ELEVENTH INTERNATIONAL CONFERENCE ON ELECTRICAL MACHINES, DRIVES AND POWER SYSTEMS

Supported by IEEE Bulgaria Section

ELMA 2005

PROCEEDINGS

VOLUME 1

15-16 September 2005
Sofia, BULGARIA

ELEVENTH INTERNATIONAL CONFERENCE ON
ELECTRICAL MACHINES, DRIVES AND POWER SYSTEMS

ELMA 2005

15 – 16 September 2005, Sofia, BULGARIA

PROCEEDINGS

VOLUME 1

Supported by IEEE Bulgaria Section

Organised by:

Union of Electronics, Electrical Engineering and Telecommunications (CEEC)
Technical University of Sofia
Technical University of Varna
Technical University of Gabrovo

ELMA 2005 – XI International Conference on Electrical Machines, Drives and Power Systems

15 – 16 September 2005, Sofia, BULGARIA

Proceedings

Printed by AVANGARD, Sofia, Bulgaria

Number of copies: 150

Printing of this edition has been financially supported by
The Technical University of Sofia

ELMA 2005
ISBN 954-902-09-5-9

These Proceedings are reviewed by members of The Steering Committee.

ELMA 2005 is sponsored by:

- SIEMENS BG
- ABB Bulgaria
- ELPROM TRAFO CH Kjustendil
- ELDOMINVEST Varna
- ELPROM Harmanli
- ELPROM – ZEM Sofia
- HYUNDAY HEAVY INDUSTRIES
- CERB Sofia
- SPARKY ELTOS Lovech
- ELMOT Veliko Tarnovo
- ABB-Avangard Sevlievo
- ZAVN Dobrich
- IEEE Bulgaria Section
- ELPROM - ILEP
- ELPROM – IEP
- ELMA Troyan
- UNITRAF Sokolovo
- DIT-M Sofia
- TROYAN MOTOR
- INOVATICS Sofia
- Rousse University “Angel Kunchev”
- ELISOT Sofia
- DENI-EN-K Sofia
- TO-NTS Varna
- EMNM – TU Sofia

STEERING COMMITTEE

INTERNATIONAL STEERING COMMITTEE MEMBERS

Viktor BESPALOV	Technical University of Moscow, Russia
Gancho BOJILOV	Technical University of Sofia, Bulgaria
Stanislaw BOLKOWSKY	SEP, Warsaw, Poland
Milan CHUNDEV	University “Sts. Cyril & Methodius”, Skopie, Macedonia
Manuel Perez DONSION	Vigo University, Spain
Gerhard DREGER	VDE – Frankfurt, Germany
Pancho DUNDAROV	CEEC, Bulgaria
Masato ENOKIZONO	Oita University, Japan
Bulent ERTAN	Middle East Technical University, Ankara, Turkey
Antonios KLADAS	National Technical University of Athens, Greece
Istvan KROMER	VEIKI RT, Hungary
Vladimir LAZAROV	Technical University of Sofia, Bulgaria
Afef LEBOUC	LEG – INPG, France
Jiŕi LETTL	CVUT – Prague, Czech Republic
Gerard MEUNIER	LEG – INPG, France
Emil MITEV	Polytechnic Radom, Poland
Gilles NOTTON	University of Corsica, France
Viktor PETROUSHIN	Odessa Polytechnic Institute, Ukraine
Michel POLOUJADOFF	University Pierre and Marie Curie, Paris, France
Ioan POPA	University of Craiova, Romania
Viktor POPOV	Technical University of St. Petersbourg, Russia
Mircea RADULESKU	Technical University of Cluj-Napoca, Romania
Saifur RAHMAN	Virginia Tech, USA
Christian SCHAEFFER	LEG –INPG, France
Wolfgang SCHROPPEL	Technical University of Chemnitz, Germany
Sergey SHIRINSKY	Technical University of Moscow, Russia
Emil SOKOLOV	Technical University of Sofia, Bulgaria
Dimitar SOTIROV	Technical University of Sofia, Bulgaria
Henryk SUPRONOWICZ	Warsaw Polytechnic, Poland
John TEGOPOULOS	National Technical University of Athens, Greece
George TODOROV	Technical University of Sofia, Bulgaria
Osami TSUKAMOTO	Yokohama National University, Japan
Christian VASSEUR	University of Lille, France
Ivan VASSILEV	CEEC, Bulgaria

CONFERENCE CHAIRMEN

Emil SOKOLOV	Technical University of Sofia
Pancho DUNDAROV	CEEC

EXECUTIVE COMMITTEE

Chairman:

Vladimir LAZAROV	Technical University of Sofia, Bulgaria

Secretariat:

George TODOROV	Technical University of Sofia, Bulgaria
Ivan VASSILEV	CEEC, Bulgaria
Yuli STAFUNSKI	Technical University of Varna, Bulgaria
Zahari ZARKOV	Technical University of Sofia, Bulgaria

Conference Internet Site: http://elma2005.tu-sofia.bg

NATIONAL ORGANIZING COMMITTEE MEMBERS

Kondyo ANDONOV	Rousse University
Rumen ATANASOV	Bulgarian Chamber of Electrical Engineering
Dimitar BAKARDJIEV	Technical University of Sofia
Dimitar DIMITROV	Technical University of Varna
Lyubomir DIMITROV	Technical University of Varna
Peter DINEFF	Technical University of Sofia
Krum GERASIMOV	Technical University of Varna
Petar GORANOV	Technical University of Sofia
Vasil GOSPODINOV	Technical University of Sofia
Nikola GRADINAROV	Technical University of Sofia
Marin HRISTOV	Technical University of Sofia
Kostadin ILIEV	Technical University of Sofia, branch Plovdiv
Todor IONKOV	Technical University of Sofia
Dimitar JETCHEV	Technical University of Sofia
Maria KANEVA	Technical University of Sofia
Milka KONSULOVA	Technical University of Gabrovo
Sava KONTROV	Technical University of Varna
Anastasia KRASTEVA	Technical University of Sofia
Rumen KUNCHEV	Technical University of Sofia
Iliana MARINOVA	Technical University of Sofia
Deshka MARKOVA	Technical University of Gabrovo
Nikolai MICHAILOV	Rousse University
Miho MIHOV	Technical University of Sofia
Mincho MINCHEV	Technical University of Sofia
Petar NAKOV	Technical University of Sofia
Petko NOTOV	Technical University of Sofia
Angel PACHAMANOV	Technical University of Sofia
Lazar PETKANCHIN	Technical University of Sofia
Vasil PIPEROV	Technical University of Sofia
Emil RATZ	Technical University of Sofia
Georgi RASHKOV	Rousse University
Plamen RIZOV	Technical University of Sofia
Nikola SHOYLEV	University of Chemical Technology and Metallurgy, Sofia
Yuli STAFUNSKI	Technical University of Varna
Rumiana STANCHEVA	Technical University of Sofia
Stefan TABAKOV	Technical University of Sofia
Raina TZENEVA	Technical University of Sofia
Hristo VASSILEV	Technical University of Sofia
Pencho VENKOV	Technical University of Sofia
Pencho VLADIMIROV	Technical University of Gabrovo
Ivan YATCHEV	Technical University of Sofia
Kiril ZAHARINOV	Technical University of Sofia

TABLE OF CONTENTS

Volume 1

INVITED PAPERS

ELECTRICAL MACHINES I

POWER SYSTEMS AND DISTRIBUTION SYSTEMS I

ELECTRICAL DRIVES

TECHNOLOGIES, NEW MATERIALS AND COMPONENTS I

ELECTRICAL MACHINES II

ELECTRICAL MACHINES III

Volume 2

GENERAL PROBLEMS IN ELECTRICAL ENGINEERING

TECHNOLOGIES, NEW MATERIALS AND COMPONENTS II

ENERGY GENERATION AND DISTRIBUTION

ELECTRONICS

ELECTRICAL MACHINES IV

POWER SYSTEMS AND DISTRIBUTION SYSTEMS II

TECHNOLOGIES, NEW MATERIALS AND COMPONENTS III

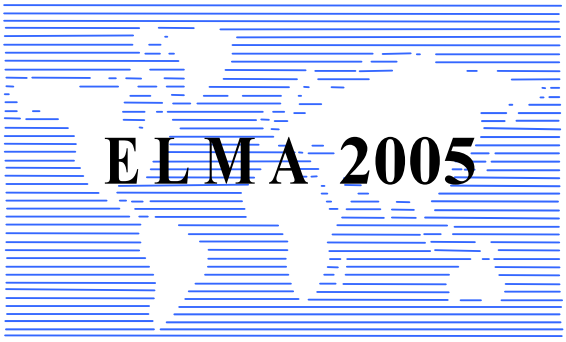

INVITED PAPERS

Energy Strategies in a Liberalised Electricity Industry

István Krómer

Abstract: *National energy strategy is a major concern because our future energy framework will be a major determinant of society's structure and life-style, as it is now. In this paper I explore the obstacles to energy strategic planning and implementation created by the society's conflicting targets for energy supply, economic growth and environment. There are economic, social, environmental and political interventions that harass any long term energy project. The approach outlined in the paper uses a forward – backward analysis to account for the threats and problems inherent in the emerging scenarios.*
Keywords*: Energy strategy, Multicriteria analysis*

Introduction

A number of major energy-related challenges face the world as it moves to the 21 st century. Dependence of hydrocarbons is growing increasing the vulnerability to supply disruptions and price spikes. Electricity outages threaten the rapidly growing information technology based service industry. Despite ongoing improvements in air quality, air pollution from burning hydrocarbons continues to grow, global climate change threatens to impose significant long-term costs and more extreme weather.

The prosperity and well being of future generation will be strongly affected by the manner in which the nations respond to these challenges. This paper aims to present a multicriteria approach modelling the abundant and conflicting factors influencing the success of energy strategies.

Recent changes in the electricity industry

Worldwide the electricity industry is undergoing a substantial process of restructuring, with an emphasis on introduction of competition in the generation sector.

There are other factors also forcing the electricity industry to change. These factors have included low natural gas prices (prior to 2000), substantial improvement in the efficiency of gas-fired combustion turbines and combined cycle systems, heightened public interest and concern for the environment and its protection.

The restructuring of the electricity industry and the recent catastrophic disturbances have fed concerns of the general public, legislators and governments regarding the reliability of their electricity supply. We inherited a robust and reliable electricity system from the regulated industry. After the reregulation of the electricity, the institutional structure, utility cost control and the customer relationship went through dramatic changes.

Some examples:

- Due to the unbundling, the roles were separated and the number of players increased
- The generating companies became market oriented
- The investment in new technologies must result increased profit even in short run.

Electricity market seems to be able to attract investment in generation capacity. The prices are the key drives of investment activity. However, it is not easy to implement market reform to ensure reliable outcome. The debate continues whether market price signals are strong enough to stimulate continuous, timely and well balanced investments or boom and bust cycles or unbalanced ambitions can occur.

Strategic planning hierarchy

Electricity planning is subject to a large degree of uncertainty, due, among others, to aspects like: economic growth, cost and availability of fuels and technologies, environmental regulation, public opinion etc.

The probalistic analysis can be considered as a suitable way for handling uncertainties. However, it is really difficult to assign probabilities any of the different events considered. Instead of relying on predictions of probabilities, we can use scenarios based on a multicriteria analysis. Scenarios help the decision makers to understand the role of uncertainties and allow them for preparing more informed decision by revealing strategic threats and new opportunities.

This report was intended to present a multicriteria approach modelling the abundant and conflicting factors influencing the success of energy strategies. A forward-backward planning process is used.

Forward process

The forward process is a description of the traditional scenario making determined by the actors who pursue their objectives, policies and individual ideas.

The backward process is used as a prescriptive mechanism to determine which policies the actors will pursue to attain their desired outcome.

Finally the second forward process tests the implementation of the strategies.

The first forward process provides a mapping of the environment in which the energy strategies are proposed (Fig. 1).
The first three levels in the decision hierarchy contain the focus, the major actors and their most important objectives. The focus is a sustainable energy future. Delivering sustainability has become a general priority of the energy strategies. The 2004 World Energy Congress drew the conclusion that sustainable energy systems are achievable, but the challenges are numerous and need to be buckled if sustainability is to be achieved in this century.

If a party (i.e. regulatory agency or a branch of government) facing a problem of public interest, a broad range of stakeholder groups should be involved. From this broad range we selected four different player groups: investors, regulators, system operators and public interest groups for the given analysis.
In order to asses how well potential scenarios fulfil the actors' objectives we selected five objective categories: economy, reliability of supply, health and environment, societal aspects and technology development.
The economic objectives include the economic feasibility and competitiveness of new power plants on a liberalized power market.
Reliability objectives must consider both adequacy and security that is both long term system expansion planning and short-term operational concerns. Adequacy and security are both complements and substitutes. Most regulators want to hold reliability performance constant at pre-regulatory level or even improve reliability performance. They are concerned about the apparent luck of investment in generation. On the other hand, to maintain the supply security is a major challenge to the system operators.
Health and environmental objectives include the human health effects, the global climate change concerns and waste management issues. Overstretched environmental and sustainability ambitions can jeopardize the reliability of energy supply.
The societal objectives were extended to employment, risk aversion and terror threats.

The introduction of the decision-makers preferences in the process is fundamental since it reflects their attitude toward different risks considered.

The fourth level of the forward process outlines the fuel mix-technology scenarios may be available for generation for the time horizon considered. We have to maintain a diversified generation mix to mitigate risks that is to keep open all the options for a diversified and sustainable primary energy structure.
World Energy Council envisages that the global energy mix will show great diversity (coal, oil, gas, nuclear, hydro, wind, solar etc.) and none of this sources is expected to have more than a 30 % share of the market.

The actual contribution of different fuels/technologies may vary according to the weight of different actors and their priorities.

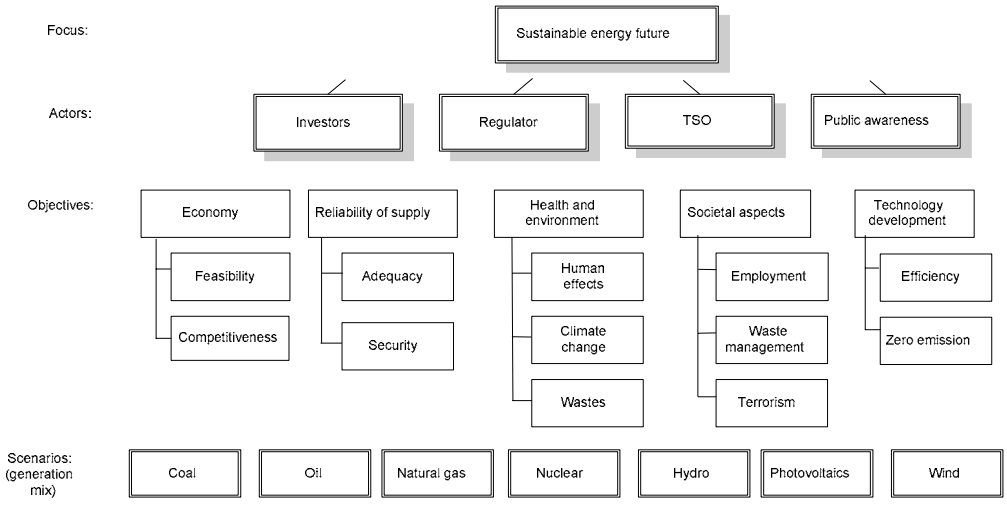

Figure 1: Planning hierarchy: forward process I.

The set of objectives used to evaluate the alternatives in public decision problems is the foundation on which the analysis rests. Various weighting schemes have been used on the level of main objectives. If equal weights are applied (balanced case) the combined cycle natural gas is the top performer fuel-technology options (Fig. 2), but in the emission control focused case nuclear energy ranks clearly better than gas (Fig. 3). It is clearly seen that in both cases all fuel-technology options are represented by an important share. Coal and oil are in relative terms generally at the low end while natural gas having a quite stable position. The multicriteria ranking provides relatively robust scenarios.

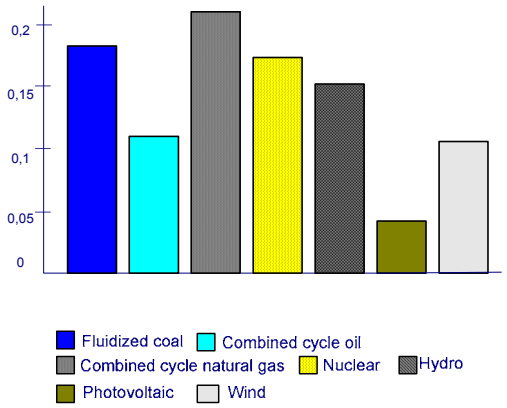

Figure 2: Balanced objectives generation mix

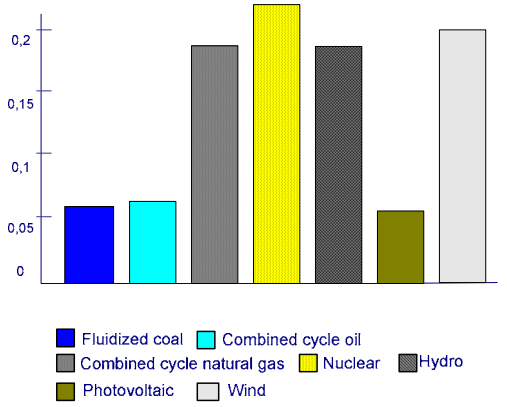

Figure 3: Emission control

Backward process

The focus of the backward process (Fig. 4) is the desired future and we explore the policies the actors will pursue to attain it. In recent years a number of uncertainty analysis proceed in the opposite direction of the traditional way of defining strategy options. Starting with available scenarios they assess and compare uncertainties associated with these scenarios.

Thus the second level contains the projected scenarios which are two of the probable outcomes from the forward process in our analysis. The third level includes the problems encountered in implementing the proposed strategic scenarios.

The move toward competition results in higher than normal uncertainty about the shape of reform and future market operations. Such a risk may delay or make more costly the financing of the investment. Regulatory risk encompasses two different type of uncertainty. Namely risk at the time of reform is announced and carried out and the ongoing risk of unpredictable regulatory interventions. Regulatory risk at the time of reform largely depends on the scope of reform. The ongoing regulatory risk relates to a lack of clarity about the objectives and future direction of regulation and energy policy. Increasing regulatory discretion and regulatory involvement will increase ongoing regulatory risk.

Another critical factor that is external to the generation industry is the availability and price of fuels. A comparison of the annual consumptions volume with reserves reveals that current primary energy consumption is in inverse ratio to the reserve situation. Today, consumption of energy sources with the lowest reserve levels is the highest. An extension of the natural gas fueled power generation would aggravate the already unbalanced reserve consumption ratio.

Tradable emission permits are increasingly regarded as a versatile instrument of the environmental regulation. Beside the benefits of the introduction of emission trading there are several drawbacks: companies with growth ambitions will be crippled in their development by emission limits, or companies having reached high energy efficiency standards must incur higher specific reduction costs than those still having high emission levels.

The transmission to a more competitive environment in the electricity industry has resulted in dramatic decline in the level of R and D funding in both the public and private sector throughout the industrial world and a shift in the focus towards achieving short-term results.

In democratic societies, decision-making process has increasingly involved the public as legitimate partners often creating a risk that the communication would be driven by non experts. In addition, the implementation of the right-to-know principle now introduced in many national and international laws and regulations has meant that many assessment procedures now include public participation.

The fourth level contains the most influential actors in terms of ability to implement the energy

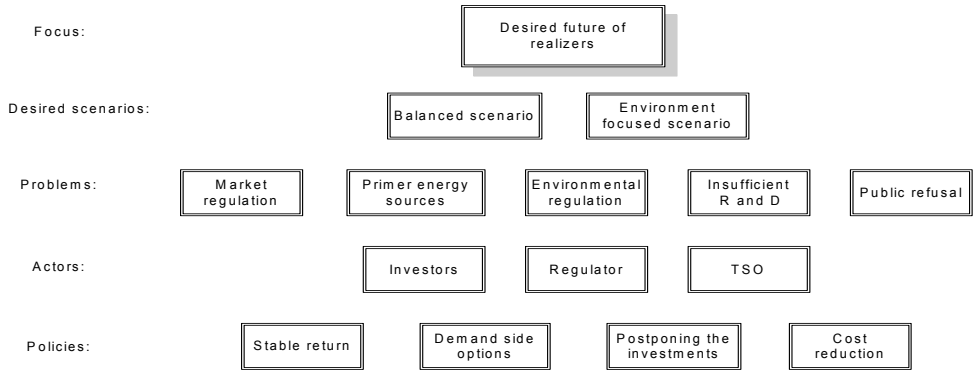

Figure 4. Planning hierarchy: backward process

strategies. The fifth level of the backward process represents its basic reason, it contains the policies serving the interests of the major players. They include pursuit of stable return, demand side response, postponing investments, cost cutting. While the others are self consistent, the demand side options need an explanation.

The costumer demand side participation is considered an efficient market tool which significantly reduces uncertainty of medium and long term electricity capacity margin sufficiency and enhance overall system reliability. Major efforts are undertaken to deliver the necessary methodology, business process, infrastructure, implementation plans for the rapid deployment of demand response into electricity markets.

Second forward process

In the second forward process the actors are the same as in the backward process. The objectives of the major players to pursuit the desired future are cleared up by the help of the backward process. The focus of this exercise can be considered as a customized strategy since the second forward process tests the implementation of the policies suggested in the backward process.

The result show by way of example that nuclear and coal options are not exactly pretenders to the throne. The increase of the renewable source is not very spectacular apart from wind power. The liberalisation of energy markets increases the amounts of cross border trading of electricity. The initial role of interconnections (supplying emergency electricity) changed radically with the start of market opening and some of the interconnections were becoming heavily congested.

Due to the uncertain investment climate and lower costs, the refurbishment of existing plants is more attractive than building new plants. The same trend applies to conventional and nuclear power plants. However, under competitive pressure only the most efficient plants are likely to survive. Power plant manufacturers and operators have always been striving for increasing the efficiency of the power plants. The average efficiency of power plants presently ranges world wide about 30 %, meanwhile the available technologies permit efficiencies between 45 and 58 % depending the fuel used. The efficiency increases are not restricted for new power plant construction, but successful retrofitting of existing plans by optimized plant components is common practice. With optimised procedures and advanced IT a higher flexibility of plants can be achieved

The cost of electricity from utility scale wind system has dropped by more than 80 % over the last 20 years. Costs are continuing to decline as more and larger plants are built and advanced technology is introduced. While wind generation is fast proving to be a valuable option in combating greenhouse effects, the reality is that actual energy production will always deviate from scheduled production and the cost of balancing wind power can be significant. Due to the lack of controllability in its output, wind power is not considered a viable source of generation flexibility.

Transforming today's centralised power system into something closer to a smart, distributed network to provide a reliable power supply and to make possible innovative new energy services may seem like a return to electricity's roots over a century ago. The emergence of micro grids made up of all sorts of distributed generators including fuel cells, wind and solar power is apparent. Onsite generation and distributed power generation can help to resolve a large number of power issues, however, a complete return to that model would be inexpedient.

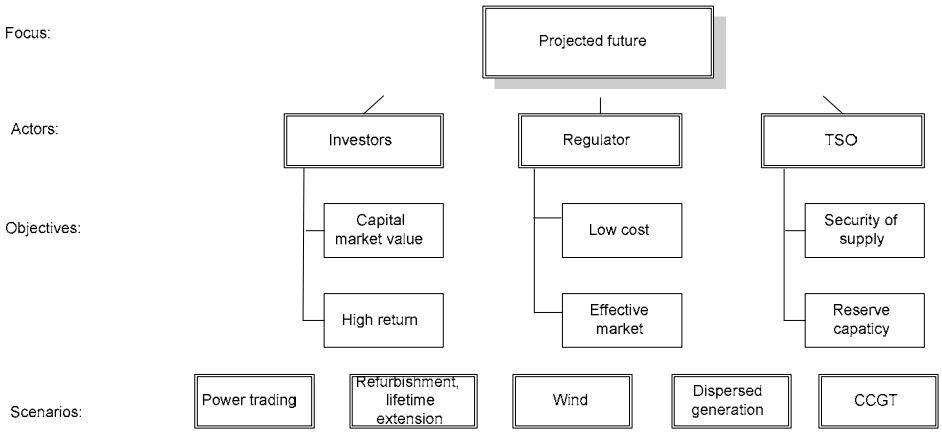

Figure 5. Planning hierarchy: forward process II.

The current market preference for gas-fired power generation for base load power plants can be explained by the perceived lower cost of gas-fired generation. The characteristics of the combined cycle gas turbine, its low capital cost and its flexibility have also added to its attractiveness. These investment trends result in an increase of the gas-fired capacity mostly at the expense of oil-fired capacity. However, the operational flexibility of gas-fired generators is constrained by the limitations on offtake arrangements with the gas network.

Conclusions

The key findings of this study show that the emerging generation mix that differs considerable from the robust fuel-mix/technology options with greater reliance on gas-fired and dispersed generation can be expected to increase the vulnerability of power systems. Without significant advances in demand side behaviour, load following requirements on generation will continue to increase.

To ensure an adequate framework for the development of future electricity production we need an efficient regulatory environment and market operation, realistic climate and environmental goals, efficiency driven support of new technologies and a diversified generation structure.

István Krómer *– Professor, DSc.*
Institute for Electric Power Research, H-1251 Budapest P. O. Box 80 Hungary, E-mail: i.kromer@veiki.hu

R&D Status of HTS Power Applications in Japan

Osami Tsukamoto

Abstract: *Application of superconductor, especially high temperature superconductor (HTS), can be effective solutions of recently emerging difficulties in electric power utilities by improving efficiency and compactness, increasing power density, breaking capacity limits of electric power devices and creating new functional devices. Therefore, presently many countries in the world are conducting R&D projects of HTS power apparatuses vigorously. In the paper, R&D status of HTS power applications including LTS ones in Japan is reviewed.*

Keywords: *HTS, Power application, YBCO, Power cable, SMES*

Introduction

The following critical issues on electric power system are emerging in recent information technology and environment conscious society.

- Highly dense electricity demands in metropolitan area and vastly expanding demands for communication capacity.
- High cost of land in metropolitan area.
- Needs for long distance bulk power transmission and inter-connection of power systems, especially in Japan.
- Keen demands for high quality and reliable electricity.
- Steady increase of renewable power systems introduced to the power grid causing instability of the grid.
- Deregulation / market place for electricity.
- Environmental issues / saving energy, high efficiency.
- NIMBY (Not In My Back Yard)
  BANANA (Build Absolutely Nothing Anywhere NeAr)

There is a strong fear due to those issues that difficulties occur in the near future to maintain the stable and reliable operation of the power system. Those difficulties might occur in many countries in the world.

Application of superconductor, especially high temperature superconductor (HTS), can be effective solutions of those difficulties by improving efficiency and compactness, increasing power density, breaking capacity limits of electric power devices and creating new functional devices. Therefore, presently many countries in the world, USA, Japan, Korea, China and countries in EU are conducting R&D projects of HTS power apparatuses vigorously. Electric power companies in Japan are expecting to solve their problems by applications of superconductivity and are involved in the R&D activities on superconducting devices as active players. In USA, Office of Electric Transmission and Distribution Department of Energy published in 2003 a report "Grid 2030" which reported on future delivery system of electricity. The report says the followings. HTS have the potential to revolutionize electric power delivery. The prospect of transmitting large amounts of power through compact underground corridors, even over long distances, with minimal electrical losses and voltage drop, could significantly enhance the overall energy efficiency and reliability of the electric system, while reducing fuel use, air emissions, and physical footprint.

Key Superconducting power apparatuses are;

- Power cables
- Transformers
- Fault current limiters
- Flywheel energy storage system
- SMES
- Generators.

In this back ground NEDO (New Energy and Industrial Technology Development Organization) have conducted and are conducting five, in total, national R&D projects related to superconducting power apparatuses including a project of fundamental material technology developments with firm supports from the electric power companies. There are also in-house R&D activities conducted by private sectors.

National projects conducted by NEDO

Out of five NEDO projects, four for superconductor power applications and one for fundamental material technology development for HTS applications. Presently, 3 out of the 5 projects have been finished successfully and two are on going. One project will be restarted in 2005JFY. Terms of the five projects are shown in Fig.1. Japanese fiscal year is from April to March of the next year.

Fundamental material technology developments for HTS applications

The first phase of this project was established in 1998 JFY to develop technologies for high critical current density (J_c) coated conductors, bulk materials and electronic devices and the first two technologies are related to power applications. Coated conductors such as YBCO conductors have higher J_c in high magnetic field than Bi/Ag sheathed wires at 77K but technology to make long conductors is to be developed. The second phase of this project was established in 2002JFY to develop YBCO and REBCO coated conductors of long length and high current for power applications. The term of phase II project is 5 years. Targets of the phase II project are summarized in Table.1. In the end of the project

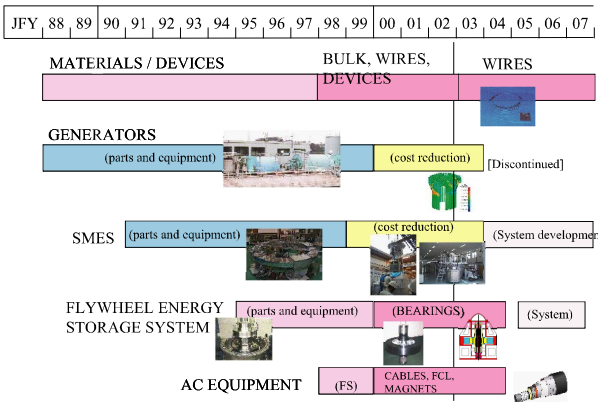

Fig.1. R&Ds projects conducted by NEDO (JFY : Japanese fiscal year is from April to March in next year)

Table 1

Goals for the phase II project of coated conductors

Specifications	Interim Targets (2005)		Final Targets (2007)	
	High Performance Type	Low Cost Type	High Performance Type	Low Cost Type
Length (m)	200m		500m	
I_c	Ic=200A/cm-w (@77K,0T)		Ic=300A/cm-w (@77K,0T)	
	Ic=20A/cm-w (@77K,3T)	----------	Ic=30A/cm-w (@77K,3T)	----------
Production Rate	----------		5m/h	
Cost	Selection of Promising Process for the Target of Low Cost		$100/kAm (@77K,0T)	$70 /kAm (@77K,0T)

processes will be developed to fabricate practical coated conductors in power applications even from the stand point of cost. Interim review is to be held in 2005JFY. Recent achievements are explained in reference [1] and listed in Table 2. At the present, YBCO conductors of 90m length with critical current I_c =210A and of 200m length with I_c =88A have been developed and the interim target of 200m length and I_c =200A is expected to be fulfilled.

Table 2

Present status of Ic·L competition in the world

	Ic L	Affiliation	Ic(A)	L(m)	Process
1st	15900	SRL-ISTEC	159	100	YBCO(PLD)/CeO2(PLD) /GZO(IBAD)/Hatelloy
2nd	13230	Fujikura	126	100	YBCO(PLD)/CeO2(PLD) /GZO(IBAD)/Hatelloy
3rd	(12870)	Sumitomo	110 (Ic min.)	117	HoBCO(PLD)/CeO2(PLD) /GZO(IBAD)/Hatelloy
4th	10050	IGC	104	97	YBCO(MOCVD)/STO/MgO(Cap)/MgO(IBAD)/Y2O3/Al2O3/Hatelloy
5th	8550	Chubu Electric Power Company	95	90	YBCO(MOCVD)/CeO2(PLD) /GZO(IBAD)/Hatelloy
6th	7000	IGC	100	70	YBCO(PLD)/STO/MgO(Cap)/ MgO(IBAD)/Y2O3/Al2O3/Hatelloy
7th	6374	AMSC	186	34	YBCO(TFA-MOD)/CeO2/ YSZ/Y2O3/Ni-W
8th	1440	SRL-ISTEC	90	16	YBCO(TFA-MOD)/CeO2(PLD) /GZO(IBAD)/Hatelloy

R&D fundamental technology for superconducting generators -Super GM / Phase II-

In the previous Super GM project, a 70MW model superconducting generator with LTS (Low temperature superconductor) field windings and copper armature windings was successfully developed (Fig.2) and tested [2], and the technical feasibility of a superconducting generator has been demonstrated. However, it has turned out to be clear that a superconducting generator made on the technical basis of the model superconducting generator developed in the previous project was not cost competitive to a conventional one. Therefore, it was planed in the phase II of the Super GM project to develop technology for the cost reduction. R&D of fundamental

Fig.2. 70MW superconducting generator developed by the Super GM project (Phase I) at the test site. The generator (left side) was driven by a synchronous motor (right side).

technology for scaling up to 600MVA class machines is also included in the project because one of the most promising applications of superconducting generators was a 600MW class for the combined cycle. Technology to reduce the cost was developed by 50% increasing the output power density. Techniques were developed to increase the current densities of both of the superconducting field windings and copper armature windings by 30% and demonstrated by making model coils of both of the field and armature windings. A rotor using HTS was investigated but significant merits to use HTS were not found for a large scale superconducting generator. This project was finished in 2003.

R&D superconducting magnetic bearing for flywheel energy storage

In the project elementary technology for a radial type superconducting bearing for a 100kWh class flywheel energy storage (FWES) has been developed and the magnetic bearing system combining superconducting bulk magnetic bearings (SMB) and active control magnetic bearing (AMB) has been verified by making a 10kWh class test model of FWES (Figs.3 and 4). This model achieved stable operation of the rotor at 11,250rpm corresponding 5kWh energy storage.

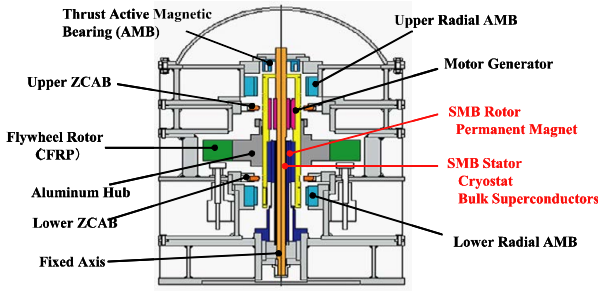

Rating Rotation Speed		15,860 rpm	*SMB*	*Levitation Force Density*	0.36 kg/ cm²
Stored Energy		10 kWh class		*Type*	Radial
Flywheel	*Rotor Weight*	425 kg	*AMB*	*Thrust*	PID Control
	Diameter	1,000 mm		*Radial*	Zero Power Control
	Rotation Inertia	2.61x10⁵ kg·cm²	*Vacuum Degree*		1.0x10³ Torr
Motor Generator Capacity		15 kW	*Hight of the Vacuum Chamber*		2,513 mm

Fig.3. 10kwh class flywheel energy storage test system

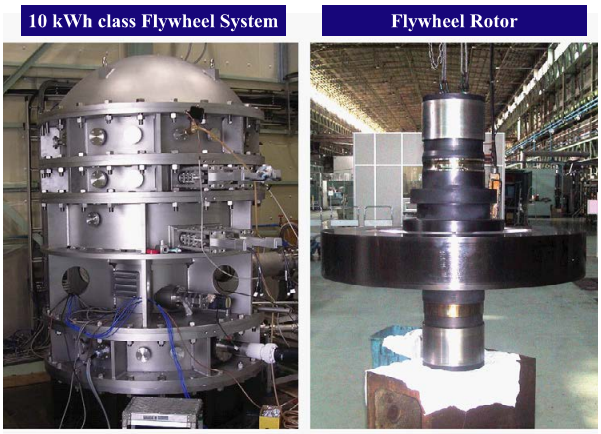

[*Ishikawajima-Harima Heavy Industries Co., Ltd.*]

Fig.4. Views of 10kWh class flywheel system and flywheel rotor

R&D of fundamental technologies for superconducting AC power equipments

This project is called Super ACE (ACE stands for AC Equipment). In the Super ACE project, the following R&Ds have been performed;

a) Superconducting power cable,
b) Thin film super to normal transition type current limiter,
c) HTS magnet technology for a transformer and a reactor of a rectifier type current limiter,

i) Superconducting power cable

To realize a practical power cable with large current capacity and low AC losses, it is necessary to develop techniques to assemble elemental HTS tape wires into a cable homogenizing current distribution among the wires together with techniques to reduce AC losses in the wires. Development of efficient cooling system for a long cable is also necessary. In this project, a 500m long single phase HTS cable was developed [3] and tested in a layout with various sections including 10m up and down section simulating installation on a bridge over a river and an underground section (Fig.5). A configuration and specifications of the cable is shown in Fig.6. The performances of the 500m cable were demonstrated in the test. A short circuit test was performed using 10m long piece of the cable and it was shown that the cable survived 315kA/0.5s duration test with no damages and after the test the cable recovered the superconducting state. A low AC loss cable of short length was also developed and achieved 1W/m loss at 3000Arms and 60Hz.

ii) Thin film current limiter

A super to normal transition type fault current limiter (a resistive type FCL) using thin film HTS is simple and compact and, therefore, most promising. In the project the following R&Ds were performed to develop the fundamental technology for the resistive type FCL.

a) R&D of a high voltage (6.6kV) FCL by series connection of the thin film elements.
b) R&D of a large current FCL (1kA) by parallel connections of the thin film elements.

HTS conductors for FCL should be highly resistive in

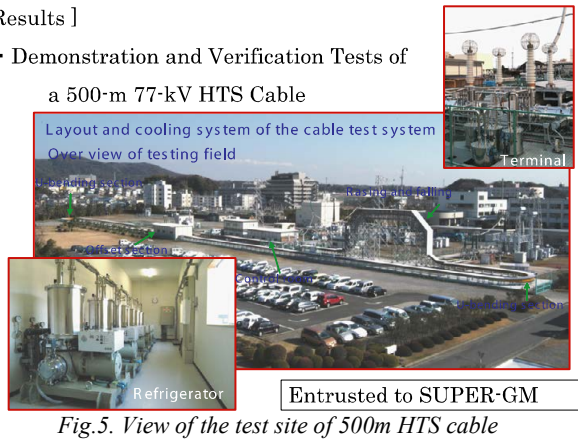

Fig.5. View of the test site of 500m HTS cable

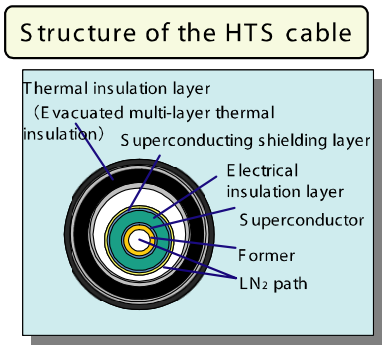

Item	Configuration		O.D. (approx. mm)
Conductor	Former	SUS spiral tube Hollow Cu stranded conductor (250mm^2)	28
	Superconductor	Ag sheathed Bi2223 tape (0.25 mm^t ×4 mm^w)	30
Electrical insulation layer	Electrical Insulation (Insulation thickness: 8 mm)	Polypropylene laminated paper	48
Shielding layer	Superconducting shielding layer	Ag sheathed Bi2223 tape (0.25 mmt ×4 mmw)	58
Thermal insulation layer and tubes	Inner tube	SUS	92
	Vacuum thermal insulation layer	Evacuated multi-layer thermal insulation	—
	Outer tube	SUS	124
	Oversheath	PVC	133

Fig.6. Configuration and specifications of the 500m HTS cable

the normal state and thin film HTS conductors have appropriate properties for FCS. However, when a thin film conductor is quenched by over current a quench is initiated at a local spot where the conductor is heated locally and a hot-spot appears. That hot-spot gives damages to the conductor. Therefore, a key to develop a thin film FCL is to solve the hot-spot problem. A good solution for the hot-spot problem was invented. Indium thermal shunts are attached to the thin film YBCO to conduct heat and the current at a quenched spot to the nickel substrate on which YBCO layer is deposited. It was demonstrated that a FCL unit in which 40 of the current limiting elements of this configuration were connected in series limited a short circuit current by withstanding 11.9kV (Fig.7) [4]. Investigations were also conducted to control currents in the current limiter elements to be uniform in the parallel connections. A 1kA module was developed (Fig.8) and tested successfully. Combining those techniques the technology to realize a 6.6kV/1kA resistive type FCL has been developed.

iii) HTS magnet technology

Technologies for two kinds of magnets, AC magnets for transformers and pulse magnets for reactors of rectifier type FCL, were developed.

To develop technology for AC magnets for a 66~77kV/10MVA transformer, the followings are performed;

- Development of 66~77kV current leads/bushings,
- Development of assembled conductors with transpositions,
- Development of cooling system (Combination of a GM refrigerator and circulation pump).

Based on those developments, a model single phase transformer, 66kV/6.9V-10MVA was developed and tested successfully to verify the technology developed (Fig.9).

To develop technology for pulse magnets for the reactors of a rectifier type FCL, thermal and electric behaviors of a pulse magnet were studied by making model coils and techniques of electric insulation system were developed. Based on these studies a 66kV/100A class reactor type FCL was developed (Fig.10) and tested

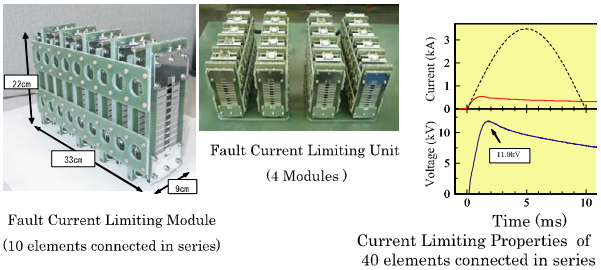

Fig.7. High voltage resistive type FCL with 40 of current limiting elements and test result

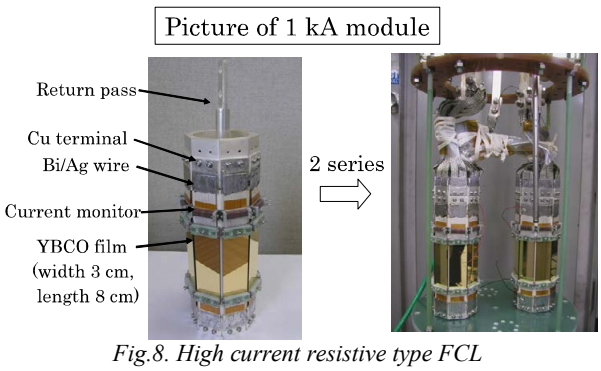

Fig.8. High current resistive type FCL

Single phase model transformer

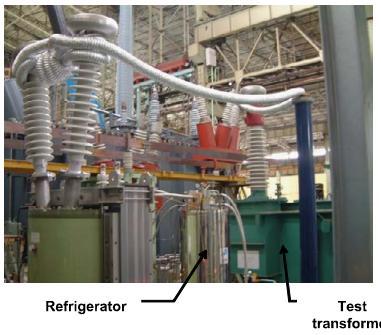

Withstanding voltage test

Fig.9. Views of 66kV/6.9kV-10MVA single phase HTS model transformer

successfully.

R&D of SMES

In the previous SMES project (Phase I: 1991FY-1998FY), technical feasibility of a small scale LTS SMES was demonstrated. However, it was pointed out that cost should be reduced to about one tenth of the cost projected in the study of the phase I for a small scale SMES to be cost competitive to other alternative devices. Based on this result, the phase II project was planned in 1999 to develop cost reduction technology for LTS SMES. Technical feasibility study of HTS SMES was also included in the phase II project. The objectives of the LHS SMES project were to realize cost competitive LTS 100MW/15kWh SMES for power system stabilization and 100MW/500kWh SMES for compensation of load fluctuations and frequency control. Cost reduction technology was studied from both sides of conductors and coil configurations. The cost assessment resulted in that aluminum stabilized NbTi cable in conduit conductor (CICC) and externally copper stabilized NbTi CICC were suitable for the SMES for the power system stabilization and that for load fluctuation compensation, respectively, and that the multi-pole solenoid arrangement was suitable for both applications (Fig.11). To verify the technology a model solenoid coil of stored energy 2.9 MJ and a multi-pole magnet consisting of 4 solenoid coils were constructed for the system stabilization and load fluctuation compensation

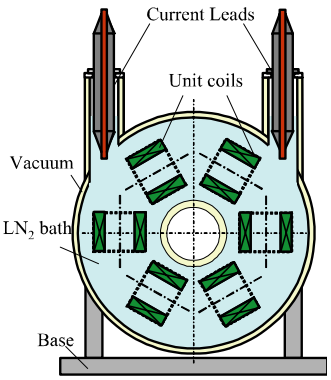

Fig.10. View and configuration of reactor magnet of 66kV/750A HTS FCL

SMESs, respectively (Fig.12) [5], and tested successfully. 10,000 times charging and discharging operations of the model magnet for load fluctuation compensation were conducted and durability for repeated operations of SMES was demonstrated.

Based on those R&D results a new NEDO project on SMES (phase III) has been started in 2004 as a 4 year project. Purpose of this project is to develop proto-type 10MW/20MJ LTS SMES for electric power system stabilization. More cost reductions of the power conditioner and superconducting magnets are pursued. R&Ds of highly reliable refrigeration system and HTS coils are also included in the project. The developed SMES will be tested being connected to a utility power grid to demonstrate merits of the SMES in a real power grid.

In-house R&D activities conducted by private sector

Some of major electric power companies in Japan have conducted and are conducting their own in-house projects for superconductor power applications. Major activities are as follows.

Tokyo Electric Power Company (TEPCO), the largest electric company in Japan is covering Tokyo metropolitan area where the density of the demand is very high and the demand itself is still growing. To cope with this situation TEPCO was interested in superconducting power cables which are for replacements of conventional power cables placed in tunnels. They developed and

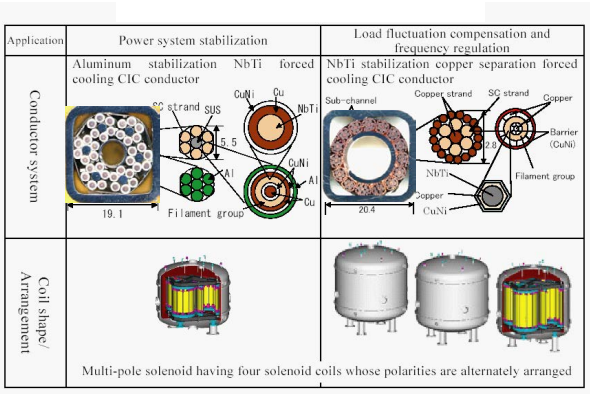

Fig.11. Configurations of conductors and coil arrangements for SMES

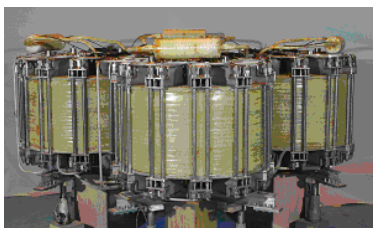

Four Pole 10MJ NbTi Coil Superconducting Model Coil

Thermal Shied for 80K

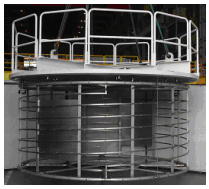

Fig.12. 500kWh SMES for fluctuating load compensation and frequency control

successfully tested in 2003 with Sumitomo Electric Industries, Ltd. 100m long 66kV/1kA 3ϕ cable which could fit to the conduits for conventional power cables (Fig.13) [6].

Chubu electric company is also interested in R&Ds of SMES and LTS FWES. They developed a 5MW/ 5MJ LTS SMES and are conducting a field test introducing the SMES for the power quality improvement to a factory of large size liquid crystal displays (LCD) for color TVs. In this factory, one voltage sag of ~ 0.1sec may cause a damage coasted $5M and it was demonstrated that the SMES compensated voltage sags caused by multiple-lightenings and saved productions from the damages. Pod motors with HTS field windings/Copper wire armature windings and also all HTS windings are being developed Ishikawajima Harima Heavy for ship propulsion motors (Fig.14). There are other in-house projects on superconducting FCL, transformers, HTS ship propulsion mortars etc. These private R&D activities significantly contribute to the National projects and vise-virsa.

Concluding remarks

Engineering feasibilities of LTS power apparatuses, generators and small scale SMES, were demonstrated and the R&D stage has shifted to demonstration of economic feasibility. After the on-going R&D projects it is expected that pilot models are developed and that LTS power apparatuses will be introduced to the real power system. Technical feasibility of HTS applications, power cable, FCL, flywheel energy storage and transformers were demonstrated by the ongoing R&D projects and it is expected that after R&Ds of pilot models, HTS power apparatuses also start to be introduced to real power systems in the near future. Keys for the HTS power applications including industrial ones to come into the real world are reduction of HTS wire cost and development of reliable, efficient and low cost refrigerators. Many efforts are paid to the cost reduction of the wires but less effort have been paid to the development of the refrigerators. Now is the time to put more effort to develop the refrigerators suitable for HTS apparatuses.

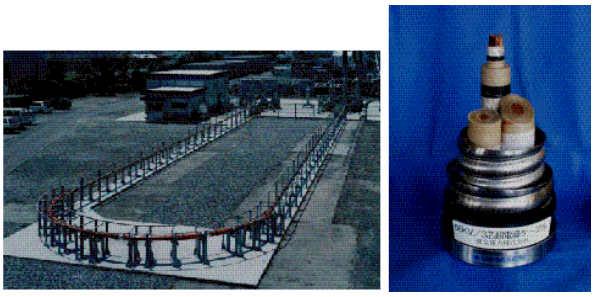

Fig.13. 100m long 66kV/1kA 3ϕ HTS cable (TEPCO/SUMITOMO)

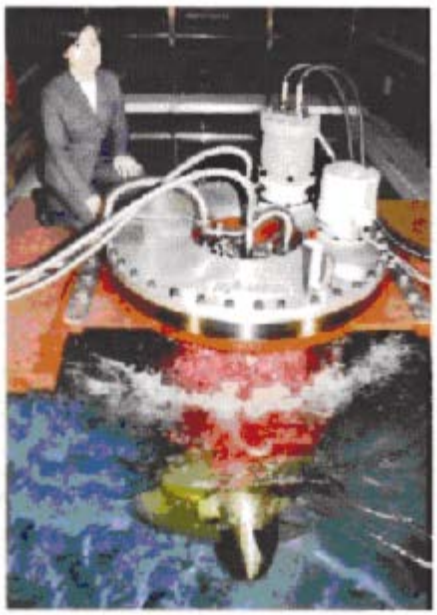

Fig.14. HTS pod-motor propeller tested in water (HTS field winding/Cu armature windings)

References

[1] Y. Iijima, K. Kakimoto, Y. Sutoh, S. Ajimura, and T. Saitoh, "Development of Long Y-123 Coated Conductors for Coil-Applications by IBAD/PLD Method", *IEEE Trans. on Applied Superconductivity*, Vol. 15, No. 2, pp. 2590-2595, 2005

[2] K.Yamaguchi, M.Takahashi, R.Shiobara, T.Taniguchi, H.Tomeoka, M.Sato, H.Sato, Y.Chida, M.Ogihara, R.Takahashi, H.Kusafuka, "70MW Class Superconducting Generator Test", *IEEE Trans. On Applied Superconductivity*, Vol.9, No.2, pp. 1209-1212, 1999

[3] K. Ueda, O. Tsukamoto, S. Nagaya, H. Kimura, and S. Akita, "R&D of a 500m Superconducting Cable in Japan", *IEEE Trans. on Applied Superconductivity*, Vol. 13, No. 2, pp. 1946-1951, 2003

[4] S. Torii, H. Kameda, T. Kumano, H. Sakaki, H. Kubota, and K. Yasuda, "Operation Tests for SN Transition Superconducting Fault Current Limiter in the Power System Simulator", *IEEE Trans. on Applied Superconductivity*, Vol. 15, No. 2, pp. 2134-2137, 2005

[5] H. Ohsaki, S. Taniguchi, S. Nagaya, S. Akita, S. Koso, M. Tatsuta, "Development of SMES for power system control: present status and perspective", *Physica C 412-414*, pp. 1198-1205, 2004

[6] S. Honjo, M. Shimodate, Y. Takahashi, T. Masuda, H. Yumura, C. Suzawa, S. Isojima, and H. Suzuki, "Electric Properties of a 66kV 3-Core Superconducting Power Cable System", *IEEE Trans. on Applied Superconductivity*, Vol. 13, No. 2, pp. 1952-1955, 2003

Osami Tsukamoto – *Professor, Dr., Faculty of engineering Yokohama National University, 79-5 Tokiwadai, Hodogaya-ku, Yokohama, JAPAN.*
e-mail: osami@tsukalab.dnj.ynu.ac.jp

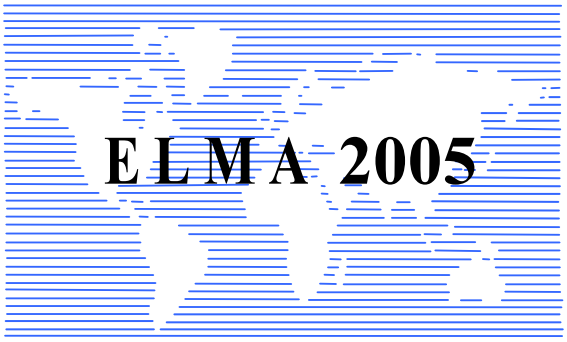

ELECTRICAL MACHINES I

The Nonlinear Model of a Switched Reluctance Motor

Eleonora Darie, Emanuel Darie

Abstract: *In this work on present the simple nonlinear model of the switched reluctance motor (SRM), it can include all the important effects inherent to the SRM. As input, the model requires the main motor geometry, number of turns, some characteristics of the used magnetic material, and only one precalculated or measured magnetization point.*

Keywords: *modeling, reluctance motor, electrical drive.*

Introduction

The SRM has very simple, cost effective construction, but determining its performances is difficult because of highly nonlinear relation between the torque and the excitation current. The nonlinearity is greatly affected by intense saturation of the corners of partially overlapping stator and rotor poles. The energy conversion principles show that accurate calculation of produced torque may be obtained from the relations between the phase current (i), flux-linkage (Ψ) and regular rotor position (θ). Therefore, most of the existing SRM models are based on previously provided magnetization curves (Ψ-i) for a number of rotor position angles [2]-[4]. These magnetization characteristics can be obtained from measurements on existing motor or from sufficiently precise numerical calculations such as finite element analysis [1], [5] or some other method. The performance of SRM drive strongly depends on applied control. The drive system comprising signal processing, power converter and motor must be designed as a whole for the specific application. Therefore, a model suitable for CAD must be able to predict the static and the dynamic characteristics with enough accuracy. Some models, as those based on gage curve use empirical knowledge and need only a few precalculated points of the of the magnetization (Ψ-i) curves. The gage curve models have ability to include into account all main nonlinearities. However they are unable to include effects of mutual interaction between two or more simultaneously excited phases, which are important in designing SRM drive with four or larger number of motor phases. A number of nonlinear SRM models, using magnetic theory [3], [4], [5], have been developed. These reluctances have physical meaning and are found from fundamental and some empirical considerations and knowledge. As an input it requires the motor geometry, some specific points of iron core B-H curve, and only one precalculated or measured magnetization (Ψ-i) point. If some other magnetization points are known, the model allows correction of some parameters for more accuracy. The model of SRM is suitable to be used for CAD of SRM drives as support in searching for optimal motor geometry, optimal number of turns, choice of power converter topology and rating of semiconductors. This model of SRM uses equivalent magnetic circuit of the motor as a set of reluctances linked in series and in parallel. These reluctances have had physical meaning and are found from fundamental and some empirical considerations and knowledge. The model of SRM allows including into account mutual interaction between phases as well as the nonlinearities. As an input it requires the motor geometry, some specific points of iron $B = f(H)$ and only one recalculated or measured magnetization point.

Basic concept

In determining the basic equation which gives relation between flux linkage (Ψ), phase current (i) and rotor position (θ) it is assumed that reluctance of SRM magnetic circuit can be represented by five reluctances in series linked in series. The relation on represent as:

$$i_k = \frac{\Psi}{N^2} \sum_{j=0}^{4} R_j \,, \tag{1}$$

where N is number of turns, and reluctances R_j are defined as:

$$R_j = \frac{l_j}{\mu_j A_j}, \tag{2}$$

where: l_j, μ_j and A_j are the length, permeability and the cross section area, respectively, of the corresponding part of flux path. All parts of reluctances R_j (j = 0, 1, … ,4) consist of two identical portions. The reluctances R_1, R_2, R_3, and R_4 are associated with the stator yoke, two rotor poles, respectively. The reluctances R_0 include the air parts and narrow high saturable parts of stator and rotor pole corners (Fig. 2). This reluctance varies with rotor position (θ) and with the flux density (B) while the other reluctances vary only with the flux density. Precise determination of reluctance R_0 is very difficult. In the proposed model it is represented in the form of two reluctances in series and one in parallel with them, as shown in Figure 1.

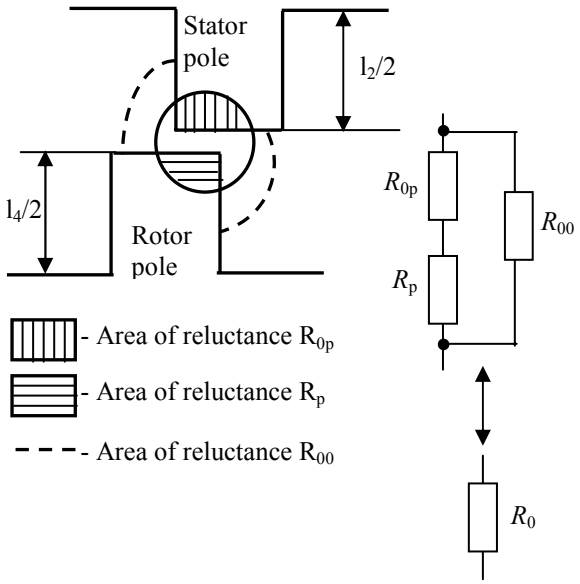

Fig.1. Reluctance R_0 of SRM.

Thus, reluctance R_0 can be found from:

$$(3) \qquad i_k = \frac{1}{R_{00}} + \frac{1}{R_{0p} + R_p},$$

The reluctance R_p in (3) stands for the rotor and the stator pole corners, which come into saturation earlier than the other iron parts of the motor. This effect is the consequence of the small air gap in overlapped portion of stator and rotor poles, and the large lengths on the other air paths through which flux "flows". R_{0p} includes the reluctance of the air gap. When the flux has relatively small values, it almost entire flows through the parts with reluctances R_{0p} and R_p. However, with the greater value of the flux, the flux density in R_p increases, and the value of reluctance R_p increases, too. Therefore, the influence of the other flux paths becomes significant. All the other air parts for the flux flowing are represented by reluctance R_{00}. In order to simplify further considerations, the expression (1) can be written as:

$$(4) \qquad i(\theta,\Psi) = \frac{\Psi R_0}{N^2} + \frac{\Psi}{N^2}\sum_{j=1}^{4} R_j = \\ = i_0(\theta,\Psi) + i_{fe}(\Psi)$$

Where the current i_0 is determined to the reluctance R_0 and the current i_{fe} is related to the other reluctances. In the proposed model, for the cases when only one phase is exited, the entire flux flows through the paths R_j (j = 0 to 4), i.e. the leakage flux is neglected. The results of FE analysis show that the leakage flux has a small value, though its influence is not negligible when the saturation. Level of the iron core is higher. In the nonlinear model, these phenomena are included indirectly. If more than one phase is excited, the parts of the reluctances R_1 and R_4 must be divided in the portions with different fluxes. For example, when the two phases are simultaneously excited, the fluxes in these parts are equal to the sum or the difference of the phase fluxes. Thus, the nonlinear model can be easily applied for multiphase regime.

The Dynamic model of SRM

Some Simplifications in Determining Reluctance R_0

From (2) and from Fig. 1, for calculation of reluctance R_0 three effective parameters must be known. However, if, for reluctance R_0, we take $\mu = \mu_0$ and $l = 2g$ (g - the air gap length), only the effective cross section area A_0 will be the unknown variable:

$$(5) \qquad R_0 = \frac{2g}{\mu_0 A_0}.$$

Thus, the problem of calculation of the reluctance R_0 is reduced to the determination of the effective area A_0 that is function of flux linkage (ψ) and rotor position (θ). On the other hand, reluctances R_{00}, R_{0p} and R_p can be written as:

$R_{00} = \frac{l_{00}}{\mu_{00} A_{00}}$, $R_{0p} = \frac{l_{0p}}{\mu_{0p} A_{0p}}$, $R_p = \frac{l_p}{\mu_p A_p}$, where l_{00}, l_{0p} and l_p are effective lengths, A_{00}, A_{0p} and A_p are effective cross section areas, and μ_{00}, μ_p and are the relevant permeability's. It is obvious that $\mu_{00} = \mu_{0p} = \mu_0$, $l_{0p} = 2g$ and that the areas A_{0p} and A_p are approximately equal to the cross section area of overlapping rotor and stator poles (Fig. 2). Therefore, if we take $A_{0p} = A_p$, and, in order to reduce number of variables, on take $l_{00} = 2g$, than, using (3) and (5), we obtain:

$$(6) \qquad A_0 = A_{00} + \frac{A_p}{1 + \xi \frac{\mu_{p0}}{\mu_p}},$$

The saturation in the area of reluctance R_p is modelled by the Frohlich curve:

$$(7) \qquad B_p = \frac{B_{mp} H_p}{\frac{B_{mp}}{\mu_{p0}} + H_p}.$$

Here B_{pm} is the maximum flux density with a typical value of $2T$ for most commonly used materials. From $B_p = \frac{\Psi_p}{N H_p}$, where Ψ_p is the portion of flux linkage Ψ, which flows through the areas with reluctances R_p and R_{0p}, the permeability μ_p can be expressed from (7) as:

(8) $$B_p = \frac{B_p}{H_p} = \mu_{p0}\left(1 - \frac{\Psi_p H_p}{B_{mp} N A_p}\right),$$

The unknown variable Ψ_p can be found from the equation:

(9) $$R_{00}\left(\Psi - \Psi_p\right) = \left(R_p + R_{0p}\right)\Psi_p .$$

Combining equations (4), (5), (6), (8), (9), the relationship between flux linkage ψ, rotor position θ and current i_0 can be expressed as:

(10) $$i_0 = \left[c_{05}\left(1 - c_{01}\right)\Psi - c_{01}c_{02} + c_{01}\sqrt{\left(\Psi - c_{03}\right)^2 + c_{04}^2}\right],$$

where:

$$c_{01} = \frac{A_p}{2\left(A_p + A_{00}\right)}, \qquad c_{02} = B_{mp} N\left[A_p + \left(1 + \xi\right)A_{00}\right],$$

$$c_{03} = B_{mp} N\left[A_p + \left(1 - \xi\right)A_{00}\right],$$

$$c_{04}^2 = c_{02}^2 - c_{03}^2 = 4\xi B_{mp}^2 N^2 A_{00}\left(A_p + A_{00}\right),$$

$c_{05} = \frac{2g}{\mu_0 N^2 A_{00}}$. Coefficients $c_{0k}\left(k = 1,2,\ldots,5\right)$ are functions of only three variables (A_{00}, A_p, and ξ). Hence, determination of current i_0 is further simplified. For the small flux linkage (Ψ), the reluctance R_0 is dominant due to a high permeability of no saturated iron in all the

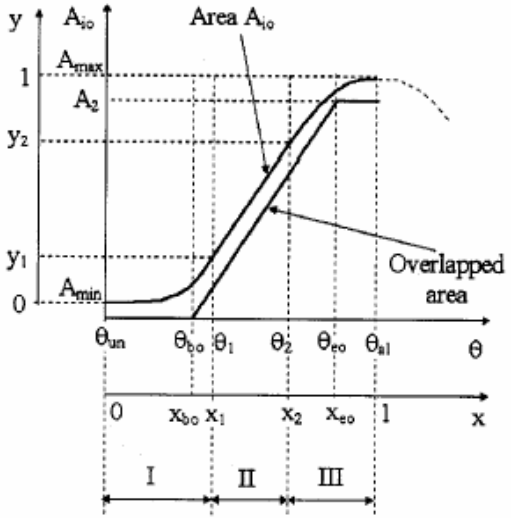

Fig. 2. Shaping area A_{i0}.

Permeability μ_p has also very high values and, therefore, reluctance R_0 is almost independent of flux linkage (Ψ). As a consequence we can define the area $A_{i0} = A_0\left(\theta, \Psi \cong 0\right)$ as function only of rotor position (θ). The area A_{i0} has the same shape as unsaturated phase inductance. Figure 2 shows this shape resembles. A minimum value A_{min} of the aria A_{i0} is the unaligned rotor position (θ_{un}) and the maximum value A_{max} is attained at the aligned rotor position (θ_{al}).

Determination the Reluctance of the Iron

For determining the i_{fe} in (4), the reluctances R_1, R_2, R_3, R_4, in (2) must be found from the flux linkage ψ. These reluctances represent the overall iron reluctance excluding the area of the reluctance R_p. The lengths l_j and the areas A_j (j=1 to 4) in (2) depend on the SRM construction and are shown in Figure 1. Each parameter μ_j, corresponding to the reluctance R_j (j=1 to 4) can be calculated from *B-H* curve for which we used the form:

(11) $$\frac{H_j}{H_s} = \gamma\frac{B_j}{B_s} + 1 - \gamma\left(\frac{B_j}{B_s}\right)^{\alpha},$$

where H_j and B_j are respectively field intensity and flux density in the area of reluctance R_j, and γ, α, H_s and B_s are constants defining the *B-H* curve. The point (B_s-H_s) on the curve should have the value so that for the flux density B_j smaller than B_s, the reluctance R_j (j=1 to 4) is respectively low in comparison with reluctance R_0. Also, when the flux density B_j tends to reach the value B_s, the influence of saturation effect becomes significant (typical value of B_s is within 1,1 T and 1,3 T). Parameter γ has value from 0,6-0,7 for the most commonly used iron. If we chose exponent α so that (20) matches well the real *B-H* curve, we will get poorer results for magnetization Ψ-*i* curves in the saturation region due to the leakage flux becoming more pronounced. Value of α varies from 7-13 for different irons and motor constructions. In the case that one Ψ-*i* point in the saturation region for the aligned position, the coefficient α can be determined more precisely.

Calculation of the torque

Instantaneous torque can be calculated by defining magnetic co energy W_m' as a function of rotor position θ and phase current i, or by defining magnetic energy W_m as a function of rotor position θ and flux linkage Ψ. Referring to (4), magnetic energy W_m can be obtained as:

(12) $$W_m = \int i\,d\Psi = \int i_0\,d\Psi + \int i_{fe}\,d\Psi = W_{m0} + W_{mfe}.$$

In (12) the energy W_{m0}, related to the current i_0, varies with rotor position θ and flux linkage ψ. As consequence, the produced torque T is determined as:

$$T = -\frac{\partial W_m}{\partial \theta} = -\frac{\partial W_{m0}}{\partial \theta} - \frac{\partial W_{mfe}}{\partial \theta} = \tag{13}$$
$$= \frac{\partial W_{m0}}{\partial \theta}.$$

Energy $W_{m0} = \int i_0 \, d\psi$ can be determined by substituting i_0 from (10).

Finally:

$$T = -\frac{\partial W_{m0}}{\partial A_{i0}} \frac{dA_{i0}}{d\theta}. \tag{14}$$

The torque can be obtained by solving (14), or approximately as:

$$T = -\frac{W_{m0}(\psi,\theta) - W_{m0}(\psi,\theta - \Delta\theta)}{\Delta\theta}. \tag{15}$$

where $\Delta\theta$ is a small step in the calculations of rotor position θ.

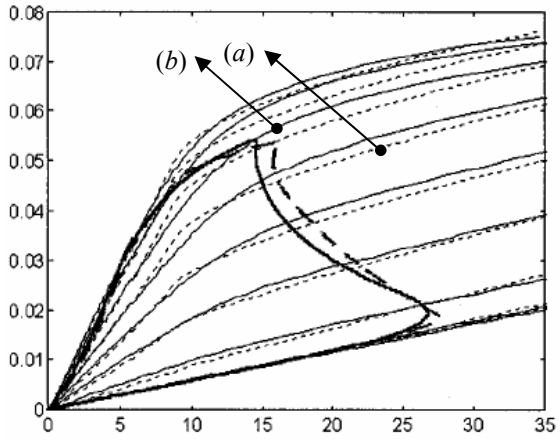

Fig. 3. Magnetization curves (from unaligned to aligned positions with 5^0) for SRM obtained by Miller model (a) and by nonlinear model of SRM (b).

The dynamic modelling of SRM is based on two variables i.e. rotor position θ and flux linkage Ψ, which is calculated from the equation:

$$\psi = \int_0^t (v - Ri)\,dt \frac{2g}{\mu_0 A_0}. \tag{16}$$

where: v – is the voltage applied to the phase winding, R is the phase resistance and i- is the phase current obtained from (4) for previous rotor position: θ-$\Delta\theta$. For starting the SRM simulation, only the unaligned inductance is needed (in order to obtain the area A_{min}. All the other parameters can be calculated from the motor dimensions and magnetizations B-H data of the magnetic material. For better results, the aria A_{max} can be precisely defined, if the unsaturated inductance is calculated. The SRM non linear model are elaborated and used in the Matlab/Simulink simulation of a 6/4 SR machine. Simulation results of used method and of the Miller method on shown in Fig. 3.

The magnetization (Ψ-i) curves from unaligned to aligned rotor position with step of 5^0 are shown in Fig. 3.

Conclusions

In this paper a simple and effective model of the SRM has been presented. It can include all the important effects inherent to the SRM. As input, the model requires the main motor geometry, number of turns, some characteristics of the used magnetic material, and only one precalculated magnetization (Ψ-i) point. If some other magnetization points are known, the model allows correction of some parameters for more accuracy. Because of its features, the model is suitable to be used for CAD of SRM drives as support in searching for optimal motor geometry, optimal number of turns, choice of power converter topology and rating of semiconductors. The model gives good instantaneous shapes of current and torque, and, therefore, it may be used for optimisation in control, as it is determination of optimal turn on and turn off angles in firing-angles control, shaping current waveforms for minimizing torque ripple or maximizing torque per ampere.

Acknowledgements

The authors would like to thank for many helpful comments and suggestions aimed this work.

References

[1] Pulle, D. W. J. New database for switched reluctance drive simulation, IEEE, 1991, Proceedings, Vol. 138, pp. 331-337.

[2] Torrey D. A., Lang, J. H. Modelling a nonlinear variable-reluctance motor drive, IEE Proceedings, 1990, vol. 137, pp. 314-326.

[3] Faiz, J. F. Aspects of design optimisation for switched reluctance motors, IEEE Trans, on Energy Conversion, 1993, Vol. 8, pp. 704-713.

[4] Radun, A. V. Design considerations for the switched reluctance motor, IEEE Trans. on Industry Applications, 1995, vol. 31, pp. 1079-1087.

[5] Miller, T. J. E. Switched Reluctance Motor and Their Control. Hillsboro/London: Magna Physics, Oxford University Press, Hillsboro, 1993.

Eleonora Darie *– Ph. D., Technical University of Civil Engineering, Pache Protopopescu 66 Str., Bucharest, Romania.*
e-mail: eleonora_darie@yahoo.com.

Emanuel Darie *– Ph. D., Police Academy, Privighetorilor 1-2 Str., Bucharest, Romania.*
e-mail: edarie@yahoo.com.

The Control of Switched Reluctance Drives

Eleonora Darie, Emanuel Darie

Abstract: *This work describes the aspects of the topology and control of a switched reluctance drive are considered and compared with the topology and control of conventional AC drives. The focus herein lies on the control of switched reluctance drives. The switched reluctance drive is necessary for a flywheel energy storage system for use in for instance an UPS. It is shown that for this application, switched reluctance drives have some essential advantages compared to conventional AC drives.*

Keywords: *switched reluctance machines, generator, flywheel storage, drive control.*

Introduction

The switched reluctance machine drives have gained considerable attention among researchers due to several reasons. First of all, the rotor construction is simple and robust, as it consists of pure (laminated) steel with neither permanent magnets, nor electrical windings, while the stator can be easily manufactured as the windings are not distributed but concentrated around the salient poles. Secondly, the machine is cost-effective in comparison with induction machines, while it is claimed to have a comparable or even higher efficiency and power to volume ratio. In this work, the main aspects of principal operation, inverter topology and control of switched reluctance machines are reviewed. Also, the use of the switched reluctance machine as a generator is considered and for this purpose a short review of publications in this matter is performed. Finally, the application in a flywheel energy storage system is considered and it is shown that this application permits to exploit most of its specific advantages. In a switched reluctance machine, only the stator presents windings, while the rotor is made by steel laminations without conductors or permanent magnets. The switched reluctance machine motion is produced by the variable reluctance in the air grip between the rotor and the stator.

Principle operation of Switched Reluctance Machines

Although switched reluctance machines are in fact synchronous machines, their operation and control differs fundamentally from conventional rotating-field AC machines, such as induction or permanent magnet synchronous machines.

Torque Development

Torque production in reluctance machines is achieved by the tendency of the rotor to move to a position where the inductance, and hence the magnetic field energy, of the excited winding is minimized [1]. An example of a 6/4 switched reluctance machine is shown in fig. 1. This three-phase machine is denoted 6/4 because it has six stator and four rotor poles. In the position shown, the resulting torque tends to rotate the rotor in clockwise direction towards the aligned position. If the rotor continues past the aligned position, due to its inertia, the attractive force between the poles produces a braking torque. To eliminate this negative torque, the current must be switched off while the poles are separating. The ideal current waveform is therefore a series of pulses synchronized with aligning rotor poles and stator poles. By exciting the stator windings of the different phases each time two rotor poles approach the appropriate stator poles, a continuous torque production and rotation of the rotor is achieved. In generator mode, windings are excited during the separation of the respective poles, yielding a braking attraction. The requirement for an optimized current shape makes it impossible to run such a machine directly from the grid. A power electronic inverter with a control based on feedback of the rotor position is a necessity.

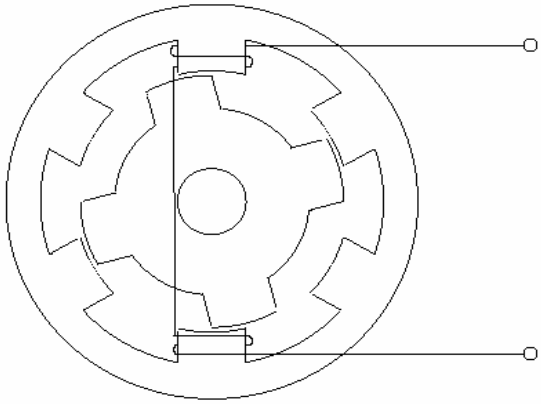

Fig.1. The 6/4 switched reluctance machine with one phase excited.

Circuit equations

The general voltage equation of an electrical coil with a resistance R and with $\Psi(t)$ representing the instantaneous flux coupled with this coil, can be written as:

$$u = R \cdot i(t) + \frac{d\Psi(t)}{dt}. \quad (1)$$

While, in case of a switched reluctance machine the inductance L is a complex function of position and

(through the non-linear ferromagnetic hysteresis phenomenon) current:

$$\Psi(t) = L \cdot (i(t), \theta(t)) \cdot i(t) \ , \ \frac{d\theta}{dt} = \omega_m \ , \tag{2}$$

where θ is the mechanical angle of the rotor position and ω_m is the rotational speed.

Using (1) and (2), the dynamic phase voltage equation of a switched reluctance machine with the rotor position θ and the rotational speed ω_m, neglecting mutual coupling effects, can be stated as follows:

$$u_{ph} = R \cdot i(t) + \left[L(t) + (i(t) \frac{\partial L(i,\theta)}{\partial i} \right] \frac{di}{dt} + + i(t) \frac{\partial L(i,\theta)}{\partial i} \omega_m \tag{3}$$

The last term is the back electromotive force (emf) e of the switched reluctance machine:

$$e = \omega_m \cdot i \cdot \frac{\partial L(i,\theta)}{\partial \theta} \ . \tag{4}$$

Hence, the induced voltage contains information about the rotor position. This property can be exploited for position feedback without a shaft sensor.

With constant current, (4) is linked to both increase in magnetic field energy and produced mechanical power. In unsaturated conditions, both terms equal each other, and torque can be expressed as:

$$T = \frac{i^2}{2} \cdot \frac{\partial L(i,\theta)}{\partial \theta} \ . \tag{5}$$

When $\frac{\partial L}{\partial \theta} > 0$ the torque is positive and electrical power is converted into mechanical output (motoring), while when $\frac{\partial L}{\partial \theta} < 0$ the torque is negative and mechanical power is converted into electrical power (generating). Note that the produced torque is independent of the direction of the current, since i^2 is always positive. With the machine driven in saturation, although (5) being no longer valid, these conclusions remain true.

Inverter Topology

As torque is independent of the direction of the current, the flux-linkage and the current, as well as the topology of the inverter circuit, may be unipolar. This mode of operation is preferred because it permits a simpler form of controller. However, to be able to switch off the current while the poles are aligned (in motoring mode), a negative voltage must be applied to enforce this fast current change in the relatively large inductance of the pole winding. The half-bridge phase can supply current in only one direction. This circuit is capable of operating the machine as a motor and generator. Several other circuits are possible besides, using less power electronic switches and employ various means to produce the reversed voltage [2]÷[6]. However, in general these circuits either compromise the performance of the machine or require additional components, while the fault-tolerant operation, more in particular the impossibility to have a shoot-through, of the drive is destroyed.

Control of Switched Reluctance Motor

The control of electrical machines is typically achieved through several control loops. Fig. 2 shows the basic control scheme of a servo drive [1]. The outer control loops are generally similar for all drive types, while the inner torque loop differs in switched reluctance machines fundamentally from other electrical machines. Much of the classical theory of torque control in electric drives is based on the DC machine, in which torque is proportional to flux multiplied by current. The flux and current are controlled independently, be it through mathematical transformations in AC field-oriented control. Generally speaking, in classical DC and AC

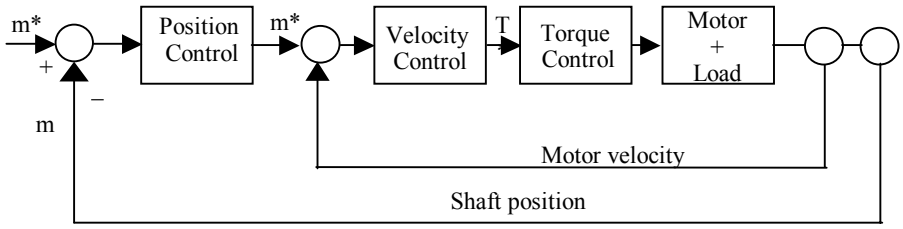

Fig.2. ***Servo drives control system.***

machines, the flux is maintained constant while the current is varied in response to the torque demand. In switched reluctance machines, unfortunately, there is no straightforward equivalent of field-oriented control. Pulses of phase current, synchronized with the rotor position, produce torque in the switched reluctance machine. The flux in each phase must usually be built up from zero and returned to zero each stroke. The inner torque loop consists of controlling timing and regulation of these pulses. Usually there is no torque sensor and therefore the torque control loop is not closed. Because the switched reluctance motor drive cannot be characterized by a simple torque constant k_T (torque/ampere), smooth torque control must be achieved through feed-forward torque control algorithms, incorporating some kind of motor model.

Switched Reluctance machine as a generator

Current control of the switched reluctance machine in generating is identical to motoring mode. The only difference is timing of current pulses. The objective of the generator control is normally to keep the DC-link voltage at the desired value. Unlike field-oriented AC machines, power generation is not continuous but pulse-wise. A DC-link capacitor must be retained to provide excitation power during the fluxing interval, more in particular during the first part of each stroke. The DC-link voltage decreases during the fluxing interval, and increases during the de-fluxing interval. The variation or ripple in the DC-link voltage depends on the energy needed to build up the flux each stroke and the DC-link capacitance. The essence of its instability is the proportionality of the excitation power to the back-electromotive force (emf). If the load is too small, the DC-link voltage rises exponentially towards infinity, and if the load is too large, the DC-link voltage falls towards zero. For this reason it is necessary to feedback the DC-link voltage or to control the average output current independently of the DC-link voltage. The controller must maintain the average DC-link voltage constant in much the same way as it must maintain a constant average torque in motoring mode. Since the switched reluctance machine is singly excited, like the induction machine, a DC source is necessary during start-up from cold, i.e. with the machine not magnetized and no voltage on the DC-link capacitor. The efficiency of the switched reluctance generator is very similar to the efficiency of the switched reluctance motor. The main difference is that the losses in the converter can be reduced as in the generator, the bulk of the current flows through the diodes having in general less conducting losses than the switching devices.

Application in flywheel energy storage

In flywheel energy storage, electrical energy is stored in the form of kinetic energy. As the amount of stored energy is proportional to the square of the rotation speed, a high-speed, low-loss operation is desired. In view of its application in for instance an uninterruptible power supply system (UPS) or a dynamic voltage restorer (DVR), reliability and immediate and fast energy transfer is key. Hence, primary requirements for the motor/generator of a flywheel energy storage system can be summarized as: high output power capability, fast response on sudden energy demand (for example when a voltage dip occurs), ability of the rotor to withstand high speeds, ability of the rotor to operate in vacuum with adequate.

Conclusions

The basic operation of a switched reluctance machine is reviewed for the motor as well the generator operation; thereby illustrating its advantages over other types of standard AC drives. The four-quadrant operation is appropriate for the operation as flywheel energy storage. It is especially very useful for high-speed operation due to its mechanical properties and low losses.

Acknowledgements

The authors would like to thank for many helpful comments and suggestions aimed this work.

References

[1] Cameron, D. E., Lang, J. H. The Control of High-Speed Variable-Reluctance Generators in Electric Power Systems. IEEE Transaction on Industry Applications, 1993, Vol. 6 pp. 1106-1109,

[2] Vukosavic S., Stefanovic V.R. SRM Inverter Topologies: A Comparative Evaluation, IEEE Transaction on Industry Applications, 1991, Vol. 6, pp. 1034-47.

[3] Kjaer, P. C., Cossar, C. Switched Reluctance Generator Control using an Inverse Machine Model, International Conference on Electrical Machines, 1994, Proceedings, pp. 380-385.

[4] Sawata, T., Kjaer, P. C., Miller, T. J. E. A Control Strategy for the Switched Reluctance Generator, Conference on Electrical Machines, 1998, Proceedings, pp. 2131-2136.

[5] Darie, E., Darie, E. Linear and non-linear Model Simulation of a Switched Reluctance Motor, Buletinul Institutului Politehnic din Iaşi, 2004, Tomul L (LIV) Fasc. **5**, pp. 1275-1279.

[6] Ray, W. F., Ebrahim, M. T. A novel high speed switched reluctance generator, European Conference on Power Electronics and Applications, 1995, Proceedings, Vol. 3, pp. 811-816.

Eleonora Darie *– Ph. D., Technical University of Civil Engineering, Pache Protopopescu 66 Str., Bucharest, Romania.*

e-mail: eleonora_darie@yahoo.com.

Emanuel Darie *– Ph.D., Police Academy, Privighetorilor 1-2 Str., Bucharest, Romania.*

e-mail: edarie@yahoo.com.

New Methods in Flux Measurement and Static Torque Calculation in a 7.5 kW SR Machine

Feriha Erfan Kuyumcu, Kadir Yılmaz, Mevlut Karacor

Abstract: *The determination of parameters of a Switched Reluctance Motor is highly difficult and complex due to magnetic flux linkage which is dependent on stator current and the displacement angle of the rotor. In this study, the magnetic flux linkage and static behaviour of the motor were examined experimentally. The results obtained from the experiments are unique as no other results are available. In order to achieve these results an electronic circuit was designed to obtain the incremental inductance. Hence the analytical functions using the parameters of current and constant rotor angle were curve fitted to experimental data by using computer programmes. The last section of the paper deals with the curve-fitting of the variation of magnetic flux to a cosine and exponential function, with torque changes obtained for 7.5 KW SR Motor.*

Keywords: *Switched Reluctance Motor, Flux Linkage, Incremental Inductance, Static Torque.*

Introduction

A recent study of the literature shows that there is a growing interest in Switched Reluctance Motors. The improved simplicity of design and high performance are two of the advantages to be considered in variable speed drive applications. The continuing improvements in power electronic devices, magnetic materials and design have increased the importance of an SRM over a conventional machine due to the absence of a rotor winding and the independence of stator phase current direction [1]. But the determination of the static behaviour of an SRM is highly complex due to the salient pole construction on both the rotor and the stator, and the non linearity of the magnetic circuit. The air gap between the stator and rotor has maximum and minimum values which correspond to the aligned and unaligned positions. The difference between these values is very large. Therefore, the magnetic flux varies widely with respect to a small change in the rotor displacement angle. Generally, the magnetic saturation is a frequently encountered phenomenon in an SRM, and the numerical methods applied to the non-linear analysis may be obtained in references [2,3].

The most important parameters of the magnetic flux are dependent on the current and the rotor displacement angle. The static behaviour of an SRM is thus obtained in terms of (θ) and (i). The variation of magnetic flux is obtained experimentally by using a test circuit, as shown in section 2. The experimental results obtained with the analogue circuit are compared with those obtained by an alternative method. The results are good, especially in the minimum inductance region, though these experiments are completely different with respect to one another. In the fourth section the results of the experiments, for magnetic flux and inductance, were used to reduce the difference between the new analytical functions and their originals. Primarily the co-energy and then the torque characteristics are calculated from the function which is presented in the last section.

II. The Flux Linkage Measurement Method Using A Power Transistor Test Circuit

The measurement of magnetic flux linkage in an SRM is described in this section. The flux linkage, in terms of applied voltage and phase resistance, is given below as

$$\Phi(\theta,i) = \int_0^t \left[V_{(t)} - R.i_{(t)}\right]dt \qquad (1)$$

Where V(t), i(t) and R are, respectively, the instantaneous value of applied voltage to phase winding, phase current, and resistance of winding. The Oulton 132S type, 8/6 pole, 7.5kW Switched Reluctance Motor was used in this experiment. Before starting the experiments, the rotor displacement angle θ was marked on a scale in equally spaced angles relative to the aligned position.

A. Test Circuit

The measured resistance of phase winding is used to calculate the voltage drop. Figure 1 shows the block diagram of the test circuit used to measure the flux linkage. The parameters and the design of the circuit were calculated according to energy stored in the magnetic field, and the IGBT was used as a power switch. In order to estimate the maximum of the surge current (approx 70A), the energy stored in the minimum inductance region was considered by using the magnetization curve.

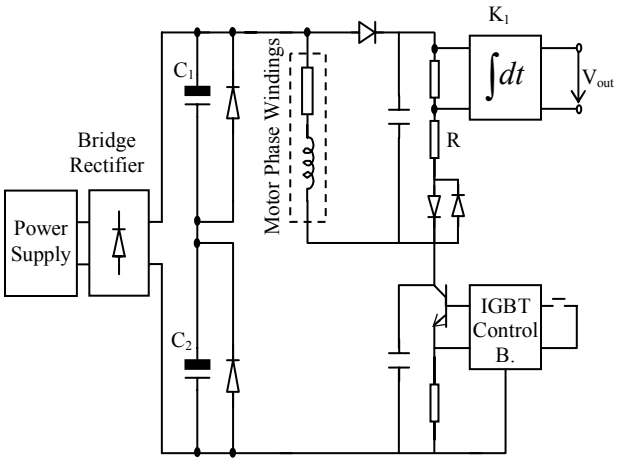

Fig.1 – Simplified diagram of the flux linkage measurement test circuit for one phase of the motor.

The values of the current ranged from 10 to 60 Amperes, in steps of 10A, to measure the magnetic flux accurately. The time constant of the integrator's output voltage, which is proportional to the magnetic flux linkage, was selected so as to be larger than that of the stator current. The integrator's output voltage developed by magnetic flux linkage is due to integral constants, as described below,

$$\Delta V_{out} = -\int_0^{\infty} \frac{V_L}{C.R}\,dt = \frac{\Phi}{C.R} \tag{2}$$

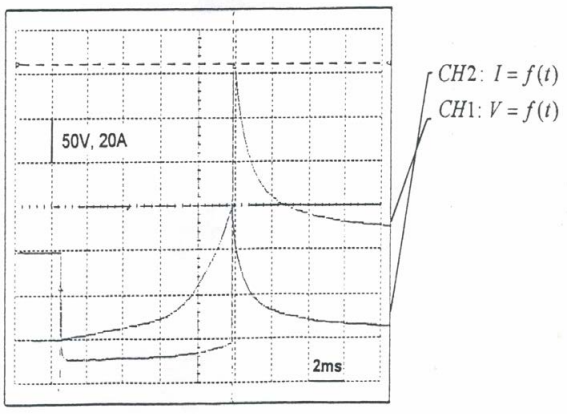

Fig.2 - Applied voltage and current profiles to the motor phase winding with the test circuit (θ=50°).

Thus, the value of the time constant of the integrator's circuit is limited by the value of the output voltage. Hence the magnetization characteristic of the motor was obtained in terms of the stator current and displacement angle. Figure 2 shows the profiles of the applied voltage and current to the stator winding where the amplitude of the current is adjusted by the use of feedback resistance.

The upper curve of figure 2 shows the variation of applied voltage at θ=50° where the inductance is almost maximum, while the lower curve represents the stator pulse current at 60 Ampere at the same displacement angle.

B. Test Results Of The Flux Measurement

Total pole arc of the Switched Reluctance Motor, (which has 8/6 pole numbers), is described as 360/Nr=60°. The experiments were conducted for a 30° displacement angle, started from an aligned position where the angle of displacement was assumed as zero. Since there were two variables, known as the angle and current, the current was varied from 10A to 60A in 10A steps for every angle. This experiment was repeated for each phase to check the differences. But the results obtained were very close in all cases.

The integrator's output signal and the applied phase current are presented in figure 3.

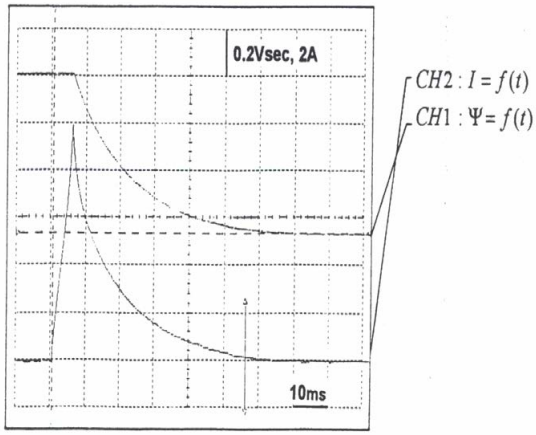

Fig.3 - Time variation of pulse current and flux with rated integrator gain (θ= 50°).

The flux linkage, due to the gain of integrator, decreases exponentially and takes negative values. The figure 4 shows the variation of magnetic flux linkage against the rotor displacement angle, θ at pre-selected amplitudes of stator current As is observed in figure 4 the origin of the angle is taken as 60° where the poles are in the aligned position.

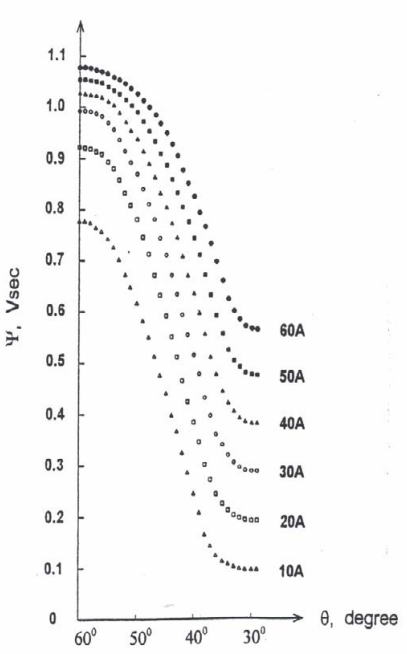

Fig. 4-The measured flux linkage against rotor angular displacement at different current amplitudes.

As the rotor moves away from the stator axis, the displacement angle is increased in the negative direction. Since there are 6 poles in the rotor, the angle between the two consecutive poles is 60 degrees and the first 30° section is repeated in the second 30° section. Therefore, the variation of the magnetic flux against the angle shows a maximum and minimum corresponding to the minimum and maximum airgap on the stator pole axis. The region of the curve, between the maximum and minimum, shows an almost linear variation of flux with the angle. This is the region where the negative torque is developed and considered for the motor operation.

The magnetic flux remains almost constant at the "dead zone" region and is caused by differences between stator and rotor pole arcs. The inductance of the motor phase winding for every current range at the unaligned position is almost equal, ($L_{min}=\psi/i$) . The differences between minimum and maximum inductance variation, (ΔL), for the maximum current value at the aligned position, is decreased.

III. An Alternative Measuring Method For The Incremental Inductance In The SR Motor

An alternative measuring method for the incremental inductance of the SR Motor will be explained in this section. This is an alternative method selected for the purpose of checking the accuracy of the previous results.

A. The Design of the Test Circuit and the Determination Of Incremental Inductance

The general voltage equation of a phase winding in an SRM was given in equation (1). Since the ψ and i are the functions of time and angle, this equation may be written as

$$V_{(t)} = R.i(t) + \frac{\delta\Phi}{\delta i}.\frac{di}{dt} + \frac{\delta\Phi}{\delta i\theta}.\frac{d\theta}{dt} \quad (3)$$

Where, R.i(t) is the voltage drop at the phase winding resistance, ($\delta\psi/\delta i$).(di/dt) is the voltage at the incremental inductance and ($\delta\psi/\delta\theta$).($d\theta/dt$) is the speed dependent back electromotor force (emf). Hence the incremental inductance for a constant angle is given by

$$L_{inc}(\theta, i) = \frac{\delta\Phi}{\delta i}\Big|_{\theta=const.} \quad (4)$$

The circuit presented in Figure 5 was designed to determine the incremental inductance of a phase winding. A small AC current with different DC offsets was applied to the phase winding using Darlington transistors. The incremental inductance is determined as given below by the application of the AC signal to the phase winding (where ω is the angular frequency of applied AC signal).

$$L_{inc} = \frac{1}{\omega}\sqrt{\left(\frac{V_{(t)}}{i(t)}\right)^2 - R^2} \quad (5)$$

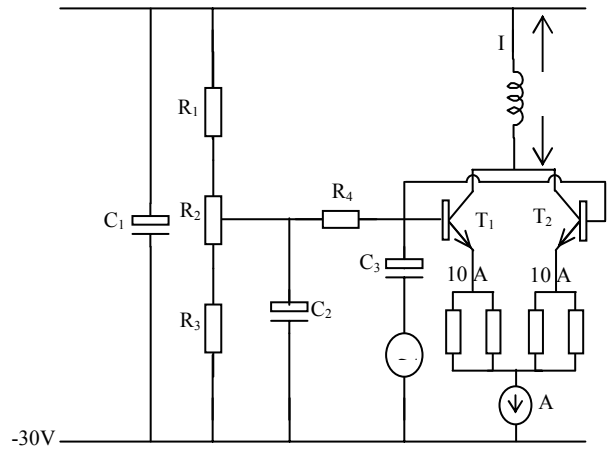

Fig.5 - The circuit used in determining the incremental inductance.

This process was repeated at θ = 50° and θ = 30°. When the rotor angle was set to 50° the test circuit given in figure 1 was used and the current was increased in 5 Ampere steps up to 60 Amperes to measure the magnetic flux as accurately as possible. The standard derivation of experimental flux values for each current value at the constant rotor position is found to be almost equal and has a very small value, as $\sigma = 0.3.10^{-3}$. The circuit shown in figure 5 was employed to measure the incremental inductances at same rotor angles as before and at I= 20 A. The same process was repeated at θ=30°

B. The Comparison of Two Sets of Experimental Results

By using the Matlab packet program, 5.th degree polynomial and cubic spline methods, the curve fitting was achieved for the magnetic flux values obtained by the method described in section 2. The variation of incremental inductance obtained through the use of polynomials is presented in figure 6. L_{inc} =f (I); (θ=const.) is obtained by taking the differential of the flux curve. There is a 4% difference between the values determined by the cubic spline method and the measurement made at I= 20A.

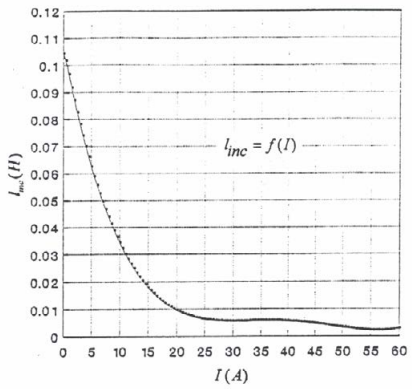

Fig. 6 - The variation of incremental inductance determined through 5.th degree polynomials at a constant rotor position (θ=50°).

The incremental inductance at θ= 30° was experimentally determined as L_{inc} =9.63mH by the use of the circuit given in figure 5. The magnetic flux values obtained by the employment of figure 1 were used to compute the slope of the curve. The Ψ-i variation for the minimum inductance value could be acceptable as a linear function, thus it can be described as a classic linear variation as

$$(6) \qquad \left.\begin{array}{l} I(t) \Rightarrow x \\ \Phi \Rightarrow y \end{array}\right\} \; y = ax + b$$

Hence, the slope of variation can be expressed as

$$(7) \qquad l_{inc} = m = \frac{n.\sum xy - \sum x.\sum y}{n.\sum x^2 - \left(\sum x\right)^2} = 9.681mH$$

The incremental inductance which was calculated as the slope of linear function by using the experimental flux data is l_{inc}=9.681mH. At the same position the incremental inductance was experimentally determined as l_{inc}=9.63mH by the use of the circuit given in figure 5 for the 20A current range. The maximum error, for the minimum inductance, obtained through different methods of measurements and calculations was ≈0.5%. The comparison of the two methods is presented in Table 1.

Table 1. The comparision of two different test results.

I=20A (DC)	θ=50°	By using magnetic flux data	Cubic Spline Metod	I_{inc}=10.11mH
			5th order polynomials	I_{inc}=9.6mH
		Measuring directly		I_{inc}=10.07mH
	θ=30°	By using magnetic flux data	Slope of linear function	I_{inc}=9.681mH
			5th order polynomials	I_{inc}=9.675mH
		Measuring directly		I_{inc}=9.63mH

IV. THE DETERMINATION OF THE TORQUE CHARACTERISTIC

It is not possible to calculate easily the co-energy and therefore the torque, in the SRM, by using an equivalent circuit diagram as with conventional machines, because the flux varies with the rotor angle and current The torque produced in the SR Motor with the constant phase current is computed as the rate of change of the co-energy of the magnetic field with the variable displacement angle θ,

$$(8) \qquad T(\theta, i) = \int_0^i \Phi(\theta, i) di \Big|_{i=const.} \qquad \text{(Nm)}$$

The integration applied to the magnetic flux at any rotor position *0,* determines the co-energy as

$$W'(\theta,i)=\int_0^i \Phi(\theta,i)di\big|_{\theta=const} \quad \text{(joule)} \tag{9}$$

The analytical function of the torque expression is obtained by using the experimental results of magnetic flux being dependent on the two parameters.

A. The Analytical Description of The Magnetic Flux Linkage

In order to determine the static torque variation, the method of determination of the magnetic flux variation is described in this section. One of the functions of the magnetic flux, in terms of the rotor position, is approached by cosine functions, while the other is approached to exponential functions by using experimental results. The function given below comprising four constants is as follows

$$\psi(\theta,i)=a_1(\theta).\left[1-e^{a2(\theta).i}\right]+a_3(\theta).\left[1-e^{a4(\theta).i}\right] \tag{10}$$

These constants, a_1, a_2, a_3 and a_4 are closely related to the rotor position. The constants given in exponential functions do not change with the rotor displacement angle (as mentioned in the recommended methods) to define the non-linear functions of the motor [4]. In this work the constants *"a" are* used in the solution above (equation 10) in terms of displacement angle and current. The numerically determined function approaches that obtained experimentally. The experimentally determined variation in inductance against angle is obtained for each value of stator current at all positions of the rotor poles. Hence, the inductance corresponding to different stator currents is almost unchanged and reaches the minimum at around 30 degrees of rotor position. Thus the variation of L against *0* is given as

$$L(\theta)=\frac{L}{2}.\left[1+\cos(Nr.\theta)\right]+\frac{L_{\min}}{2}.\left[1-\cos(Nr.\theta)\right] \tag{11}$$

Lmin is assumed constant, where the y-/ relationship is nearly linear. In figure 7, the flux which is the function of stator current and rotor angle, is presented here, in the θ axis where the current is taken as a parameter.

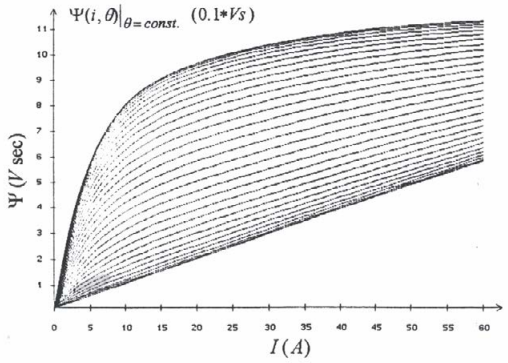

Fig.7- The numerically defined flux versus current trajectories for constant.

It shows that the maximum flux is achieved at the aligned position. The flux decays as it moves away from that position. The calculated magnetization curves are presented in figure 7 for constant rotor angle. The characteristic may be carried to large boundaries by using mathematical solutions. The main aim in this chapter is to determine the static torque.

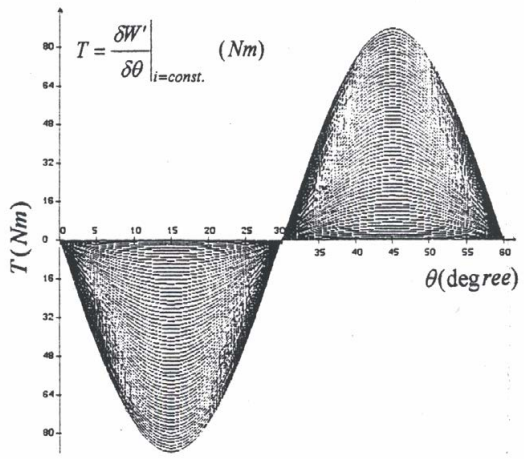

Fig.8 - The torque curve obtained by numerical function.

In figure 8 the variation of the total torque is presented by taking the stator current as a parameter.

The total energy function of the motor is

$$\psi.i=W+W' \tag{12}$$

$$W=\psi.i-\int_0^i \psi(i,\theta)di \tag{13}$$

After describing the energy function (by using equation 12 and 13), an average was taken for a total of θ_i = 30° of the rotor displacement angle for the constant current value given by

$$\overline{W} = \frac{1}{\pi/6} \int_0^{\theta_i} W(\theta, i) d\theta \Big|_{i=const.} \quad \text{(Joule)} \tag{14}$$

The average torque is calculated for θ = 30° as

$$\overline{T} = -\overline{W} . \frac{\theta . Nr}{2.\pi} \quad \text{(Nm)} \tag{15}$$

While it is operating at maximum speed, the average torque T_{ort}= 39.55Nm is calculated for the average value of measured current (I_{ort}=8.44A.). On the other hand the measured output torque of the DC load generator was 40.1 Nm at the same working condition. In this study, the calculated average torque has been found to be very close (i.e. 1.37%) to the directly measured dynamic torque at the same speed and current condition.

V. CONCLUSION

In this paper, the performance characteristics of an SR test motor, were obtained with the effect of saturation being taken into consideration. The magnetic flux linkage of the SR motor, which is related to the stator phase current and rotor displacement angle, was measured experimentally. The accuracy of the values was compared with the incremental inductance which was designed to obtain the incremental inductance values from a completely different circuit. The comparison of the two methods shows very close agreement between the two sets of results, especially for the unaligned position. By using the experimental data, analytical functions were graphically obtained and dependent on two variables. Equally, the magnetic flux linkage values were fitted to exponential and cosine functions. Therefore, energy, co-energy and electromagnetic torque changes were obtained for the 7.5 kW SR test motor. These characteristics were calculated for one phase over a rotor displacement range of 60°.

VI. REFERENCES

[1] W.,F., Ray, P.,J., Lawrenson, R.,M.,Davis, J.,M., Stephenson, N.,N.,Fulton, R..J.,Blake, "High-Performance Switched Reluctance Brushless Drives", IEEE Transactions on Industry Applications, Vol.lA-22, No.4, July/August 1986.

[2] J.,M., Stephenson, J.,Corda, "Computation of torque and current in doubly salient reluctance motors from nonlinear magnetisation data", Proc. IEE, Vol.126, No.5, pp.393-396, 1979.

[3] T.,J.,E., Miller, M.,McGiIp, "Nonlinear theory of the switched reluctance motor for rapid computer-aided design", IEE Proceedings, Vol.137, Pt.B, No.6, pp.337-347, November 1990.

[4] J.,V., Byme, J.,B., O'Dwyer, "Saturable variable reluctance machine simulation using exponantial functions", Proc. Int. Conf. on Stepping Motors & Systems, pp.11-16, 1976.

Feriha Erfan Kuyumcu *– Professor, Dr., Faculty of Electrical Engineering, Kocaeli University, 41300., Kocaeli, TURKEY*
e-mail: erfan@kou.edu.tr

Kadir Yilmaz *– Dr., Technical Education Faculty, Department of Electrical Education, Kocaeli University, 41300., Kocaeli, TURKEY*
e-mail: kayel@kou.edu.tr

Mevlut Karacor *– Ph.D. Student, Faculty of Electrical Education, Kocaeli University, 41300., Kocaeli, TURKEY*
e-mail: mkaracor@kou.edu.tr

Computing Phase Resistance Value of Short Pitched and Fully Pitched Switched Reluctance Motors by using Parametric CAD Model

Kadir Yılmaz, Abdulkadir Cengiz

Abstract— *This paper proposes computing phase resistance value of conventional switched reluctance motor (SRM) and fully pitched switched reluctance motor (FPSRM) by using parametric CAD model. The FPSRM is a relatively new variation of the conventional SRM. FPSRM retains all of the structural simplicity of the conventionally wound SRM. The effect of end winding in machine modelling is very significant issue that should be considered in the way of performance prediction. Short-pitch SRM has inherently shorter end winding than full-pitch SRM. Longer end winding yields higher phase resistance and this will eventually impact the thermal performance of the motor along with electromechanic performance. This paper presents an approach to compare full-pitch SRM with short-pitch one by considering the end winding effect. Earlier works considered this effect based on experimental studies and hand-on experience of motor construction. Our aim is to include the end winding effect to the model by using tools such as Finite Element Analysis (FEA) and Computer Aided Design (CAD). For these purposes, phase resistance computation in both types of SRM.*

Introduction

There is increasing attention toward Switched Reluctance Motors (SRM) for several applications such as automotives, home appliances, aerospace industry etc. High torque output over wide range of speed, robustness, less maintenance are main advantages of SRM among others. On the other hand, high torque ripple, acoustic noise, rotor sensor requirements are mainly cited disadvantages of SRM [1, 2]. SRM has double salient structure where stator hosts phase coils whereas the rotor has no winding at all. In its conventional structure, stator windings are wound around a single tooth of stator. During the last ten years, researchers have proposed several different winding structures in an effort to further increase power density of the conventional SRM [3,4]. One of these proposed approaches has been to use mutual inductance between phase windings to perform electromechanical energy conversion. The sole structural difference of this approach is the phase windings which are wound around several stator teeth. Depending on the span of the coils these motors are named as full or fractional-pitch winding SRM. Another name for full-pitch SRM, which has been commonly used in the literature, is mutually coupled switched reluctance motor (MCSRM) due to the torque production mechanism based on mutual inductance between phases. Both names will be interchangeably used in this paper. On the other hand, like most of the similar publications appeared in the literature, in this paper conventional SRM will be sometimes referred as short-pitch SRM.

Figure 1 shows short pitched winding structure with one phase conducting. Figure 2 is unipolar excitation of fully pitched winding with two phase conducting. Regardless of the winding configuration, SRM has both spatial and magnetic nonlinearities that must be considered when designing either the magnetic structure or the control.

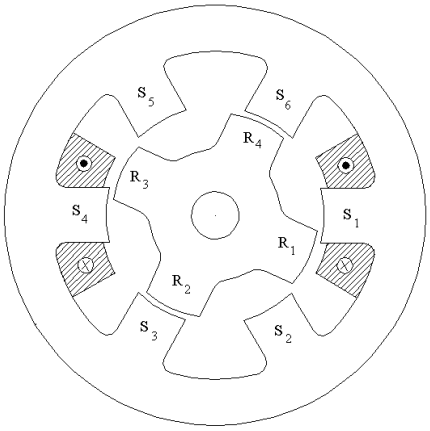

Fig. 1. Short pitched SRM..

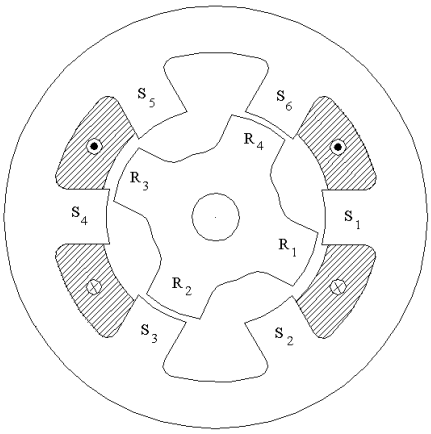

Fig. 2. Fully pitched SRM..

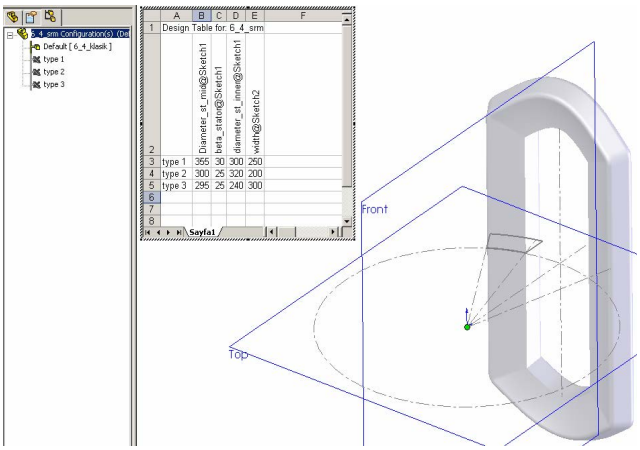

Fig. 3. Design Table structure for three types of a SRM model

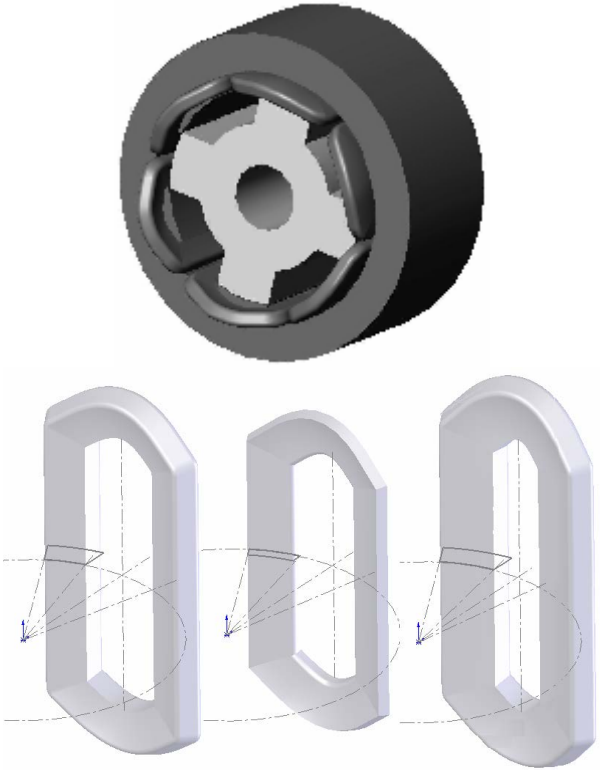

Fig.4. 3D solid-models for the short pitched SRM winding structures.

In a conventional SRM there is complete magnetic decoupling between phases, so that torque is produced entirely due to the rate of change of winding self inductance. This effectively limits each phase to contributing to positive torque production to one half of electrical cycle [2]. If the same motor is wound with fully pitched windings then it can be shown that the new configuration produces torque entirely as a result of changing mutual inductances between phases while maintaining a unipolar excitation pattern. Compared with the conventional SRM, better utilization of the electric circuit results in each phase contributing to positive torque production for at least three thirds of one electrical cycle. Therefore, for many configurations, significantly greater torques are predicted for a given frame size.

Depending on the excitation strategy used in mutually coupled SRM, positive torque generation mechanism takes different form. A unipolar converter may be used to drive fully pitched winding SRM and this mode of operation has been described by Barras et al [5]. By using a converter that can supply unipolar phase currents, phase current form factor can be improved and torque ripple reduced. When the fully pitched winding machine is operated from an asymmetric half bridge the maximum device duty cycle is 2/3 because each phase is excited for two thirds of the electrical cycle. Machine efficiency is significantly increased due to better utilization of the electric circuit, but device conduction and switching losses are approximately double.

The effect of end winding in machine modelling is very significant issue that should be considered in the way of performance prediction. Short-pitch SRM has inherently shorter end winding than full-pitch SRM. Longer end winding yields higher phase resistance and this will eventually impact the thermal performance of the motor along with electromechanic performance. This paper presents an approach to compare full-pitch SRM with short-pitch one by considering the end winding effect. Earlier works [3,4] considered this effect based on experimental studies and hand-on experience of motor construction. Our aim is to include the end winding effect to the model by using tools such as Finite Element Analysis (FEA) and Computer Aided Design (CAD). For these purposes, phase resistance computation in both types of SRM.

Computing Phase Resistance Value of Two SRMs by Parametric Cad Model

Unlike the conventional SRM, winding structure is full-pitch type and it covers the entire slot in MCSRM. Since the winding lengths of these two machines will be different due to the end winding effects, the amount of increase in the phase resistances has to be taken into account during the analysis. Since physical dimensions of the machines remain unchanged, both machines must operate under the same magnetic operating conditions or with equal copper losses. Copper winding volume per phase is calculated for both machines by using their 3D parametric representations with the SOLIDWORKS^{TM} .These results are then utilized for estimating changes in phase resistance. As an improvement to the previous methods where phase resistance increase can only be estimated experimentally after constructing the motors [2,3], the proposed method in this paper will enable the designers to accurately estimate the phase resistance ahead of machine construction.

For the calculations of the changes in the winding volumes the "sweep command" of the SOLIDWORKS^{TM}, a parametric 3D solid modeling

program has been utilized. In this method, various cross-sections along the body's spine and a guide line, on which these cross-sections will be swept through, are necessary. At first step, planes at various angles, on which cross-sections would be placed, were constructed. Next, depending on the number of turns and wire diameter, a cross-section has been formed and then placed on the planes in a way to represent the slices on the trajectory. Finally, these cross-sections have been swept or lofted on the guide line and the solid model has been formed as shown Fig 3-4. In parametric design, degree of freedoms in the models is reduced to become zero by introducing geometric constraints and by introducing dimensional relation between the factors, which form winding structure. While each winding volume is created, 4 parameters of the motor are defined and the rest of the constraints are derived based on those four parameters as shown in Fig.5. The four parameters are stator middle diameter, inner stator diameter, stator pole arc and axial length of the motor.

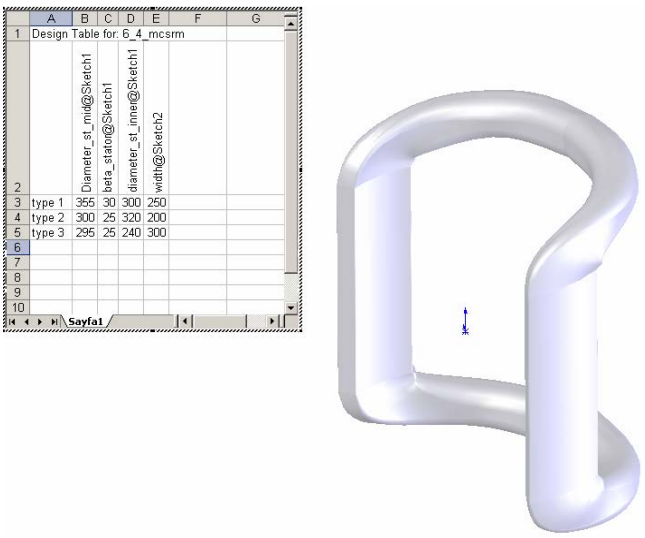

	A	B	C	D	E	F	G
1	Design Table for: 6_4_mcsrm						
2		Diameter_st_mid@Sketch1	beta_stator@Sketch1	diameter_st_inner@Sketch1	width@Sketch2		
3	type 1	355	30	300	250		
4	type 2	300	25	320	200		
5	type 3	295	25	240	300		
6							
7							
8							
9							
10							

Sayfa1

Fig 5. Design Table structure for three types of a MCSRM model.

In parametric CAD programs, desired measures and parameters are transferred to an EXCEL file by "Design Table" function and after certain arrangements, it would be possible to derive several models out of one model as shown in Fig.6. In this study, new models with different dimensions are created by this method out of initial SRM and MCSRM models. Therefore, users can select the desired winding type and they can easily create new winding geometry by adding new entries to the parameters existing in the "Design Tables" menu. So, by parametric model, a quick solution to compute winding volume increase is obtained when a conventional SRM is wound as mutually coupled SRM. Fig.6 shows winding structures for different and MCSRMs.

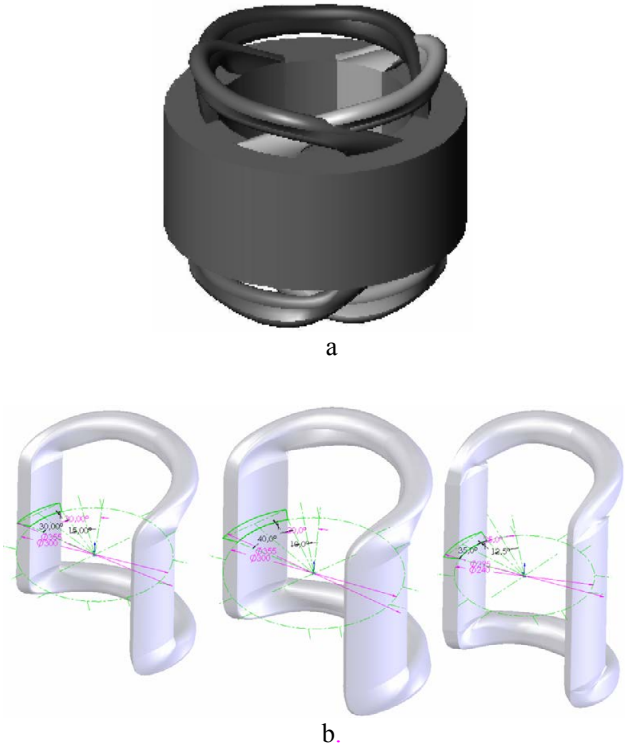

a

b.

Fig 6. 3D solid-models for the fully pitched SRM winding structures

Numerical calculations for different geometries have been done with the "mass properties" command of the program. As a result of these calculations, an increase between 59%-62% has been observed between MCSRM and conventional SRM windings. Comparison between the winding volumes of the short pitched SRM and fully pitched SRM shown in Table I. This increase will reflect itself at the resistance value for a fixed slot cross section area and filling factor since resistance will be proportional with the winding length.

Table 1. Copper winding volume per phase is calculated for both SRM and bipolar excited MCSRM

	Number of winding	Volume per winding (mm^3)	Total volume (mm^3)
Conventional SRM	6	658.4	3950.4
MCSRM	3	2106.43	6319.29
% Volume increasing			0.599658262

Conclusions

This paper presented an approach to compare full-pitch SRM with short-pitch one by considering the end winding effect by using parametric CAD model. Studies performed showed that for the same motor geometry, Short-pitch SRM has inherently shorter end winding than full-pitch SRM. Therefore, FPSRM has more copper losses than conventional SRM due to the longer end winding. Longer end winding yields higher phase resistance and this will eventually impact the thermal performance of the motor along with electromechanic performance. If comparison is to be made under equal thermal conditions, then current level of MCSRM has to be reduced to attain the same copper losses. This paper presented include the end winding effect to the model by using tools such as Finite Element Analysis (FEA) and Computer Aided Design (CAD). For these purposes, phase resistance computation in both types of SRM.

References

[1] T.J.E. Miller, "Switched Reluctance Motors and Their Control", Oxford University Press, Oxford, 1993.

[2] P.J. Lawrenson, J.M. Stephenson, P.T. Blenkinsop, J. Corda, and N.N. Fulton, "Variable Speed Reluctance Motors", IEE Proc. Inst. Elect. Eng, Vol. 127, pt. B, July 1980, pp. 253-265.

[3] B.C.Mecrow, "Fully-Pitched Winding Switched Reluctance and Stepping Motor Arrangements", IEE Proc. Elect. Power Appl. Part B, Jan 1993, pp. 61-70.

[4] B.C. Mecrow, "New Winding Configuration For Doubly Salient Reluctance Machines", IEEE Trans. On Industry Applications, November 1996, pp. 1348-1356.

[5] P.G. Barrass, B.C. Mecrow, A.C. Clothier "Unipolar Operation of Fully-Pitched Winging Switched Reluctance Drives" Proceedings of the IEE conference, Sept. 1995, Vol. 412, pp. 252-256.

[6] M. Garip, Y. Ozoglu, E.Mese, and F. Arslan, "Excitation Comparison for Mutually Coupled Switched Reluctance Motors", Proc. of the ICMCA conference, Sept. 2002.

[7] Solid Works Inc., Theory Manual - Revision 9, 1997.

Kadir Yılmaz – *Kocaeli University, Technical Education Faculty, Department of Electrical Education, Kocaeli 41300, Turkey*

e-mail: kayel@kou.edu.tr

Abdulkadir Cengiz – *Kocaeli University, Technical Education Faculty, Department of Mechanical Education, Kocaeli 41300, Turkey*

e-mail: akcengiz@kou.edu.tr

Dynamic Model and Steady-State Characteristics of the Induction Motor at Variable Frequency

Doru Adrian Nicola, Daniel Cristian Cismaru and Aida Cornelia Bulucea

Abstract *In paper it is presented a dynamical model and they are established the static characteristics and they limits at variable frequency of the induction machine. The chosen manner it is new and it offers the possibility of geometrical interpretations. They are analyzed the workings of practical interest (at m=ct. and p_i=ct.).The paper contains graphic representations for concrete dates. The obtained results are entirely compatible with those established in reference by other methods.*

Keywords: *Induction Motor, Variable Frequency, Structural Model, Steady-state Characteristics*

Introduction

Both in the industrial drives domain at variable speed and in the modern electric traction domain (urbane and railway) it is made more and more much appeal at the induction motors with the cage rotor. Their great advantage it is constituted by the mechanical robustness. But, for to obtain a variable controlled speed, this type of motor requires a three-phase supply with adjustable frequency and voltage [1], [2], [3] . In same time, the command and control circuits are clearly more complicated than in the d.c. motors case [3], [4], [5] etc..

If the dynamic regime performances depend only on the control method adopted, the steady-state regime characteristics at variable frequency will be exclusively established by the induction motor parameters within the frameworks of the supply exigencies imposed. But, till now, the information's watching the behavior at variable frequency of the induction motor were being established somehow "up-side down", by the working results extrapolation at f_s=50Hz=ct.. The method leads at heavy results, without the possibility some interpretation [6], [7]. As compared with those as before, in the paper it is proposed a new establishment methodology of the steady-state regime characteristics, at any supply frequency of the induction motor.

The obtained results are simply and they permit geometrical interpretation. For generalization, the all relations will be expressed in relative quantities (p.u.).

Mathematical equations and dynamic model

Like complex electromechanical system, any induction motor can be decomposed or recomposed from two big functional parts (an electromagnetic part and a mechanical part) like in fig.1 [7], [8].

Physical, only the electromagnetic part of induction motor it is connected at the W_{el} source of electrical energy. Phenomenological, it answers by the formation process of currents, of magnetic fluxes and of electromagnetic torque. The electromagnetic part it is governed by the electromagnetism laws. Particularly, it can be exposed the magnetic saturation, too.

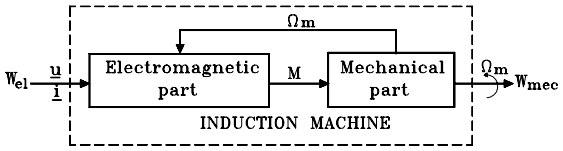

Fig.1. Functional parts of induction motor

Unlike the mechanical part it is independently of the rotor type, it includes only the turning masses inertia and it is integrated in the mechanical system, being governed by the classic mechanical laws.

Like specific features, those two functional parts they are interconnected through the M (electromagnetic torque) and Ω (mechanical angular speed of rotor) intern interaction quantities.

For the electromagnetic part of the induction motor it is adopted the mathematical model with space phasors [2], [5], [6] etc. Moreover, the equations will be presented in relative quantities (p.u.). In these conditions, in the common reference system, turning with the ω_s speed, the induction motor equations (with the rotor referred at stator) they are described by the equations (in p.u.):

$$
\begin{aligned}
&\underline{u}_s = r_s \cdot \underline{i}_s + \frac{1}{\omega_n} \cdot \frac{d\underline{\phi}_s}{dt} + j\,\nu_s \cdot \underline{\phi}_s \\
&0 = r'_r \cdot \underline{i}'_r + \frac{1}{\omega_n} \cdot \frac{d\underline{\phi}'_r}{dt} + j \cdot \nu_r\, \underline{\phi}'_r \\
&\underline{\phi}_s = \underline{\phi}_m + x_{s\sigma} \cdot \underline{i}_s; \quad \underline{\phi}'_r = \underline{\phi}_m + x'_{r\sigma} \cdot \underline{i}'_r \\
&\underline{i}_s + \underline{i}'_r = \underline{i}_m; \quad \phi_m = f(i_m) \\
&\nu_r = \nu_s - n \\
&m = Re\{j \cdot \underline{i}_s^* \cdot \underline{\phi}_s\} = Im\{\underline{i}_s \cdot \underline{\phi}_s^*\} = Im\{\underline{i}_s \cdot \underline{\phi}_m^*\}
\end{aligned}
\tag{1}
$$

In the above equations only main flux saturation was considered. Effects of the magnetic saturation upon the leakage flux were neglected. Also, the iron losses were neglected.

Magnetization characteristic of the machine Φ_m=f(i_m) is given numerically through points.

Corresponding to the mathematical dynamic model equations, in fig.2 it is shown the structural diagram for the saturated electromagnetic part of the induction motor.

For the unsaturated motor, when x_m=ct., we have:

$$\underline{\phi}_m = x_m \cdot \underline{i}_m = x_m \cdot (\underline{i}_s + \underline{i}'_r) \tag{2}$$

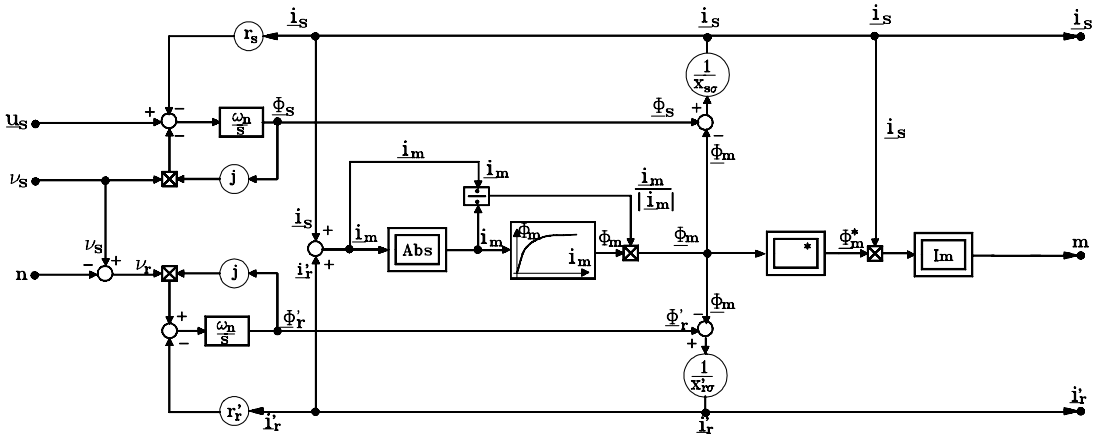

Fig.2. Structural model for electromagnetic part of the saturated induction motor

and the part afferent the $\underline{\Phi}_m$ main flux (from the structural diagram) it is simplified like in fig.3.

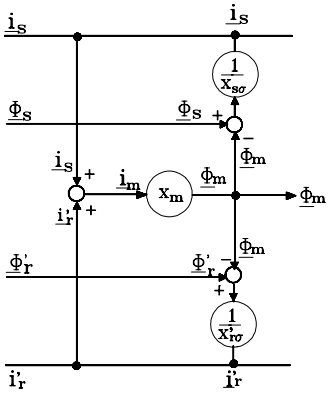

Fig.3. Linear model of $\underline{\Phi}_m$ flux

Moreover, with $x_s=x_m+x_{s\sigma}$ and $x_r'=x_m+x_{s\sigma}'$, the $\underline{\Phi}_s$ and $\underline{\Phi}_r'$ magnetic fluxes expressions from (1) they become:

$$(3) \qquad \underline{\phi}_s = x_s \cdot \underline{i}_s + x_m \cdot \underline{i}'_r; \quad \underline{\phi}'_r = x_m \cdot \underline{i}_s + x'_r \cdot \underline{i}'_r$$

whence, like in the references [4], [5], [7] they are found the currents:

$$(4) \qquad \underline{i}_s = \frac{\underline{\phi}_s - \frac{x_m}{x'_r} \cdot \underline{\phi}'_r}{\sigma \cdot x_s}; \quad \underline{i}'_r = \frac{\underline{\phi}'_r - \frac{x_m}{x_s} \cdot \underline{\phi}_s}{\sigma \cdot x_s}$$

and the structural diagram for the unsaturated induction motor it becomes identically like in the clasical reference.

Steady-state operation at variable frequency

For the determination of the steady-state regime equations at the supply with variable frequency of the induction motor, in the (1) general equations they are made the following explanations:

1. The common reference frame it is chosen a turning one, with the synchronism speed corresponding to the supply frequency.

2. It is considered only the fundamental waves influence, neglecting the harmonics of the supply converters. In the synchronous reference frame, the all space phasors from (1) they will be by the complex quantities type with the constant arguments.

3. The sinusoidal steady-state regime supposes as well the constant modules for the space phasors. Therefore, in (1) we will have $d\underline{\Phi}_s/dt=0$ and $d\underline{\Phi}'_r/dt=0$.

With these explanations, in steady-state regime, the (1) general model equations are reduced at:

$$\underline{u}_s = r_s \cdot \underline{i}_s + j\nu_s \cdot \underline{\phi}_s; \; 0 = r_r' \cdot \underline{i}_r' + j\nu_r \cdot \underline{\phi}_r'$$

$$(5) \qquad \underline{\phi}_s = x_s \cdot \underline{i}_s + x_m \cdot \underline{i}_r'; \; \underline{\phi}_r' = x_m \cdot \underline{i}_s + x_r' \cdot \underline{i}_r'$$

$$m = Im\{\underline{i}_s \cdot \underline{\phi}_s^*\}; \; \nu_r = \nu_s - n$$

If in the fluxes equations it is separated the main flux $\underline{\Phi}_m=x_m\cdot\underline{i}_m$ (with $\underline{i}_m=\underline{i}_s+\underline{i}_r'$) by the leakage fluxes $\Phi_{s\sigma}=x_{s\sigma}\cdot\underline{i}_s$ and $\Phi_{r\sigma}'=x_{r\sigma}\cdot\underline{i}_r'$, to the (3) system it can be associated the equivalent circuit (in p.u.) from fig.4.

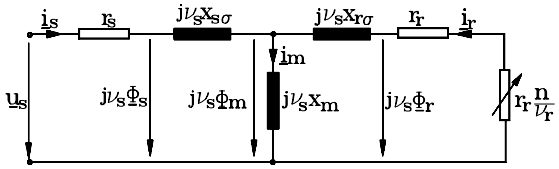

Fig.4. Equivalent scheme of induction motor (in p.u.)

Because, at the supply frequency variation it is modified and the voltage, from technical and economical reasons, they will be approached separately two variation domains, that is:

- the underrated frequencies domain (when Φ_s=ct.) and the ν_{smin} minimum frequency determination;
- the overrated frequencies domain (when u_s=ct.) with the ν_{smax} maximum frequency explanation.

Working at underrated frequencies

For the m electromagnetic torque insurance, in the

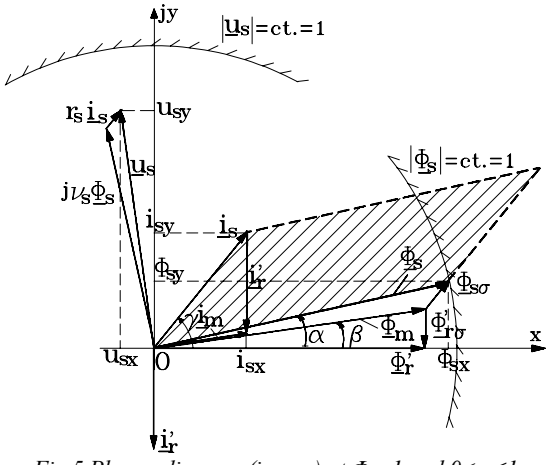

Fig.5 Phasor diagram (in p.u.) at Φ_s=1 and $0<\nu_s\leq 1$

$0<\nu_s\leq 1$ underrated frequencies domain it is modified the u_s voltage amplitude, so that the $\underline{\Phi}_s$ flux it remain with constant magnitude.

At any ν_s=ct.<1 and $|\underline{\Phi}_s|$=ct.=1, the phasor diagram (in p.u.) of induction motor it is presented in fig.5.

It illustrated geometrically the functional relations among voltages, currents and fluxes, when the motor must supplied so that at any $0<\nu_s\leq 1$, the $\underline{\Phi}_s$ stator flux it will describe the circle arc with radius $|\Phi_s|$=ct.=1.

In this geometrical representation, because:

$$m = Im\{\underline{i}_s \cdot \underline{\phi}_s^*\} = |\underline{i}_s| \cdot |\phi_s| \cdot \mathbf{sin}(\gamma - \alpha) \tag{6}$$

the m electromagnetic torque (in p.u.) it is numerically equal with the hachured area size from fig.5.

The physical existence of the mechanical movement, so $n\geq 0$, it leads at the minimum value of ν_{smin} stator frequency:

$$n = \nu_s - \nu_r \geq 0 \quad \Rightarrow \quad \nu_{s\,\mathbf{min}} \geq \nu_{r\,\mathbf{max}} \tag{7}$$

Working at overrated frequencies

From insulation reason, in the overrated frequencies domain it appears the u_s=ct.=1 so that the $\underline{\Phi}_s$ stator flux it will decrease inverse proportionally with the ν_s frequency:

$$\Phi_s \approx \frac{u_s}{\nu_s} \tag{8}$$

what it leads at a considerable decrease of the electromagnetic torque.

At the u_s=ct.=1 limitation constraint, the phasor diagram of induction motor at working with $\nu_s>1$ it is represented in fig.6.

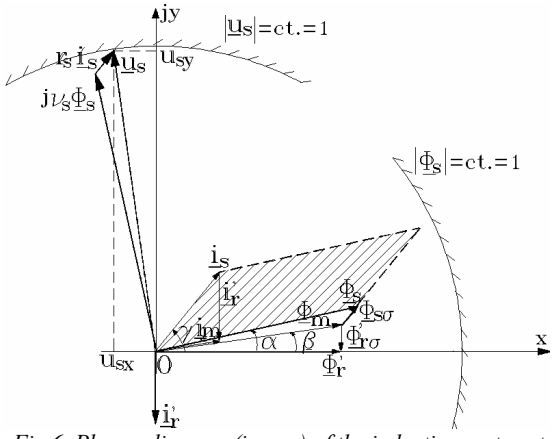

Fig.6. Phasor diagram (in p.u.) of the induction motor at u_s=ct.=1 and ν_s>1

Here the hachured area (delimited by $\underline{i}_s$ and $\underline{\Phi}_s$ phasors) it is numerically equal with electromagnetic torque quantity developed by motor at overrated frequencies.

The maximum value of ν_{smax} stator frequency it will be conditioned physically still of the mechanical movement existence of rotor through the relation among torques:

$$m \geq m_{ext} \tag{9}$$

Steady-state characteristics at variable frequency

The original idea which it was at the basis of the static characteristics establishment at variable frequency of the induction motor it contains two elements, meaning:

1. The choice of the x, jy complex frame with the real axis superposed the $\underline{\Phi}_r$ phasor direction (see fig.5 and fig.6) and

2. The choice of the $\underline{\Phi}_s$ phasor like independent complex variable.

Thus, if between the (5) equations the rotor current i_r' is eliminated, after which it is utilized the decomposition:

$$\begin{aligned} &\underline{u}_s = u_{sx} + j \cdot u_{sy}\,; \quad \underline{i}_s = i_{sx} + j \cdot i_{sy} \\ &\underline{\phi}_s = \phi_{sx} + j \cdot \phi_{sy}\,; \quad \underline{\phi}_r' = \underline{\phi}_r' + j \cdot 0 \end{aligned} \tag{10}$$

the steady-state regime at variable frequency of the induction motor it will be described, on components, by the following system of equations (in p.u.):

$$\begin{aligned} &u_{sx} = r_s \cdot i_{sx} - \nu_s \cdot \phi_{sy}\,; \; u_{sy} = r_s \cdot i_{sy} + \nu_s \cdot \phi_{sx} \\ &\phi_{sx} = \sigma x_s \cdot i_{sx} + \frac{x_m}{x_r'} \cdot \phi_r'\,; \quad \phi_{sy} = \sigma x_s \cdot i_{sy} \\ &\phi_r' = x_m \cdot i_{sx}\,; \quad i_{sy} = \nu_r \cdot \frac{x_r'}{r_r'} \cdot \frac{\phi_r'}{x_m} \\ &m = \phi_{sx} \cdot i_{sy} - \phi_{sy} \cdot i_{sx}\,; \quad \nu_r = \nu_s - n \end{aligned} \tag{11}$$

Through the elimination of the Φ_r' rotor flux, after a few mathematical processing, the (11) equations can be brought at the canonical form:

$$\begin{aligned} &u_{sx} = \frac{r_s}{x_s} \cdot \phi_{sx} - \nu_s \cdot \phi_{sy}\,; \; u_{sy} = \frac{r_s}{\sigma x_s} \cdot \phi_{sy} + \nu_s \cdot \phi_{sx} \\ &i_{sx} = \frac{\phi_{sx}}{x_s}\,; \quad i_{sy} = \frac{\phi_{sy}}{\sigma x_s}\,; \quad m = \frac{1-\sigma}{\sigma x_s} \cdot \phi_{sx} \cdot \phi_{sy} \\ &\nu_r = \frac{r_r'}{\sigma x_r'} \cdot \frac{\phi_{sy}}{\phi_{sx}}\,; \quad n = \nu_s - \nu_r \end{aligned} \tag{12}$$

From (12) equations, the induction motor characteristics can be presented both in trigonometric form (with geometrical interpretations) and in algebraic form like below.

Trigonometric form

If $\alpha=\mathrm{Arg}\{\underline{\Phi}_s\}$, see fig.7, then the orthogonal components of the $\underline{\Phi}_s$ phasor they are given by:

$$\phi_{sx} = \phi_s \cdot \mathbf{cos}\,\alpha\,; \quad \phi_{sy} = \phi_s \cdot \mathbf{sin}\,\alpha \tag{13}$$

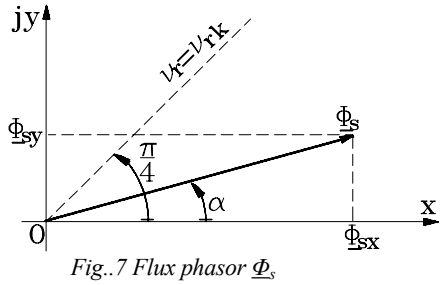

Fig..7 Flux phasor $\underline{\Phi}_s$

With the (13) substitutions, from the (12) equations can be quickly established the static characteristics of the induction machine at any value ν_s of the supply frequency. These are:

$$i_s=\sqrt{i_{sx}^2+i_{sy}^2}=\frac{\phi_s}{x_s}\sqrt{\cos^2\alpha+\frac{\sin^2\alpha}{\sigma^2}}$$

$$m=m_k\cdot\sin 2\alpha\,;\quad m_k=\frac{1-\sigma}{2\sigma\cdot x_s}\cdot\phi_s^2$$

(14)
$$\nu_r=\nu_{rk}\cdot tg\alpha\,;\quad \nu_{rk}=\frac{r_r'}{\sigma x_r'}\,;\quad n=\nu_s-\nu_r\geq 0$$

$$u_{sx}=\phi_s\cdot(-\nu_s\cdot\sin\alpha+\frac{r_s}{x_s}\cdot\cos\alpha)$$

$$u_{sy}=\phi_s\cdot(\nu_s\cdot\cos\alpha+\frac{r_s}{\sigma x_s}\sin\alpha)$$

$$u_s=\sqrt{u_{sx}^2+u_{sy}^2}$$

The α argument of the $\underline{\Phi}_s$ flux it depends only by the ν_r rotor frequency magnitude. At $\alpha\pm\pi/4$ the electromagnetic torque will be maximum ($\nu_r=\nu_{rk}$). For $\alpha\in(0,\pi/4]$ the induction machine will work like motor. For $\alpha\in[-\pi/4,0)$ the machine will work like generator ($m<0$, $\nu_r<0$).

Algebraic form

If between the (14) equations it is eliminated the α angle, with the substitutions:

(15)
$$tg\alpha=\frac{\nu_r}{\nu_{rk}}\,;\ \sin\alpha=\frac{tg\alpha}{\sqrt{1+tg^2\alpha}}\,;\ \cos\alpha=\frac{1}{\sqrt{1+tg^2\alpha}}$$

the static characteristics of the induction machine can be brought at the algebraic form, like below:

(16)
$$i_s=\frac{\phi_s}{x_s}\cdot\sqrt{\frac{1+(\frac{1}{\sigma}\cdot\frac{\nu_r}{\nu_{rk}})^2}{1+(\frac{\nu_r}{\nu_{rk}})^2}}\,;\quad \nu_{rk}=\frac{r_r'}{\sigma x_r'}$$

(17)
$$m=\frac{2m_k}{\frac{\nu_r}{\nu_{rk}}+\frac{\nu_{rk}}{\nu_r}}\,;\quad m_k=\frac{1-\sigma}{2\sigma x_s}\cdot\phi_s^2\,;\quad n=\nu_s-\nu_r$$

(18)
$$u_s=\phi_s\cdot\sqrt{\nu_s^2+2\nu_s(1-\sigma)\frac{r_s}{x_s}\cdot\frac{\frac{1}{\sigma}\cdot\frac{\nu_r}{\nu_{rk}}}{1+(\frac{\nu_r}{\nu_{rk}})^2}+(\frac{r_s}{x_s})^2\cdot\frac{1+(\frac{1}{\sigma}\frac{\nu_r}{\nu_{rk}})^2}{1+(\frac{\nu_r}{\nu_{rk}})^2}}$$

The (16), (17), (18) relations are likewise with those established on other ways in [1], [2], [5], [7] etc..

Characteristics of induction motors at constant Φ_s flux

In the underrated stator frequencies interval, at any ν_r=ct. (α=ct.), the Φ_s flux is influencing both the i_s current and the m electromagnetic torque.

In other that the induction machine develops the same torque, like in the rated regime, in the (14) equations it is imposed the Φ_s=1 condition. They result the static characteristics at constant flux:

(19)
$$i_s=\frac{1}{x_s}\cdot\sqrt{\cos^2\alpha+\frac{\sin^2\alpha}{\sigma^2}}$$
$$m=\frac{1-\sigma}{2\sigma x_s}\cdot\sin 2\alpha\,;\quad \nu_r=\nu_{rk}\cdot tg\alpha\,;\quad n=\nu_s-\nu_r$$

For α=ct., they result i_s=ct., m=ct. and ν_r=ct. at any $\nu_s\leq 1$. In this case the stator flux phasor will be, as well, constant $\underline{\Phi}_s=1\cdot e^{j\alpha}$=ct.. Definitely, this condition it is ensured by the u_{sx} and u_{sy} components constraint of the supply voltage at any $\nu_s\leq 1$, as below:

(20)
$$u_{sx}=-\nu_s\cdot\sin\alpha+\frac{r_s}{x_s}\cdot\cos\alpha$$
$$u_{sy}=\nu_s\cdot\cos\alpha+\frac{r_s}{\sigma x_s}\cdot\sin\alpha$$

The $i_s=f_1(\alpha)$, $m=f_2(\alpha)$, $\nu_r=f_3(\alpha)$ dependencies for Φ_s=1 and any $\nu_s\leq 1$ they are named the static characteristics. They are illustrated in fig.8.

At the $\underline{\Phi}_s=1\cdot e^{j\alpha}$=ct. condition guarantee, at any $\nu_s\leq 1$, the induction machine performances depend exclusively only by the i_s current magnitude. Thus, by the α elimination with the substitutions:

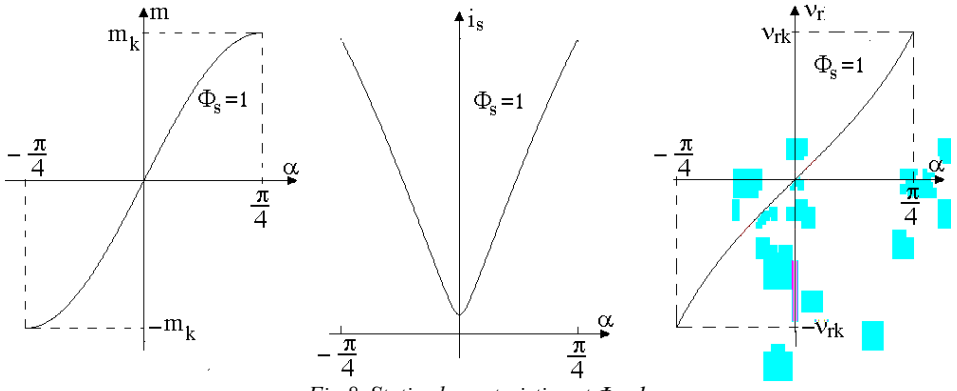

Fig.8. Static characteristics at Φ_s=1

(21) $\sin\alpha = \pm\sigma\sqrt{\frac{(x_s i_s)^2 - 1}{1-\sigma^2}}\ ;\ \cos\alpha = \sqrt{\frac{1-(\sigma x_s i_s)^2}{1-\sigma^2}}$

they result:

(22) $$\nu_r = \pm\frac{r_r'}{x_r'}\cdot\sqrt{\frac{(x_s i_s)^2 - 1}{1-(\sigma x_s i_s)^2}}\ ;\quad n = \nu_s - \nu_r$$
$$m = \frac{\pm 1}{(1+\sigma)x_s}\cdot\sqrt{[(x_s i_s)^2 - 1]\cdot[1-(\sigma x_s i_s)^2]}$$

Here, the "+" sign corresponds to the motor regime and the "-" sign corresponds to the generator regime.

The rated values, like motor, they are obtained for $i_s=1$ and $v_s=1$. They result:

(23) $$\nu_{rn} = \frac{r_r'}{x_r'}\cdot\sqrt{\frac{x_s^2 - 1}{1-(\sigma x_s)^2}}\ ;\quad m_n = \frac{\sqrt{[x_s^2 - 1]\cdot[1-(\sigma x_s)^2]}}{(1+\sigma)x_s}$$
$$n_n = 1 - \nu_{rm}$$

Implicitly, it results, as well,

(24) $$\alpha_n = tg^{-1}\{\sigma\sqrt{\frac{x_s^2 - 1}{1-(\sigma x_s)^2}}\}$$

For $\alpha=\alpha_k=\pm\pi/4$ they are obtained the maximum torque point coordinates:

(25) $$i_{sk} = \frac{1}{\sigma x_s}\cdot\sqrt{\frac{1+\sigma^2}{2}}\ ;\quad m_k = \frac{1-\sigma}{2\sigma x_s}$$
$$\nu_r = \nu_{rk}\ ;\quad n_k = \nu_s - \nu_{rk}$$

Characteristics at constant P_i power

In the overrated frequencies domain it can be neglected $r_s\underline{i}_s$ as compared with the $jv_s\Phi_s$ term from the voltages equation. Because at $v_s>1$ we must take into account the insulation restriction ($u_s=1$), from (14) we have:

(26) $$u_{sx} = -\nu_s\phi_s\sin\alpha\ ;\ u_{sy} = \nu_s\phi_s\cos\alpha\ ;\ \sqrt{u_{sx}^2 + u_{sy}^2} = 1$$

It results:

(27) $$\phi_s = \frac{1}{\nu_s}$$

At $u_s=1$ and $v_s>1$ the induction machine will work with weakening flux. Moreover, $\alpha=\alpha(v_s)$. The static characteristics at $v_s>1$, obtained from (14), where it is taken into account (27), will have the expressions:

(28) $$i_s = \frac{1}{\nu_s x_s}\cdot\sqrt{\cos^2\alpha + \frac{\sin^2\alpha}{\sigma^2}}\ ;\quad \nu_r = \frac{r_r'}{\sigma x_r'}tg\alpha$$
$$m = \frac{1-\sigma}{2\sigma x_s}\cdot\frac{1}{\nu_s^2}\cdot\sin 2\alpha\ ;\quad n = \nu_s - \nu_r$$

In the (28) relations, $\alpha=\mathrm{Arg}\{\underline{\Phi}_s\}$ varies with v_s. At $v_s=v_{sM}$ we have $\alpha=\pi/4$. The $\alpha=\alpha(v_s)$ law it is obtained from the $p_i=$ct. condition, where $p_i=m\cdot v_s$ represents the internal power of the induction machine. It results:

(29) $$\frac{\sin 2\alpha}{\nu_s} = \frac{1}{\nu_{sM}} = ct.$$

Here v_{sM} represents the maximum frequency for which it is still possibly the working with $p_i=$ct.. For $p_i=p_{in}=m_n\cdot 1$, we obtain:

(30) $$\nu_{sM} = \frac{1-\sigma}{2\sigma x_s}\cdot\frac{1}{p_{in}} = \frac{m_k}{m_n}$$

or with m_n given by (23):

(31) $$\nu_{sM} = \frac{1-\sigma^2}{2\sigma\sqrt{[x_s^2 - 1]\cdot[1-(\sigma x_s)^2]}}$$

Moreover, at the induction machine working (like motor) with $v_s>1$ and $p_i=$ct., the (27) and (29) relations permit the geometrical interpretation obtainment from fig.9. Thus, at the v_s stator frequency increase from 1 at v_{sM}, the $\underline{\Phi}_s$ phasor extremity (with the $\Phi_s=1/v_s$ module and $\alpha=1/2\cdot\arcsin(v_s/v_{sM})$ argument) it is moved away on the curve (a) from A through B to C, like in fig.9.

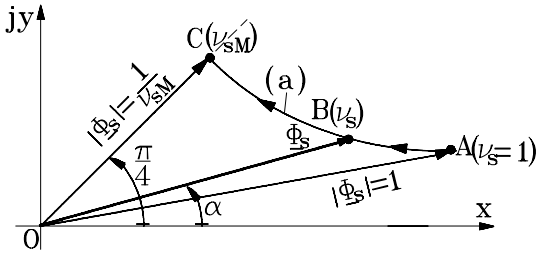

Fig.9. Geometrical place of $\underline{\Phi}_s$ phasor at $v_s>1$ and $p_i=ct.$

Definitely, on the $\sin 2\alpha = v_s/v_{sM}$ relation and substitutions basis:

(32) $$\sin^2\alpha = \frac{1-\sqrt{1-\sin^2 2\alpha}}{2}\ ;\quad \cos^2\alpha = \frac{1+\sqrt{1-\sin^2 2\alpha}}{2}$$
$$tg\alpha = \frac{1-\sqrt{1-\sin^2 2\alpha}}{\sin 2\alpha}$$

from (22) they are obtained the static characteristics at $p_i=$ct. and $v_s>1$ in the form:

$$i_s = \frac{1}{\nu_s\cdot x_s}\cdot\sqrt{\frac{1+\sigma^2}{2\sigma^2} - \frac{1-\sigma^2}{2\sigma^2}\cdot\sqrt{1-(\frac{\nu_s}{\nu_{sM}})^2}}$$

(33) $$m = \frac{1}{\nu_s}\cdot m_n\ ;\quad n = \nu_s - \nu_r$$
$$\nu_r = \frac{r_r}{\sigma x_r}\cdot[\frac{\nu_{sM}}{\nu_s} - \sqrt{(\frac{\nu_{sM}}{\nu_s})^2 - 1}\,]$$

They are available only for $v_s<v_{sM}$. The static characteristics at $p_i=p_{in}=$ct. they are represented in fig.10.

Limit characteristics at $v_s>v_{sM}$

At higher values $v_s>v_{sM}$ of the supply frequency within the framework of the $u_s=1$ restriction they remain available the (27) and (28) relations. On the other hand, the working with the constant power it is not more possible. The limit values of the static characteristics result for $\alpha=\pi/4$, obtaining successively:

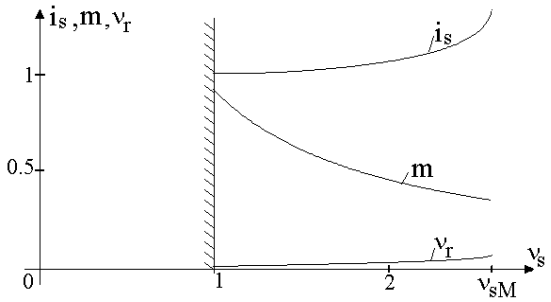

Fig.10. Static characteristics at constant power

$$i_s = \frac{1}{\nu_s \sigma x_s} \cdot \sqrt{\frac{1+\sigma^2}{2}}\ ; \quad m = \frac{1-\sigma}{2\sigma x_s} \cdot \frac{1}{\nu_s^2} = \frac{m_k}{\nu_s^2} \tag{34}$$

$$n = \nu_s - \nu_r\ ; \quad \nu_r = \nu_{rk} = \frac{r_r'}{\sigma x_r'}$$

In this case the $\underline{\Phi}_s$ phasor occupies the OC direction from fig.9, but with module magnitudes $\Phi_s=1/\nu_s$ by more and more small.

Conclusions

The paper approach by a new manner the static characteristics determination at the working with variable frequency of the induction machine.

They are analyzed separated the working at constant flux (when the torque is, as well, constant), the operation with constant electromagnetic power and at limit (for $\nu_s>\nu_{sM}$) the working with maximum torque.

Each of these regimes is accompanied by geometrical interpretations. All the relations are expressed in p.u.. The exposed method is general and perfect compatible with the established results by the other methods in reference.

Annex

In the (1) system equations, all the quantities they have been related at the values corresponding to the working rated point (n index). Explicitly, like reference quantities they have been chosen the following [2], [3] :

- for the phase voltages :$U_{ref}=\sqrt{2}\cdot U_n$
- for the phase currents $I_{ref}=\sqrt{2}\cdot I_n$
- for pulsations $\omega_{ref}[s^{-1}]=\omega_n=2\pi f_n[Hz]$
- for fluxes $\psi_{ref}=\sqrt{2}\cdot U_n/\omega_n$
- for powers $S_{ref}=3\cdot U_n\cdot I_n$
- for the mechanical angular speed $\Omega_{ref}=\omega_n/p$
- for torque $M_{ref}=S_{ref}/\Omega_{ref}=3\cdot U_n\cdot I_n\cdot p/\omega_n$
- for resistances and impedances $Z_{ref}=Z_n=U_n/I_n$ and
- for inductances $L_{ref}=\psi_{ref}/I_{ref}=U_n/(\omega_n I_n)$.

The quantities expressed in p.u. they are written with small letters. Particularly, in (1), n it is the relative rotor speed, ν_s is the relative stator frequency and ν_r is the relative speed of the rotor, as below:

$$n = \frac{\omega_m}{\omega_n} = \frac{\Omega_m}{\Omega_n}\ ; \ \nu_s = \frac{\omega_s}{\omega_n} = \frac{f_s}{f_n}\ ; \ \nu_r = \frac{\omega_r}{\omega_n}$$

The parameters taken into consideration at the graphic representations they have the following values (in p.u.): r_s=0,01867; r_r=0,01493; $x_s=x_r$=4,41123; x_m=4,3089; σ=0,04585

References

Bühler,H. Convertisseurs statiques, PPUR, Lausanne, 1991.

Bühler,H. Électronique de réglaje et de commande,PPUR, Laussanne 1990.

Bühler,H. Réglaje de systémes d'électronique de puissance, PPUR, Lausanne (1997).

Murphy,J.M.D., F.G. Turnbull Power electronic Control of AC Motors, Pergamon Press, 1988.

Boldea,I., S.A. Nasar Vector Control of AC Drives, CRC Press, 1992.

Chatelain,I. Machines électriques, PPUR, Lausanne,1989.

Nicola, D.A. Electrotehnică, transformatoare şi maşini electrice Vol.II, Ed. Sitech, Craiova, 1998.

Nicola, D.A. and D.C. Cismaru, Considerarea saturaţiei fluxului principal la modelarea şi simularea maşinii de inducţie, SIELMEC'99, Vol.I, pg.35-38, Chişinău, 1999.

Doru Adrian Nicola - *Professor, Dr., Electromechanical Faculty, University of Craiova, Bd. Decebal, Nr.5, Craiova, ROMANIA, e-mail: dnicola@em.ucv.ro.*

Daniel Cristian Cismaru - *Lecturer, Dr., Electromechanical Faculty,University of Craiova, Bd. Decebal, Nr.5, Craiova, ROMANIA, e-mail: dcismaru@em.ucv.ro*

Aida Cornelia Bulucea - *Associate Professor, Dr., Electromechanical Faculty, University of Craiova, Bd. Decebal, Nr.5, Craiova, ROMANIA, e-mail: abulucea@em.ucv.ro.*

Optimum Design and Performance Analysis of Three-Phase Induction Motor

A. Gökhan YETGİN, A. İhsan ÇANAKOĞLU, K. Nur BEKİROĞLU, Sibel ZORLU

Abstract: *In this paper, an algorithm for the 3-phase asynchronous motor is presented. Dimensions of geometric forms for desired stator and rotor bar types are obtained via this algorithm by inputting nominal values of the motor and flux densities. By using these dimensions, equivalent circuit parameters are calculated by simulation and experimentally for no-load and short circuited conditions and the performance analysis is carried out. Dimensions obtained with the software for three 3-phase squirrel cage asynchronous motors with powers of 3, 5.5 and 45 kW respectively and experimental results are presented comparatively in the form of tables.*

Keywords: *Induction motor, optimum design, equivalent circuit parameters, steady-state analysis, computer program.*

1. Introduction

The aim in motor design is to manufacture motors that have desired characteristics with high efficiency and low cost values. Structural optimization ideas in mechanical engineering are described in early 1960's [1]. After the petroleum crisis as the energy costs increased, some researchers like Buschart and Diamant, started to investigate the optimization of induction motors and they have used methods such as Neural Network, Fuzzy Logic, and Genetic Algorithm [2].

In order to analyze the performance of induction motors, the equivalent circuit parameters must be calculated. Generally, five methods are used for calculating induction motor parameters in terms of present data [8].

1. Calculating parameters using motor design data

This method requires detailed information such as stator and rotor geometry and material parameters. Since this method has close relations with physical facts, it gives the most correct answer but because it is bound to numerical solution methods such as finite element analysis, it is the most expensive one [12, 13].

2. Calculating parameters using steady state motor model

This method uses iterative solutions based on steady state equations of induction motor [10]. This is the most common parameter calculation method because the motor values are easily obtained [8].

3. Calculating parameters in frequency domain

This is a method based on frequency response of the motor in rest position. Motor parameters are calculated using obtained transfer function [9]. The greatest advantage of this method is that it gives the most correct results [8].

4. Calculating parameters in time domain

Motor parameters are measured in time domain and modeling parameters are adjusted so they confirm measured values. In this model, since it is not possible to observe measurement amounts of all parameters, motor model should be simplified [11]. The disadvantages of the model are; its cost and difficulty in obtaining data to be used in calculations [8].

5. Calculating parameters in real time

This method requires parameter prediction technique using simplified induction motor model. Using this model, updating motor parameters is rather faster. Parameters are predicted by adjusting driver system controls of the induction motor [3].

In this study, first and second methods are chosen for calculation of equivalent circuit parameters because all the data required for motor model calculation is available. The results of first and second method and the data given by the manufacturer are compared in tables.

2. Description of the Program and Methods Used

The discriminatory value between small and mid-scaled induction motors is considered as 100 kW. Motors with capacity lower than 100 kW, consist of a single stator and rotor pack [6]. In low power motors, the stator iron pack is manufactured using single metal sheets. The rotor is similarly packed using metal plates and the rotor bars are casted in slots [7]. In this study, computer software is developed in order to design motors up to 100 kW power. With this software, a continuous control is achieved over the parameters that have great importance on motor from many aspects. Stator, rotor and air gap magneto-motor force, stator and rotor winding current density values, loss and efficiency values are important parameters that are controlled by the software [5].

Input values for the software are primarily the label values of the motor to be designed (nominal values such

as; power, voltage, current, power factor, efficiency, rpm, frequency). B-H and magnetic loose characteristics of the material to be used in the stator and rotor core, are typed into the software for iterative calculations. In Figure-1, the process diagram of induction motor design is given. According to this diagram, all the constructional data of the motor (stator and rotor dimensions, inner and outer diameters and dimensions of stator and rotor slots) are obtained from the software. Magnetically and electrical load values are controlled within the software. If these values are not equal or not close to each other, the design returns to first step and all the values are re-calculated. If all the steps are successfully completed, I_o magnetizing current, equivalent circuit parameters, loss and efficiency values are calculated. Performance values are checked and if they are very different from aimed values, the calculation process starts from the first step using new current density and new λ packing ratio values. When all the values are convenient, the operation characteristically curves of the motor are plotted and nominal working point is determined. Figure-2 shows the section that the input data is typed into the software. Figure-3 shows the section that the calculated values of the stator are given.

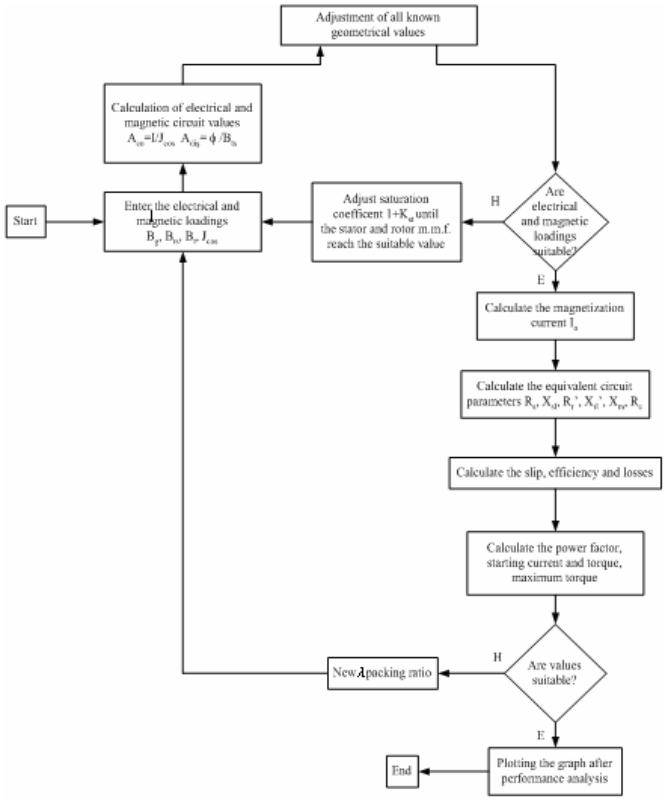

Figure-1. Algorithm used for design

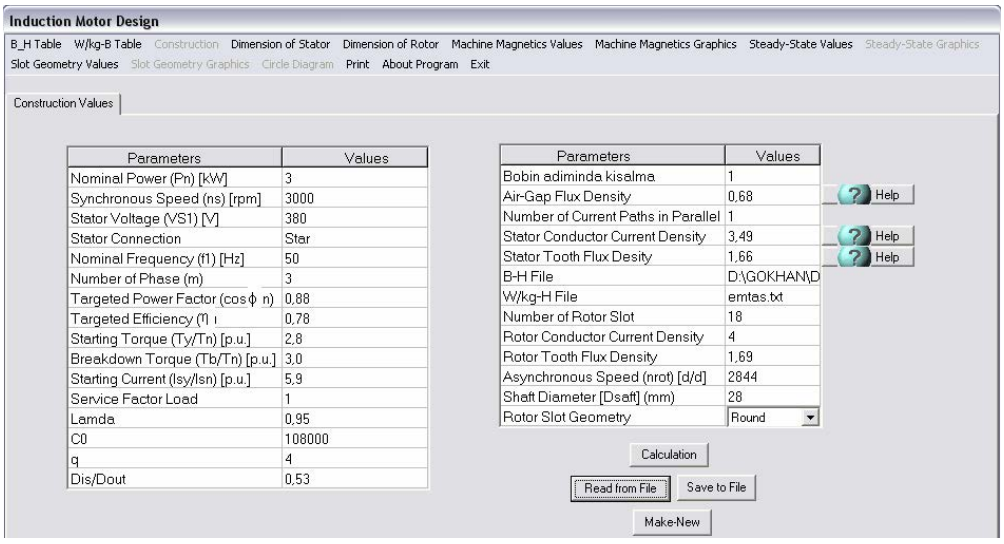

Figure-2. Entering data

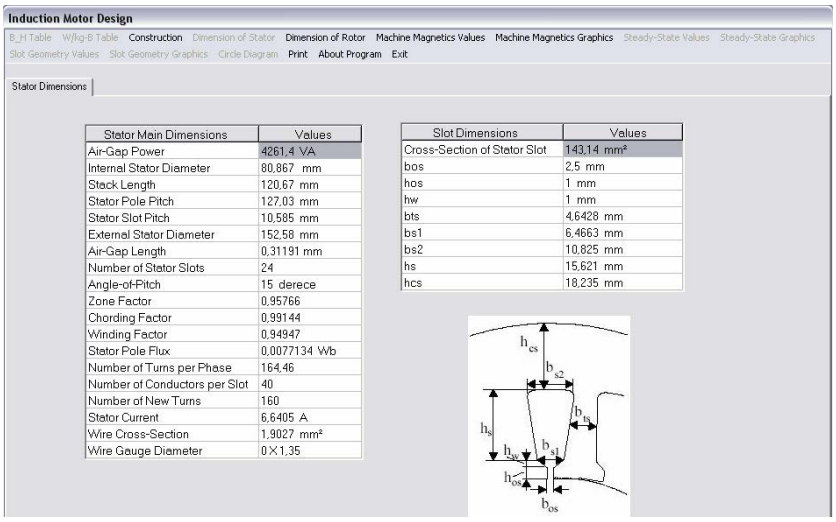

Figure-3. Results for the stator

One of the most important points of induction motor equivalent circuit determination is the stator and rotor slot geometry [5]. In this study, three different slot geometries determined by NEMA standards for three different motor power values are used.

2.1. Stator Slot Calculation

Stator slot form must be selected in order to obtain the best operation characteristics for the motor to be designed. All three slot forms are selected round. Figure-4 shows the slot form and values used in the calculations.

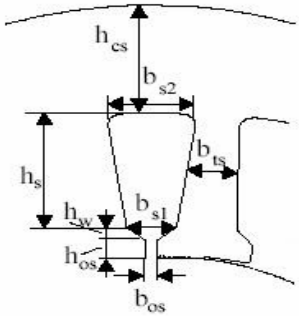

Figure-4. Stator slot geometry

The stator slot area that the conductors will be placed is calculated using following equation (K_d filling rate) [6]:

$$A_{su} = \frac{\pi d_{co}^{\,2} a_1 w_{11}}{4K_d} \quad (1)$$

Where, d_{co} is conductor diameter, a_1, number of parallel bars, and w_{11}, total number of windings in the slot. The equations used to calculate other important parameters of stator slot are as follows [5,6];

Upper diameter of stator slot;

$$b_{s1} = \frac{\pi(D_{is} + 2h_{os} + 2h_w)}{N_s} - b_{ts} \quad (2)$$

N_s : Number of stator slots.

Lower diameter of stator slot;

$$b_{s2} = \sqrt{4A_{su}\,\tan\frac{\pi}{N_s} + b_{s1}^{\,2}} \quad (3)$$

Stator slot height;

$$h_s = \frac{2A_{su}}{b_{s1} + b_{s2}} \quad (4)$$

Stator slot dorsal height;

$$h_{cs} = \frac{D_{out} - (D_{is} + 2(h_{os} + h_w + h_s))}{2} \quad (5)$$

D_{out} : stator outer diameter, D_{is} : stator inner diameter.

Stator slot teeth width;

$$b_{ts} = \frac{B_g \tau_s}{B_{ts} k_{fe}} \quad (6)$$

Here, B_g is the air gap selected at the beginning of the design. B_{ts} is the current density value of the stator teeth. τ_s is polar step, and k_{fe} is the ratio of the voltage induced in the coil, to voltage applied to the stator.

2.2. Rotor Slot Calculation

Generally, rotor slot form is considered as an independent design parameter. Lately, re-design of the rotor slots, by using numerical analysis methods, is possible examining electromagnetic performance analysis of squirrel-cage induction motors based on numerical methods [4]. Among the rotor slot forms shown in Figure 5, the one with the minimum leakage reactance and the maximum moment value is the slot form shown as Figure 5.(a), and this form is the most preferred one [17]. Also, three different rotor slot forms are used for three different motors and these are given in Figure-5 in power values order.

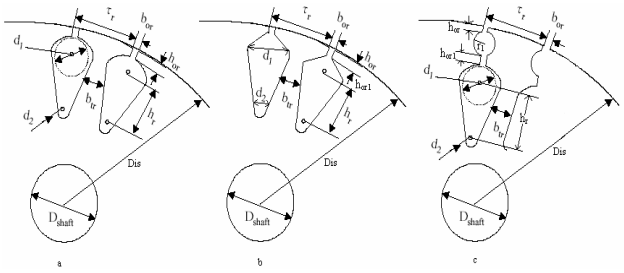

Figure-5. Rotor slot geometry a) Round b) Egg-Shaped c) Double Cage

For a 3 kW motor, the slot form shown in Figure-5-a is selected and the given equations are derived accordingly [6].

Rotor slot area;

$$A_b = \frac{\pi}{8}(d_1{}^2 + d_2{}^2) + \frac{(d_1 + d_2)h_r}{2} \quad (7)$$

N_r : Number of rotor slots.

Rotor slot upper diameter;

$$d_1 = \frac{\pi(d_{is} - 2h_{or}) - N_r b_{tr}}{\pi + N_r} \quad (8)$$

Rotor slot lower diameter;

$$d_2 = \sqrt{\frac{8\tan\frac{\pi}{8}A_b - d_1{}^2(\pi\tan\frac{\pi}{N_r} + 2)}{\pi\tan\frac{\pi}{N_r} - 2}} \quad (9)$$

Rotor slot height;

$$h_r = \frac{d_1 - d_2}{2\tan\frac{\pi}{N_r}} \quad (10)$$

Rotor slot dorsal height;

$$h_{cr} = \frac{\phi}{2Lb_{cr}} \quad (11)$$

B_{tr} : Chosen rotor teeth flux density.

Rotor slot teeth width;

$$b_{tr} = \frac{B_g}{k_{fe}B_{tr}} \quad (12)$$

3. Motors Used for the Design

Three squirrel-cage induction motors of 3, 5,5, and 45 kW power values are selected for the design. The label values and values selected for design are given in Table-1. These values are the input values of the software. For all three motors, stator slot geometry is determined for round slot form. One of the most important point in motor parameter selection is that rotor slot forms are different for the three motors. Also the frequency, voltage and pole number values of the 5.5 kW motor are different from the other two.

Table-1.

Motor Parameters

Motor Parameters		**Motor 1**	**Motor 2**	***Motor 3***
Nominal Power	[kW]	3	5,5	*45*
Stator Voltage (L-L)	[V]	380	460	*380*
Connection		Star	Star	*Delta*
Nominal Frequency	[Hz]	50	60	*50*
Number of Phase		3	3	*3*
Nominal Power Factor		0.88	0.83	*0.91*
Nominal Efficiency	[%]	0.78	0.89	*0.91*
Synchronous Speed	[rpm]	3000	1800	*3000*
Nominal Speed	[rpm]	2844	1764	*2965*
Number of Stator Slot		24	36	*36*
Number of Rotor Slot		18	28	*40*
Air-Gap Flux Density	[Tesla]	0.68	0.726	*0.65*
Stator Tooth Flux Density	[Tesla]	1.66	1.45	*1*
Rotor Tooth Flux Density	[Tesla]	1.69	1.6	*0.92*
Stator Conductor Current Density	[A/mm^2]	3.49	4.35	*3*
Rotor Bar Current Density	[A/mm^2]	4.0	4.0	*3.05*
Shaft Diameter	[mm]	28	35	*55*
Stator Slot Geometry		Round	Round	*Round*
Rotor Slot Geometry		*Round*	*Egg-Shaped*	*DoubleCage*

4. Design Results

Table-2.

Comparison of motor parameters

Parameters	Symbol	M 1 Calculation	**M 1 Measurement**	M 2 Calculation	**M 2 Measurement**	M 3 Calculation	**M 3 Measurement**
Stator out diameter	d_{out} *[mm]*	152.58	150	179.67	180	341.84	340
Air-Gap length	*g [mm]*	0.31	0.3	0.34	0.35	0.892	0.9
Flux density	*[T]*	0.0077	0.0081	0.0061	0.0058	0.0388	0.0415
Num. of conductor per slot	o_{ss} *[piece]*	40	42	36	32	18	20
St. slot mouth openness	b_{os} *[mm]*	2.5	2.5	2,2	2.2	2.7	2.7
St. slot wedge height	h_w *[mm]*	1.0	1.0	1.0	1.0	1.0	1.0
St. tooth width	B_{ts} *[mm]*	4.64	4.84	5.1	4.75	6.46	6.7
St. slot bottom width	b_{s1} *[mm]*	6.46	6.5	4.97	5.42	10.52	11
St. slot up width	b_{s2} *[mm]*	10.82	9.88	8.55	9.16	15.63	15.06
Rt. slot mouth height	h_{or} *[mm]*	0.5	0.5	0.5	0.5	2.2	2.25
Rt. tooth width	b_{tr} *[mm]*	6.03	6.1	5.9	5.88	5.76	5.6
Rt. slot height	h_r *[mm]*	13.37	13.5	18.18	20	20.57	20.45
Rt. back iron height	h_{cr} *[mm]*	7.97	6.8	15.46	13.4	22.84	21.3

For all three motors, some of the construction values are given in Table-2 in comparison with the data given by the manufacturer.

Calculation: Values obtained as a result of design in computer software.

Measurement: Values of ELSANAS Electrical Motors A.S.

After comparison of design results and measurement values, it is found that design results are correct with little errors.

5. Calculation of Equivalent Circuit Parameters

5.1. Calculation of Equivalent Circuit Parameters by Using Dimensions

The following formulas are used to calculate equivalent circuit parameters in Fig. 6 by using dimensions of the motor [6].

Stator phase resistance R_1;

$$R_1 = \rho \frac{l w_1}{A_{co} a_1} \tag{13}$$

ρ: resistivity value, *l:* coil lenght, A_{co}: wire cross-section area.

Rotor phase resistance R_2;

$$R_2 = \frac{4m_1}{N_r}(w_1 k_{w1})^2 R_{be} \tag{14}$$

m_1 : number of phase, k_{w1} : stator winding factor, R_{be} : rotor short circuit ring resistance.

Stator leakage reactance X_1 ;

$$X_1 = 2\mu w_1 l \frac{w_1^2}{pq}(\lambda_s + \lambda_{ds} + \lambda_{ec}) \tag{15}$$

λ_s, λ_{ds}, λ_{ec} are respectively values for permeance, short circuit ring permeance and specific geometric permeance, depending on different slot geometries.

Rotor leakage reactance X_2;

$$X_2 = \frac{4m_1}{N_r}(w_1 k_{w1})^2 X_{be} \tag{16}$$

X_{be} *:* rotor short circuit ring leakage reactance.

Magnetization reactance X_m, is calculated as follows depending on the magnetization current I_o.

$$X_m = \sqrt{\left(\frac{V}{I_o}\right)^2 - R_1} - X_1 \tag{17}$$

5.2. Calculating Equivalent Circuit Parameters Using Steady-State Motor Model

The single phase equivalent circuit parameters of the three-phase induction motor shown in Figure-6 can be calculated by no-load and short-circuit tests [14]. The parameters calculated with this method are constant. However, rotor parameters such as R_2 and X_2 change with rotor current frequency [15]. In this case, rotor current is important in double-slotted or deep bar slotted motors. A well known case is that the increase in resistance value of each conductor related to the material with temperature increase. Consequently, parameters vary with temperature variation [16].

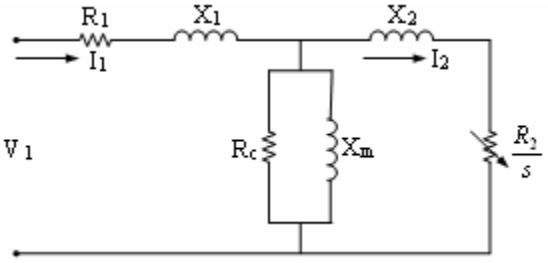

Figure-6. Single phase equivalent circuit of three phase induction motor

Some formulas used in the steady state method are given below [5].

Stator phase resistance R_1 for star connection;

(18) $$R_1 = \frac{1.05 V_{dc}}{2 I_{dc}}$$

Equivalent total resistance R_{kd} ;

(19) $$R_{kd} = \frac{P_k}{I_{kd}^2}$$

Equivalent total impedance Z_{kd} ;

(20) $$Z_{kd} = \frac{V_{kd}}{I_{kd}}$$

Equivalent total reactance X_{kd} ;

(21) $$X_{kd} = \sqrt{Z_{kd}^2 - R_{kd}^2}$$

V_{dc} and I_{dc} : DC voltage and current of motor windings, P_k : Short circuit power, V_{kd} and I_{kd} : Short circuit voltage and current.

Equivalent circuit parameters obtained from use of dimensions and experiments are given in Table-3 for the 3 kW motor in comparison.

Table-3.

Parameters for a motor of 3 kW

Parameters	Computer Program Values	Experimental Values
R_1 [Ω]	1.145	1.141
R_2 [Ω]	0.983	1.057
X_1 [Ω]	1.4	1,56
X_2 [Ω]	2.93	3.09
X_m [Ω]	80.65	78.41
R_c [Ω]	231.44	242

In Figures 7, 8 and 9, the curve 1 represents catalogue values, curve 2 represents construction values obtained from the software, and curve 3 represents experimental data.

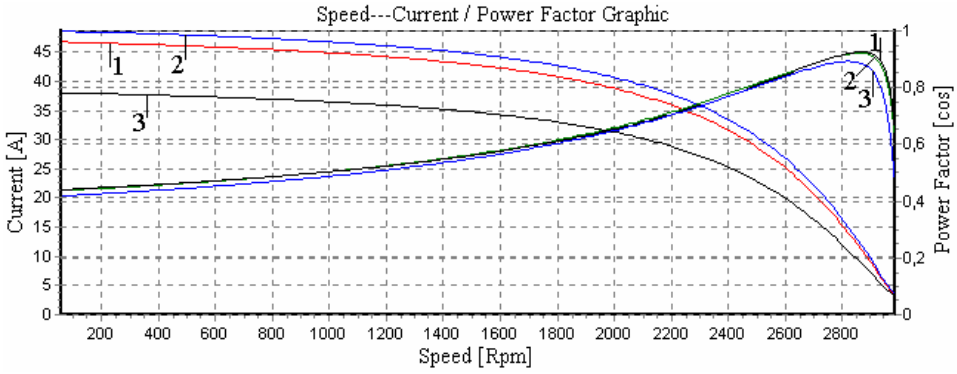

Figure-7. Current-Speed / Power Factor-Speed graphs for a motor of 3 kW

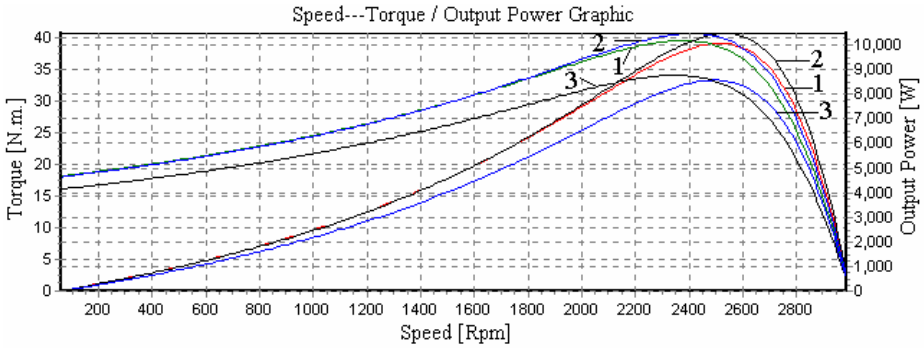

Figure-8. Torque-Speed / Output Power-Speed graphs for a motor of 3 kW

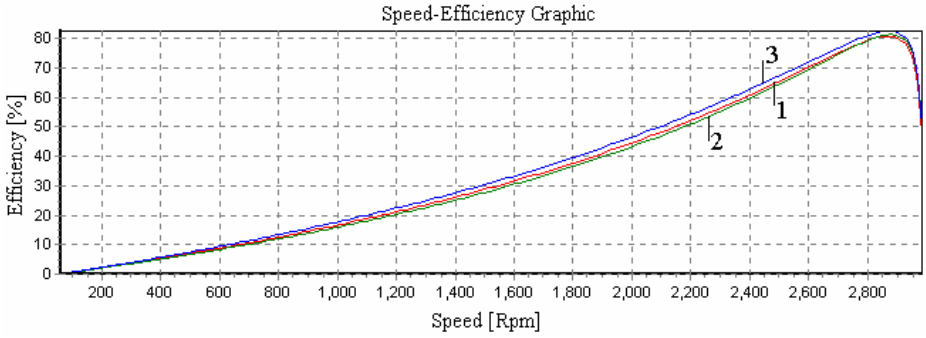

Figure-9. Efficiency-Speed graphs for a motor of 3 kW

6. Conclusion and Recommendations

In this study, two different methods used for induction motor design are described and resulting data is given in comparison as tables and figures. An algorithm is developed for design and motor dimensions are determined using this algorithm. When the results of algorithm data are compared, the error ratios are as follows; for the 3 kW motor 4.54 %, for the 5.5 kW motor 5.45 % and for the 45 kW motor 3.04 %. Considering that these values are errors of total motor design, it is found that they are rather low ratios. The point to be mentioned is that the air gap length value that has great importance for rotational motors is very close to measured values for three motors. This result confirms a homogenous magnetic field over the rotor and stator core and supports correct design results. When the other parameters of the motors given in Table-2 are examined, it can be found that the values support each other. Especially, motor outer diameter and the number of turns to be placed on stator slots that has significant influence on motor loss value are very close to measured values.

When the motor characteristically curves are examined, it can be seen that the obtained curves and the test curves for the 3 kW motor support catalogue values.

In Table-3, that the equivalent circuit parameters of the motors are shown, it can be found that the values resulting from design are very close to test results.

The design is found to be successful according to the values obtained by following these results.

Acknowledgements

Authors want to thank ELSANAS A.S. Motor Factory (Ankara / TURKEY) for giving the opportunity to use their laboratories.

References

[1] S., Palko, T., Jokinen, Optimization of Squirrel Cage İnduction Motors Using Finite Element Method and Genetic Algorithms, Conference Publication No.444 IEEE, EMD 97 1-3, pp 21-25, Sempemter, 1997.

[2] M., R., Feyzi, H., V., Kalankesh, Optimization of Induction Motor Design by Using the Finite Element Method, pp 845-850.

[3] J., Stephan, M., Bodson, J., Chiasson, Real Time Estimation of the Parameters and Fluxes of Induction Motors, IEEE Transactions on Industry Applications, 30(3), pp 746-759, 1994.

[4] V., A., Galinda, X., M., L., Fdez, J., A., D., Pinto, A., P., Coimbra, Parametric Study of Rotor Shape on a Cage Induction Motor, pp 441-446.

[5] A., G., Yetgin, Induction Motor Design, Dumlupınar Universitesi Elektrik-Elektronik Mühendisliği Bölüm Semineri, Mayıs 2003.

[6] I., Boldea, S., A., Nasar, The Induction Machine Handbook, CRC Pres LLC, Washington, D.C., 2002, pp 133-159.

[7] O., Gürdal, Electric Machine Design, 1.Baskı, Atlas Yayın Dağıtım, 2001, ss 97-129.

[8] D., Lindermeyer, H., W., Dommel, A., Moshref, P., Kundur, An Induction Motor Parameter Estimation Method, Electrical Power and Energy Systems 23, pp 251-262, 2001.

[9] J., R., Willis, G., J., Brock, J., S., Edmonds, Derivation of Induction Motor Models from Standstill Frequency Response Test, IEEE Transactions on Power Energy Conversion, 4 (4), pp 608-615, 1989.

[10] B., K., Johnson, J., R., Willis, Tailoring Induction Motor Analytical Models to fit Known Motor Performance Characteristics and Satisfy Particular Study Needs, IEEE Transactions on Power Systems, 6(3), pp 965-969, 1991.

[11] P., Ju, E., Handschin, Z., N., Wei, U., Schluecking, Sequential Parameter Estimation of a Simplified Induction Motor Load Model, IEEE Transactions on Power Energy Conversion, 11(1), pp 319-324, 1996.

[12] R., Belmans, Magnetic Field Analysis in Squirrel Cage Induction Motors, IEEE Transactions on Magnetics, 28 (2), pp 1367-1370, 1992.

[13] D., Dolinar, G., Stumberger, B., Grear, Calculation of the Linear Induction Motor Model Parameters Using Finite Elements, IEEE Transactions on Magnetics, 34 (5), pp 3640-3643, 1998.

[14] C., Grantham, D., Seyoum, D., Indyk, D., Mckinnon, Calculation of the Parameters and Parameter Variations of an Induction Motor and the Effect of Measurement Error.

[15] E., J., Brown, C., Grantham, Determination of The Parameters and Parameter Variations of a 3-Phase Induction Motor Having a Current Displacement Rotor, Proc. IEEE, 122 , No.9, pp 919-921, 1975.

[16] C., Grantham, H., Y., Tabatabaei, Rapid Parameter Determination for use in the Control High Performance Induction Motor Drives, IEEE 1999 International Conference on Power Electronics and Drive Systems, PEDS'99, Hong Kong, pp 267-272, July 1999.

[17] A., I., Çanakoğlu, A., G., Yetgin, 2003, Calculation of Slot Leakage Inductance for Induction Motor, D. P. U., Fen Bilimleri Enstitüsü Dergisi, Eylül 2003, Sayı 4, ss 175-185, Kütahya.

A. Gökhan Yetgin - *Ph.D. Student, Faculty of Engineering, Sakarya University, Dept. of Elc.-Elt. Eng., Campus of Esentepe, 54187, Adapazarı, TURKEY.*
e mail: agyetgin@sakarya.edu.tr

A. İhsan Çanakoğlu - *Ph.D., Faculty of Engineering, Dumlupınar University, Dept. of Elc.-Elt. Eng., Campus of Esentepe, 43100, Kütahya, TURKEY.*
e mail: canakoglu@sakarya.edu.tr

K. Nur Bekiroğlu - *Ph.D., Yildiz Technical University, Faculty of Electrical and Electronics, Department of Electrical Engineering, Istanbul, TURKEY.*
e mail: nbekir@yildiz.edu.tr

Sibel Zorlu - *Ph.D., Yildiz Technical University, Faculty of Electrical and Electronics, Department of Electrical Engineering, Istanbul, TURKEY.*
e mail: zorlu@yildiz.edu.tr

Influence of equivalent circuit parameters of the induction machine on its energy characteristics

Pencho Vladimirov, Deshka Markova, Dimitar Spirov

Abstract: *Mathematical methods have been developed for defining the electric losses in the stator and rotor windings, efficiency, the slip which ensures maximum efficiency, maximum efficiency, power factor and energy efficiency, by means of the space vector. Through the design of experiment method the adequacy of the models obtained has been studied, as well as the influence of the induction machine parameters upon the above mentioned target functions.*

The developed models enable the research and optimization of the energy efficiency of the induction machines and drives.

Keywords: *induction machine parameters, energy characteristics, space vectors, design of experiment, polynomial models*

Introduction

Researches show that the greatest consumers of the energy, which is produced in the world, are the electric motors, which transform 60-65% of this energy. Due to their well-known advantages, the asynchronous motors have the widest application – specialists think that these are 80-90% of all motors used. The limited energy resources and the continuously increasing price of energy determine the significance of the modern researches related to the definition and improvement of the energy parameters of the electric motors and drives. The improvement of the energetics of the electric motors, the electric drive systems and the mechanisms and machines as a whole is expressed mostly in reduction of the exploitation consumption of energy.

A method of designing three-phase asynchronous electric motors with low power, in which criteria for optimal parameters are developed and used, such as maximum efficiency, maximum energy efficiency, etc., is developed in [1].

A method for calculation of the efficiency of the systems for electric driving of mechanisms with cycle action is presented in [2].

The energetics of the electric drives for production mechanisms is studied in [3], wherein the factors influencing the energy consumption and the ways to reduce it, have been analyzed. Methods, algorithms and models have been developed for defining the power of the losses and the power, which is exchanged with the electricity grid, by means of unadjustable and adjustable in various ways asynchronous electric drives. A method has been presented for defining and optimizing the energy per cycle, and the average annual energy consumption. Systems for electric driving with minimum energy consumption have been developed.

The object of this work is to develop mathematical models for defining the electric losses in the stator and rotor windings, the efficiency, the slip, which ensures maximum efficiency, the maximum efficiency, the power factor and the energy efficiency, by using the space vectors in relative units. By means of the design of experiment method the influence of the induction machine parameters upon the above mentioned target functions for general purpose asynchronous motors will be investigated.

Mathematical models

In view of the possibility to study the energy characteristics of the induction machines in both dynamic and steady-state modes, it is convenient to use the differential equations for the space vectors. The mathematical models are developed and the studies are performed on the base of the general assumptions [4], without considering the core losses.

The equations of the voltages of the induction machine in a coordinate system which rotates with arbitrary speed are:

$$u_s = R_s i_s + \frac{d\psi_s}{dt} + j\omega_k \psi_s ,$$

$$0 = R_r i_r + \frac{d\psi_r}{dt} + (\omega_k - \omega_r)\psi_r ,$$

$$\psi_s = L_s i_s + L_m i_r ,$$

$$\psi_r = L_m i_s + L_r i_r ,$$

$$\psi_m = L_m (i_s + i_r),$$

$$\omega_{sl} = \omega_k - \omega_r ,$$

where ω_k, ω_r and ω_{sl} are the electrical angular speeds of the coordinate system, the rotor, and the slip, respectively.

In order to obtain the complex equations describing the steady operation modes of the induction machine from the differential equations of the induction machine we have to replace the operator of the differentiating $\frac{d}{dt}$ with $j\omega$ [4].

Upon selecting $\omega_k = 0$ we make as transformation of the variables to the coordinate system α, β, fixedly connected to the stator of the machine. In result:

$$\begin{aligned}
&\dot{U}_s = R_s\dot{I}_s + j\omega_s\left(L_s\dot{I}_s + L_m\dot{I}_r\right) = \\
&= R_s\dot{I}_s + jX_s\dot{I}_s + jX_m\dot{I}_r \\
&0 = R_r\dot{I}_r + j\left(\omega_s - \omega_r\right)\left(L_m\dot{I}_s + L_r\dot{I}_r\right) = \\
&= R_r\dot{I}_r + j\omega_s s\left(L_m\dot{I}_s + L_r\dot{I}_r\right) \\
&0 = \frac{R_r}{s}\dot{I}_r + jX_m\dot{I}_s + jX_r\dot{I}_r
\end{aligned} \tag{1}$$

where: $X_s = \omega_s L_s$ is the full inductive resistance of the stator phase;

- $X_r = \omega_s L_r$ is the full inductive resistance of the rotor phase;

- $X_m = \omega_s L_m$ inductive resistance of mutual induction for one rotor or stator phase.

The space vectors $\dot{U}_s$, $\dot{I}_s$ and $\dot{I}_r$ remain variables, but they have the same circular frequency, equal to the circular frequency of the power supply ω_s of the stator windings.

Upon selecting $\omega_k = \omega_r$ we perform a transformation of the variables to the coordinate system d, q, fixedly connected to the rotor of the machine. In result we obtain voltage equations equal to those from (1). The space vectors $\dot{U}_s$, $\dot{I}_s$ and $\dot{I}_r$ remain variables, but they have the same circular frequency, equal to the circular frequency ω_r, i.e. the frequency of the rotor currents.

Upon selecting $\omega_k = \omega_s$ we perform a transformation of the variables to the coordinate system x, y, which rotates with synchronous angular speed ω_s of the machine field relative to the stator. In result we obtain voltage equations equal to those from (1). The space vectors $\dot{U}_s$, $\dot{I}_s$ and $\dot{I}_r$ remain constant quantities. In many cases of researching the dynamics of the AC-machines, the possibility to replace the sine variables with constant quantities significantly simplifies the modeling, the analysis of the results from the modeling, and the control of the electric drives.

In the development of the mathematical models we will use coordinate system x, y with the complex equations (1), which have been received for it and which describe the steady operation mode of the induction machine. It is necessary to obtain expressions for the components of the electric losses in the stator windings $p_{e\pi 1}$ and in the rotor windings $p_{e\pi 2}$ in steady operation modes by means of the space vectors.

The expression for the electric losses in the stator winding in dynamic and steady modes is:

$$p_{e\pi 1} = R_s\left(i_{sx}^2 + i_{sy}^2\right) = R_s I_s^2, \tag{2}$$

In a similar way we find the electric losses in the rotor winding:

$$p_{e\pi 2} = R_r\left(i_{rx}^2 + i_{ry}^2\right) = R_r I_r^2, \tag{3}$$

Using the Cramer formulas from (1) we define i_{sx}, i_{sy}, i_{rx}, i_{ry}, I_s, I_r, and after substitution and transformation we obtain:

$$p_{e\pi 1} = \frac{U_s^2 R_s\left(\left(\frac{R_r}{s}\right)^2 + X_r^2\right)}{\left(R_s\frac{R_r}{s} - X_s X_r + X_m^2\right)^2 + \left(R_s X_r + \frac{R_r}{s}X_s\right)^2}, \tag{4}$$

$$p_{e\pi 2} = \frac{U_s^2 X_s^2 R_r}{\left(R_s\frac{R_r}{s} - X_s X_r + X_m^2\right)^2 + \left(R_s X_r + \frac{R_r}{s}X_s\right)^2}, \tag{5}$$

where $U_s = \sqrt{\frac{3}{2}}U_{\phi m} = \sqrt{3}U_{\phi}$ is the space vector of the stator voltage with zero initial phase.

In the researches, it is convenient to represent the components of the losses in relative units – relative to the base power $P_{б} = 3U_{н}I_{н} = \frac{3}{2}u_{б}i_{б} = \frac{3}{2}z_{б}i_{б}^2 = \frac{3}{2}\frac{u_{б}^2}{z_{б}}$.

After substitution and transformations the expressions assume the following form:

$$p_{e\pi 1}^{*} = \frac{p_{e\pi 1}}{P_{б}} = \frac{R_s^{*}\left(\left(\frac{R_r^{*}}{s}\right)^2 + X_r^{*2}\right)}{\left(R_s^{*}\frac{R_r^{*}}{s} - X_s^{*}X_r^{*} + X_m^{*2}\right)^2 + \left(R_s^{*}X_r^{*} + \frac{R_r^{*}}{s}X_s^{*}\right)^2}, \tag{6}$$

$$p_{e\pi 2}^{*} = \frac{p_{e\pi 2}}{P_{б}} = \frac{X_m^{*2}R_r^{*}}{\left(R_s^{*}\frac{R_r^{*}}{s} - X_s^{*}X_r^{*} + X_m^{*2}\right)^2 + \left(R_s^{*}X_r^{*} + \frac{R_r^{*}}{s}X_s^{*}\right)^2}. \tag{7}$$

The check via calculations show that the results for p_{el1} and p_{el2}, obtained with the help of the above mentioned mathematical models, are equal to the results, obtained by using the Π-equivalent circuit [1].

It is known, that the full mechanical power of the motor shaft is expressed with the equation:

$$P'_R = P_\delta(1-s) = I_r^2 \frac{R_r}{s}(1-s). \quad (8)$$

The active power which is fed to the motor is defined with the expression:

$$P_1 = p_{el1} + P_\delta = I_s^2 R_s + I_r^2 \frac{R_r}{s}. \quad (9)$$

The efficiency referring to the full mechanical power of the motor shaft will be:

$$\eta_R = \frac{P'_R}{P_1} = \frac{I_r^2 \frac{R_r}{s}(1-s)}{I_s^2 R_s + I_r^2 \frac{R_r}{s}}. \quad (10)$$

After replacing with the expressions for I_s and I_r, and after transformation we receive:

$$\eta_R = \frac{X_m^2 \frac{R_r}{s}(1-s)}{R_s\left(\left(\frac{R_r}{s}\right)^2 + X_r^2\right) + \frac{R_r}{s}X_m^2}. \quad (11)$$

The expression obtained (11) η_R is the same as the one, obtained for η_R with the usage of the Π-shaped equivalent circuit in [1]. The maximum value of the efficiency η_R regarding the quantity $\frac{R_r}{s}$ is obtained from the equation $(\eta_R)' = 0$. After a series of transformations the following expression [1] is obtained:

$$\left(\frac{R_r}{s}\right)^2 - 2R_r\frac{R_r}{s} - \left(X_m^2\frac{R_r}{R_s} + X_r^2\right) = 0. \quad (12)$$

Bearing in mind that from the two solutions of equation (12) for the motor operation mode the sign "+" is meaningful, then the following expression is obtained [1]:

$$\frac{R_r}{s} = R_r + \sqrt{R_r^2 + X_m^2\frac{R_r}{R_s} + X_r^2}. \quad (13)$$

By eliminating R_r, the expression (13) acquires the form:

$$s_R = \frac{1}{1+\sqrt{1+\left(\frac{X_r}{R_r}\right)^2 + \frac{X_m^2}{R_s R_r}}}, \quad (14)$$

where s_R is the slip, which renders the maximum value of the efficiency η_R.

By multiplying the numerator and the denominator of the under-square quantities with z_δ^2, the following expression for the slip s_R is obtained:

$$s_R = \frac{1}{1+\sqrt{1+\left(\frac{X_r^*}{R_r^*}\right)^2 + \frac{X_m^{*2}}{R_s^* R_r^*}}}. \quad (15)$$

In order to obtain the expression for $\eta_{R\max}$ the expression (15) have to be substituted in (11). After substitution and transformation the following expression is obtained [1].

$$\eta_{R\max} = \frac{1}{\frac{2R_s R_r}{X_m^2}\frac{1}{s}+1}. \quad (16)$$

By multiplying the numerator and the denominator of the fraction expression in (16) with z_δ^2, for the efficiency $\eta_{R\max}$ the next expression is obtained:

$$\eta_{R\max} = \frac{1}{\frac{2R_s^* R_r^*}{X_m^{*2}}\frac{1}{s}+1}. \quad (17)$$

The power factor $\cos\varphi$ is defined by the expression:

$$\cos\varphi = \frac{P}{S} = \frac{p_{el1} + P_\delta}{U_s I_s} = \frac{I_s^2 R_s + I_r^2 \frac{R_r}{s}}{U_s I_s}.$$

After replacement with the expressions for I_s and I_r, and after transformation we receive expression (18). By multiplying the numerator and the denominator of (18) with z_δ^3, the expression for the power factor $\cos\varphi$ changes in expression (19). Very often, along with the expressions for the efficiency and $\cos\varphi$ their product is used too, which is called energy efficiency η_e. In the case, when the efficiency is defined through the full mechanical power of the motor shaft $\eta_e = \eta_R \cos\varphi$. After replacing with the expressions (11) for η_R and with (19) for $\cos\varphi$ we receive the expression (20).

(18) $$\cos\varphi = \frac{\left(\left(\frac{R_r}{s}\right)^2 + X_r^2\right)R_s + X_m^2\frac{R_r}{s}}{\sqrt{\left(\frac{R_r}{s}\right)^2 + X_r^2}\sqrt{\left(R_s\frac{R_r}{s} - X_sX_r + X_m^2\right)^2 + \left(R_sX_r + \frac{R_r}{s}X_s\right)^2}},$$

(19) $$\cos\varphi = \frac{\left(\left(\frac{R_r^*}{s}\right)^2 + X_r^{*2}\right)R_s^* + X_m^{*2}\frac{R_r^*}{s}}{\sqrt{\left(\frac{R_r^*}{s}\right)^2 + X_r^{*2}}\sqrt{\left(R_s^*\frac{R_r^*}{s} - X_s^*X_r^* + X_m^{*2}\right)^2 + \left(R_s^*X_r^* + \frac{R_r^*}{s}X_s^*\right)^2}},$$

(20) $$\eta_e = \eta_R\cos\varphi = \frac{X_m^{*2}\frac{R_r^*}{s}(1-s)}{\sqrt{\left(\frac{R_r^*}{s}\right)^2 + X_r^{*2}}\sqrt{\left(R_s^*\frac{R_r^*}{s} - X_s^*X_r^* + X_m^{*2}\right)^2 + \left(R_s^*X_r^* + \frac{R_r^*}{s}X_s^*\right)^2}}.$$

Results

In the study of a certain electromechanical object it is observed, that some of the qualities, properties or parameters, interesting for us, depend on several quantities $X_1, X_2, ...X_n$, that is, there is a function of several variables $Y = f(X_1, X_2, ..., X_n)$. To obtain more information, we set a certain combination of influences X, for which we receive the relevant value of Y. In most cases we do not know the type of the function, therefore the power series expansion is considered:

(21) $$Y = B_0 + B_1X_1 + ... + B_nX_n + ... + B_{12}X_1X_2 + ... + B_{n-1,n}X_{n-1}X_n + B_{11}X_1^2 + ... + B_{nn}X_n^2,$$

The quantity Y is called the target function, and the variables $X_1, X_2, ...X_n$, whose influence we investigate, are called factors. When assigning values to the factors, a value for the target function is obtained. In the common cases the factors are quantities with sizes, as their numerical values may considerably differ one from another. Therefore, it is not operated with the actual factor values, but with the so-called encoded factor values, obtained by means of linear transformation [5]. For the encoding, an output area of the experiment shall be selected, i.e., upper and lower limits must be set for each factor - $X_{i\min}$ and $X_{i\max}$. A new scale is selected for each factor, so that the value of $X_{i\min}$ would correspond to -1, and of $X_{i\max}$ to +1.

The expression of Y, obtained in a polynomial form, represents a secondary model of the actual function. The degree of the model obtained may be different, depending on the requirements for simplicity and adequacy of the model. On this base, a second degree plan is selected – an orthogonal composition B-plan.

It is necessary to find through the design of experiment method more simple and convenient polynomial expressions for the influence of the parameters of the equivalent circuit of the induction machine upon the electric losses in the stator windings $p_{e\pi1}^*$, the electric losses in the rotor windings $p_{e\pi2}^*$, the efficiency. η_R, the slip s_R, which ensures maximum η_R, the efficiency $\eta_{R\max}$, the power factor $\cos\varphi$, and the energy efficiency η_e.

The parameters of the equivalent circuit of the common induction machines in relative units vary within the following limits: $R_s^* = 0{,}01 \div 0{,}08$; $R_r^* = 0{,}02 \div 0{,}08$; $X_{\sigma s}^* = 0{,}06 \div 0{,}14$; $X_{\sigma r}^* = 0{,}06 \div 0{,}16$; $X_m^* = 1{,}2 \div 4{,}0$.

The range of variation of the factors in actual and encoded forms is given in Table 1.

Table 1. Range of variation of the factors in actual and encoded forms

Factor	I		II		III		IV		V	
Level	R_s^*	x_1	R_r^*	x_2	$X_{\sigma s}^*$	x_3	$X_{\sigma r}^*$	x_4	X_m^*	x_5
Lower	0.01	-1	0.02	-1	0.06	-1	0.06	-1	1.2	-1
Middle	0.045	0	0.05	0	0.1	0	0.11	0	2.6	0
Upper	0.08	+1	0.08	+1	0.14	+1	0.16	+1	4	+1

All possible combinations of the factors can be represented as a table, called plan of experiment. This table contains the value of the target function for the relevant combination of the factors and with its help the polynomial coefficients are calculated.

The degree of proximity of the obtained approximating expression to the actual functional dependence of the researched function upon the relevant factors is evaluated with the difference between the actual value and the value which is calculated with the approximating expression for a certain experiment. A basic element of the criteria is so-called residual sum of the quadratic differences [5]:

$$S = \sum_{u=1}^{N} \left(Y_u - \overline{Y}_u\right)^2$$

By means of this sum, the adequacy dispersion is calculated:

$$\sigma_{a\partial}^2 = \frac{S}{f_{a\partial}},$$

where $f_{a\partial} = N - l$, N is the number of freedom degrees, and l is the number of the coefficients being defined. In the research of electromechanical objects it is convenient to use the following widely applied criterion for the adequacy of the approximating expression obtained [5]:

$$\delta = \sigma_{a\partial} \le m,$$

where $\sigma_{a\partial}$ is the adequacy dispersion, and m is the admissible value for the accuracy of reproducibility of the function.

For the polynomial model of $p_{e\pi 1}^*$, $p_{e\pi 2}^*$, η_R, η_R s_R,. $\eta_{R\max}$, $\cos\varphi$ и η_e depending on the parameters of the equivalent circuit of the induction machine, for δ it is obtained $\delta_{pel1} = 0{,}096$, $\delta_{pel2} = 0{,}132$, $\delta_{\eta R} = 6{,}574.10^{-3}$, $\delta_{sR} = 0{,}11$, $\delta_{\eta R\max} = 4{,}556.10^{-3}$, $\delta_{\cos\varphi} = 4{,}418.10^{-3}$ and $\delta_{\eta e} = 8{,}237.10^{-3}$, respectively.

The mathematical dependencies obtained as a result of the experiment may be considered as an instrument for the research of the energy characteristics of the asynchronous electric motor. The polynomials $p_{e\pi 1}^*$, $p_{e\pi 2}^*$, η_R, s_R, $\eta_{R\max}$, $\cos\varphi$, η_e = $f(R_s^*, R_r^*, X_{\sigma s}^*, X_{\sigma r}^* X_m^*)$ enable, in particular, the solution of the following tasks [5]:

to precisely evaluate the influence of the parameters on the energy characteristics;

to define the "existence zones" for certain values of the target functions;

to investigate the obtained functional dependencies for the determination of the optimal parameters, which ensure the necessary energy characteristics;

The B-plan of second degree confirms the direction and the degree of influence of the factors upon the function being researched, and the coefficients before the quadratic members take into account the non-linearity of the function.

When exploring the influence of the parameters of the equivalent circuit of the induction machine upon $p_{e\pi 1}^*$, $p_{e\pi 2}^*$, η_R, η_R s_R,. $\eta_{R\max}$, $\cos\varphi$ and η_e for the mechanism parameters we assume load torque M* = 1 and coefficient of inertia FI = 2, respectively.

The investigation about the influence of the equivalent circuit parameters of the induction machine upon its energy characteristics have been carried out for 4 constant values of the slip in the operation part of its mechanical characteristic: $s = 0{,}02$, $s = 0{,}04$, $s = 0{,}06$ and $s = 0{,}08$.

The influence of the equivalent circuit parameters upon the target functions for the case when s = 0,06 = *const* is analysed below.

For the polynomial model for $p_{e\pi 1}^*$ the expression (22) is obtained. From the analysis of the polynomial model for $p_{e\pi 1}^*$ for s = 0,06 it is found that: the increase in R_s^* and R_r^* results in significant linear rise of $p_{e\pi 1}^*$; the increase in $X_{\sigma s}^*$ causes an enhancement of $p_{e\pi 1}^*$, reaching maximum value at $X_{\sigma s}^* \approx 0{,}1$; the increase in $X_{\sigma r}^*$ leads to rise of $p_{e\pi 1}^*$, reaching maximum value at $X_{\sigma r}^* \approx 0{,}14$; the increase in X_m^*

results to decrease of p^*_{en1}, reaching minimal value at $X^*_m \approx 3{,}3$.

For the polynomial model for p^*_{en2} the expression (23) is obtained. From the analysis of the polynomial model for p^*_{en2} for s = 0,06 it is found that: the increase in R^*_s results in significant linear decrease of p^*_{en2}; the increase in R^*_r causes a considerable linear enhancement of p^*_{en2}; the increase of X^*_{os} leads to rise of p^*_{en2}, reaching maximum value at $X^*_{os} \approx 0{,}1$; the increase of X^*_{or} results in increase of p^*_{en2} and reaching maximum value at $X^*_{or} \approx 0{,}14$; the increase of X^*_m leads to decrease of p^*_{en1}, reaching minimum value at $X^*_m \approx 3{,}3$.

For the polynomial model for s_R the expression (24) is. From the analysis of the polynomial model for s_R for s = 0,06 it is found that: the increase in R^*_s and R^*_r results in significant nearly linear increase of s_R; s_R does not nearly depend on X^*_{os}; the increase in X^*_{or} leads to rise of s_R reaching maximum value at $X^*_{or} \approx 0{,}1$; the increase of X^*_m results in significant nonlinear decrease of s_R.

For the polynomial model for $\eta_{R\max}$ the expression (25) is obtained. From the analysis of the polynomial model for $\eta_{R\max}$ for s = 0,06 it is found that: the increase in R^*_s and R^*_r results in significant nearly linear decrease of $\eta_{R\max}$; $\eta_{R\max}$ does not nearly depend on X^*_{os}; the increase in X^*_{or} leads to decrease of $\eta_{R\max}$, reaching minimum value at $X^*_{or} \approx 0{,}12$; and the increase in X^*_m causes significant nonlinear growth of $\eta_{R\max}$.

For the polynomial model for $\cos\varphi$ the expression (26) is obtained. From the analysis of the polynomial model for $\cos\varphi$ for s = 0,06 it is found that: the increase in R^*_s results in slight rise of $\cos\varphi$, reaching maximum value at $R^*_s \approx 0{,}05$; the increase in R^*_r causes a considerable linear growth of $\cos\varphi$, reaching $\cos\varphi = 1$; the increase in X^*_{os} leads to slight nonlinear increase of $\cos\varphi$, reaching maximum value at $X^*_{os} \approx 0{,}12$; the increase in X^*_{or} results in significant nearly linear decrease of $\cos\varphi$; the increase in X^*_m leads to insignificant nonlinear decrease of $\cos\varphi$.

For the polynomial model for η_e the expression (27) is obtained. From the analysis of the polynomial model for η_e for s = 0,06 it is found that: the increase in R^*_s causes a considerable linear enhancement of η_e; the increase in R^*_r results to a considerable rise of η_e, reaching maximum value at $R^*_r \approx 0{,}065$; the increase in X^*_{os} leads to slight growth of η_e, reaching maximum value at $X^*_{os} \approx 0{,}13$; the increase in X^*_{or} results in significant nearly linear decrease of η_e; and the increase in X^*_m leads to considerable rise of η_e reaching maximum value at $X^*_m \approx 3{,}5$.

$$
\begin{aligned}
(22)\quad & p_{en1}{}^* = 4{,}562.10^{-3} + 0{,}339R_s{}^* + 0{,}295R_r{}^* + 1{,}509.10^{-2}X_{os}{}^* + 1{,}479.10^{-2}X_{or}{}^* - 1{,}555.10^{-2}X_m{}^* + \\
& + 3{,}3R_s{}^*R_r{}^* + 3{,}515.10^{-3}R_s{}^*X_{os}{}^* + 7.054.10^{-2}R_s{}^*X_{or}{}^* - 0{,}127R_s{}^*X_m{}^* - 1{,}227.10^{-2}R_r{}^*X_{os}{}^* + \\
& + 1{,}391.10^{-2}R_r{}^*X_{or}{}^* - 0{,}109R_r{}^*X_m{}^* + 1{,}051.10^{-2}X_{os}{}^*X_{or}{}^* - 1{,}096.10^{-4}X_{os}{}^*X_m{}^* - 2{,}314.10^{-3}X_{or}{}^*X_m{}^* - \\
& - 0{,}105R_s^{*2} - 0{,}14R_r^{*2} - 7{,}677.10^{-2}X_{os}^{*2} - 4{,}814.10^{-2}X_{or}^{*2} + 4{,}05.10^{-3}X_m^{*2}
\end{aligned}
$$

$$
\begin{aligned}
(23)\quad & p_{en2}{}^* = 2{,}899.10^{-2} - 2{,}666.10^{-2}R_s{}^* + 0{,}904R_r{}^* + 8{,}91.10^{-3}X_{os}{}^* + 8{,}707.10^{-3}X_{or}{}^* - 2{,}976.10^{-2}X_m{}^* - \\
& - 0{,}721R_s{}^*R_r{}^* + 3{,}439.10^{-4}R_s{}^*X_{os}{}^* - 6{,}464.10^{-3}R_s{}^*X_{or}{}^* + 1{,}744.10^{-2}R_s{}^*X_m{}^* - 2{,}353.10^{-2}R_r{}^*X_{os}{}^* + \\
& + 3{,}965.10^{-2}R_r{}^*X_{or}{}^* - 0{,}203R_r{}^*X_m{}^* + 2{,}141.10^{-2}X_{os}{}^*X_{or}{}^* - 1{,}679.10^{-4}X_{os}{}^*X_m{}^* - 1{,}504.10^{-3}X_{or}{}^*X_m{}^* - \\
& - 6{,}089.10^{-2}R_s^{*2} - 0{,}117R_r^{*2} - 4{,}698.10^{-2}X_{os}^{*2} - 3.10^{-2}X_{or}^{*2} + 5{,}522.10^{-3}X_m^{*2}
\end{aligned}
$$

(24)
$$s_R = 1{,}265.10^{-2} + 0{,}546R_s^* + 0{,}443R_r^* + 3{,}178.10^{-2}X_{\sigma s}^* + 1{,}883.10^{-2}X_{\sigma r}^* - 1{,}683.10^{-2}X_m^* + \\ + 3{,}008R_s^*R_r^* - 4{,}68.10^{-2}R_s^*X_{\sigma r}^* - 0{,}102R_s^*X_m^* + 2{,}07.10^{-2}R_r^*X_{\sigma r}^* - 8{,}518.10^{-2}R_r^*X_m^* + \\ + 1{,}215.10^{-3}X_{\sigma r}^*X_m^* - 1{,}664R_s^{*2} - 1{,}325R_r^{*2} - 0{,}159X_{\sigma s}^{*2} - 0{,}103X_{\sigma r}^{*2} + 3{,}384.10^{-3}X_m^{*2}$$

(25)
$$\eta_{R\max} = 0{,}975 - 1{,}108R_s^* - 0{,}881R_r^* - 5{,}851.10^{-2}X_{\sigma s}^* - 4{,}808.10^{-2}X_{\sigma r}^* + 3{,}396.10^{-2}X_m^* - \\ - 5{,}867R_s^*R_r^* - 8{,}801.10^{-2}R_s^*X_{\sigma r}^* + 0{,}213R_s^*X_m^* + 4{,}343.10^{-2}R_r^*X_r^* + 0{,}166R_r^*X_m^* + \\ + 2{,}287.10^{-3}X_{\sigma r}^*X_m^* + 3{,}284R_s^{*2} + 2{,}594R_r^{*2} + 0{,}293X_{\sigma s}^{*2} + 0{,}185X_{\sigma r}^{*2} - 6{,}9.10^{-3}X_m^{*2}$$

(26)
$$\cos\varphi = 0{,}998 + 5{,}156.10^{-2}R_s^* + 1{,}534R_r^* + 0{,}109X_{\sigma s}^* - 0{,}801X_{\sigma r}^* - 2{,}708.10^{-3}X_m^* - \\ - 0{,}196R_s^*R_r^* + 3{,}407.10^{-3}R_s^*X_{\sigma s}^* + 0{,}101R_s^*X_{\sigma r}^* - 4{,}169.10^{-3}R_s^*X_m^* - 0{,}622R_r^*X_{\sigma s}^* + \\ + 12{,}68R_r^*X_{\sigma r}^* + 3{,}037.10^{-2}R_r^*X_m^* + 0{,}338X_{\sigma s}^*X_{\sigma r}^* - 7{,}832.10^{-3}X_{\sigma s}^*X_m^* - 2{,}357.10^{-2}X_{\sigma r}^*X_m^* - \\ - 0{,}496R_s^{*2} - 20{,}992R_r^{*2} - 0{,}387X_{\sigma s}^{*2} - 0{,}902X_{\sigma r}^{*2} + 5{,}935.10^{-4}X_m^{*2}$$

(27)
$$\eta_e = 0{,}938 - 0{,}383R_s^* + 1{,}06R_r^* + 9{,}372.10^{-2}X_{\sigma s}^* - 0{,}766X_{\sigma r}^* + 1{,}111.10^{-2}X_m^* - \\ - 5{,}495R_s^*R_r^* - 5{,}702.10^{-3}R_s^*X_{\sigma s}^* + 1{,}109.10^{-2}R_s^*X_{\sigma r}^* + 0{,}163R_s^*X_m^* - 0{,}577R_r^*X_{\sigma s}^* + \\ + 11{,}968R_r^*X_{\sigma r}^* - 0{,}172R_r^*X_m^* + 0{,}31X_{\sigma s}^*X_{\sigma r}^* - 7{,}293.10^{-3}X_{\sigma s}^*X_m^* - 1{,}981.10^{-2}X_{\sigma r}^*X_m^* - \\ - 0{,}394R_s^{*2} - 19{,}669R_r^{*2} - 0{,}319X_{\sigma s}^{*2} - 0{,}824X_{\sigma r}^{*2} - 3{,}473.10^{-3}X_m^{*2}$$

Conclusion

Mathematical methods have been developed for defining the electric losses in the stator and rotor windings, efficiency, the slip which ensures maximum efficiency, maximum efficiency, power factor and energy efficiency, by means of the space vectors in relative units. Through the design of experiment method polynomial methods have been developed for taking into account the influence of the equivalent circuit parameters of the induction machine upon the above mentioned target functions. The adequacy and the operation capacity of the models obtained has been confirmed, and the above mentioned relations have been studied for general purpose asynchronous electric motor. The developed polynomial models enable the research and optimize the energy efficiency of the induction machines and the electric drives.

References

[1] Popadin S. V., S. D. Peltekov, Electric micro-machines, part IV, VMEI-Varna, 1977 (in Bulgarian)

[2] Jordanov S., G. Daskalov, K. Kutryanski , A method to calculate the efficiency of systems for electric driving of mechanisms with cycle action, Electrical Engineering and Electronic 1996, № 9-10, pp. 3-6 (in Bulgarian)

[3] Kutryanski K. P., Energy-saving electric drives of production mechanisms – selection and optimization, dissertation for obtaining PhD degree", Sofia, 1999 (in Bulgarian)

[4] Kopilov I. P., Electrical machines, Moscow, Higher School 2000, p.607 (in Russian)

[5] Ivobotenko B. A. at all, Design of experiment in electromechanics, Moscow, Energy, 1975, p.184 (in Russian)

Pencho Vladimirov *– Assoc. Prof. Dr., Department of Electrical Engineering, Technical University – Gabrovo, 4, Hadgi dimitar str., 5300 Gabrovo, Bulgaria, pvlad@iname.com*

Deshka Markova *– Assoc. Prof. Dr., Department of Electrical Engineering, Technical University – Gabrovo, 4, Hadgi dimitar str., 5300 Gabrovo, Bulgaria, markova@tugab.bg*

Dimitar Spirov *– Ph.D. Student, Department of Electrical Engineering, Technical University – Gabrovo, 4, Hadgi Dimitar str., 5300 Gabrovo, Bulgaria,dimitar_spirov@abv.bg*

Model of the Temperature Regime of a Three-Phase Induction Motor

Ivan Evstaiev and Nicolay Mihailov

Abstract: *The quality protection of a three-phase induction motor is very important. It is necessary to determine the engine condition, to protect it from failure. Powering off the engines without necessity is troubling the technological process. That's why the modeling of the temperature is an important problem when developing software for a specialized electronic device for protection of asynchronous engines. In this article is synthesized a model of the temperature regime of a three-phase induction motor, for use in an electronic protection device. Based on the physical process analysis in the stator and the rotor, an algorithmic model, estimating the temperature regime in accordance with the running and nominal current and the time-current characteristic, is suggested. The synthesized model is designed for electronic devices for protection of small asynchronous engines.*

Keywords: *three-phase induction motor; electronic device; model*

Introduction

The temperature regime of a three-phase induction motor (TIM) is a primary factor, determining the flawless exploitation. That is why the modeling of the temperature of a TIM is an important problem when developing software for a specialized electronic device for protection of asynchronous engines. Sometimes the temperature is being controlled with a sensor installation on the coil. This approach usually creates a lot of problems when using the engine, and also adds delays when heavily loaded, because of the inertness of the sensor, which is sometimes unwanted.

There are articles in which the modeling of the temperature regime described is reduced to modeling of the time-current characteristic of a TIM or to approximation with an aperiodic process [3,2]. The disadvantage in this case is that the temperature is not being used and the device is using empiric criteria. This way also leads to difficult control of the current temperature, when the engine is heavily loaded.

The goal of the publication is to synthesize a model of the temperature regime of a TIM. The model is to be used with electronic devices for protection of small engines.

Basic hypothesis and dependencies of the modeling Instructions for Authors

The variation of the temperature changes of an asynchronous engine shows that when the loading is less than the nominal, the temperature exchange between the coils, the stator and the rotor is good enough. This is quite different when the engine is heavily loaded, especially when starting or in a standstill rotor regime. In such a situation, the coils release a lot of energy, which cannot be absorbed by the body fast enough. That is why the temperature of the coils starts to rise and there is a danger of damage.

These specific features are taken into account when synthesizing the model.

When developing the model, we assume that the TIM is a homogenous body, having some temperature. The variation of the temperature depends on the electricity used of the TIM and on the dependency between the running and the nominal current. This dependency is used to determine how to impact the change of the temperature.

It is also taken into account that with nominal loading and nominal outside conditions, the engine can work for unlimited time. It is assumed that with nominal loading, the temperature rises to the maximum allowed after some time.

When the charge is less than the nominal, the engine temperature is a function of the running and nominal current.

The temperature also depends on the loading. If the loading is equal to the nominal one, after a long period of time, the temperature becomes close to that of shutting down. If it is less than the nominal, the temperature is also less.

With big loadings, the energy is not emitted fast enough from the coils, and they are heated much faster. In this case the temperature changes are being estimated by using the time-current characteristic of the engine. The temperature changes of the engine are calculated so that for a given charge, the engine is supposed to shut down after some time, depending on the time-current characteristic for the given conditions.

Algorithmic model

In block 1 the initial conditions are defined (Fig. 1). In block 2 the running current of the engine is checked – it is compared with the nominal current. It is well- known that the current of the engine is an indicator for its loading. If the running current is greater than the nominal the formulas in block 3 are used. Based on the time-current characteristic of the engine the time left until the engine overheats is calculated. Using this time, the count of the discrete values is determined: the changing of the temperature for a fixed time and the maximum allowed temperature the engine could reach at such loading. This temperature is the maximum possible.

If the running and the nominal current are equal, block 6 comes after block 4. The temperature change for a fixed time is determined using the time-current

characteristic, the time for which the engine is being heated to the maximum temperature. The maximum temperature is also the maximum allowed.

If the running current is lower than the nominal one, the change of the temperature is lowered in proportion with the lowering of the current (block 5). The maximum possible temperature is less than the nominal one – it is in proportion with the loading.

In block 7, 8 and 11 the sign of the temperature change is determined. If the running value of the current is more than that in the previous moment, the sign is positive (block 8). Otherwise it is negative (block 11).

Initial conditions

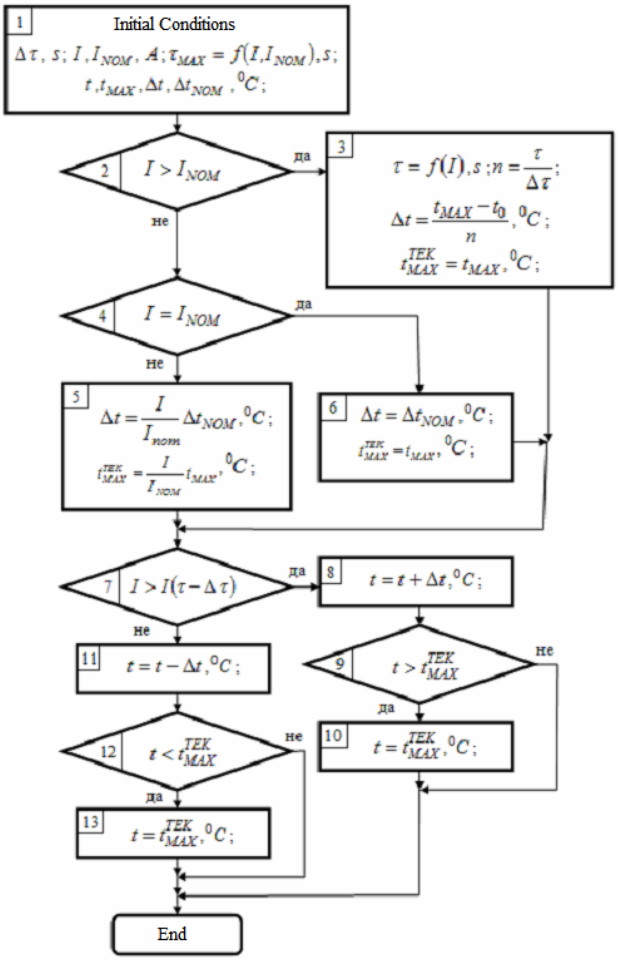

Fig.1.Algorithmic model of the temperature regime of a three-phase induction motor.

Blocks 9, 10, and 12, 13 correct the maximum and the minimum change of the temperature of the engine respectively.

The parameters used in the algorithm are the following: I is the running current of the asynchronous engine, I_{NOM} -the nominal current of the asynchronous engine, $t, t_0, t_{MAX}, \Delta t, \Delta t_{NOM}$ - current, basic, maximum, allowed temperature for time interval $\Delta\tau$ and the temperature change for time $\Delta\tau$ with nominal loading, t_{MAX}^{TEK} - the maximum temperature that can be reached for a specific loading, τ - the current time, $\tau_{MAX} = f(I, I_{NOM})$ - the time-current characteristic of the asynchronous engine, τ_{MAX} - the time needed to reach the maximum allowed temperature of the engine for a specific loading, $\Delta\tau$ - the discretization time.

Main results and conclusions

The physical dependencies determining the temperature regime of a three-phase induction motor are analyzed.

An algorithmic model of the temperature regime of an asynchronous engine for use with electronic device is synthesized.

The synthesized algorithmic model has the ability to adapt constantly to the changes in the loading of the engine, and to simulate its temperature.

References

[1] Minchev D. Automatic Control of Electric Drives. Sofia, Machinery, 1987.

[2] Yakov V., E. Kouzmanov, G. Georgiev. General Structure and Operational Algorithm of Protection device for a 3-phase Asynchronous Engine. Electrical Machinery and Electronics, 1-2. 1999, pp. 22-26.

[3] Fiaher A., et al. Digital Motor Protection with New Thermal Replica of the Rotor Circuit. Engineering&Automation, XIII.1991. 1, pp. 22-25.

Ivan Evstatiev *– Assoc. Professor, PhD, Faculty of Electrical and Electronic Engineering, "Angel Kunchev" University of Rousse, 8 Studenska Str., 7017 Rousse, BULGARIA.*
e-mail: ievstatiev@ecs.ru.acad.bg.
Nicolay Mihailov *– Assoc. Professor, Dr., Faculty of Electrical and Electronic Engineering, "Angel Kunchev" University of Rousse, 8 Studenska Str., 7017 Rousse, BULGARIA.*
e-mail: mihailov@ru.acad.bg.

Applications of Infrared Thermography to Diagnose Electrical Machines

Lyubormir Dimitrov **Velko Naumov**

Abstract. *In the following article have been considered different applications of Infrared Thermography (Thermovision) to diagnose electrical machines. Pointed out are also the advantages of the predictive maintenance of machines with important functions and spheres of effective application of this diagnostic method.*
Examples of usage of thermography to evaluate the technical condition of induction motors have also been given out.
Keywords: *Infrared Thermography, Diagnose, Elecrtical Mashines*

Introduction

Modern systems for technical maintenance of electrical machines are based on methods for pre-evaluation of the technical condition. These are more economy effective compared to planned maintennance methods, when the necessary repair procedures take place on particular periods. It brings more benefits to use such systems rather than off-line methods to determine the technical condition and identify incipient faults in the motor.

A very powerful means for such diagnosis proving the necessity of preventive maintenace is the Infrared Thermography (IR Thermography). In this way, the infrared radiation emitted by the examined motor object is used. The image received after scanning the thermal emissions shows a picture of different temperature distribution in different points or regions allowing conclusions about the technical condition. Currently, there are lots of various modern instrumentation [1] able to save and recall thermal vision files [Fig.1] for further analysis. This is a major advantage during the procedure of machine diagnosis and preventive maintenance.

During measurement surface contact to follow temperature changes of the object is not necessary. Thermography or thermovision is applied in many industrial branches for condition monitoring of motors and different devices.

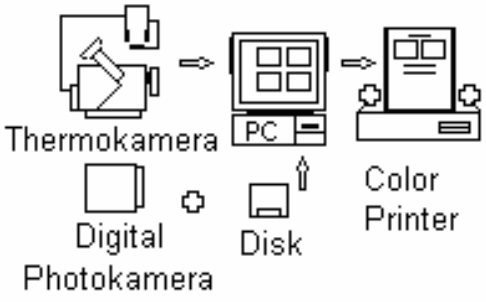

Fig.1.Thermal vision instrumentation.

The aim of this article is to show the possibility of using the infrared thermography (thermovision) to diagnose the electrical machines.

In such machines there are many failures of various kind. The thermo-monitoring application allows basic identification of the following faults: defective rotor and rotor windings, defective stator windings, poor or defective isolation of the windings, incipient faults in the stator package, cooling problems and bearing damages [2].

Thermal Monitoring Methods

While using technical Condition Monitoring method, one should have in mind three sources of faults:

- **mechanical sources:** this includes bearings, rotor de-balance, loosen joints, bad drive couplers, bad end windings, brush vibrations broken brush holders;
- **aerodynamic sources,** with regard to cooling system features: turbulence, ventilation etc.
- **electromagnetic sources** such as static and dynamic excentricity of the air gap, changes in the air gap magnetic conductivity, broken or short-circuit windings, debalance of phase currents, broken rotor bars, pulsation of theelectromagnetic moment, magnitostriction effect.

Thermal condition monitoring of the separate electrical motor construction elements could be carried out when there are troubles such as those given in Table 1.

Problems (Table.1) that appear could be observed and discovered by surface thermal temperatures or thermal images comparison during same operating conditions. The term “overheating” from Table1 shows a temperature rise in the corresponding construction element above its normal thermal conditions.

Table1

Thermal Condition Monitoring of the Electrical Motors

Machine body:
Overheating and cooling
Cooling system failures
Bad electrical contacts
Rotor and rotor windings overheating

Stator:
Stator package – hot places in frame
Bad stator windings
Front connection of stator windings – cracks in isolation
Bearing and bearing joint overheating:
Bad coupling, bent shaft, damaged bearing components – balls, rollers, rings, separators, bad lubrication, loosen elements, overtightened drive belts
Collector-brush apparatus overheating :
Brushes, brush holders, collectors, bad contacts between brushes and current conductor elements.

Experimental results

Fig.2 shows two different thermal images of a working induction motor where cooling problems appear after overload.

The term "overheating" from Table1 shows a temperature rise in the corresponding construction element above its normal thermal conditions.

Thermocouples incorporated in the stator to follow temperature changes are also known as conventional method for thermal monitoring. This method is not always applicable especially in industries, where thermal processes predominate and some devices determine high temperature for the motor surroundings.

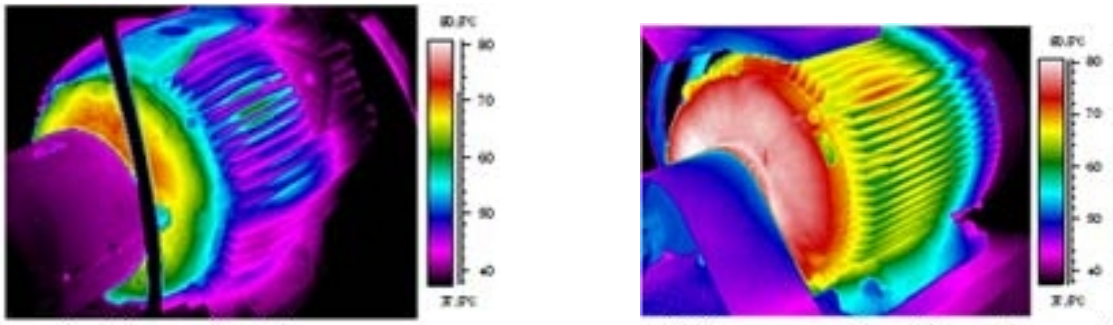

Fig.2.Two different Thermal images of a working induction motor.

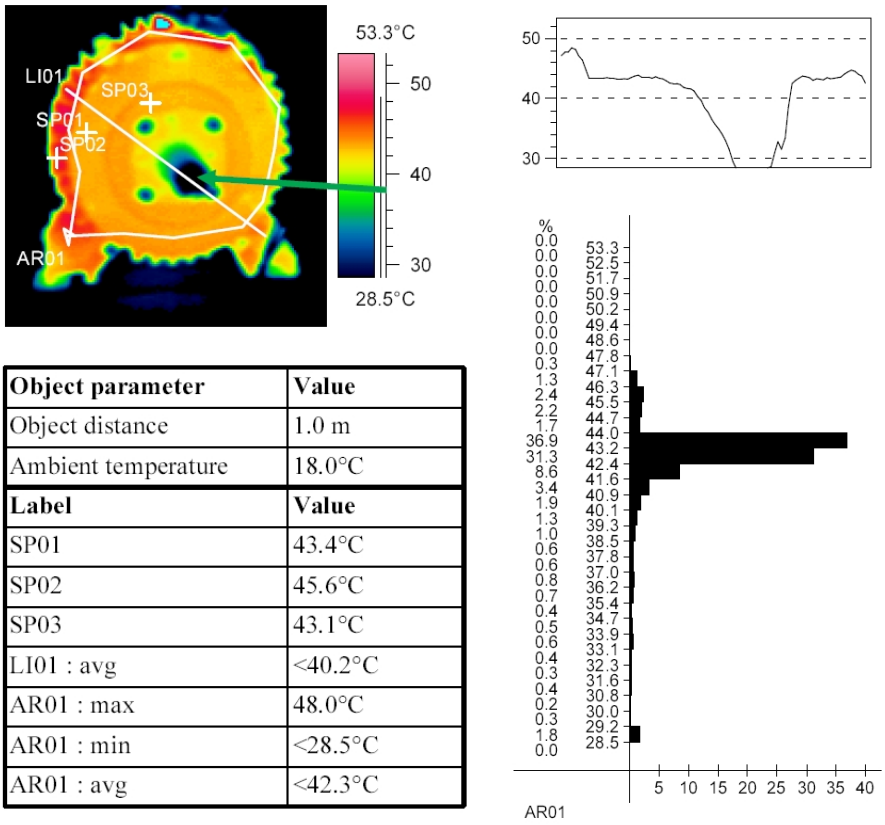

Object parameter	Value
Object distance	1.0 m
Ambient temperature	18.0°C
Label	**Value**
SP01	43.4°C
SP02	45.6°C
SP03	43.1°C
LI01 : avg	<40.2°C
AR01 : max	48.0°C
AR01 : min	<28.5°C
AR01 : avg	<42.3°C

Fig.3.The temperature Distribution of the front Bearing of induction Motor type MO180 M-2

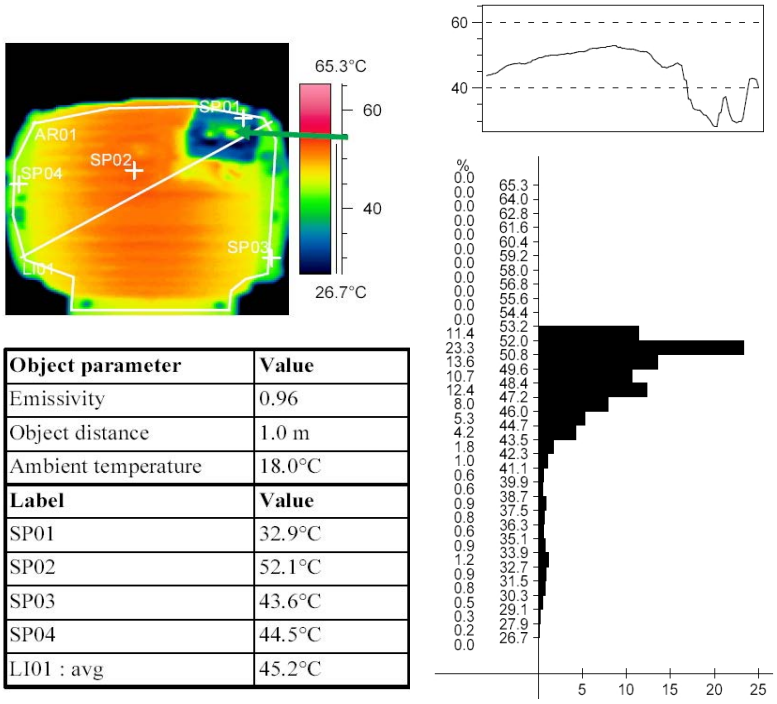

Object parameter	Value
Emissivity	0.96
Object distance	1.0 m
Ambient temperature	18.0°C
Label	**Value**
SP01	32.9°C
SP02	52.1°C
SP03	43.6°C
SP04	44.5°C
LI01 : avg	45.2°C

Fig.4.Thermal images of the outer surface of an induction motor type MO180 M-2.

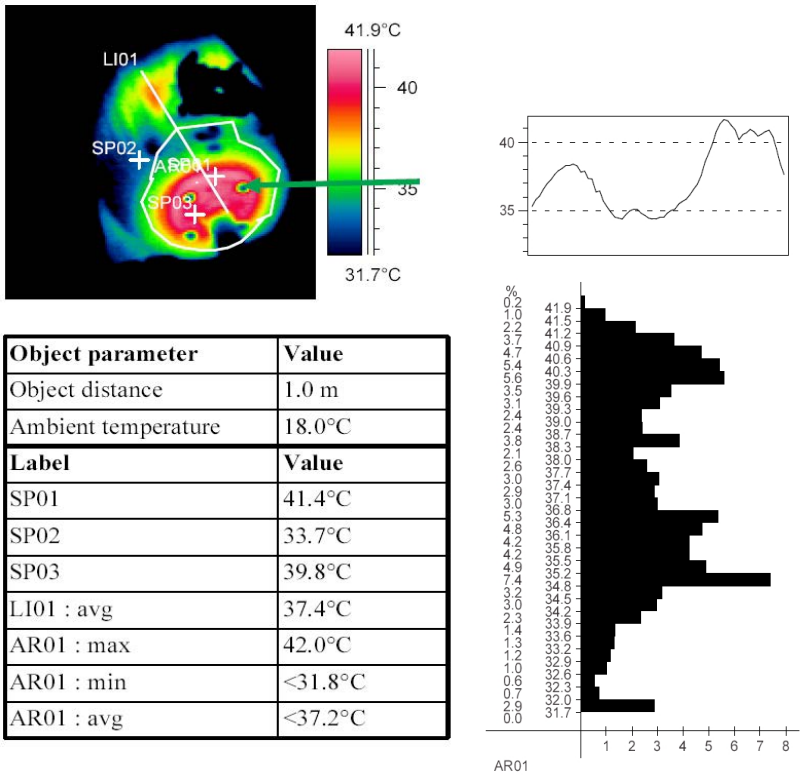

Object parameter	Value
Object distance	1.0 m
Ambient temperature	18.0°C
Label	**Value**
SP01	41.4°C
SP02	33.7°C
SP03	39.8°C
LI01 : avg	37.4°C
AR01 : max	42.0°C
AR01 : min	<31.8°C
AR01 : avg	<37.2°C

Fig.5.Thermal images of the outer surface of an Induction Motor.

Besides this additional isolation of these thermocouples is necessary, especially in high voltage machines. In this sense, the main advantage of the distant contactless monitoring is that it does not require electrical isolation of the machine and delivers thermal information about the condition of different parts in particular. Temperature measurements and thermal vision is carried out when the machine is in operation during full load conditions.

All motors and generators have one normal condition thermal vision (image) and also defined maximum operating temperatures for different parts or elements.

All motors and generators have one normal condition thermal vision (image) and also defined maximum operating temperatures for different parts or elements.

On Fig.3, Fig.4, Fig.5 are shown thermal images of the outer surface of ab induction motor, type MO180 M-2, taken by software developers Agema Infrared Systems AB. The temperature distribution of the front bearing shield is on Fig.3. Also shown are the temperatures of

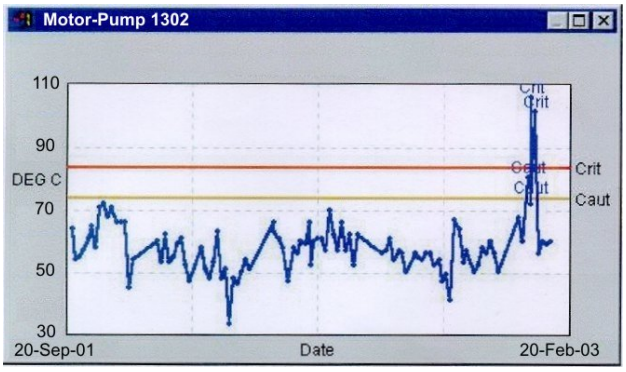

Fig.6.

three random surface points as well as the temperature change - line LI01, together with a heat histogram of region AR01. This allows to determine the hottest spots in the corresponding construction elements and hence to take preventive precautions. In this case, it is not necessary because the temperatures are below critical limits. The temperature distribution on the stator surface is shown on Fig.4 there's a picture of the terminal box. The temperature values in the terminal connectors are normal and do not show loosened or poor electrical contact.

The overheating in the front bearing shield is identified on Fig.5. During the Temperature changes of separate elements of construction in time period (Trend Monitoring) is of crucial importance for the maintenance staff. Such kinds of devices are well developed by companies-manufacturers of thermographic equipment. Actually this allows prediction of the future condition of elements.

Fig.6 shows the temperature changes of an induction motor bearing for 18 months period having indications for replacement because the critical temperature values have been exceeded.

Conclusions

The research carried out above show that infrared thermography (thermo vision) having large application in many industrial spheres is effective especially for preventive maintenance of electrical machines

Despite the big initial expenses for its introduction, these could be easily compensated by the corresponding decrease in repair costs and non-operational period expenditures.

Nowadays, most of the modern insurance companies set as a requirement companies to have such equipment in order to decrease risks of fire in large enterprises and different industrial units. EU countries envisage introduction of normative documentation to regulate the utilization of thermo-vision applications in specific industries.

All this determines the great interest in such applications during operation of electrical machines.

References

[1]. Thomas R. "Using infrared thermography as a diagnostic tool". Machine, Plant & Systems Monitor, Jan./Feb. 1999 p.11-16

[2.] "Analyzing mechanical systems using infrared thermography", AIRT 2001, p.1-11

[3.] Copp. R., Pieroway A., "Infrared in Predictive Maintenance", Machine, Plant & Systems Monitor, Sep./Oct. 1999 p.22-23

Lyubomir Dimitrov –*AssociateProfessor,Dr,*
Electrical Faculty Technical University of Varna,Studentska Str.1 ,9000Varna,BULGARIA
e-mail :lubo.dimitrov@mail.bg
Velko Naumov-*AssociateProfessor,Dr,*
Mechanical Faculty Technical University of Varna,Studentska Str.1 ,9000Varna,BULGARIA

Vibration and Acoustic Noise of Switched Reluctance Motor

Vladimir Kuzmichev

Abstract: *The paper presents a method for magnetic component prediction of switched reluctance motors (SRM) vibration and acoustic noise. Oscillation theory of the distributed-parameter mechanical systems is the base of it. Analytical equations for modal frequencies definition of stator core and numerical calculation of magnetic forces are utilized in the method. Computation results of the 3-phase 12/8 SRM vibration behavior are presented.*

Keywords: *switched reluctance motor, vibration, acoustic noise*

Introduction

Switched reluctance motors are viable contestants for a lot of number of practical applications due to their high reliability and efficiency, wide speed range at constant power and fast dynamic response. Structure simplicity and low manufacture cost make them extremely attractive for many companies and firms producing electrical machines. SRMs have been used in drives for automatic sliding door, air compressors, washing machines, air conditioning system for passenger trains, vacuum cleaning systems and etc. The world output of them was increased eight times last decade and goes on increasing. In spite of that there is not a definite opinion about the future of the electrical machines type among the scientists. There are many problems in their theory which have not got standard and comprehensive decisions as yet. Accurate analytical prediction of SRMs vibration and acoustic noise is one of them.

Vibration and acoustic noise are considered one of the main SRMs drawbacks, which limit their industrial and domestic application. Indeed double salient poles machine which is the "heart" of SRM is inherently vibration and noise prone in the sense that it has pulsed excitation and a mechanical structure that is more susceptible to resonance than "smooth-air-gap" machines. But there are many examples quiet SRMs now. Thus there is every reason to believe that high level of SRMs vibration and acoustic noise is only the problem of their optimal design. Calculation of these characteristics is an inherent part of it.

The task of vibration behaviour prediction for any motor type is a quite complicated problem. Difficulties of it for the case of SRM is to the most part of its aspects have not been examined as yet.

Many scientists try to solve the problem. Most of their articles describe solutions of the local tasks such as calculation modal frequencies, impact of stator winding and end-bells on modal shapes and etc [1, 2]. These investigations are very important. But each of them itself can not solve general problem. Some articles contain different variants of its solution. But the explanation of the proposed procedures often is not clear. So it is an extremely difficult to use them in practice. Thus, there are a lot of publications on the subject and many scientists make an every effort to develop the method for estimation of SRMs vibration characteristics. But in spite of that this task has not got a comprehensive solution yet.

The main goal of the publication is to generalize information from various publications on the subject of vibration and acoustic noise of SRMs and after that to develop the method for accurate analytical prediction of the magnetic component of their vibration and acoustic noise. Section 1 of the paper contains a brief review of vibration and acoustic noise sources in SRM. Section 2 includes some basic material about magnetic component of their vibration and noise. In Section 3 description of the mathematical model to calculation of vibration and acoustic noise are presented. Section 4 contains description of the method for magnetic component prediction of vibration and noise and some calculation results of magnetic component of the 3-phase 12/8 SRM vibration and acoustic noise.

1 Vibration and acoustic noise sources in SRMs

Sources of vibration and acoustic noise in SRM can be divided into four broad categories: magnetic, mechanical, aerodynamic and electronic. Fig. 1 shows the broad classification of them [3]. The various sources are described below.

The cause of magnetic vibration and noise is electromagnetic forces acting on the exciting stator poles.

Mechanical sources can be divided into the next sections: self, load-induced and auxiliaries.

The reason of the electrical machines self vibration is the stator structure. Stator has natural frequencies. When frequency of an exciting force coincides with one of stator natural frequencies, resonance occurs, leading to vibration and acoustic noise.

The load-induced source of vibration and noise include vibration and noise due to coupling the test machine with a load and due to mounting of the machine on the foundation.

The auxiliary mechanical sources of vibration and noise in SRM include the vibration and noise due to bearings and rotor unbalance.

Cooling of SRM by air, water or oil is the cause of the acoustic noise.

The electronic sources of vibration and noise in SRM arise due to the harmonics contained in the applied voltage and in the current.

Analysis of vibration and acoustic noise sources in SRM shows they do not differ from the ones in the other types of variable-speed drives.

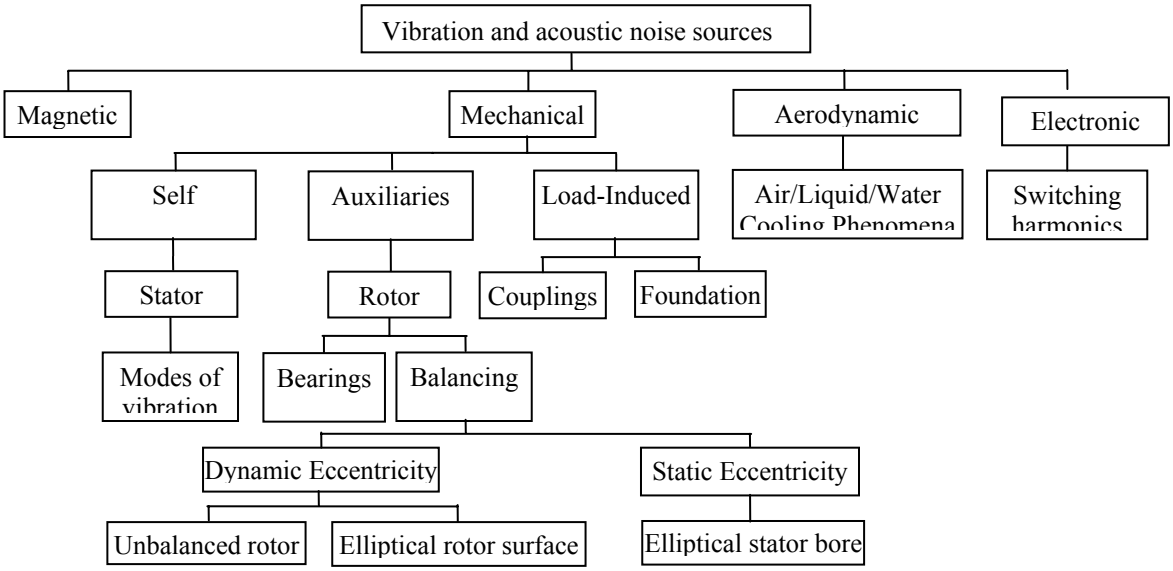

Fig. 1. Vibration and acoustic noise sources in SRM [3].

Also it should be mentioned that bearings and cooling systems of all types of electrical machines are the same. In addition to that stators of all of them have natural frequencies. Thus, mechanical and aerodynamic components of vibration and acoustic noise in all types of electrical machines may be calculated by the general methods. So there are no any reasons to develop a new method for estimation of these components of vibration and noise in SRM.

On the contrary space and time distribution of the exciting electromagnetic forces is different for every type of motors. Therefore more practical task is to develop the method for estimation of magnetic component of vibration and noise of SRMs.

2 Magnetic component of SRMs vibration and noise

As it was stated above the electromagnetic forces acting on the exciting stator poles are the cause of SRMs magnetic vibration and noise. They have two components: radial one F_{ai} and azimuth one F_{ri} (Fig. 2). Their distribution along poles is nonuniform. Components of electromagnetic force act only on the part of stator pole which is overlapped by the rotor one at the moment. Irregularity of the radial force distribution leads to generation of bending moment M_{1i} acting on stator poles.

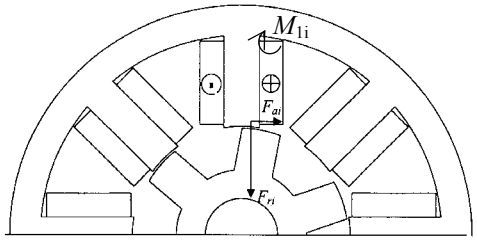

Fig. 2. Components of electromagnetic force and bending moment acting on stator poles i of the 4-phase 8/6 SRM.

Electromagnetic forces and bending moment ovalizes stator yoke which leads to vibration and noise. For vibration analysis it is important to know the space and time distribution of force components and bending moment.

Space distribution of electromagnetic forces and bending moment along the air gap depends on stator geometry. It may be described with the help of Dirac delta function $\delta(\varphi)$

$$F_r(\varphi,\ t)=\sum_{i=1}^{2p}F_{ri}(t)\cdot\delta(\varphi-\varphi_i), \tag{1}$$

$$F_a(\varphi,\ t)=\sum_{i=1}^{2p}F_{ai}(t)\cdot\delta(\varphi-\varphi_i), \tag{2}$$

$$M_1(\varphi,\ t)=\sum_{i=1}^{2p}M_{1i}(t)\cdot\delta(\varphi-\varphi_i), \tag{3}$$

where $F_{ri}(t)$, $F_{ai}(t)$, $M_{1i}(t)$ are the time distribution of electromagnetic forces and bending moment, acting on stator poles i; $p=\frac{N_s}{m}$ is the number of SRM poles pairs; N_s is the number of SRM stator poles; m is the number of phases; φ is an angular coordinate; i is a pole number.

In practice it is more convenient to use equations (1) – (3) written in the next form

$$F_r(\varphi,\ t)=F_{r0}(t)+\sum_{r=2p}^{\infty}F_r(t)\cdot sin(r\cdot\varphi), \tag{4}$$

$$F_a(\varphi,\ t)=\sum_{r=2p}^{\infty}F_a(t)\cdot sin(r\cdot\varphi), \tag{5}$$

$$M_1(\varphi,\ t)=\sum_{r=2p}^{\infty}M_1(t)\cdot sin(r\cdot\varphi), \tag{6}$$

where r is a space harmonic number of force components or moment.

Analytical calculation of the electromagnetic force components and bending moment time distribution is very difficult due to non-sinusoidal voltage, current and flux waveforms in SRMs. Usually they are calculated by some numerical methods. Typical time distribution of the electromagnetic force components and bending moment is

represented in Fig. 3, 4. These force components and bending moment waveforms were calculated in Flux2D for 3-phase 12/8 SRM operating with power 1 kW and speed 3000 rpm.

Waveforms of force components and bending moment in SRMs are non-sinusoidal. Their spectrums have (Fig. 3, 4) a lot of number harmonics. Each of them must be taken into account to accurate calculation of SRMs vibration and acoustic noise.

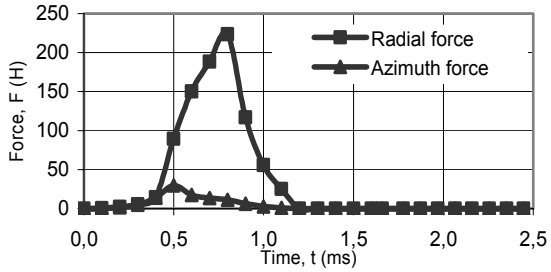

Fig. 3. Electromagnetic force components acting on stator pole of 3-phase 12/8 SRM operating with power 1 kW and speed 3000 rpm.

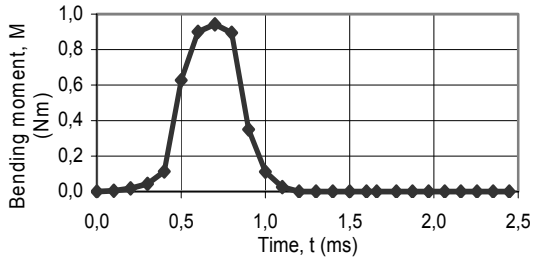

Fig. 4. Bending moment acting on stator pole of 3-phase 12/8 SRM operating with power 1 kW and speed 3000 rpm.

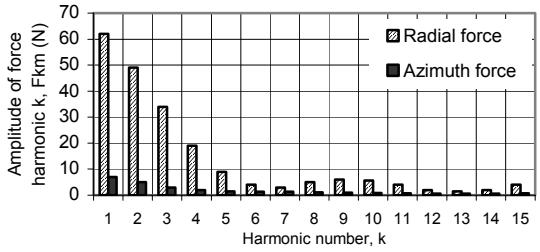

Fig. 5. Spectrums of the electromagnetic force components acting on stator pole of 3-phase 12/8 SRM operating with power 1 kW and speed 3000 rpm.

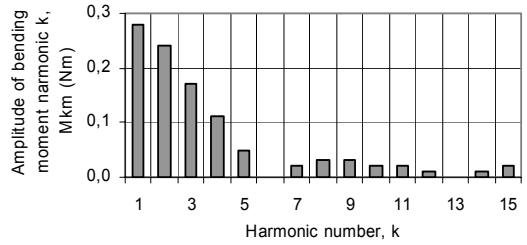

Fig. 6. Spectrum of the bending moment acting on stator pole of 3-phase 12/8 SRM operating with power 1 kW and speed 3000 rpm.

Azimuth component of the electromagnetic force in electrical machines is multiple times less than the radial one. Many scientists recommend to neglect it. But some results of their investigations show that this recommendation is not correct in general case.

Form the point of view mechanics the stator core is a distributed-parameter oscillation system. Such systems have a lot of mode shapes. Each of them has order r and natural frequency f_{cr}.

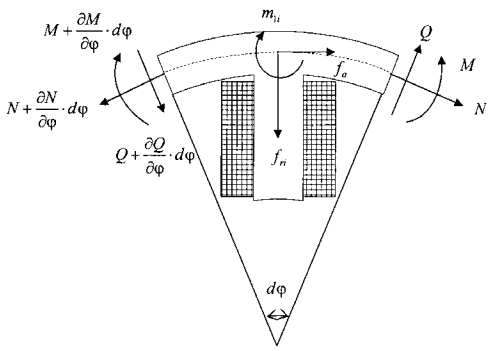

Fig. 7. Typical element of the stator core oscillation system.

Orders of modes which may be excited in SRM are depend on both stator and rotor geometry. If there is not rotor eccentricity they may be defined by the next expression

$$r = 2p \cdot k \tag{7}$$

where k=1, 2, 3 … if p=1, k=0, 1, 2, 3 … if p>1.

Modes with odd orders are excited in addition to modes with orders which are defined from equation (7) only in the case if there is static or dynamic eccentricity of rotor.

At the end of the section it should be noted every harmonic of electromagnetic force or bending moment excites modes of all orders. But excitation energy each of them is not the same. The nearly harmonic frequency to the mode one the higher energy of its excitation.

3 Mathematical model for SRMs vibration and noise prediction

It is standard to use dynamical model of the thin ring to describe the transverse vibration of SRM stator core. The average radius R_{sy_av} of such ring is equal to average one of the real stator yoke. Poles and coils are taken into account by added masses.

The thin ring with added masses is an oscillation system with distributed-parameters and multi degree of freedom. Its typical element is presented in Fig. 7. Such elements have two degree of freedom: radial one x_1 and azimuth one x_2. The equations of their motion are given by the equilibrium conditions of forces and moments:

$$\begin{cases} -N-\dfrac{\partial Q}{\partial \varphi}-\left(R_{sy\_av}\cdot f_{ri}-M_i\cdot R_{sy\_av}\cdot\dfrac{\partial^2}{\partial t^2}x_1\right)=m_0\cdot R_{sy\_av}\cdot\dfrac{\partial^2}{\partial t^2}x_1 \\ -\dfrac{\partial N}{\partial \varphi}+Q+R_{sy\_av}\cdot f_{ai}-M_i\cdot R_{sy\_av}\cdot\dfrac{\partial^2}{\partial t^2}x_2=m_0\cdot R_{sy\_av}\cdot\dfrac{\partial^2}{\partial t^2}x_2 \\ -\dfrac{\partial M}{\partial \varphi}+Q\cdot R_{sy\_av}-m_{1i}\cdot R_{sy\_av}+\chi_i\cdot R_{sy\_av}\cdot\dfrac{\partial^2}{\partial t^2}\varphi=0 \end{cases}, \tag{8}$$

where i is the element number; $f_{ai} = \frac{F_a(\varphi,t)}{2\cdot\pi\cdot R_{sy\_av}\cdot l_\delta}$, $f_{ri} = \frac{F_r(\varphi,t)}{2\cdot\pi\cdot R_{sy\_av}\cdot l_\delta}$ are the density of radial and azimuth components of electromagnetic force along the element length l_δ;

$m_{1i} = \frac{M_1(\varphi,t)}{2\cdot\pi\cdot R_{sy\_av}\cdot l_\delta}$ is the density of bending moment along the element length; $m_0 = \frac{M_{ys}}{2\cdot\pi\cdot R_{sy\_av}\cdot l_\delta}$ is the equivalent mass; M_{ys} is the stator yoke mass; $M_i = \rho_s\cdot\frac{2\cdot p\cdot b_{ps}\cdot h_{ps}}{2\cdot\pi\cdot R_{sy\_av}\cdot d\varphi}$ is the distribution density of added masses; b_{ps}, h_{ps} are the width and the height of the stator pole; ρ_s is the stator steel density; $\chi_i = \frac{\rho_s\cdot b_{ps}\cdot h_{ps}^3}{3\cdot R_{sy\_av}\cdot d\varphi}$ is the specific polar moment of inertia of added masse area.

Assume that: elements of thing ring are not extensible and deformation due to shear stresses is neglected quantity. In this case there is the next relationship between radial and azimuth deformations

$$x_1 = -\frac{dx_2}{d\varphi}. \tag{9}$$

Using the relationship (9) and applying property of natural modes orthogonality it is not difficult to get equations of motion of the whole thin ring and next the equations of stator core motion.

If harmonic k of electromagnetic forces and bending moment excites radial and azimuth modes with order r the equations of stator core motion are

$$\frac{d^2}{dt^2}x_{1k}(t) + 2\cdot\zeta_{rr}\cdot\omega_{rr}\cdot\frac{d}{dt}x_{1k}(t) + \omega_{rr}^2\cdot x_{1k}(t) = \tag{10}$$
$$= \frac{1}{m_{rr}}\cdot\frac{r^2\cdot F_{rk}(t)}{\pi\cdot R_{sy\_av}\cdot l_\delta\cdot\left(r^2+1\right)},$$

$$\frac{d^2}{dt^2}x_{2k}(t) + 2\cdot\zeta_{ar}\cdot\omega_{ar}\cdot\frac{d}{dt}x_{2k}(t) + \omega_{ar}^2\cdot x_{2k}(t) = \tag{11}$$
$$= \frac{1}{m_{ar}}\cdot\frac{r\cdot\left[F_{ak}(t) - \left(r^2-1\right)\cdot\frac{M_{1k}(t)}{R_{sy\_av}}\right]}{\pi\cdot R_{sy\_av}\cdot l_\delta\cdot\left(r^2+1\right)},$$

where $F_{rk}(t)$, $F_{ak}(t)$ are the harmonic k of the radial and azimuth electromagnetic force components acting on the one stator pole; $M_{1k}(t)$ is the harmonic k of the bending moment acting on the one stator pole;

$\zeta_{rr} = \frac{c_{rr}}{2\sqrt{k_{rr}m_{rr}}}$, $\zeta_{ar} = \frac{c_{ar}}{2\sqrt{k_{ar}m_{ar}}}$ are the damping ratios of the radial and azimuth modes shapes r;

$\omega_{rr} = \sqrt{\frac{k_{rr}}{m_{rr}}}$, $\omega_{ar} = \sqrt{\frac{k_{ar}}{m_{ar}}}$ are the angular natural frequencies of radial and azimuth modes r;

E is the Young's modulus of stator core steel;

$k_{rr} = k_{ar} = \begin{cases} \frac{E\cdot J}{R_{sy\_av}^4}\frac{r^2\cdot\left(r^2-1\right)^2}{\left(r^2+1\right)}, & \text{if} \quad r \ge 2 \\ \frac{E\cdot h_{ys}}{R_{ys\_av}^2}, & \text{if} \quad r = 0 \end{cases}$ are the stiffness of radial and azimuth modes r;

$m_{ar} = m_0\left[1 + \frac{\frac{J_i}{R_{sy\_av}^2}\cdot\left(r^2-1\right)^2+1}{r^2+1}\cdot\frac{N_S\cdot M_{ps}}{M_{ys}}\right]$ is the azimuth mass of mode r;

$m_{rr} = m_0\left[1 + \frac{N_S\cdot M_{ps}}{M_{ys}}\right]$ is the radial mass of mode r; M_{ps}, M_{ys} is a weight of stator pole and stator yoke.

It is clear the equations (10), (11) are the equations of a simple oscillator. Thus, stator core vibration due to excitation of mode r by harmonic k of the radial and azimuth electromagnetic force components and bending moment can be represented as linear superposition of two simple oscillators rippling.

Waveforms of the electromagnetic force and bending moment have a lot of harmonics. Each of them may excite infinite aggregate of stator core modes. Therefore the dynamic model of stator core is multitude of oscillators' pairs (Fig. 8).

Solutions of the dynamic model equations are the next expressions

$$x_{1km} = \frac{F_{rkm}}{k_r}\cdot\frac{r^2}{\pi\cdot R_{sy\_av}\cdot l_\delta\cdot\left(r^2+1\right)}\cdot k_{grk}, \tag{12}$$

$$x_{2km} = \frac{F_{akm} - \left(r^2-1\right)\cdot\frac{M_{1km}}{R_{sy\_av}}}{k_r}\cdot\frac{r}{\pi\cdot R_{sy\_av}\cdot l_\delta\cdot\left(r^2+1\right)}\cdot k_{gak}, \tag{13}$$

where x_{1km}, x_{2km} are amplitudes of radial and azimuth oscillations;

$k_{ga(r)k} = \frac{1}{\sqrt{\left(1-\frac{\omega_k^2}{\omega_{a(r)r}^2}\right)^2 + \left(0{,}03\cdot\frac{\omega_k}{\omega_{a(r)r}}\right)^2}}$ are the amplification factors for radial (r) and azimuth (a) oscillations.

Amplitudes of velocity and acceleration response may

be calculated by multiplication (12), (13) by factors ω_k and ω_k^2 accordingly. Total amplitudes of harmonics k of displacement x_{km}, velocity x'_{km} and acceleration x''_{km} response are

$$x_{km} = \sqrt{\sum_{r=0}^{n}\left(x_{1mr}^2 + x_{2mr}^2\right)}, \quad (14)$$

$$x'_{km} = \sqrt{\sum_{r=0}^{n}\left(\left(x'_{1mr}\right)^2 + \left(x'_{2mr}\right)^2\right)}, \quad (15)$$

$$x''_{km} = \sqrt{\sum_{r=0}^{n}\left(\left(x''_{1mr}\right)^2 + \left(x''_{2mr}\right)^2\right)}. \quad (16)$$

To definition of acoustic pressure level may be used excretion which is represented in [4].

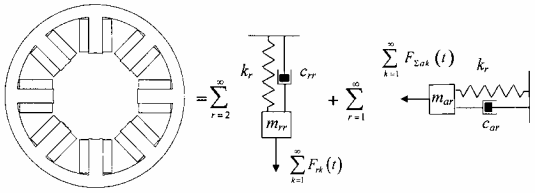

Fig. 8. Dynamic model of stator core.

4 Method for magnetic component prediction of SRMs vibration and acoustic noise

Method for magnetic component prediction of SRMs vibration and acoustic noise by mathematical model which was described in this paper is quite simple. It contains three stages. The waveforms of the electromagnetic forces and bending moment must be defined at the first stage. The second stage is to define modes orders which will be excited in the SRM. Third stage is the most difficult. It is to calculate vibration and acoustic noise by the proposed model.

This method has been used to define vibration and acoustic noise characteristics of the 3-phase 12/8 SRM operating with power 1 kW. Waveforms of electromagnetic forces and bending moment for the case are shown in Fig. 3, 4. In the calculations the modes with orders 0, 4 and 8 were taken into account. The results of the calculations are present in Fig. 9-11.

Conclusion

Mathematical model and method for magnetic component prediction of SRMs vibration and acoustic noise is presented. The model takes into account both radial and azimuth components of the electromagnetic force acting on stator pole.

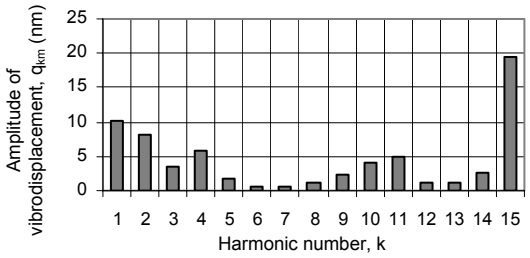

Fig. 9. Vibrodisplacement spectrum of the 3-phase 12/8 SRM operating with power 1 kW and speed 3000 rpm.

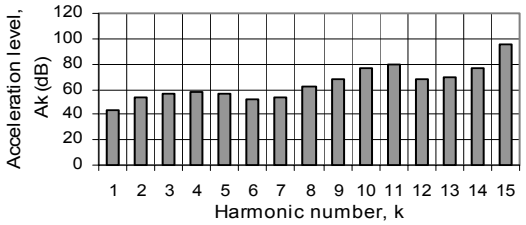

Fig. 10. Acceleration level spectrum of the 3-phase 12/8 SRM operating with power 1 kW and speed 3000 rpm.

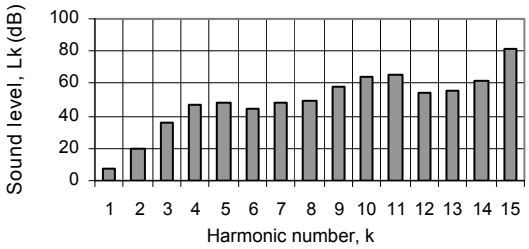

Fig. 11. Spectrum of an acoustic pressure level of the 3-phase 12/8 SRM operating with power 1 kW and speed 3000 rpm.

References

[1] Cai W., Pillay P., Tang Z., "Impact of Stator Windings and End-Bells on Resonant Frequencies and Mode Shapes of Switched Reluctance Motors," *IEEE Trans. on Ind. Appl.*, vol. 38, NO. 4, July/August 2002. pp.1027-1036.

[2] Hong J.-P., Ha K.-H, Lee J., "Stator Pole and Yoke Design for Vibration Reduction of Switched Reluctance Motor," *IEEE Trans. on Magnetics*, vol. 38, NO. 2, March 2002. pp. 929-932.

[3] Krishnan R., "Switched Reluctance Motor Drives: Modeling, Simulation, Analysis, Design and Application," *Boca Raton, FL, USA: CRC Press*, 2001. 450 p.

[4] Anwar M.N., Husain I., "Radial Force Calculation and Acoustic Noise Prediction in Switched Reluctance Machines," *IEEE Trans. on Ind. Appl*., vol. 36, NO. 6, November/December 2000. pp.1589-1597.

Vladimir Kuzmichev *– Assistant Professor, PhD, Institute of Electrical Engineering, Moscow Power Engineering Institute (Technical University), Krasnokazarmennaya Str., 14, 111250 Moscow, RUSSIA*
e-mail: kuzmichevva@mpei.ru.

Information and Methodical Issues of Technologic Forecasting for Electrical Machines Reliability at the Design Stage

Victor V. Popov and Igor A. Arseniev

Abstract : *The idea of the reliability supply of the electric machines by means of modern information technologies (IT) is posed in the paper. The importance of creation of the united database system with data on the system reliability for the needs of wide range of specialists is stressed. This database should be further transformed to the knowledge base. The methodological foundations of the reliability prediction illustrated by prognosis of no-failure turbogenerator operation are analyzed.*

Keywords: *Reliability support automated system, electrical machines, reliability forecasting.*

Introduction

The positive experience of turbogenerators reliability ensuring for the modern power systems is accumulated by the present time. It is reached with the help of different and usually independent technical and organizational arrangements, which are organized during the creation or exploitation periods of the turbo generators. The richest experience of making such arrangements is collected during the turbogenerators operation, where their reliability as the element of the power system is realized. At the same time the technical level and the effectiveness of such arrangements on the other stages of the tubrogenerator lifecycle are also raised. Thus, the automated systems of technical designing, production and testing processes support aimed to raise turbogenerators reliability are being successfully developed. The methodology of technical diagnostics with the use of modern IT has shown its effectiveness. The issue of the integration of all these arrangements as the interactive components within one united system could be stated as one of most actual ones. This system has to be based on the united methodological basis. IT for design, testing, regulation and control stages being successfully applied in the electric machines building and electrotechnology are recommended to become such basis.

The concept of the turbogenerators reliability control systems is presented below. It is based on system analysis and it joins different aspects of using IT for reliability provision (ITRP). Some methodological principals for tubbogenerators reliability support at the design stage are discussed within the framework of developing automated system for reliability provision of turbogenerators (ASRP).

The concept of the system for reliability control of turbogenerators by the use of IT.

The structural scheme of the ASRP is presented on the figure 1. It consists of the local systems and subsystems, joined within a closed adaptive system. You can see here the following components:

- CAD – computed-aided design system.
- CAM - computed-aided manufacturing system
- CAT- computed-aided testing system
- CAO- computed-aided operation control system. It consists of two subsystems: computed-aided regulation and control (CARC) and computed-aided technical diagnostics and prognostics (CATDP).

It is important that ASPR has also database (DBS) and knowledge base (KB) systems and tutor system (TS) as its natural components.

The complex diagnostic and reliability forecasting system is on the upper level of the control.

The ITRP concept as it follows from the structural scheme of the ASRP presented at figure 1, links together the different stages technologies. It is realized by different systems and subsystems. In that way the ITRP development solves not only the problem of the components integration. It also improves the role and widens the functionality of each of them. Actually, creation of the united database system for reliability aspects with its further transformation to the knowledge base, supporting by the tutor systems can becomes an essential factor for improving qualification of the wide range of specialists. If we use such system in the frames of higher schools by founding special centers, like the Center of studying specialists for “Electrosila” company at St. Petersburg State Polytechnical University (CSS), we’ll radically raise the quality of the students’ education. The graduates will become not the “young specialists”, but the “young professionals”, conceived the experience of many years of turbogenerators design and operation.

The use of IT as a basis of the presented system has become possible owing to mathematical methods (MM) and programming systems (PS) for each subsystem. It is necessary to develop such MM and PS, which ensure mathematical models of high correspondence, in order to reach appropriate trustworthiness to forecast the conditions of turbogenerators reliable operation.

The CAD system plays an important role in ASRP. The CAD system has to solve now not only the problems of optimizing the constructions characteristics and parameters owing to different criteria of consumer quality maintenance, but it has also to estimate the probability of inadmissible derivations of the parameters owing to different possible defects appeared during the periods of the production and exploitation. That’s why in the ASRP system the CAD components have to provide additional support by using appropriate MM and PS for computational modeling of different operating modes in order to

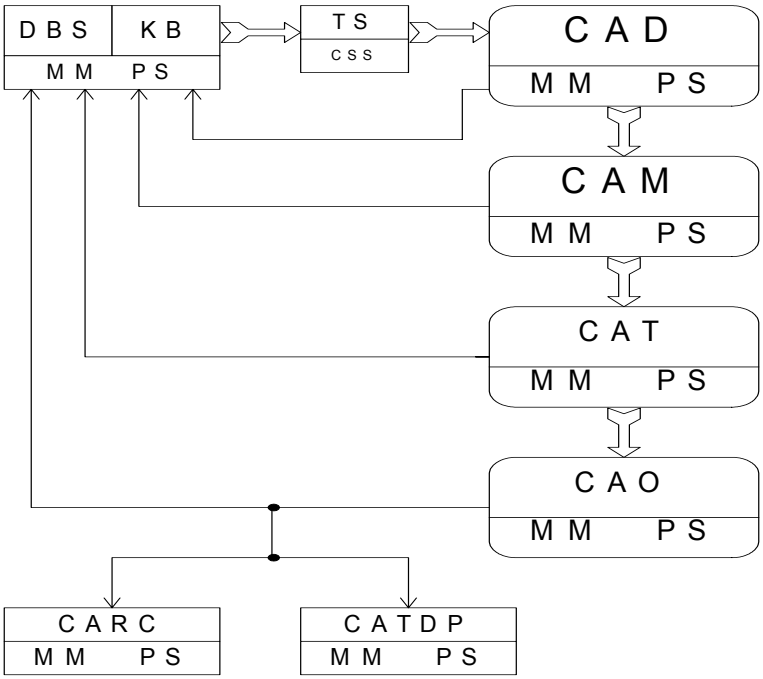

Fig.1. The structural scheme of the automated system for reliability provision of turbogenerators– ASRP.

discover global and local peculiarities spatial and temporal distributions of complicated physical fields and processes in main elements and units.

According to experience, the dangerous for turbogenerator normal operation effects usually appear in the local zones, which have local features in their structure or properties. The operation mode affects on the local intensity of different physical processes.

However it can be strengthened by different defects that appear during the manufacturing or exploitation periods. It is obvious that the stochastic mathematic models should be used for the examination of physic fields and processes in the local zones with probable defects. The numerical realization of such models is much more complicated than of determined ones. Interpretation of results from the stochastic models also becomes complicated. But it provides possibility to evaluate the probability of inadmissible for safety reasons influences in local zone of turbogenerators during different operation modes. The factor of parametric reliability (the probability of reliable work) can be considered as the probability of excess by the different physical influences their permissible limits.

The complex numerical study of the parametric reliability factors on the range of the whole variety of criteria, allow us to estimate the probability of tubrogenerator no-failure operation. It also helps to control the processes of turbo generator's production and exploitation.

The forecasting methods of turbogenerator's elements reliability with the use of modern IT

The reliability forecasting of elements means the estimation of the physical influences inadmissible excess. Evaluated probability is considered as a factor of parametric reliability (the probability of reliable work).

Let's illustrate the methods of such estimation on the sample of rotor's heat deregulation, which can appear under his asymmetric heating. This problem is especially actual for turbogenerators with full water cooling, where owing to high effectiveness of water cooling the asymmetric heat of their rotors is very probable. It was found out during the experiments, that the difference of temperatures in the diametrical points of the rotor surface could cause the inadmissible level of vibrations. The reason of the asymmetric heating of the rotor can become different sorts of defects, irregular the symmetric thermal flux and heat exchange. These defects appear in a random way during the production ore exploitation periods. So it is necessary to make the estimation the influence of all factors or at least of the most important ones which are possible to cause the asymmetric heat of the rotor in order to take this into account during the production and operation stages. Such factors could become dispersions and deflections in the sizes of hydraulic cooling channels, the contacts of electric and heat resistances between structural elements of the rotor etc. The distribution and intensity of mentioned above factors within the rotor's volume have a stochastic nature. Many of them could be defined using the law of probability. So it is possible and reasonable to forecast the probable level of the vibrations, caused by these factors. The forecasted values of probability could be considered as a factor of rotor parametric vibration in conditions heath deregulation. The method of such forecasting is described in [1, 2]. It is based on solving the following three interrelated boundary problems:

- thermal conductivity, which defines temperature distribution within the rotor volume;
- thermoelasticity, which defines rotor's curves after heat deformations;

- rotor fluctuations forced by disbalance of forces caused by thermoelastic curve.

A picture of the electromagnetic and eddy currents distribution in abnormal functioning mode is the input information for solving the problems of rotor heat deregulation. Modern computers and programming package allow us to solve the considered tasks in three-dimensional target setting. But the use of such universal programming systems, designed for research and development, for electrical machines design. First, these packages could be hardly used integrated parts in CAD systems. Second, it demands higher requirements to computer configuration and user qualification. Besides that, the user has to formulate the goal of calculations and results processing for the need of electric machine design. Thus the development of specialized programming systems for the limited types of areas with reductive input data definition and automated results processing is still an actual task for engineering.

Special programmed complex for calculation rotor's constructive elements thermal stability is worked up on the department of the electric machines St. Petersburg State Polytechnical University.

The most difficult part of this complex is a block of the calculation of the eddy currents distribution in the rotor's structure, capable to reveal the zones of their local concentration. Eddy current activities in these local zones determine the level of the electric, heat and thermodynamic influence on the rotor. It is important to take into account not only three-dementional geometry and physical characteristic constructive element, but also all local features of the constructive structure of the rotor.

The specialized programming system for computation of the thermal durability of the rotor structural elements of the power turbogenerators in different operation modes has been developed at the "Electrical Machines" chair of St. Petersburg State Polytechnical University.

The most complicated part of the system is the module for calculation of the distribution of eddy currents within the rotor volume of complicated configuration. The system can find out the zones of their local concentration. The density of eddy currents in such local zones defines the level of additional electromagnetic, heat and thermodynamic influences to the constructive rotor elements and, consequently, the level of the elements and rotor reliability. Solving such kind of problem, it is important to take into account not only the geometry and physical characteristics of the rotor elements, but also the local peculiarities of the rotor structure, where the intensity of physical effects become the key factor for the no-failure turbogenerator running.

In such conditions it becomes possible to estimate the thermal durability of the rotor within abnormal modes, i.e. to estimate the admissible values of value and duration of the opposite currents. It becomes possible to study electromagnetic and heating processes only within the limited volume of the rotor, i.e. only in the parts with the highest density of eddy currents and caused by them thermal flux [3].

Refuse from global analysis of the temperature field of the turbogenerator's rotor within abnormal modes, characterizing by drastic demonstration of surface effect, do not limit information about the most intensive heating zones. It allows to reduce the shape of the research zone and the number of calculating procedures within computational model of interconnected electromagnetic and heath fields. Herewith the possibility to take into account the local particularities of the structure of the rotor and different contact phenomena on the surfaces of the interfacing parts of the separate constructive details, defining so called fretting corrosion, appears. It is important that this possibility does not require additional computing resources. Within such particularities are, for instance, are the effects on surface resistances of the rotor constructive elements, which are called fretting processes. The detailed exploration of fretting fatigue [4] showed the essential influence of such processes on the mechanical durability of the rotor's structure elements. The electric and heat resistances between the contacted surfaces of the constructive elements can also influence on the distribution of eddy currents, especially in the local zones of their concentration. Obvious that the fretting processes can fundamentally influence on the distribution of local zones with high density of heat and thermomechanical processes.

To illustrate all discussed above the picture of spread of tangentia eddy current (f = 100 Hz) within the frontal rotor zones, flowing from the jag to the wedge of the contact area AB, is presented on figure 2.

Here you can find also the distribution of the current density within the width of the contact area in conditions of ideal contact of the jag with the wedge and uniform distribution of contact electric resistance between them. The current densities are shown here in parts of their value in the middles of the surfaces of the jag and the wedge correspondingly. It is seen that different contact conditions influence essentially on the eddy current distribution especially near the edge of the contact area.

The MM and PS for the computational realization of mentioned above border problems and for calculation the probability of the fact that the vibration amplitude will not exceed the admissible value in conditions of considered defects were carried out at the "Electric Machines" department.

As an illustration of the results, received by described methods, the forecast of no-failure operation of the rotor of the turbogenerator T3B-800 with full water cooling in conditions of heat deregulation is presented on figure 3. This heat deregulation is caused by technological dispersion of the real canals profiles on the parallel branches of the cooling system (curves 1). This forecast defines the dependency of no-failure operation probability P from admissible vibration amplitude Aadm i.e. the probability of the fact that the level of the vibration amplitude will not exceed the admissible value. 125The probability P is determined for two values of bearings compliance: L1=0.1•10-4 mm/N and L2=0.746•10-4 mm/N.

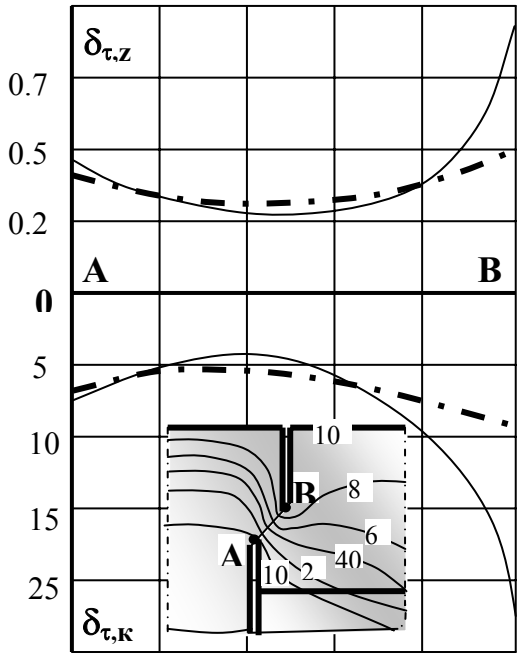

Fig.2. The influence of contact resistance on the eddy current density distribution

———— Ideal contact

— ·— · — · With contact resistance

In the calculation it was supposed that the coefficient of hydraulic friction in a separate parallel cooling branch could be considered as a variate distributed by the normal law with defined average of distribution and average square-law deflection. Under such assumptions, confirmed by practice, the numeric characteristics of the variates of hydraulic resistance and water discharge in the separate cooling branch were defined.

For the illustration of other technological defects influence the probability of no-failure operation of the same turbogenerator in conditions of the possible heat deregulation, caused by technological dispersal of the isolation thickness on energizing coil slots are presented on the same figure (curves 2). One can see that the influence of some technological factors on vibratory reliability of the rotor could be essential.

Conclusions

- Continuously expanding IT possibilities, constantly developing automated systems, which support technological processes at all turbogenerator's lifecycle stages, make the problem of ASRP creation actual.
- The role of the CAD systems greatly increases within the framework of ASRP. CAD allows to forecast the turbogenerator's parametrical reliability by the given criteria during the design stage. Such forecasts allow to concretize the demands for technical tolerance for the component parts and to create prerequisites for the purposeful control of the production and exploitation processes.
- It is necessary to continue the R&D for raise the precision of the reliability forecast at the design stage. The most important trend is developments of the turbogenerator' systems analysis methodology and research of dynamics of stochastic characteristics of turbogenerator' structural parameters during the exploitation processes.

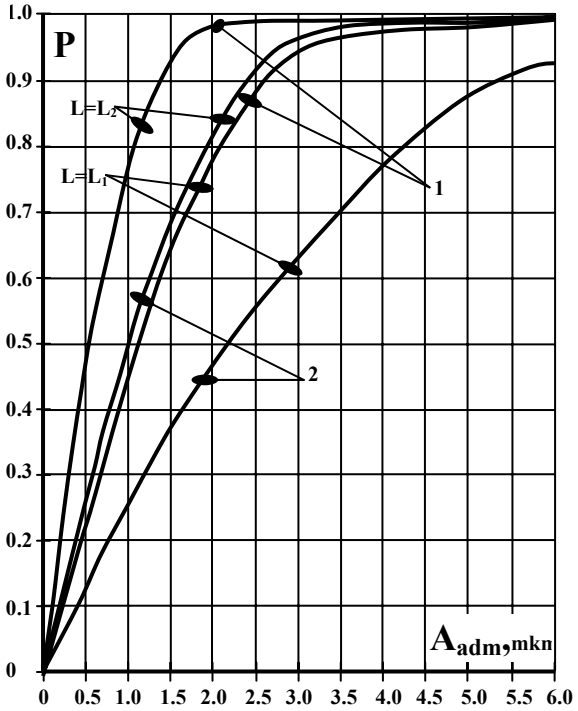

Fig.3. No-failure operation prognosis for the turbogenerator T3B-800 in conditions of possible heat deregulation.

References

[1] Мартьянов М.В., Попов В.В. Методика и результаты численного моделирования тепловой разбалансировки роторов турбогенераторов с водяным охлаждением. – Изв. Вузов. Энергетика, №5, 1984.

[2] Мартьянов М.В., Попов В.В., Федоренко В.В. – Прогнозирование тепловой разбалансировки массивных роторов синхронных машин – Электротехника, 1992, № 1.

[3] Арсеньев И.А., Попов В.В. К расчету термической стойкости конструктивных элементов массивного ротора при оценках надежности крупных синхронных машин на стадии проектирования. Известия АН «Энергетика». Отделение физико-технические проблемы энергетики. №3, 1999, с.112-118

[4] Штилерман И.З. – Об одной модели фреттинг-усталости.- ОАО «Электросила» СПБ, 2001.

***Victor V. Popov** – Professor, Faculty of Electrical Mechanic, St.Petersburg State PolitechnicalUniversity, 29 Politehnicheskaja Str., 193318 StPetersburg, RUSSIA. e-mail: elmash@mebil.stu.neva.ru*

***Igor A. Arseniev** – engineer, Faculty of Electrical Mechanic, St.Petersburg State PolitechnicalUniversity, 29 Politehnicheskaja Str., 193318 StPetersburg, RUSSIA.*

e-mail: elmash@mebil.stu.neva.ru

Complex Electronic Protection of the Low-Voltage Three-Phase Induction Motors

Gabriel Nicolae Popa, Iosif Popa and Sorin Deaconu

Abstract: *In present, majority of industrial drives are made with low voltage motors. Are used especially three-phase cage induction motors, because are robust, simple and have high reliability. An important problem for electrical drives is the protection of low-voltage three-phase induction motors; the mean operating time depends by protection made. The paper presents a complex electronic protection for low voltage three-phase induction motors that are made with 8 bits microcontroller.*

Keywords: *electronic, protection, induction, motor, microcontroller*

Introduction

Nowadays, the major part of the industrial equipment is driven by low-voltage electric motors. For this purpose are used mainly three-phase induction motors, because these are robust, have a simple constuction and have a high reliability in operation.

A problem of special importance is the protection of low-voltage induction electric motors, because their protecting mode depends on their operating life. The protections of low-voltage induction electric motors should act for interrupting of electric power supply when a defect occurs in the electric supply installation, in the machine or in motor's overload operationg regime. The main types of defects that appear during the operation of three-phase induction motors are: two-phase or three-phase short-circuits between the stator winding solenoids, short-circuits between the windings of the solenoids from the same phase, interruption of a solenoid, putting to mass of the conductors of statoric solenoids, or complex defects such as short-circuits accompanied by putting to mass, interruptions with putting to mass, short-circuits with contact rezistance at the defect's site, interruptions of conductors with rezistance at the defect's site, etc. For the three-phase induction electric motors with coiled rotor, the same defects can appear also in the rotor's winding.

The complex protection presented further is based on a Motorola MC68HC05B6 microcontroller. The process computer CC/Basic (initiation board with MC68HC05B6 microcontroller) is a compact element, destined for measurement, management and adjustment, having even the capacity to transmit and store the data.

The processors' technique has been developped very much, in such way that in the actual modern life it is indipensable in almost all electric devices, leading the process by means of their "intelligence" contained in the system's memory. Programming of a microcontroller is usually very complicate and needs a voluminous knowledge and expensive development devices. By C-Control system are opened possibilities through this technique for any user. The CC/Basic process computer is an important step in programming of microcontrollers for solving the problems concerning the measurement, control and adjustment of processes, however these having limitations at the border of very complex problems. The CC/Basic process computer contains a microprocessor, which allows, by means of a dedicated software, the programming in Basic language (high level language), thus avoiding the difficult programming in assembling language [4,5].

The main microcontrollers advantage is the software that replace a complex logic circuit, without a hardware change. That, the protection for low voltage induction motors may be made with these electronic devices.

Electronic Protection's Hard Structure

The program achieves the protection of a three-phase induction motor at short-circuit, overload, asymmetry of the currents over an imposed value, against starting and operation in two phases and minimal voltage, by measuring the efficient values of currents and voltages.

The protection is achieved as follows [2,3]:

- at short-circuit, by permanent measuring of the current; if the current's value, from any of the phases, is higher than $7 \cdot I_n$ then it has place the instantaneous release of the main contactor K_1 (≈0,02s). Within the starting period, if the current can reach to this limit, then acts the protection to short-circuit. Therefore, is necessary that the adjusted value of the short-circuit current I_{SC} to fulfil the condition:

(1) $$I_{SC} = 1{,}2 \cdot I_p ,$$

where I_p is the motor's staring current.

(2) $$I_p = k_p \cdot I_n ,$$

in which $k_p \in [4{,}5\text{-}7)$ [-], and I_n is the motor's rated current;

- at overload, by continuous measurement of the current and time-delayed cutting-off of the K_1 contactor depending on the overload current's value. Is considered that the motor runs in overload regime when the current, from any of the phases, is ranged within $I_S \in [1{,}05I_n\text{-}7I_n)$. The release time of the contactor K_1 is calculated by:

(3) $$t = \frac{k_S}{I_S^2} ,$$

where k_S [$A^2 \cdot s$] depends on the protected motor's power, and I_S [A] is the overload current;
- asymmetry between the phases' currents, by measuring the currents, and if the asymmetries are higher than 20%, then the contactor is released instantaneously (≈0,02s);
- against starting in two phases, by measuring the voltages on each phase. If one voltage is 0V then the motor doesn't start;
- against functioning in two phases, by permanent measuring of the currents on the three phases. If there is no current on one of the phases, then is achieved the instantaneous release of the contactor K_1;
- voltage minimal, by continuous measuring of the voltage on the three phases, and if one of the phase voltages u_f:

(4) $$u_f < 0,7 \cdot U_{fn}$$

where U_{fn} is the phase rated voltage, then the release is instantaneous.

In fig.1 is presented the connecting mode of the three-phase induction motor to the system with microcontroller. Permanently are measured the current on the three phases I_R, I_S, I_T (with three AC transformers –alternative voltage fig.1 T_{CR}, T_{CS}, T_{CT}) and the phase voltages U_{R0}, U_{S0}, U_{T0} (with three voltage lowering transformers T_{UR}, T_{US}, T_{UT}). Thus, in the secondaries of the six transformers shall be obtained alternative voltages of small values [1,3].

Because at analog-digital inputs of the microcontroller are allowed only continuous voltages within 0-5V, the voltages from the secondaries of the six transformers should be rectified (with bi-alternance precision rectifiers), filtered (with active go-down filters) and then amplified (with operational amplifiers). All these are represented as block scheme in fig. 2, named as "Alternative voltage – continuous voltage converter". The convertors' outputs are connected to six analog-digital ports AD_1, …, AD_6 of the system with microcontroller.

The system with microcontroller has START key, S_{START} for running the program, one for RESET, S_{RESET}, a key for checking the protection marked with S_3 connected to the port P_3 and a key S_4 for resetting the protection connected to the port P_4. The contactor K_1 (for electric power supply of the motor), is controlled by the relay K_2 which is connected to the port P_1. In case when the protection releases the contactor K_1 and the defect was remedied, then by the key S_4 is reset the protection. If the protection does not reset, then is pressed the key S_{RESET}, then the key S_{START}. Periodically, the protection can be verified (even when is phisycally connected to the protected motor) by the key S_3. During verification, the contactor K_1 does not turn on. The key S_3 has the role to disconnect the inputs of the analog-digital ports AD_1,…, AD_6 connecting itself to six potentiometers P_{CR}, P_{CS}, P_{CT}, P_{UR}, P_{US}, P_{UT} by which can be verified the protection to all type of defects with the contactor K_1 released. Thus, the current potentiometers P_{CR}, P_{CS}, P_{CT} are scaled at the following marks: I_n; $1,05 \cdot I_n$; $1,2 \cdot I_n$; $2 \cdot I_n$; $3 \cdot I_n$; $7 \cdot I_n$; $10 \cdot I_n$. For the values ranged between $[1,05\text{-}7) \cdot I_n$ is simulated the overload, and for the values higher or equal with $7 \cdot I_n$ – the short-circuit. On the voltage potentiometers P_{UR}, P_{US}, P_{UT} are scaled the positions $0,7U_n$ şi U_n. If the voltage is lower than $0,7 \cdot U_n$ should act the minimal voltage protection. The protection's normal operation or verification is determined by the key S_3, which, if it's not pressed, makes that the ports P_5 and P_6 (to which are connected the relays K_5 and K_6 with three contacts normally opened and three contacts normally closed fig.1) to be on 0 logic, otherwise these are on 1 logic. When on the ports P_5 and P_6 the applied signals have the logic value 1, they turn-on the relays K_5 (for current) and K_6 (for voltage) which connect the inputs of analog-digital convertors to the potentiometers P_{CR}, P_{CS}, P_{CT}, (simulate the phase currents) and P_{UR}, P_{US}, P_{UT} (simulate the phase voltage). By adjusting of the potentiometers to different values, could be simulated both simple and combined defecte, more complex.

As warning elements are used LEDs which have the following destination (fig.1):
- LED 1 (D_1 connected to the port P_9) indicates the protection's voltage supply;
- LED 2 (D_2 connected to the port P_{10}) indicates the turning on of the contactor K_1;
- LED 3 (D_3 connected to the port P_{11}) indicates the protection to short-circuit;
- LED 4 (D_4 connected to the port P_{12}) indicates the protection to overload;
- LED 5 (D_5 connected to the port P_{13}) indicates the protection to asymmetry between the currents;
- LED 6 (D_6 connected to the port P_{14}) indicates the anti-bi-phase and voltage minimal protection;
- LED 7 (D_7 connected to the port P_{15}) indicates the starting period of the motor;
- LED 8 (D_8 connected to the port P_{16}) indicates the protection's verification with the contactor K_1 released.

All the LEDs (1,…,8) are supplied through limit resistances R_{lk}, k=1,…,8 of 1,8KΩ. In case of a defect, the contactor releases (non-time-delayed or time-delayed, depending on the defect's type), and the defect's related LED remains on. During the motor's starting period, the LED 7 turns on.

If it's desired the protection's verification, the procedure is as follows: after suppling the protection with electric power from the voltage stabilizer, should be pressed in order the keys S_{START} and S_3, to verify the protection, during the break of 1s (when all the warning LEDs are off). After this time, the LED 8 and the LED 1 are turning on and the contactor K_1 is not turning-on (verification is made by turning-off or turning-on of the LED 1). At the ports AD_1, …, AD_6 are connected the potentiometers P_{UR}, P_{US}, P_{UT}, P_{CR}, P_{CS}, P_{CT} , which, by adjusting, simulate different defects. At determination of the defect, the LED 1 turns off, and one ore more of the LEDs which indicates the type of defect (LEDs 3, 4, 5, 6) are turning on. The protection's re-turning on is made with S_4. If the system blocks itself, are pressed S_{RESET}, then S_{START}, after which can be simulated other defects.

If it's desired the motor's protection, after supplying with voltage is pressed the key S_{START}. In case of a defect, this is remedied, after which is pressed the key S_4, and if the system blocks itself, are pressed in order the keys S_{RESET} and S_{START}.

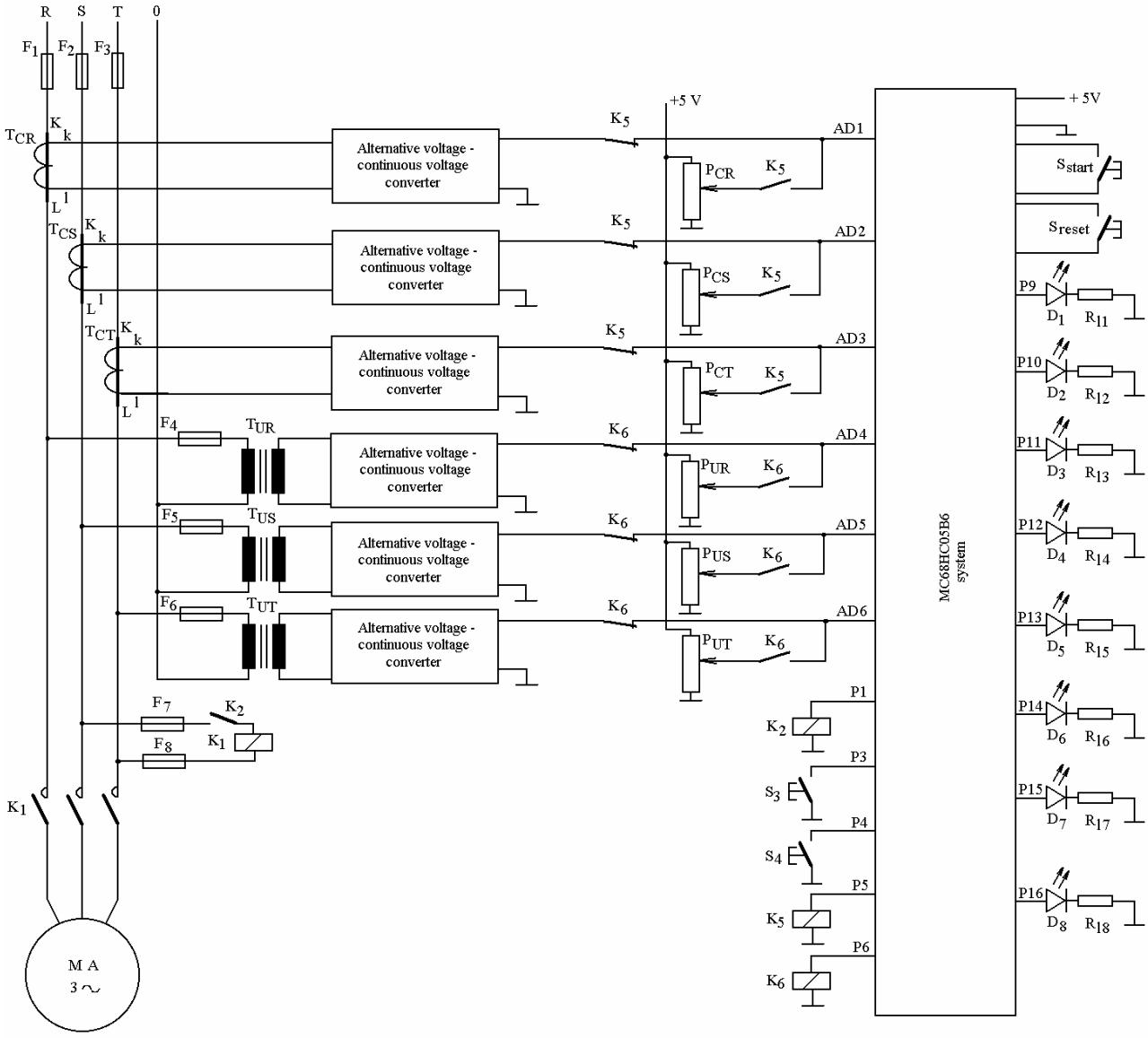

Fig.1. Principle diagram of the complex electronic protection.

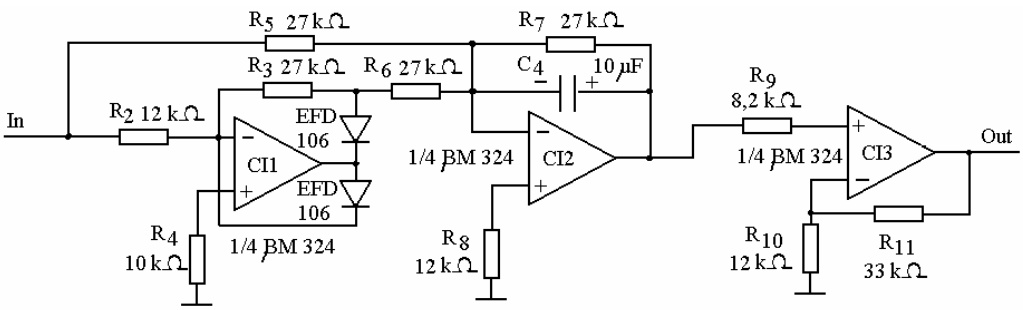

Fig.2. The converter used for the "alternative voltage-continuous voltage" conversion fig.1.

In fig. 2 is presented the "alternative voltage-continuous voltage" converter, used in collecting of phase currents and voltages of the protected motor from fig.1 [1]. The circuit's input In is connected to all the outputs of the secondaries of the current or voltage transformers, and the output Out is connected to the analog-digital ports AD_1, …, AD_6. CI1 together with the auxiliary components is a precision bi-alternance rectifier, CI2 together with R_7, C_4, R_8 is an active go-down filter, and CI3 with R_9, R_{10}, R_{11} is a non-inverter amplifier. The components R_{10} and R_{11} determine the amplifying factor. In the converter are used operational amplifiers of βM324 type.

The convertors AD_1, …, AD_6 are on 8 bit. The problem is that the system with microcontroller to sieze the value $1{,}05 \cdot I_n$ (the minimum value for which is considered overload). That means that to a value of $0{,}05 \cdot I_n$ (5% from I_n) should correspond at least a voltage U_p=19,4[mV]. The minimum voltage from the convertor's output should be:

$$U_{In} = \frac{I_n}{0{,}05 \cdot I_n} \cdot U_p , \quad (5)$$

After making the calculations, is obtained U_{In}=388[mV]. It is selected a voltage U_{In}=400[mV] (corresponding to the rated current I_n). At a voltage U_{In}=400[mV], after making the coversion, is obtained the decimal value U_{InZ}=21 (which, in fact, shows from how many intervals of U_p=19,4[mV] is formed the voltage at input into the analog-digital port). In table 1 are presented the voltage values at the output of the converter from fig.2 for different values of the overload currents.

Table 1

Voltages at the current converters' outputs U_{IS}[mV] from fig.2 and their decimal values U_{ISZ}[-] interpreted by microcontroller depending on the overload currents

I_s[A]	I_n	$1.05I_n$	$1.1I_n$	$1.15I_n$	$1.2I_n$	$1.25I_n$	$1.35I_n$	$1.45I_n$	$1.55I_n$
U_{IS}[mV]	400	420	440	460	480	500	540	580	620
U_{ISZ}[-]	21	22	23	24	25	26	28	30	32

I_s[A]	$1.7I_n$	$2I_n$	$2.05I_n$	$3I_n$	$4I_n$	$5I_n$	$6I_n$	$6.95I_n$	$7I_n$
U_{IS}[mV]	680	800	820	1200	1600	2000	2400	2700	2800
U_{ISZ}[-]	35	41	42	62	82	103	124	139	144

At overload, is calculated the time after which the time-delayed contactor K_1 releases, according to the formula (2). In order to sieze the minum voltage ($0{,}7 \cdot U_n$) is necessary that ate the convertor's output from fig.2 to be at least the voltage U_p. So, to the rated voltage U_n should correspond a voltage:

$$U_{Un} = \frac{U_n}{0{,}7 \cdot U_n} \cdot U_p , \quad (6)$$

The decimal value recognized by the microcontroller if of U_{UnZ}=21. To $0{,}7 \cdot U_n = U_{min}$ corresponds a voltage at the output of the "alternative voltage-continuous voltage" convertor of U_{Umin}=280 [mV], which has the decimal value of U_{UminZ}=14. This is the minimum voltage to which the motor still can operate.

The electronic protection permanent measure the currents and the voltages and achive the following:

- shortcircuit protection, with instantaneous release; for $I_S \geq 7 \cdot I_N$, t=0.02s (I_s-defect current, I_N – nominal current, t – release time);
- thermal overload release, the release are made with time delay t that depends by overload current I_S (according with motor thermal curve $K_s = I_S^2 \cdot t$); for $I_S=(1.05 \div 7) \cdot I_N$ and t=(7060÷0.02) [s];
- asymmetry currents protection, when one phase is with 20% bigger than other;
- starting and working in two-phase protection, with instantaneous release;
- minimum voltage protection; if the voltage is lower than a set voltage value ($0.7 \cdot U_N$), with instantaneous release.

The currents and voltages measure are made with current and voltage transformers and with alternating voltage/direct voltage convertors. The convertors output signals are transmission to microcontroller. The complex electronic protection is compact and may be used to a large motor powers (up to tenths KW), with a minimum modification in software (change of variable parameters).

The Protection's Logic Diagram

In fig. 3 is presented the logic diagram of the electronic protection's main program, achieved with MC68HC05B6 microcontroller. Is mentioned that both the current transformers T_{CR}, T_{CS} and T_{CT} (fig.1) and the voltage transformers T_{UR}, T_{US}, and T_{UT} operate in the non-saturated area.

Further is explained in detail the logic diagram of the program from fig.3.

By pressing the key S_{START}, the contactor K_1 and the relays K_5 and K_6 are releasing. Further, is achieved a break of 1s. Meanwhile, could be made the protection's verification by pressing the key S_3. If the key S_3 is pressed, it follows the verification sub-routine, thus achieveing another break of 1s; the LEds 1,…, 8 (for warning) are turning-off, and the LED 1 is turning-on (indicates the functioning of the protection). To the constant K is given the biggest positive value, K=32767 and is activated the anti- bi-phase protection sub-routine. If this sub-routine siezes a defect, it follows the contactor's releasing routine; thus, if K_5 and K_6 are released, it follows the contactor's turning-on routine,

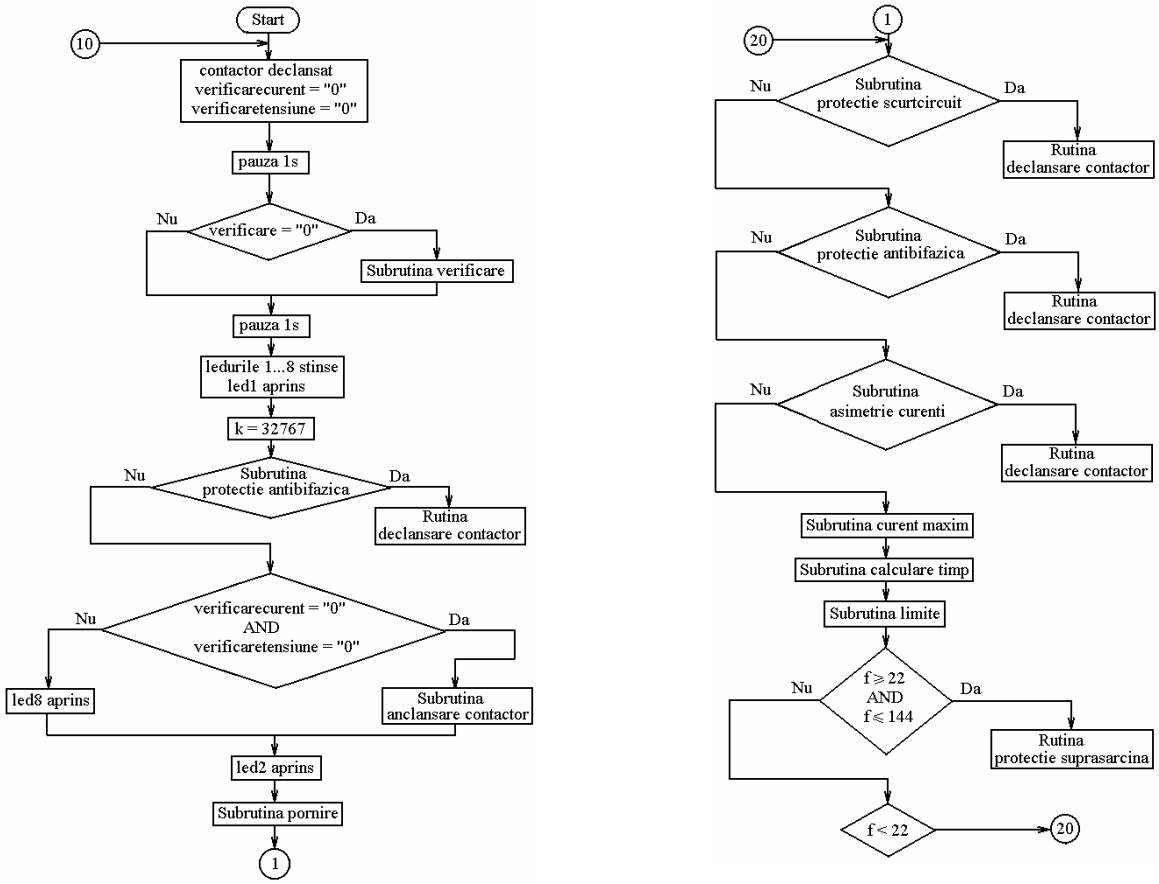

Fig.3. The logic diagram of the electronic protection's main program

thus the LEDs 8 (warning that the protection is under verification) and 2 (indicates the contactor's K_1 turning-on, when the motor M is supplied with voltage) are turning on. It follows the starting sub-routine, then the short-circuit protection sub-routine; if there is a defect, then operates the contactor's release routine, thus is activated the anti- bi-phase protection sub-routine; if there is a defect, it follows the contactor's release routine, thus operates the currents' verification sub-routine; if it is seized a defect, then it follows the contactor's release routine, thus to maximum current sub-routine, then to time calculation sub-routine and limits sub-routine. If $22 \leq f \leq 144$ (f corresponds to the maximum values of the currents from the three phases at a given moment, and 22 and 144 represent the limit values of the overload current), it follows the overload protection routine, thus for $f<22$ is made a skip to label 20, after that following the same verifications.

The program, after it was compiled (after compilation were obtained 721 octets) was sent on the serial interface RS232 to the system with microcontroller and stored in EEPROM.

Experiments

It was verified the protection's functioning to all types of defects mentioned in the beginning. In fig. 4 was drawn the experminetal protection's characteristic in semi-logarithmic co-ordinates. Within the range $I_S \in [1{,}05\text{-}7) \cdot I_n$ is achieved the overload protection, obtaining the times given in table 2, and at short-circuit, when $I_S \geq 7 \cdot I_n$ the release time of the contactor K_1 is of 0,02s.

The overload currents I_S[A] and the release times t[s] obtained experimentally, at overload and short-circuit, after which was drawn-up the characteristic from fig.1.

In case if the protection siezes a defect, is turning-on the LED (or LEDs) corresponding to the type of defect (short-circuit, anti- bi-phase, overload, voltage minimal), indicating also the moment when the defect took place (before starting, during starting or after starting).

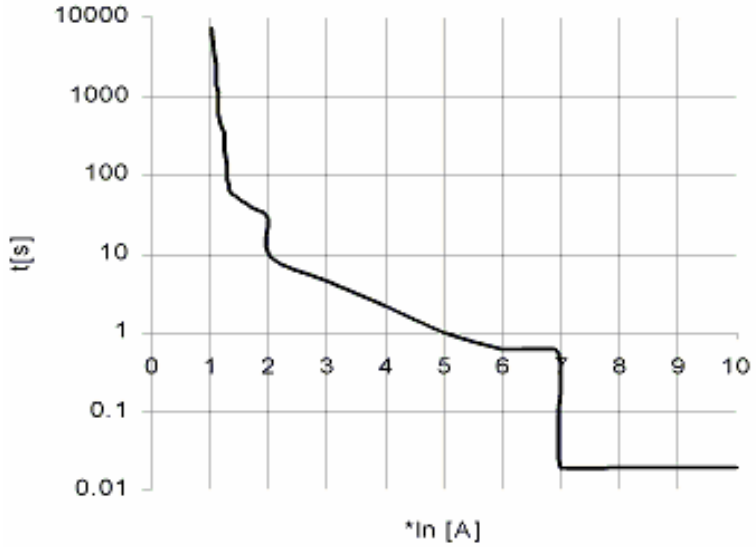

Fig.4. Protection characteristic of the system with microcontroller.

Table 2

The overload current when $I_S \in [1.05\text{-}7)\cdot I_n$ and short-circuit current, when $I_S \geq 7\cdot I_n$ which was drawn-up the characteristic from fig.4

$I_s[A]$	$1.05I_n$	$1.1I_n$	$1.15I_n$	$1.2I_n$	$1.25I_n$	$1.35I_n$	$1.45I_n$	$1.55I_n$
t[s]	7060	1763	772	450	75	64	53	46

$I_s[A]$	$1.7I_n$	$2I_n$	$2.05I_n$	$3I_n$	$4I_n$	$5I_n$	$6I_n$	$7I_n$
t[s]	39	28	9,3	4,41	2,15	1	0,6	0,02

Conclusions

It's been achieved a complex protection that can be used for a wide range of motors (with powers up to tens of KW), the single modifications that should be done, at changing of the protection from one motor to another, must be the starting limits (starting sub-routine), in such way to obtain starting periods dependant on the motor powers and on the amplifying factor of the CI3 circuits from the "alternative voltage-continuous voltage" convertors (fig.2) in order to obtain at output voltages of 400[mV] both at measuring of the rated currents and of the rated voltages.

References

[1] Drăgulănescu N. Agenda radioelectronistului, ediția a II-a, Editura Tehnică, București, 1989.
[2] Fransua Al.,Saal C., Țopa I. Acționări electrice, Editura Didactică și Pedagogică, București, 1975.
[3] Popa I., Popa G.N. Dispozitive electronice cu structură cablată și programată, de protecție a motoarelor asincrone trifazate de joasă tensiune, Editura Mirton, Timișoara, Romania, 2000.
[4] *** . C-Control/Basic Steuercomputer, Conrad Electronic GmbH, Germany, 1997.
[5] *** . C-Control/Basic Starterboard, Conrad Electronic GmbH, Germany, 1997.

Gabriel Nicolae Popa *– Lecturer, Ph.D., Faculty of Engineering Hunedoara, „Politechnica" University of Timisoara, Revolutiei str. no 5, Hunedoara, ROMANIA, e-mail: gnpopa@fih.utt.ro*

Iosif Popa *– Associate Professor, Ph.D., Faculty of Engineering Hunedoara, „Politechnica" University of Timisoara, Revolutiei str. no 5, Hunedoara, ROMANIA, e-mail: ipopa@fih.utt.ro.*

Sorin Deaconu *– Associate Professor, Ph.D., Faculty of Engineering Hunedoara, „Politechnica" University of Timisoara, Revolutiei str. no 5, Hunedoara, ROMANIA, e-mail: sorind@fih.utt.ro.*

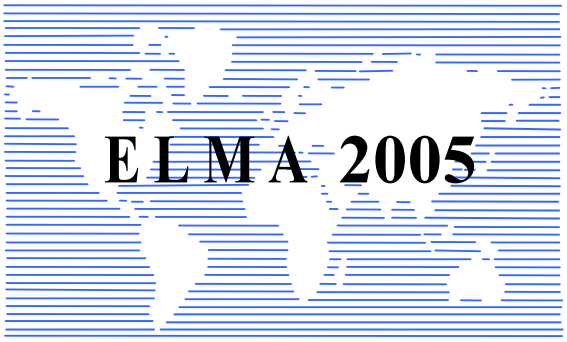

POWER SYSTEMS AND DISTRIBUTION SYSTEMS I

Voltage stability- essence, methodology and analysis

Petko Notov, Rad Stanev

Abstract: *The reasons for appearance of voltage instability, the way it processes and the consequences are being clarified. The program for static analysis of voltage stability STATUS is being presented, after which the methods used are described: method of V-P and V-Q curves, method of V-Q sensitivity and the method of the modal analysis of the state matrix. A comparison between the described methods is made and the method of Q-V modal analysis of the state matrix is approved, as most perspective.*

Keywords: *voltage stability, static analysis, modal analysis, V-Q sensivity, V-P and V-Q curves*

Introduction

Considering the tendencies of the Bulgarian power system development, which is a part of the united European power system (UCTE), ensuring the voltage stability will become more important for guaranteeing the integrity of the system and the quality of the electrical power, supplied to the electricity consumers. Although the problem is extremely important and up-to-date, until now in Bulgaria was no programme realisation, which could allow its detailed study. Voltage stability of an electrical power system (EPS) represents its ability to maintain continually admissible voltages, while being subjected to control and disturbing influences upon the equipment of which it contents. Operating conditions in which this ability is disrupted are possible- spontaneous and uncontrollable change, beyond the admissible limits of bus voltages in some areas of the electrical network, known as voltage instability (collapse) are observed. The duration of the process is between a few seconds and a few minutes.

Voltage instability is a failure process with local nature. The power supply in the affected area is disrupted. Because the failure states have cascading development after such processes, the power union splits into non-synchronously working parts or completely disintegrates. An elementary case of voltage instability is the tumble of induction motors (loss of their stability), supplied by a distant power source, after switching operations in the system [1]. The most common disintegration of concentrated* EPCs is observed after a voltage collapse in an area, after failure of one or more overloaded power lines, which connect it to the other parts of the system. Such processes may appear after decline of powerful and loaded generators, because of loss of excitation and also because of transformers, compensation devices, switching on heavy loads and wrong operative switching operation, incorrect operation and failures of system automation, etc. The voltage profile and stability are significantly affected by the operation of the synchronous generators and compensators, the other sources of reactive power (capacitor batteries, so called "FACTS"[2], etc), by the characteristics of the loads, by the operation of the voltage adjustment devices (the excitation systems of the synchronous machines, the OLTCs, etc.) in the EPC, by the co- ordination between the devices of the system automation themselves and between the relaying protections.

The nature of the problem discussed consists of the inability of the EPS to cover the necessities of reactive power in the unstable area.

Voltage instability- mechanisms and scenarios

Different scenarios for appearance and growth of voltage instability [2] are possible, like the following exemplary one:

The EPS is in a post- failure state, due to loss of generating units close to the load centre in a given area. Under these conditions the high- voltage power lines, which connect that area with the EPS appear to be overloaded. The resources of reactive power, necessary to support the voltage levels in the area are significantly decreased. A high- voltage power line falls off, because of being overloaded. The remaining power lines take its load, which leads to increase of reactive power losses over them. A lack of reactive power appears in the supplied area. The voltages, close to the load centre decrease significantly.

The generators' AVRs try to recover the voltage over their buses by injecting reactive power in the system. Through the transformers and the power lines extra reactive power flow passes and they increase the voltage drop in each of these elements, thus they decrease the voltages in the load buses even more.

The voltage decrease in the vicinity of the load centre reflects on the state of the distribution networks, too. By the means of the OLTCs of the transformers in the lowering substations, the voltages on the buses to which loads are connected are temporarily (for 2-4 minutes) recovered to the levels, before the disturbance. The switching of the taps of the OLTCs causes the load on the high voltage lines to increase. Because these lines are preliminary overloaded, the reactive power, necessary for transfer („loss" of reactive power) becomes too high [3]. The reactive power, emitted by the generators increases,

* *Concentrated* are the EPSs, whose systemsforming networks consist of many contours, formed by relatively short power lines, powered by robust power stations. Such are the EPSs of the European countries, including the Bulgarian EPS.

and one by one, they reach the limit of the reactive power they can render (when reaching the maximum admissible excitation current under the influence of AVR). When a generator reaches this state, the voltage over his terminals starts decreasing. As a result the current in its stator circuit grows in such a way, that it keeps its external active power, determined by the load. This process leads to turning off the overloaded generators, this way. Their share in covering the load of the systems is taken by the remaining generators, which get rapidly overloaded and their protections disconnect them one by one from the network.

The reactive power produced by the shunt capacitors and natural capacities of the power lines decrease in square with the voltage decrease, which additionally extends the described failure process.

When the voltages at the buses of the system- forming high- voltage network decrease, the transfer capabilities of power transfers decrease, too [1], i.e. the disruption of the synchronous stability (by shift angle of the generators) of the EPS – dynamic and/or transient becomes possible- i.e. some of the synchronous motors start swinging spontaneously, which is their reasons turning off or to fall cascadely out of synchronism, which leads to disruption of the power supply in separate areas or in the whole country.

The STATUS program

The STATUS program allows power flow solution in normal, stressed, including critical steady states and application of voltage stability static analysis. On the basis of static analysis the sensitive and predisposed to instability points and other "weak" places in the network are localized and technical measures for increase of stability, optimization of electrical states, support of the voltage profile and the quality of electrical power are defined. For application of the voltage stability static analysis, the STATUS program uses the method of V-P and V-Q curves, the method of V-Q sensitivity and the method of Q-V modal analysis of the state matrix, described below.

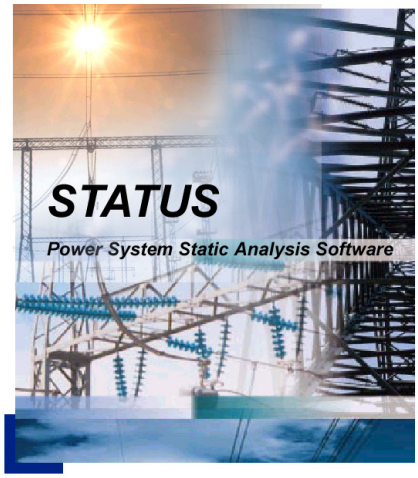

Methods

The basic methods for voltage stability static analysis, which at present have practical application, will be presented.

V-P and V-Q curves [2]

The method of V-P and V-Q curves is the oldest method, which is used for voltage stability analysis. This method examines the way the voltage changes, when increasing the load. The method has the essential advantage of staying close to the physical aspect of the problem and due to this reason it is extremely evident. The V-P and V-Q curves show how close (in MW and MVAr) is a system to the verge of voltage instability.

At first, we will examine the V-P curve (fig. 1). The points in the upper part of the V-P curve are stable. For them a small load increase is connected with a small voltage rise. At the critical point, at which the transferred power is maximum, the system is at the verge of stable state. In this point every load increase leads to significant (theoretically infinite) voltage reduction.

The points, which belong to the lower part of the curve are unstable. In order to guarantee the stable operation of the system it is necessary for it to have some reactive power reserve.

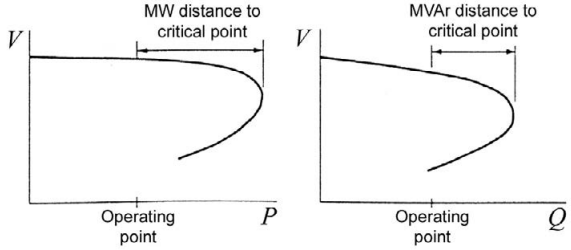

Fig.1. V-P and V-Q curves.

The voltages at the distinct network buses will vary significantly and some of the buses may preserve acceptable voltage levels, but the loss of voltage stability will arise at one and the same load, regardless the voltages in the distinct buses. Voltage instability starts in the most unstable bus and quickly spreads to the other weak links. That is the reason why the most unstable bus is the one with the lowest V-P curve.

The same reasoning are valid for the V-Q curves, too, with the difference that in that case the voltage change when increasing the load is estimated. Because V is influenced more by Q, than by P, in many cases application of the V-Q curves may appear to be more proper.

The V-P and Q-V curves may be calculated for particularly chosen load buses, for selected areas of the system or for the whole tested system. These curves are acquired by solving a number of power flows. Although these procedures may be automated, the calculation time is too long and they cannot provide the information, necessary for getting to the heart of the processes, causing instability. In addition, we shall note, that the

procedures are aimed towards particular buses, i.e. the stability characteristics are acquired by separately stressing each bus. This may lead to getting unrealistically distorted results for the system stability as a whole.

V-Q sensivity [2,4]

Let the bus equations, describing the pseudo steady state of an EPS are described in the known linearized form:

$$(1) \qquad \begin{bmatrix} \Delta \mathbf{P} \\ \Delta \mathbf{Q} \end{bmatrix} = \underbrace{\begin{bmatrix} \mathbf{J}_{P\theta} & \mathbf{J}_{PV} \\ \mathbf{J}_{Q\theta} & \mathbf{J}_{QV} \end{bmatrix}}_{\mathbf{J}} \cdot \begin{bmatrix} \Delta \theta \\ \Delta \mathbf{V} \end{bmatrix},$$

where

$\Delta \mathbf{P}$ - incremental change in bus real power,

$\Delta \mathbf{Q}$ -incremental change in bus reactive power injection,

$\Delta \theta$ - incremental change in bus voltage angle,

$\Delta \mathbf{V}$ - incremental change in bus voltage magnitude,

$\mathbf{J}$ - Jacobian matrix.

The system stability is influenced by **P** and **Q**. Although it may be presumed that the active power **P** preserves at each operating point and to examined only the connection between the increments of the bus voltage **V** and the reactive power **Q**. In that case

$\Delta \mathbf{P} = \mathbf{0}$ and therefore

$$(2) \qquad \Delta \mathbf{Q} = \mathbf{J}_{\mathbf{R}} \Delta \mathbf{V},$$

where

$$(3) \qquad \mathbf{J}_{\mathbf{R}} = \mathbf{J}_{QV} - \mathbf{J}_{Q\theta} \mathbf{J}_{P\theta}^{-1} \mathbf{J}_{PV}$$

is the reduced Jacobian matrix [1]. Equation (2) shows that:

$$(4) \qquad \Delta \mathbf{V} = \mathbf{J}_{\mathbf{R}}^{-1} \Delta \mathbf{Q}.$$

The matrix $\mathbf{J}_{\mathbf{R}}^{-1}$ is called ***V-Q*** *reduced Jacobian matrix,* whose i[th] diagonal element defines the **V-Q** *sensitivity* at the i[th] bus [2].

V-Q sensitivity at each bus of the network defines the slope of the ***Q-V*** curve for the respective bus when calculating the pseudo stable state. Positive sensitivity witnesses steady state. At that state, the less the sensitivity, the more stable is the EPS. With decreasing the stability, the sensitivity grows, reaching infinity at the verge of stability. Negative ***V-Q*** sensitivity is an indication of unstable operation.

The advantage of this method is that it gives information for the system stability as a whole and precisely defines the areas, where instability may appear. The substantial shortcoming, which the method showed when examining some systems is that it gives a clear distinction of the most unstable areas hardly in immediate vicinity of the critical point.

Q-V modal analysis [2,4]

Voltage stability in EPS may be defined by calculating the eigenvalues and the eigenvectors in the reduced Jacobean matrix $\mathbf{J}_{\mathbf{R}}$, defined with the equation (3). Let [2,4]

$$(5) \qquad \mathbf{J}_{\mathbf{R}} = \xi \Lambda \eta,$$

where

ξ - right eigenvector matrix of $\mathbf{J}_{\mathbf{R}}$;

η - left eigenvector matrix of $\mathbf{J}_{\mathbf{R}}$;

Λ - diagonal eigenvalue matrix of $\mathbf{J}_{\mathbf{R}}$.

From equation (5)

$$(6) \qquad \mathbf{J}^{-1}{}_{\mathbf{R}} = \xi \Lambda^{-1} \eta$$

Substituting in equation (4) gives:

$$(7) \qquad \Delta \mathbf{V} = \xi \Lambda^{-1} \eta \, \Delta \mathbf{Q}$$

or

$$(8) \qquad \Delta \mathbf{V} = \sum_i \frac{\xi_i \eta_i}{\lambda_i} \Delta \mathbf{Q},$$

where

ξ_i is the i[th] column right eigenvector of $\mathbf{J}_{\mathbf{R}}$;

η_i is the i[th] row left eigenvector of $\mathbf{J}_{\mathbf{R}}$;

Each eigenvalue λ_i and the corresponding right and left eigenvectors ξ_i and η_i define the i[th] mode of Q-V response. Since $\xi^{-1} = \eta$, equation (7) may be written as:

$$(9) \qquad \eta \Delta \mathbf{V} = \Lambda^{-1} \eta \, \Delta \mathbf{Q}$$

or

$$(10) \qquad \mathbf{v} = \Lambda^{-1} \mathbf{q},$$

where

$\mathbf{v} = \eta \Delta \mathbf{V}$ is the vector of modal voltage variations

$\mathbf{q} = \eta \, \Delta \mathbf{Q}$ - vector of modal reactive variations.

Eqation (10) contents uncoupled first order equations. Thus for the i[th] mode can be written

$$(11) \qquad \mathbf{v_i} = \frac{1}{\lambda_i} \mathbf{q_i}$$

because Λ^{-1} from (10) is a diagonal matrix, whereas $\mathbf{J}^{-1}{}_{\mathbf{R}}$ in (4) in general is nondiagonal.

With $\lambda_i > 0$, the i[th] modal voltage $\mathbf{v_i}$ an the i[th] modal reactive power $\mathbf{q_i}$ variations are along the same direction, indicating that the sysitem is voltage stable.

With $\lambda_i < 0$, the i[th] modal voltage $\mathbf{v_i}$ an the i[th] modal reactive power $\mathbf{q_i}$ variations are along opposite directions, indicating that the sysitem is voltage unstable.

The magnitude of each modal voltage variation $\mathbf{v_i}$ equals the inverse of λ_i times the magnitude of the

modal reactive power variation $\mathbf{q_i}$. Thus the magnitude of λ_i determines the degree of stability of the i[th] modal voltage. The smaller the magnitude of positive λ_i, the closer the i[th] modal voltage is to beeng unstable.

With $\lambda_i = 0$, the i[th] modal voltage collapses because any incremental change in that modal reactive power causes infinite change in the modal voltage.

The magnitude of the eigenvalues can provide a relative measure of the proximity to instability. Eigenvalues do not, however, provide an absolute measure because of the nonlinearity of the problem. To find the MW and MVAr distance to voltage instability, the system is stressed incrementally until it becomes unstable and the modal analysis is applied at each operating point.

The modal analysis can be extended by finding the following participation factors [4]:

- Bus participatin factors

The relative participation k in mode i ce is given by the bus participation factor

(12) $$P_{ki} = \xi_{ki}\eta_{ik}.$$

From equation (3.44) we see that P_{ki} determines the contribution of λ_i to the V-Q sensivity at bus k. For all small eigenvalues bus participation factors are determining the areas prone to instability. The sum of all the bus participations for each mode is equal to unity because the right and left eigenvectors are normalized. The size of bus participation in a given mode indicates the effectiveness of remedial actions applied at that bus in stabilizing the mode.

- Branch participation factors

With the angle and voltage variations for both sending and receiving ends known, the linearized change in branch reactive loss can be calculated. The relative participation of branch *j* in mode i is given by the participation factor

(13) $$P_{ji} = \frac{\Delta Q_{loss \quad for \quad branch \quad j}}{\max\left|\Delta Q_{loss \quad for \quad all \quad branches}\right|}.$$

Branch participation factors indicate, for each mode, which branches consume the most reactive power in response to an incremental change in reactive load. Branches with high participation are either weak links or are heavily loaded. Branch participation are useful for identifying to alleviate voltage stability problems.

- Generator participation factors

Analogous to the case of branch participation, for a given reactive power variation, voltage and angle variations are determined at each machine terminal. These in turn are used to compute the change in reactive power output for each machine. The relative participation factor of machine m in mode i is given by the generator participation factor

(14) $$P_{mi} = \frac{\Delta Q_{m \quad for \quad maschine \quad m}}{\max\left|\Delta Q_{\quad for \quad all \quad machines}\right|}.$$

Generator participation factors indicate for each mode which generators supply the most reactive power in response to an incremental change in system reactive loading. Generator participation factors provide important information regarding proper distribution of reactive reserves among all the machines in order to maintain adequate voltage stability margin.

Like the V-Q sensitivity method, the modal analysis method gives information for the system stability as a whole and clearly distinguishes the areas, where instability could appear. In addition, through the participation factors, the Q-V analysis gives information for the mechanism in which instability takes place and the role, which the distinct elements of a EPS play in the process. Another advantage, which the modal analysis shows, compared to V-Q sensitivity is that it clearly distinguishes the unstable areas in the initial stable state, far before reaching the critical point.

Conclusion

Taking into consideration the wide literature survey made and the examination of many systems at the methods described, using the STATUS program, it can be recapitulated that the modal analysis method of the state matrix gives the most complete estimation of the processes, taking place into EPS in cases of voltage instability.

Acknowledgments

The authors would like to express their sincere thanks to eng. St. Stannev who offered us help in English.

Literature

[1] Нотов, П., К.Герасимов, Преходни процеси в електроенергийните системи, София, 1997.

[2] Taylor, C.W. Power System Voltige Stability, McGraw-Hill,Inc., 1996.

[3] Под ред. проф. В.А.Веникова, Электрические системы, том 2 Электрические сети, М. 1971.

[4] Kundur, Prabha, Power System Stability and Control, 1994

Petko Notov – *Professor, Dr., Faculty of Electrical Engineering, Technical University of Sofia, 8 Kl. Ohridski Str., 1000 Sofia, BULGARIA. e-mail: notov@tu-sofia.bg*

Rad Stanev – *Ph.D. Student, Faculty of Electrical Engineering, Technical University of Sofia, 8 Kl. Ohridski Str., 1000 Sofia, BULGARIA e-mail: r_stanev@yahoo.com*

Voltage stability static analysis of distribution networks

Rad Stanev, Petko Notov

Abstract: *This article presents the examination of distribution networks using the program for voltage stability static analysis STATUS. An example with a real network is examined. On the basis of static analysis the sensitive and predisposed to instability points and other "weak" places of the network are localized and measures for stability increase, optimization of the electric states, support of the voltage profile and the quality of the electrical power are determined.*

Keywords: *voltage stability, static analysis, distribution networks, power flow, electrical power quality*

Introduction

Voltage stability is an extremely important problem both for transfer and distribution networks. Application of static analysis in distribution networks, except for voltage stability, gives precious information and for that, how optimal is the power flow in the system, in what degree the requirements for voltage profile and power quantity are fulfilled, which are the weak places in the network and what remedies shall be applied.

Test system

Static analysis of voltage stability will be presented in an existing 21 bus, 0,4 kV distribution network with uniformly distributed, symmetric, purely active load (Fig. 1). All the quantities are presented in named units.

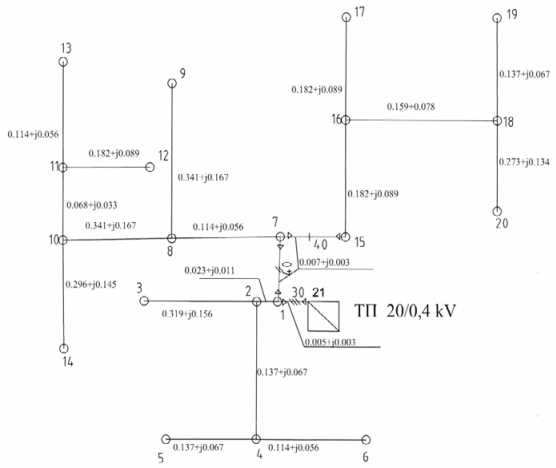

Fig 1. One- line scheme of the tested system

Voltage profile and V-P curves

The results from the solution of the power flow problem in the initial steady state and in the critical state are shown in table 1 and 2 respectively. The codes for bus types are: 0 - slack bus, 1- PV bus and 2 - PQ bus.

Table 1

Power flow solution in the initial steady state

Bus	Type	V	θ	P	Q
-	-	V	rad	kW	kVAr
1	2	399,09	-0,0013	-0,7415	0
2	2	398,19	-0,0024	-5,1909	0
3	2	395,4	-0,0058	-3,4606	0
4	2	395,79	-0,0053	-4,2021	0
5	2	395,28	-0,0060	-1,4831	0
6	2	395,44	-0,0058	-1,2359	0
7	2	398,12	-0,0023	-1,8009	0
8	2	388,86	-0,0133	-8,6514	0
9	2	385,58	-0,0174	-3,7078	0
10	2	372,18	-0,0341	-7,6627	0
11	2	370,86	-0,0358	-3,9549	0
12	2	369,89	-0,0371	-1,9775	0
13	2	370,48	-0,0363	-1,2359	0
14	2	369,60	-0,0375	-3,2134	0
15	2	397,75	-0,0027	-2,2600	0
16	2	389,08	-0,0132	-5,6852	0
17	2	388,16	-0,0144	-1,9775	0
18	2	384,68	-0,0187	-6,1796	0
19	2	384,15	-0,0194	-1,4831	0
20	2	382,56	-0,0214	-2,9662	0
21	0	400	0	71,673	1,2835

Table 2

Power flow solution in the critical state

Bus	Type	V	θ	P	Q
-	-	V	rad	kW	kVAr
1	2	395,25	-0,0053	-2,8167	0
2	2	391,70	-0,0095	-19,717	0
3	2	380,64	-0,0232	-13,145	0
4	2	382,22	-0,0213	-15,962	0
5	2	380,19	-0,0238	-5,6335	0
6	2	380,82	-0,0231	-4,6946	0
7	2	389,87	-0,0090	-6,8407	0
8	2	330,85	-0,0592	-32,862	0
9	2	315,55	-0,0817	-14,084	0
10	2	207,97	-0,2263	-29,106	0
11	2	198,44	-0,2481	-15,023	0
12	2	191,26	-0,2657	-7,5113	0
13	2	195,70	-0,2549	-4,6946	0
14	2	188,60	-0,2715	-12,206	0
15	2	388,23	-0,0105	-8,5844	0
16	2	349,82	-0,0560	-21,595	0
17	2	345,86	-0,0615	-7,5113	0
18	2	330,01	-0,0833	-23,473	0
19	2	327,65	-0,0867	-5,6335	0
20	2	320,38	-0,0976	-11,267	0
21	0	400	0	353,480	44,837

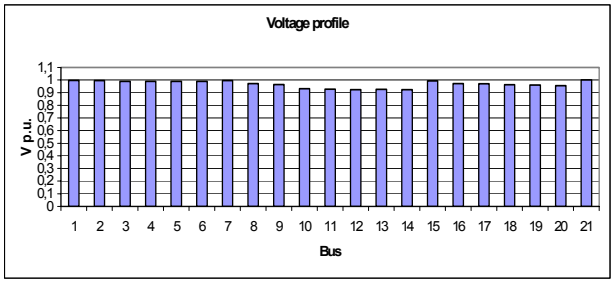

Fig.2.Voltage profile in the initial steady state.

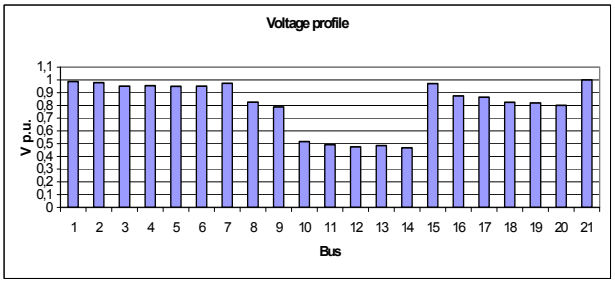

Fig.3. Voltage profile in the critical state

Graphically presented results of fig. 2, 3 and 4 allow the busses with decreased voltage to be localized.

The buses in the system may be conventionally divided into three groups:

- Buses with sensitive to load change voltage

In the initial steady state there are five buses only, with voltage under the minimum admissible magnitude of $0{,}95U_{rated}$. These are the buses, outermost from the transformer substation- buses 10, 11, 12, 13 and 14. These buses remain with the lowest voltage both in the maximum and the critical state.

On drawing to the critical state, the slope of the V-Q curve rises and just before the critical state the tangent to the curve practically becomes parallel to the ordinate. So that even in case of minimum load increase, significant (teoretically infinite) voltage decrease is observed. This, by itself witnesses voltage stability loss.

- Buses with slightly sensitive to load change voltage.

Buses 8, 9, 16, 17, 18, 19 and 20 have acceptable voltages in the initial steady state, but in the maximum and the critical state, they decrease their voltages under the admissible rates. Buses 8 and 9, which are close to the first group of buses (10,11,12,13 and 14), have a more sensitive voltage, than buses 16,17,18,19 and 20. In the critical state the slope of their V-Q curves significantly rises.

- Buses with insensitive to load change voltage.

These are all the other unmentioned buses (1,2,3,4,5,6,7 и 15). They are in the vicinity of the transformer substation. These buses retain admissible voltages in almost the whole system stressing process. For them, even immediately before the critical state, the small load changes lead to small voltage changes, which witnesses that they are in a steady, voltage stable state.

As we can see the voltages at the distinct network buses vary significantly and some of the buses preserve acceptable voltage levels, but the voltage instability arises at one and the same load, regardless the voltages in the distinct buses.

The voltage stability margin is 353,480kW + j44,837kVAr. The distance from the maximum registered state to the voltage stability margin is 112,890kW + j28,395kVAr or in %, compared to the critical state- 31,9% for active power and 63,3% for reactive power.

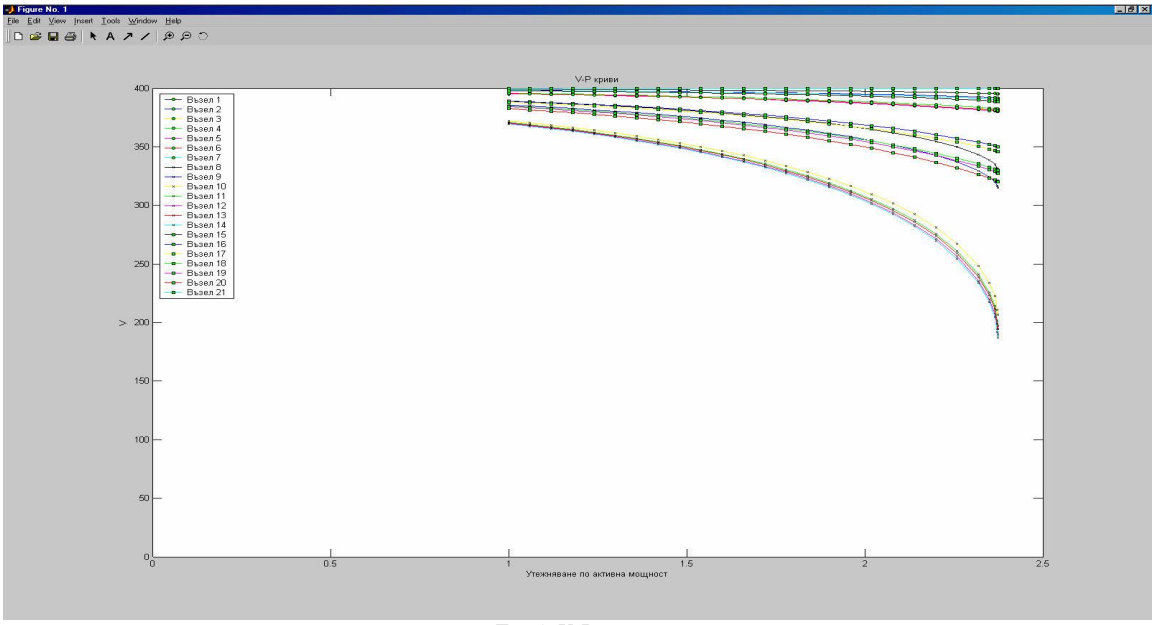

Fig.4. V-P curves

Power losses in the power lines

Table 3 shows the active and reactive power line losses in the initial steady state and in the critical state. The power line losses in the critical state are approximately 45 times greater than the losses in the initial steady state.

Figure 5 shows the active power losses in the process of stressing the state. Alike is the kind of the graphic of the reactive loss in the lines (Fig. 6).

The power loss graphics (Fig. 5 and 6) represent one of the main aspects of voltage instability, too, and namely- the system inability to transfer reactive power from the generation to the consumption place. This is visible, especially in the critical state, when the losses in the weak links significantly grow, and the transfer capability significantly decreases, i.e. the lines figuratively said, get "stuck".

The graphics show, that the weakest links (branches) in the system are (8,10), (7,8) and (15,16). These are the most heavily loaded links, which consume the greatest quantity of active and reactive power.

Table 3

Active and reactive power line loses in the initial and in the critical state

Line (from,to)	Line loses in the initial state	Line loses at the critical point
-	kW + *j*kVAr	kW + *j*kVAr
(21,1)	0,16058 + 0,09635i	03,968 + 02,381i
(1,2)	0,03549 + 0,01697i	00,544 + 00,260i
(2,3)	0,02444 + 0,01195i	00,380 + 00,186i
(2,4)	0,04193 + 0,02051i	00,650 + 00,318i
(5,4)	0,00193 + 0,00094i	00,030 + 00,015i
(4,6)	0,00111 + 0,00055i	00,017 + 00,009i
(1,7)	0,13345 + 0,05719i	03,741 + 01,603i
(15,7)	0,01971 + 0,00845i	00,367 + 00,157i
(7,8)	0,73855 + 0,36280i	26,914 + 13,221i
(8,9)	0,03153 + 0,01544i	00,679 + 00,333i
(8,10)	0,80639 + 0,39492i	40,254 + 19,714i
(10,11)	0,02545 + 0,01235i	01,313 + 00,637i
(11,12)	0,00520 + 0,00254i	00,281 + 00,137i
(11,13)	0,00127 + 0,00062i	00,066 + 00,032i
(10,14)	0,02237 + 0,01096i	01,240 + 00,607i
(15,16)	0,40865 + 0,19983i	07,792 + 03,810i
(16,17)	0,00472 + 0,00231i	00,086 + 00,042i
(16,18)	0,12181 + 0,05976i	02,425 + 01,189i
(18,19)	0,00204 + 0,00100i	00,040 + 00,020i
(18,20)	0,01641 + 0,00806i	00,338 + 00,166i
Total:	2,6031 + 1,2835i	91,124 + 44,837i

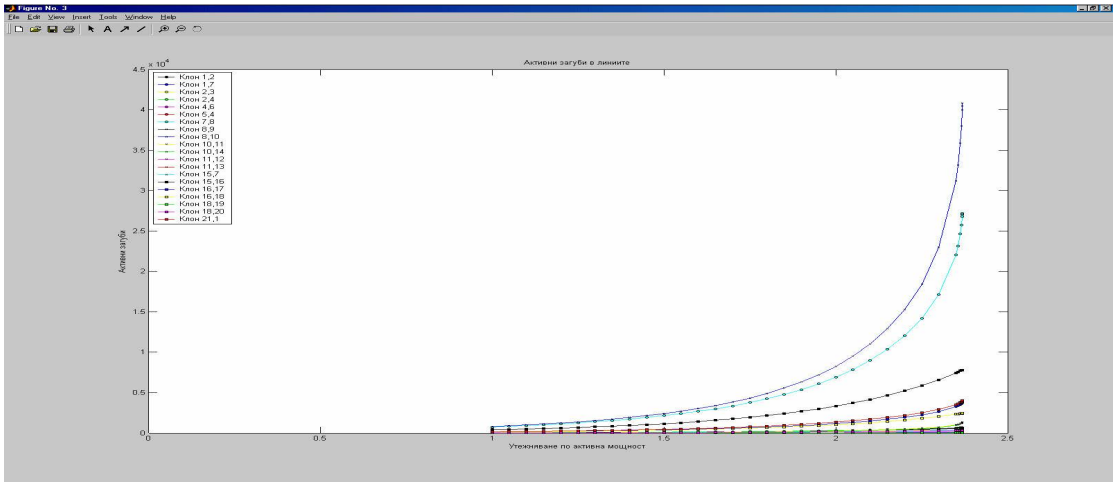

Fig.5. Active losses in the process of stressing the state.

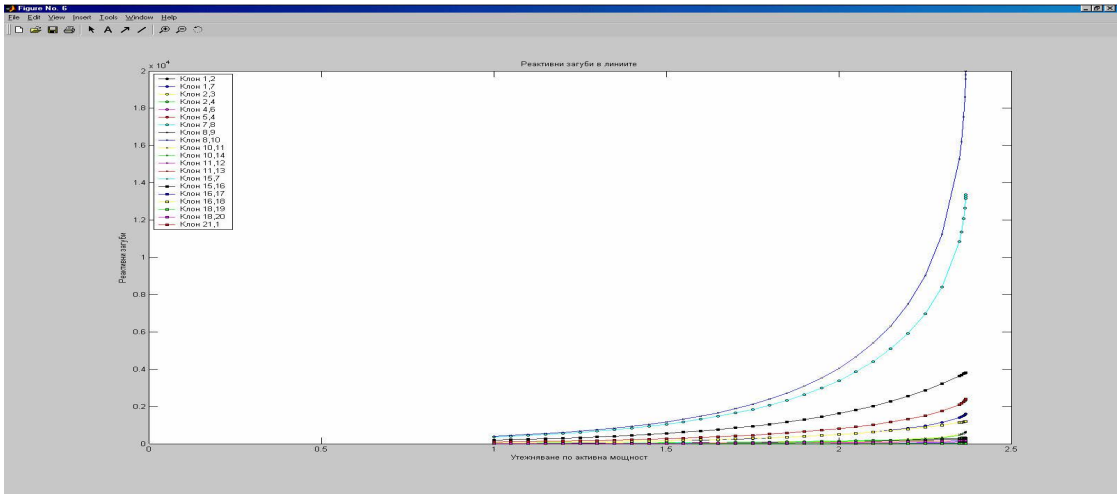

Fig.6. Reactive losses during the stressing process

Self V- Q sensitivities.

The V-Q sensitivity at every bus determines the slope of the V-Q curve for the given operation state. The positive sensitivity witnesses stable operation. The smaller the sensitivity, the more stable is the EPS. When stability decreases, sensitivity grows until reaching infinity on the verge of stability. Vice versa, the negative V-Q sensitivity is an indication of unstable operation. Because physical stability and mathematical stability by the Newton- Raphson method are directly interconnected, when reaching the critical point, the iteration process falls off convergency.

Table 4

Self V-Q sensitivities

Bus №	V-Q sensitivity in the initial steady state	V-Q sensitivity in the critical state
1	0,0000	0,0000
2	0,0000	0,0000
3	0,0004	0,0004
4	0,0002	0,0002
5	0,0004	0,0004
6	0,0003	0,0004
7	0,0000	0,0000
8	0,0002	0,0005
9	0,0006	0,0010
10	0,0006	0,0048
11	0,0007	0,0055
12	0,0010	0,0064
13	0,0009	0,0061
14	0,0010	0,0063
15	0,0000	0,0000
16	0,0003	0,0003
17	0,0005	0,0006
18	0,0005	0,0006
19	0,0006	0,0008
20	0,0008	0,0010

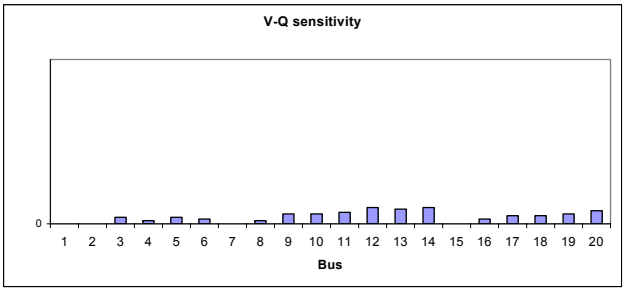

Fig.7. V-Q sensitivities in the initial steady state

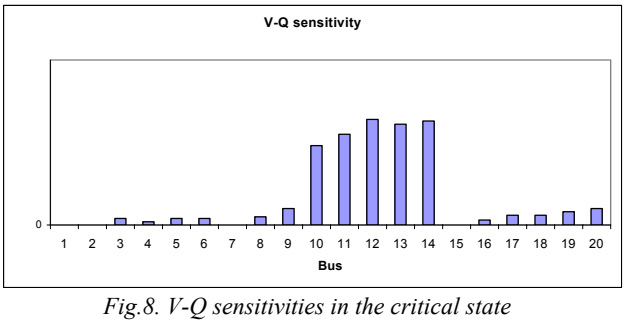

Fig.8. V-Q sensitivities in the critical state

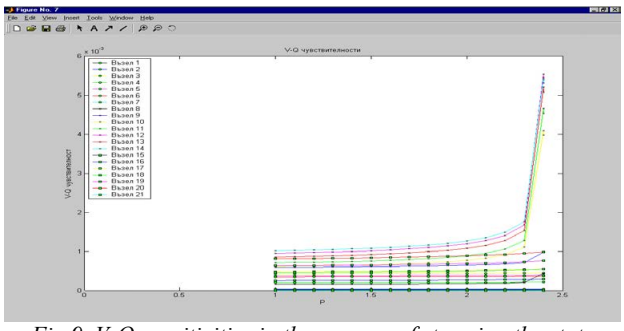

Fig.9. V-Q sensitivities in the process of stressing the state

The buses with the greatest V-Q sensitivities, are the most voltage unstable buses and for the specific system they are buses from 10,11,12,13 and 14 (fig. 8). Figures 6, 7 and 8 show one of the disadvantages of the method of V- Q sensitivities and namely- it gives clear distinction of the most unstable buses, only in the closest vicinity to the critical state.

Modal analysis

Except by the method of V-P and V-Q curves and the method of the V-Q sensitivities, the STATUS program allows static analysis of voltage stability by the method of Q-V modal analysis of the state matrix, too [4]. The application of the modal analysis allows the participation factors of the buses and the branches of the system in the least stable mode to be determined.

Bus participation factors

For all small eigenvalues the bus participation factors define the areas, which are predisposed to voltage instability in the greatest degree.

Table 5

Participation factors of the buses in the initial steady state and in the critical state

Bus №.	Bus participation factors in the initial steady state	Bus participation factors in the critical state
1	0,0000	0,0000
2	0,0000	0,0000
3	0,0000	0,0000
4	0,0001	0,0000
5	0,0001	0,0000
6	0,0001	0,0000
7	0,0001	0,0001
8	0,0130	0,0122
9	0,0171	0,0132
10	0,1580	0,1652
11	0,1869	0,1894
12	0,2159	0,2139
13	0,2043	0,2045
14	0,2015	0,2005
15	0,0001	0,0001
16	0,0004	0,0001
17	0,0004	0,0001
18	0,0006	0,0002
19	0,0006	0,0002
20	0,0007	0,0002

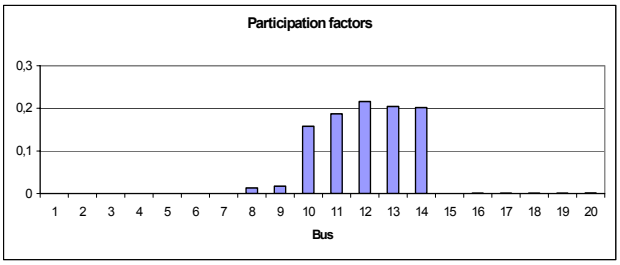

Fig.10. Bus participation factors in the initial steady state

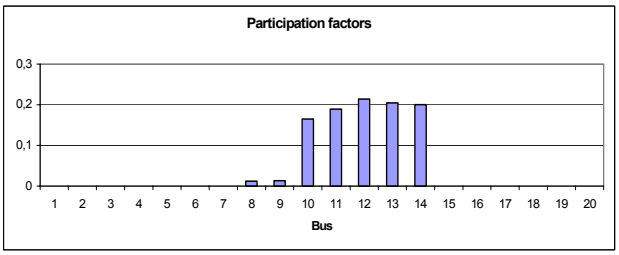

Fig.11. Bus participation factors in the critical state

The sum of all the bus participations for each state is equal to 1, because the left and right eigenvectors are normalized. The size of the participation factor shows in what degree will the applied for the stability measures contribute for increasing the state stability as a whole. In the examined system buses 10,11, 12, 13 and 14 differ with a great participation factor, and the participation of all the other buses are close to 0, i.e. the mode is localized.

From figures № 10 and 11 is visible an important advantage of the modal analysis method over the V-Q sensivity method, and namely that it clearly distinguishes the unstable areas early in the initial steady state, far before reaching the critical point.

Branch participation factors

The participation factors of the branches in each state show which branches consume the greatest quantity of reactive energy, as a result of load increase. Branches with great participation factor are either weak or overloaded lines. For the examined network in the initial steady state the greatest participation factors have branches (7,8), (8,10) and (15,16). At the critical state of stability loss, branches (7,8) and (8,10) keep their great participation factors. These are branches, which connect the transformer substation with the voltage unstable area, comprised of the buses with sensitive voltage (buses 10, 11, 12, 13 and 14). On their account the participation factor of branch (15,16) decreases in the critical state.

Table 6

Branch participation factors in the initial steady state and in the critical state

Power line between buses (from, to)	Branch participation factors in the initial steady state	Branch participation factors in the critical state
(21,1)	0,2440	0,1196
(1,2)	0,0430	0,0130
(2,3)	0,0303	0,0093
(2,4)	0,0519	0,0159
(5,4)	0,0024	0,0007
(4,6)	0,0014	0,0004
(1,7)	0,1448	0,0807
(15,7)	0,0214	0,0079
(7,8)	0,9187	0,6680
(8,9)	0,0391	0,0167
(8,10)	1,0000	1,0000
(10,11)	0,0313	0,0323
(11,12)	0,0064	0,0070
(11,13)	0,0016	0,0016
(10,14)	0,0278	0,0309
(15,16)	0,5060	0,1904
(16,17)	0,0058	0,0021
(16,18)	0,1513	0,0594
(18,19)	0,0025	0,0010
(18,20)	0,0204	0,0083

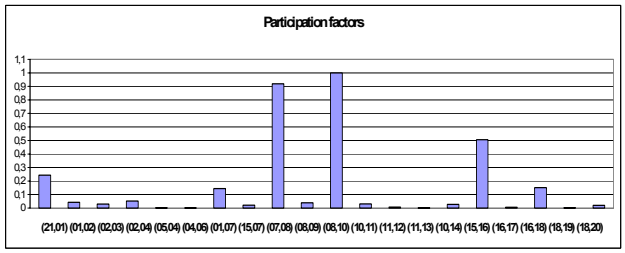

Fig.12. Branch participation factors in the initial steady state

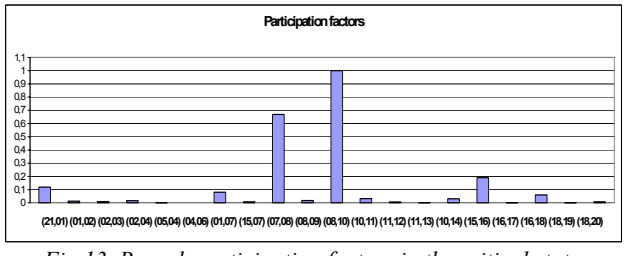

Fig.13. Branch participation factors in the critical state

Conclusion

1. The analysis made by the methods of the V-P curves, the V-Q sensitivity and the Q-V modal analysis show that the system is statically voltage stable. In all the system states realized, the system is away enough from the voltage stability margin, i.e. in the examined operational conditions the system has the necessary stability reserve.

2. From the viewpoint of electrical power quality improvement, it is reasonable to mount measurement, control and registration equipment in the buses with sensitive voltage, in order to track the state parameters.

3. In order to improve the quality of the electrical power, to optimize the electrical states and to increase voltage stability, the flow capacity of branches (7,8) , (8,10) and (15,16) shall be increased.

Acknowledgements

The authors would like to express their sincere thanks to Eng. St. Stannev who offered us help in English and to Associate Professor, Dr. Marin Botsov for presenting us the tested system.

References

[1] Нотов, П., К.Герасимов, Преходни процеси в електроенергийните системи, София, 1997.

[2] Taylor, C.W. Power System Voltige Stability, McGraw-Hill,Inc., 1996.

[3] Под ред. проф. В.А.Веникова, Электрические системы, том 2 Электрические сети, М. 1971.

[4] Kundur, Prabha, Power System Stability and Control, 1994.

Petko Notov *– Professor, Dr., Faculty of Electrical Engineering, Technical University of Sofia, 8 Kl. Ohridski Str., 1000 Sofia, BULGARIA. e-mail: notov@tu-sofia.bg*

Rad Stanev *– Ph.D. Student, Faculty of Electrical Engineering, Technical University of Sofia, 8 Kl. Ohridski Str., 1000 Sofia, BULGARIA e-mail: r_stanev@yahoo.com*

Usage of graphic systems for the solution of technological problems of control by operational modes both availability index of product of electric equipment of electrical networks and electrical power systems

Youri Koubarkov, Valery Goldshtein

Abstract: *In the report the outcomes of mining IAC "Pegas" for the automated management static and dynamic display indispensable for the solution of a problem of operation of business of electrical networks, and also items of information on the equipment ES are shown on the basis of information and functional model. The purpose of construction of an entity set model consists in detection of all parameters of a power system and definition of connections between them. The purpose of construction of functional model is the detection of problems solved in a management system, and connections between them.*

Keywords: *information, electrical system, substations, distributive networks, equipment of substations.*

Introduction

IAC "Pegas" is intended for the automated management static and dynamic display indispensable for the solution of a problem of operation of business, and also items of information on the equipment of an electrical power system and modes of its activity [1].

In a tendered complex the opened all-level systems combining a functions of technological and technological operation of business of electrical networks and ensuring maximum accessible information environment for operational services on the operating registration of a condition of the equipment of an electrical power system 0,4-110 kV and calculations of modes of its activity realised.

The concept of the open system IAC "PEGAS" guesses a capability practically of its unlimited extension by technological units and modules, and also miscellaneous information bases indispensable for maintenance of control by power firms at acceptance of the justified technical and economical solutions and measures.

IAC "PEGAS" envisions federating with corporate economical, geoinformation and operative - dispatching systems both systems of the registration of the electric power and control of its quality. At partial or full absence of the called systems IAC will realise a minimum indispensable set of their functions.

Assigning of a complex

- maintenance of leaving out of staff about a structure and characteristics of the established equipment of an electrical power system, its current condition, consumption and losses of the electric power, other generalized characteristics of primary activity. The information should be called directly from the scheme. Access to the schemes - from any workstation of a corporate network.
- maintenance of engineering staff of manufacturing services by means of authentic and visual mapping and control of a condition of the particular equipment of substations (SS) and distributive networks (DN), secondary circuits and devices, means of the registration, telemechanics, communication. Maintenance by help information, means of the registration of defects, deviations, applications, duties, rights etc.
- the solution of rated - analytical problems of control of modes of an electrical power system by engineering staff of manufacturing services.
- maintenance of activity of operative - dispatching staff by the information on a current condition of the equipment of an electrical power system. Applying of the unified library of the schemes in a simulator of operating switchings, operating log-book and operative - information complex.

Virtual mapping of hardware systems

The operations and operatings with the graphically mapped scheme of a system are designed as it is possible more adequately for operations and operatings in a substantial electrical system. For example, the switched - off position of the disconnecting switch, conclusion of a member from operative conditions, change of the operating status of the electrical vehicle is mirrored in the scheme with the help of change of its colour. The editor of corporation "Modus" will be used as the base editor.

Common federating of the data

"Pegas" enables to use one database for the electrical, mechanical, logical and physical characteristics of system members. These data can be used as for a different kind of calculations (normal mode, short-circuit currents, mechanical calculation etc.), and for a task of the characteristics of similar members at their attachment in the scheme. This federating of the data provides identity of the characteristics of one-type members for the scheme and reduces a volume of an input information.

Simplification of input datas

"Pegas" allows to prepare the database of the detail information for each electrical vehicle included in the scheme. At the subsequent data entry member, again placed on the scheme, needs only realization of updating of the selected information or simplly its selection from the database.

Pursuant to the set up concepts "Pegas" consists of four subsystems:

- of the purely graphic editor "Modus" permitting to work directly in a visual mode with the schemes of electrical networks and electrical power systems, executed in single line representation.
- databases, where all indispensable normative - help information on members imaged with the help of the graphic editor is stored.
- the installations both corrections of parameters and their values or characteristics of members placed on a field of mapping.
- of the rated - analytical modules permitting to design electrotechnical and other calculations for the mapped scheme of an electrical system.

The concept of creation of the distributed database of a network infrastructure "Power system"

The problem of creation of the database of a network infrastructure (further - Infrastructure) is more than actual problem, as from quality of the registration of the information, its conformity at any moment of time to a substantial condition of business a volume, received by firm, of the proceeds on implementation directly depends. The insecure registration, unauthenticity, absence of the indispensable information can by a unpredictable image have an effect on such relevant problems as calculation with the viewers, calculation of losses in networks [2].

Let's describe the requirements shown to a network infrastructure:

- **Unified information space**

The key requirement meaning, that anyone object / property should be present only at the single copy. Any subdivision, which one should is necessary to receive access to this object it to receive, that should be provided with the applicable means. The physically given requirement will be realised with the help of a unified database server, or organization of a system of duplicating of the information between database servers of subdivisions.

- **Consistence of the information**

Follows from problems of unified information space and means, that in the database there should not be no parts of the information, which one contradicts each other.

- **Absence of duality of the information**
- **Arrangement of executed operations**

Any operation, which one requires participation of several subdivisions should be technically realised in such a way. The operating originated by one subdivision should be transmitted to anothers on a chain of interplays.

- **Effectiveness of the information**

The effectiveness of the information should be not less often 1 time per day.

- **Information entirety.**

Structure and the pattern of the information should provide fulfilment all existing(present) at present in Energosbyt, electronetwork firms and CDS of problems, or should provide a principled capability of the solution of all these problems.

Corporate system on the equipment and modes of electrical networks

Leading particulars of corporate system are:

- database of the electronetwork equipment with binding to the schemes of objects consisting from storehouse(depot) of tabular datas and storehouse of the schemes of objects (substations, lines, feeders, secondary circuits, scheme of feeders with arrangement of the bearings etc.). The unequivocal conformity of the data on the scheme and in the tables is provided with means of the appendices of federating of the schemes and database of the corporation “Modus”.
- external sources of obtaining of the periodic and sporadic information - database OIC (operating position of switches); the database of the financial and economic information "«ICAR" (accession numbers, wearing of the equipment, lists of operation personnel etc.); the database “Energosbyt” (information on motion of meters on the substations).
- system of inquirys for activity of the specialists and executives who are not having special opening-up, with the database and schemes. The system is under construction on the special Web-server accessible from a corporate network and a network of affiliate through a standard Internet - browser.
- set of computational problems working in local area networks of affiliate. The list of problems can change depending on needs. It is expedient to include in a launch facility problems which are included in a structure of the operational complex in view of applying of new capabilities of graphic mapping of outcomes.
- simulator of operating switchings - component of the corporation ”Modus”. The activity of a simulator on the substantial operational schemes will allow to improve the quality opening-ups of operation personnel. There is an appendix "«Simulator" as component of the corporation ”Modus”.
- AWP of the manager. A set of problems for maintenance of operating activity of the manager of firm. Processing of the applications, maintenance by the operating documentation, help information, means of the registration of defects, deviations, duties be right etc. Management of the operating log-book (can the program of the corporation “Modus”) is utilised. The component «Adviser of the manager » can be realised in further.

Dynamic system controls of modes of networks 0,4-110 kV

At creation of a system the following problems are resolved:

1. Scheming of an electrical power system of firm.
2. Compiling the schemes of SS-6-110 kV.

3. Mining pattern of the integrated database on leading particulars of an electrical power system, selection of the format of data storage with possibility of using of available DB such as Oracle-8 or Access, mining of pattern of packages of a storage of information of different assigning (for electrical calculations, for exploitation, for the financial documents etc.), selection and optimization of a volume of the storable information and places of its storage (network, server, local machine), mining of a module of unequivocal conformity of the data presented on the schemes, drawn by the graphic editor and in the tables of a DB with possibility of using of means of different applications. Mining of providers both sampling of parameters of members and parameters of a mode simplified reference(reversal) to the data located in a DB, usage of standard means of a DBMS. Mining of capabilities of escalating of volumes of the storable information, and also capability of increase of quantity of members, schemes of feeders and regions.

4. List of the tables of normative - help information of including substation, transformers power and measuring, lines, switches, reactors, dischargers etc.

5. Management of base of the equipment and measuring instruments on substations, including

- Base of the equipment,
- Passport(certificate) of transformers,
- Base of measuring instruments on substations;
- Formation of the schedule - schedule of repair of the equipment and replacement of insulating oil.

6. System development of binding of external sources of obtaining of the periodic and sporadic information to the schemes, drawn by the graphic editor and to the tables of the database.

7. Mining possibility of using of the integrated database for the solution of many problems (calculation RPA, etc.) [3].

8. Computational problems on a network 6-110 kV:

- steadied (normal and emergency);
- power dissipations both electric power in an electrical power system and its separate members [4];
- an estimation of a level of commercial losses [5];
- short-circuit currents (three-phase and twophase);
- relay protection of power transformers (MCP, MCS);
- relay protection of lines (MCP, MCS and distance protection);
- relay protection of lines 6-10 kV from single-phase ground faults;
- relay protection synchronous and asynchronous motors (MCP, MCS);
- construction of cards of selectivity for five stages at usage of the relay assembly with the dependent and independent characteristics;
- calculation of parameters of the schedules(charts) of loads;
- calculation of adjustments of arcing ground suppressor;
- calculation of ferroresonance overstressings on substation 110-500 kV.

9. Mining AWP of the manager with a set of problems for his operating activity (processing of the applications, maintenance by the operating documentation, help information, means of the registration of defects, deviations, duties, rights and so further) and management of the operating log-book and with an outlook of implementation of a component " Adviser of the manager ".

References

[1] Rule of the device of electric sets. 6 is..- M.: Energoatomizdat, 1985.

[2] Loss of the electric power in electrical networks of power systems / V. T. Vorotnitskiy, Y. S Zelezko, I. H. Kazantsev etc.; Under red. I. H. Kazantsev. M.: Energoatomizdat, 1983.

[3] Directives on calculation of short-circuit currents and selection of electric equipment / Under red. B.N.Neklepaev, - M.: ENAS, 2002. - 152 p.

[4] RD 34.20.501-95. Operating instructionses of power plants and networks of Russian Federation, "RAO EES of Russia" 24.08.1995., 15 is. (with change №1, Minenergo of Russian Federation 17.07.2000 and "RAO EES of Russia" 23.06.2000).

[5] Technique of calculation of normative (technological) losses of the electric power in electrical networks approved by the command Minpromenergo of Russia from 3.02.2005 № 21.

Youri Koubarkov *– Professor, CSc., Faculty of Electrical Engineering, Technical University of Samara, Pervomaiskay Str., 18 Samara, RUSSIA. e-mail: tsara@sama.ru.*

Valery Goldshtein *– Professor, DSc., Faculty of Electrical Engineering, Technical University of Samara, Pervomaiskay Str., 18 Samara, RUSSIA.*

Prony Analysis and its Application in Studies of Inter-Area Oscillations in the Former Second UCTE Synchronous Zone

Chavdar Ivanov, Krum Gerasimov, Bozhidar Pavlov and Yulian Rangelov

Abstract: *This paper presents the results of an analysis of the inter-area oscillations in the former Second UCTE Synchronous Zone. The Prony analysis is applied in analyzing of the active power deviations recorded in the Bulgarian Electric Power System (EPS) at more significant disturbances in the Second UCTE Synchronous Zone. A special software tool in MATLAB has been designed to perform the Prony analysis. About 100 real disturbances that include about 625 records of active power deviations have been considered. These records are obtained by the recorder systems of the Bulgarian Transmission System Operator (NEK EAD). The results show a good performance of the investigated power system for damping of the inter-area oscillations.*

Keywords: *inter-area oscillations, damping, Prony analysis, Second UCTE Synchronous Zone.*

I. Introduction

Inter-area oscillations are associated with the swinging of many generators in one part of the electric power system against the generators in the other parts. They are caused by two or more groups of closely coupled generators being interconnected by weak ties. The natural frequency of these oscillations is typically in the range of 0,1 Hz to 1 Hz. The characteristics of inter-area oscillations are complex and in some respects significantly differ from the characteristics of local plant oscillations [1].

Inter-area oscillations in the former Second UCTE Synchronous Zone and its damping have been frequently discussed during the preparatory activities on reconnection between the First and the Second UCTE Synchronous Zones. Improvement of inter-area oscillations damping is one of the measures that should be taken in order to meet the UCTE requirements. Additionally, a stability study has been carried out to identify the necessary damping measures to be taken against the inter-area oscillations.

These and other facts became the reason of modernizing the control equipment of a number of units in the Bulgarian EPS and the other power systems in the Second UCTE Zone. New excitation systems with digital automatic voltage regulators (AVR) and power system stabilizers (PSS) [2] were installed in the Bulgarian EPS.

This new situation necessitated the launching of inter-area oscillations analyses and assessment of the Bulgarian EPS behaviour. Some real disturbances and damping measures against inter-area oscillations have been simulated.

The Bulgarian EPS operates synchronously with the other power systems in the Second UCTE Zone. Therefore this analysis shows the damping performance of the Bulgarian EPS, as well as the damping performance of the entire Second UCTE Zone.

After the resynchronization between the First and the Second UCTE Synchronous Zones on 10 October 2004, the frequency range of the inter-area oscillations was changed because of the power system enlargement.

The analysis shows a large degree of damping performance in the whole inter-area oscillations frequency range and the results from this analysis are valid not only for the situation before the reconnection, but also for the situation after reconnection to the UCTE.

Section II of this paper is a short description of Prony Analysis and its application for the purposes of this study. The software tool that performs Prony analysis is also described. The location of recorders and the period of analysis are discussed in Section III. Section IV presents the results of this study, which are summarized in Section V.

II. Prony Analysis and its Application

Background of Prony Analysis

Complete understanding of power system oscillations generally requires a combination of analytical tools. A lot of work has been done trough the years to develop mathematical techniques and tools for analyzing the oscillatory behaviour of the power systems. The special tools applied in the study of power system oscillations can be put into two basic groups: modal analysis and modal identification [1], [3], [4].

The Modal Analysis involves defining of the typical modes of a power system model, with linearization round a specific operating point. The modal analysis is not discussed in this paper.

In contrast to it, the Modal Identification involves defining of the typical modes of the power system dynamic behaviour obtained either from system measurements or from transient stability simulations using a non-linear model. The Prony Analysis is a typical example for a modal identification technique.

First published in 1795, the Prony Analysis is a mathematical strategy for fitting a series of damped sinusoids to an observed function *y(t)* [5], [6]

$$(1)\quad y(t) = Cx(t) = \sum_{i=1}^{n} B_i e^{\lambda_i t} = \sum_{i=1}^{Q} A_i e^{\lambda_i t} \cos\left(2\pi f_i t + \varphi_i\right)$$

The approximating function is given by

$$(2)\quad \hat{y}(k) = \sum_{i=1}^{P} B_i z_i^k$$

where *B* is a residue and $z_i = e^{\lambda_i \Delta t}$.

The approximating function $\hat{y}(k)$ has a structure and an underlying theory very similar to that of a Fourier series. The Prony Analysis extends the Fourier Analysis by direct estimation of frequency, damping, strength, and

relative phase of the modal components which are present in a recorded signal.

The Prony Analysis can be used as an addition to the Modal Analysis, which allows model validation and investigation of non-linear effects in the EPS [1].

Application of Prony Analysis

Due to the specific application of the Prony Analysis the MATLAB based tool has been developed. The backbone of this tool is the MATLAB function *prony*, which finds a filter with a certain numerator order, denominator order, and having the impulse response in the initial data. A loop in a developed algorithm gives the appropriate order of the filter nominator and denominator. The main aim of the algorithm is to find this appropriate order in which the impulse response of the filter fits to the recorded active power deviation obtained from a certain recorder. The algorithm has several stages:

- Load data – the user selects which record will be analyzed;
- Selection of time interval for analysis;
- De-noising – the tool uses wavelet concept to de-noise the initial data, if necessary;
- Apply function prony with minimum order of the filter;
- Calculation of signal to noise ratio (*SNR*)

$$SNR = \frac{-20\log\left\|\hat{y}(k) - y(k)\right\|}{\left\|y(k)\right\|} \tag{3}$$

where $\|\ \|$ denotes the usual root mean square norm and the *SNR* is in decibels, dB.

The reconstructed signal $\hat{y}(k)$ will usually fit to $y(k)$ inexactly. Signal to noise ratio is used as a measure for the quality of this fitting.

- Calculation of the poles and residues of the filter;
- Obtaining of modal properties for each modal component of the recorded signal:

- The eigenvalues (λ_i)

$$\lambda_i = \mathrm{Re}\left(\lambda_i\right) \pm j\,\mathrm{Im}\left(\lambda_i\right) = \sigma_i \pm j\omega_i \tag{4}$$

$$\lambda_i = \frac{\log\left(\lambda_{zi}\right)}{\Delta t} \tag{5}$$

where λ_{zi} is the pole in *z* domain.

- The initial amplitudes (A_i) and phases (φ_i)

$$A_i = 2\left|r_i\right|, \quad \lambda_i = \sigma_i \pm j\omega_i \tag{6}$$

$$A_i = \left|r_i\right|, \quad \lambda_i = \sigma_i \tag{7}$$

$$\varphi_i = \arctan\left(\frac{\mathrm{Im}\left(r_i\right)}{\mathrm{Re}\left(r_i\right)}\right).\frac{360}{2\pi} \tag{8}$$

where r_i is a residue.

- The oscillation frequency is given by

$$f_i = \frac{\omega_i}{2\pi}, \text{ Hz} \tag{9}$$

- The oscillation damping ratio is defined to be

$$\xi_i = \frac{-\sigma_i}{\sqrt{\sigma_i^2 + \omega_i^2}}.100\ , \% \tag{10}$$

The damping ratio determines the rate of decay of the amplitude of the respective oscillation. The minimum acceptable level of damping below which the power system cannot have a satisfactory operation, is not clearly defined. According to the world practices [1], the minimum acceptable damping ratio is typically within the range from 3 % to 5 %. It means that the amplitude of the inter-area oscillations is damped down from 15 *s* to 13 *s*.

The tool developed for performing this algorithm has a user-friendly graphical interface, which is shown on Fig.1.

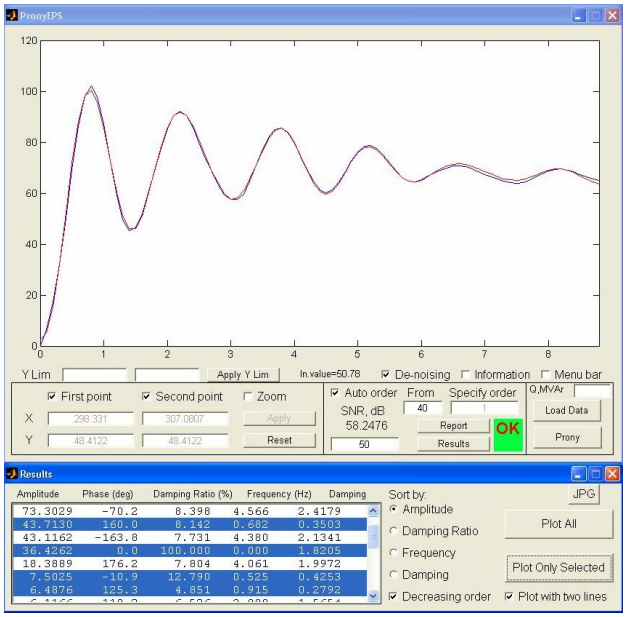

Fig. 1. Main dialog window of the software.

Validation of the Developed Software

The software validation is done in the following cases:

- Analysis of initially known compound signal

$$\begin{aligned} y(t) = {} & 0{,}6.e^{-0{,}02t}\cos\left(2\pi.0{,}12.t + \frac{85\pi}{180}\right) + \\ & + 1{,}2.e^{-0{,}03t}\cos\left(2\pi.0{,}7.t + \frac{65\pi}{180}\right) + \\ & + 1{,}25.e^{-0{,}04t}\cos\left(2\pi.1{,}1.t + \frac{35\pi}{180}\right) + \\ & + 0{,}3.e^{0{,}05t}\cos\left(2\pi.1{,}5.t + \frac{15\pi}{180}\right), \end{aligned} \tag{11}$$

where $t = 0, 0.1, 0.2, \ldots, 10\ s$.

The results are shown in Table 1.

Table 1.

Results initially known compound signal

A	φ, deg	ξ, %	*f*, Hz
0.3	15	-0.531	1.5
0.6	85	2.652	0.12
1.2	65	0.682	0.7
1.25	35	0.579	1.1

- Comparison of the results (Table 2) from the analysis of active power deviations at generator outage (unit 5, 500 MW output power) in Kozloduy NPP with frequency response of 1000 MW units in Kozloduy NPP. The frequency response tests were carried out a week before this generator outage so that a comparison of the results could be made.

Table 2

Results of active power deviation analysis

units	Frequency at peaks in frequency response, Hz	Frequency obtained from the recorded signals, Hz
5	0.9	0.97
	0.7	0.692
6	0.9	0.863
	0.7	0.753

The results presented in Table 2 show that the modal identification of dominant frequencies at this disturbance fit to dominant frequencies in frequency responses. The analyzed disturbance stimulates the local plant oscillations coming from these units.

III. Recorders and Period of Analysis

The recorders in the Bulgarian EPS are maintained by the Bulgarian Transmission System Operator (National Electric Company- NEK EAD). They are installed in the Bulgarian border substations and power plants. The data from 17 recorders have been analyzed in this study. Five of the recorders are installed in the border substations to record the deviations in the Bulgarian tie-lines, and the rest of recorders are installed in power plants.

- Recorders in the border substations, 400 kV tie-lines: Dobrudzha s/s (BG) – Isaccea s/s (RO); Kozloduy NPP (BG) – Tantareni s/s (RO); Sofia West s/s (BG)-Nis s/s (YU); Blagoevgrad s/s (BG) - Thessaloniki s/s (GR).
- Recorders in power plants: Kozloduy NPP, Varna TPP, Bobov Dol TPP, Maritsa East 2 TPP.

The observation period was from the beginning of 2003 to 10 October 2004 - the reconnection between the First and the Second UCTE Synchronous Zones.

IV. Some Results of the Analysis

About 100 real disturbances in the Second UCTE Zone that include about 625 records of active power deviations have been analyzed. About 2000 dominant modal components in the frequency range from 0.1 Hz to 3 Hz have been obtained as a result of the these records analysis. The results are presented in diagrams shown below.

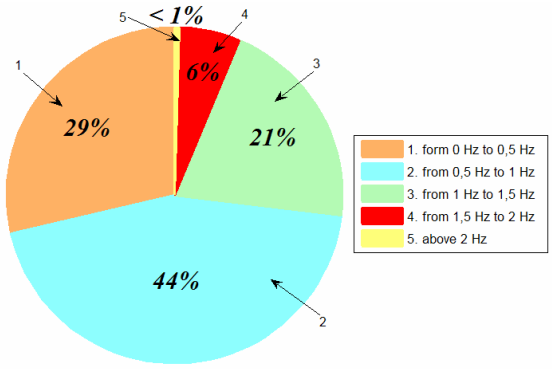

Fig. 2. Modal components by frequency ranges

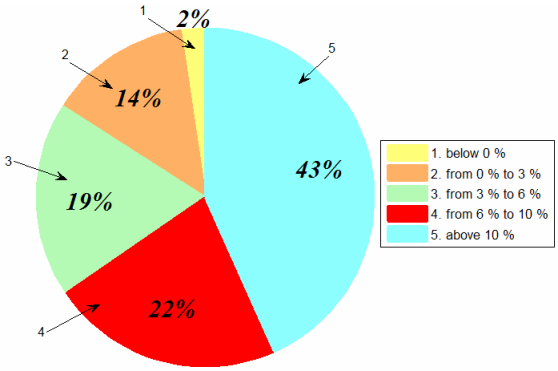

Fig. 3. Damping ratio of modal components.

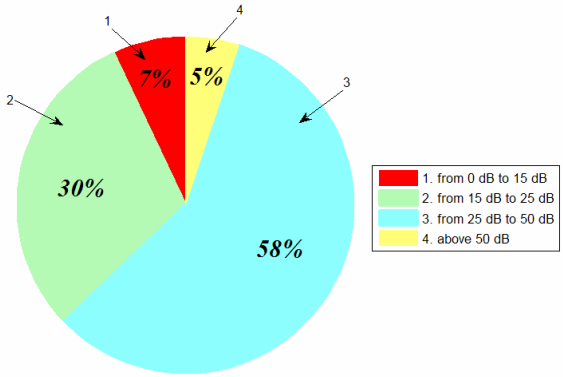

Fig. 4. Signal to noise ratio (SNR)

Figures 2, 3, 4 and 5 show the following:

- Because of the location and type of disturbances, the oscillations with frequency below 1 Hz are prevailing (73 %, Fig. 2) in the modal components obtained. The frequencies higher than 1 Hz are obtained mainly from the recorders in the power plants where local modes are observed.
- The typical frequencies of the inter-area oscillations in the Second UCTE Zone are in a frequency range from 0.5 Hz to 0.8 Hz.
- The modal components with a damping ratio higher than 3 % are 84 % (Fig. 3) of all the modal components. This shows a good damping performance of the power system oscillations in the Second UCTE Zone

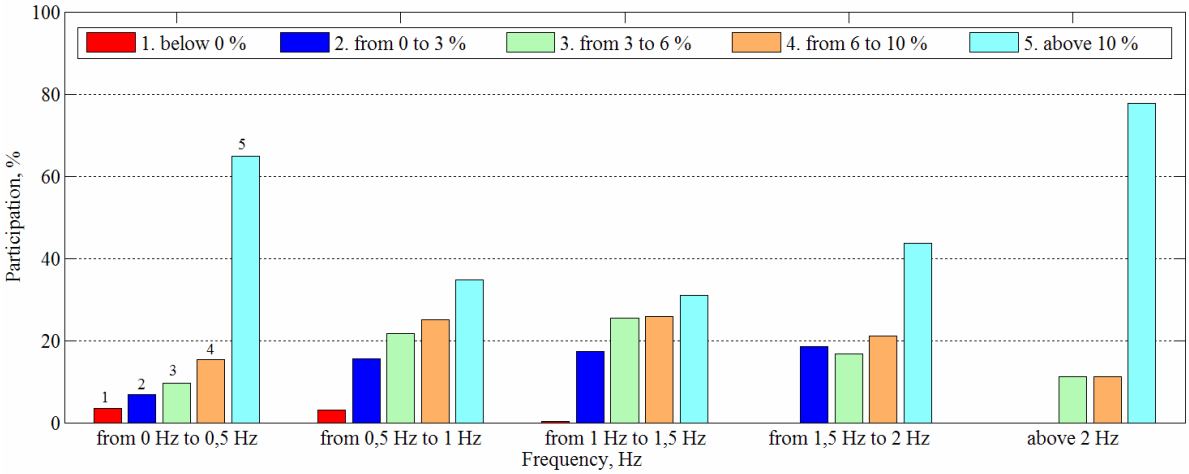

Fig. 5. Damping ratio of modal components by frequency ranges

- The computed unstable modes (2%, Fig. 3) are not realistic, because actually only long-lasting oscillations occurred, however with non-increasing amplitude. This numerical effect may be caused by the insufficient time interval for the Prony analysis [7]. Besides, these unstable modes can be neglected, because their amplitude is 30-50 times smaller than the amplitude of the main modal component of the respective recorded signal.
- Only 7 % of the recorded signals have been analyzed at a signal-to-noise ratio below 15 dB (Fig. 4). This ensures the analysis accuracy.
- About 85 % of the modal components in a frequency range from 0.5 Hz to 1 Hz have a damping ratio higher than 3 %. This proves the damping performance in this frequency range.
- About 65 % of the modal components in the frequency range from 0 Hz to 0.5 Hz have a damping ratio higher than 10 %. This is a good indicator that after the reconnection between the First and the Second UCTE Synchronous Zones the power system oscillations damping will not be affected and will remain as good as before the reconnection.

V. Summary

The results of this analysis can be summarized as follows:

1. The inter-area oscillations in the former Second UCTE Synchronous Zone have a good damping performance.

2. The frequency range of recorded inter-area oscillations is from 0.5 to 0.8 Hz. After the reconnection of the two UCTE synchronous zones the most probable value is about 0.2 Hz. This statement has been confirmed by the analysis of the reconnection process and the analysis of some disturbances having occurred after that.

3. The developed software is a valuable tool that implements the Prony Analysis and it can be used in further studies of analyses of low frequency oscillations and power system model verification.

Periodic analyses of the inter-area oscillations damping at future disturbances within the UCTE will be made in order to check the power system damping performance in Eastern Europe.

References

[1] CIGRE Technical Brochure on control of power system oscillations, Task force 38-01-07, Final report, July 1996.

[2] Pavlov, B. The electric power system of Bulgaria on its way to UCTE. Power Engineering Society General Meeting, 2003, IEEE Volume 1, 13-17 July 2003.

[3] Kundur, P. Power System Stability and Control. New York: McGraw-Hill Inc., 1993.

[4] Rogers, G. Power System Oscillations. Boston: Kluwer Academic Publishers, 2000.

[5] Hauer, J. F. Application of Prony analysis to the determination of modal content and equivalent models for measured power system response. IEEE Trans. Power System, pp. 1062-1068, Aug.1991.

[6] Hauer, J. F. Initial results in Prony analysis of power system response signals. IEEE Trans. Power System, pp. 80-89, Feb.1990.

[7] Breulmann, H., E. Grebe, M. Lösing, W. Winter, R. Witzmann, P. Dupuis, M.P. Houry, T. Margotin, J. Zerenyi, J. Dudzik, PSE S.A., J. Machowski. Analysis and damping of inter-area oscillations in the UCTE/CENTREL power system. CIGRE 38-113, Session 2000.

Chavdar Ivanov *– Expert in System Analyses and Transmission Planning Department, National Dispatch Center, Bulgarian National Electric Company (NEK), 5 Veslets Str., 1040 Sofia, BULGARIA. e-mail: ch.ivanov@ieee.org*

Krum Gerasimov *– Associate Professor, Dr., Faculty of Electrical Engineering, Electrical Power Engineering Department, Technical University of Varna, 1 Studentska Str., 9010 Varna, BULGARIA. e-mail: k.gerasimov@tu-varna.edu*

Bozhidar Pavlov *– Head of System Analyses and Transmission Planning Department, National Dispatch Center, Bulgarian National Electric Company (NEK), 5 Veslets Str., 1040 Sofia, BULGARIA. e-mail: bpavlov@ndc.bg*

Yulian Rangelov *– Assistant Professor, Faculty of Electrical Engineering, Electrical Power Engineering Department, Technical University of Varna, 1 Studentska Str., 9010 Varna, BULGARIA. e-mail: j.rangelov@tu-varna.edu*

Selection of PSS Gain Based on Impedance Matching

Chavdar Ivanov, Olof Samuelsson and Krum Gerasimov

Abstract: *This paper presents an approach for PSS gain selection based on impedance matching concept. The presented approach is used for improvement of the damping of the inter-area oscillations. In order to clarify this method a spring-mass mechanical system and a simple two-area power system are investigated.*

Keywords: *power system oscillations, damping, inter-area oscillations, impedance matching, PSS gain.*

I. Introduction

Inter-area oscillations are associated with the swinging of many generators in one part of the electric power system against generators in other parts. They are typically caused by groups of closely coupled generators being interconnected by weak ties. The natural frequency of these oscillations is typically in the range of 0,1 Hz to 1 Hz. The characteristics of inter-area oscillations are complex and differ from the characteristics of local plant oscillations [1]. A power system stabilizer (PSS) is often used to provide a supplementary signal to the generator excitation system. The basic function of the PSS is to provide positive damping torque to power swing modes [2]. To this aim PSS must produce a component of electrical torque on the rotor, which is in phase with speed deviations.

The calculation of PSS settings has been widely discussed over the past years. Based of the concept of damping and synchronizing torques developed on the shaft of a generator, a technique was presented for PSS tuning for a single machine infinite bus system [3]. Using this approach a practical procedure for PSS tuning is presented in [2]. Compensation for the phase response over an appropriate frequency range is used in determing the transfer function of PSS. A further test is performed to determine the PSS gain. This test consists of raising the gain until the onset of instability is observed. Then the PSS gain is set to $1/3^{rd}$ of this value.

Several methods of the design of compensation for PSS are used in practice. Some of them are summarized in [1], [4], [5].

The wave-based analysis of electromechanical disturbances has been recently discussed in [8], [9]. In [8] electromechanical waves in power system were modeled as a way to understand observations from phasor-angle measurement devices in the field. These electromechanical waves are manifest in the mechanical shaft dynamics of electrically coupled generators.

Modal analysis of linearized models [10] represents the dynamics via superposition of simple standing (rather than traveling) motions. The traveling wave perspective is important for a basic understanding of power system dynamics because it directly relates spatial and temporal information [9].

The possibility of control actions to eliminate wave reflections at the edges of a grid is realized in [9]. This is accomplished in a manner analogous to impedance matching of transmission lines.

The results presented in this paper are obtained by software as EUROSTAG, MATLAB and EUROMAT toolbox. EUROMAT toolbox is used to transfer linearized model from EUROSTAG to MATLAB [6].

Section II of this paper deals with mechanical model and its electrical equivalent. The possibility for application of the proposed approach for PSS gain selection is presented in Section III. The results from this investigation are summarized in Section IV.

II. Mechanical model and its electrical equivalent

Electromechanical dynamics of power system can be transformed into purely mechanical or electrical systems. Fig. 1 shows a spring-mass model that exhibits the dynamics of the inter-area mode. The generic damping component in a spring-mass model is a viscous damper *d* (Fig. 1).

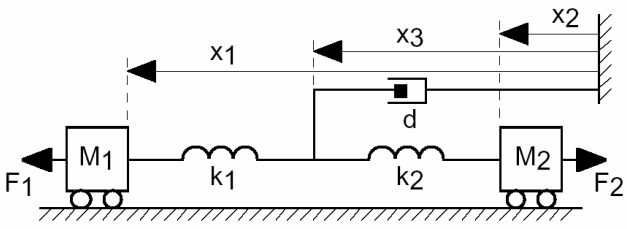

Fig. 1. Spring-mass model of an inter-area mode.

When moving one of the ends relative to the other the damper develops a counteracting force proportional to the velocity of the motion. Introducing a damper would intuitively damp an oscillating motion of the masses as the swing energy is dissipated in the damper.

Application of the equivalent variables and parameters in mechanical and electrical systems [6], [7] to the mechanical system, shown in Fig. 1, gives a state space description that agrees with the circuit of Fig. 2. Energy stored in the capacitors C_1 and C_2 corresponds to the kinetic energy stored in the swinging masses of the power system. Similarly energy stored in the inductors $_{L1}$ and L_2 is equivalent to potential energy in the power system. The conductance R represents the damper.

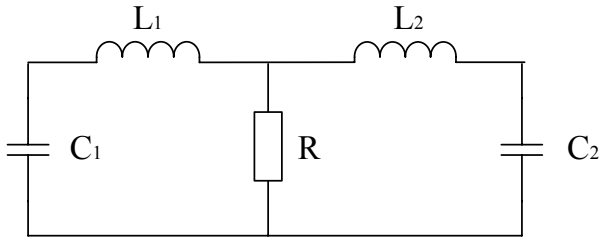

Fig. 2. Electric equivalent to the spring-mass inter-area mode system with one damper.

For this circuit active and reactive power are well defined. Active power is dissipated in the conductance, while reactive power quantifies the energy oscillating between the lossless inductors and capacitors. Consequently the oscillation is damped as its energy is dissipated as active power. If R is equal to zero, the electric system is a pure LC-circuit with undamped oscillatory mode. Setting R to infinity yields LC-circuits with different resonance frequencies.

The maximum damping is achieved when maximum active power is dissipated in the damper. In case of R equal to zero or infinite both yield zero damping since in the first case the current is zero, while in the second case the voltage is zero. By modeling the circuit as R connected to a two-pole with impedance Z, the condition for maximum power is conveniently formulated as that of impedance matching

$$R = |Z| \tag{1}$$

Root locus of the spring-mass inter-area mode model is shown in Fig. 3. In addition, the detailed view of root locus around eigenvalue with the best damping ratio is shown in Fig. 3a.

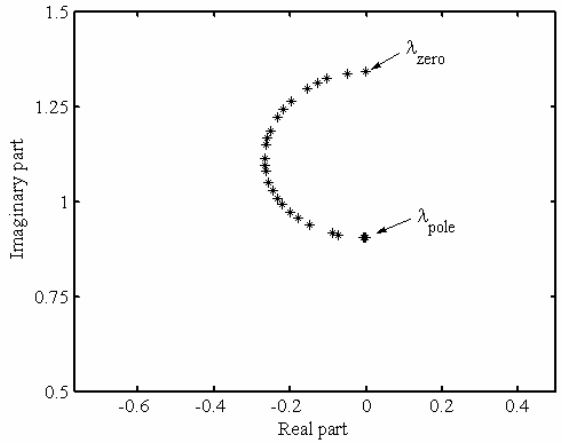

Fig. 3. Root locus of the spring-mass inter-area mode model.

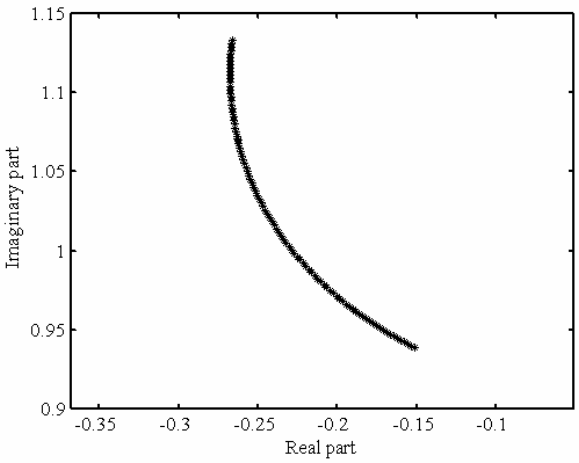

Fig. 3a. Root locus of the spring-mass inter-area mode model (zoom in).

In this paper the criteria for the maximum damping of inter-area oscillation is considered to be the maximum damping ratio of the oscillation. The damping ratio determines the rate of decay of the amplitude of the given oscillation [10]. It is defined to be

$$\xi_i = \frac{-\sigma_i}{\sqrt{\sigma_i^2 + \omega_i^2}} .100,\ \% \tag{2}$$

where σ_i and ω_i are real and imaginary parts of eigenvalue λ_i that describes the oscillatory mode with frequency

$$f = \frac{\omega_i}{2\pi},\ Hz \tag{3}$$

The maximum damping ratio for root locus shown in Fig. 3 is 23.85 % and it is achieved by gain of the damper K_d=1.3433.

According to terms of wave-based analysis and impedance matching concept presented in [11], [12] the optimum gain of damper is considered to be

$$K_{d,opt} = \frac{1}{M_{opt}} \tag{4}$$

where M_{opt} is the magnitude of the transfer function between force and velocity at ω_{opt} that is called optimum frequency. Fig. 4 presents Bode plot of this transfer function. The optimum frequency is given by

$$\omega_{opt} = \sqrt{\omega_z . \omega_p},\ \frac{rad}{s} \tag{5}$$

where ω_z and ω_p are frequencies of zero and pole of the system.

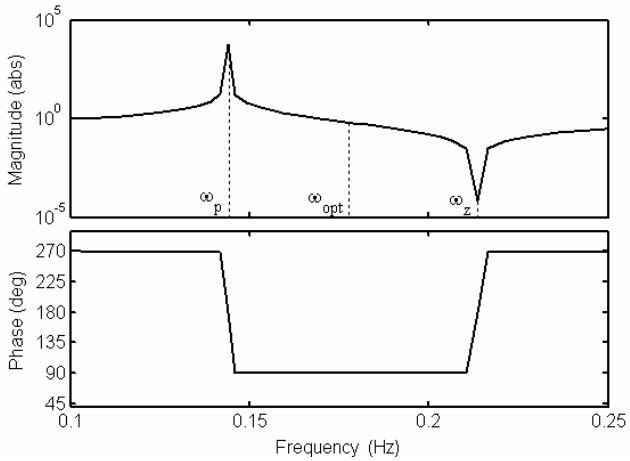

Fig. 4. Bode plot of the spring-mass model with one damper with gain K=0.

Equation (5) represents the geometric average of these two frequencies.

For studied case ω_p=0.9045 rad/s and ω_z=1.3416 rad/s. Using (5) ω_{opt} is equal to 1.1016 rad/s. Then the optimum gain is derived by (4)

$$K_{d,opt} = \frac{1}{M_{opt}} = \frac{1}{0.7427} = 1.3465 \qquad (6)$$

The comparison of the results obtained by root locus with the results from presented approach shows the accuracy of this method.

In order to check the accuracy of the method in case of different initial dampings (d_i) in the system, the root locus at these initial dampings is investigated. The root locus is plotted in Fig. 5.

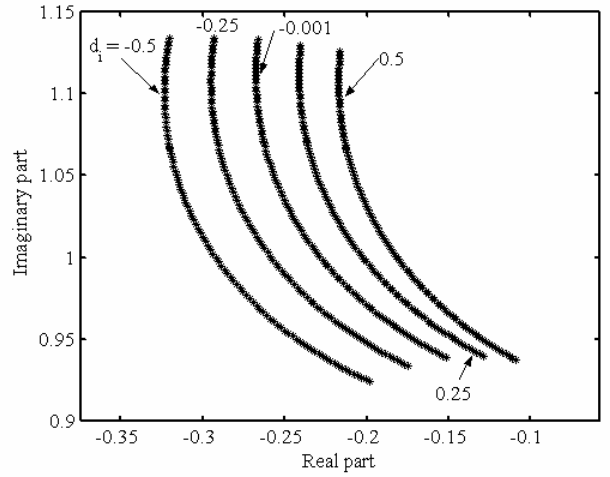

Fig. 5. Root locus of the spring-mass model at different initial damping.

As it can be seen from Fig. 5 the different initial damping affects the eigenvalues of the system. The dependence of the results for the damping ratios and the optimum gains in respect to initial damping can be seen in Fig. 6 and in Fig. 7. The optimum gains and the damping ratios are plotted for both ways of obtaining: impedance matching and root locus.

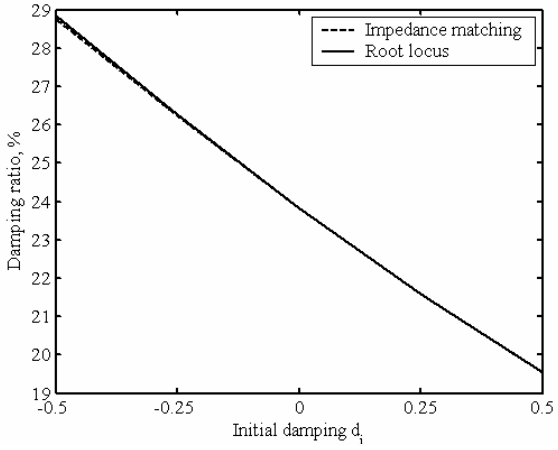

Fig. 6. Damping ratio = f (Initial damping) for spring-mass model.

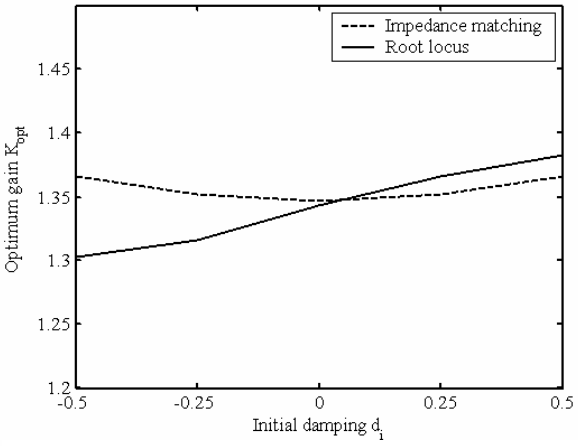

Fig. 7. Optimum gain = f (Initial damping) for spring-mass model.

The accuracy of this approach is more affected when a big amount of initial damping is introduced. This can be considered as a disadvantage of the approach, but it is well known that damping ratio about 30 % is a good constraint for real systems.

III. A two-area power system

The system consists of two similar areas connected by a weak tie. This system is often used to study fundamental nature of inter-area oscillation [10]. The diagram of the simple two-area power system is depicted in Fig. 8 and the data for this system are given in Appendix I.

This system has two local modes and one inter-area mode. The characteristics of these modes are given in Table 1.

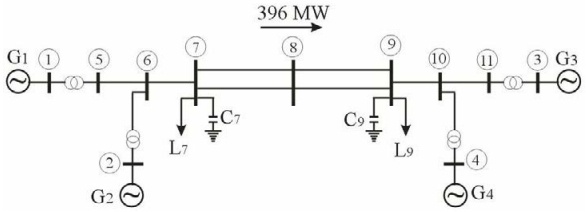

Fig. 8. A simple two-area power system.

Table 1.

Characteristics of inter-area modes

Mode	λ_i	ξ_i, %	*f, Hz*
Local 1	-0.7046±j6.158	11.37	0.98
Local 2	-0.6885±j5.963	11.47	0.95
Inter-area	0.0671±j3.4395	-1.95	0.55

T

he root locus of a two-area power system inter-area mode is plotted in Fig. 9. Only the PSS of generator G3 is activated. The maximum damping ratio 10.35 % and it is achieved by gain of the PSS KPSS=77.7.

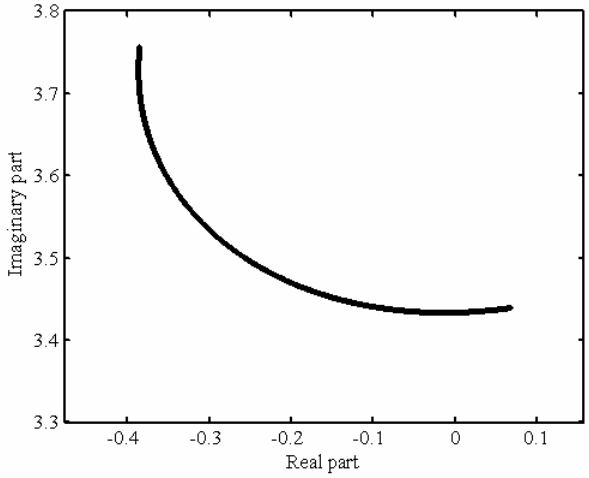

Fig. 9. Root locus of a two-area power system inter-area mode.

The Bode plot of the transfer function $\Delta\omega/\Delta V_{ref}$ is plotted in Fig. 10.

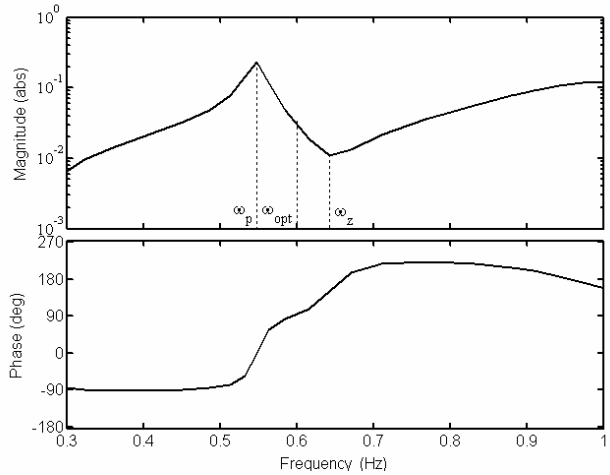

Fig. 10. Bode plot of the transfer function $\Delta\omega/\Delta V_{ref}$ at PSS gain KPSS=1.

Applying the proposed approach we have ω_p=3.44 rad/s and ω_z=4.03 rad/s. Using (5) ω_{opt} is equal to 3.7233 rad/s. Then the optimum gain is derived by (4)

$$K_{PSS,opt} = \frac{1}{M_{opt}} = \frac{1}{0.013} = 76.9 \quad (7)$$

where M_{opt} is considered to be

$$M_{opt} = \left(\left| \frac{\Delta\delta}{\Delta V_{ref}} \right| - \left| \frac{\Delta P}{\Delta V_{ref}} \right| \right)_{\omega_{opt}} \quad (8)$$

and $\Delta\delta$ is rotor angle deviations.

Due to specific application of PSS, the PSS lead-lag filters must be tuned to provide the required phase compensation before applying this proposed approach.

IV. Conclusions

The comparison of the results obtained by root locus with the results from presented approach shows the accuracy of this method. The gain selection of damping devices is clarified for two systems: a spring-mass mechanical system and a simple two-area power system.

Despite the numerical discrepancy, the concept of impedance matching is valuable as it provides a condition for maximum damping that has a physical interpretation.

The possibility for using this method in practice for online selection of PSS gain is considered as a future work. Different types of PSS at different by scale power systems will be also investigated in our future work.

Appendix I

The data for a two-area power system in given below.

1) Generators

U_n=24 *kV*; P_n=1000 *MW*; x_d=x_q=2.35; x'_d=x'_q=0.452; x''_d=x''_q=0.318; *xl*=0.172; r_a=0; T'_{d0}=T'_{q0}=8.8 *s*; T''_{d0}=T''_{q0}=0.12 *s*; K_D=1; *H*=5.65.

2) Lines

Table A.1.

Lines data

Buses	U_n, *kV*	*R, p.u.*	*X, p.u.*	*B, p.u.*
5-6; 10-11	220	0.0025	0.025	0.04375
6-7; 9-10	220	0.001	0.01	0.0175
2x(7-8); 2x(8-9)	220	0.011	0.11	0.1925

3) Transformers and Loads

Table A.2.

Transformers and loads data

Buses	U_{n1}, *kV*	U_{n2}, *kV*	S_n, *MVA*	*R, p.u.*	*X, p.u.*	*B, p.u.*
5-1; 6-2; 10-4; 11-3	220	24	1260	0.0018	0.143	-0.0054

P_{L7}=967 *MW*; Q_{L7}=100 *MVAr*; Q_{C7}=406 *MVAr*;
P_{L9}=1767 *MW*; Q_{L9}=100 *MVAr*; Q_{C9}=396 *MVAr*.

4) Excitation system

- AVR – ABB UNITROL with following settings

K_A=150; T_r=0.02 *s*; T_A=1 *s*; T_{A1}=12 *s*; T_B=6 *s*; T_{B1}=0.1 *s*; T_E=0.004 *s*;

- PSS – classical model. The PSS input is generator rotor speed signal.

T_W=10 *s*; K_{STAB}=20; T_1=0.05 *s*; T_2=0.02 *s*; T_3=3 *s*; T_4=5.4 *s*;

References

[1] CIGRE Technical brochure on control of power system oscillations, Task force 38-01-07, Final report, July 1996.

[2] Larsen, E. V. and D. A. Swann. Applying power system stabilizers. Parts I, II and III, IEEE Trans. Power App. Syst., vol. PAS-100, pp. 3046-3077, Nov./Dec. 1981.

[3] De Mello, F. P., and C. Concordia. Concepts of synchronous machine stability as affected by excitation control, IEEE Trans. Power App. Syst., vol. PAS-88, pp. 316-329, Apr.1969.

[4] Gibbard, M. J. and D. J. Vowles. Reconciliation of methods of compensation for PSSs in multimachine systems, IEEE Trans. Power Systems, vol.19, No.1, pp. 463-472, Feb. 2004.

[5] Kundur, P., M. Klein and M. Zywno. Application of power system stabilizers for enhancement of overall stability, IEEE Trans. Power Systems, vol.4, pp. 614-626, May 1989.

[6] Samuelsson, O. Power system damping. Structural aspects of controlling active power, PhD Thesis, Lund University, 1997.

[7] Samuelsson, O. and B. Eliasson. Damping of electro-mechanical oscillations in a multimachine system by direct load control, IEEE Trans. Power Systems, vol.12, pp. 1604-1609, Nov. 1997.

[8] Thorp, J. S., C. E. Seyler and A. G. Phadke. Electromechanical wave propagation in large electric power systems, IEEE Trans. on Circuits and Systems – I: Fundamental Theory and Applications, vol.45, No.6, pp. 614-622, June 1998.

[9] Lesieutre, B. C., E. Scholtz and G. C. Verghese. A zero-reflection controller for electromechanical disturbances in power systems, 14th PSCC, Sevilla, 24-28 June 2002.

[10] Kundur, P. Power System Stability and Control, New York: McGraw-Hill Inc., 1993.

[11] Ojima, H., K. Nagase and Y. Hayakawa. Wave-based analysis and wave control of damped mass-spring systems, IEEE Proceedings of the 40th Conference on Decision and Control, Orlando, Florida, USA, pp. 2574-2579, Dec. 2001.

[12] Ojima, H., K. Nagase and Y. Hayakawa. A study on the impedance matching controller for uniformly varying damped mass-spring systems, Proceeding of the American Control Conference, Denver, Colorado, USA, pp. 2821-2826, June 4-6, 2003.

Chavdar Ivanov *– Expert at System Analyses and Transmission Planning Department, National Dispatching Center, Bulgarian National Electric Company (NEK), 5 Veslets Str., 1040 Sofia, BULGARIA. e-mail: ch.ivanov@ieee.org.*

Olof Samuelsson *– Associate Professor, Dr., Department of Industrial Electrical Engineering and Automation, Lund Institute of Technology, Lund University, Lund, SWEDEN. e-mail: olof.samuelsson@iea.lth.se.*

Krum Gerasimov *– Associate Professor, Dr., Faculty of Electrical Engineering, Electrical Power Engineering Department, Technical University of Varna, 1 Studentska Str., 9010 Varna, BULGARIA. e-mail: k.gerasimov@tu-varna.edu.*

Determination of the optimal repair cost limit under minimal repair of the electrical equipment

Svetlana Tzvetkova

Abstract *The paper gives mathematical model to determination of the optimal repair cost limit under minimal repair of the electrical equipment for a Weibull distributed time-to-failure and exponentially distributed repair cost. With the bounds for the optimal repair cost limit, a simple algorithm to obtain the optimal repair cost limit is developed.*

Keywords: *minimal repair, optimal repair cost limit, time-to-failure, electrical equipment.*

Introduction

When operating electrical equipment fails, it must be repaired or replaced to continue in operation. In [1] are introduced periodic replacement policies with minimal repairs, in which a electrical equipment is replaced at time T and undergoes minimal repairs between replacements. In many situations where an electrical equipment failure occurs, the concept of minimal repair is important. The idea of minimal repair is that if the electrical equipment fails, a repair can be made which does not materially change the condition of the electrical equipment from its condition immediately before failure. A minimal repair occurs when the failed electrical equipment is not treated so as to return it to "as new" condition but is instead returned to the average condition for a working electrical equipment of its age.

Examples include complex systems where the repair or replacement of one component does not materially affect the condition of the whole system.

In order to alleviate a forced repair immediately prior to the scheduled replacement time, in [2] is proposed a replacement policy based on failure number, which is more cost effective. However, these policies are based on a constant repair cost which is less than the replacement cost, and closed – form solutions are available only for Weibull time-to-failure distribution. In practice, the repair cost is a random variable. There can be no guarantee that a repair cost will be less than the replacement cost. The decision to repair or replace a failed unit may depend on the estimated repair cost. This policy is called repair limit replacement policy [3]. In this policy, there is no preventive replacement. Whenever a unit fails, it is first inspected and the repair cost is estimated. If the estimated repair cost exceeds certain amount, known as "repair limit", then the failed unit is not repaired but replaced. So, the repair limit is a limit on the amount of money which can be spent on the repair of the electrical equipment. The values of the repair limits are dependent on the type, age and in some cases on the location of the electrical equipment. The repair limits thus provide an economic replacement policy.

The paper gives bounds for the optimal repair cost limit under minimal repair of the electrical equipment for a Weibull distributed time-to-failure and exponentially distributed repair cost. With those bounds, a simple algorithm to obtain the optimal repair cost limit is developed.

Mathematical model to determination of the optimal repair cost limit

The following notation are used:

λ - Weibull scale parameter, $\lambda > 0$,

β - Weibull shape parameter, $\beta \geq 1$,

u - average estimated repair cost,

r - average replacement cost of the electrical equipment,

c - repair cost limit,

$\Phi(c)$ - average cost per unit time for repairs and replacement,

$\Gamma(x)$ - the gamma distribution function.

The assumptions that are made are:

1. The electrical equipment follows a Weibull failure distribution with survivor function age t

$$\overline{F}(t) = \exp\left[-(\lambda t)^{\beta}\right]. \tag{1}$$

2. The estimated repair cost follows a negative exponential distribution with average u. The probability that the repair cost will exceed a cost limit c is

$$\overline{G}(c) = \exp\left(-\frac{c}{u}\right) = 1 - G(c). \tag{2}$$

3. Replacement cycle begins at $t = 0$ and ends at replacement.

Based on the above assumptions and notation, [4] has shown that the average cost per unit time for repairs and replacement is

$$\Phi(c) = \frac{\lambda \exp\left(-\frac{c}{\beta u}\right)}{\Gamma\left(1+\frac{1}{\beta}\right)}\left[r - u - c + u\exp\left(\frac{c}{u}\right)\right]. \tag{3}$$

The optimum repair cost limit c^*, obtained by setting the derivative of $\Phi(c)$ equal to 0, is the root of the following equation

(4) $$c+u(\beta-1)\left[\exp\left(\frac{c}{u}\right)-1\right]=r.$$

Generally, the optimum repair cost limit c^* is less than the average replacement cost of the system r except when $\beta=1$, then $c^*=r$. It is never optimal to set $c=0$ when $r\neq 0$. For this reason, we assume that $\beta>1$ and $r>0$.

Let

(5) $$f(c)=c+u(\beta-1)\left[\exp\left(\frac{c}{u}\right)-1\right]-r.$$

Then

$$f(0)=0+u(\beta-1)\left[\exp\left(\frac{0}{u}\right)-1\right]-r=-r<0,$$

$$f(r)=r+u(\beta-1)\left[\exp\left(\frac{r}{u}\right)-1\right]-r>0,$$

and f is continuous and strictly increasing function. Therefore, the root of equation (4) is unique and $c^*<r$.

If is replaced $\exp\left(\frac{c}{u}\right)$ with $1+\frac{c}{u}+\frac{c^2}{2u^2}$ in equation (4), the following equation is obtained

(6) $$c+u(\beta-1)\left[\frac{c}{u}+\frac{c^2}{2u^2}\right]=r,$$

$$c+c(\beta-1)+c^2\frac{(\beta-1)}{2u}=r,$$

or

(7) $$c^2+\frac{2u\beta}{(\beta-1)}c-\frac{2ur}{(\beta-1)}=0.$$

Then the solution of equation (7) is

$$c_U^*=\frac{-\frac{2u\beta}{(\beta-1)}+\sqrt{\left(-\frac{2u\beta}{(\beta-1)}\right)^2+\frac{8ur}{(\beta-1)}}}{2}$$

or

(8) $$c_U^*=-\frac{u\beta}{(\beta-1)}+\sqrt{\left(-\frac{u\beta}{(\beta-1)}\right)^2+\frac{2ur}{(\beta-1)}}.$$

c_U^* is the only positive solution of equation (7). Also, it is obvious that $c_U^*<r$.

On the other hand, if is replaced $\exp\left(\frac{c}{u}\right)$ with $\frac{2+\frac{c}{u}}{2-\frac{c}{u}}$ in equation (4), the following equation is obtained

(9) $$c+u(\beta-1)\left[\frac{2+\frac{c}{u}}{2-\frac{c}{u}}-1\right]=r.$$

From (9) is obtained

(10) $$c^2-(2\beta u+r)+2ru=0.$$

Let

$$D=(2\beta u+r)^2-8ru=4\beta^2u^2+4\beta ur+r^2-8ru$$

and

$\beta=1+\alpha$, where $\alpha>0$.

Then

(11) $$D=4(1+\alpha)^2u^2+4(1+\alpha)ur+r^2-8ru=$$

$$=(2u-r)^2+8\alpha u^2+4\alpha^2u^2+4r\alpha u>0.$$

So, equation (9) has two positive roots. The lesser one is

(12) $$c_L^*=\frac{(2\beta u+r)-\sqrt{(2\beta u+r)^2-8ru}}{2}.$$

From

(13) $$c_U^*+u(\beta-1)\left[\exp\left(\frac{c_U^*}{u}\right)-1\right]-r>$$

$$>c_U^*+u(\beta-1)\left[\frac{c_U^*}{u}+\frac{(c_U^*)^2}{2u^2}\right]-r=0$$

we have $f(c_U^*)>f(c^*)=0$. Since f is strictly increasing function, therefore

(14) $$c_U^*>c^*>0.$$

Since $\beta>1$ and

(15) $$-16\beta u^2+16u^2<0.$$

Then we have

(16) $$4\beta^2u^2-16\beta u^2+16u^2+4ur\beta-8ur+r^2<$$

$$< 4\beta^2 u^2 + 4ur\beta + r^2 - 8ru .$$

So

$$4(\beta^2 - 4\beta + 4)u^2 + 4ur(\beta - 2) + r^2 < \quad (17)$$

$$< (2\beta + r)^2 - 8ru .$$

Hence

$$2(\beta - 2)u + r < \sqrt{(2\beta u + r)^2 - 8ru} . \quad (18)$$

Also, we have

$$(2\beta u + r) - \sqrt{(2\beta u + r)^2 - 8ru} < 4u , \quad (19)$$

$$\frac{(2\beta u + r) - \sqrt{(2\beta u + r)^2 - 8ru}}{2} < 2u . \quad (20)$$

Consequently

$$\frac{c_L^*}{u} < 2 . \quad (21)$$

On the other hand, from $0 < \frac{c_L^*}{u} < 2$ and from [5] where $e^x < \frac{2+x}{2-x}$ for $0 < x < 2$ we have

$$f(c_L^*) = c_L^* + u(\beta - 1)\left[e^{\frac{c_L^*}{u}} - 1 \right] - r < \quad (22)$$

$$< c_L^* + u(\beta - 1)\left[\frac{2 + \frac{c_L^*}{u}}{2 - \frac{c_L^*}{u}} - 1 \right] - r =$$

$$= 0 = f(c^*) .$$

So, we have $f(c_L^*) < f(c^*)$. Since f is strictly increasing function, then,

$$c_L^* < c^* . \quad (23)$$

Finally, since $c_U^* < r$.

Therefore

$$c_L^* < c^* < c_U^* < r . \quad (24)$$

The algorithm

Step 1: Input of data for β, u и r .

Step 2: Let $\varepsilon > 0$.

Step 3: Calculation of c_U^* by equation (8) and c_L^* by equation (12).

Step 4: Set $c_L = c_L^*$ and $c_U = c_U^*$.

Step 5: Calculation of $c_{OIIT} = \frac{c_L + c_U}{2}$.

Step 6: If $|f(c_{OIIT})| < \varepsilon$, do to step 8. Otherwise, go to step 7.

Step 7: If $|f(c_{OIIT})| > 0$, set $c_U = c_{OIIT}$.

If $|f(c_{OIIT})| < 0$, set $c_L = c_{OIIT}$. Then go to step 5.

Step 8: $c^* = c_{OIIT}$ and exit the optimal repair cost limit.

Conclusion

The repair limit is a limit on the amount of money which can be spent on the repair of the electrical equipment.

In the paper is working out mathematical model for determination the optimal repair cost limit (equation (8) and equation (12)) under minimal repair of the electrical equipment. Using given algorithm is easy to find the bounds for the optimal repair cost limit. The basic information for this are:

- the time-to-failure distribution of the electrical equipment,
- the distribution of repair cost,
- the costs of repair and replacement.

References

[1] Barlow, R. E, L. C. Hunter. Optimum preventive maintenance policies. Operations Research, Vol. 8, 1960, pp. 90-100.

[2] Park, K. S. Optimal number of minimal repairs before replacement. IEEE Transactions on Reliability, Vol. R-28, 1979, pp. 137-140.

[3] Hastings, N. A. J. The repair limit replacement method. Operational Research, Vol. 20, 1989, pp. 337-349.

[4] Park, K. S. Cost limit replacement under minimal repair. Microelectronics and Reliability, Vol. 23, 1983, pp. 347-349.

[5] Chung K. J., Optimal repair cost limit for a consumer following expiry of a warranty. Microelectronics and Reliability, Vol. 34, 1994, pp. 189-192.

Svetlana Tzvetkova *– Senior Assistant, Dr., Faculty of Electrical Engineering, Technical University of Sofia, 8 Kl. Ohridski Str., 1000 Sofia, BULGARIA.*
e-mail: stzvet@tu-sofia.bg

A NEW APPROACH TO MODELLING HIGH VOLTAGE THREE-PHASE PIPE TYPE CABLE USING CONFORMAL MAPPING

J Moshtagh and Raj K. Aggarwal, senior member, IEEE

Abstract: *In the modelling of underground cables, in particular the per unit length series impedance Z and the per unit length shunt admittance Y, EMTP software makes certain assumptions and approximations; this inevitably gives rise to inaccuracies when simulating the voltage and current waveforms under fault conditions. This paper presents a new approach to the modelling of the cable's Z and Y parameters using conformal mapping (CM), which avoids the assumptions and approximations associated with the EMTP software thereby increasing the simulation accuracy. In order to make a comparison between the Z and Y parameters and in the simulated transient voltage and current signals attained via the EMTP and CM methods, a practical radial three-phase pipe type cable is analysed. The results confirm the validity and higher accuracy of the new proposed method.*

Keywords: conformal mapping, cable modelling, EMTP, pipe type cable

INTRODUCTION

There has been an upsurge in the usage of underground distribution systems in recent years. In this respect, increased competition due to the deregulation of the power industry and the demand to provide better service to the customers having increasingly sensitive loads, makes the development of reliable and accurate fault location methods for distribution systems an important issue. One of the most important factors in accurate fault location is to develop an accurate model of a cable which then needs to be integrated into an overall distribution system model. Essentially, there is a need to determine accurately, the per unit length impedance and admittance of a cable, which in turn determine the relationships between current, voltage, attenuation and velocity of travelling waves in the transient state.

A number of models have been proposed to date. These models can be classified into the following two main groups; time domain and frequency domain models. With regard to the advantages and disadvantages of these techniques, in reference [1], the presented model belongs to the class of time-domain, frequency-dependent methodology. It overcomes the main limitations of existing time-domain cable models, that is, it takes into account the frequency dependence of the modal transformation matrices. This model is compatible with the time domain solution, such as the one used in the EMTP. In many analyses of overhead line parameters, approximations ignoring eddy currents in conductors can be assumed. However, in close conductors, such as underground cables, the AC parameters vary significantly with frequency and conductor spacing. In references [2] and [3], on which the EMTP model is based, the distributions of current density due to proximity and skin effects are determined analytically by solving the differential equation for penetration of currents in the conducting material and appropriately applying boundary conditions. But, for eccentric conductors such as a three-phase cable, inner conductors are replaced with an assumed small circle which is concentric with outer conductor such as pipe or armour. In all the aforementioned methods and also in EMTP model it is assumed that permeability μ for conductors and pipe is constant. Thus in order to determine μ throughout the pipe, in reference [4], the magnetic field intensity in each element of the pipe is solved using the finite-element method. In reference [5], the cable is divided into a large number of cells as the field is assumed to be constant within each cell and a linear integration is performed for the voltage using Finite-Difference Time Domain (FDTD) method.

In the modelling of a three-phase cable, the main problem arises by virtue of the fact that the three conductors are positioned off centre within the pipe or armour and it is principally due to this that some estimations and approximations are made in the EMTP model; a direct consequence of the latter is that the mathematical representation of the impedance and admittance in a pipe type cable in the EMTP software includes infinite series formulations of the flux linkage and the proximity effects; this of course is based on some approximations in the configuration of cable. However, with regard to CM's ability to transform an isotropic region into a symmetrical and much simpler region, the mathematical equations for the calculation of Z and Y take a simplified form and eliminate such approximation which changes the configuration of cable.

Herein, the EMTP method for calculating Z and Y is firstly reviewed followed by outlining the attributes of CM and then, based on ref. [6], simplification of the mathematical equations for calculating Z and Y is carried out. Finally, a practical radial three-phase pipe type cable is analysed and a comparison is made between the results attained using the EMTP and CM models. It should be noted that according to reference [1], time domain method in the EMTP model is compatible with the J Marti model associated with frequency-dependent parameters. The performance of the EMTP cable model is compared with the CM model, the latter being based on the Bergeron model which is time-domain based.

THREE-PHASE CABLE MODEL IN EMTP

Cable model in EMTP is based on Brown and Rocamora's calculations and results shown in ref. [6], but these calculations are based on such assumptions which have been considered in Emanuel approach mentioned in ref. [7]. These assumptions are as follows:

1. The cylindrical conductors are replaced with infinitesimally thin sheets.

2. The displacement currents and dielectric losses are neglected.
3. The finite thickness of the pipe wall is neglected since current penetration is assumed to be confined under transient conditions.
4. The pipe is considered to have constant permeability.

First assumption is associated with the configuration of the conductors inside the pipe, as a typical configuration of a three conductor cable shown in fig. (1) is replaced with a concentric conductor shown in fig. (2). Before dealing with eliminating this assumption as a result increasing the accuracy of cable model, following is dealt with reviewing on the EMTP model.

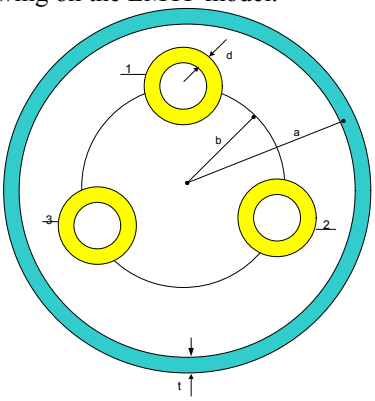

Fig. 1. Typical configuration of a three conductor's cable

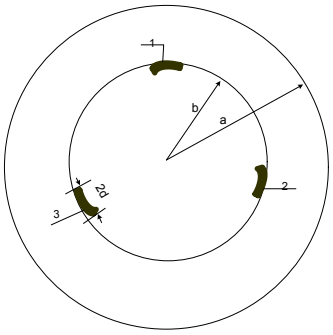

Fig. 2. Assumed configuration of three conductor's cable

According to reference [8], Z_{phase} matrix in a three-phase cable becomes:

$$[z_{phase}]=\begin{bmatrix} [z_{self-a}] & [z_{mutual-a-b}] & [z_{mutual-a-c}] \\ [z_{mutual-b-a}] & [z_{self-b}] & [z_{mutual-b-c}] \\ [z_{mutual-c-a}] & [z_{mutual-c-b}] & [z_{self-c}] \end{bmatrix} \quad (1)$$

Each impedance in $[Z_{self}]$ depends on $Z_{insulation}$, $Z_{tube\text{-}in}$, $Z_{tube\text{-}out}$ and $Z_{tube\text{-}mutual}$ as follows:

$$z_{insulation}=\frac{1}{2\pi} j\omega\mu_o\mu_r \ln(r/q) \quad (2)$$

μ_r = permeability of insulation

$\mu_o = 2*10^{-4}$ H/Km

r=outside radius of insulation (or tube)

q=inside radius of insulation (or tube)

$$z_{tube-in}=\frac{\rho m}{2\pi qD}\left[I_O(mq)*k_1(mr)+k_o(mq)*I_1(mr)\right] \quad (3)$$

$$z_{tube-out}=\frac{\rho m}{2\pi rD}\left[I_O(mr)*k_1(mq)+k_o(mr)*I_1(mq)\right] \quad (4)$$

$$z_{tube-mutual}=\rho/(2\pi rqD) \quad (5)$$

Where, $D=I_1(mr)*k_1(mq)-I_1(mq)*k_1(mr)$; (6)

$$m=\sqrt{j\omega\mu/\rho} \quad (7)$$

and I_O,I_1,K_0 and K_1 are Bessel functions.

Also:
$$[z_{mutual-a-b}]=\begin{bmatrix} z_{ab} & z_{ab} & z_{ab} \\ z_{ab} & z_{ab} & z_{ab} \\ z_{ab} & z_{ab} & z_{ab} \end{bmatrix} \quad (8)$$

Where Z_{ab} is the mutual impedance between conductors 1 and 2 as shown in Fig. 3.

Compared to the geometry of the single-core cable, the geometry of the three-phase or the pipe-type cable is more complex for two reasons:

a) The single-core cables inside the pipe are not concentric with respect to the pipe.
b) The steel pipe is magnetic and subject to current-dependent saturation effects.

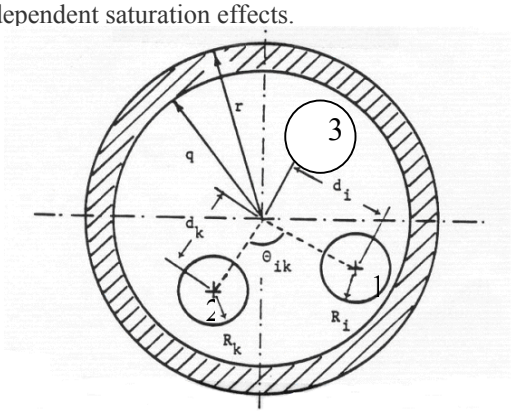

Fig. 3. Pipe type multi single-core cable

Depending on the thickness of the pipe, the two states can be evaluated as infinite and finite pipe thicknesses, respectively. However with reference to Eq. (9), the depth of penetration in the pipe becomes:

$$d_{pipe}=\frac{\sqrt{2}}{|m|}=503*\sqrt{\frac{\rho_{earth}(\Omega m)}{\mu_r f(Hz)}} \quad (9)$$

and with typical values of $\rho_{pipe}=5*10^{-8}$, f=50 Hz and μ_r=200, d will be less than 1.5mm. In practice, the thickness of pipe is larger than 3 mm, and hence in this paper, only infinite pipe thickness (no earth return) is analysed. In this case, no voltage will be induced on the outside of the pipe and consequently, the pipe is the return path instead of earth as shown in Fig. 3.

The self impedance of the loop between the sheath and the pipe (or armour) consists of three terms; the first term $Z_{sheath\text{-}out}$ is the same as in Eq.(4), but the second term becomes:

$$Z_{insulation}=\frac{j\omega\mu_0}{2\pi}\ln\left[\frac{q}{R_i}*\left(1-\left(\frac{d_i}{q}\right)^2\right)\right] \quad (10)$$

The third term is given as:

$$z_{pipe-in}=\frac{j\omega\mu_0\mu_r}{2\pi}[(\frac{k_0(mq)}{mqk_1(mq)})+$$

$$(2*\sum_{n=1}^{\infty}\left(\frac{d_i}{q}\right)^{2n} * \frac{k_n(mq)}{n\mu_r k_n(mq) - mqk'_n(mq)})] \quad (11)$$

Taking m from Eq.(7), and $\mu = \mu_{o*}\mu_r$=permeability of the pipe, k_n=modified Bessel function of the second kind of order n, k_n'=derivative of k_n and also the mutual impedance Z_{ab} (mentioned in Eq.(8)) between the two outermost loops formed by armour (pipe) and sheath becomes:

$$z_{ab} = \frac{j\omega\mu_0}{2\pi}\left\{\begin{array}{l}\ln\frac{q}{\sqrt{d_i^2+d_k^2-2d_id_k\cos\Theta_{ik}}} + \mu_r\frac{k_0(mq)}{mqk_1(mq)} \\ +2*\sum_{n=1}^{\infty}\left(\frac{d_id_k}{q^2}\right)^n \cos(n\Theta_{ik})*(2\mu_r\frac{k_n(mq)}{n\mu_r k_n(mq)-mqk_n(mq)} - \frac{1}{n})\end{array}\right\} \quad (12)$$

The admittances for pipe-type cables according to Fig.1 configuration becomes Eq.(13).

$$[y_{phase}] = j\omega[P_{phase}]^{-1} \quad (13)$$

Where $[P_{phase}]$ is a potential coefficient matrix given as:

$$[p_{phase}] = \begin{bmatrix}[p_a] & 0 & 0\\ 0 & [p_b] & 0\\ 0 & 0 & [p_c]\end{bmatrix} + \begin{bmatrix}[p_{aa}] & [p_{ab}] & [p_{ac}]\\ [p_{ba}] & [p_{bb}] & [p_{bc}]\\ [p_{ca}] & [p_{cb}] & [p_{cc}]\end{bmatrix} \quad (14)$$

Where:

$$[P_a] = \begin{bmatrix}p_1+p_2+p_3 & p_2+p_3 & p_3\\ p_2+p_3 & p_2+p_3 & p_3\\ p_3 & p_3 & p_3\end{bmatrix} \quad (15)$$

With

$$p_i = \frac{1}{c_{i\,i}} = \frac{\ln(r/q)}{2\pi\varepsilon_o\varepsilon_r} \quad (16)$$

and also $[p_{ii}]$ *and* $[p_{ik}]$ in the second term is a 3*3 matrix with 9 equal elements as follows:

$$p_{ii} = \frac{1}{2\pi\varepsilon_0\varepsilon_r}\ln\left[\frac{q}{R_i}*\left(1-\left(\frac{d_i}{q}\right)^2\right)\right] \quad (17)$$

$$p_{ik} = \frac{1}{2\pi\varepsilon_0\varepsilon_r}\ln\left[\frac{q}{\sqrt{d_i^{\,2}-d_k^{\,2}-2d_id_k\cos\theta_{ik}}}\right] \quad (18)$$

The admittance matrix is then deduced by inverting [p_{phase}], as has been shown in Eq.(13).

The new approach (presented herein) for a more accurate cable model is on the basis of simplifying and amending Eqs.(10,11,17) (ii. diagonal terms of Eqs.(1,14)) and Eqs. (12,18) (ii. mutual terms of Eqs.(1,14)) by using CM. It should be noted that the diagonal terms of Eqs. (1,14) are related to a single-core pipe type cable and hence are determined using the methodology given in ref. [9].

THE CONFORMAL MAPPING METHOD

In order to modify the equation for calculating Z and Y, in this paper Eqs. (10,11,12,17,18) are modified for a three-phase cable by transforming eccentric circles into concentric circle by using the CM method. It should be mentioned that for a limited range of eccentric conductor locations, reference [10] achieves this transformation using CM. However, firstly only a single conductor pipe type cable is considered, secondly, the depth of penetration of pipe and the thickness of the outer layer of conductor (e.g. armour) is neglected and thirdly, the employed conformal transformation has some limitations, such as the distance between the centre of the two eccentric circles is dependent on the radius of circles. The transformation employed in ref. [10] is:

$$W = (Z-a) / (Z+a) \quad (19)$$

Herein, the employed transformation does not have the three aforementioned limitations. This is essentially to avoid any complexities and approximations (as in other methods) in determining Z and Y. Moreover, modifications to the five aforementioned equations associated with impedance and potential coefficient matrices are divided into two parts as follows: diagonal terms (Eqs.(10,11,17)) and off-diagonal terms (Eqs.(12,18)).

A. Diagonal terms of Z and P

In order to calculate the diagonal terms of Eqs.(1,14), the methodology adopted herein is similar to that of a single-core pipe type cable, its extension to a three-phase pipe type being relatively simple. As a first step, a conformal transformation is determined that transforms eccentric circles into concentric circles in two stages. The first transformation is: $Z=Z_1/R_1$ that transforms single-core pipe type cable into Fig. 4, ie.:

$$x_1=(d+q)/R_1 \quad \& \quad x_2=(d-q)/R_1 \quad (20)$$

As d= distance between two centres of core and pipe

.q= the radius of core and R_1= the inner radius of pipe

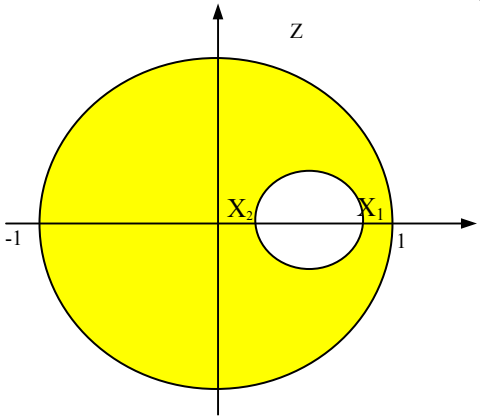

Fig. 4. Pipe type (unit radius) single core

The second transformation is:

$$W_1 == (z-a)/(aZ-1) \quad (21).$$

This transformation transforms Fig. 4 into Fig. 5.

Also the transformation $W_2=\ln(W_1)$ transforms Fig.5 into two parallel lines with distance $\ln(R_o)$.

As shown in Figs. 4 & 5, the transformation W_1 transforms x_1 to $-R_o$ and x_2 to R_o; thus R_o & 'a' become:

$$a = [1+x_1x_2+\sqrt{(1-x_1^2)(1-x_2^2)}]/(x_1+x_2) \quad (22)$$

$$R_o = [1-x_1x_2+\sqrt{(1-x_1^2)(1-x_2^2)}]/(x_1-x_2) \quad (23)$$

Also from the two parallel lines that are a cross section of two parallel plates, capacitance per unit length is:

$$C_{equal}=\varepsilon_o.A/D = 2\pi\varepsilon_o/\ln R_o \ (F/m) \quad (24)$$

With regard to Fig. 6, the capacitance between circles C_1 & C_3 is deduced from Eq. (24) and the capacitance between circles C_1 & C_2 becomes:

$$C_{1\text{-}2}=2\pi\varepsilon_o/\ln(r/q) \quad (25)$$

Here r is the radius of circle C2, q is the radius of circle C1 and the radius of circle C_3 is unity.

The capacitance between circles C_2 & C_3 becomes:

$$C_{2\text{-}3} = 2\pi\varepsilon_o/\ln(R_o q/r) \quad (26)$$

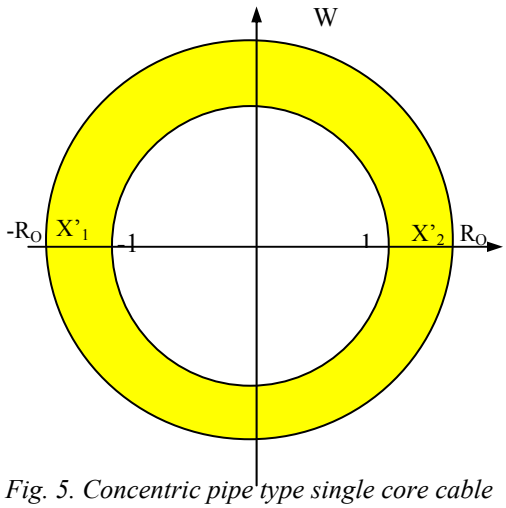

Fig. 5. Concentric pipe type single core cable

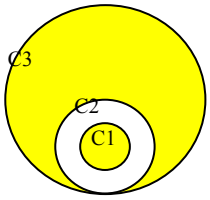

Fig. 6. Three eccentric circles

Since the capacitance is considered ideal, it is related to the inductance at infinite frequency by[8]:

$$C= (\mu_o.\varepsilon_o)/L \quad (27)$$

Thus Eqs. (10) & (17) become Eqs. (28) and (29), respectively. It should be noted that the permittivity between circles C1 and C2 is $\varepsilon_o\varepsilon_r$ and between circles C2 and C3 it is ε_o in pipe type cable, but in a three-phase cable, both of them are $\varepsilon_o\varepsilon_r$.

$$Z_{insulation} = \frac{j\omega\mu_0\mu_r \ln(r/q)}{2\pi} + \frac{j\omega\mu_0 \ln(R_o.q/r)}{2\pi} \quad \text{(pipe type cable)}$$

$$= \frac{j\omega\mu_0\mu_r \ln R_o}{2\pi} \quad \text{(three-phase cable)} \quad (28)$$

$$P = \ln[(r/q)^{*}(R_o.q/r)^{\sigma}]/(2\pi\varepsilon_o\varepsilon_r) \quad \text{(pipe type cable)}$$

$$= \ln R_o/(2\pi\varepsilon_o\varepsilon_r) \quad \text{(three-phase cable)} \quad (29)$$

If the depth of penetration of the pipe and the thickness of the outside of the conductor is taken into account, the aforementioned transformation transforms Fig.7 into Fig.8.

It can be observed that the inside of the pipe is transformed to the outside of the pipe and hence $Z_{pipe\text{-}in}$ is obtained from Eq. (4) by replacing r (the outside radius of pipe) to N (scale factor) and q (the inside radius of pipe) to N*r. r has been shown in Fig.(7). Thus $Z_{pipe\text{-}in}$ in Eq.(11) now becomes:

$$z_{pipe-in} = \frac{\rho m}{2\pi ND}\left[I_O(mN) * k_1(mNr) + k_o(mN) * I_1(mNr)\right] \quad (30)$$

where D is:

$$D= I_1(mN)*k_1(mNr)-I_1(mNr)*k_1(mN) \quad (31)$$

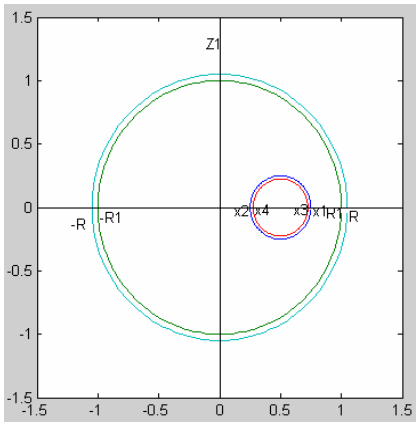

Fig. 7. Two eccentric circles (including thickness)

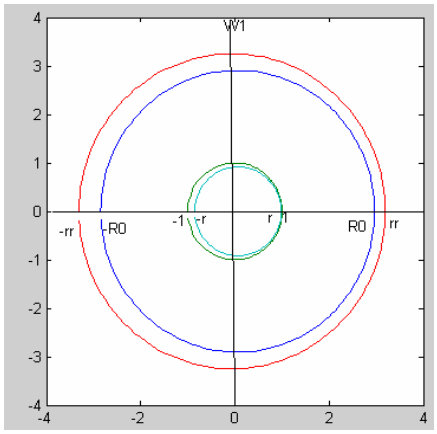

Fig. 8. CM transformation of Fig. (7)

Although it can be seen from Fig. 8 that all circles are not completely concentric, since the depth of penetration in the pipe at power frequency is less than 1.5mm, and the thickness of the armour or sheath is much smaller than its outer radius, Fig. 8 is a valid approximation of four concentric circles, and is certainly more accurate than neglecting the effect of depth of penetration in pipe and thickness of armour (or sheath) altogether, as in the EMTP model.

In order to find the maximum matching between the four circles in Fig. 8, thereby maximising the accuracy of the CM model, a coefficient k is introduced in the transformation. Thus we have:

$$W_1 = \frac{Z - ka}{kaZ - 1} \quad (32)$$

k causes the transformation of four circles to be more concentric. Thus if the thickness of conductor is b, k becomes:

$$k = M + \sqrt{M^2 - \frac{1}{a^2}} \quad (33) \text{ as: } \quad M = \frac{(x_1 - b)(x_2 + b) + 1}{a(x_1 + x_2)} \quad (34)$$

Because of the various transformations that have been used to transform Fig.7 to Fig.8, there is scaling on Z_{pipein}

[10], and hence a scale factor or metric coefficient N should be taken into account. N is the ratio of distances in the original Z_1-plane to the corresponding distances in the transformed W_1-plane. Hence it is defined as:

$$N = R_1 \left| \frac{(ka)^2 - 1}{(ka)^2 + 1} \right| \qquad (35)$$

Appendix 1 shows the various stages in the calculation of N.

B. Off-diagonal terms of Z and P matrices

This section deals with modifying the mutual terms of Z and P (or Y according to Eq. (13)) matrices.
As mentioned in ref. [6], the axial voltage drop depends on the flux linkage and the axial electric field at the pipe wall as follows:

$$\frac{\partial V}{\partial x} = -I(R + j\omega L) = -\frac{d\lambda}{dt} + E_x(r_1) \qquad (36)$$

This paper will only deal with flux linkage and modification of P (Eq.(18)) and L (first and fourth terms of Eq.(12)) and hence Y and Z, respectively. In order to obtain the mutual impedance terms, a two-conductor system is analysed as shown in Fig.9. If conductor 1 is carrying a current that is returning in the pipe, the mutual flux linkage with conductor 2 is in the region between conductor 2 and the pipe. The flux linkage becomes:

$$\frac{d\lambda_{2(1)}}{dt} = j\omega \oint A_{2(1)}.dl_2 = j\omega[A_1(r_1,\theta) - A_1(r_{12},\theta_{12})] \qquad (37)$$

Where A is the vector potential within the pipe and θ_{12} has been shown in Fig. (3).

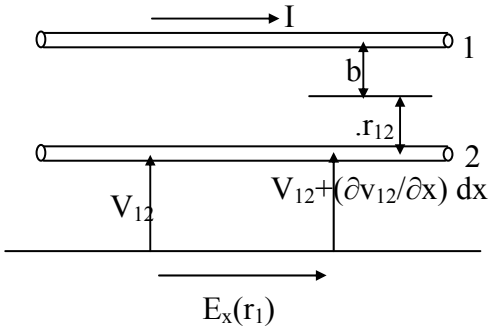

Fig.9. Two conductor system

With regard to Eq.(37), and in order to find the quantity of the mutual flux linkage between conductor 2 and the Armour associated with conductor 1, reference should be made to a three-phase cable which is shown in Fig. (10).

As can be seen, fluxes generated by conductor 1 produce a set of circles in which the centre moves from α_1 to 0 on the axis x. Thus in order to find the amount of the flux generated by conductor 1 that flows between conductor 2 and the armour, we need to find a circle with centre α_4 and radius R_4.

Referring to Eqs.(28,36) and the CM method, the first and fourth terms of Eq.(12) become:

$$Ij\omega L = \frac{d\lambda}{dt} = Ij\omega \frac{\mu_o \mu_r}{2\pi} \ln R_o(x_{14}, x_{24}) \qquad (38)$$

Then, P_{12} is derived as follows:

$$P_{12} = \frac{1}{2\pi.\varepsilon_o.\varepsilon_r} \ln R_o(x_{14}, x_{24}) \qquad (39)$$

Appendix 2 shows how X_{14} and X_{24} are obtained. In conclusion, P_{12} and $R_o(x_{14},x_{24})$ are obtained from Eq.(39) and Eq.(23), however in the latter equation, instead of x_1 and x_2, x_{14} and x_{24} should be used, respectively

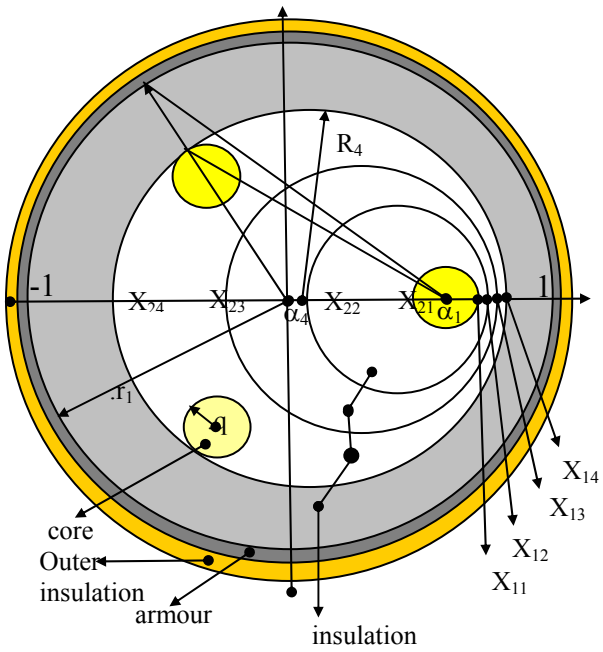

Fig. 10. Generation of flux linkage in a three-phase cable

DISTRIBUTION SYSTEM CONFIGURATION AND PARAMETERS

In order to do a comparison of the Z and Y parameters between the EMTP and CM methods, a practical three-phase underground distribution network shown in Fig. 11 has been considered.

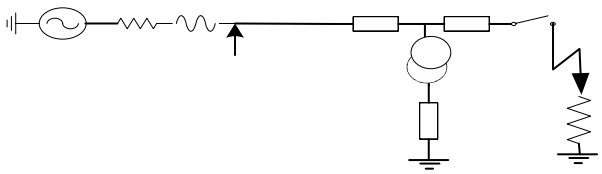

Fig. 11. Practical 3-phase underground distribution network

The specifications of the various elements in Fig (11) are as follows:
Source: V_L = 11kV, f=50Hz, X_s:R_s=10, X_s=2Ω, R_s=0.2Ω
Switch1: closing time =5 ms
Fault resistance R_f=0.1 ohms,
Step time for sampling =10 μs i.e. F=100kHz.
Cables: XLPE, Three-phase pipe type cable (core + grounded sheath)
Core: r_{in}=0, r_{out}=6.1mm, ρ=2.3*10^{-8} Ω.m, μ_r=100
Sheath: r_{in}=10mm, r_{out}=11mm, ρ=17*10^{-8} Ω.m, μ_r=100
Insulation between core and sheath: thickness=3.9mm, ε_r=3

Insulator between pipe and sheath: ε_r=8
Pipe: r_{in}=4cm, r_{out}=4.5cm, ρ=25*10^{-8} Ω.m, μ_r=100
Transformer: S=315 kVA
Winding 1 : V_L=11kV, R_p=1Ω ., X_p= 9 . Ω
Winding 2 : V_L=400V, R_s= 0.44 mΩ., X_s= 3.6 mΩ
Magnetizing Branch: R_M=1000 GΩ
Load= V_L=400 Vrms , 3phase λ, P_L=102.626 kW, Q_L=76.733 kVAR,

It should be noted that all voltage and current signals are simulated using the EMTP software.

DISCUSSION OF RESULTS

This section comprises of two parts. In the first part, a comparison is made between the various cable parameters, principally to highlight the differences observed between the two types of cable models using, the EMTP and the CM models. The results shown in Table 1 typify the differences experienced in some of the important parameters of a 3-phase pipe type symmetrical cable. It should be mentioned that although the three conductors are symmetrically placed, they are nonetheless eccentric resulting in a complex and non-linear interaction amongst the various electrical variables.

Table 1- Characteristic of three-phase cable

	EMTP Model	CM Model
R_1 ohm/meter	6.8e-4	10.1803e-4
R_0 ohm/meter	6.78e-4	10.1584e-4
XL_1 ohm/meter	1.2654e-3	1.16085e-3
XL_0 ohm/meter	1.2734e-3	1.1652e-3
XC_1 mho/meter	1.0607e-7	1.0607e-7
XC_0 mho/meter	1.0607e-7	1.0607e-7
Velocity Mode1	2.6175e+7	2.62e+7
Velocity Mode2	2.6243e+7	2.623e+7
Velocity Mode3	2.6243e+7	2.623e+7
Attenuation Mode1	2.60193e-2	3.9027e-2
Attenuation Mode2	2.61673e-2	3.9156e-2
Attenuation Mode3	2.61673e-2	3.9156e-2

First of all considering the symmetrical components (both series and shunt impedances), it is apparent that the resistive elements of the series impedances are relatively much higher in the case of the CM model compared to the EMTP model. This can be directly attributed to the fact that unlike the EMTP model, the depth of penetration in the pipe has been taken into account in the CM model; this is particularly important from a practical point of view, in view of this fact that the depth of penetration is less than the thickness of the pipe. However, there is only a small difference between the reactive elements of both the series and shunt impedances. Modal parameters are a very important indicator of the behaviour of a cable (or line) particularly under transient conditions. It is clearly evident from Table 1 that whilst the velocity of propagation of the three modes (one earth and two aerial) are little different in the two models, the attenuation is significantly higher in the case of the CM model compared to the EMTP model. The modal transformation employed is shown in ref. [8]. Although not shown here, similar differences in the cable characteristics have also been observed in the case of an asymmetrical cable.

In order to ascertain the effect of the aforementioned differences in the cable parameters an both voltage and current signals under faults, an extensive series of fault studies were carried out by integrating the two cable models into a typical 11 kV distribution system as shown in Fig 11. In all cases, the point of observation of the waveforms is 'A' and all faults considered are at point 'B' in Fig 11. The sampling rate is 100 kHz and for all faults involving earth, the fault resistance is 0.1 Ω.

First of all considering an a-phase-earth fault at voltage maximum, Figs 12-15 show a comparison in the voltage and current waveforms attained via the two models. Comparing the voltage waveforms (Figs 12 and 14) it is

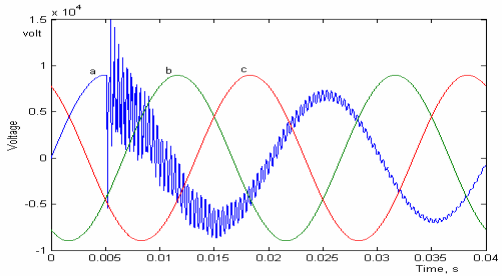

Fig. 12. Voltage signals, phase a-earth fault EMTP model

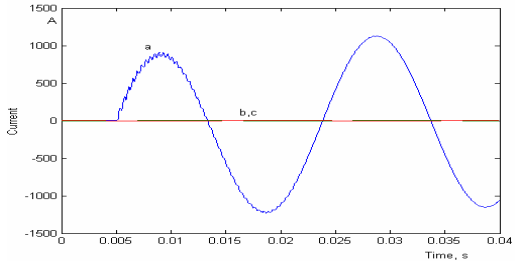

Fig. 13. Current signals, phase a-earth fault EMTP model

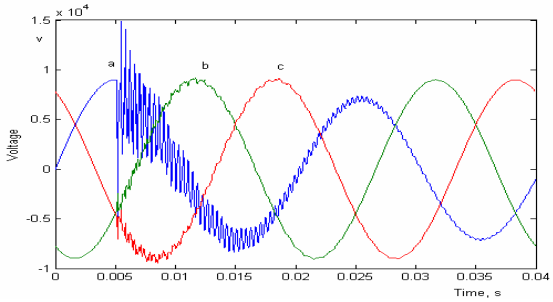

Fig. 14. Voltage signals, phase a-earth fault CM model

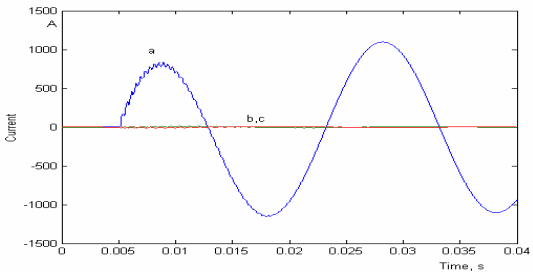

Fig. 15. Current signals, phase a-earth fault CM model

apparent that the initial distortion on the faulted a-phase is much the same for the two models. Importantly, the transients in the case of the CM model die down much faster than in the case in the EMTP model; this clearly shows the effect of higher attenuation associated with the CM model (as discussed previously) which manifests itself into the increased damping effect. Interestingly, some distortion is also observed on the two healthy phases b and c in the case of the CM model. When considering the current waveforms (Figs 13 and 15), the transients are significantly smaller than those on the voltage waveforms and importantly, there is little difference in distortion between the two models; this is somewhat expected by virtue of the fact that in a highly inductive circuit (cable or line) current signals are predominantly power frequency and swamp over any high frequency distortions. When considering a b-c-phase fault, Figs 16-19 depict the differences observed in the waveforms for the two models considered. First of all looking at the voltage waveforms (Figs 16 and 18), it is apparent that although the initial distortion is nearly the same for the two models, the transients take significantly longer to die down in the case of the EMTP cable model.

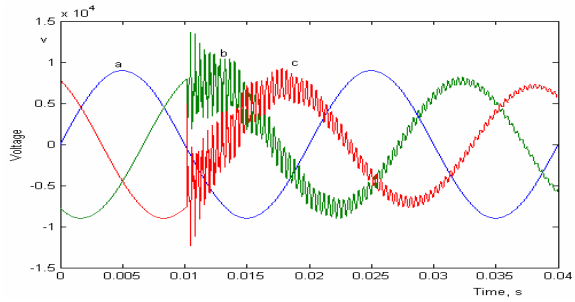

Fig. 16. 3-phase Voltage waveforms, b-c fault, EMTP model

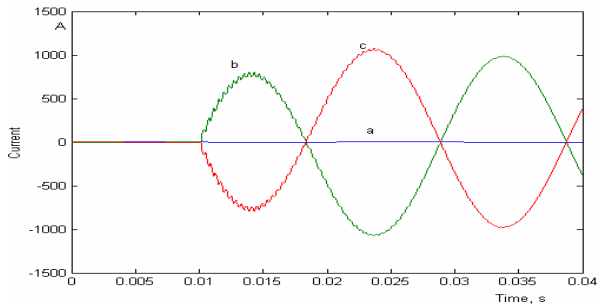

Fig. 17. 3-phase Current waveforms, b-c fault, EMTP model

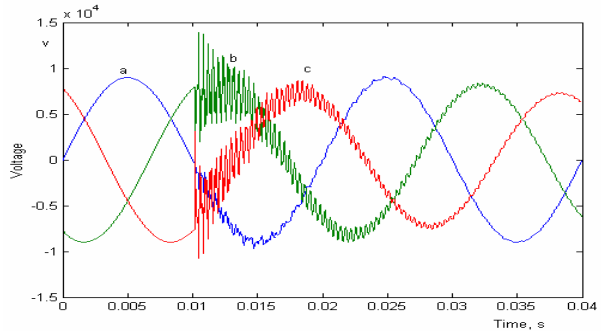

Fig. 18. 3-phase Voltage waveforms, b-c fault, CM model

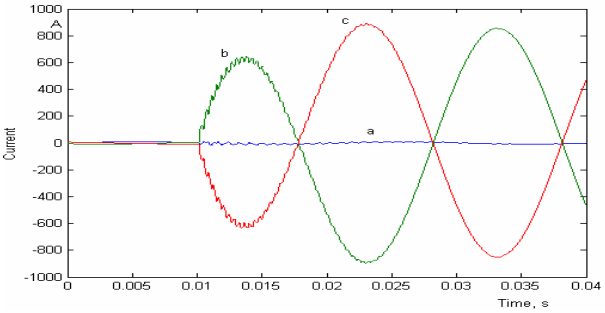

Fig. 19. 3-phase Current waveforms, b-c fault, CM model

In the absence of the earth resistivity playing a part for this type of a fault, the differences in the attenuation constants between the two models (these are higher for the CM model), manifest themselves into the increased damping effect in the case of the CM model. Here again like the single phase to ground fault, there is also distortion on the healthy 'a' phase in the case of the latter. The current waveforms are little different for the two models as shown by Figs 17 and 19.

Although not shown herein, similar observations to the foregoing have been made in the case of a 3-phase fault and for faults on a system employing an asymmetrical cable i.e there is much faster attenuation on the fault phases in the case of the CM cable model in all fault cases.

CONCLUSION

This paper presents a new approach to the calculation of the crucially important parameters Z and Y (series impedance and shunt admittance) of a commonly employed 3-phase pipe type cable in a low voltage distribution system. It is clearly demonstrated that the conformal mapping (CM) approach adopted herein overcomes a number of approximations associated with the EMTP based cable model, which makes certain approximation in the configuration of the cable when the conductors are eccentric. The CM method overcomes this assumption by mathematically transforming the eccentric circles into concentric circles. The results presented clearly demonstrate the differences observed in the cable parameters via the two cable models. The greatest impact is on the attenuation constant (this is a function of both Z and Y), that for the more accurate CM model being higher than that for the EMTP model. The net effect of the latter is that the high frequency transients superimposed upon the power frequency voltage and current waveforms are attenuated much faster in the case of the more accurate CM model compared to the EMTP model and this is the case for all types of faults. Equally important, some distortion is also observed on the healthy phases(s) in the case of the CM model and this is distinctly absent in the EMTP model largely due also to the approximations and their impact on the mutual coupling amongst conductors in the case of latter.

The foregoing is an important advancement in the accurate modelling of the fault transient phenomena in

underground cables particularly in view of the fact that some of the developments in techniques of accurate fault detecting /location are heavily depended on extracting information from accurately modelled voltage and current signals under faults.

REFERENCES

[1] L.Marti, "simulation of transients in underground cables with frequency-dependent modal transformation matrices",IEEE transaction on power Delivery, July 1988

[2] J.A.Tegopoulos & E.E.Kriezis, "Eddy current distribution in cylindrical shells of infinite length due to axial current", Part I: shells of one boundary, IEEE, PAS, 1971

[3] J.A.Tegopoulos & E.E.Kriezis, "Eddy current distribution in cylindrical shells of infinite length due to axial current", Part II: shells of finite thickness, IEEE, PAP, 1971

[4] X.B.Xu & G.Liu & P.Chow, "A finite-element method solution of the zero-sequence impedance of underground pipe-type cable", IEEE transaction on power Delivery, JAN.,2002

[5] D.L.Paul, C.J.Railton & I.J.Craddock, "Full-wave modelling of coaxial cables by FDTD technique", electronics letters 10th Oct. 2002 vol.38 no.21
Sep./Oct. 2002

[6] G.W.Brown & R.G.Rocamora, "surge propagation in Three-phase cables", Part I –unsaturated pipe, IEEE ,PAS , Jun./Feb. 1976

[7] Emanuel, A. and Doepken Jr. H. C. "Calculation of losses in steel enclosures of three-phase bus or cable", IEEE PAS-93, November 1974, PP. 1758-1767.

[8] EMTP Theory book

[9] J Moshtagh & R K Aggarwal, "A new approach to single-phase pipe type cable modelling using conformal mapping", UPEC 2004

[10] R. Schinziger & A. Ametani, "surge propagation characteristics of pipe enclosed under ground cables". IEEE, PAS, Sept. 1978

APPENDIX I

Scale factor N is the ratio of distances in the original Z_1-plane to the corresponding distances in the transformed W_1-plane. Hence it is defined by:

$$N = \left|\frac{dZ_1}{dW_1}\right| = \left|\frac{dZ_1}{dZ}.\frac{dZ}{dw_1}\right| \qquad \text{(A1-1)}$$

With regard to : $Z=Z_1/R_1$ therefore : $Z_1=R_1Z$ and

$$dZ_1 / dR_1 = Z \qquad \text{(A1-2)}$$

and $W_1 = \frac{Z-ka}{kaZ-1}$ therefore:

$$kaZW_1 - W_1 = Z - ka \Rightarrow Z = \frac{W_1 - ka}{kaW_1 - 1} \qquad \text{(A1-3)}$$

Since this is an analytic function, it can be differentiated directly with respect to W_1, as:

$$\frac{dZ}{dW_1} = \frac{(ka)^2 - 1}{(kaW_1 - 1)^2} \qquad \text{(A1-4)}$$

To find the absolute value of dZ/dW_1, W_1 is expressed as: $W_1=\cos\theta + j\sin\theta$; because the radius of the pipe in W_1-plane is unity, it leads to the following:

$$\left|\frac{dZ}{dW_1}\right| = \left|\frac{(ka)^2 - 1}{1 + (ka)^2 - 2ka\cos\theta}\right| \qquad \text{(A1-5)}$$

Thus:

$$N = R_1\left|\frac{(ka)^2 - 1}{1 + (ka)^2 - 2ka\cos\theta}\right| \qquad \text{(A1-6)}$$

N is seen to be a function of θ. With N appearing dominantly in the denominator of Eqs.(30) & (31), the average values of 1/N should appear where point by point evaluations of N are not undertaken [10]. In this case, the cosθ term vanishes so that the N takes the form:

$$N = R_1\left|\frac{(ka)^2 - 1}{(ka)^2 + 1}\right| \qquad \text{(A1-7)}$$

APPENDIX II

In order to find the circle(α_4,R_4), some calculations are done as follows:

$x_{14}=x_{11}+k.(1-x_{11})$ (A2-1)

$x_{24}=x_{21}-k.(1+x_{21})$ (A2-2)

$\alpha_1=(x_{11}+x_{21})/2$ (A2-3)

$\alpha_4=\alpha_1-k.\alpha_1$ (A2-4)

k is a percentage of the full distance between the origin to the centre as shown in Fig. 10 ; for example $x_{11} \to 1$, $x_{12} \to -1$ or $\alpha_1 \to 0$.

From Fig(9), it can be concluded that:

$$R_4 = x_{11}^2 + \alpha_4^2 - 2\alpha_4.x_{11}\cos 120 \qquad \text{(A2-5)}$$

$$R_4 = x_{14} - \alpha_4 \qquad \text{(A2-6)}$$

From Eq.(A2-5, A2-6) k is obtained as follows:

$$k^2 - Mk + N = 0 \Rightarrow k = \frac{M}{2} - \sqrt{\frac{M^2}{4} - N} \qquad \text{(A2-7)}$$

As : $M = (2d^2 + x_{11}(d-1) + d + 1)/d^2$ (A2-8)

And $N = (x_{11}^2 + d^2 + x_{11}(d-1) + d)/d^2$ (A2-9)

After calculating k, x_{14} and x_{24} can be derived from Eqs.(A2-1) and (A2-2) respectively.

Jamal Moshtagh*: received the B.S. degree in Electrical Power Engineering from Sharif University of Technology (Iran) in 1989 and the M.S. degree in the same field from Kh. Nasir University of Technology (Iran) in 1995. He is currently a Ph.D student at the University of Bath (UK). His areas of interest include power distribution systems analysis, application of Intelligent systems in Power Distribution Systems. He has published more than 10 papers in aforementioned field.*

R K Aggarwal*: received the B.S. and Ph.D degrees from the University of Liverpool, U.K., in 1970 and 1973, respectively. Currently, he is a Professor and Head of the Electrical Power and Energy Systems Group of the Department of Electronic and Electrical Engineering at the University of Bath, U.K. His main research interests include Power System Modelling and Application of Digital-Technology and AI to protection and control. He has published many technical papers and c0-authored four text books.*

Calculation of the Safety Conditions from High Touch and Step Voltages in the Grounding System of REK Bitola – Suvodol

Nikolce Acevski, Risto Ackovski and Mile Spirovski

Abstract: *In this paper, beside the results of calculation, are described and elaborated mathematic models which are applied for solution of problem with transfer of potential. Appropriate algorithm is made as programmed package which is used for analysis or better says, for anticipation of the conduct of al grounding system (GS) in the area of the mine when faults to ground appeared in the system 110 kV for the present situation.*

Keywords: *groundings, transferred potentials, safety conditions, touch and step voltages*

Introduction

Because of the nearness of the sources of REK Bitola as well as because of the meaning of the mine "Suvodol" problem of transferred potentials is especially expressed. Cables in the network are with rubber isolation that contains three-phase conductors as well as additional signal conductors made by cooper with relative big section. So all objects in part of the mine (operative stations, diggers, transport tapes, engines and the other consumers on medium (MV) and low voltage (LV)) are mutual galvanic harnessed and together with their groundings, they formed GS of the mine. At appearance of fault to ground at station 110/6 kV/kV of the mine or the network 110 kV in nearness of the mine, that power is distributed at all GS (tower groundings on 110 kV transmission lines (TL), grounding on substation 110/6 kV/kV and groundings by individual MV consumers). For mutual galvanic connection of groundings from supplied objects at 6 kV networks, at appearance of fault to ground in 110 kV network, by metal pieces of equipment may occur potentials appreciably higher of potential by ambient soil. The problem with transfer of potentials also is expressed with the systems for transport of soil and chats, as and substation TS MV/LV by 6 kV network in mine, where groundings of that TS are sources of current field and dangerous voltage of touch and step on their near in time of fault in HV network.

Grounding System - Model

Netlike Grounding - Model

Small part of the current (in this case just 9,4 %) that is injected in GS of the mine will go to the earth over netlike grounding of TS 110/6kV/kV "Suvodol". Accuracy of the final results of the analysis for the potentials of GS of the mine is little connected with the accuracy of the calculated grounding resistance R_{ts} of the netlike grounding. For this calculation we will use simplified way the entirely netlike grounding will be modelled with one horizontal panel which equivalent diameter has the same parameter A as the netlike grounding itself.

$$D_{ek} = \sqrt{4 \cdot A / \pi} = 1{,}128 \cdot \sqrt{A}\,, \tag{1}$$

For calculation of the resistance we will use the following expression [9], where is $\rho = 100\Omega m$:

$$R_{TS} = \frac{\rho}{2 \cdot D_{ek}} = 0{,}725\Omega\,, \tag{2}$$

Modelling of Transmission Lines

When TL is performance with protective rope; it participates of the transfer of the currents and potentials when fault to ground appeared in the system 110kV. Therefore, in replacement scheme in the network of GS every TL ought to be presented on the same way, with so-called "π-scheme" [9]. In power network of the mine "Suvodol" exist only one TL provided with protective rope. That is TL 110kV TS 110/6 "Suvodol"-TS 400/110 Bitola2", who is consecution like two systematic (with two independent threat on phase conductors 2x3xA1/C240/40mm²) with length l=2,7 km, type of protective rope Fe III 50mm² .

According to [9], for impedance per kilometre length of protective rope we can get:

$$\underline{z} = \left(0{,}05 + \frac{1000\rho_{Fe}}{S_{Fe}}\right) + j\left(\log\frac{2D_e}{d} + 0{,}0157\mu_r\right) \tag{3}$$

$$\underline{z} = (4{,}24 + j1{,}24)\Omega / km$$

With D_e is indicated equivalent depth of the return path of current in the earth, which is according to Carson model depend of ρ and frequency f and it can be calculated with:

$$D_e = 658\sqrt{\rho / f} = 930{,}6m\,, \tag{4}$$

As we know number of aperture 12, for average cost of aperture amount a=225 m, than for impedance of average aperture we will have:

$$\underline{Z}_r = a \cdot \underline{z} = (0{,}954 + j0{,}279)\Omega / aperture\,, \tag{5}$$

According to [9], TL with more than 10 apertures is treated like infinite TL, without making any important mistake in modelling. TL may be equivalent with it entering impedance:

(6) $\underline{Z}_{VL} = \sqrt{R_{ST} \cdot \underline{Z}_r} - 0{,}5 \cdot \underline{Z}_r = (2{,}04 + j0{,}22),$

Where $R_{st} = 6{,}5\Omega$ is average value of grounding resistance on the separates towers of TL.

Modelling of Cables 6 kV and Characteristics of their Models

Every cable looked together with returned path through earth, can be presented with one I-removal scheme, i.e. with one ordinal impedance $\underline{Z}=\underline{z}\cdot l$. Longitudinal impedance that is impedance of unit length $\underline{z}$ in this case will be [9]:

(7) $$\underline{z} = r + jx = \left(\frac{1000}{\kappa \cdot S} + 0{,}05\right) + j \log \frac{D_e}{D_s},$$

According to these formulas, in context of above mentioned, there are estimated parameters by unit length of the all types of cables that are used in 6 kV supply network of the mine in table 1. $r20$ is the active resistance at temperature of 20°C.

Modelling of Groundings on TS 6/X kV/kV

Each TS 6/x kV/kV which has own grounding with known grounding resistance R, in removal scheme of GS will be node, so-called "grounding place", and the grounding itself in removal scheme will be modelled with cross located active resistance R. According to this, before matrix forming [Y] on GS, is necessary to be determinate grounding resistances of all grounding places and for this reason we need to know ρ as well as the geometry of groundings.

Accessory Groundings – Model

Accessory groundings of different types of mine objects and machines are modelling of identical way like groundings of substation TS 6/x kV/kV. Beside that, each grounding in qualified grounding place (that can be introduced of the accessory grounding) will introduce one active resistance established cross in equivalent scheme in GS. We can say that it happens that more grounding are galvanic connected in one grounding place. In that case, in removal scheme of GS will appear as parallel connected active resistance as there are different groundings; galvanic connected with the grounding place.

Surface Groundings –Model

According to [9], grounding resistance of transporters/tracks with length l and equivalent diameter d on the surface of earth at average ρ is:

(8) $$R = \frac{\rho}{\pi \cdot l} \cdot \ln \frac{2l}{d},$$

According, to this, if the track is located on the area of earth and if it is linked on one end with GS and it is free on the other sight, than it can be treated like elementary grounding, that in equivalent scheme GS on individual grounding place will entered active resistance R. As both ends of track are galvanic connected for different grounding places, then in removal scheme of GS the track will have to introduce with π-scheme.

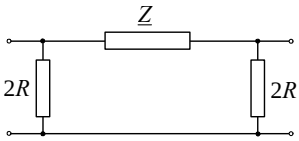

Fig. 1. π–removal scheme for transporters/track

Parameter $\underline{Z}$ of ordinal branch in π– scheme is [9]:

(9) $\underline{Z}=[\rho_{Fe}\, l/S + 0{,}05] + j\cdot[0{,}1445\cdot\log(2D_e/d) + 0{,}0157\cdot\mu_r]$,

Diggers and other machines and mine objects that have big step upon area, with their caterpillars realize good power contact with earth. If we like to determine all characteristics of this grounding (distribution of the potentials upon the land; voltage per step etc) then step upon area of digger will have to model as precise as possible, and in a whole will be noted the geometry of the problem.

Analyses shows that step upon areas of diggers, transporters and other equipment, satisfactory can be modelled with individual netlike GS, horizontally placed in earth on certain small depth h. Thereat, netlike GS will need to have the same geometry like geometry of step upon area of digger/machine, and own modelling itself can be successfully done if step upon area is changed with heavy network on horizontal tracks, placed on small distance from one another (e.g. D=50 sm.), buried in small depth (e.g. h=5 sm).

Estimation of Currents and Potentials in Grounding System

When one-phase fault to ground appear in 110 kV patch board of mine "Suvodol" that is of arbitrarily place of TL 110 kV TS 110/6 "Suvodol"-TS 400/110 "Bitola 2", comes to flux of currents per grounding of station. Current which fluxes per this grounding, and the potential of grounding, V_z, measured in relation of reported land (item which is located enough from GS), depends on the quantity of current of fault to ground, as well as on the location of the fault. The analyses show that most unfavourable case, from aspect of the quantity of potential of grounding, is for one-phase fault to ground produced in the station. The whole current of fault doesn't go into the earth, but just one part of it, which will be indicated with I_z. Component I_z represents current that is "injecting" in GS and we can call it current through GS. This current in different ways, flows through earth to source of current, i.e. to station 400/110 "Bitola 2". If with $\underline{Z}_z$ we indicate complex "enter impedance of the whole GS at station 110/6 "Suvodol"and if we note $Z_z = |Z_z|$ will have:

(10) $$V_z = Z_z \cdot I_z ,$$

So for determination of the potential V_z it will be needed, on one side, to be known entering impedance Z_z. Quantity of current I_z may be calculated if the parameters of the system 110 kV are known. The value of the equivalent impedance Z_z of whole GS needed for estimation of potential V_z may be received in two ways: with direct measuring or with estimation. In this paper it is calculated with computer programme based on the method of independent voltages.

In the paper it is supposed that current on fault to ground is known, produced in TS 110/6 "Suvodol". In the same time, in the estimations is operated with subtranzient currents of fault to ground because they are the biggest. Data for value of the current of one-phase fault to ground in power system of R.M. are received from competent offices. The case note as maximum current is in connection with maximum regime of power system of R.M., with all aggregates of operation, and minimum currents is for regime in which one aggregate is out. The current I_z =17196 A that is injected in GS in mine is calculated like in [6].

After according current I_z is estimated by known (calculate or measured) value of entered impedance $Z_z = Z_{ek}$, calculate the potential V_z=1215 V in netlike grounding, node SO.

After determination of potential V_z on the place of fault, we can determine potentials and for other groundings in the region of the mine. For this purpose it is less complicated to practice matrix algebra and potentials of cables, and after those currents through branches of GS, are calculated with usage of method of independent voltages. As first task that can be established, will be (with use of Cirhof laws) the determination of currents in whole GS.

It's very useful, particularly when the calculations are made by computer, if there are used matrix methods. In the algorithm according to which is produced the programme package Suvodol, is used matrix approach for solution of the problem of distributing of currents and transfer of potentials in GS in the mine. Solution of mentioned problem is done with help of matrix of impedances, [*Z*], of GS [18]. For this purpose, primary, according to known plot of feeder 6kV and their known parameters, is generated so-called matrix of admittances [*Y*] of GS, [18]. With its inversion we have matrix [*Z*].

(11) $$[Z] = [Y]^{-1}$$

Then, potentials $\underline{V}(i=1,N)$, of the separate groundings are determined with help of:

(12) $$V_i = Z_{is} \cdot I_Z \; ; \; i = 1,2, ..,N,$$

With $Z_{is}\,(i=1,N)$ are elements in the column "*s*" of matrix [*Z*], hereby, with "*s*" is indicated the index of node that is referred to grounding.

Results of the Estimation

Whole network 6 kV is divided, on:

1. Coal system (SJ);
2. First system (S1);
3. Second system (S2) and
4. Zero system (S0).

That is made, so we can see what is the stake of each of the systems of the mine in drop off of total current I_z although it's partial GS are galvanic connected in the central separation (node "SO") through it's grounding type "CENTRAL", and they are treated like that in the estimations as well. The results are shown in table 2.

When we evaluate the attained results, if estimated voltages of touch and step are in the permitted borders, we need to respect:

1. Time of duration of one-phase fault to ground.
2. Allowed voltages of touch and step, depending on the time of disconnecting.

According to the results from the studies [1], [2], time of disconnection of fault to ground made in the station 110kV of mine is t=0,1 s. In the American standard (ANSI/IEEE Std80-1986), simple formulas are added for calculation of permitted voltages of touch and step. The lowest values in these voltages are one to cases when person is in contact with metal areas. In that case, permitted voltage of touch, for man who has 70 kilograms is calculated with:

(13) $$\Delta U_{ddoz} = \Delta U_{cdoz} = 157 / \sqrt{t} ,$$

According to [5] if the time of disconnection is *t*=0,1s, allowed voltage of step out of station is 320 V, but in case when roads of public traffic are considered, that voltage is 180V. Question for height of allowed voltage of touch is treated also in [5]. According to article 29 of this Rule, if time of disconnection of fault to ground is 0,1 s allowed voltage of touch is 300 V. From this point we can make the conclusion that if time of disconnection of fault to ground produced in 110 kV network is 0,1 s, allowed voltage of touch/step, is 300 V.

Measures for Eliminating Dangers

From the received results, we can see that maximum voltages of steps are regular for 40-60 % smaller than maximum voltages of touch, so we can conclude that dangers in 6 kV network in mine when fault to ground appear in 110 kV system are voltages of touch. In table 3 are present nodes of network that have maximum potential difference of touch that exceeds the value of 200V. In it there are shown voltages of nodes *U*(V), ρ (Ωm) as well as the voltages of touch ΔU_d and potential difference of touch ΔE_d. (4.8)

Table 1. *Longitudinal parameters of used type of cables*

ordinal	Label of cable	Outlying diameter mm	Active resistance r_{20} Ω/km	Reactive resistance x at ρ = 50 Ω·m	Reactive resistance x at ρ = 100 Ω·m	Reactive resistance x at ρ = 200 Ω·m
1	EpN78 3x25+3x10	51	0,676	0,690	0,712	0,734
2	EpN78 3x35+3x10	54	0,676	0,688	0,710	0,731
3	EpN78 3x50+3x16	60	0,423	0,679	0,700	0,722
4	EpN78 3x70+3x16	65	0,423	0,673	0,695	0,717
5	EpN78 3x95+3x25	67	0,271	0,669	0,690	0,712
6	EpN78 3x120+3x25	76	0,271	0,664	0,686	0,708
7	EpN78 3x185+3x25	117	0,271	0,646	0,668	0,690
8	PP41 3x95/25	45	0,814	0,645	0,667	0,689
9	PP44 3x95/25	45	0,814	0,645	0,667	0,689
10	PHP41 3x185/25	54	0,814	0,634	0,656	0,677
11	PP44 3x185/25	54	0,814	0,634	0,656	0,677

Table 2 *Distribution of injected currents and equivalent impedances per separated systems of the mine for total injected current* I_z *=1000A*

	S i s t e m	I_r	I_x	I	φ		Z
/	/	(A)	(A)	(A)	(o)	%	Ω
1	Coal (SJ)	277.62	-19.71	278.32	-4.06	26.7	0.25376
2	First (S1)	217.72	-50.86	223.58	-13.15	21.5	0.31589
3	Second (S2)	151.09	-16.38	151.98	-6.19	14.6	0.46472
4	Zero (S0)	255.55	-1.06	255.55	-0.24	24.5	0.27637
5	Netlike grounding	70.64	67.11	97.44	43.53	9.4	0.72481
6	110 kV TL	27.37	20.89	34.43	37.35	3.3	2.05105
	Total	1000.00	0.00	1000.00	0.00	100.0	0.07063

Table 3. *Nodes in network 6 kV in which* $\Delta E_d > 200$ *V*

	System	node	Grounding type	ρ (Ωm)	U (V)	ΔE_c (V)	ΔE_d (V)	ΔU_d (V)
1	(SJ)	RP6	RP16	40	770	139	201	189
2	(SJ)	RP78	RP78	40	908	127	296	279
3	(SJ)	DOM.TRAFO	RP16	100	1168	210	305	264
4	(S2)	TS4	RP16	100	1184	213	309	267
5	(S2)	RP5	RP16	50	778	140	203	188
6	(S2)	ES10	BG_JL3	40	558	275	296	279
7	(S0)	RP910	RP78	40	903	126	294	277
8	(S0)	PRP	PRP	100	814	197	385	333

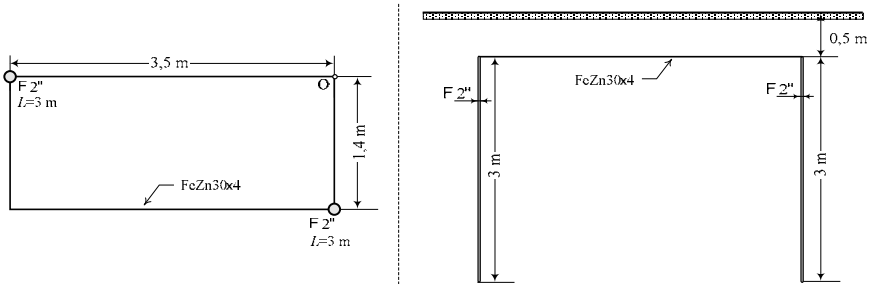

Fig.2. Grounding type PRP

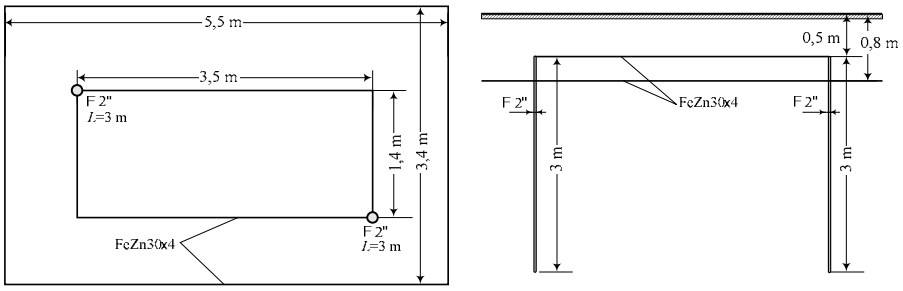

Fig. 3. New grounding type PRP 2

But if we adopt the measure for danger ($\Delta U_{d.doz} = \Delta U_{\sim.doz} = 300$ V) then in 6 kV network in the mine danger of more higher voltage of touch will appear one in the knot PRP in zero system ($\Delta U_d = 333$ V).
Solution of this problem can be done in more than one way but the simplest are the following:
1. Installation of additional ring around the object, 1m of its margins and at depth of 0,8m.
2. Asphalting the path around the object with width of at least 1m.

Here is analyzed and discussed the first method, which is cheaper. Asphalting will occur if there isn't objective limitation for installation of the additional ring around the object itself.

For that reason permanent grounding type PRP (figure 2) that is consisted of just one rectangular ring with sizes axb=3,5x1,4m buried in depth $h_1 = 0,5$ m and two vertical plug F2" that are 3 m long, we will add another rectangular ring with dimensions a2xb2=5,5x3,4m, buried in depth $h_2 = 0,8$ m and this way we will have new grounding that will be called type PRP2 (fig. 3). Characteristics of this new type of grounding are explored in program package "ZAZEM" and it is concluded that the biggest potential differences of touch and step are by the length in direction of 0-A (fig. 4.).

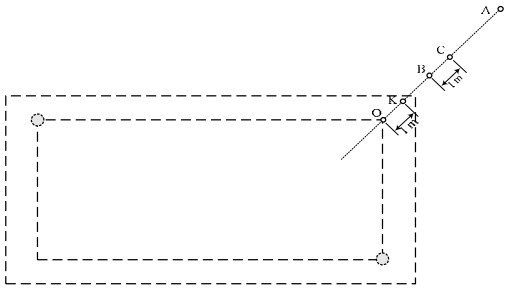

Fig 4. Estimation of potentials in the surface of earth

On the fig. 5. φ_K ($\varphi_K = \varphi_{min}$) in the critical item *k*, that is located 1m from the edge of object, and the lowest when the potential difference of touch ΔE_d is difference between potential φ_0 of the object and φ_K, in item k:

(14) $$\Delta E_d = \varphi_0 - \varphi_K ,$$

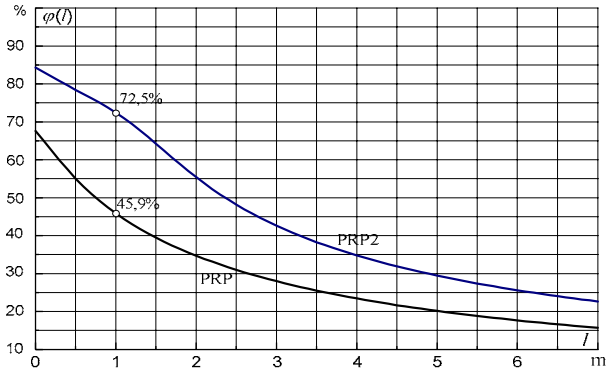

Fig.5. Distribution of potentials per length of critical direction 0-A

From here, for maximum potential difference of touch:

$\Delta E_d = 54,1\%$ for permanent grounding type PRP

$\Delta E_c = 27,5\%$ for new grounding type PRP2.

So, after putting second, additional, contour, we obtain new, grounding type PRP2, at which maximum voltage of touch will be reduced of the value $\Delta U_d = 169$ V. Besides these analyses, there are calculated potentials differences of step ΔEc. Calculations show that the biggest potential difference of step is again in direction 0-A, between the points B and C which are alienated 1m from one to another. Essential characteristics of groundings type PRP and PRP2 are shown in table 4, (grounding resistance, potential differences of touch and step.

Table 4. *Characteristics of groundings type PRP and PRP2*

Grounding type	R_Z, (Ω)	ΔE_c (%)	ΔE_d (%)
PRP	11,35	21,7	54,1
PRP2	8,05	17,2	27,5

Conclusion

1. The biggest danger of transferred potentials in 110kV network in region of mine “Suvodol” at REK –Bitola is when fault to ground appear in TS 110/6kV/kV.
2. The highest potentials in MV network of mine are those in so-called “maximum regime” when all sources in power system of R.M. are on.
3. Time of disconnection for the current that is produced is estimated that is t = 0,1s. For this time in the paper is suggested that as a criteria of dangerous to be accepted $\Delta U_{d.doz} = \Delta U_{c.doz}$ = 300 V.
4. For this adopted criteria for safety is obtained that real danger of higher voltage of touch is noticed only with one grounding, in the node PRP (ΔU_d = 333 V).
5. It is suggested the grounding in this TS 6/0,4 kV to be improved with adding one rectangular contour around the object. Alternative, the whole zone around the object should be asphalted.
6. Currents of fault to ground after building of 400kV relation Bitola2-Amindeo, will be bigger at least for 40-60%. That will provoke enlargement of dangers from transferred potentials in MV network of the mine for approximately the same percent and appearance of new dangerous places in MV network, tab. 3.

References

[1] R. Ackovski, D. Rajicic, R. Taleski i A. Dimitrovski, "Modeliramje na kusite vrski, zazemjuvackiot sistem i presmetka na potencijalite na zazemjuvacite vo reonot na rudnikot 'SUVODOL' pri pojava na kusa vrska vo sistemot 110 kV", ETF - Skopje, Skopje, mart 1991.

[2] R. Ackovski, D. Rajicic, A. Dimitrovski i R. Taleski, ″Analiza na karakteristikite na tipskite zazemjuvaci vo reonot na rudnikot 'Suvodol' pri REK 'Bitola'", ETF - Skopje, juni 1991.

[3] D. Vidanovski, M. Stojanovski, B. Dungovski i N. Stojanovski "Analiza za sprecuvanje na izvoz na opasni potencijali po transporterite vo Rudnik Suvodol". 1993 g.

[4] R. Ackovski, R. Taleski, A. Dimitrovski: Strucna recenzija na elaboratot "Analiza za sprecuvanje na izvoz na opasni potencijali po transporterite vo Rudnik Suvodol", ETF-Skopje, 1994 g.

[5] Pravilnik za tehnickite normativi na elektricni postrojki i uredi vo rudnicite so povrsinska eksploatacija na mineralni surovini. "Sl. list na SFRJ br. 66/87".

[6] N. Acevski, "Prilog kon modelite za resavanje i analiza na zazemjuvaci i zazemjuvacki sistemi", doktorska disertacija ETF-Skopje, 2003.

[7] Industrija kablova "M. Pijade"-Svetozarevo. Katalog za SVERPEN kabli 1 i 6 kV.

[8] V. Srb: "Kabelska tehnika", Zagreb 1970.

[9] J. M. Nahman: "Uzemljenje neutralne tacke distributivnih mreza" Naucna knjiga Beograd, 1980.

[10] J. M. Nahman: "Struje kratkih spojeva i njihovo prekidanje". ETF-Beograd, 1975.

[11] R. Ackovski: "Visokonaponski mrezi i sistemi", ETF-Skopje, 1995.

[12] D. Rajicic: "Analiza na EES", ETF-Skopje, 1996.

[13] B. Stefanini: "Prijenos elektricne energije", Zagreb, 1968

[14] J. M. Nahman: "Metoda proracuna slozenih uzemljivaca na digitalnim racunarima i opste karakteristike uzemljivaca". XI Strucno savjetovanje, Ohrid, 1972.

[15] J. M. Nahman: "Numericki postupak za proracun medjusobnih otpornosti tankih pravolinijskih provod-nika". casopis "Elektrotehnika" ELTHB2 27, br. 1-2/1984.

[16] A. Hukic: "Proraun iznoenja potencijala iz TS 110/35/6 HAK putem metalnog plasta 6 kV kablova. casopis "Elektrotehnika" ELTHB2 29, br. 1-2/1986.

[17] D. Salamon: "Analiza tipicnih uzemljivaca na povrsinskom kopu rudnika uglja REIK "Kolubara". Casopis "Elektrotehnika" ELTHB2 27, br. 1-2/1984.

[18] H. E. Brown: Solution of Large Networks by Matrix Methods, John Wiley&Sons, Inc. N.Y. 1975.

Nikolce Acevski *– Associate Professor, Ph D., Faculty of Technical Sciences, St. Cl. Ohridski University 7000 Bitola,R.MACEDONIA*
e-mail: nikola.acevski@mofk.gov.mk

Risto Ackovski *– Full Professor, Ph D., Faculty of Electrotehnics, St. Cyril and Metodius University 1000 Skopje R.MACEDONIA.*

Mile Spirovski *– Faculty of Technical Sciences, St. Cl. Ohridski University 7000 Bitola R.MACEDONIA*

Dynamic Voltage Restorer with Zero Sequence Compensation

Mehmet Tumay, K. Cagatay Bayindir, M. Ugras Cuma and C. Onur Tokunc

Abstract: *In this paper, a three-phase four-wire Dynamic Voltage Restorer (DVR) which can mitigate zero sequence components under unbalanced faults is presented. Zero sequence components result in the high insulation costs and asymmetry of the phases and magnitudes of the terminal voltages. Zero sequence currents will flow through the neutral wire in three-phase four-wire systems unless zero sequence compensation is applied. The developed DVR model and case studies for unbalanced faults are presented in this paper.*

Keywords: *voltage sags, zero sequence compensation*

Introduction

Power quality disturbances such as voltage sags, voltage swells and short duration outages on sensitive equipment can often lead to valuable data loss and long production downtimes [1]. Voltage sags are one of the major power quality problems faced. With the increasing use of power electronic based equipments, the loads are becoming more sensitive to voltage sags.

A variety of devices have been designed to mitigate disturbances in power systems, DVR can provide the most cost effective solution to mitigate the voltage sags by establishing the proper voltage quality level that is required by customer [2]. DVR restores the load voltage to its pre-fault value within a few milliseconds.

A three-phase unbalanced source voltage can be decomposed into a zero-sequence component, a positive-sequence component, and a negative-sequence component by using symmetrical components transformation. Generally, distribution systems use a three phase three-wire topology or a three-phase four-wire topology. The use of Y-Y winding with the neutrals grounded in transformer connection allows propagation of zero sequence components to the loads when an unbalanced fault takes place [3].

Most of the faults that occur on power systems are unsymmetrical faults, which may consist of unsymmetrical short circuits, unsymmetrical faults through impedances, or open conductors [4]. Therefore the zero sequence components will necessarily appear due to unbalance of three phase voltages in the system. A disadvantage of the zero sequence components is, as well as the higher insulation cost, the asymmetry of the phases and magnitudes of the terminals voltages. Zero sequence currents can cause large voltage drops because of the voltages induced by the coupling inductances of the lines [5]. Therefore a control algorithm is required to control the positive, negative, and zero sequence voltages injected during the unbalanced fault period. Thus the influence of the zero-sequence components must be considered when a DVR is designed.

Control algorithms for three-phase three-wire DVR are presented in [6] and [7]. But zero sequence components, having negative effects on the distribution system, are not considered. This paper presents a method to restore positive sequence and compensate both the negative and zero sequence of the load voltages.

System Configuration

A typical three-phase four-wire distribution line with DVR is modeled under Matlab/Simulink for presentation of the proposed method. Fig.1 shows the studied model.

The control strategy of the DVR should be designed to detect the voltage sags in the supply voltage and apply the necessary missing voltage as soon as possible. A three phase four-wire DVR is modeled and simulations are carried out to show the performance of the proposed control strategy.

The DVR is designed to compensate both balanced

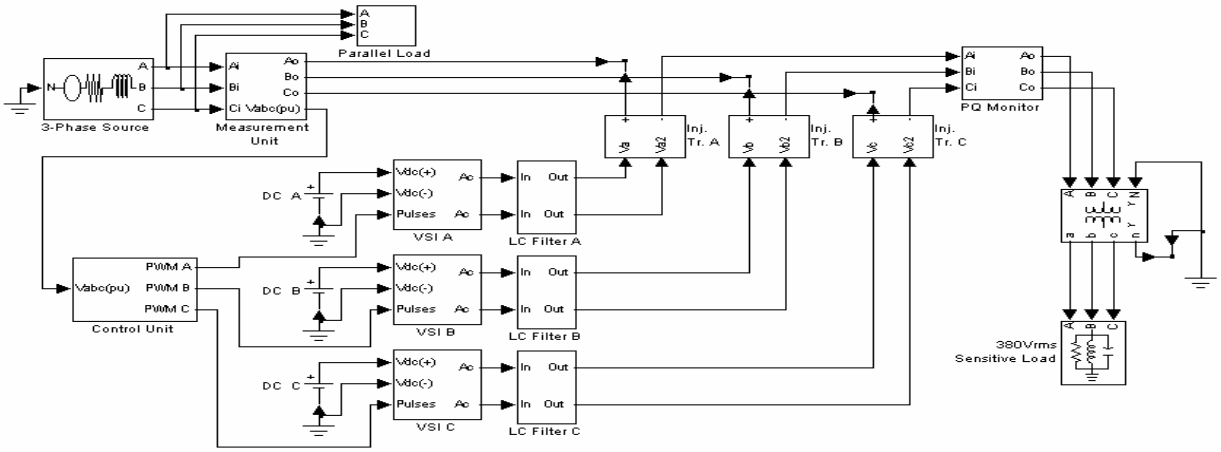

Fig.1. Modeled DVR topology

and unbalanced voltage sags. Under unbalanced voltage sag conditions, it is clear that the missing voltages of three phases will not be same. Three single-phase bridge inverters are used to inject three independent missing voltages.

One of the important problems of the DVR that should be solved is the attenuation of the high order harmonics generated by the voltage source PWM inverter. Basically there are two types of filtering systems that may be applied to the DVR, inverter side filtering and line side filtering. In this study inverter side filtering is used. Inverter side filtering scheme has the advantage of being closer to the harmonic source, thus high-order harmonic currents are prevented to penetrate into the series injection transformer.

Three single-phase injection transformers are used to inject the independent missing voltages to the line.

Parallel load contains shunt loads connected to the supply feeder and fault generating elements, constituting the fault that causes the voltage sag.

Proposed Control Method

Due to the three-phase four-wire system, a control algorithm is required to control the positive, negative, and zero sequence voltages injected during the unbalanced fault period. Three independent reference signals are generated by the control unit. Fig.2 shows the diagram of the control circuit.

In the proposed control strategy the source side terminal voltages V_a, V_b, V_c are transformed into d-q-0 components with the Park Transformation as in [7];

$$C = \begin{bmatrix} 1 & -1/2 & -1/2 \\ 0 & \sqrt{3}/2 & -\sqrt{3}/2 \end{bmatrix}, \quad (1)$$

$$R(\theta) = \begin{bmatrix} \cos(\theta) & -\sin(\theta) \\ \sin(\theta) & \cos(\theta) \end{bmatrix}, \quad (2)$$

$$\begin{bmatrix} V_d \\ V_q \end{bmatrix} = \frac{2}{3}.R(\theta).C.\begin{bmatrix} V_a \\ V_b \\ V_c \end{bmatrix}, \quad (3)$$

$$V_0 = \frac{1}{3}(V_a + V_b + V_c) \quad (4)$$

For simplicity, the transformation matrix is written separately for d, q and 0 components.

As mentioned in [7], in case of source voltage unbalance, two rotating coordinate systems should be used for proper operation of the controller. The former will rotate counterclockwise direction, called as the positive sequence synchronous reference frame (PSRF), while the latter will rotate in the clockwise direction, called as the negative sequence synchronous reference frame (NSRF), with the angular frequency of the system in the stationary reference frame. However, this is not satisfactory to control zero sequence components in the system. A zero sequence compensator also should be added. In this study a zero sequence compensator is added to the system and simulations are carried out to show the effectiveness of the proposed method.

For effective control without phase shift in steady state, the positive and negative sequence components that have DC values should be separated. In order to achieve this differential controller method is used. Fig.3 and Fig.4 show the block diagram of this process.

The DC values of positive and negative sequence SRF are then compared with reference constants. The errors and zero sequence components processed through PI controllers are used as reference d-q-0 components for the inverse Park transform. The outputs of inverse transform are the reference PWM signals and compared with a carrier wave to generate the firing pulses to the Voltage Source Inverter (VSI).

The positive sequence rotates counterclockwise and the negative sequence rotates clockwise direction in the stationary reference frame, when they are shown in positive sequence SRF, the positive sequence becomes a

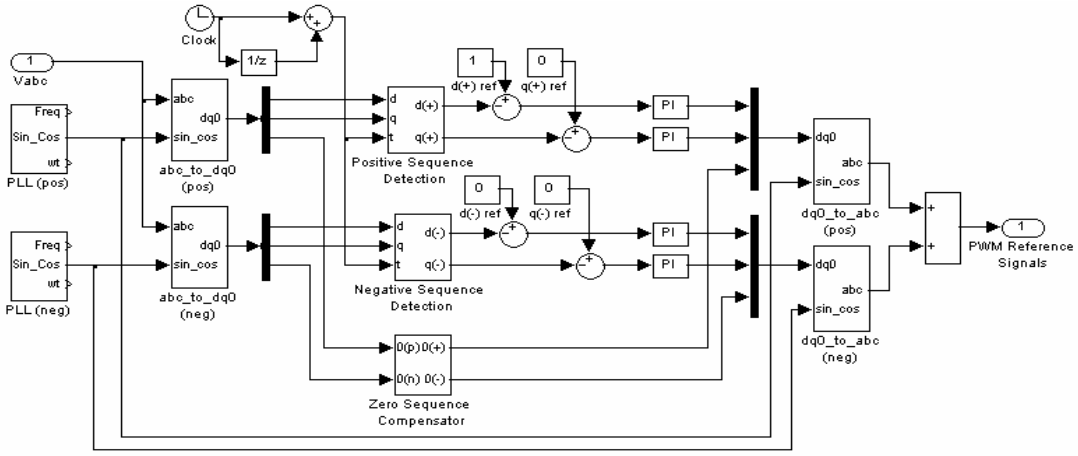

Fig.2. Block diagram of control circuit

DC component and the negative sequence a 100Hz component [7].

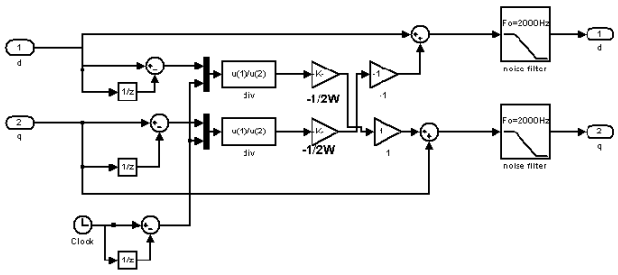

Fig.3. Positive sequence detection

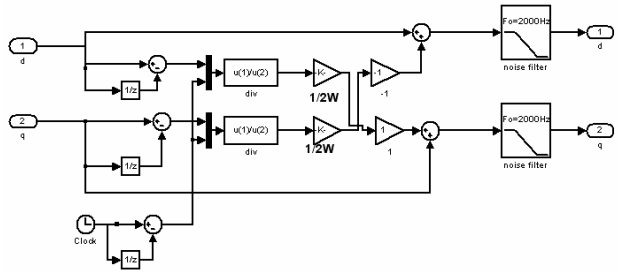

Fig.4. Negative sequence detection

Equation (3) is composed of both positive and negative sequence components. This is expressed as;

$$(5) \qquad \begin{bmatrix} V_{d(p)} \\ V_{q(p)} \end{bmatrix} = \begin{bmatrix} V_{dp} \\ V_{qp} \end{bmatrix} + R(-2\omega t) \begin{bmatrix} V_{dn} \\ V_{qn} \end{bmatrix}$$

Equation (6) shows (5) differentiated in time domain;

$$(6) \qquad \begin{bmatrix} V'_{d(p)} \\ V'_{q(p)} \end{bmatrix} = (-2\omega t) R(\frac{\pi}{2}) R(-2\omega t) \begin{bmatrix} V_{dn} \\ V_{qn} \end{bmatrix}$$

where,

$V_{d(p)}$ is the positive sequence d component,

$V_{q(p)}$ is the positive sequence q component,

V_{dp} is the positive sequence d component of the positive sequence SRF

V_{qp} is the positive sequence q component of the positive sequence SRF

V_{dn} is the negative sequence d component of the positive sequence SRF

V_{qn} is the negative sequence q component of the positive sequence SRF

Equation (6) is rotated by 90° and divided by -2 ω , as follows;

$$(7) \qquad -\frac{1}{2\omega} R(\frac{\pi}{2}) \begin{bmatrix} V'_{d(p)} \\ V'_{q(p)} \end{bmatrix} = R(\pi) R(-2\omega t) \begin{bmatrix} V_{dn} \\ V_{qn} \end{bmatrix}$$

Since the sum of a vector and the same vector phase shifted by 180° becomes zero, the sum of equation (3) and (7) leaves only positive sequence component that is a DC component for positive sequence SRF.

$$(8) \qquad \begin{bmatrix} V_{d(p)} \\ V_{q(p)} \end{bmatrix} - \frac{1}{2\omega} R(\frac{\pi}{2}) \begin{bmatrix} V'_{d(p)} \\ V'_{q(p)} \end{bmatrix} = \begin{bmatrix} V_{dp} \\ V_{qp} \end{bmatrix}$$

Similarly, the negative sequence components can be calculated as follows;

$$(9) \qquad \begin{bmatrix} V_{d(n)} \\ V_{q(n)} \end{bmatrix} + \frac{1}{2\omega} R(\frac{\pi}{2}) \begin{bmatrix} V'_{d(n)} \\ V'_{q(n)} \end{bmatrix} = \begin{bmatrix} V_{dn} \\ V_{qn} \end{bmatrix}$$

where,

$V_{d(n)}$ is the negative sequence d component,

$V_{q(n)}$ is the negative sequence q component

Under normal circumstances, the source voltage only includes positive sequence components. An unsymmetrical fault causes negative sequence currents to flow in a three-phase three-wire system while both negative and zero sequence currents will flow in a three-phase four-wire system. For efficient sag compensation, following reference d and q components are chosen.

$$(10) \qquad V_{dref(p)} = 1,$$

$$(11) \qquad V_{qref(p)} = 0,$$

$$(12) \qquad V_{dref(n)} = 0,$$

$$(13) \qquad V_{qref(n)} = 0$$

Elimination of zero sequence components disrupting the symmetry of the phases is an important aspect of this study. In order to eliminate the zero sequence components, the reference zero component for the inverse Park transform with 180° phase shift have to be generated. The zero sequence compensator consisting of PI controllers has this capability.

Case Studies

Designed DVR is examined under different case studies to reflect the real problems.

Single-phase to ground fault

Most faults in power systems are single-phase to ground faults. In this case study, single-phase fault was simulated and analyzed. The status of zero sequence current is observed. The %40 voltage sag occurred at phase A between 0.1s and 0.2s.

To demonstrate the performance of the proposed control method under unbalanced voltages in four-wire topology, two simulations are carried out. In the first simulation, there is no zero sequence compensator, while in the second; the zero sequence compensator is included.

The simulation results without zero sequence compensator are depicted below. Fig.5 shows the source voltage. Fig.6 shows the restored load voltages by DVR.

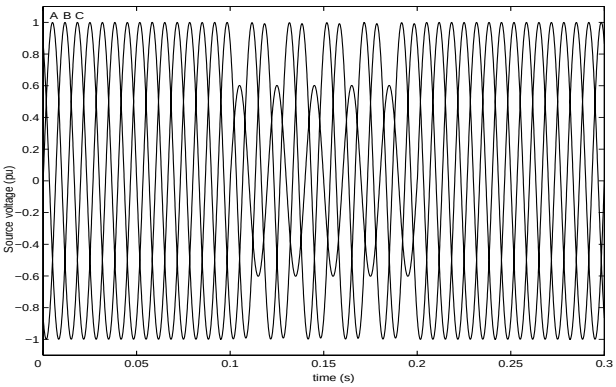

Fig.5. Source voltages, phase A, phase B, phase C

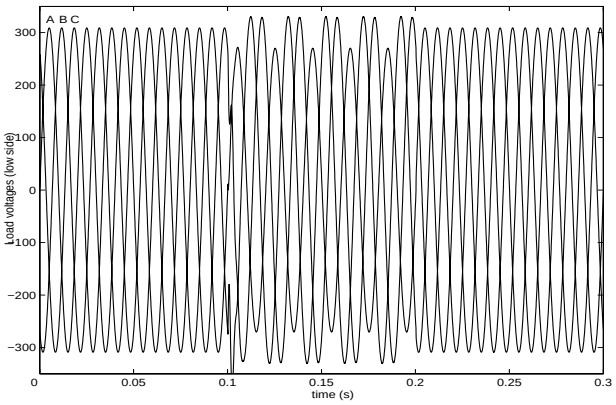

Fig.6. Restored load voltages without zero compensator

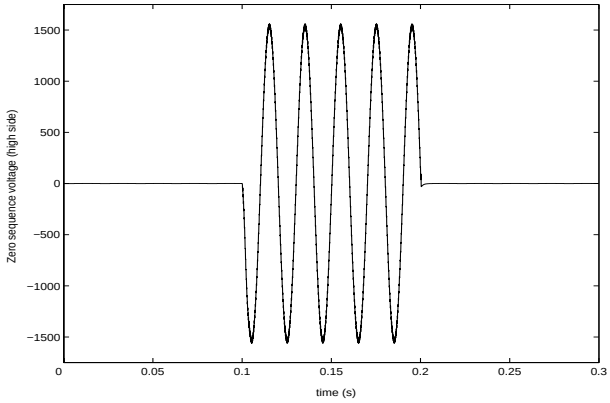

Fig.7. Zero sequence voltage (high side)

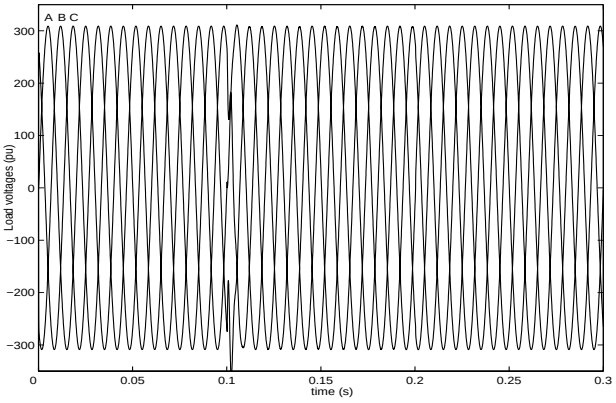

Fig.8. Restored load voltages with zero compensator

From Fig.6, it can be seen that non-faulted voltages of phases B and C increase above their nominal values. On the other hand, the faulted phase A voltage is not restored as a result of neutral point voltage increase due to the zero sequence currents. Fig.7 shows the zero sequence voltage.

Zero sequence compensator is included in the second simulation. Fig.8 shows the restored load voltage, while Fig.9 shows the compensated zero sequence voltage for the second simulation.

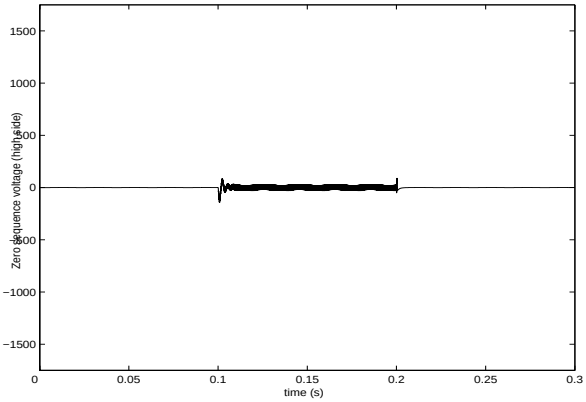

Fig.9. Zero sequence voltage (high side)

Two phase to ground fault

Two-phase fault was simulated and analyzed. The status of zero sequence is observed. The %30 voltage sag occurred at phase B and C between 0.1s and 0.2s.

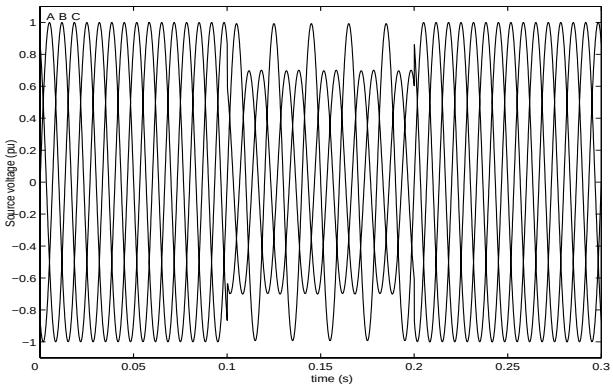

Fig.10. Source voltages

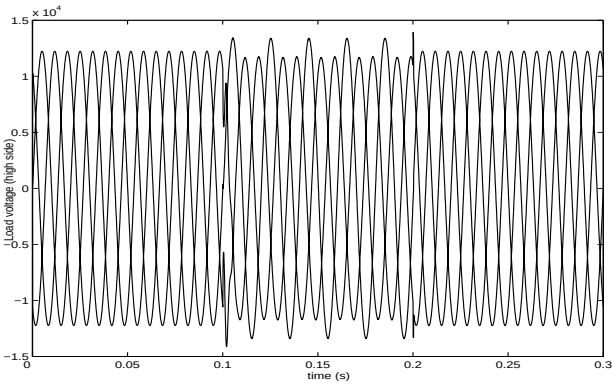

Fig.11. Restored load voltages without zero compensator

Fig.10 shows the source voltage. Fig.11 is the restored load voltage without zero sequence compensator. Fig.12 depicts the restored load voltage with zero sequence compensator.

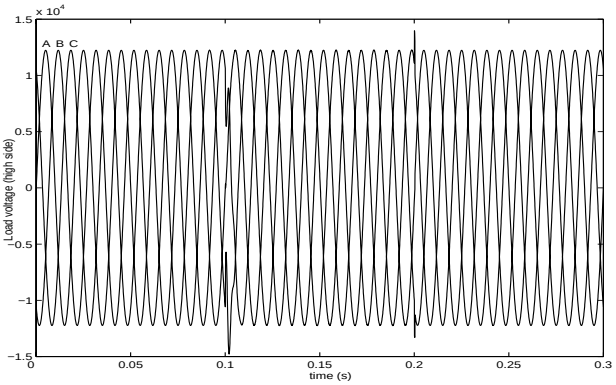

Fig.12. Restored load voltages with zero sequence compensator

Conclusion

In this study, a DVR mitigating balanced and unbalanced voltage sags with zero sequence compensation is proposed. Without mitigating zero-sequence components restored load voltages are distorted in systems where transformer connection with Y-Y winding with the neutrals grounded is used. Simulation results for different case studies are presented to verify the effectiveness of proposed method.

References

[1] Elmitwally, A., Kandil, M.S., Elkateb, M. A Fuzzy-controlled Versatile System for Harmonics, Unbalance and Voltage Sag Compensation. Power Engineering Society Summer Meeting, IEEE, 2000, Vol.3, pp.1439-1444.

[2] Jurado, F., Valverde, M., Carpio, J. Voltage Sag Correction by Dynamic Voltage Restorer based on Fuzzy Logic Control. Canadian Conference on Electrical and Computer Engineering, IEEE, 2003, Vol.1, pp.421-424.

[3] Zhan, C., Arulampalam, A., Jenkins, N. Four-wire Dynamic Voltage Restorer based on a Three Dimensional Voltage Space Vector PWM. IEEE Transactions on Power Electronics, IEEE, July 2003, Vol.18, Iss.4, pp.1093-1102.

[4] Grainger, J.J., Stevenson, W.D. Power System Analysis. McGraw-Hill Science/Engineering, 1994

[5] Chung, I.Y., Park, S.Y., Moon, S.I., Park, J.K. The Control and Analysis of Zero Sequence Components in DVR System. Power Engineering Society Winter Meeting, IEEE, 2001, Vol.3, pp.1021-1026.

[6] Fitzer, C., Barnes, M. Voltage Sag Detection Technique for a Dynamic Voltage Restorer. IEEE Transactions on Industry Applications, IEEE, 2004, Vol.40, Iss.1, pp.203-212.

[7] Jung, H.J., Suh, I.Y., Kim, B.S., Kim, R.Y., Choi, S.Y., Song J.H. A Study on DVR Control for Unbalanced Voltage Compensation. Applied Power Electronics Conference and Exposition, IEEE, 2002, Vol.4, pp.1068-1073.

Mehmet Tumay *– Associate Professor, Faculty of Engineering and Architecture, Department of Electrical and Electronics Engineering, University of Cukurova, 01330, Balcalı, Yuregir, Adana, TURKEY. e-mail: mtumay@cu.edu.tr.*

K. Cagatay Bayindir*– Ph.D. Student, Faculty of Engineering and Architecture, Department of Electrical and Electronics Engineering, University of Cukurova, 01330, Balcali, Yuregir, Adana, TURKEY. e-mail: cbayindir@isdemir.com.tr.*

M. Ugras Cuma *– MS.c. Student, Faculty of Engineering and Architecture, Department of Electrical and Electronics Engineering, University of Cukurova, 01330, Balcali, Yuregir, Adana, TURKEY. e-mail: mehmet@eemb.cu.edu.tr.*

C. Onur Tokunc *– Electrical and Electronics Engineer, e-mail: onurtokunc@yahoo.com*

Fuzzy Logic Control of Dynamic Voltage Restorer

Mehmet Tumay, M. Ugras Cuma, Ahmet Teke, K. Cagatay Bayindir

Abstract: *This paper presents Fuzzy Logic Control (FLC) of Dynamic Voltage Restorer (DVR). The purpose of this study is detecting voltage sags on the line and injecting the missing voltage to the system. In this study, a new control method for DVR is presented by combining a FLC with a carrier modulated PWM inverter. The proposed control scheme is simple to design, flexible in cost and has excellent voltage regulation capabilities. The simulations under balanced and unbalanced sag conditions verify the performance of the designed DVR.*
Keywords: *dynamic voltage restorer, fuzzy logic controller, power quality, voltage sag*

Introduction

The voltage generated by power stations has a sinusoidal waveform with a constant frequency. Any disturbances to voltage waveform can cause problems related with the operation of electrical and electronic devices. Users need constant sine wave shape, constant frequency and symmetrical voltage with a constant rms value to continue the production. This increasing interest to improve efficiency and eliminate variations in the industry has resulted more complex instruments sensitive to voltage disturbances such as voltage sag, voltage swell, interruption, phase shift and harmonic. Voltage sag is considered the most severe since the sensitive loads are very susceptible to temporary changes in the voltage [1].

Dynamic Voltage Restorer (DVR) is a new approach used to mitigate voltage sags and improve power quality. DVR is a series connected power electronic controller that mitigates the voltage sags in the power system and restores the load voltage to the pre-fault voltage value. The primary advantage of the DVR is keeping the users always on line with constant and high quality voltage thereby providing continuity of production. [1-4]. DVR restores the load voltage to its pre-fault value within a few milliseconds. It has become a cost effective solution for the protection of sensitive loads from disturbances primarily voltage sags.

Modern pulse-width modulated (PWM) inverters capable of generating accurate high quality voltage waveforms form the power electronic heart of the new Custom Power devices like DVR. Because the performance of the overall control system largely depends on the quality of the applied control strategy, a high-performance controller with fast transient response and good steady state characteristics is required. Various linear and nonlinear control strategies have been proposed for DVR and fuzzy logic based controllers belong to the nonlinear group. It appears that the nonlinear control is more suitable than the linear type since the converter is truly a nonlinear system [5]. The advantages of fuzzy logic controllers over conventional controllers are that they do not need an accurate mathematical model; they can work with imprecise inputs and can handle non-linearity.

The fuzzy logic controller is used as a substitute for the conventional PI controller [2]. The three-phase source voltages are transformed into d and q coordinates. The reference values for V_d and V_q are compared with these transformed values and voltage errors are obtained. These errors are processed by two FL controllers evaluating 81 linguistic rules [2]. Resulting outputs are re-transformed into three-phase domain and compared with a carrier signal to generate Pulse Width Modulated (PWM) inverter signals.

The proposed method does not include any transformations. Three-phase source voltages are directly processed by a FL controller to improve the response time of DVR. The number of rules is decreased to 49 to achieve better performance. The proposed DVR has the capability of both balanced and unbalanced voltage sag compensation. Details of proposed DVR and simulation results for different case studies are presented below.

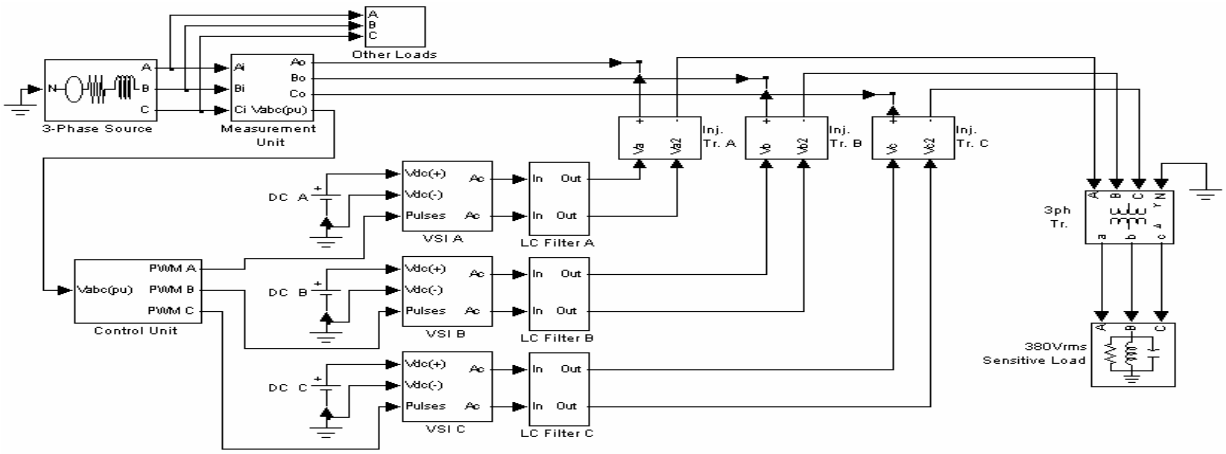

Fig.1. Configuration of designed system

Proposed DVR Configuration and Controls

The Matlab / Simulink model of proposed DVR is shown in Fig.1. Three single-phase full bridge PWM inverters consisting of IGBT switches are used to produce compensating voltages. The inverter side filters eliminate PWM inverter harmonics. The advantage of the inverter side filter is that it is on the low-voltage side of the series transformer and is closer to the harmonic source. Using this scheme the high-order harmonic currents are prevented from penetrating into the series transformer, thus reducing the voltage stress on the transformer [6]. The three phase adjacent parallel loads create balanced or unbalanced fault at desired time and size. Maximum single-phase injection capability is %50 of nominal value.

The block diagram of proposed DVR controller is shown in Fig.2. In the proposed method PLL is applied to each supply phase independently. The PLL for each phase tracks the phase of network voltage phasor and generates a reference signal with magnitude of 1 locked to supply frequency for each phase. The supply voltage for each phase is converted to per unit and error is obtained from the difference of reference PLL generated signal and actual supply voltage converted to per unit. Error and error rate are the inputs for the fuzzy logic controller. Output of the fuzzy logic controller is fed to the PWM generator to produce switching pulses for the voltage source inverter. This method can easily be implemented in real time and there are no current publications in this method as mentioned in [7].

The DVR should supply the unchanged load voltage with minimum energy consumption for injection due to the high cost of capacitors. The available voltage injection strategies are (1) pre-sag, (2) phase advance, (3) voltage tolerance and (4) in-phase method [8].

The proposed controller employs in-phase injection method. This method has following advantages:

- Quick calculation ability during the compensation process of sag,
- Less complex control algorithm than phase advance and voltage tolerance method,
- Less disturbances to the load,
- Optimum solution when the DVR has limited voltage injection capacity.

The phase angles of the pre-sag and load voltage are different but the most important criteria for power quality that is the constant magnitude of load voltage is satisfied as shown in Fig.3.

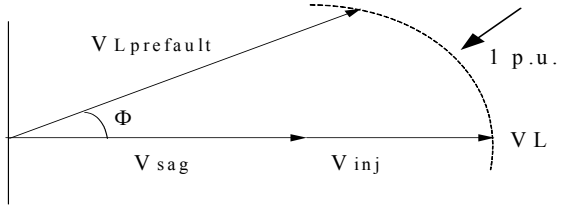

Fig.3. Vector diagram of in phase method

(1) $$|V_L| = |V_{Lprefault}|$$

(2) $$V_{inj} = MV_p$$

V_L, $V_{Lprefault}$, V_{inj}, M and V_p represent load voltage vector, voltage vector before sag, injected DVR voltage vector, maximum voltage sag to be compensated and rated rms voltage of the primary feeder respectively. All points on the arc have the same rms value (1 p.u.) with different phase angles.

For most practical cases a more economical design can be achieved by only compensating the positive and negative sequence components of the voltage disturbance seen at the input of the DVR. This option is reasonable because for a typical distribution bus configuration the zero sequence part of a disturbance will not pass through the step down transformer because of infinite impedance for this component. This zero sequence blocking function is achieved by delta winding of the load-side step down transformer [9]. The proposed DVR can compensate positive sequence and negative sequence components and this is verified with simulations for different case studies.

Direct feed-forward-type control model is preferred in the proposed controller. To maximize dynamic performance direct feed-forward-type control architecture should be applied in the control concept of DVR. With this concept a fast response time (approximately 1 ms) can be achieved to compensate voltage sags [9].

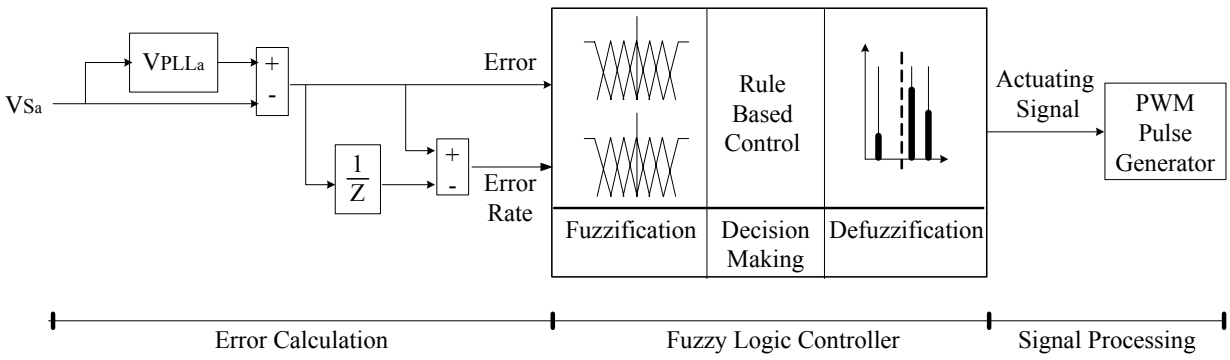

Fig.2. Block diagram of proposed control method

Proposed Fuzzy Logic Controller

In FL modeling, the operator's experience, defining the input and output variables of the system and understanding how these variables are processed by control mechanism has more influence than mathematical modeling of the system. The following advantages make FL superior to other conventional methods:

- Reliable and fast response
- High voltage accuracy and low distortion of output
- Robustness for nonlinear load conditions, sudden load changes and system parameter variations
- Less rule and data storage than traditional controllers
- Excellent control of nonlinear systems that would be difficult or impossible to model mathematically.

The fuzzy logic controller for the proposed DVR has two real time inputs measured at every sampling time, named error and error rate and one output named actuating-signal for each of the phases. The input signals are fuzzified and represented in fuzzy set notations by membership functions. The defined 'if … then …' rules produce the linguistic variables and these variables are defuzzified into control signals for comparison with a carrier signal to generate PWM inverter gating pulses.

The measured source voltages V_a, V_b, and V_c are converted into p.u. values. The error is calculated from the difference between source voltage data and the Phase Locked Loop (PLL) data for each phase as shown in Fig.2. The error rate is the rate of change of error. For phase A, the error and error rate are defined as,

$$err_A = V_{PLL_A} - V_{S_A} \tag{3}$$

$$\Delta err_A = err_A(n) - err_A(n-1) \tag{4}$$

Fuzzy logic control involves three steps: fuzzification, decision-making and defuzzification. Fuzzification transforms the non-fuzzy (numeric) input variable measurements into the fuzzy set (linguistic) variable that is a clearly defined boundary. In the proposed controller, the error and error rate are defined by linguistic variables such as large negative (LN), medium negative (MN), small negative (SN), small (S), small positive (SP), medium positive (MP) and large positive (LP) characterized by memberships. The memberships are curves that define how each point in the input space is mapped to a membership value between 0 and 1. The membership functions belonging to the other phases are identical. Membership functions for the inputs are shown in Fig.4.

The If-then rules define a Fuzzy Inference System (FIS) by connecting the input to the output. Fuzzy inference process is realized by one of the Mamdani or Sugeno methods [4]. Fuzzification of inputs and applying the fuzzy operator are completely the same in both methods. The main difference is that the output membership functions of the used Sugeno-type are linear or constant. It provides higher performance, accuracy to nonlinear dynamic systems under various operating conditions. The output is defined by linguistic variables such as negative big (NB), negative medium (NM), negative small (NS), zero (Z), positive small (PS), positive medium (PM) and positive big (PB) characterized by memberships. The membership function of output variable is shown in Fig.5. The solution of defuzzification process results from equation (5)

$$U = \frac{\sum_i y_i \mu(y_i)}{\sum_i \mu(y_i)} \tag{5}$$

where U denotes the crisp value of the output, y_i represents the normalized controller output for the ith interval and $\mu(y_i)$ is the associated membership grade.

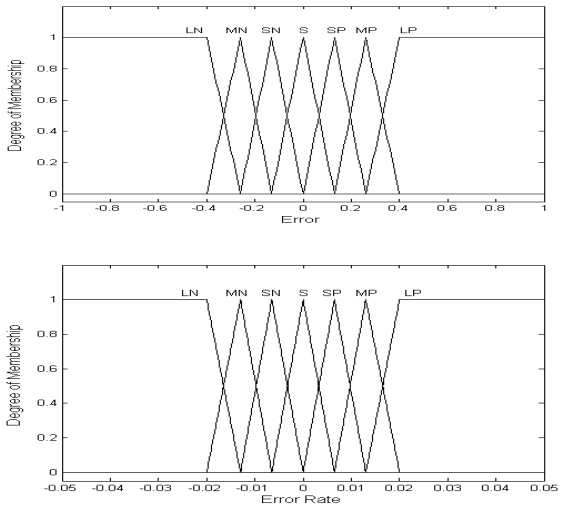

Fig.4. Membership functions for inputs

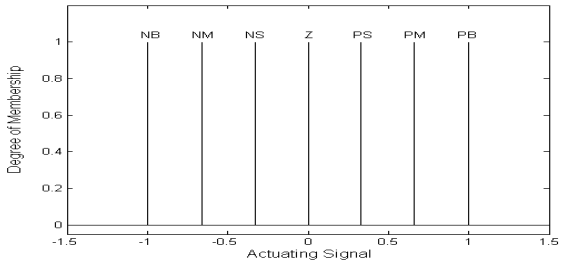

Fig.5. Membership function for output

Table 1

Fuzzy decision table

		Error Rate						
		LP	MP	SP	S	SN	MN	LN
Error	LP	PB	PB	PB	PM	PM	PS	Z
	MP	PB	PB	PM	PM	PS	Z	NS
	SP	PB	PM	PM	PS	Z	NS	NM
	S	PM	PM	PS	Z	NS	NM	NM
	SN	PM	PS	Z	NS	NM	NM	NB
	MN	PS	Z	NS	NM	NM	NB	NB
	LN	Z	NS	NM	NM	NB	NB	NB

There are 49 rules to carry out optimum control action and each rule expresses an operating condition in the system as shown in Table 1. The person's experience and knowledge about the system behavior help to define the rules. The correct combinations of these rules improve the system performance. All rules are evaluated in parallel and the order of the rules is not important. The decision table for fuzzy logic control rules is shown in Table 1.

The outputs of FLC process are the control signals that are used in generation of PWM inverter switching signals by comparing a carrier signal. The generation of switching signals for single phase of the system is shown in Fig.6 where the configuration will be the same for other phases.

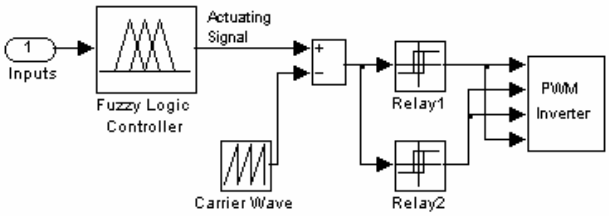

Fig.6. Generation of PWM switching signals

The relay element gives output when the input of itself is greater than 0. The upper relay element is set to give output when the input of itself is greater than 0. The output of lower relay is the complement of upper one. The output of the fuzzy controller is set to take values between -1 to 1. The carrier signal is set to take values between -0,9 to 0,9 with a frequency of 2 KHz.

Case Studies

The performance of the designed DVR is evaluated under Matlab / Simulink. The system runs at 50 Hz frequency and sample time is chosen to be 100 μs. The total period of simulation for each case is 0.4s and the simulation parameters are given in Table 2.

Table 2

Simulation parameters

Power Supply	15000Vrms, 50 Hz Supply resistance, R = 0.04 Ω
Sensitive Load	380 Vrms, 50 kVA, 0.95 p.f.
Load Transformer	15000/380 Vrms, 55 kVA
Injection Transformer	92/3460 Vrms, 15 kVA
DC Link	150 V
LC Filter	L=2.8mH, C=75μF

Case 1: Single-phase to ground fault

Most of the faults are single-phase line to ground faults (SLGF). The SLGF occurs on phase A resulting in 60% decrease from nominal value between the period 0.1s and 0.3s. Fig.7 shows the remaining voltage, injected voltage and load voltage at SLGF. Phase A voltage of sensitive load and average load power are maintained at almost 1 p.u.

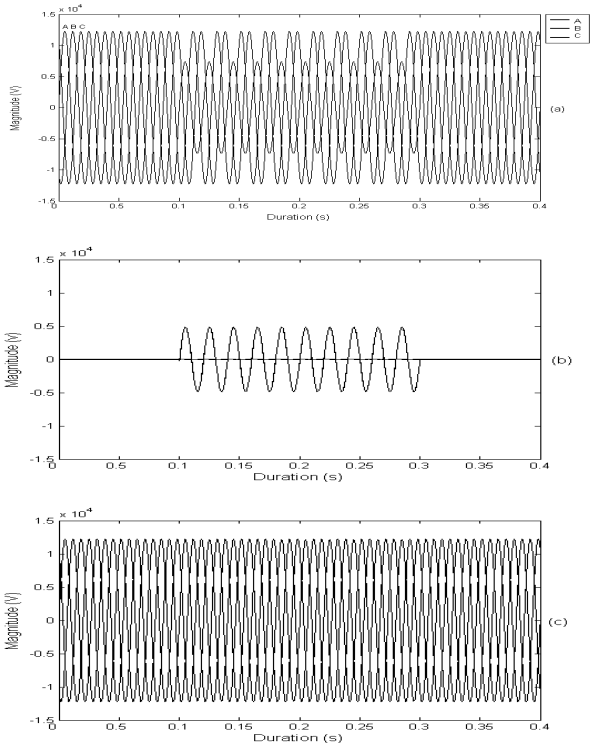

Fig.7. Case 1: The source (a), injected (b) and load (c) voltages

Case 2: Three-phase Balanced Fault

In Case 2, the three-phase balanced fault occurs. 60% voltage sag takes place between the period 0.1s and 0.3s. Fig.8 shows the remaining voltage, injected voltage and load voltage under balanced three-phase sag.

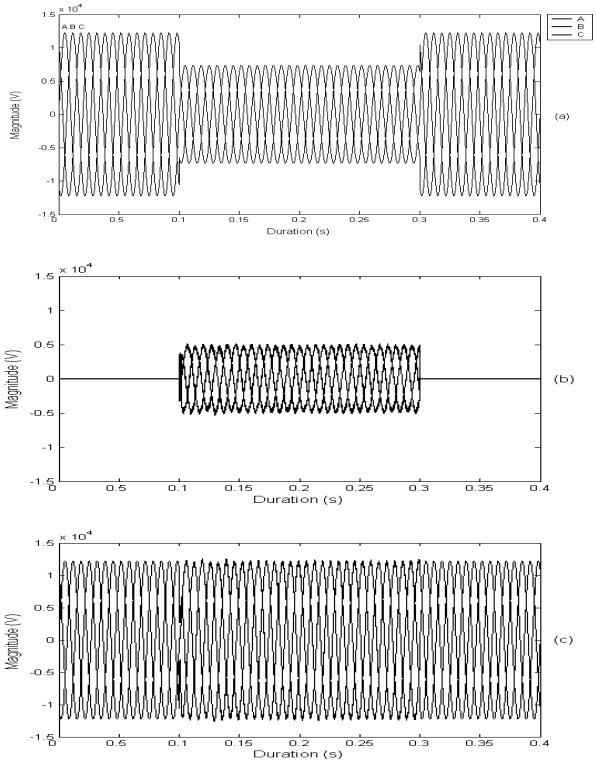

Fig.8. Case 2: The source (a), injected (b) and load (c) voltages

During Case2 period, all the phase voltages of sensitive load are maintained at [0.99-1.02] p.u. and average load power is 0.99 p.u.

Case 3: Three-phase Unbalanced Fault

In Case3, A phase, B phase and C phase voltages are decreased to 60%, 70% and 80% from their nominal values between the period 0.1s and 0.3s. Fig.9 shows the remaining voltage, injected voltage and load voltage at three-phase unbalanced sag.

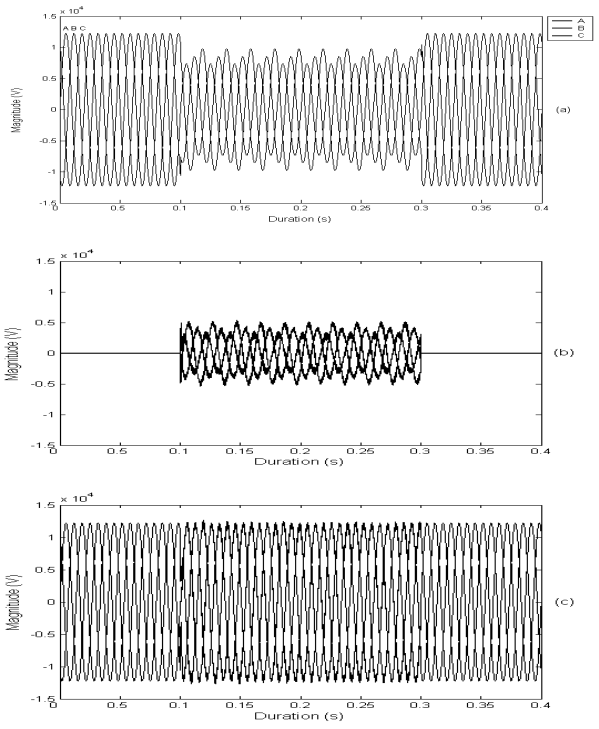

Fig.9. Case3: The source (a), injected (b) and load (c) voltages

During unbalanced sag period, the values of A phase, B phase and C phase voltages are maintained at [0.99-1.02], [0.98-1.02], and [0.99-1.06] p.u. respectively. The average load power is 0.98 p.u.

Conclusion

By adapting advanced FL control technique in generation of reference signals for PWM, a high level of efficiency and dynamic performance of DVR are both achieved. The simulation results show that the DVR compensates the sags quickly and provides excellent voltage regulation under various operating conditions. The proposed method does not involve any transformation resulting in quicker response compared to the conventional control methods.

FL control of DVR is new in literature and the proposed control method can easily be applied for superior performance and as an alternative control method for conventional or complex system configurations.

References

[1] Nguyen, P.T., Saha, T.K. Dynamic Voltage Restorer against Balanced and Unbalanced Voltage Sags: Modeling and Simulation. Power Eng. Soc. Gene. Meeting, IEEE, 2004, Vol.1, pp.639-644.

[2] Jurado, F., Valverde, M., Carpio, J. Voltage Sag Correction by Dynamic Voltage Restorer based on Fuzzy Logic Control. Int.Conf. CCECE 2003, IEEE, 2003, Vol.1, pp.421-424.

[3] Nielsen, J.G., Newman, M., Nielsen, H., Blaabjerg, F. Control and Testing of a Dynamic Voltage Restorer (DVR) at Medium Voltage Level. IEEE Tran. On Power Electronics, Vol.19, Iss.3, pp.806-813.

[4] Ramachandaramurthy, V.K., Arulampalam, A., Fitzer, C., Zhan, C., Barnes, M., Jenkins, M. Supervisory Control of Dynamic Voltage Restorers. IEE Proceedings on Generation, Trans. And Distribution, 2004, Vol.151, Iss.4, pp.509-516.

[5] Jurado, F. Neural Network Control for Dynamic Voltage Restorer. IEEE Tran. On Industrial Electronics, 2004, Vol.51, Iss.3, pp.727-729.

[6] Zhan, C., Ramachandaramurthy, V.K., Arulampalam, A., Fitzer, C., Kromlidis, S., Barnes, M., Jenkins, M. Dynamic Voltage Restorer based Voltage-Space-Vector PWM Control. IEEE Tran. On Industry Applications, 2001, Vol.37, Iss.6, pp.1855-1863.

[7] Fitzer, C., Barnes, M., Green, P. Voltage Sag Detection Technique for a Dynamic Voltage Restorer. IEEE Tran. On Industry Applications, 2004, Vol.40, Iss.1, pp.203-212.

[8] Chung, I.Y., Won, D.J., Park, S.Y., Moon, S.I., Park, J.K. The DC Link Energy Control Method in Dynamic Voltage Restorer System. Electrical Power and Energy Systems, ELSEVIER, 2003, Vol.25, Iss.7, pp.525-531.

[9] Daehler, P., Affolter, R. Requirements and Solutions for Dynamic Voltage Restorer, A Case Study. Power Eng. Soc. Winter. Meeting, IEEE, 2000, Vol.4, pp.2881-2885.

Mehmet Tumay *– Associate Professor, Faculty of Engineering and Architecture, Department of Electrical and Electronics Engineering, University of Cukurova, 01330, Balcalı, Yuregir, Adana, TURKEY. e-mail: mtumay@cu.edu.tr.*

M. Ugras Cuma *– MS.c. Student, Faculty of Engineering and Architecture, Department of Electrical and Electronics Engineering, University of Cukurova, 01330, Balcali, Yuregir, Adana, TURKEY. e-mail: mehmet@eemb.cu.edu.tr.*

Ahmet Teke *– MS.c Student,, Faculty of Engineering and Architecture, Department of Electrical and Electronics Engineering, University of Cukurova, 01330, Balcali, Yuregir, Adana, TURKEY. e-mail: ahmetteke@yahoo.com*

K. Cagatay Bayindir *– Ph.D. Student, Faculty of Engineering and Architecture, Department of Electrical and Electronics Engineering, University of Cukurova, 01330, Balcali, Yuregir, Adana, TURKEY. e-mail: cbayindir@isdemir.com.tr.*

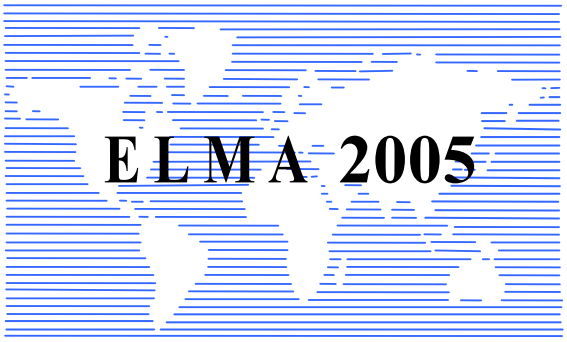

ELECTRICAL DRIVES

Modelling and Simulation of an Electrical Drive with Induction Motor Controlled with Neuro-Fuzzy Regulator

Cătălin Constantinescu

Abstract: *The paper presents the results which are obtained after the simulating of an electrical drive system with asynchronous motor where a classic regulator was replaced with a neuro-fuzzy one, then, in order to improve the answer, with a hybrid one (classic and neuro-fuzzy).*

Keywords: *neuro-fuzzy control, induction motor*

Introduction

Starting with a classical structure (proposed by MathWorks Inc.) for space vector driving, the speed regulator (standard PI) was replaced with a neuro-fuzzy regulator (ANFIS network). In that way are presented the comparative results obtained following many trainings of the neuro-fuzzy network.

Neuro – fuzzy control

To train the neuro-fuzzy controller, data pairs were generated using complex signal generators. In first stage the model used to generate these pairs (fig. 2) has a sample and hold period of 10 ms, when the frequencies of the signals at the regulator input were 1Hz respectively 1/512 Hz (both signals are double-ramp type), the simulation time is 256 seconds. Computation of these data (proper training) was made using a Matlab program.

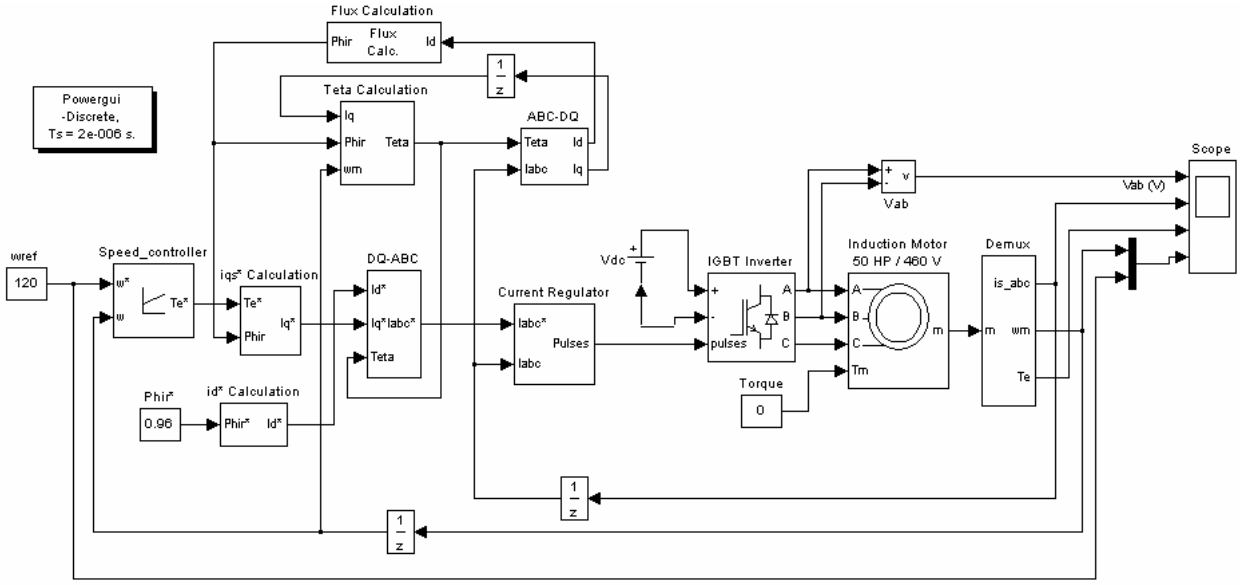

Fig.1 Space vector control for induction motor

In this program are specified the number of the fuzzy sets established for the inputs, respectively for outputs, their type, and, also, the number of training epochs.

After this first training stage an ANFIS network was obtained and the rules surface (fig. 3) confirms the correctness of this network (the shape of the surface is almost like one for a classic PI regulator). Therefore, the next model that is considered has an ANFIS network instead of the classic regulator. (fig. 4). Following the simulations, a decrease for the time to reach the stabilized regime was obtained (even the overshoot was eliminated) but the error is bigger that the one obtained with the classic regulator (fig. 5,6).In the case of the PI speed regulator the speed begin to stabilize aproximatively after 1,5 seconds.In the case of NF (neuro-fuzzy) regulator this time decreases at aproximatively 0,9 seconds.

Since the behavior of a neuro-fuzzy network (hence the behavior of a neuro-fuzzy structure) depends very much on the data set used for his training, knowing the models previously described, more scenery to generate data were pictured.

The first change was the increase of the inputs variation domain (from 200 rad/s to 250 rad/s).

For a closer analyze, in the next simulations the speed profile is formed from three stages and the load is proportional with speed. The time considered for each simulation was 5 seconds.

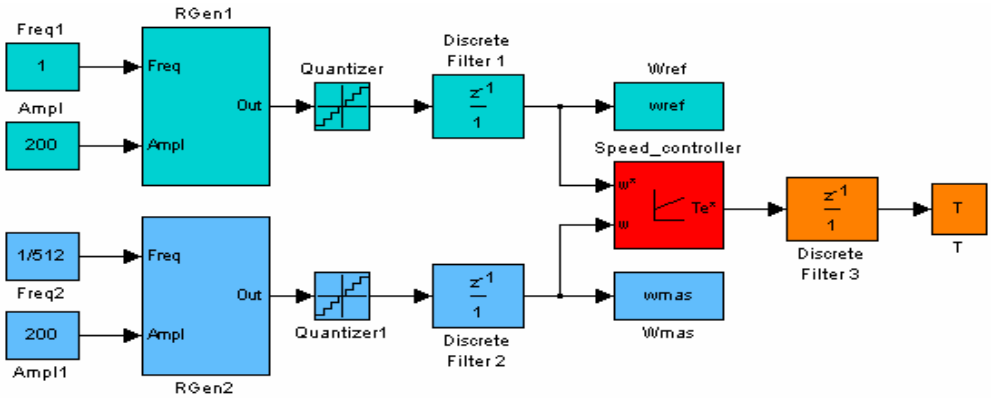

Fig.2 Generating data pairs for training the ANFIS network

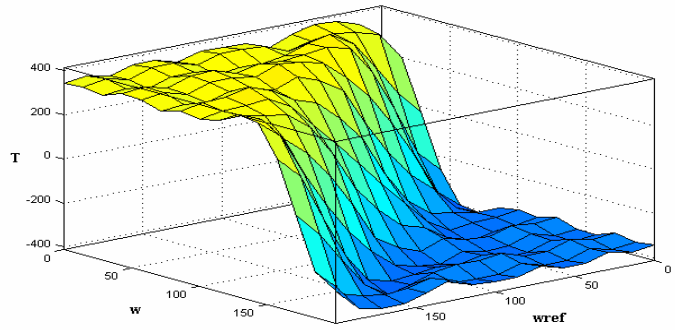

Fig. 3 Rules surface for the ANFIS network

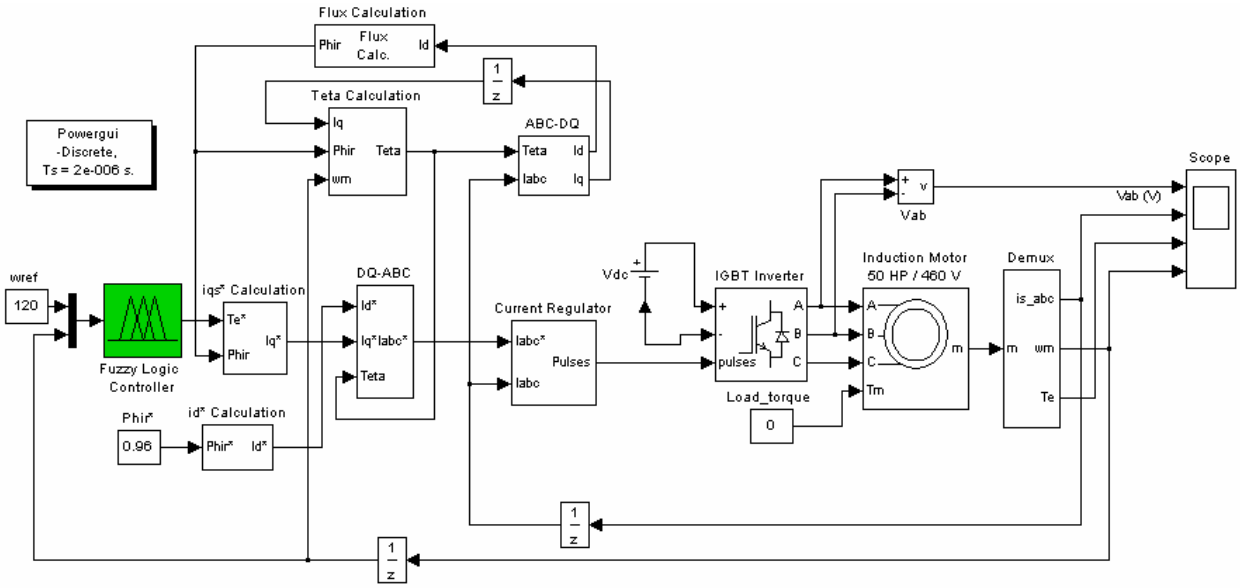

Fig. 4 Space vector control with neuro-fuzzy speed regulator

The simulation results obtained after the mentioned change shows an improvement for the system's response time, meaning that the error was decreased.

The next change of the training data generation conditions consisted in the increase of the superior limit for the speed regulator output (T_{max} was increased from 300 to 350 Nm). In this case, too, an error decrease is obtained and, in the same time, a better time is realized.

An improvement is, also, that the time period between two samples is smaller (practically the number of training pairs is doubled) and, in the same time, the output of the speed regulator is increased again (to 400Nm).

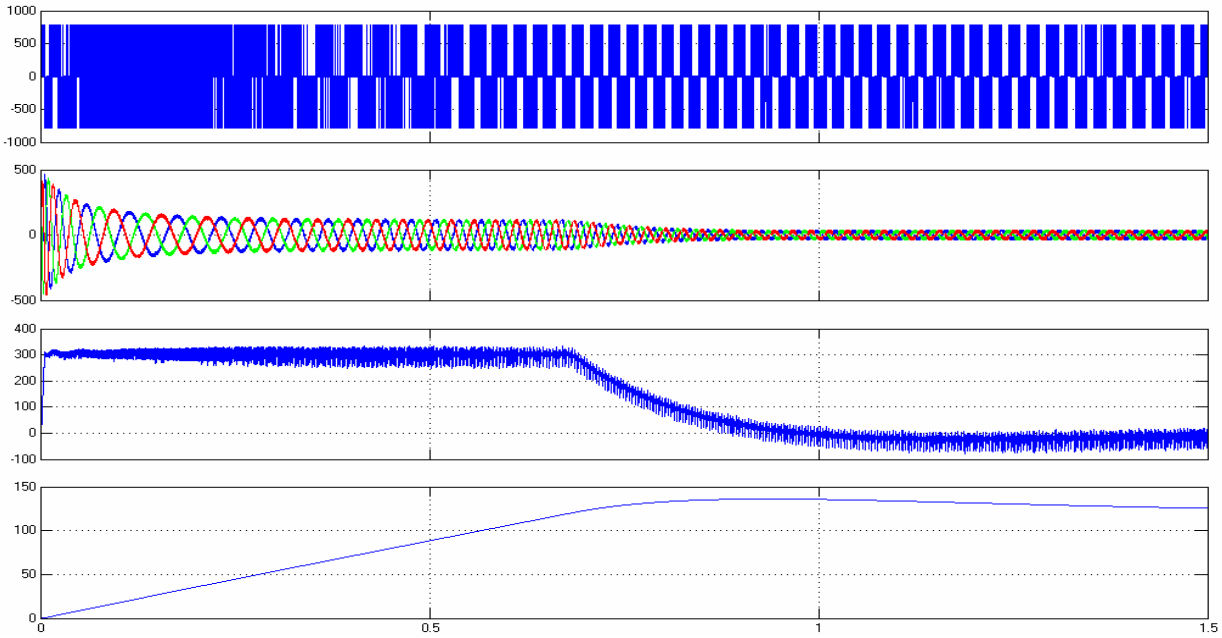

Fig. 5 The simulation results for a space vector control system with classic speed regulator (are presented in order, voltage between two phases, currents, torque and speed; sampling rate = 2μs)

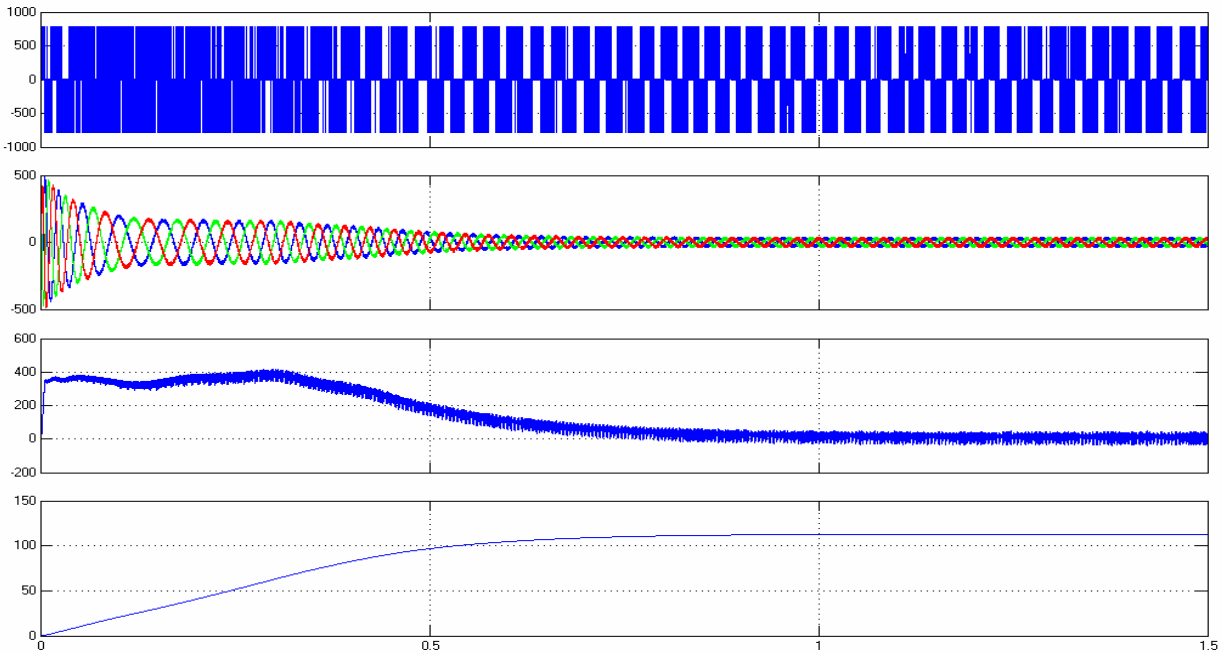

Fig. 6 Simulation results for the space vector control with neuro-fuzzy speed regulator after the first training

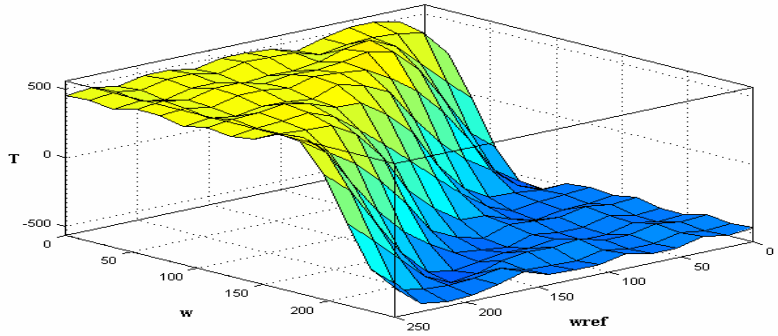

Fig. 7 Rules surface for the final NF regulator

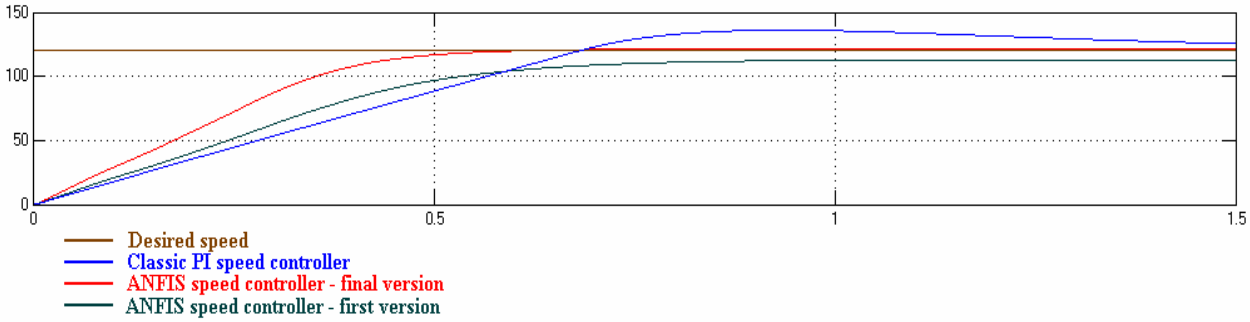

Fig. 8 Comparative results between the classic PI regulator, the initial NF regulator and the final NF regulator in the initial simulation conditions (the torque is zero and reference speed is constant)

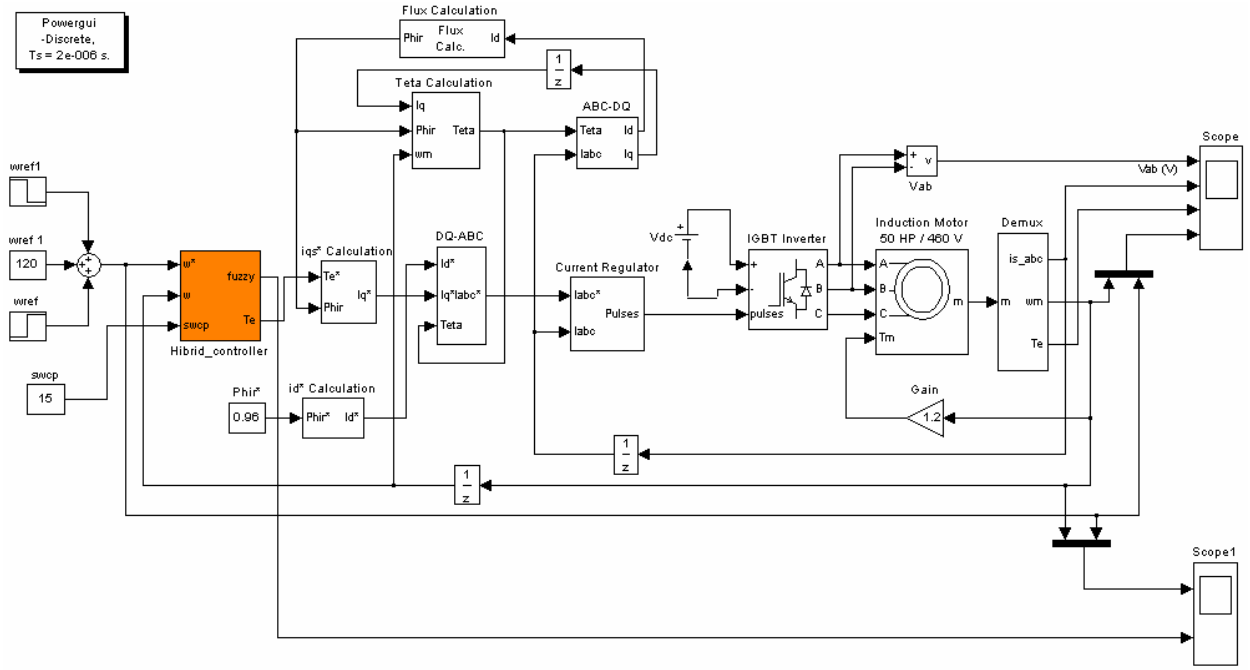

Fig. 9 Model for hybrid space vector control of an induction motor

The last change of the training context consisted in decreasing 5 times the sampling rate (the number of training pairs = 256000 – sample and hold at each millisecond; simulation is made for 256 seconds time period).

Overall, the improvement it seems to be not spectaculars, but is obvious. More, in the case of the initial simulating conditions for the electrical drive (when load is zero and constant speed), a better behavior is observed for the final neuro-fuzzy regulator comparatively to the PI regulator, especially for a certain speed range – fig.8.

These conclusions leads to the idea to combine these two drive techniques in order to obtain better global results. Knowing that at bigger speed errors the NF speed regulator has a better behavior and at small errors the classical regulator has a better response, the simplest method to combine these two structures consists in switching the responses of the two regulators taking into account the error (fig. 9,10). Mathematically the model it will be not so complicated and as for the implementation the model can be realized.

The results obtained following the simulation are obvious superior to the control with classic regulator and, also, to the control with neuro-fuzzy speed regulator (decrease the time to reach the prescribed value, decrease the overshoot, decrease the stationary error).

Better results were obtained in the case of using a hybrid speed regulator with double switching (there are two switching thresholds; when the error is between the two threshold, the command is given by the PI regulator, in that way the command is NF type) – fig. 11,12.

In this case a decrease for the time to reach the stabilized regime is observed and, also, the overshoot is reduced. In some situations, maintaining the motor's speed in a certain domain is given even by switching the outputs for the two regulators of the hybrid controller with double ramp. (fig. 13).

Conclusion

[1] Few interesting aspects about neuro-fuzzy and/or classic control for electrical drive system with asynchronous motor were exposed after the simulations. Therefore, is obvious that a good answer of a system with

neuro-fuzzy control depends on a good training of an unconventional regulator, which consists in choosing the appropriate training context. It is observed a very good behavior of the system when NF system control is combined with the classic one, even in this case the advantages given by the neuro-fuzzy control are, someway, altered (for example a bigger interval for the sample and hold period is accepted).

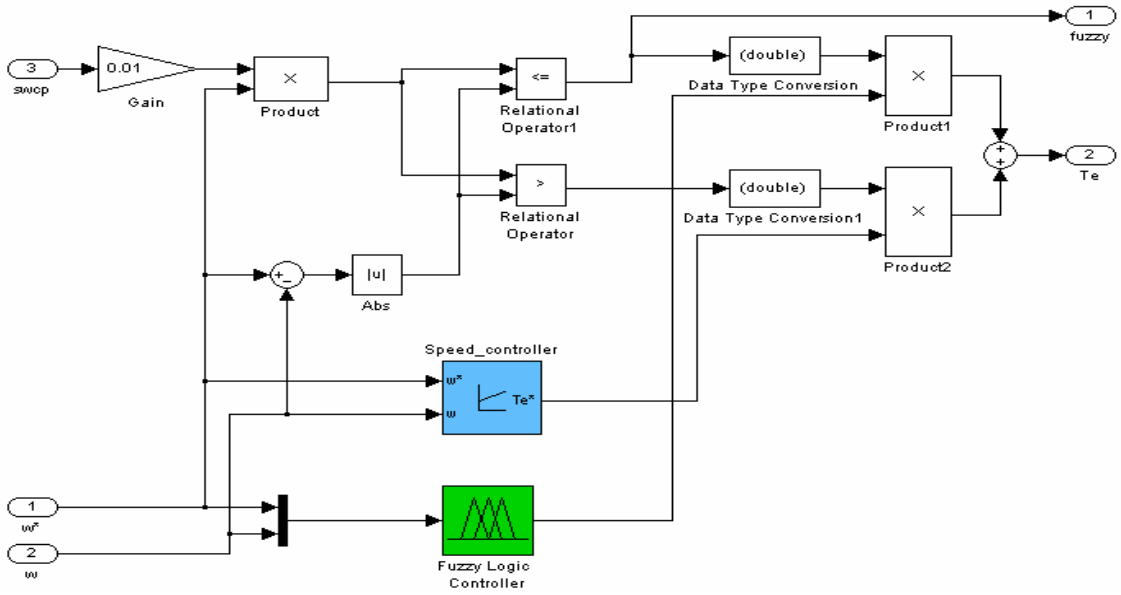

Fig.10 Model for discriminating between neuro-fuzzy and classic control (hybrid speed regulator)

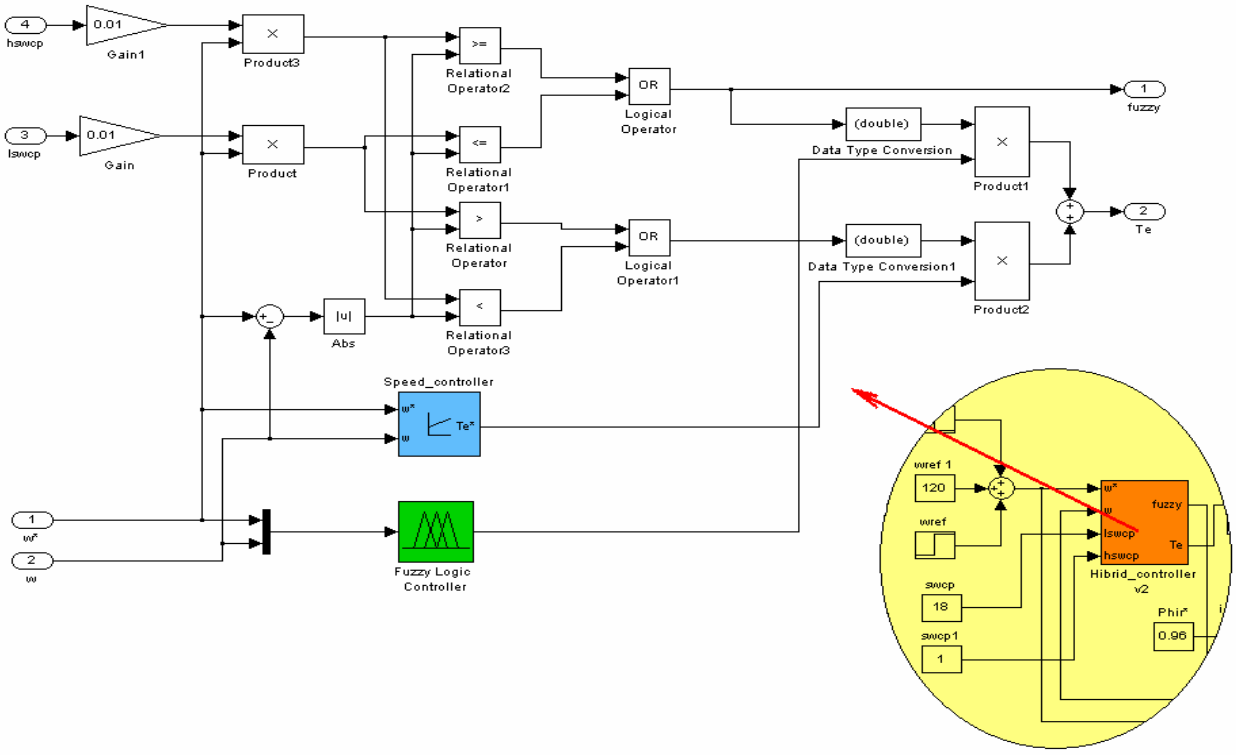

Fig.11 Hybrid speed regulator with double switching

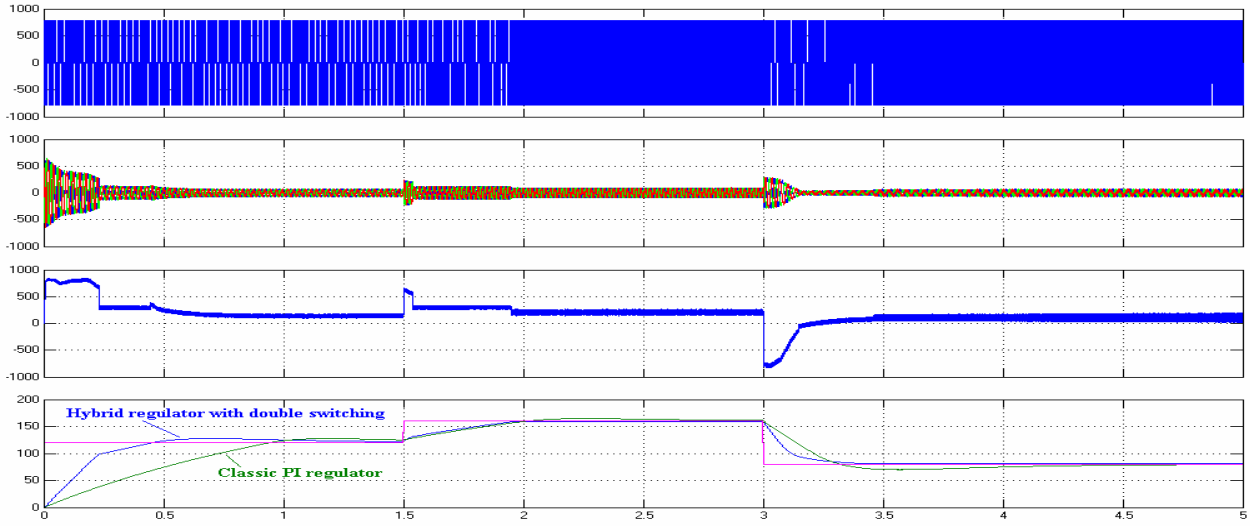

Fig. 12 Obtained results after the simulation of the drive system with hybrid regulator and compare with the speed obtained in the case of the classic control

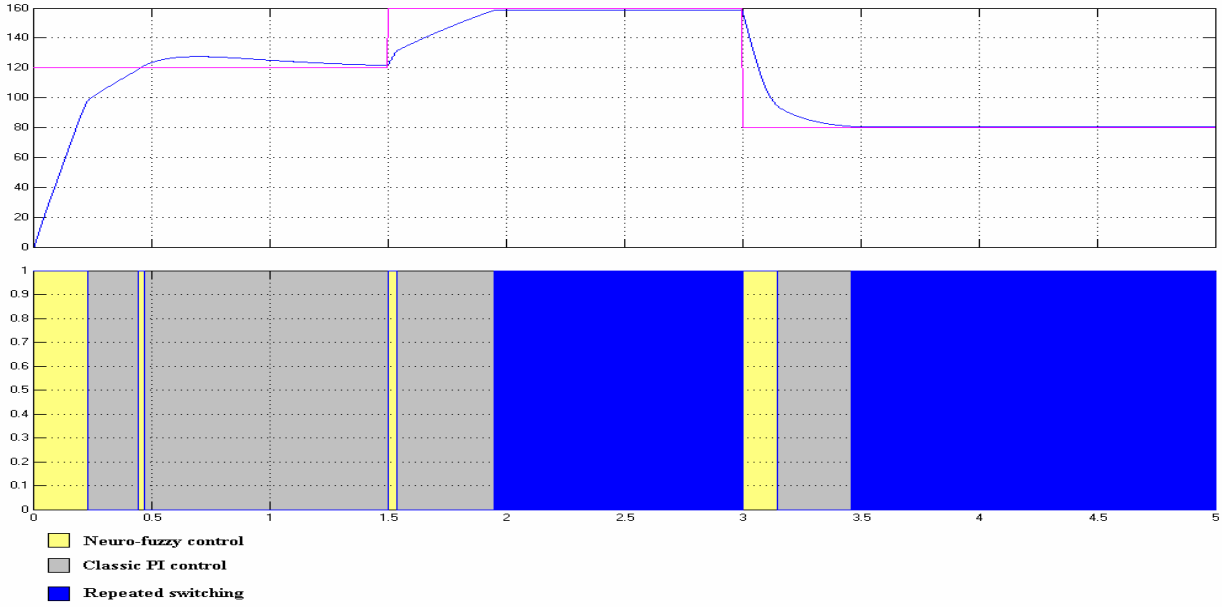

Fig. 13 Regulator's switching zones

References

[1] Jang Jyn-Shing Roger. ANFIS: Adaptive – Network – Based Fuzzy Inference System. IEEE Transactions on Systems, Man, and Cybernetics; vol. 23; no. 3, May / June 1993.

[2] Lin Chin-Teng, Lee C.S. George. Neural Fuzzy Systems: A Neuro-Fuzzy Synergism to Intelligent Systems. Prentice Hall PTR, 1996; ISBN 0-13-235169-2.

[3] Lygeros J., Godbob D.N., Coleman C.P., Model Based Fuzzy Logic Control. Inteligent Machines and Robotics Laboratory, University of California, Berkeley.

[4] Parthy A., Shahkarami M., Hanitsch R. A Contribution to Fuzzy Controlled Induction Motors. Proceedings SPEEDAM, Sorrento – Italy, June, 1998.

[5] Razik H., Baghli L., Rezzoug A. Neuro-Fuzzy Speed and Current Control of an Induction Motor. Proceedings Electrimacs'99 ISBN 972-98257-0-X.

[6] Strietzel R., Welsch W. Tuning of Linear and Fuzzy PI Controllers. 5th Symposium on Automatic Control and Computer Science, Iaşi, 1995.

[7] Vas Peter. Artificial-Intelligence-Based Electrical Machines and Drives. Application of Fuzzy, Neural, Fuzzy-Neural, and Genetic-Algorithm-Based Techniques. Oxford University Press, New York, 1999, ISBN 019859397X.

Cătălin Constantinescu *– Lecturer, Ph.D., Faculty for Electromechanical Engineering, University of Craiova, 107 - Decebal Blv., 200440, Craiova, ROMANIA. e-mail:cconstantinescu@em.ucv.*

A Half Bridge Converter for Motoring and Regenerating Operation of a DC Motor, Using a PWM Method Current Control

Marian Pearsica

Abstract: *DC motor controllers using Power MOS devices can be used in many speed control and servo applications giving excellent drive performance. Basic principles relating to DC motor specifications and drive frequency are presented. The pulse width modulated (PWM) method of switched-mode voltage control is discussed with reference to armature current control, and hence output torque control of DC motors. The paper presents the functional units designing, which compose the controller.*

Keywords: *DC Motor, half bridge converter, controller.*

Introduction

DC motor controllers using Power MOS devices have a series of advantages, and the most important are the next:

- Power MOS choppers can operate at a higher switching frequency, giving reduced noise, interference, and current ripple. These devices allow the obtaining a good dynamic system response.
- The principle control variable in the PWM motor control system is "duty cycle", δ. Motor torque and velocity can be tightly controlled, by controlling the PWM duty cycle and motor current.

Figure 1 presents the torque speed characteristics for motoring and regenerating operation of a DC motor (two quadrant operation). The braking with recovery (for regenerative operation) is used when the motor is engaged to a higher rotational speed than the rotational speed at the operation without load, n_0.

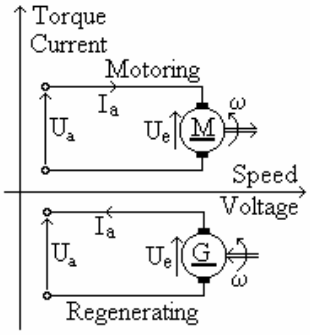

Fig.1. Torque and speed characteristics for two quadrant operation.

When the DC machine operates as a motor, this one is supplied from the supply network with a U_a voltage, the current coming in the armature winding through the positive brush. If the rotational speed becomes higher than n_0, the back voltage induced across the armature conductors exceeds the supply voltage value, as consequence in the armature winding is induced a current I_a, opposite to the initially current. The electromagnetic torque changes the sense and the DC motor becomes a generator which transforms the mechanical energy into electrical one which is returned to the supply network achieving a recovery of energy.

The armature induced emf, which is measured at brushes, is equal with the value of the induced voltage in a way of current because the ways of current are parallel connected [1]. Relation (1) describes the armature induced emf:

$$(1) \qquad U_e = \frac{p}{a} N \frac{n}{60} \phi = K_e \, n \phi; \quad K_e = \frac{p}{a} \frac{N}{60}$$

Where: p is the number of poles pairs, a – the number of current way pairs, N – the number of actives conductors of the rotor, n – the rotational speed of the rotor which is measured in rotations per minute, ϕ – the inductor magnetic flux of a pole.

The steady state operation of the motor is described by the relation:

$$(2) \qquad I_a = \frac{U_a - U_e}{R_a} = \frac{U_a - K_e \, n \phi}{R_a}$$

Where: U_a represents the armature voltage supply, I_a – the armature current, R_a – the armature winding resistance, U_e – the armature induced emf.

For normal motor operation U_a and I_a are positive and the motor is operating in its "first quadrant". By reducing U_a below U_e such that I_a is negative, the motor will operate in its second quadrant that is regenerating or braking.

The electromagnetic torque is described by the relation:

$$(3) \qquad M = \frac{P}{\Omega} = \frac{U_e \cdot I_a}{\Omega} = \frac{p N \phi I_a}{2 \pi a} = K_M \, \phi \, I_a$$

Where: P is the electromagnetic power of the motor and Ω is the angular rotational speed of the rotor.

Figure 2 presents the mechanical characteristics of a DC motor with parallel excitation for regenerative operation. In order to obtain different braking torque it is used a variable rheostat (R_v) serially connected to an external DC circuit which is connected to the armature coils. At a rotational speed, $n > n_0$, electromagnetic torque is negative and it becomes a braking torque, producing the braking of the motor until its rotational speed decreases at the n_0 value. If the rotational speed

becomes lower than n_0 value, the motor will produce again a positive torque and it will operate in normal motor mode.

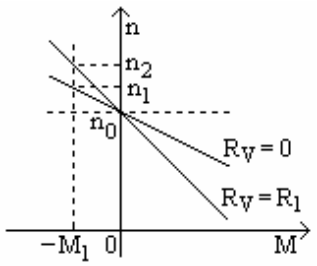

Fig.2. Mechanical characteristics of a DC motor with parallel excitation for regenerative operation.

Two quadrant converter

Figure 3 shows a half bridge chopper circuit for motoring and regenerating operation [7]. The average voltage applied to the motor, and hence its rotational speed, is controlled by varying the duty cycle of the switch T_1. For regenerative operation the DC motor acts as the active power source, and the regenerating current is controlling by varying the duty cycle of the switch T_2. The negative armature current increases through the switch T_2 and the armature inductance when T_2 is on.

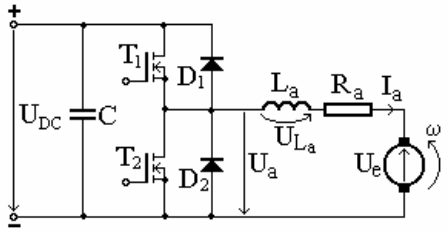

Fig.3. Half bridge chopper circuit.

The switching waveforms for the circuit, for motoring operation, are presented in figure 4. During motoring operation the transfer function of the converter is given by the relation:

$$U_a = \frac{t_{on} \cdot U_{DC}}{T} \quad (4)$$

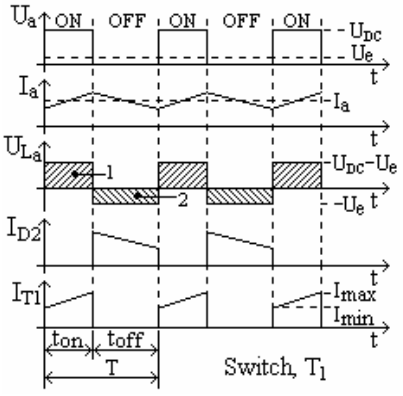

Fig.4. Switching waveforms for motoring operation.

The relevant circuit waveforms for regenerating operation are shown in figure 5, showing the equal areas of the inductor. During regeneration the transfer function of the converter is given by the relation:

$$U_a = \frac{t_{on} \cdot U_{DC}}{T} \quad (5)$$

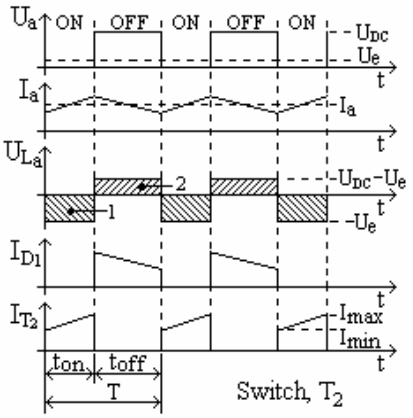

Fig.5. Switching waveforms for regenerating operation.

Figure 6 presents a schematic arrangement for two quadrants controller, showing the outer speed control loop and the inner current control loop.

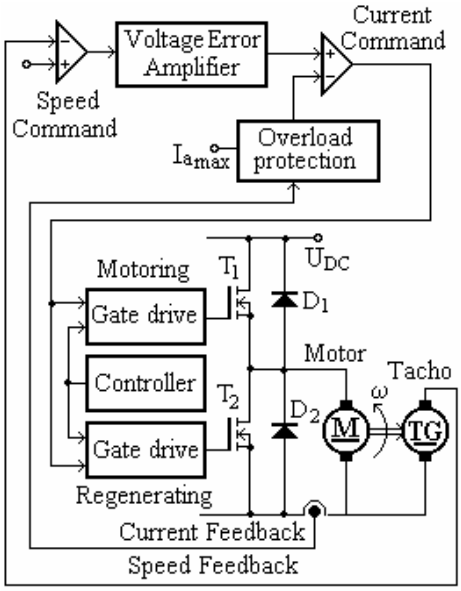

Fig.6. Schematic arrangement for two quadrants controller.

The voltage error signal gives the current reference command, and the current command signal is compared with the actual motor current in the inner control loop [3].

PWM current control

A way of controlling motor current it is to control the switching sequences to the main Power MOS devices. The devices can be switched a constant frequency using a PWM method current control [6, 7]. Figure 7 presents the controller circuit diagram and its component circuits [5]: steady voltage (B_1), slow-start circuit (B_2), commutation circuit (B_3), pulse generator (B_4), error amplifier (B_5), PWM chopper (B_6), overload protection circuit (B_7), supply voltage variations protection circuit (B_8).

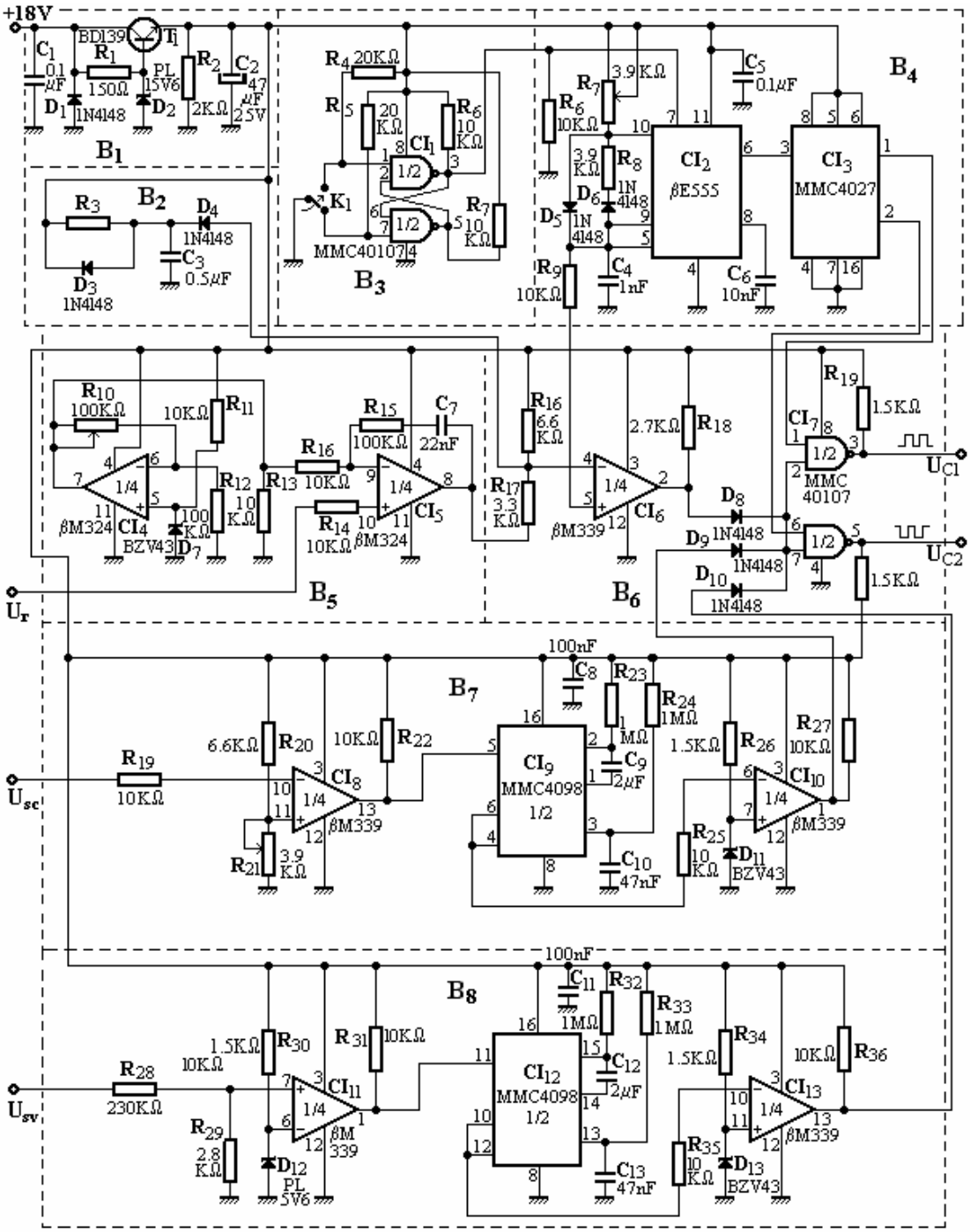

Fig.7. Controller circuit diagram.

The presented controller circuit is proposed for the current adjustment through the winding armature using a PWM method current control. Frequency may be fixed at any value from 1 kHz to 100 kHz and duty cycle adjusted at any point from 0 to 98%. Protection circuitry includes cycle-by-cycle current limiting, over current protection, soft start capability, voltage protection and feedback loop protection circuits. The device contains a voltage reference (CI_4, D_7) which is connected to the inverting input of the error amplifier (CI_5). The feedback signal (U_r) is obtained from either a tachogenerator or from a signal proportional to the armature voltage (the feedback signal must be scaled to centre about the voltage reference level.

At start-up the duty cycle is adjusted to be long enough to give sufficient motor starting torque. The initial motor current is given by the equation:

$$L_a \frac{di_a}{dt} + R_a \cdot i_a = U_{DC} \tag{6}$$

Where: L_a is the armature winding inductance.

During the interval t_{on}, the rise of motor current prior

to armature rotation is given by the equation:

$$(7) \qquad i_a = \frac{U_{DC}}{R_a}\left[1 - \exp\left(-\frac{t}{\tau_a}\right)\right]$$

Where: τ_a is the electrical time constant of the motor, $\tau_a = L_a/R_a$.

The current in the motor windings rises exponentially at a rate governed by average supply voltage and motor inductance. During the interval t_{off} the switching element T_1 is off and motor current decays through the diode D_2 (Fig. 3) at a rate dependant upon the external circuit constants and internal motor leakage currents, according to the equation:

$$(8) \qquad i_a = I_1 \exp - \left(\frac{t - \delta T}{\tau_a}\right)$$

Where: I_1 is the current at the end of the first pulse and it is nearly 60% of i_a maximum value, $I_{amax} = U_{DC}/R_a$. For a PWM waveform with a period T the ratio of pulse width to switching period is denoted by δ.

The motor current at the end of the period, T, remains at a level I_2, which is then the starting current for the next cycle. As soon as rotation begins, back emf is generated, and the motor equation becomes:

$$(9) \qquad L_a \frac{di_a}{dt} + R_a \cdot i_a = U_{DC} - U_e$$

An approximate expression for the average motor current is given by the equation:

$$(10) \qquad I_{ave} = \delta \frac{U_{DC} - U_e}{R_a}$$

Figure 8 presents the gate drive circuit to command the switching element (2 power MOSFET transistors BUK 438-800 A, parallel connected) [5].

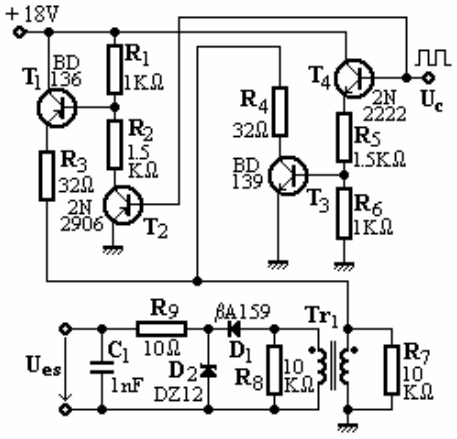

Fig.8. Gate drive circuit

The power transistors are driven using the coupling transformer Tr_1. The respective circuit assures the necessary gate current for charging and respectively discharging the entry capacities gate-source (C_{gs}) of the MOSFET transistors which were used, in a very short period.

The switching elements command using the coupling transformers assures a controlled increase of the drain currents of the power transistors by applying a linear variable voltage on the gate.

Conclusion

DC motor speed control can be achieved using switch mod DC-DC chopper circuits.

For many applications the motor control system is operated at switching speeds in the range 1kHz to 100kHz.

Power MOS devices are ideally suited for this type of converter. The advantages of power MOS devices include their simple gate drive requirements, rugged performance, easy of use in parallel configurations, switching performances.

Motor torque and velocity can be tightly controlled by controlling the PWM duty cycle and motor current.

By PSpice simulation [4] was tested in time and frequency domains the half bridge chopper circuit, and it was analyzed its stability. The obtained signal levels have a good concordance with calculated values [5].

References

[1] Bidian, D. Electrotehnica si masini electrice. Editura Academiei Academiei Fortelor Aeriene, Brasov, 1997.

[2] Kassakian, J., G. Principles of Power Electronics. Addison-Wesley Publishing Company, 1991.

[3] Riine, K. A Digitally Controlled Zero Voltage – Switching Full Bridge Converter. Proceedings, 1994.

[4] Radoi, C. SPICE – Simularea si analiza circuitelor electronice. Editura Amco Press, Bucharest, 1994.

[5] Pearsica, M. Circuit de comanda si reglare a curentului prin infasurarea rotorica la motoarele de curent continuu. Revista Academiei Fortelor aeriene, Nr. 1, Brasov, mai 2004.

[6] Pearsica, M., Influenta modului de comanda PWM asupra functionarii motorului de curent continuu. A VIII-a Ses. de Com. St., Academia Fortelor Terestre, Sibiu, June 2004.

[7] * * * Power Semiconductor Applications. Philips Semiconductor Inc., 1994.

Marian Pearsica *– Associate Professor, Dr., Department of Electronic and Computer Science, "Henri Coanda" Air Force Academy, Mihai Viteazu St. 160, 500183, Brasov, Romania.*
e-mail: marianpearsica@yahoo.com

Plant Control using Digital Sensors that introduce a Delayed and Sampled Output

Afzal Chamroo, Christian Vasseur and Haoping Wang

Abstract: *This article deals with the control of linear plants that deliver delayed and sampled output. We propose a control theory which makes use of a class of piecewise continuous systems and that enables sampled tracking. A mathematical approach of the dynamics of our control command is given. This approach uses only the delayed and sampled output vector as feedback. Moreover, a computer simulation example is presented so as to enhance the theoretical aspect. The method shows relialability and robustness against slight time-variations of the plant's parameters.*

Keywords: *tracking, sampled tracking, sampled feedback, delayed output, piecewise continuous systems*

Introduction

The goal of the present article is to develop a control stragegy that enables tracking on linear plants in cases where the only available feedback is the plant's delayed and sampled output vector. This is often the case when we deal with control architectures that make use of digital calculators and digital sensors that are time consuming in what concerns step calculations.

The particular type of output that is studied here brought us to consider a sampled type control technique. In that point of view, Kabamba [3] was the first to propose the sampled control commands for linear plants using a generalised sampled-data hold function. Urikura and Nagata [11] developed an optimised control method for sampled-data systems, by reducing ripples between sampling instants. Otherwise, Yamamoto [13] proposes an optimisation using a hybrid control system, based on the notion of functions defined piecewisely.

Considering the hybrid notion introduced by Decarlo [2], Koncar and Vasseur [4-6] have established, more recently, a class of control systems whose evolution is described by switchings. The chronology of these switchings is defined by a set of sampling instants $S = \{t_k, k = 0,1,2,...\}$ called "switching instants". These controllers are referred to as piecewise continuous systems (PCS). In this approach, the control input of the plant is defined from two input spaces: the first space U^r allows control between switching instants, while the second input space V^s enables control at the switching instants. Referring to the classification of Tittus and Egardt [10], this class of control systems has hybrid properties and extends the concept of compound control realised by Laurent [7] and Vasseur [12]. According to Branicky's taxonomy of hybrid systems [1], these control units are characterised by autonomous switchings and controlled impulses.

It is well established in [6] that the use of PCS controllers enables sampled tracking on linear plants by undertaking a *state* feedback. However, in our case, we must adapt appropriately the method in [6] so as to define a controller no longer based on state feedback, but on an *output* feedback, which is, moreover, delayed and sampled.

In this paper, we start by defining the particular nature of the output signal considered for feedback. An overview of the construction and behaviour of a PCS is given in the second section, as well as its use in sampled tracking. Then we show how the use of a PCS controller can be adapted in our case. Moreover, the equations of the whole closed loop structure are established in view of taking into account the delayed nature of the output. The reader can find at the end of the paper a typical example raising delayed and sampled output while controlling a mobile cart by camera.

The Particular Sensor Output

The plant which we consider in our study is a usual general linear *nth* order system that we represent by its state and output equations as follows:

(1a) $x'(t) = A.x(t) + B.u(t)$,

(1b) $y(t) = C.x(t)$,

with $A \in \Re^{n \times n}$, $B \in \Re^{n \times r}$ and $C \in \Re^{m \times n}$ being the real, characteristic matrix of the system, and $x(t) \in \Sigma^n$, $u(t) \in U^r$ and $y(t) \in Y^m$ representing respectively the state, the input and the output of the plant.

However, in our case, we consider that neither the state $x(t)$, nor the output $y(t)$ of the plant is available. The only data to which we can access comes from a digital sensor that "observes" the output $y(t)$ and delivers it in a sampled and delayed format. The sampling period of the sensor being t_e and the delay associated being $N.t_e$, we define the sensor data as such:

(1c) $z(t) = y^*(t - N.t_e)$,

with N being a positive integer and (*) representing sampling with a period of t_e.

In our study, we assume that N and t_e are known constants.

An illustrating example can be the case where processed data accessed from a digital camera constitute

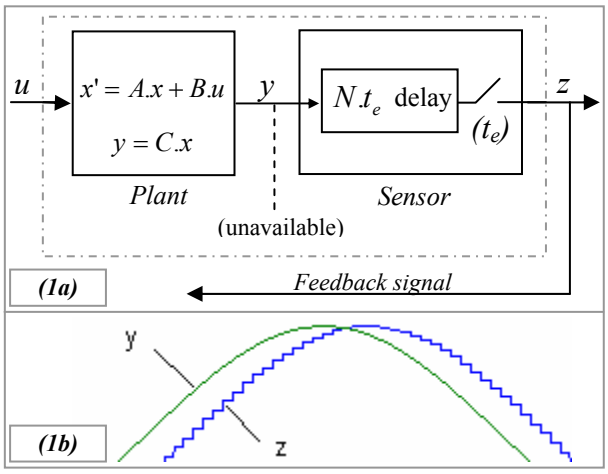

Fig.1a. The plant-sensor entity,
Fig.1b. Output signals for N=4.

the output $z(t)$ of a "visual" sensor. In that case, the t_e sampling period corresponds to the delivery of image information where t_e represents the time for an image shooting. For what concerns the delay, it represents the time necessary for image processing.

In this study, we assume that this delay is a multiple of the sampling period. This means actually that N snapshots are necessary to obtain the required data.

The whole statement of this section is summarised in Fig.1 above, where $N = 4$.

Piecewise Continuous Systems as Controllers

The principle of PCS control is to build an associated PCS system whose output constitutes the input of the plant. According to [6], we make use of a PCS system to define a particular PCS controller whose behaviour can be summarised as follows:

(i) The state of the PCS controller is switched to forced values at regular intervals of period t_e, which is the sample rate of the sensor. The corresponding switching set is represented by $S = \{k.t_e, k = 0,1,2,...\}$.

(ii) The equations describing the behaviour of the controller are:

(2a) $\lambda'(t) = \alpha.\lambda(t)$, $\forall t \in]k.t_e, (k+1)t_e[$,

(2b) $\lambda(k.t_e^+) = \delta.\psi(k.t_e)$, $\forall k = 0,1,2,...$,

(2c) $w(t) = \gamma.\lambda(t)$, $\forall t$.

Equation (2a) describes the continuous evolution of the controller's state $\lambda(t) \in \Sigma^{\hat{n}}$ upon $]k.t_e, (k+1)t_e[$, $\alpha \in \Re^{\hat{n}\times\hat{n}}$ being the state matrix of the controller. The only parameter that defines the behaviour of the controller's state in this interval of time is α which can take an arbitrary value. Usually, it is fixed such that the PCS is stable between switching instants.

Equation (2b) defines the controller's state at switching instants, by means of a bounded discrete input

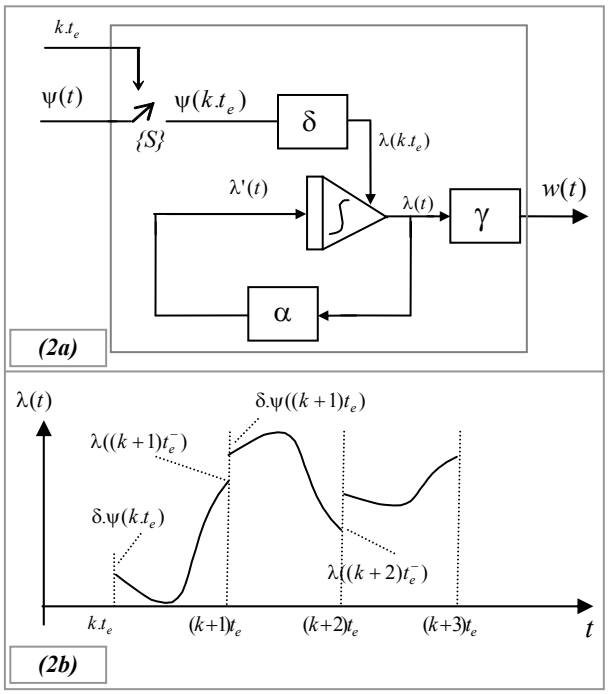

Fig.2a. Realisation diagram,
Fig.2b. State evolution of a PCS controller

$\psi(k.T_e) \in V^s$, and according to the linear relationship characterised by the matrix $\delta \in \Re^{\hat{n}\times s}$.

Equation (2c) is the output equation of the controller, characterised by the full rank matrix $\gamma \in \Re^{\hat{m}\times\hat{n}}$. The output $w(t) \in Y^{\hat{m}}$ constitutes the input command to be fed to the plant.

Fig.2a gives the realisation diagram of a PCS controller and Fig.2b shows its state's evolution.

It is shown in [6] that if the state of the plant is available, it is possible to define $\psi(t)$ and δ so as to achieve discrete tracking of a $c(t)$ state trajectory by the plant's state $x(t)$ at each switching instant and with one sampling period delay: $x((k+1)t_e) = c(k.t_e)$, $\forall k = 0,1,2,...$. The parameters α and γ are chosen arbitrarily.

Note that from now on, the discrete values of every function will be considered as being sampled at t_e period and to simplify the notations, any time function $f(t)$ at a given $k.t_e$ instant will be written as $f(k.t_e) = f_k$ $\forall k = 0,1,2,...$. Moreover, dealing with PCS gives rise to discontinuous signals. Thus, if any signal $f(t)$ is discontinuous, we shall consider the right value at the discontinuity since the switchings at each $k.t_e$ imply consequences occuring at every $k.t_e^+$. However, for simplification sake, the notation f_k will be used, instead of the strict one: $f_k^+ = f(k.t_e^+)$.

Control Strategy

The idea is to make use of the PCS controller defined above in order to achieve sampled tracking of a state trajectory $c(t)$ by the plant's inaccessible state $x(t)$ with a delay equal to a period of the sensor's sample time. Hence, we will define a control strategy to ensure $x_{k+1} = c_k \ \forall k = 0,1,2,...$ by using only $z(t)$, defined in (1c), as feedback signal.

Thus, the method we'll propose should allow us to observe: $z_{k+N+1} = C.c_k \ \forall k = 0,1,2,...$, with $C \in \Re^{m \times n}$ being the output matrix of the plant as described formerly.

For better comprehension, we will proceed by step:

(i) The PCS controller playing the main role of our method, we will first show how to define its matrix $\psi(t)$ and input δ to achieve $x_{k+1} = c_k$ in cases where *state* feedback is possible.

(ii) Then, we'll describe how the same goal can be achieved with a *delayed state* feedback.

(iii) Thus we only need to reconstitute the delayed state from the *delayed output* and use the approach of step (ii).

In every case, the controller's output is linked to the plant's input, thus $u(t) = w(t)$.

State Feedback

In this case, the behaviour of the closed loop system can be given by the following equation set:

(3a) $x'(t) = A.x(t) + B.u(t), \quad \forall t,$

(3b) $\lambda'(t) = \alpha.\lambda(t), \quad \forall t \in \left]k.t_e,(k+1)t_e\right],$

(3c) $u(t) = \gamma.\lambda(t), \quad \forall t,$

(3d) $\lambda_k = \delta.\psi_k, \quad \forall k = 0,1,2,...$.

By integration, the first three equations allow us to write in a sampled format, the next step value x_{k+1} of the state as a function of its previous one x_k:

(4) $x_{k+1} = f.x_k + M.\lambda_k$, with

$$f = e^{At_e} \text{ and } M = f.\int_0^{t_e} e^{-A\tau}B.\gamma.e^{\alpha\tau}d\tau .$$

In order to realise the discrete tracking which is defined above, we only have to fix down the tracking condition which is $x_{k+1} = c_k$, where $c(t)$ is the desired state trajectory. Thus, from (4) we have:

(5) $\lambda_k = M^{-1}\{c_k - f.x_k\}$

Equation (5) gives the switching value of the controller's state, under the condition that M^{-1} exists [6]. Hence, in this case, we are able to define the PCS controller with:

$\delta = M^{-1}$ and $\psi(t) = c(t) - f.x(t)$,

α and γ chosen arbitrarily.

Delayed State Feedback

Here, we assume that the most recent information available on the state at current time is $x(t - N.t_e) = x_{k-N}$, due to an imaginary sensor that delivers the state with a delay of $N.t_e$. We can

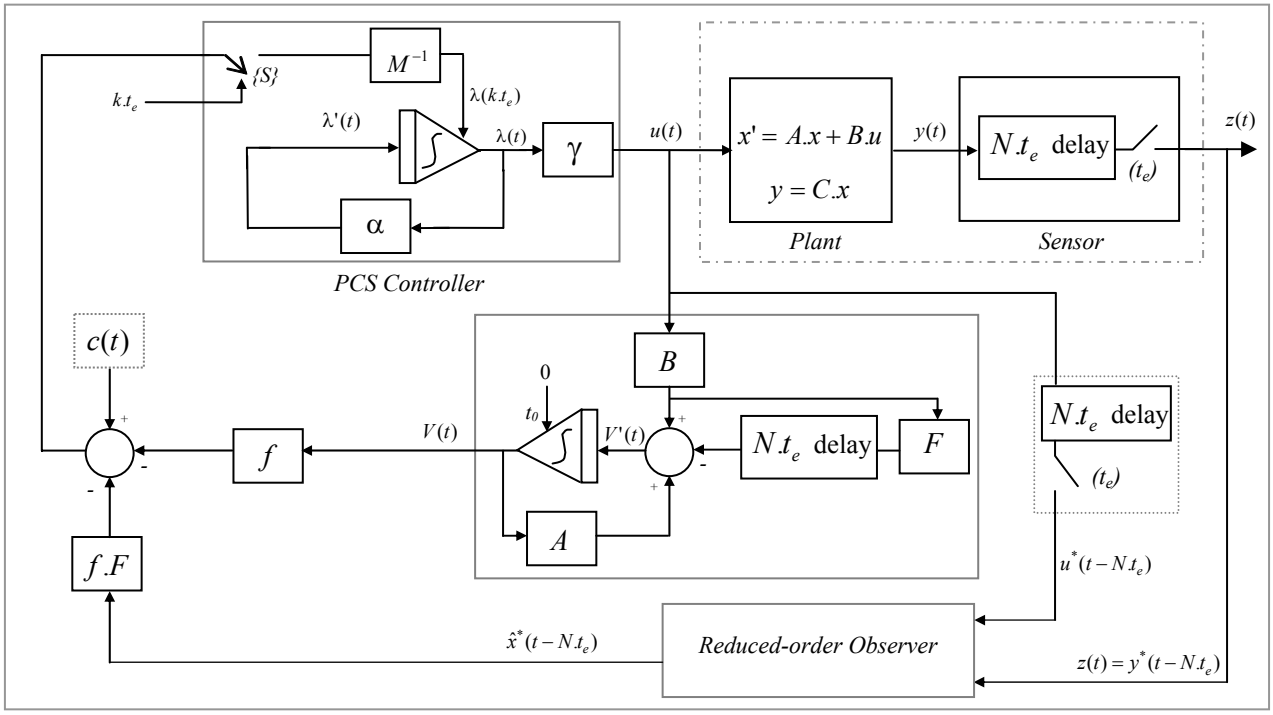

Fig.3. Block diagram of the whole closed loop structure using delayed output feedback

nevertheless write down mathematically equation (4) as before. However, x_k being unavailable, it must be calculated from x_{k-N} as follows:

(6) $x_k = F.x_{k-N} + V_k$, with

$$F = e^{A.N.t_e} \text{ and } V_k = F.\int_{(k-N)t_e}^{kt_e} e^{-A\tau} B.u(\tau).d\tau .$$

Note that in practice, V_k can be calculated as being the solution to the following differential equation:

(7) $V'(t) = A.V(t) + B.u(t) - F.B.u(t - N.t_e)$, with $V(0) = 0$.

Thus, by replacing the calculated value of x_k (6) in equation (4), we obtain:

(8) $x_{k+1} = f.(F.x_{k-N} + V_k) + M.\lambda_k$

Now, with the same tracking condition as in the former case, and assuming that M is invertible, we define the PCS controller with:

$$\delta = M^{-1}$$
$$\text{and } \psi(t) = c(t) - f.(F.x(t - N.t_e) + V(t))$$

Delayed Output Feedback

At this stage, we only have to reconstitute the delayed plant's state x_{k-N} using the available sensor data $z(t)$ so as to bring us back to the previous case.

This is easily realised using a discrete reduced-order observer [8] [9], that takes as input signals $z(t) = y^*(t - N.t_e)$ and $u^*(t - N.t_e)$. The observer thus outputs an estimate of the delayed plant's state, $\hat{x}^*(t - N.t_e)$.

Using the same tracking condition $x_{k+1} = c_k$, we can therefore ensure $z_{k+N+1} = C.c_k \ \forall k = 0,1,2,\ldots$.

Fig.3 represents the detailed architecture of the closed loop structure in the case of sampled and delayed output feedback. Note that the sampled nature of the delayed output is supported by the PCS controller which switches at the sample rate of the digital sensor.

Computer Simulation Example

In view of validating our method we have simulated, by means of Matlab®/Simulink®, the behaviour of the whole closed loop structure shown in Fig.3. This computer simulation reflects the control of a real system which is described below. As shown in Fig.4, this system consists of the visual position control of a moving cart.

The Plant

The plant which is considered here is a cart that moves along a horizontal and straight line segment. The cart is powered by an electric motor by means of a notched belt. The plant's state is composed of the real position and speed of the cart, while its output is given by the real position only:

$$x = \begin{bmatrix} x_1 \\ x_2 \end{bmatrix} = \begin{bmatrix} real\ position \\ real\ speed \end{bmatrix},\ y = x_1 ,$$

The motor is of a brushless type. It is driven in +/-10V by a dSpace® computer input/output card via a power amplifier. Supplied with 240V (mono), it can offer a nominal couple of 3.0Nm with a power of 200W. Identification with a second order approximation of the amplifier-motor-cart set has shown a time constant of 8.3ms and an overall gain of 2.9m/S/V.

Hence, we assume that the plant can be defined by the following state representation:

$$A = \begin{bmatrix} 0 & 1 \\ 0 & -120 \end{bmatrix},\ B = \begin{bmatrix} 0 \\ 350 \end{bmatrix} \text{ and } C = \begin{bmatrix} 1 & 0 \end{bmatrix}$$

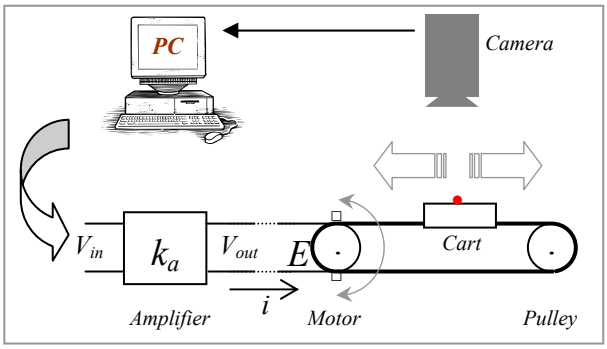

Fig.4. Visual control

The Sensor

The aim of the experiment is to realise a visual position control of the cart. Thus, the sensor is a "artificial vision" system that observes an infrared LED fixed on the cart, as shown in Fig.4. This vision system is constituted of a motionless digital infrared CCD camera connected to a computer allowing image processing. The camera is positionned above the cart and observes its motion. Thus, after a location operation, the artificial vision system outputs the position of the cart in a t_e-sampled format, with a delay equal to $N.t_e$:

$z(t) = x_1^*(t - N.t_e)$, with (*): sampling at t_e.

The Associated PCS Controller

In this simulation, we make use of the strategy for delayed output feedback as explained formerly. The delayed state is reconstituted by using the output $z(t)$ of the artificial vision system. The appropriate inputs (as defined in the "strategy" section) are fed to the PCS controller, whose internal parameters are chosen as such:

$$\alpha = \begin{bmatrix} -0.1 & 0 \\ 0 & -0.2 \end{bmatrix},\ \gamma = \begin{bmatrix} 1 & 1 \end{bmatrix}$$

The Aim of the Experiment

In the present example, the goal is to be able to realise sampled position tracking of a desired trajectory by the cart. According to our method's requirement, we have to define a state trajectory, which is here chosen to be:

$$c(t) = \begin{bmatrix} c_1(t) \\ c_2(t) \end{bmatrix} = \begin{bmatrix} \sin(\omega.t) \\ \omega.\cos(\omega.t) \end{bmatrix} \text{ with } \omega = 2\,\text{rad/s}$$

In this example, $c_2(t)$ is bound to be the derivative of $c_1(t)$, since they represent the desired speed and position trajectories.

As specified previously, our method should ensure $x_k = c_{k-1}$ and thus $z_k = C.c_{k-N-1}\ \forall k = 0,1,2,\ldots$. The results obtained are shown in Fig.5 and Fig.6.

Note that in order to better illustrate the results, the values of t_e have been chosen to be relatively big as compared to real cases. Moreover, to show that the tracking occurs at each switching instant, the desired trajectory has been delayed appropriately, for comparison sake.

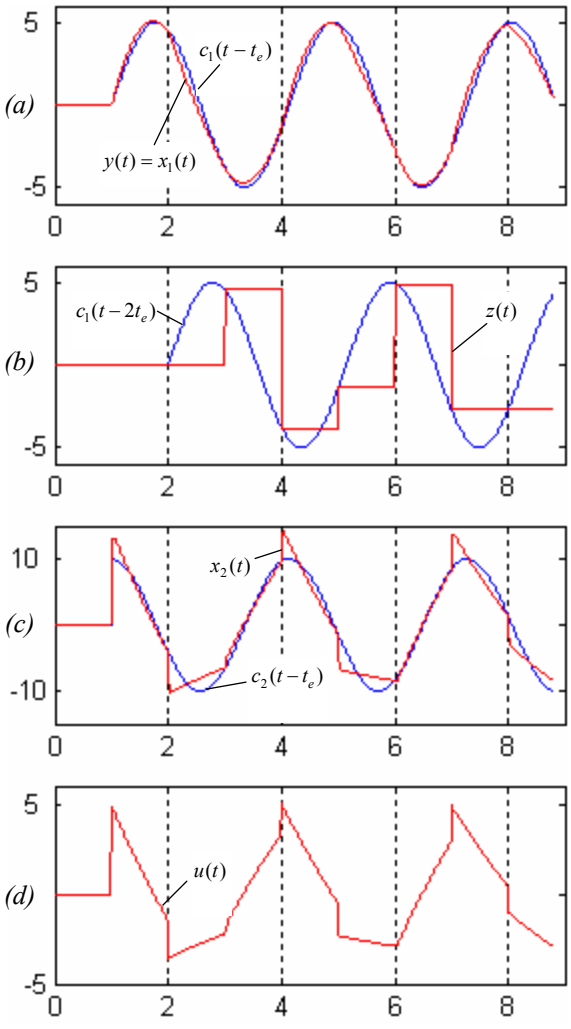

Fig.5. Tracking, $t_e = 1s$ and $N = 1$

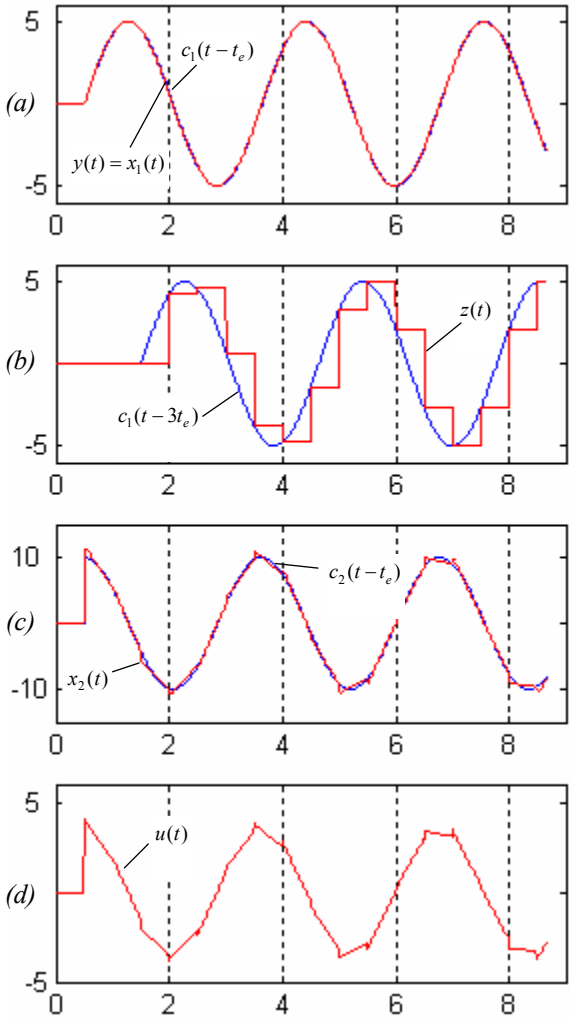

Fig.6. Tracking, $t_e = 0.5s$ and $N = 2$

Results Comment

Fig.5 and Fig.6 illustrate the result of sampled tracking using two different type of sensors. In both cases, the sensor gives rise to a delay of 1s, but the values of t_e and N differ.

Fig.5a and Fig 6a show sampled tracking of $c_1(t)$ by the plant's output $y(t)$ which is here equal to the real cart position $x_1(t)$. Note that the $y(t)$ curve intersects that of $c_1(t-t_e)$ at every $k.t_e$, thus showing t_e-sampled tracking with a delay of t_e. Similarly, Fig.5c and Fig 6c show how the second state variable (speed) reaches its desired trajectory at switching instants.

In the same way, Fig.5b and Fig 6b, represent sampled tracking of $c_1(t)$ by $z(t)$ with a delay of $(N+1).t_e$.

Fig.5d and Fig 6d illustrate the control command fed to the plant. Coming out of a PCS controller, we can notice its piecewise continuous nature.

Note that though we have shown the state's evolution for demonstration sake, we do not use it for feedback, since we assume it to be unavailable.

Conclusion

The method that we present in this paper is appropriate for control of linear plants in cases where the only available feedback comes from a sensor delivering the plant's output vector in a delayed (of $N.t_e$) and sampled (at t_e) format. The control unit is based on a PCS controller whose switching matches the sample rate t_e of the sensor, thus designed for sampled feedback. Moreover, the use of PCS control has been adapted in cases this sampled feedback is delayed. The method, thus ensures sampled tracking at every $k.t_e \ \forall k = 0,1,2,...$, with a delay of t_e concerning the state and one of $(N+1).t_e$ concerning the sensor's output such that $x_k = c_{k-1}$ and $z_k = C.c_{k-N-1} \ \ \forall k = 0,1,2,...$.

Computer simulations showed that the method is reliable and moreover robust against time-variations of the plant's parameters (A and B).

Although the main goal of the paper is to deal with a delayed and sampled *output* vector, the reader can also find techniques in cases of *state* and delayed *state* feedback. Those techniques are easily implemented, and also proved to be robust, even in the presence of noise in the state signal.

Note that in every case, the PCS controller show better efficiency for small values of t_e, which is the period at which the PCS controller's state switches. However, in cases of sampled feedback, the best that can be done to optimise the controller is to switch at a period equal to the sampling period of the feedback data.

As a perspective of our study, works are presently being carried out to optimise the PCS controller to ameliorate its behaviour between switching instants so as to enhance the tracking in this interval, especially in cases where t_e is relatively high. This optimisation is based on that given in [6].

Furthermore, we are undertaking real time experiments to test the present method on the real system of Fig.4.

Acknowledgements

This work is supported by the European Union under Grants 15010/02Y0064/03-04 CAR/Presage N° 4605 Obj. 2-2004:2 - 4.1 – N° 160/4605.

References

[1] Branicky, M.S., Borkar, V. and Mitter, S.K. A unified framework for hybrid control. In *Proceedings IEEE Conf. Decision Contr.*, Lake Buena Vista, 1994, pp. 4228-4234.

[2] Decarlo, R.A., Branicky, M.S., Peterson, S. and Lennartson, B. Perspective and results on the stability and stabilization of hybrid systems. In *Proceedings of the IEEE*, Vol. 88, No. 7, 2000, pp. 1069-1082.

[3] Kabamba, P.T. *Control of Linear Systems Using Generalized Sampled-Data Hold Functions*. IEEE Transactions on Automatic Control, Vol. 32, No. 9, 1987, pp. 772-783.

[4] Koncar, V. and Vasseur, C. *Systèmes à fonctionnement par morceaux et poursuite échantillonnée.* APII-JESA, Vol. 35, No. 5, 2001, pp. 665-689.

[5] Koncar, V. and Vasseur, C. *Piecewise functioning systems: bi-sampled controllers.* Studies in Informatics and Control Vol.11, No.2, 2002.

[6] Koncar, V. and Vasseur, C. *Control of linear systems using piecewise continuous systems.* IEE Control Theory & Applications , Vol. 150, n° 6, pp.565-576, 2003.

[7] Laurent, F. Sur la commande d'un filtre linéaire par des impulsions multimodulées. *C.R. Acad. Sc*, Paris, t. 270, pp. 288-289.

[8] Leondes, C. and Novak, L. *Reduced-order observers for linear discrete-time systems*. IEEE Transactions on Automatic Control, Vol. 19, No. 1, 1974, pp. 42-46.

[9] Luenberger, D.G. *An Introduction to Observers*. IEEE Transactions on Automatic Control, Vol. 16, No. 6, 1971, pp. 596-602.

[10] Tittus, M. and Egardt, B. *Control Design for Integrator Hybrid Systems.* IEEE Transactions on Automatic Control, Vol. 43, No. 4, 1998, pp. 491-500.

[11] Urikura, S. and Nagata, A. *Ripple-Free Deadbeat Control for Sampled-Data Systems.* IEEE Transactions on Automatic Control, Vol. 32, No. 6, 1987, pp. 474-482.

[12] Vasseur, C. Contribution à l'étude des systèmes échantillonnés commandés par impulsions multimodulées, Ph.D. Thesis, University Lille 1, Villeneuve d'Ascq, France, 1972.

[13] Yamamoto, Y. *A Function State Approach to Sampled Data Control Systems and Tracking Problems.* IEEE Transactions on Automatic Control, Vol. 39, No. 4, 1994, pp. 703-713.

Afzal Chamroo *– Ph.D. Student, LAGIS[1], USTL[2].*
e-mail: chamroo@i3d.univ-lille1.fr.

Christian Vasseur *–Professor, LAGIS[1], USTL[2].*
e-mail: christian.vasseur@univ-lille1.fr.

Haoping Wang *– Ph.D. Student, LAGIS[1], USTL[2].*
e-mail: haopingwong@hotmail.com.

[1]Laboratoire d'Automatique, Génie Informatique & Signal (UMR CNRS 8146),

[2]Université des Sciences et Technologies de Lille, 59655 Villeneuve d'Ascq, FRANCE.

SIMULINK Models of Direct Self Control Used in Electrical Traction with Induction Motors

Daniel Cristian Cismaru, Doru Adrian Nicola and Aida Cornelia Bulucea

Abstract *In the paper it is presented the DSC mathematical modelling used on the locomotives with traction induction motor. They are built the associated structural diagrams of those three configuration of DSC, which they permit a fast implementation into a simulation soft. By means of these models they are achieved simulations which they permit the validation of the mathematical models. SIMULINK models can be used as such or with certain simplifications into a more complex associated construction of the study through simulation of the locomotives end electrical trains.*

Keywords: *SIMULINK Models, DSC, Asynchronous Motors, Electric Traction, Mathematical Modelling*

Introduction

The **D**irect **S**elf **C**ontrol (DSC), invented by Depenbrock [2], has been implemented successfully by ABB (ADTRANZ) through the MICAS microcomputer traction control system utilization [4]. Unlike the vector control, in the implementations case on the locomotives with traction induction motor, the DSC diagram structure like specific feature it has three different configurations corresponding to a three stator frequency domains: (0, $f_{sN}/3$], ($f_{sN}/3$, f_{sN}] and (f_{sN}, f_{smax}]. All those three configurations have however like common elements two identical calculus blocks, corresponding to the traction induction motor and the voltage-source inverter.

The used model in the implemented control diagrams with MICAS it has at basis the equivalent diagram of traction induction motor with the concentrated leakage inductivities in the rotor mesh [4], [8].

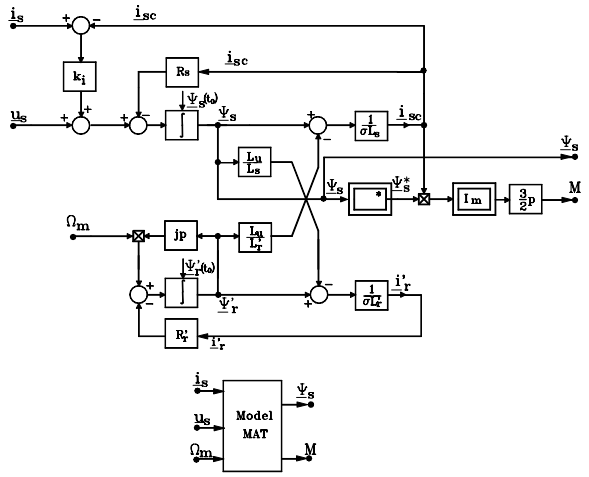

Fig.1. Traction induction motor model used in the DSC

Unlike, in the paper it is presented an equivalent model, built on the mathematical model basis of the written traction induction motor electromagnetic part with vector phasors in the (α_s,j·β) stator reference frame [6]:

$$\underline{u}_s = R_s \cdot \underline{i}_s + \frac{d\underline{\psi}_s}{dt};\ 0 = R_r' \cdot \underline{i}_r' + \frac{d\underline{\psi}_r'}{dt} - j \cdot \omega_m \cdot \underline{\psi}_r' \quad (1)$$

$$\underline{\psi}_s = L_s \cdot \underline{i}_s + L_u \cdot \underline{i}_r';\ \underline{\psi}_r' = L_u \cdot \underline{i}_s + L_r' \cdot \underline{i}_r'$$

$$M = \frac{3}{2} \cdot p \cdot Im\{\underline{i}_s \cdot \underline{\psi}_s^*\}$$

The (1) mathematical model can be brought in the shape of:

$$\frac{d\underline{\psi}_s}{dt} = \underline{u}_s - R_s \cdot \underline{i}_s;\quad \frac{d\underline{\psi}_r'}{dt} = j \cdot p \cdot \Omega_m \cdot \underline{\psi}_r' - R_r' \cdot i_r' \quad (2)$$

$$\underline{i}_s = \frac{\underline{\psi}_s - \frac{L_u}{L_r'} \cdot \underline{\psi}_r'}{\sigma L_s};\quad \underline{i}_r' = \frac{\underline{\psi}_r' - \frac{L_u}{L_s} \cdot \underline{\psi}_s}{\sigma L_r'}$$

$$M = \frac{3}{2} \cdot p \cdot Im\{\underline{i}_s \cdot \underline{\psi}_s^*\}$$

where $\sigma = 1 - \frac{L_u^2}{L_s \cdot L_r'}$ it represents the leakage coefficient of motor.

By means of the (2) equations it is built the structural diagram and the mask block of the induction motor electromagnetic part. Moreover, through the introduction of a supplementary input variable, the obtained $\underline{i}_s$ stator current vector, which it will be compared with the $\underline{i}_{sc}$ calculated adequate value, it is obtained the used traction induction motor model in the DSC (fig.1).

For the $\underline{\psi}_s = \psi_{s\alpha} + j \cdot \psi_{s\beta}$ vector projections being, on the β_r, β_s and β_t axes they are used the calculus relations:

$$\psi_{s\beta r} = \psi_{s\beta}$$

$$\psi_{s\beta s} = -\frac{\sqrt{3}}{2} \cdot \psi_{s\alpha} - \frac{1}{2} \cdot \psi_{s\beta} \quad (3)$$

$$\psi_{s\beta t} = \frac{\sqrt{3}}{2} \cdot \psi_{s\alpha} - \frac{1}{2} \cdot \psi_{s\beta}$$

Within the framework of this model, on the $f_{2wR,S,T}$ switching functions and the voltage value basis from the DC-link circuit, must calculated the $\underline{u}_s$ supplied stator voltage vector by the voltage-source inverter (fig.2).

Because when $f_{2wR}=1 \Rightarrow u_{RO}=+\frac{u_d}{2}$ and when $f_{2wR}=0 \Rightarrow u_{RO}=-\frac{u_d}{2}$ then it is obtained like reference:

$$u_{RO}=f_{2wR}\cdot\frac{u_d}{2}-(1-f_{2wR})\cdot\frac{u_d}{2} \quad (4)$$

Entirely alike

$$u_{RO}=(2\cdot f_{2wR}-1)\cdot\frac{u_d}{2}$$

$$u_{SO}=(2\cdot f_{2wS}-1)\cdot\frac{u_d}{2} \quad (5)$$

$$u_{TO}=(2\cdot f_{2wT}-1)\cdot\frac{u_d}{2}$$

Thus it results the function which it defines the block corresponding to the voltage-source inverter (fig.2)

$$\underline{u}_s=\frac{2\cdot u_d}{3}\cdot(f_{2wR}+a\cdot f_{2wS}+a^2\cdot f_{2wT}) \quad (6)$$

For all those three regimes, the traction induction motor will be fed from a voltage-source inverter commanded by the $f_{2wR,S,T}$ signals. From two phases they are collected the stator currents, and through the intermediation of a speed transducer it is known the Ω_m mechanical angular speed of the motor rotor, too. These variables together with voltage value from the DC-link circuit they are taken by the control diagram.

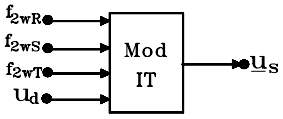

Fig.2. Voltage-source inverter model

DSC in high speed domain

At high speed, traction induction motor is working with $U_s=U_{sN}$, $\psi_s<\psi_{sN}$, $f_s>f_{sN}$ and reference data of the ψ_s^* stator flux it is obtained at the output of the torque PI controller (fig.3).

The $\underline{i}_s$ stator current vector is calculated by means of the measured value of the i_{sR} and i_{sT} currents and from the obtained condition of an equilibrated system, too, and $\underline{u}_s$ on the previously presented inverter model basis.

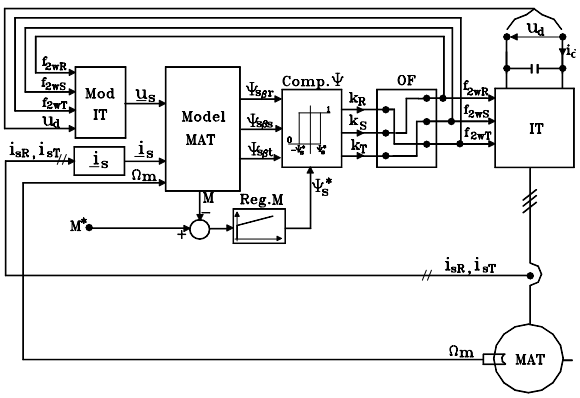

Fig.3. DSC diagram in high speed domain

Those three components of the $\underline{\psi}_s$ flux vector they are calculated with the (3) equations. Through the comparing, in the two position controller (Comp.ψ), of those three components of flux with the ψ^* reference data, they result the k_R, k_S, k_T signals. After the order of these signals in the signal select (OF), they result the $f_{2wR,S,T}$ switching functions of the voltage-source inverter.

DSC in medium speed domain

In this working regime ($U_s<U_{sN}$, $\psi_s=\psi_{sN}$, $f_{sN}/3\le f_s\le f_{sN}$), the control diagram has a few modifications given the previous case (fig.4):

- the reference data of ψ^* flux corresponds the rated value of the stator flux, and
- the difference between the reference data and the instantaneous value of torque it is compared in the Comp.M block (alike with Comp.ψ), having like result the m_z signal with two possibly values 0 and 1 (fig.5).

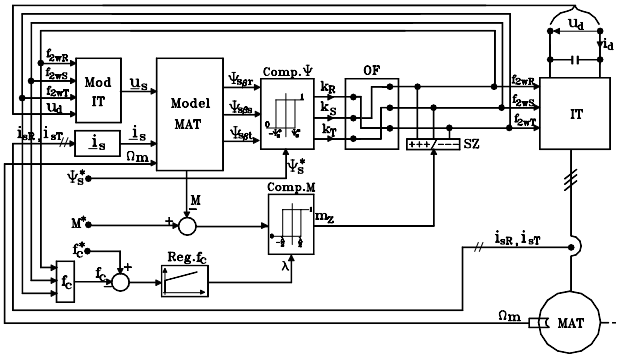

Fig.4. DSC diagram in medium speed domain

The λ variation interval width of the torque, which it characterizes the Comp.M comparing block of the torques, it is given by the switching frequency controller. This PI controller has at input the difference between the reference data of the switching frequency and the instantaneous value of the same deducted switching frequency on the $f_{2wR,S,T}$ signals basis.

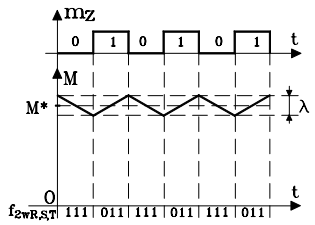

Fig.5. Diagram of m_z signal formation

The m_z signal value influences the $f_{2wR,S,T}$ signals values, thus:

- if $m_z=1$, then the $f_{2wR,S,T}$ signals keep them the resulted values from the OF;
- if $m_z=0$, then the $f_{2wR,S,T}$ signals take an imposed value by the SZ, like:

111 or 000 depending on their previous values, so that we have only a modification (for example 101 → 111 and 001 → 000) (fig.5).

Through the Comp.M block intermediation it is achieved the fastest intervention about the torque, which it is made to pulsate at nearly three times of the f_c switching frequency.

ISC in low speed domain

In the low speed domain ($U_s<U_{sN}$, $\psi_s=\psi_{sN}$, $f_s<f_{sN}/3$), the control diagram presents important modifications given the previous cases (fig.6). It is observed the utilization of a different control like principle, based on the PWM modulation and named the **I**ndirect **S**elf **C**ontrol or **I**ndirect **S**tator-quantities **C**ontrol (ISC).

Those two used controllers (for torque and flux) are by P type. The used calculus relations within the framework of the controllers and a new blocks are:

- for the flux controller

$$k_{\psi s} = p_{\psi} \cdot \frac{\psi_s^* - \psi_s}{\psi_s^*} \quad with \quad p_{\psi} < 1 \tag{7}$$

- for the torque controller

$$\Delta x_d = p_M \cdot \frac{4}{3} \cdot \frac{\sigma \cdot L_s}{(1-\sigma)\cdot p} \cdot \frac{M^* - M}{\psi_s^{*2}} \quad with \quad p_M < 0{,}5 \tag{8}$$

where Δx_d it is the dynamic angular displacement of $\underline{\psi}_s$ (established by a modification of the instantaneous value of the M torque given by the M^* reference data);

- the static angular displacement of $\underline{\psi}_s$

$$\Delta x_{st} = T_p \cdot \omega_s \quad with \quad T_p = \frac{1}{2 \cdot f_c} \tag{9}$$

- the rotor angular speed

$$\omega_r = \frac{R_r'\cdot(1-\sigma)}{\sigma \cdot L_s} \cdot tg\{\frac{1}{2} arcsin[\frac{M}{M^*} \cdot (\frac{\psi^*}{\psi_s})^2]\} \tag{10}$$

- the $\Delta\underline{\psi}_s$ variation

$$\Delta\underline{\psi}_s = [e^{j\cdot\Delta x} \cdot (1 + k_{\psi s}) - 1] \cdot \underline{\psi}_s \tag{11}$$

- the $\underline{u}_s$ stator voltage

$$\underline{u}_s = R_s \cdot \underline{i}_s + \frac{\Delta\underline{\psi}_s}{T_p} \tag{12}$$

In the end, within the framework of the PWM block, the $\underline{u}_s$ voltage it is decomposed in those three components corresponding to the traction induction motor phases, compared with the triangular signal by f_c frequency, resulting thus the $f_{2wR,S,T}$ signals command of the inverter. Because of the PWM modulation, the current is very near to sinusoidal wave. Through the simple elimination of this block it is obtained a model of the ISC, which it take account only by the feeding voltage fundamental of the traction induction motor.

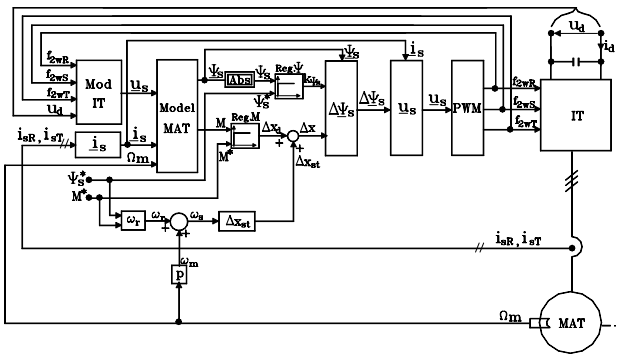

Fig.6. ISC diagram in low speed domain

SIMULINK models

On the presented mathematical models basis associated with the DSC can be created SIMULINK models, having the same topology structure. Through adequate completions or simplifications can be achieved models which they permit the study through simulation of the different phenomenon specific to the electrical traction.

Simplified SIMULINK model of ISC

For the working study of the traction induction motor in the ISC case, without the consideration of the voltage-source inverter model, it is built its SIMULINK model (fig.7).

The used model contains two mask blocks:

- MAS1, the model corresponding to the traction induction motor [7];

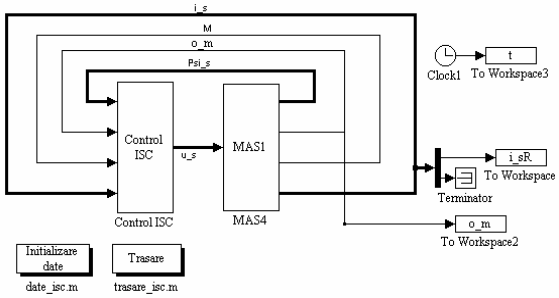

Fig.7. ISC SIMULINK model without consideration of voltage-source inverter model

- Control-ISC (fig.8), which it has the structure achieved in accordance with the ISC diagram.

By means of this model (fig.7) it has been simulated a transient state corresponding to a starting, followed of a working with constant speed and then of a braking. They have been obtained, the waveforms of the M_{ref} reference torque, the M electromagnetic torque of the motor, the Ω_m angular speed, of the u_{sR} R phase stator voltage and of the i_{sR} R phase current (fig.9).

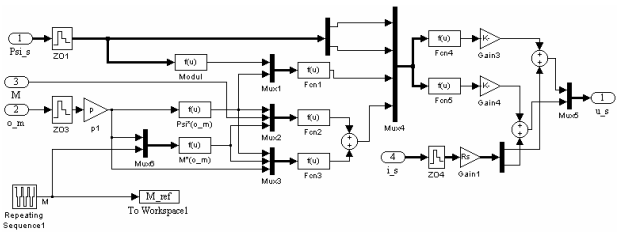

Fig.8. Structure of Control-ISC mask block from fig.7

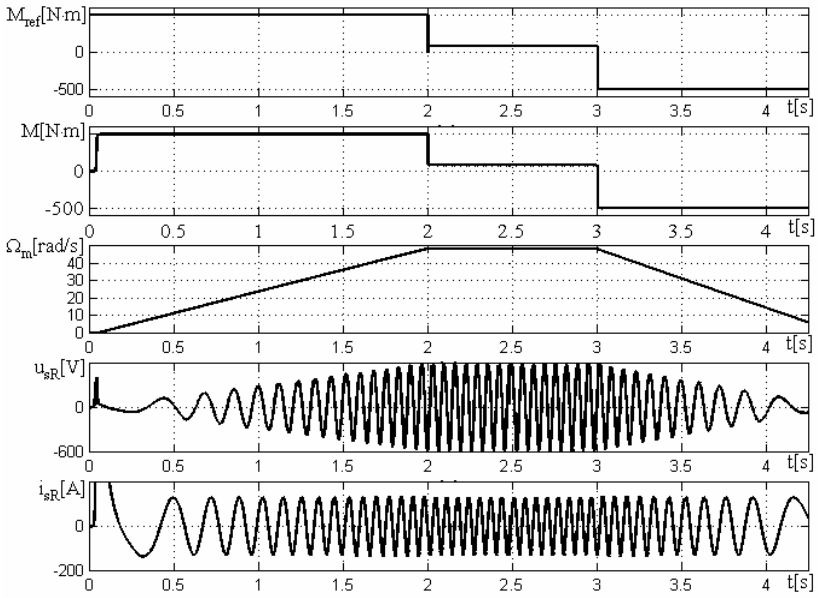

Fig.9. Waveforms of principal quantities which characterize the ISC without consideration of voltage-source inverter model

SIMULINK model of DSC

For the working study of the two levels voltage-source inverter – traction induction motor ensemble in the DSC case it is built its SIMULINK model. From physical viewpoint, this has the same structure with the ISC model (fig.7) with the substitution specification of the ISC block through the DSC block. The Control-DSC block (fig.10) contains all those three components of the DSC:

- the ISC, in the low speeds domain, modeled by the Control-ISC block (fig.8) and followed of the PWM-IT2N block, which take thus account of the voltage-source inverter working;
- the DSC, in the medium speeds domain, modeled by the Control-DSC block (fig.11) and
- the DSC-W, in the high speeds domain, modeled by the Control DSC-W block (fig.12).

Like in the case of SIMULINK model corresponding to the ISC, too, the composition of the Control-DSC and Control-DSC-W blocks it is given by the corresponding.

The selection of one among those three control types it is made depending on the speed of traction induction motor (fig.10).

For the simulation of voltage-source inverter working, after the Control-ISC block it has been inserted the PWM-IT2N block. The other two DSC blocks contain each a such Mod-IT block of generation of the voltage pulse.

By means of the DSC model it has been simulated the starting regime of system based on the DSC for the reference torque by 6000 N·m. They have been visualized the waveforms the M electromagnetic torque, of the Ω_m speed, of the voltage and current on the R phase, u_{sR} and respectively i_{sR} (fig.13).

The appeared modifications in the torque variation they are established at the passing from a control type to another. For the medium values domain the λ variation width of the torque can easily modify by means the Relay block (fig.11).

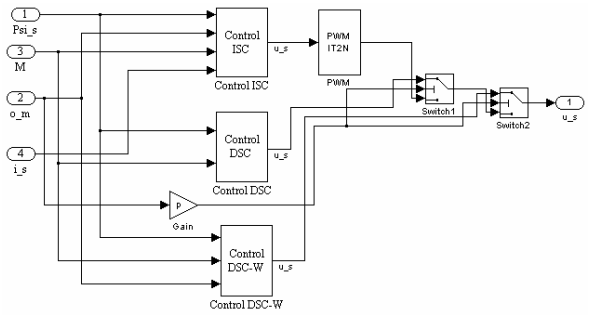

Fig.10. Structure of Control-DSC block

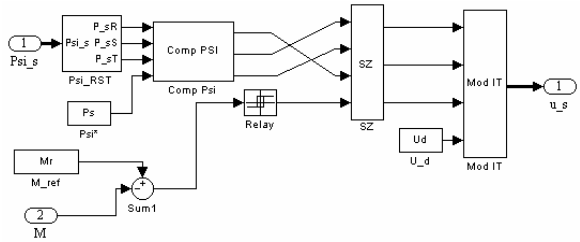

Fig.11. Structure of Control-DSC block from fig.10

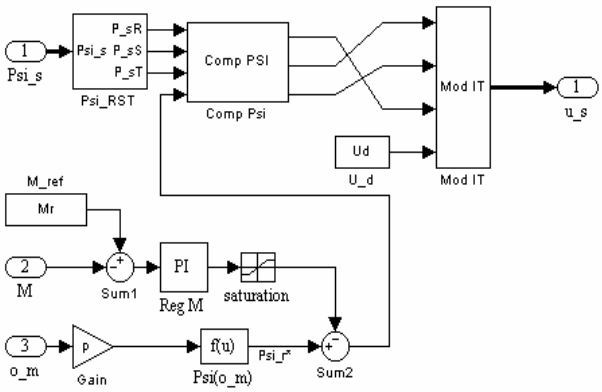

Fig.12. Structure of Control-DSC-W block from fig.10

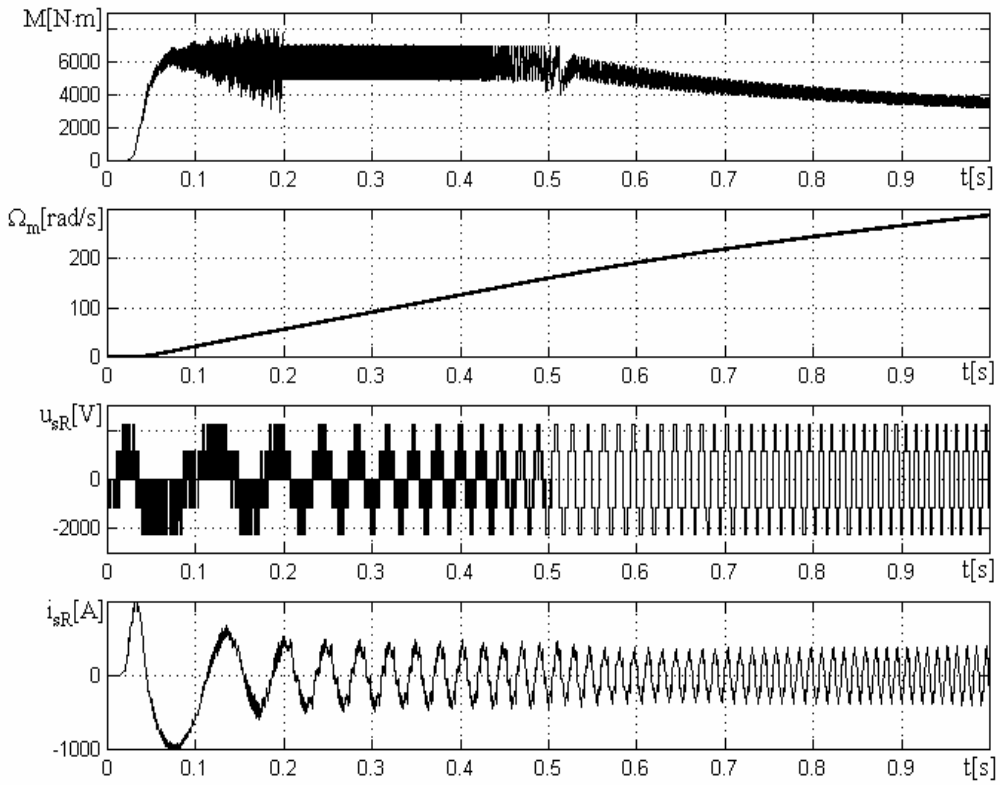

Fig.13. Waveforms of principal quantities which characterize DSC

A supplementary validation of the models correctness used for DSC it can make by means of the experimental results presented in [5]. In this sense it is used the DSC model, at which the initialization it is made with the dates of another traction motor [5].

Further on, they are presented comparatively the obtained dates experimental way with those obtained through simulation. In the last case, it appears not the voltage variation from the intermediate circuit, too, which it has been considered in simulation, like being constant. The comparisons are given graphically, through the alike diagrams juxtaposition.

They have been compared the torque and current variations on phase of the traction induction motor in three situations:

- at the DSC in the high speeds domain (DSC-W) (fig.14);
- at the DSC (fig.15);
- at the passing from the ISC to the DSC (fig.16);

The comparative analysis it underlines the elaboration correctness of the DSC specific models.

Conclusions

The used DSC in electrical traction it supposes three different configurations corresponding to a three stator frequency domains. For all these configurations they have been achieved the mathematical models of the component blocks, and they have been built structural diagrams for:

- DSC in the high speed domain (weakening field)
- DSC in the medium speed domain
- ISC in the low speed domain.

The obtained structural diagrams permit a immediate implementation into a simulation soft like MATLAB-SIMULINK, being thus usefully at the study through

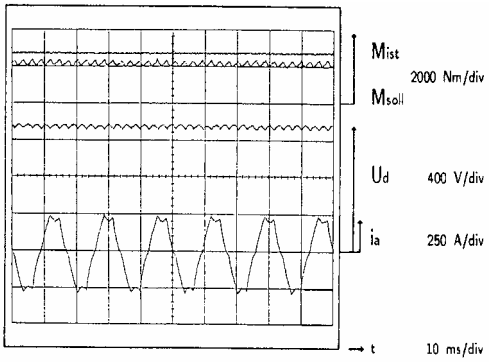

a) experimental [5]

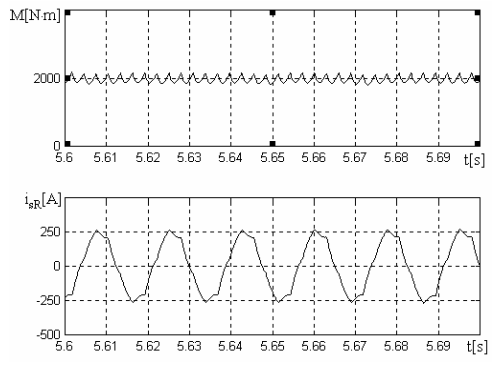

b) simulation [1]

Fig.14. Torque and phase current of traction induction motor at DSC in high speeds domain (DSC-W)

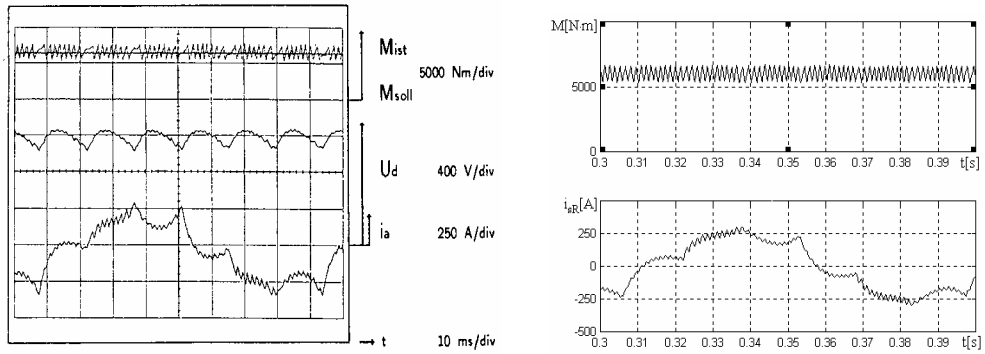

a) experimental[5] *b) simulation [1]*

Fig.15. Torque and phase current of traction induction motor at DSC

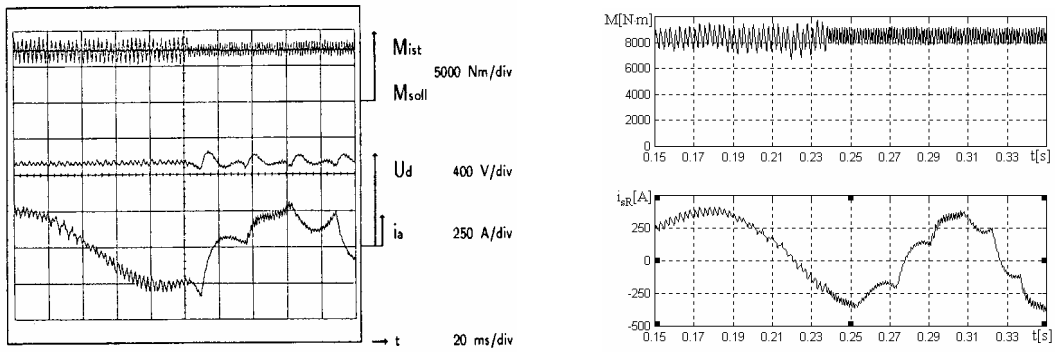

a) experimental [5] *b) simulation [1]*

Fig.16. Torque and phase current of traction induction motor at passing from ISC to DSC

simulation of phenomenons from electrical traction.

On the structural diagrams basis of DSC they have been created the SIMULINK models for:

- the ISC without the model consideration associated the voltage-source inverter and
- the DSC with all those three its configurations, the selection it is made automatically depending on the traction induction motor speed.

By means of these models they have achieved simulations which they have been praised the specific features of this control type used in electrical traction. Through the comparison with experimental results it has been validated the used models achievement correctness.

The presented SIMULINK models can be usefully within the framework of simulations by hardware-in-the-loop type, too, permitting the study through simulation of a new control strategies how they would be those based on the ISC [3], [8].

References

[1] Cismaru, D.C. Modelarea şi simularea acționărilor cu motoare asincrone specifice trenurilor de mare viteză. Ph.D Thesis, Electromechanical Faculty, University of Craiova, 2003.

[2] Depenbrock, M. Direct Self - Control (DSC) of Inverter - Fed Induction Machine. IEEE Transactions of Power Electronics, 1988, Vol.3, No.4.

[3] Hoffmann, J., M. Jänecke. Fast Torque Control of an IGBT - Inverter - Fed Three-Phase A.C. Drive in the Whole Speed Range - Experimental Results, EPE, Sevilia, 1995.

[4] Jänecke,M., R. Kremer, G. Steuerwald. Direct Self - Control (DSC), a Novel Method of Controlling Asynchronous Machines in Traction Applications, EPE, Aachen, 1989.

[5] Jänecke,M. Die Direkte Selbstregelung bei Anwendung im Traktionsbereich, VDI-Verlag GmbH, Düsserdorf, 1992.

[6] Nicola,D.A. Transformatoare electrice. Maşini asincrone . Ed. Sitech, Craiova, 1998.

[7] Nicola, D.A., D.C. Cismaru. Modelling of Voltage-Source Inverter and Traction Induction Motor Used on Electrical Vehicles, SIELMEN'03, Chisinău, 2003.

[8] Steimel,A. Control of the Induction Machine in Traction. EB, 12/1998.

Daniel Cristian Cismaru *- Lecturer, Dr., Electromechanical Faculty,University of Craiova, Bd. Decebal, Nr.5, Craiova, ROMANIA, e-mail: dcismaru@em.ucv.ro*

Doru Adrian Nicola *- Professor, Dr., Electromechanical Faculty, University of Craiova, Bd. Decebal, Nr.5, Craiova, ROMANIA, e-mail: dnicola@em.ucv.ro.*

Aida Cornelia Bulucea *- Associate Professor, Dr., Electromechanical Faculty, University of Craiova, Bd. Decebal, Nr.5, Craiova, ROMANIA, e-mail: abulucea@em.ucv.ro.*

THE INTELLIGENT DRIVE FOR PERMANENT MAGNET AC MOTORS

Eleonora Darie, Emanuel Darie

Abstract: *The work presents an intelligent control scheme for magnet AC motors with a minimum number of sensors. The scheme includes two principal sections: the rotor position estimation algorithm and the current and voltage reconstruction. In the scheme, only one current sensor is required to measure the DC link current of the inverter.*

Keywords: *modeling, reluctance motor, intelligent drive.*

Introduction

The permanent magnet AC motors have a wide range of applications because of their high efficiency, high power density and easy controllability. In order to control such motors, however, their rotor position must be known and the accuracy of motor data primarily depends upon the type of the motor used. The permanent magnet AC motors belong to the family of the synchronous AC machines and so that the constant torque can be produced only when the winding currents are precisely synchronized with the induced voltages, which can be determined from the instantaneous rotor position.

The motors are powered via the three-phase inverters that ensure the synchronization of the current, which generates switching states from the rotor position data. The conventional way of measuring the rotor position data involves some form shaft-mounted sensing devices, such Hall-Effect devices, and resolves, absolute or incremental encoders. However, these mechanical shaft-mounted position sensors have many drawbacks and therefore, their applications could be restricted.

A number of indirect rotor position detection schemes for permanent magnet AC motors has been suggested in the recent years. The expected benefits of these indirect techniques are: elimination of the electrical connections of sensors, reduced size, no maintenance, unsusceptible to the environmental factors, increased reliability and above all these, operating at zero, low and higher speeds. However, most of the indirect position detection techniques have problems when they are used in real-time system, especially at the low and zero speed range. Moreover, in order to extract the rotor position information, the earlier schemes require at least four or more voltage and current sensors in total. The current information in the drive is used to accomplish the current control loop. However, the voltage and current sensors are expensive mainly due the requirements for the isolation. Therefore, employing minimum number of sensors, which also increase the reliability of the system.

Position estimation

In the permanent magnet AC motors with trapezoidal back electromotive force (e.m.f.), the rotor position information is needed every 60^0 electrical interval to achieve the current commutation and hence the self-synchronization. Several rotor position estimation methods for such motors have been proposed in the references [1-4], which are based on the back e.m.f. sensing or the conducting states of the freewheeling inverter diodes. However, all of the methods proposed so far ultimately fail at low and zero speed due to the absence of the measurable signal, back e.m.f.

In the permanent magnet AC motors with sinusoidal back e.m.f. however, the continuous rotor position data is required. Furthermore, the continuous rotor potion information can be used to eliminate the torque ripple, which occur in the practical motor drives. A number of rotor position elimination techniques have also been reported for such motors. Some of the rotor position estimate techniques are based on the vector principle of AC motors. However, the accuracy of the measured voltages and the currents and the accurate knowledge of the motor parameters are necessary in these algorithms. Moreover, the reported methods suffer at low speeds require extensive computational power.

Other rotor position estimation techniques are based on the flux linkages, which can be obtained from the stator voltages and the currents of the motors. The flux linkage based methods operate accurately over a wide speed range and can be applied to the permanent magnet AC motors with trapezoidal and the sinusoidal back e.m.f. However, the performance of the position estimation depends very much on the quality and the accuracy of the estimated flux linkages. The motor parameter variation also affects the accuracy of the estimated rotor position in these methods.

From the mathematical model of the permanent magnet AC motors, on can be observed that that the back e.m.f. or flux linkage varies as a function of the rotor position only. Therefore, if these quantities are measured or estimated, the rotor position information can be determined. From the mathematical model of the permanent magnet AC motors, the per-phase voltage equation of the star-connected the permanent magnet AC motor can be given by:

$$v = R\,i + L\frac{di}{dt} + e\,, \qquad (1)$$

where v is the phase voltage; R is the winding resistance, i am the line current; L is the equivalent winding inductance and e is the back e.m.f. The back e.m.f., e is a function of the rotor's angular speed and the position, can be expressed as:

$$e = k_e\, \omega_r\, e(\theta_e) = \frac{k_e\, e(\theta_e)}{p} \cdot \frac{d\theta_e}{dt} \quad (2)$$

where: k_e is the back e.m.f. constant; ω_r is the rotor's angular speed; $e(\theta_e)$ is the back e.m.f. Function varies with rotor position; (θ_e) is the electrical rotor position and p is the number of pole pairs in the motor. Substituting equation (2) in (1), the increment of the rotor position within each time step can be calculated by:

$$\Delta\theta_e = \frac{(V - Ri)\Delta t - L\Delta i}{k_e \cdot e(\theta_e)} \cdot p\,. \quad (3)$$

Hence, an incremental algorithm as given below can estimate the rotor position.

$$\theta_e(k) = \theta_e(k-1) + \Delta\theta_e \quad (4)$$

If the parameters p, R, L, k_e and the function $e(\theta_e)$ are known, the rotor position θ_e can be calculated by using the data of the voltage and the current of the motor.

The algorithm is simple and easy to implement in real-time, due the less mathematical computations. The method can operate at very low operating speeds and even at zero speed. If the initial value of the rotor position has in error, it can be corrected within a short time and accurate rotor position information can be obtained. Finally, the method does not dependent upon the shape of the back e.m.f. and hence can be applied to the types of the permanent magnet AC motors.

The Voltage and the current reconstruction in the drive

In order to control the permanent magnet AC motor, it is necessary to know all of the three line currents for the current control and/or the rotor position rotor estimation. The conventional method of obtaining the line currents in the practical drive is to measure them directly. Depending upon the winding connections of the motor, at least two current sensors are needed, as in the star connected motor. However, the current sensors are usually expensive due to the requirements of the high frequency bandwidths and the electrical isolation. Measuring can reduce the number of current sensors only the DC link current of the inverter and reconstructing the three-phase line currents from the measurement. Two current reconstruction methods have already been reported in the literature [1], [2], [3].

The current and the voltage reconstruction method are based on the model of the permanent magnet AC motor drive. The switching controls signals (a three-phase inverter consisting six switching devices and six diodes can create seventy-two possible switching states), the rotor position and the speed of the motor are used in the state observer that estimates not only the three-phase currents but also the three-phase voltages of the motor. The output of the observer is the estimated DC link current, which is reconstructed from the switching control signals and the estimated three-phase currents. The estimated DC link current and the measured DC link current are subtracted to generate an error term that can be used to correct the estimated voltages and the currents. Hence the observer can not only estimate the voltages and the currents accurately at any operation condition but also compensate the parameter variations in the motor.

The complete intelligent drive system

The complete motor drive consists of the rotor position estimator and the current/voltage reconstruction sections. Figure 1 shows the block diagram of the drive system. If the DC link voltage of the inverter is constant, the drive requires only one current sensor that is used to measure the DC link. As explained above, the state observer estimates the phase currents of the motor from the switching control signals, the rotor position and the speed. The estimated three-phase currents reconstruct the DC link current by using the switching control signals. Then the error between the reconstructed DC links current is used to correct the estimated voltages and the currents in the drive. Using these estimated voltages and currents, the rotor position and the speed could be predicted from equations (1) - (4). The predicted rotor position and the speed data are fed back to the state observer for the conventional control purposes, in the reference current generator and in the current controller (hysteretic or PWM). In order to demonstrate the validity of the method, a complete drive simulation is implemented. On used the soft Lab VIEW. Figures 2, 3 show the simulated results of the current reconstruction for the two types of the motor drives, with trapezoidal (BTPM) and sinusoidal (BSPM) back e.m.f. respectively.

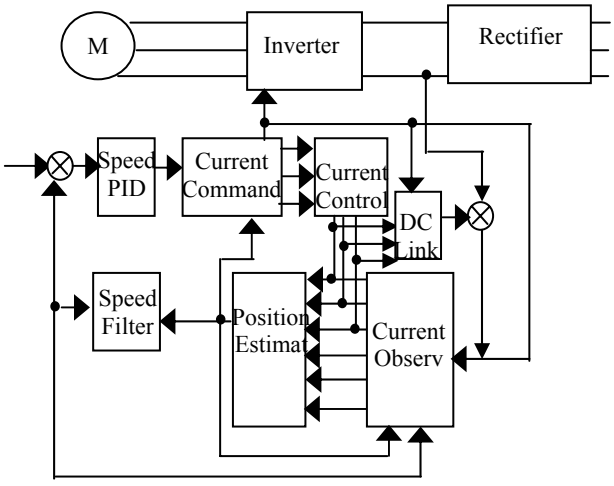

Fig.1. The complete block diagram of the intelligent motor drive system.

On observe from figures 2 and 3 that the reconstructed currents follow the actual phase currents accurately in both types of motors and under and under two typical current control mode (with and without current control). The results demonstrate that the motor parameter variations can be compensated in the state observer.

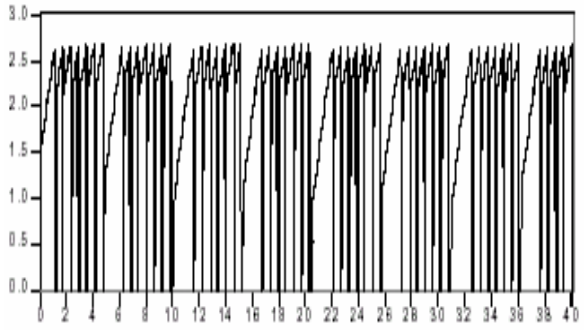

a)

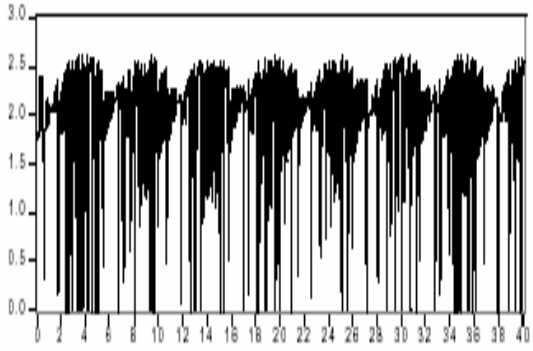

b)

Fig. 2. *The estimated steady-state current waveforms in the drive with a current control: DC link, reconstructed current of Phase 1, actual current of Phase 1 a) BTPM motor, b) BSPM motor.*

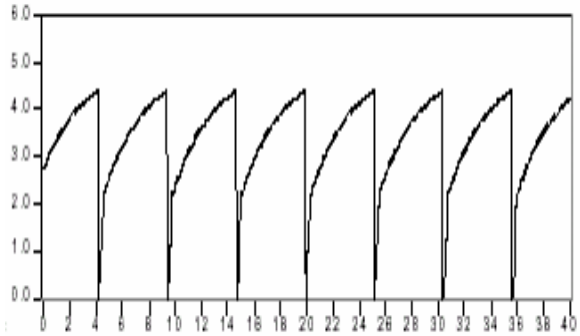

a)

Fig. 3. *The estimated steady-state current waveforms in the drive without a current control: DC link, reconstructed current of Phase 1, actual current of Phase 1 a) BTPM motor, b) BSPM motor.*

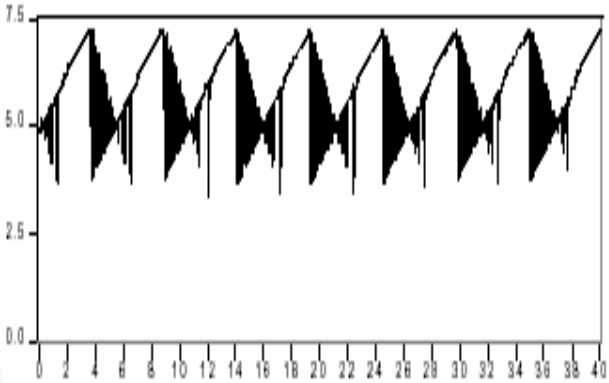

Fig. 3. b)

Conclusions

The algorithm relies on the phase voltages and the currents of the motor drive, which both are reconstructed from the measured DC link current and the switching control signals of the inverter. The state observer does not require any modification in the algorithm even if the motor type or the excitation mode is altered. The identical algorithms are used in the state observer controlling the motors with trapezoidal or sinusoidal back e.m.f.

Permanent magnet AC motors have a wide range of applications because of their high efficiency, high power density and easy controllability. In order to control such motors, however, their rotor position must be known and the accuracy of the rotor position data primarily depend upon the type of the motor.

Acknowledgements

The authors would like to thank for many helpful comments and suggestions aimed this work.

References

[1] Acarnely P.P., Eng. C. Current measurement in the three phases Brushes DC drives, IEEE Proceedings-B, 1993, Vol. 1, pp. 71-79.

[2] Acarnely P.P. Operability Criteria for Winding Currents in the three phases Brushes DC drives, IEEE Transactions on Power Electronics, 1993, Vol. 8, pp. 264-270.

[3] French C, Acarnely P.P. Direct Torque Control of Permanent Magnet Drives, IEEE Transactions on Industry Applications, 1996, pp. 1080-1088.

[4] Ogasawa S., Agagi H. An Approach to Position Sensorless for Brushes DC Motor, IEEE Transactions on Industry Applications, 1991, pp. 928-933.

Eleonora Darie *– Ph. D., Technical University of Civil Engineering, Pache Protopopescu 66 Str., Bucharest, Romania.*

e-mail: eleonora_darie@yahoo.com.

Emanuel Darie *– Ph. D., Police Academy, Privighetorilor 1-2 Str., Bucharest, Romania.*

e-mail: edarie@yahoo.com.

Galvanomagnetic Antilock Braking System

Nikola Draganov, Anatolij Alexandrov

Abstract: *The braking system is one of the most important systems providing the security of the motorcar during motion. The various modifications of antilock braking systems have the same operation algorithm embedded in them, which allows the regulation of the stopping wheels slip within a narrow range. In view of the importance of the antilock braking system for the motorcar, as well as the advantages of magneto-sensitive integrated circuits, an electronic galvanomagnetic antilock braking system has been developed, based on specialized integrated circuits MLX1881 and LM2917. The paper examines its block diagram and conceptual electric circuit. It also describes its operation algorithm and time charts.*

Keywords: *antilock braking system, magneto-sensitive integrated circuit, frequency-to-voltage converter, MOS technology*

Introduction

Locking the motorcar wheels in the course of stopping is highly undesirable, since this increases the braking distance, and along with this, the probability of skidding. The antilock system prevents the wheel lock in the case of a sudden stop, thanks to which the motorcar remains entirely controllable.

The main objective of the antilock braking system (ABS) is to maintain such a brake torque during stopping that would prevent the possibility of wheel lock, regardless of the road surfacing state, and provide the optimum braking.

The aim of the present work is synthesizing an electronic galvanomagnetic antilock braking system based on magneto-sensitive integrated circuits, taking into account their advantages and characteristic features, namely, stable transfer characteristics, temperature stability and small dimensions.

Presentation

In order to maintain the required brake torque, the ABS has to automatically change the pressure in the braking actuators, depending on the way the rotation frequency of the wheels being stopped varies. Moreover, it is necessary to provide high speed of pressure regulation, which is achieved by using high-speed pressure modulators.

The information about the wheel rotation speed is reported in most of the commonly used modifications of ABS by means of magnetic induction sensors, which determine the accuracy of the brake torque control. In view of the advantages of magneto-sensitive elements and their wide application in motorcar engineering, introducing them in braking systems increases their efficiency.

The development of the monolithic silicon IC technology makes it possible to implement the magneto-sensitive element and the electronic analogue or digital circuit on a single chip. Integrated circuits containing a Hall element have a number of advantages compared to circuits made with a discrete Hall sensor and an electronic circuit in either discrete or integral version. The most important of these are: high reliability; good temperature stability, high value of the output signal; small dimensions; economic efficiency[3, 4, 5, 6].

The new ABS has been synthesized applying a magneto-sensitive integrated circuit MLX 1881, with a Hall element, which is widely used in electronics.

The block diagram of the device is shown in Fig.1. It consists of five galvanomagnetic digital-to-analogue converters (GMDAC), a control unit (CU) and a power supply unit (power supply).

The galvanomagnetic digital-to-analogue converters have been synthesized on the basis of a magneto-sensitive integrated circuit MLX1881 manufactured by *Melexis* and an integral frequency-to-voltage converter LM2917 manufactured by *National Semiconductor*. Using these units, the rotation frequency of the motorcar wheels is monitored and converted, proportionally to the change in output voltage. The GMDAC entirely replaces the sensors for monitoring the rotation frequency of motorcar wheels that have been in common use so far.

In a GMDAC the rotation frequency is monitored by means of a magneto-sensitive integrated circuit MLX1881. Developed using MOS technology, it is capable of detecting magnetic fields with a minimum strength B_{min}=5mT. This allows it to be built in various motorcar systems. As a result of the wheel rotation, the magneto-sensitive integrated circuit (MSIC) generates a pulse series having a frequency proportional to the wheel rotation frequency. Using the frequency-to-voltage converter, the pulse series from the MSIC is converted into a proportionally varying voltage. The stable and linear conversion characteristics of the MSIC MLX1881 and of the

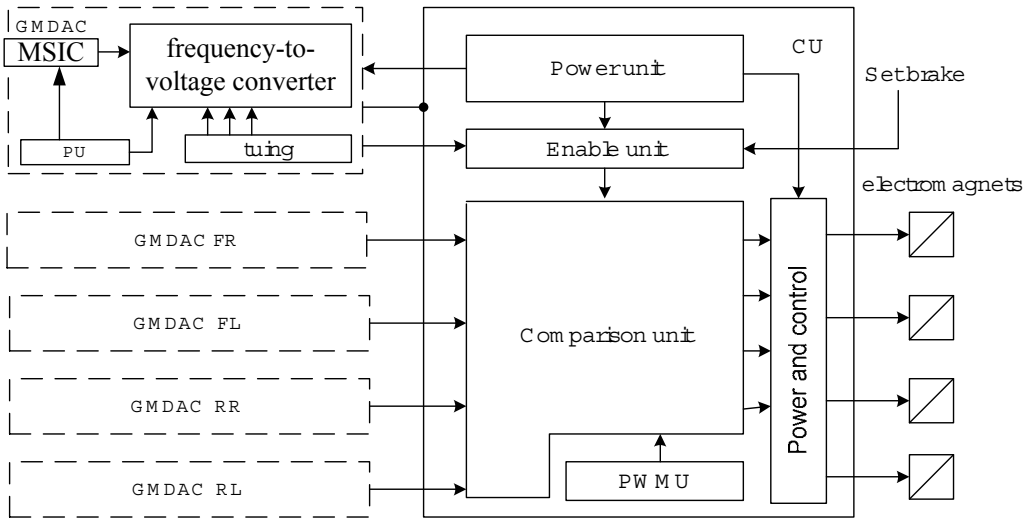

Fig. 1 Block diagram of a galvanomagnetic antilock braking system

integral converter LM2917 enable the precise monitoring of the wheel rotation frequency.

The parameters exhibited by the GMDAC, obtained after investigating it, are as follows: maximum reporting frequency f_{max}=850*Hz*, maximum output voltage for frequency f=850*Hz* and supply voltage U_{DD}=12*V* – U_{0max}=12*V*, current consumption for f=850*Hz* and U_{DD}=12*V* - I_{DD}=0,5*A*.

The control unit consists of an enabling unit (EU), a comparison and processing unit (CPU) and a power unit (PU) [1, 2].

The manner in which the system is controlled is specified in the control unit. Depending on that, the type of circuit solutions for the control unit and the power supply unit is determined. In this specific case the control is to be performed by means of pulse-width modulation of the control signal, which ensures smoothness of the characteristics and ease of implementation.

The conceptual electric circuit of the galvanomagnetic antilock braking system is shown in Fig.2, while the time charts describing its operation principle are presented in Fig.3.

When the motorcar is started, the system is supplied with a power equal to the battery supply. The operation enabling system, composed of the comparator IC5.1 and analogue switches IC4.1, IC4.2 and IC4.3, is actuated. When the motorcar drives off, due to the rotation of the information gear placed in the gearbox, the MSIC (IC1) starts generating a pulse series having a frequency proportional to the motorcar travel speed. The generated pulse series enters at the frequency-to-voltage converter (IC2) input, where it is converted into voltage level. By means of the potentiometer-type voltage divider (R4, R5) and the trimmer potentiometer PR1 the voltage level enters at the inverting input of the comparator IC5.1. An assigning voltage level from the potentiometer-type voltage divider (R6, R7) enters at the other input of the same comparator. When the motorcar speed increases, the voltage across the comparator input IC5.1 (Up2, Fig.3a) rises, and as soon as it exceeds the signal of the inverting input at the comparator output, a high level is fed to the analogue switch (IC4.1). This level sets the ABS into a stand-by mode.

Each of the four motorcar wheels has a GMDAC mounted to it, which monitors their rotation frequency during stopping. After the brake is actuated, any of the wheels is likely to lock. In this situation its rotation speed falls, which is sensed by a fall in the voltage level at its GMDAC output (Up3, Fig.3a). This signal is passed to the non-inverting input of the comparator IC3.1, while a signal (Up2, Fig.3a) from the GMDAC mounted on the gearbox is passed to its inverting input. The dynamic comparison of the two levels at the comparator IC3.1.output results in the generation of a voltage signal having an amplitude proportional to the difference between the signal showing the motorcar speed and the signal reporting the wheel speed (Up4, Fig.3б). The resultant signal is passed to the non-inverting input of comparator IC3.2, while the signal (Up5, Fig.3b) passed to the inverting input of the same comparator comes from the generator of linearly varying voltage, which is composed of integrated circuit IC5.2, resistors R20, R21, R22, R23

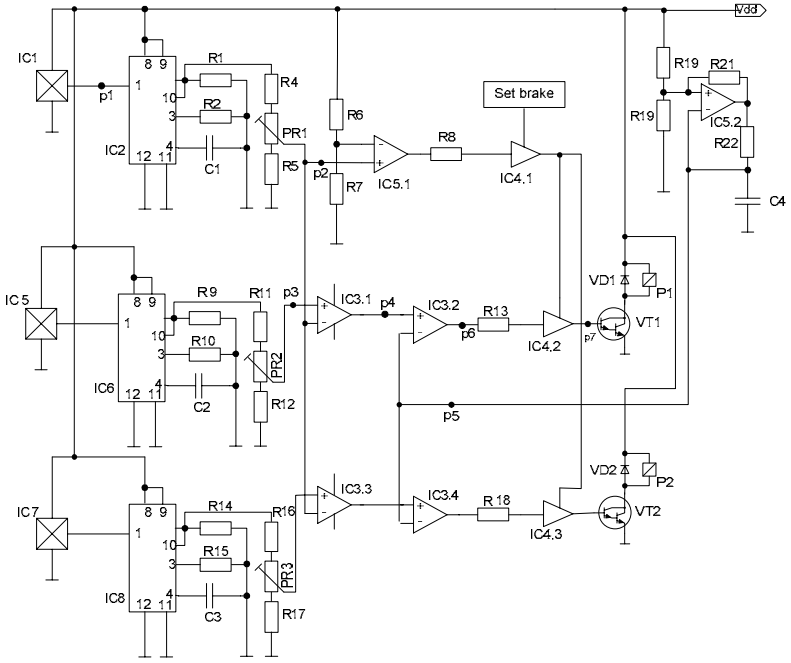

Fig.2 Conceptual electric circuit of a galvanomagnetic antilock braking system

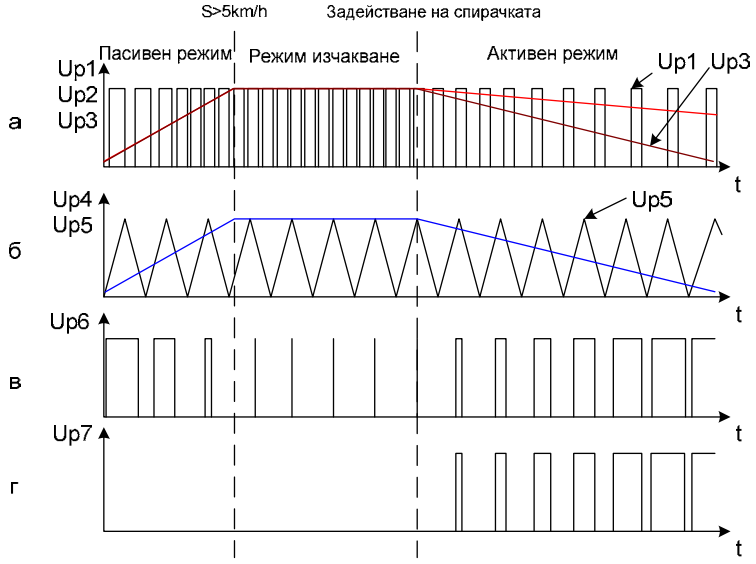

Fig.3 Time charts describing the operation of the galvanomagnetic antilock braking system

and capacitor C4. In this way a pulse series having a variable mark-to-space ratio is generated at the comparator IC3.2 output (Up6, Fig.3c). Thus, when the wheel rotation speed begins to fall sharply, the pulse width rises; therefore the brake torque will also fall so as not to lock the wheel.

The transistor VT1 controls the electromagnetic voltage modulator just at the time of pressing the brake pedal. This means that the system operates continuously, but only performs slip regulation at the time of brake actuation (Up7, Fig.3d).

It has been found out that:

1) The galvanomagnetic antilock braking system presented here has three operation modes:

- passive mode – when the motorcar speed is below the speed assigned;
- stand-by mode – when the motorcar speed is above the speed assigned;
- active mode – when the motorcar speed is above the speed assigned and the brakes are actuated.

2) The functional features of the system mainly depend on the GMDAC operation, whose conversion characteristics, in an optimum operation mode, are presented in Fig. 4. The analysis done on them shows:

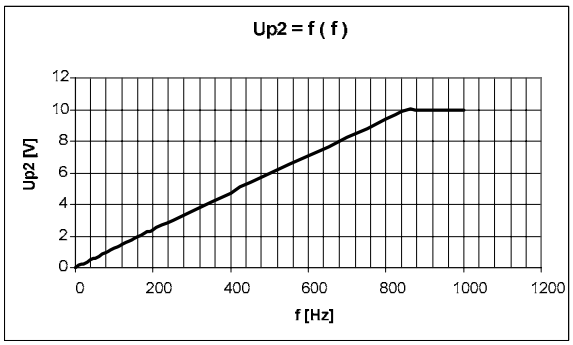

a

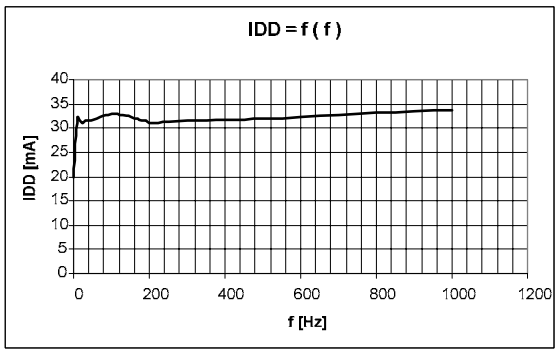

b

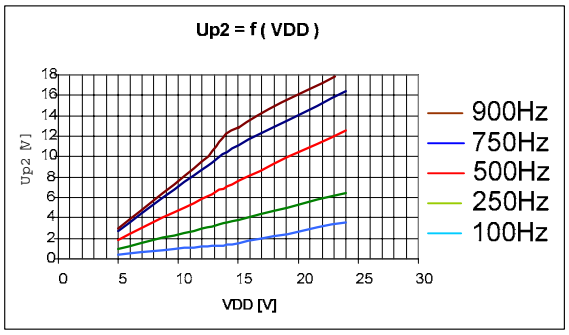

c

Fig. 4 Conversion characteristics of the galvanomagnetic digital-to-analogue converter

- The dependence Up2=F(f) (Fig. 4a), characterizing the change in the voltage across the GMDAC (Up2) output as a function of the frequency (f) of the input voltage is linear up to 850Hz, the output voltage varying from 0V to 10,2V. Above 850Hz the change in the rotation frequency of the information gear does not affect the magnitude of the output voltage and it remains equal to 10V. The transconductance over the operation range is S=850Hz/V.

- The value of the current consumption I_{DD} remains relatively constant and is within 31 ÷ 35 *mA* when the frequency varies over the range f = 10 ÷ 1000*Hz* (Fig. 4b). This is an indicator for the operation of the synthesized frequency regulator in a stationary mode.

- The characteristics $U_{P2}=F(U_{DD})$ presented in Fig. 4c exhibit the voltage variation at the GMDAC output depending on the supply voltage, in the case of input signal frequency *f*=100*Hz*; 250*Hz*; 500*Hz*; 750*Hz*; 900*Hz*, and show that regulation device sensitivity rises with the rise in frequency.

The experimental results obtained show that the galvanomagnetic regulator that has been synthesized operates steadily over the frequency range *f*=10÷850*Hz*, and its sensitivity rises with the rise in frequency.

Conclusions

1. A galvanomagnetic braking system has been developed based on a magneto-sensitive integrated circuit MLX 1881 manufactured by *Melexis* and an integral frequency-to-voltage converter LM 2917 manufactured by *National Semiconductor*. The system block diagram and its conceptual electric circuit have been elaborated. Time charts are presented, which describe its operation.

2. The galvanomagnetic antilock braking system synthesized has actuation time shorter than the time of setting the electromagnetic voltage modulator into motion, due to the dynamic nature of operation in a stand-by mode.

3. The system developed is capable of smooth regulation (modulation) of the slip torque, as a result of the introduction of pulse-width modulation of the electromagnetic voltage modulator.

4. The galvanomagnetic braking system presented here demonstrates one specific application of digital magneto-sensitive integrated circuits.

References

[1] Aleksandrov A. T., I. S. Simeonov, „Galvanomagnetic device for measuring of electric current", Bulletin of Technical university of Gabrovo, Vol. XXIV/00.

[2] Aleksandrov A., N.Draganov, "Investigation of galvanomagnetic digital-to-analog converter", ICEST 2005.

[3] Rumenin Ch., „Multisensors for magnetic field and temperature in non-contact wattmeter", magazine „Avtomatika I informatika", number 5, 1998.

[4] Takov T., „Semi-conductors sensors ", „Technics", Sofia, 1986.

[5] Göpel W., J. Hesse, J. N. Zemel, SENSORS, A Comprehensive Survey Vol. 1, "Fundamentals and General Aspects", VCH, Weinheim, 1989.

[6] Göpel W., J. Hesse, J. N. Zemel, SENSORS, A Comprehensive Survey Vol. 5, "Magnetic Sensors", VCH, Weinheim, 1989.

Anatolii Aleksandrov *– Associate Professor, Dr., Faculty of Electrical Engineering and Electronics, Department of Electronic, Technical University of Gabrovo, Hadgi Dimitar Str. 4, 5300 Gabrovo, BULGARIA.*
e-mail: alex@tugab.bg

Nikola Draganov *– Ph.D. Student, Faculty of Electrical Engineering and Electronics, Department of Electronic, Technical University of Gabrovo, Hadgi Dimitar Str. 4, 5300 Gabrovo, BULGARIA.*
e-mail: nikola_draganov@mail.bg.

Modular Framework for Electrical Drives Analysis; a Petri Nets Approach

Mircea Adrian Drighiciu

Abstract: *In many cases, an electrical drive structure can be considered such a hybrid system, defined as a mixture of continuous and discrete event systems. In this paper, an electrical drive system is considered such hybrid structure, which can change its behavior in response to generic and non – generic events. A Petri Nets approach for system modeling and analysis is presented, with several applications, explanations and comments concerning a modular hierarchical structure of the models.*

Keywords*: Hybrid Systems, Electrical Drives, Hybrid Petri Nets, Object Nets.*

Introduction

Hybrid systems have known recently considerable attention and many developments regarding their modeling and control have appeared in the literature. The most usual paradigm of a hybrid system is a supervisory control architecture, whose fundamental structure consists of a high level (supervision) where a discrete – event system models decision making, and a low level (process) where a continuous system models the process and its local control loops. The role of the supervisor model is to describe the transitions between the macro – states, which consist of the states of the continuous and the discrete – event system [2], [3], [4], [5], [6].

The behavior of the system between its states (the passage from an old to a new operating regime) is induced by the occurrence of the external asynchronous events. The higher level of the whole model treats all sequences of events (starts and ends of operations, occurrences of the unforeseen situations, internal or external disturbances etc.) without complete information regarding the evolution of the process in the elapsed time between events. The supervisory reacts to the state of the pant as perceived by it, issues commands and communicates them to the lower level. This kind of intervention may create problems in the operation of the continuous system, including deterioration of performances, even an approach to regions of instability.

For our studies, the basic idea was to consider a general hybrid structure (i.e. an DC electrical drive) such a continuous system, which can change its behavior in response to generic events (created when the state variable reaches specific values and integrated by the feeding back into the continuous system) and non – generic events (external events from the outside of the system and possible generic events of other systems). Thus, it is advantageous, if not indispensable, to be able to represent both continuous and discrete parts of the hybrid system in the same context, by a unique formalism, as far as possible [3], [4], [5], [6], [9].

In order to do the framework for hybrid systems, different approaches of modeling are used and at present is already an abundance of such paradigms, including Petri nets. Having a dual nature of a graphical tool and a mathematical object they can serve in both the theoretical and practical applications. At present, these models are frequently used for real time control and performance evaluation in a hybrid context and have become a favorite topic for the dynamic analysis of automation and production in modern technology. In this context, developed by David and Alla in the 1990s, Continuous Petri Nets, Hybrid Petri Nets and their numerous extensions, offer powerful concepts and formal techniques for expressing fundamental discrete events and continuous time behavior [2], [3], [4], [5].

Review on Hybrid Petri Nets

In a discrete Petri net, the marking of a place may correspond either to the Boolean state of a device (for example an motor is turned on or off), or to an integer (for example the number of parts in a conveyor input buffer). A general analysis method is to compute the set of reachable states and deduce the different properties of the system. But when a Petri net contains a large number of tokens, the number of reachable states explodes and this is a practical limitation of the use of Petri nets. This observation led us to define continuous and hybrid Petri nets.

An autonomous Hybrid Petri Net (HPN) [3], [5], [8] is a sextuple $Q = \{P, T, Pre, Post, \mathbf{m}_0, h\}$ such that: $P = \{P_1, P_2, \ldots P_n\}$ is a finite, not empty, set of places; $T = \{T_1, T_2, \ldots, T_m\}$ is a finite, not empty, set of transitions; $P \cap T = \varnothing$ (P and T are disjointed); h, called "hybrid function" indicates for every node whether it is a discrete node or a continuous node; Pre : $P \times T \rightarrow R^+$ or N^+, is the input incidence mapping; Post : $P \times T \rightarrow R^+$ or N^+, is he output incidence mapping $\mathbf{m}_0 : P \rightarrow R^+$ or N^+, is the initial marking.

Informally, there are two parts in a hybrid Petri net, *a discrete part* and *a continuous part*, and these parts are interconnected thanks to arc linking a discrete node (place or transition) to a continuous node (transition or place), (Fig.1). In some cases, one part can influence the behavior of the other part without changing its own marking. In other cases, the firing of a D – transition can modify both the discrete and the continuous marking.

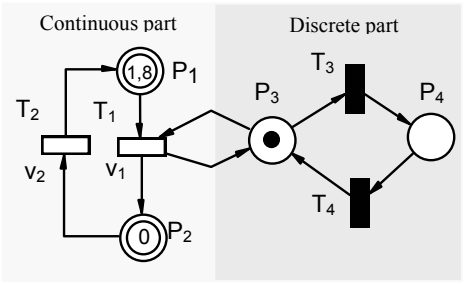

Fig.1 A Hybrid Petri Net model

The continuous places are P_1 and P_2, the continuous transitions are T_1 and T_2, the discrete places – P_3 and P_4, and the discrete transitions – T_3 and T_4. Both continuous transitions are enabled, and thus fireable. For the firing of T_1, with a firing quantity (firing speed – v_1) 0.1, the marking (1.7, 0.1, 1, 0) is obtained. A marking quantity 0.1 has been removed from P_1 and P_3, which are, input transitions, and the same quantity has been added to P_2 and P_4, which are the output transitions.

Usually, the firing speeds – associated to the continuous transitions of the net – are constants and theirs values can be the same, or different. Moreover, using basic HPN models doesn't permit to represent negative continuous variable. From their concepts and the advantages of the continuous Petri net where maximal speed can depend on time, a new class of Petri nets called Differential Petri nets has been defined [4]. Under the assumption that the continuous system can be represented by a *n* linear first order difference state equation, they are powerful enough to model in a single graph an hybrid system. An other powerful extinction of the classical structures of HPN consist by the assignation to every continuous transition a firing speed as a function, whose arguments can be the token quantities of arbitrary places of the net (Fig.2), [5], [6], [8]. The result is named *modified Petri Net*.

Here, the firing speed *v* is the speed of token flow into

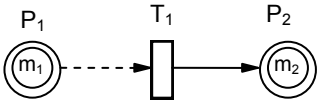

$v = f(m_1, m_2, ..., m_i, m_{i+1}, ...m_n)$

$m_1(t)$, $m_2(t)$ – quantity of tokens in P_1, P_2
$m_i(t)$, $m_{i+1}(t)$ – quantity of tokens in P_i, P_{I+1}
v – continuous transition firing speed

Fig.2 Continuous basic element of the modified net

the place P_2. The transition T_1 is always active; it can be inactivated only by the empty discrete input places. The test arc $P_1 – T_1$ does not allow token flow. This makes it possible to model subsystems without feedback: the token quantity of P_1 is not influenced [5], [6], [9]. Generally, if a single input arc is directed from P_i to P_{i+1}, the firing speed *v* is given by:

$$v = \frac{dm_{i+1}(t)}{dt} = -\frac{dm_i(t)}{dt} \quad (1)$$

For a place P_i with „ j " input arcs:

$$\dot{m}_i(t) = \frac{dm_i(t)}{dt} = \sum_j v_j \quad (2)$$

In this way, different basic elements, even non-linear coupled subsystems can be described.

Figure 3 shows such modified HPN. The continuous places are P_1 (its marking – m_1 - contains initial value of motor acceleration during starting process) and P_2 (the speed of motor, represented by the m_3 marking), the continuous transition is T_1, the discrete places P_3, P_4 and the discrete transitions - T_2, T_3.

The whole model is a synchronized HPN: the T_2 and T_3 transitions attends to be fired if those are validated and

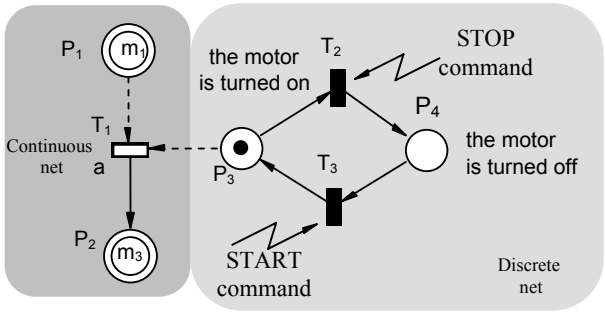

Fig.3 Hybrid Petri Net structure

only when the external associated event (START and respectively STOP commands) occurs. Also, T_1 is fired with a constant speed (authorized by the test arc $P_3 – T_1$) if the P_3 place is marked.

For the verifying of good properties of the models, algebraic techniques can be used id addition with various tools, which assures in the mean time different simulation scenarios [2], [7], [8]. Also, all proposed models can be verified comparing theirs simulation test results with others offered by the classical known programs like Matlab – Simulink, Modelica etc.

Case study

For illustrate the Petri nets paradigm in the construction methodology of the models, a DC electrical drive system was considered. Our choice was motivated by the fact that such structure is a hybrid system, also by the experimental results, which was validates the model proposed. Starting by known structure of the physical system, and using the initial linear mathematical model of the electric drive (with several usual simplifications) a basic topology of the Petri net model was constructed. Then, according with the various functional conditions of the physical system, additional structural elements was added, in aim to enhance the power of model and to obtain a modular and flexible framework – a object Petri net.

Electrical drive structure

More often, an electrical drive system is represented like a conversion chain, in which the structure composed by static converter, the acting electric engine (usually named electric motor) and the working machine is called *electrical drive* (Fig.4).

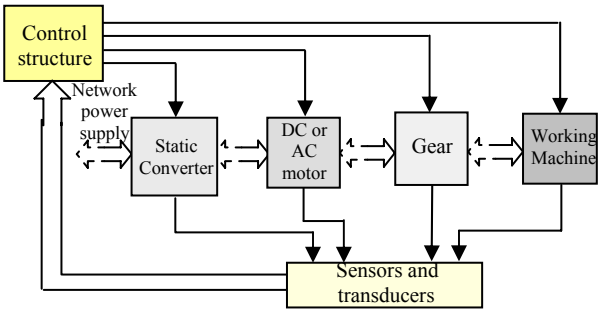

Fig.4 An electrical drive system structure

In the past decade, electric drives with electronic speed control were advantageously used in industrial applications, appliances and automotive field. The multitude of the known technological process makes that the variety of the working machines to be much more than variety of the electric motors. Taking into account the great variety of the existing working machines as well as the limited number of electric engines built with various parameters, in few cases it will be obtained the desired perfect overlapping. So it is necessary to introduce between the motor and its charge an intermediate element of adaptability, known in specialized literature as gear. This device has a double role; that of transmitting the motion and that of modifying its parameters. It does compatibility between the two elements of the system. So it could be rightly named transmitter and adapter. It has the same role of an electric transformer that performs the adaptation of the consumer to the network. Mainly it can be mechanic, hydraulic or electromagnetic, manually or automatically, adjustable or not.

It is obvious that such topology is proper to describe a hybrid and variable system structure, represented by various continuous set models, which are used successively (one or each other) for performances analysis. Thus, more particular, an electric DC drive system is possible to work loaded with rated, or greater current, obtained by the action of the static torque, in full charge - M_1 model - (the working machine WM is connected at the motor) or, if the event "disconnect the charge" occur, the behavior of motor change and the active model become M_2 (Fig.5 a. and b.).

In this way, the hybrid system will be described by continuous models (i.e. the state representation) which corresponding at the different possible structures dues at the occurrence of non – generic (external) events [8], [9]. It is know that the existing models for hybrid systems can be classified into four classes: they are automata and transition system models, dynamical system models, algebraic structure models, and programming language models. Petri Nets were also used to model hybrid systems.

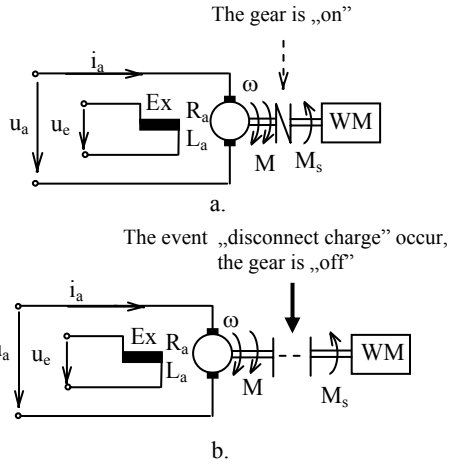

Fig.5 Explicative at the change of DC. drive structure: a) Charge connected at the output shaft; b) Charge disconnected.

Mathematical model

Usually, the initial mathematical model of an DC electric drive (Fig.5) consist of a linear equations set, which emphasizes on the one hand the system structure and stipulate the evolution rules for this one, on the other hand.

If the inductances of the armature circuits are constant values (L_a = ct., L_e = ct.), by neglecting the rotor reaction effect, also the breaking brushless voltage ($\Delta u_p = 0$), the friction in the bearings and, more over, considering that the motor is commanded by the rotor circuit (Φ = ct.), a very known mathematical model can be used [1], [8], [9]:

$$u_a = R_a \cdot i_a + L_a \frac{di_a}{dt} + e, \tag{3}$$

$$e = k_e \Phi \omega, \tag{4}$$

$$M = k_e \Phi i_a, \tag{5}$$

$$M = M_s + J \frac{d\omega}{dt} \tag{6}$$

Starting from (3)…(6) and choosing as reference the rated values of main variables, a new representation (which emphasize – at the same time – the state variables of the model) in relative coordinates is obtained:

$$u = \rho \cdot i + \rho \cdot \frac{T_a}{T_m} \cdot \frac{di}{d\tau} + \varphi \cdot \nu, \tag{7}$$

$$\varphi \cdot i = \mu_s + \frac{d\nu}{d\tau} \tag{8}$$

Between two or many stationary working regimes, the electric drive can be represented as a continuous system.

The passing from a stationary functioning point to an other is induced by occurrence of external asynchronous events (control – command signals or perturbations). In this way, input, state or output variables of the mathematical model (for a object oriented representation of the electric drive) will be associated with continuous places of Petri net model and some of mathematical model equations is possible to be considered like instantaneous firing speeds of continuous transitions. Into a modified Petri net model, by test arcs the influence of the input or perturbation variables on continuous transitions are introduced. More over, by activating at one time of some of these, the initial topology of the model is modified and the entire Petri net acquires a variable structure.

Petri net model

Considering the above and starting from a easily modification of (7) and (8) equations, the parent Petri net model of the DC motor was obtained (Fig. 6).

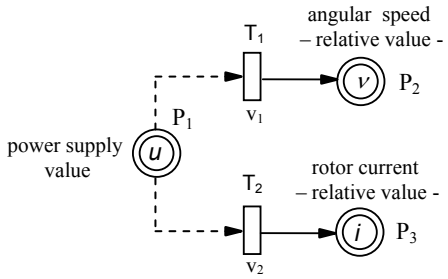

Fig.6 DC motor continuous Petri Nets model

This most simply and compact structure (the M_1 model – Fig.6) may describe the behavior of the motor without charge connected at the shaft (M_s = 0, respectively μ_s = 0). It is a modified continuous net, which its structure is identical with an other second order system; if a step command of the power supply is applied at the input (P_1 place), the continuous places P_2 and P_3 reaches during simulation the values for the state variables (the relative angular speed and the relative rotor current, respectively). This topology was obtained in the hypothesis of constant values for the electromagnetic and mechanical time constants (T_a = ct., T_m = ct.). In concordance with (1), for the firing speeds - v_1 and v_2 - of continuous T_1 and T_2 transitions was assigned respectively an expression derived in fact by (7) and (8), i.e. represented by differential equations (dependence between variables and token quantities of arbitrary places of the net):

$$\frac{di}{d\tau} = -\frac{T_m}{T_a}\cdot i - \frac{T_m}{T_a}\cdot\frac{\varphi}{\rho}\cdot \nu + \frac{T_m}{T_a}\cdot u \,, \tag{9}$$

$$\frac{d\nu}{d\tau} = \varphi \cdot i - \mu_s \tag{10}$$

Whole Petri net model structure was realized using a dedicated tool, which make possible also the analysis of the goods properties of the model via simulation (Fig.7) [7], [9], [10].

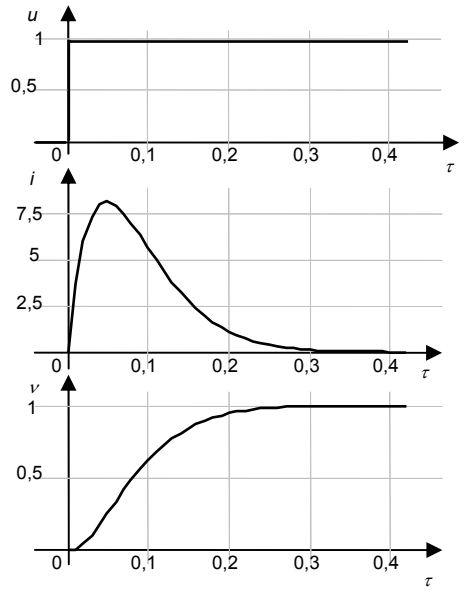

Fig.7 The results reaches by simulation during the starting process (M_s=0), for P_N = 2,64 kW, U_N = 110 V, I_N = 30 A, n_N = 1500 rpm, R_a = 0,36 ohm, L_a = 0,125 H, J = 1,2 kgm^2

The correctness of our choice in using the Peti net approach - like an alternative at different others tolls used in usual simulations scenarios for the same types of systems - to construct and analyze various models of the continuous or hybrid processes (i.e. a electric drive) was confirmed by the results of the simulation tests via the experimental results obtained on physical models Fig.8 [7],[8], [9].

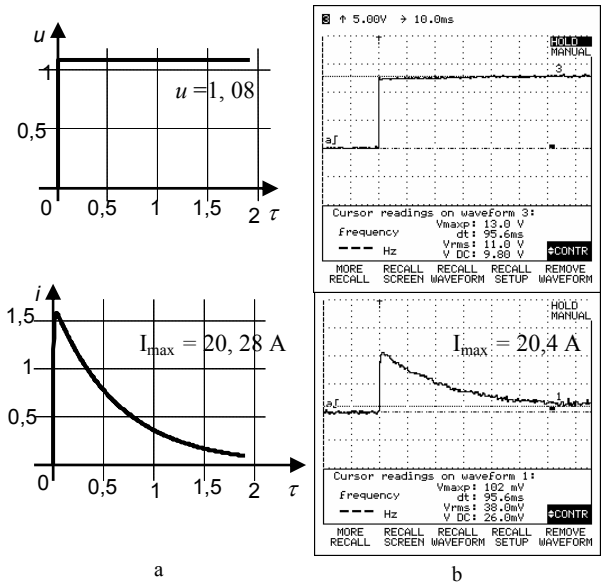

Fig. 8 The current evolution during the starting process of a real DC servo –system, for P_N = 74 W; U_N = 12 V; I_N = 13 A; n_N = 300 rpm; J = 0,0011 kgm^2; R_a = 0,6 ohmi; L_a = 0,246 mH: a) Petri net model simulation; b) Experimental results.

The basic topology of the Petri net model forms a modular structure, which can be developed by adding others functional elements, in concordance with the real physical system represented. Hence, for charge of the motor shaft subsystem, a complementary sub – net is easy to be connected, in addition as initial model. The Petri net proposed as representation is very flexible, offering at users of such techniques an immediate and useful possibility for changing the values and /or expression of the static torque at the shaft, which intervenes in the general model of the electric drive by the motion equation (6), (Fig.9) [7], [9], [10].

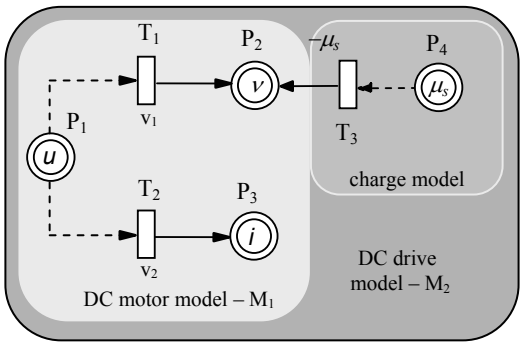

Fig.9 Continuous DC. drive model

The results of simulation tests in various working regimes are - for now – very known, but for a Petri net approaches of such hybrid structures, theses are also extremely encouraging (Fig.10).

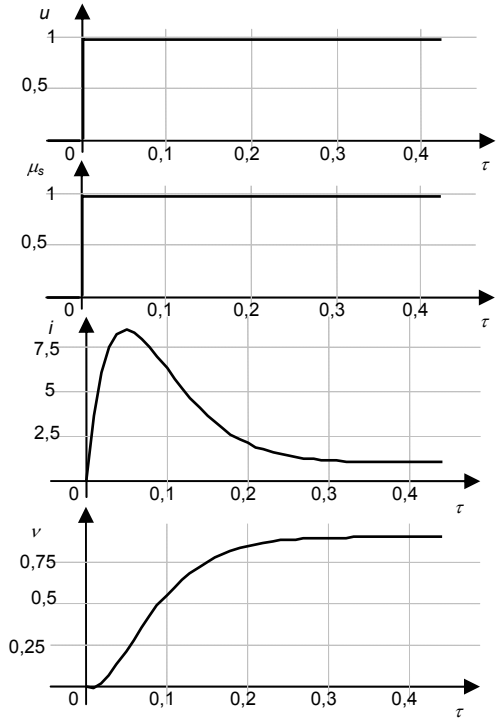

Fig.10 The evolution of main variables of the electric drive with the same values of the parameters during the starting process, in charge, with $M_s = M_N$

If the charge of motor is periodically connected and disconnected from the shaft, for such behavior representation, starting from pre-existent modular structure of the model, a hybrid Petri net was developed (Fig.11).

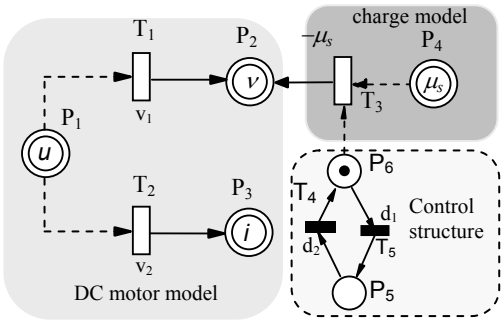

Fig.11 The Hybrid Petri net model of the electrical DC drive system.

The evolution of the system in the state space is determined by the occurrence of the external events (connect/disconnect charge), which commutes between one or other of the M_1 and M_2 models. On account of events, the hybrid system reaches a new quality and its behavior can be represented as a tree – dimensional graph (Fig.12).

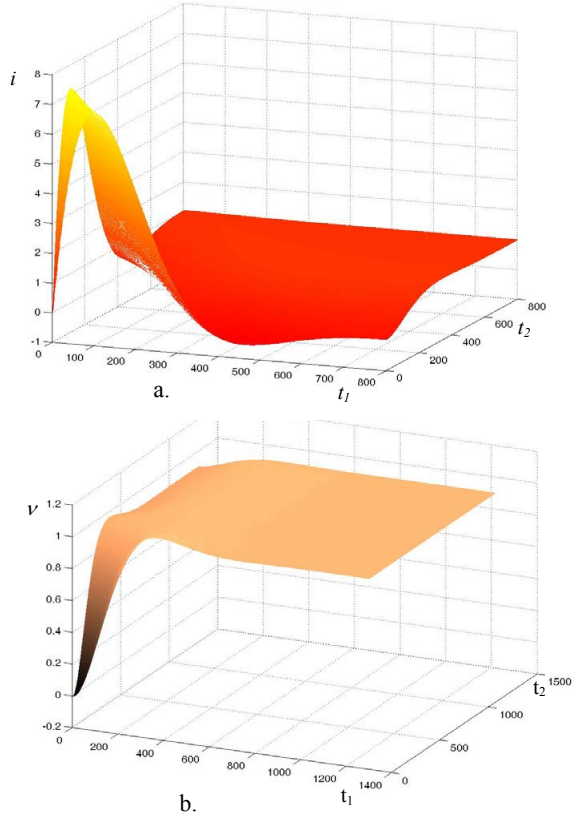

Fig.12 The reachability graphs of the hybrid system: a) rotor current; b) angular speed.

This graph (named reachability graph) describes the space of all reachable step responses of the hybrid system for arbitrary event sequences, and for various output variables.

By a easily modification of the speed associated to T_3 continuous transition (Fig.11), the model proposed can be adapted for various expressions of static torque applied at the shaft of the motor, according with the particularities of the real working process in which the electrical drive system participates.

Into a complex system, with a large topology, formed by multiple cvasi-identical dynamic sub-systems, the whole model can be composed by interconnected object sub-nets. In this way, the structure of the final Petri net model is more compact and, in the mean time, easily used for properties analysis (Fig.13). Each object net has a hierarchical multilayer structure and can be realized applying the object-oriented techniques [5], [6], [8], [11].

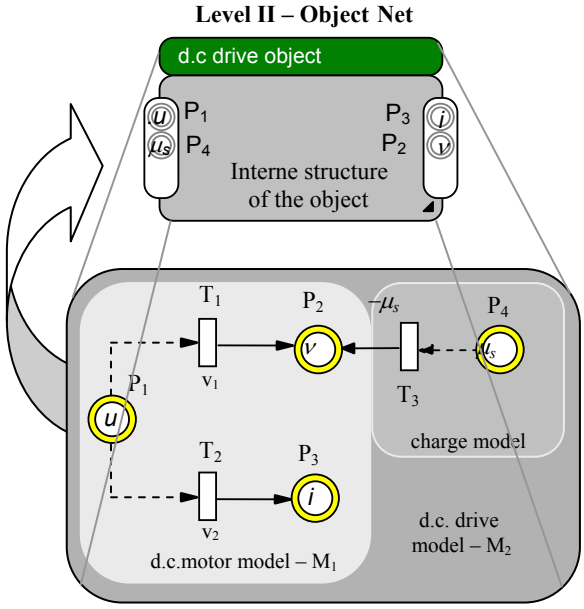

Fig.13 Hierarchical structure of the DC electric drive - object Petri Net model

Conclusions

Petri Nets are known to be powerful tools for modeling and analysis of discrete systems. The continuous and hybrid Petri Nets, extension of the basic model, allow modeling and analysis of continuous and hybrid systems on the same conceptual basis. The electrical drive systems involve both continuous and discrete variables, and their evolution is described by the combination of a continuous dynamic and a discrete one. The continuous dynamic is generally given by differential – algebraic equations and the discrete dynamic is generally modeled by automata or input – output transitions systems with a countable number of states. The paradigm of the Hybrid Petri Nets, which we are proposed is a new powerful method for analysis and our choice is motivated by the quantitative analysis facilities offered by this tool. Based on primary topology is possible to formalize the entire model by means of linear algebraic structures, then the implementation operations in various real – time command architectures may be started.

References

[1] Cantemir, L. Some principles problems concerning the electromechanical drive, Proceedings of the 9th National Conference on Electrical Drives, Craiova, 8-9 October, 1998, pp.13-19.

[2] David, R., Alla, H. Du Grafcet aux Réseaux de Petri, Hermes , Paris, 1992.

[3] David, R., Alla, H. On Hybrid Petri Nets, Discrete Event Dynamic Systems: Theory and Applications, No.11, 2001, pp.9 – 40.

[4] Demongodin, I., Koussoulas, N., T. Differential Petri nets:Representing Continuous Systems in a discrete-event world, IEEE Transaction in Automatic Control, Special Issue on Hybrid Systems, 43, 4, April 1998.

[5] Drath, R. Hybrid Object Nets: An Object Oriented Concept for Modelling Complex Hybrid Systems, Dynamical Hybrid Systems, ADPM98, Reims, 1998.

[6] Drath, R. Objektorientierte Modellierung hybrider Prozesse – Vorstellung eines neuen Werkzeuges, 42.IWK, TU Ilmenau, 1997, Bd.3, pp.533 – 540.

[7] Drath, R. Tool Visual Object Net ++, http;//www.daimi.au.dk/PetriNets/tools, section "Visual Object Net++".

[8] Drighiciu, M., A. Sur les Réseaux de Petri Hybrides, Analele Universităţii din Craiova, Seria: Inginerie Electrică, Anul 26, Nr.26, 2002, Vol. I, pp. 184 – 191.

[9] Drighiciu, M., A. A Class of Petri Nets for Hybrid Systems Representation, Analele Universităţii din Craiova, Seria Inginerie Electrică, Anul 27, Nr.27, Vol.II, 2004, pp. 63 – 68.

[10] Drighiciu M., A. Modified Hybrid Petri Nets Structure of the DC Electrical Drives, Acta Electrotehnica, Academy of Technical Sciences of Romania, Technical University of Cluj Napoca, Vol.44, No.3, 2004, pp.17 – 21.

[11] Drighiciu M., A.Petri Net Formalism for a Possible Hierarchical Structure of Complex Hybrid Systems, Proceedings of 6th International Carpathian Control Conference – ICCC 2005, Vol. II, Miskolc – Lillafured, Hungary, May 24 – 27, 2005, pp. 371 – 376.

Mircea Adrian Drighiciu *– Professor, PhD, University of Craiova, Electromechanical Engineering Faculty, Decebal Bd. No . 107, 200440, Craiova, ROMANIA. e–mail:adrighiciu@em.ucv.ro.*

Analysis, Designing, Modelling and Simulation of an Electric Driving System Equiped with Chopper Used in Electric Urban Traction

P.M. Nicolae, I.D. Nicolae, I.G. Sîrbu and V.D. Vitan

Abstract: *This paper refers to the optimal designing of a variable direct voltage regulator with IGBT on the basis of analysis, modelling and simulation of the electric driving system. The IGBT is picked out after a transient analysis using Laplace transformation, but also after the numerical simulation of IGBT operation during the conduction and blocking periods using SPICE software. Finally, the dynamic behaviour at the tram motor starting is simulated.*

Keywords: *numerical simulation, chopper, dynamic behaviour*

Introduction

The tramcars that are currently in use are not adapted to the supply line of 750 V from Craiova city. Initially designed for a direct voltage of 600 V, they are endowed with two serial direct current motors with series excitations of 300 V. Because each traction motor would have to operate to a voltage greater than the rated voltage, the solution was to introduce a series resistance in the rotoric circuit. But this solution means a low energy efficiency. Moreover, the accelerator would suffer some modifications and, in long run, some trams would be out of order due to the technical problems that appear especially in the electric driving system. Those who use these electric vehicles have often renounced to the resistance from the rotoric circuit because of the high energy consumption. This thing is reflected in the low operating time of the whole electric driving system.

A viable technical alternative is the supply of the systems through variable direct voltage regulators with IGBT components. Besides, they ensure the current control in the running and braking rates.

In order to certify that the design was made correctly, the simulation of the working rates using the designed physical parameters has often been necessary, this way avoiding the destruction of the electronic components of the designed and constructed equipment. The simulation is made in various working rates, in failure rate inclusively. That is why the numerical simulations, on the basis of the operation equations or of a specialized software (for example SPICE), are compulsory.

The Technical Solution Using Variable Direct Voltage Regulator (Chopper)

The block diagram of the motor power supply system using chopper is given in fig.1.

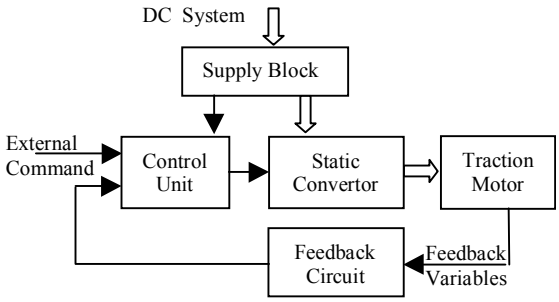

Fig.1 Block diagram of the motor power supply system

The DC motor is supplied through the static convertor from a voltage in periodical pulses. The pulse amplitude U_0 and the period T are known. Pulse width t_1 and pause duration t_2 are variable. Mean value of the supply voltage is

$$U_a = \frac{t_1}{T} \cdot U_0 . \quad (1)$$

Generally, the frequency of the voltage pulses is within the range [50…2000] Hz.

The variable direct voltage regulator can be used not only for the motor speed regulation, but also for regenerative braking, when the kinetic energy of the moving masses is turned into DC electric energy which is returned to the supply mains.

The Analysis and The Sizing of The Chopper Power Circuit

In the designing of the variable direct voltage regulator both existent supply mains parameters and traction motors parameters are considered.

Input Data

The sizing of the power circuit elements is made on the basis of the simplified equivalent scheme (fig.2).

The traction motor is a DC motor with series excitation, having the rated values: P_N=40kW, U_N=300V, I_N =140A, and starting current I_P =290A. R_m and L_m are equivalent parameters of the two series motors.

The supply voltage is U_a=750V (-30%÷+20%).

Input filter parameters are C = 1000μF, L_r = 0,6mH.

Operating frequency is f = 2kHz.

The maximum conducting period t_1 is determined imposing that the mean value of the motor terminal voltage should not to exceed its rated voltage and the mean voltage U_{med}=600V (tram supply voltage):

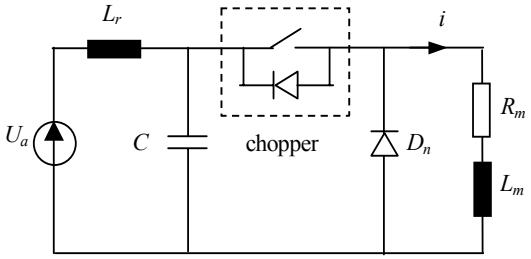

Fig.2 Simplified equivalent scheme

(2) $$T = \frac{1}{f} = 0{,}5\ ms \Rightarrow t_1 = \frac{T \cdot U_{med}}{U_a} = 4\ ms$$

The variation of the voltage mean value is determined by the variation of conducting period, while the switching period remains constant.

Mean Current Calculation through Static Convertor

The mean current through the static convertor is a fundamental criterion for IGBT module selection. In order to calculate the current mean value, one must determine the average of the current instantaneous values along a period.

During the conducting period, the system operates in a transient manner, with the following initial conditions:

a) the maximum value of the voltage across the capacitance is:

(3) $$U_{C0} = 1{,}1 \cdot U_a = 825\ V$$

b) the minimum current through L_r:

(4) $$I_{r0} = 0{,}9 \cdot I_P = 252\ A$$

c) the minimum current through L_m:

(5) $$I_{m0} = 0{,}95 \cdot I_P = 266\ A$$

These values are imposed by the limitation of the maximum ripples of the regulator input voltage, of the input current and respectively of the current through motor [5], [6].

Analysis in Transient State Using Laplace Transform

The equivalent scheme, in operational domain, for the conducting period is presented in fig.3

Solving the system written using Kirchhoff's law in operational domain, one obtains the current through motor:

(6) $$I(s) = \frac{P(s)}{Q(s)}, \quad \text{with}$$

$$P(s) = s^3 CL_m L_r I_{m0} + s^2 U_{C0} CL_r + s(L_r I_{r0} + L_m I_{m0}) + U_a$$

$$Q(s) = s[s^3 CL_m L_r + s^2 CR_m L_r + s(L_r + L_m) + R_m]$$

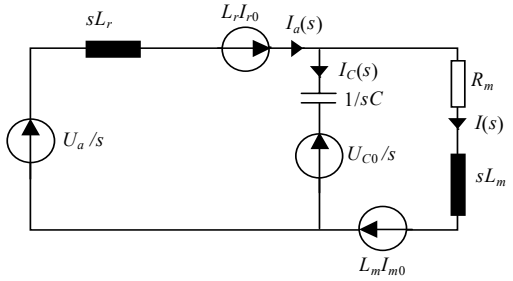

Fig.3 Equivalent scheme in operational domain

Using the above mentioned numeric data and initial conditions, this current is:

(7) $$I(s) = \frac{9{,}57 \cdot 10^{-6} s^3 + 4{,}9 \cdot 10^{-4} s^2 + 1{,}74 s + 750}{s(3{,}6 \cdot 10^{-9} s^3 + 0{,}6 \cdot 10^{-6} s^2 + 6{,}6 \cdot 10^{-3} s + 0{,}9)}$$

On the basis of Heaviside's theorems, the corresponding current in time domain is [2]:

(8) $$i(t) = 773{,}2 - 483{,}92 \cdot e^{-147t} - 23{,}84 \cdot e^{-7{,}3t} \cdot \cdot \cos(1353 \cdot t + 0{,}1076)$$

The graphical representation along a period of this function, using MATLAB, is presented in fig.4.

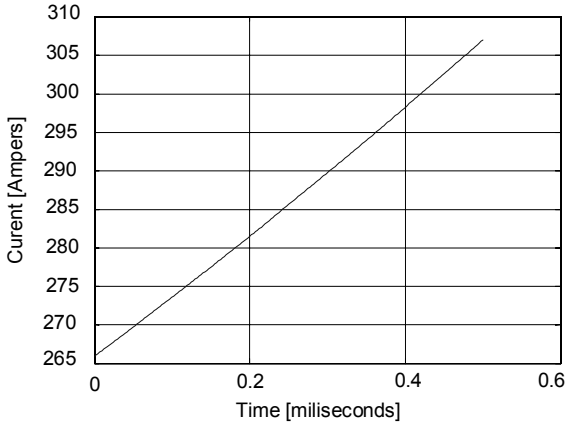

Fig.4 Current variation along the conduction period

It is noticeable that at the end of the conducting period, in the most inconvenient case (corresponding to a duration of 0,4 ms), the current does not exceed the limit required by the admissible ripple condition:

(9) $$I_{\max} = 299A \le 1{,}1 \cdot I_P$$

Numerical Simulation Using SPICE

For validation one performed the simulation along the conducting period by means of SPICE application [7] (fig.5). The simulation results, in graphic format, for the filter capacitance voltage (curve 1) and for the current through the motor (curve 2) are depicted by fig.6.

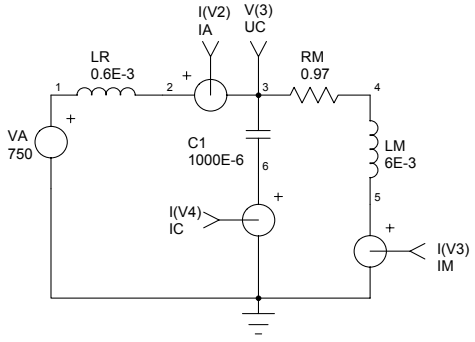

Fig.5 Equivalent SPICE *scheme along the conduction period*

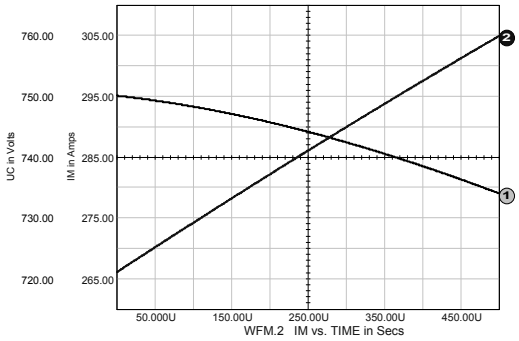

Fig.6 Simulation results along a conduction period

One observes that this result is very close to that obtained using operational method.

In a similar way, using SPICE simulation, the blocking period was analysed (fig.7,8). It comes out that in this case, both the current in the motor and the capacitance voltage are between the imposed limits, too.

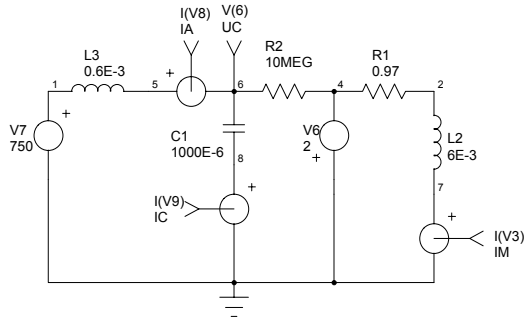

Fig.7 Equivalent scheme for the blocking period

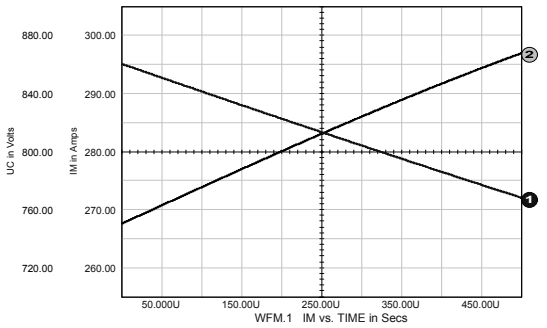

Fig.8 Simulation results along a blocking period

By making an average of the instantaneous values, a value of 283,4 A is obtained for the mean motor current and a value of 277 A for the mean chopper current. The last one is the current sizing value.

Depending on the calculated mean current and on the imposed rated voltage, a type of IGBT (the transistor with the best price-to-quality ratio) is chosen from a products catalogue. It must fulfil the conditions:

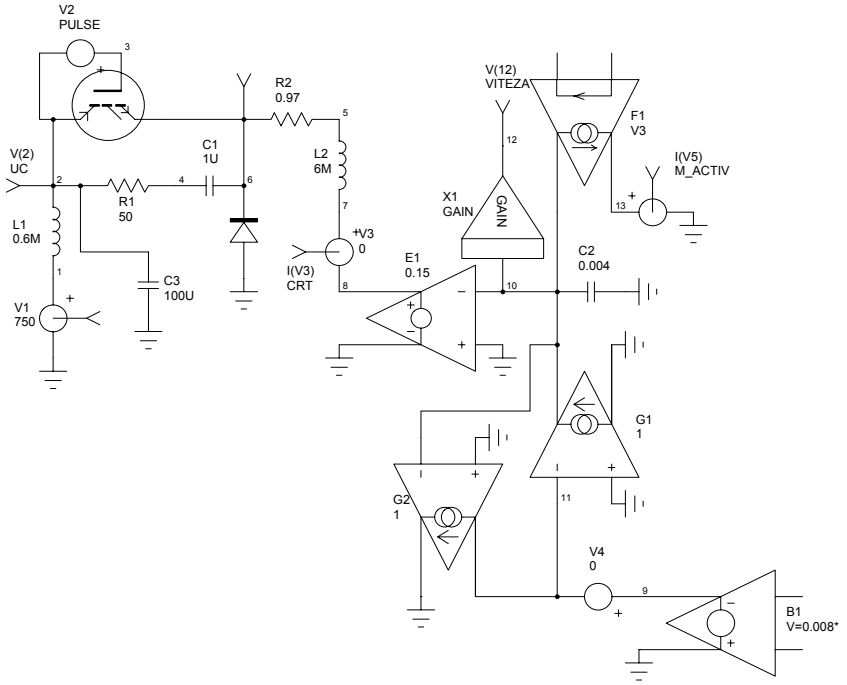

Fig.9 Modelling of the power circuit with DC motor

(10) $$I_{mean\ calculated} \le I_{mean\ catalog}$$
$$U_a \le U_{N\ catalog}$$

Numerical Simulation of The Equipment Operation

Dynamic behaviour at the vehicle motor starting was studied using numerical simulation of the power circuit (fig.9). One considers the time-variations of the load current and of the motor speed.

A model of the motor, based on the dynamic state equations [1] is used:

(11)
$$\begin{cases} u = Ri + L\dfrac{di}{dt} - e_0 \\ e_0 = -Ki\Omega \\ m = J\dfrac{d\Omega}{dt} + m_r \\ m = Ki^2 \\ m_r = f_r(\Omega) \end{cases}$$

$$R = R_a + R_e, \quad L = L_a + L_e$$

The static contactor of the voltage regulator is controlled by a source that modifies the control voltage (V2).

The simulation results are presented under two forms:

- for a duration that ensures the free components damping. Fig.10 (curve 1 – load current, curve 2 - speed) provides a general view over the operation;
- for a time positioning that is equal to a switching period (fig.11; curve 1 – IGBT control voltage, curve 2 – the current through the motor, curve 3 – input current, curve 4 – the terminal voltage of the motor). These forms offer details concerning the instantaneous values of these quantities.

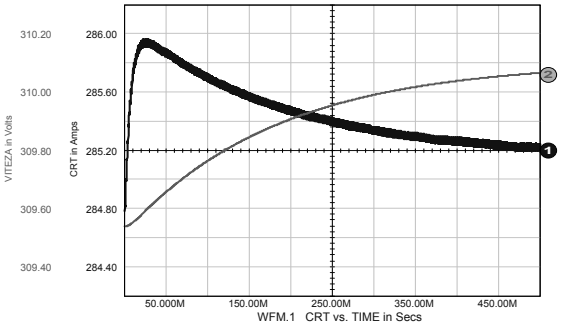

Fig.10 Simulation results along a period that ensures the free components damping

In both cases one can see that the motor current and the other parameters do not exceed the imposed values. In fig.11 one considers the case of motor power supplying along the entire period T. This is why the voltage mean value resulted approximately 742V instead of the real value of 600V.

The simulated results are in good agreement with the classic calculations.

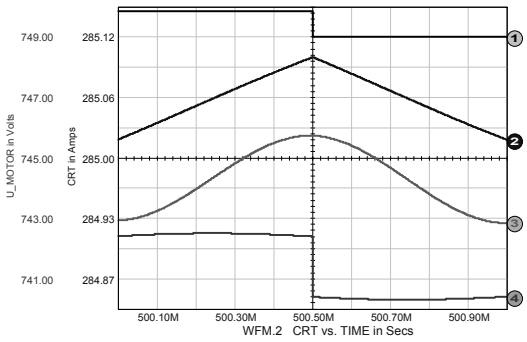

Fig.11 Simulation results along a switching period

Conclusion

The designing and the realization of the power circuit are very important in point from the energetic efficiency point of view. For this reason, the designing and realization of the control unit must also be considered.

The analysis, modelling and simulation of the driving system with chopper represent important stages of the tram driving system designing. Thus the system operational mode is anticipated and the designing might be improved. Numerical simulation method could successfully substitute a great amount of classical calculations.

Based on numerical simulations an optimal design of equipment was achieved [3], [4] and consequently it was used for equipment implementation at SC INDAELTRAC SA Company from Craiova. This work was done within the framework of a R & D project, belonging to the national program (PNCDI/ AMTRANS). The system is under way to be used at the local transport society, RAT Craiova.

Numerical simulations (made using SPICE) show a good agreement with the tests made on the test desk and afterward on the tram.

The advantages of the chopper used for an electric traction vehicle are:

- minimum 35% energy savings ;
- possibility to use the existing motors;
- motor life time increase;
- the accelerator (expensive in the fault state) is removed;
- the contacts destruction is avoided;
- the starting shocks are avoided;
- the chopper equipment is simply connected in the tram electric circuit ensemble.

References

[1] Câmpeanu, A., Introduction in a.c. Machines Dynamics (Introducere in dinamica masinilor electrice de curent alternativ- in Romanian), Ed. Academiei Române, 1998.

[2] Mandache, L., Topan, D., Sîrbu, I.G., Algorithm for Automatically Generating of Network Functions for Lumped Circuits, Annals of The University of Craiova, Electrical Engineering Serie, No.27, 2003 (printed 2004), vol.II, pp.13-18.

[3] Nicolae, I.D., Nicolae, P.M., Mandache, L., Vitan, V.D., Designing, Simulation, Implementation and Testing of Automatic Current Regulators from an Electric Driving System

with d.c. Voltage Variator Used in Electric Urban Traction, IPEC 2005, Niigata, 04 -08.04.2005, Japan.

[4] Nicolae, P.M., Mandache, L., Vitan, V.D., Hurezeanu, Gh., Analysis, Simulation and Testing of Automatic Voltage Regulators from an Electric Driving System Used in Electric Urban Traction, 7th International Conference on Applied and Theoretical Electricity ICATE 2004, Băile Herculane, Oct. 14-15, 2004, Romania, pp.513-516.

[5] Nicolae, P.M., Electric Energy Quality in Limited Electrical Power Systems (Calitatea energiei electrice în sisteme electroenergetice de putere limiată – in Romanian), Ed. Tehnică, Bucharest, 1998.

[6] Wells, J.R., Chapman, P.L., Krein, P.T., Applications of Ripple Correlation Control of Electric Machinery, Electric Machines and Drives Conference, 2003, IEEE International, vol.3, pp.1498-1503.

[7] *** Is Spice 4. User's guide, Intusoft, San Pedro, California, USA, 1998

Petre-Marian Nicolae *– Professor, Ph.D., IEEE Senior Member, Faculty of Electrotechnics, University of Craiova, Decebal Blv., no. 107, 200440 - Craiova, ROMANIA.*
e-mail: pnicolae@elth.ucv.ro

Ileana-Diana Nicolae *– Lecturer, Ph.D., Dr., Faculty of Automation, Computers and Electronics, University of Craiova, Decebal Blv., no. 107, 200440 - Craiova, ROMANIA.*
e-mail: nicolae_ileana@software.ucv.ro

Ioana-Gabriela Sîrbu *– Assistant Professor, Faculty of Electrotechnics, University of Craiova, Decebal Blv., no. 107, 200440 - Craiova, ROMANIA.*
e-mail: osirbu@elth.ucv.ro

Viorel-Dumitru Vitan *– Researcher, Faculty of Electrotechnics, University of Craiova, Decebal Blv., no. 107, 200440 - Craiova, ROMANIA.*

Realization of different methods for defining the speed in the sensorless systems for orientation of the magnetic field

Dimitar Spirov, Pencho Vladimirov

Abstract: *The well-known algorithms, models and methods for defining the speed in sensorless systems for orientation of the magnetic field have been systematized and new ones have been developed. A system has been designed for sensorless control of an induction motor. By means of this system the developed methods for defining the speed with different indexes have been researched, such as total functionality, static error, dynamic behavior, control stability at low speeds and sensitivity to changes in parameters.*

Keywords: *sensorless defining of speed, orientation of the magnetic field , static error, dynamic behavior, stability at low speeds.*

Introduction

The asynchronous electric drives with microprocessor control are used in a wide range of applications – from low cost systems to highly expensive systems with great requirements to the quality of control. In these systems, a great part of the quantities, which are necessary for the realization of the control algorithm, are calculated by the microprocessor on the base of a certain algorithm through input quantities, directly measured on the motor outputs. The angular speed of the rotor proves to be a parameter, necessary for the control system. It can be introduced by two methods – by measurements, or by calculations. The second method has a number of advantages, such as reduction of price and size of the control system, improved stability and working capacity, and elimination of measurement error [1, 2, 3]. For that purpose a series of algorithms have been developed for the calculation of the angular speed of the rotor [1, 2, 3, 5, 6, 7, 8]. In general, they may be divided into two groups – calculation along an open loop, or observation along a closed loop [1].

The purpose of this paper is to systematize the well-known ways and to make out new methods for defining the speed in the sensorless systems for orientation of the magnetic field. It is necessary to develop a system for sensorless control of an asynchronous motor with magnetic field orientation, and, with its help, to study the developed methods for sensorless estimation of the speed regarding the different indexes of the quality of the transient process of the induction machine.

Methods for calculation of the angular rotor speed

1. Calculation of the angular rotor speed along an open loop

The angular rotor speed along an open loop is estimated on the base of the voltage equations of the induction machine with short-circuited rotor, recorded in a coordinate system, which is fixedly connected to the stator (α, β):

$$u_{s\alpha} = R_s i_{s\alpha} + \frac{d}{dt}\psi_{s\alpha} \quad , \tag{1}$$

$$u_{s\beta} = R_s i_{s\beta} + \frac{d}{dt}\psi_{s\beta} , \tag{2}$$

$$0 = R_r i_{r\alpha} + \frac{d}{dt}\psi_{r\alpha} + \omega_r \psi_{r\beta} , \tag{3}$$

$$0 = R_r i_{r\beta} + \frac{d}{dt}\psi_{r\beta} - \omega_r \psi_{r\alpha} , \tag{4}$$

$$\psi_{s\alpha} = L_s i_{s\alpha} + L_m i_{r\alpha} , \tag{5}$$

$$\psi_{s\beta} = L_s i_{s\beta} + L_m i_{r\beta} , \tag{6}$$

$$\psi_{r\alpha} = L_m i_{s\alpha} + L_r i_{r\alpha} , \tag{7}$$

$$\psi_{r\beta} = L_m i_{s\beta} + L_r i_{r\beta} . \tag{8}$$

The estimation of the fluxes of the stator and the rotor basin on the measurements of the vectors of the stator voltages and currents may be obtained from the equation system above. The components of the flux of the stator are obtained from expressions (1) and (2):

$$\psi_{s\alpha} = \int (u_{s\alpha} - R_s i_{s\alpha}) dt , \tag{9}$$

$$\psi_{s\beta} = \int (u_{s\beta} - R_s i_{s\beta}) dt , \tag{10}$$

The components of the flux of the rotor can be defined with expressions (5), (6), (7) and (8). Expressions (5) and (6) define the rotor currents:

$$i_{r\alpha} = \frac{\psi_{s\alpha} - L_s i_{s\alpha}}{L_m}, \quad (11)$$

$$i_{r\beta} = \frac{\psi_{s\beta} - L_s i_{s\beta}}{L_m}, \quad (12)$$

After that we replace them in expressions (7) and (8):

$$\psi_{r\alpha} = \frac{L_r}{L_m}\psi_{s\alpha} - \frac{L_e}{L_m} i_{s\alpha}, \quad (13)$$

$$\psi_{r\beta} = \frac{L_r}{L_m}\psi_{s\beta} - \frac{L_e}{L_m} i_{s\beta}, \quad (14)$$

where $L_e = L_s L_r - L_m^2$.

1.1. Defining the angular speed of the rotor through the stator currents and the rotor fluxes

Through expressions (7) and (8) we express $i_{r\alpha}$ and $i_{r\beta}$ respectively:

$$i_{r\alpha} = \frac{\psi_{r\alpha} - L_m i_{s\alpha}}{L_r}, \quad (15)$$

$$i_{r\beta} = \frac{\psi_{r\beta} - L_m i_{s\beta}}{L_r}, \quad (16)$$

We replace them in expressions (3) and (4) and then express $\frac{d}{dt}\psi_{r\alpha}$ and $\frac{d}{dt}\psi_{r\beta}$:

$$\frac{d}{dt}\psi_{r\alpha} = \frac{R_r L_m}{L_r} i_{s\alpha} - \frac{R_r}{L_r}\psi_{r\alpha} - \omega_r \psi_{r\beta}, \quad (17)$$

$$\frac{d}{dt}\psi_{r\beta} = \frac{R_r L_m}{L_r} i_{s\beta} - \frac{R_r}{L_r}\psi_{r\beta} + \omega_r \psi_{r\alpha}, \quad (18)$$

The angular speed of the flux of the rotor $\omega_{\psi r}$ may be defined by differentiating the angle between the axle α and the flux vector.

$$\omega_{\psi r} = \frac{d}{dt}\left(arctg\left(\frac{\psi_{r\beta}}{\psi_{r\alpha}}\right)\right) = \frac{\psi_{r\alpha}\frac{d\psi_{r\beta}}{dt} - \psi_{r\beta}\frac{d\psi_{r\alpha}}{dt}}{\psi_{r\alpha}^2 + \psi_{r\beta}^2}, \quad (19)$$

In this expression, we can replace the obtained expressions for $\frac{d}{dt}\psi_{r\alpha}$ and $\frac{d}{dt}\psi_{r\beta}$:

$$\omega_{\psi r} = \frac{\psi_{r\alpha}\left(\frac{R_r L_m}{L_r} i_{s\beta} - \frac{R_r}{L_r}\psi_{r\beta} + \omega_r \psi_{r\alpha}\right) - \psi_{r\beta}\left(\frac{R_r L_m}{L_r} i_{s\alpha} - \frac{R_r}{L_r}\psi_{r\alpha} - \omega_r \psi_{r\beta}\right)}{\psi_{r\alpha}^2 + \psi_{r\beta}^2}, \quad (20)$$

For ω_r we can write:

$$\omega_r = \omega_{\psi r} - \omega_{sl}, \quad (21)$$

where ω_r and ω_{sl} are the angular frequency of rotation of the rotor and the frequency of sliding.

Replacing (20) in (21), we can express ω_{sl} :

$$\omega_{sl} = \frac{R_r L_m}{L_r}\frac{\psi_{r\alpha} i_{s\beta} - \psi_{r\beta} i_{s\alpha}}{\psi_{r\alpha}^2 + \psi_{r\beta}^2}, \quad (22)$$

The expression for the sliding frequency ω_{sl} may be represented by the electromagnetic torque M :

$$\omega_{sl} = \frac{R_r}{z_p}\frac{M}{\psi_{r\alpha}^2 + \psi_{r\beta}^2}, \quad (23)$$

where $M = z_p \frac{L_m}{L_r}\left(\psi_{r\alpha} i_{s\beta} - \psi_{r\beta} i_{s\alpha}\right)$;

z_p - number of pole pairs in the electric motor.

Replacing (19) and (22) in expression (21) and after transformation we obtain the final expression for ω_r :

$$\omega_r = \frac{\psi_{r\alpha}\left(L_r \frac{d}{dt}\psi_{r\beta} - R_r L_m i_{s\beta}\right) - \psi_{r\beta}\left(L_r \frac{d}{dt}\psi_{r\alpha} - R_r L_m i_{s\alpha}\right)}{L_r\left(\psi_{r\alpha}^2 + \psi_{r\beta}^2\right)}, \quad (24)$$

1.2. Defining the angular rotor speed through the rotor currents and the rotor fluxes

Another form for the expression of the angular rotor speed may be obtained, if the active resistance R_r of the rotor is eliminated from equations (3) and (4). We express R_r from expression (3):

$$R_r = -\frac{1}{i_{r\alpha}}\left(\frac{d}{dt}\psi_{r\alpha} + \omega_r \psi_{r\beta}\right), \quad (25)$$

We replace in (4) and express ω_r :

$$\omega_r = \frac{i_{r\alpha}\frac{d}{dt}\psi_{r\beta} - i_{r\beta}\frac{d}{dt}\psi_{r\alpha}}{i_{r\alpha}\psi_{r\alpha} + i_{r\beta}\psi_{r\beta}}, \quad (26)$$

This equation can be presented in vector form in the following manner:

$$\omega_r = \frac{i_r \times \frac{d}{dt}\psi_r}{i_r \circ \psi_r}, \quad (27)$$

where $\times$ and $\circ$ are the vector and scalar product of vectors, respectively.

1.3. Defining the angular rotor speed through stator currents and stator fluxes

The components of the rotor may be expressed through expressions (11) and (12). After replacing in expression (25) we obtain:

$$\omega_r = \frac{\left(\psi_{s\alpha} - L_s i_{s\alpha}\right)\frac{d}{dt}\psi_{r\beta} - \left(\psi_{s\beta} - L_s i_{s\beta}\right)\frac{d}{dt}\psi_{r\alpha}}{\left(\psi_{s\alpha} - L_s i_{s\alpha}\right)\psi_{r\alpha} + \left(\psi_{s\beta} - L_s i_{s\beta}\right)\psi_{r\beta}}, \tag{28}$$

If we replace expressions (13) and (14) in (27), we obtain an expression for the angular rotor speed, expressed with the stator currents and fluxes:

$$\omega_r = \frac{\left(\psi_{s\alpha} - L_s i_{s\alpha}\right)\left(L_r \frac{d}{dt}\psi_{s\beta} - L_e \frac{d}{dt} i_{s\beta}\right) - \left(\psi_{s\beta} - L_s i_{s\beta}\right)\left(L_r \frac{d}{dt}\psi_{s\alpha} - L_e \frac{d}{dt} i_{s\alpha}\right)}{\left(\psi_{s\alpha} - L_s i_{s\alpha}\right)\left(L_r\psi_{s\alpha} - L_e i_{s\alpha}\right) + \left(\psi_{s\beta} - L_s i_{s\beta}\right)\left(L_r\psi_{s\beta} - L_e i_{s\beta}\right)}, \tag{29}$$

2. Model reference adaptive systems

In the model reference adaptive systems, the outputs of two calculation models are compared. The model, which does not include calculation quantities, is noted as a reference model of the induction machine; the model, which includes the calculation quantities, may be regulated – it is an adjustable model. The error between the two models is used for the establishing of a suitable adaptive mechanism, which defines the angular rotor speed for the adjustable model.

The reference (voltage) model is obtained by replacing expressions (9) and (10) in (5) and (6), respectively, and by making simplifications:

$$\psi_{s\alpha} = \frac{L_e}{L_r} i_{s\alpha} + \frac{L_m}{L_r}\psi_{r\alpha}, \tag{30}$$

$$\psi_{s\beta} = \frac{L_e}{L_r} i_{s\beta} + \frac{L_m}{L_r}\psi_{r\beta}, \tag{31}$$

We replace the obtained expressions in (1) and (2) and then express respectively $\frac{d}{dt}\psi_{r\alpha}$ and $\frac{d}{dt}\psi_{r\beta}$:

$$\frac{d}{dt}\psi_{r\alpha} = \frac{L_r}{L_m}\left(u_{s\alpha} - R_s i_{s\alpha} - \frac{L_e}{L_r}\frac{d}{dt} i_{s\alpha}\right), \tag{32}$$

$$\frac{d}{dt}\psi_{r\beta} = \frac{L_r}{L_m}\left(u_{s\beta} - R_s i_{s\beta} - \frac{L_e}{L_r}\frac{d}{dt} i_{s\beta}\right), \tag{33}$$

After integrating the above expressions we can receive $\psi_{r\alpha}$ and $\psi_{r\beta}$.

The adjustable (current) model is expressed with equations (17) and (18). The rotor speed is calculated as the difference between the outputs of the two models:

$$\omega_r = \left(K_P + \frac{K_I}{s}\right)\left(\psi_{r\alpha i}\psi_{r\beta u} - \psi_{r\alpha u}\psi_{r\beta i}\right), \tag{34}$$

where K_P and K_I are the proportional and integral constants of the PI-regulator. The block scheme for the realization of this method is given in fig.1 [6].

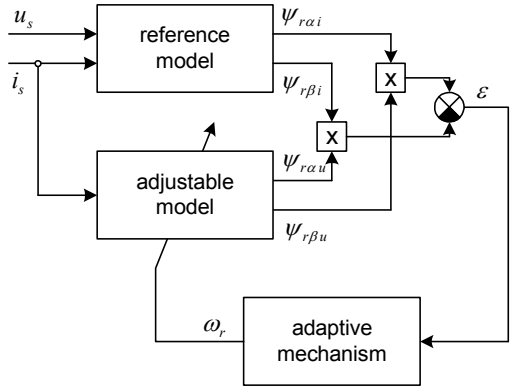

Fig.1. Block schemes for the realization of the model

3. Observer-based speed sensorless control schemes

To calculate the speed of the induction machine we have to know both quantities we can measure directly (stator voltages and currents) and quantities which are not accessible for direct measurements (flux of the rotor). We can write the model of the induction machine in the space of the status:

$$px = Ax + Bu,\ y = Cx, \tag{35}$$

The simplest approach is to realize a system, which will operate in parallel with the real system, and which can calculate the variables of the status. However, this approach does not take into account the fact, that the initial status of the system is unknown. This problem is solved by comparing the calculated output vector with the measured output vector. The difference between the two vectors may be used in order to modify the status vector in the model. This approach is called "Luenberger status observer" and is presented with the following expression [7]:

$$p\hat{x} = \left(A - LC\right)\hat{x} + Bu + Ly,\ \hat{y} = C\hat{x}, \tag{36}$$

where $\wedge$ denotes that the quantity is a calculation one, and L is the observer's matrix. The matrix L must be so selected, as to ensure a minimum error in the expression [7]:

$$p\left(x - \hat{x}\right) = \left(A - LC\right)\left(x - \hat{x}\right), \tag{37}$$

If we transform the matrix of the differential equation of the error, we will obtain a system, which is quite similar to the structure of the regulator. It shows that the matrix L shall be so calculated that the observer's poles would be proportional to these of the induction machine.

A scheme for defining the speed through a status observer is represented in Fig.2 [8].

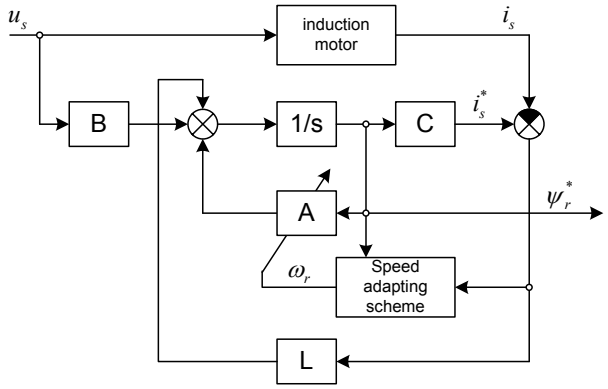

Fig.2. Scheme for defining the speed through a observer-based algorithm

The status observer, which calculates the stator current and the rotor flux is expressed with equation (36); the measured quantity being the stator current i_s . It is compared with the stator current $\hat{i}_s$ as calculated by the observer, and is fed to the speed adapting scheme. The speed is defined with the following expression:

$$\omega_r = \left(K_P + \frac{K_I}{s} \right) \left(\varepsilon_{is\alpha} \psi_{r\beta} - \varepsilon_{is\beta} \psi_{r\alpha} \right), \quad (38)$$

where K_P and K_I are the proportional and integral components of the speed regulator, respectively, and $\varepsilon_{is\alpha} = i_{s\alpha} - \hat{i}_{s\alpha}$, and $\varepsilon_{is\beta} = i_{s\beta} - \hat{i}_{s\beta}$.

Results

The model of the system for sensorless control of the induction motor, realized in the MATLAB/SIMULINK-environment is shown in Fig.3.

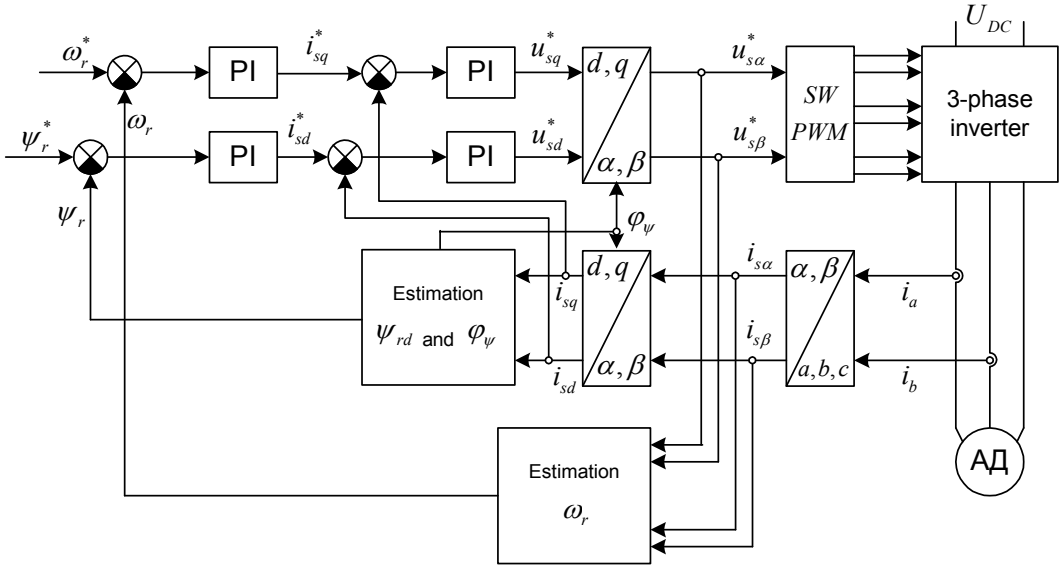

Fig.3. Model of a sensorless control system

The system includes four regulators, three coordinate converters, a three-phase inverter, a block for defining ψ_{rd} and φ_ψ with expressions (39) and (40), and a block for defining ω_r with one of the presented algorithms.

$$\psi_{rd} = \frac{L_m}{\frac{L_r}{R_r} s + 1} i_{sd}, \quad (39)$$

$$\omega_\psi = \frac{R_r L_m}{L_r} \frac{i_{sq}}{\psi_{rd}} + \omega_r, \quad (40)$$

The control is effected in the coordinate system d,q, which rotates with the speed of the rotor flux. The transformation of the quantities from the three-phase coordinate system (a,b,c) into the coordinate system, which is fixedly connected to the stator, and from into the coordinate system d,q, which rotates with the rotor flux, and vice versa, is performed in the coordinate converters by means of the Clarke transformation, and by meanes of the Park transformation and inverse Park transformation, respectively [4].

The described methods for defining the speeds are compared per different parameters of the quality of transient process of the induction machine, such as total working capacity, steady state error, dynamic behavior upon alteration of the load torques, control stability at low speeds and sensibility to parameter variations.

Steady state error. The steady state error is represented by the difference between the real and the calculated angular speed of the motor. For $\omega_r = \omega_{rн}$, in the first two algorithms for idle operation the static error is 1,01%, and when the load increases it becomes 8,45%. With the third algorithm the static error is 1,02% for both the statuses (Fig.4a). The static error has been studied also for low speeds when $\omega_r = 0.2\omega_{rн}$. In the first and the third algorithm the static error is 0,95% for both the statuses. In the second algorithm and idle operation the static error is 0,95%, and upon increasing the load it is 1,77% (Fig.4b).

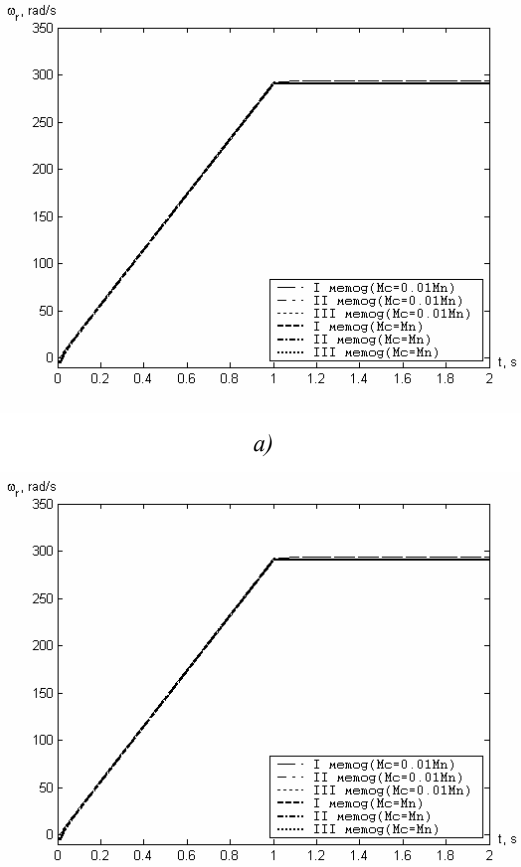

a)

b)

Fig.4. Expression of the angular rotor rotation frequency ω_r as a function of time for estimation the steady state error: a) - $\omega_r = \omega_{rн}$; b) - $\omega_r = 0.2\omega_{rн}$.

Dynamic behavior. The research is performed by introducing a short overloading with $M_c = 2M_н$ after the starting process has elapsed (in this case 1,4 s), with duration 0,2 s. For $\omega_r = \omega_{rн}$ with the first two algorithms the deviation of the rotor speed from the set values is 11,45%, and with the third algorithm it is 11,46% (Fig.5a). The deviation at low speeds when $\omega_r = 0.2\omega_{rн}$ is 15,8% with the three algorithms (Fig.5b).

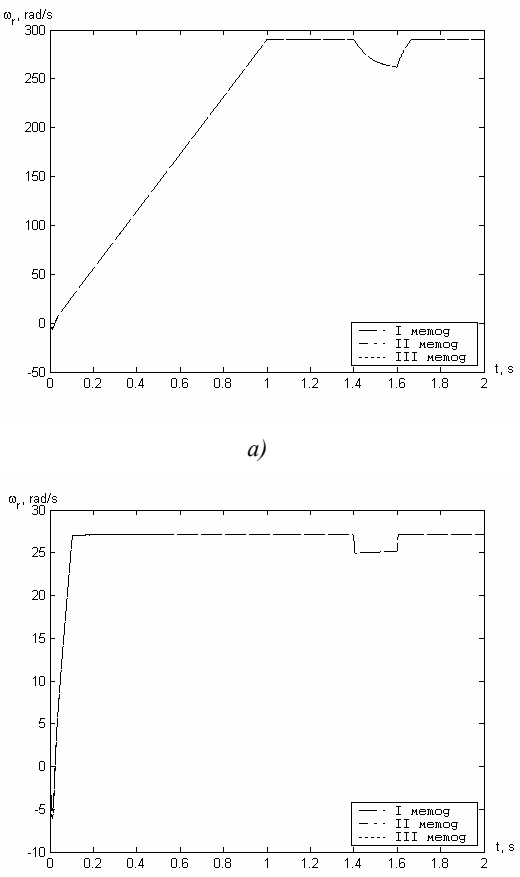

a)

b)

Fig.4. Expression of the angular rotation speed of the rotor as a function of time for estimation the dynamic behaviour: a) - $\omega_r = \omega_{rн}$; b) - $\omega_r = 0.2\omega_{rн}$.

Sensibility to parameter variations. Here, the sensibility of the algorithms to variations of the rotor active resistance R_r. For $\omega_r = \omega_{rн}$ the study is performed by introducing the change of $R_r = 1{,}4R_{rн}$ after the starting process has elapsed (in this case at 1,4 s). In the first two algorithms the deviation of the rotor speed form the set value is 9,29%, and for the third algorithm it is 7,43% (Fig.6a). The deviation at low speeds when $\omega_r = 0.2\omega_{rн}$ in the first two algorithms is 44,93%, and in the third algorithm it is 39,53% (Fig.6b).

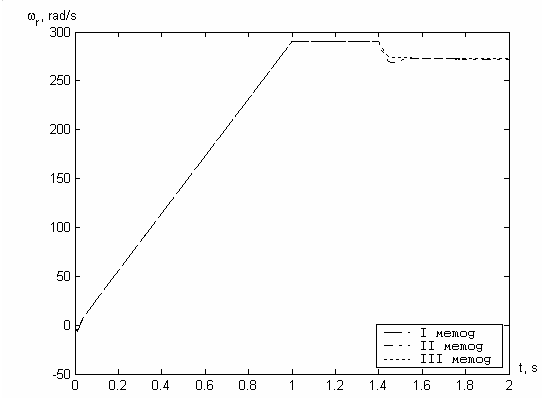

a)

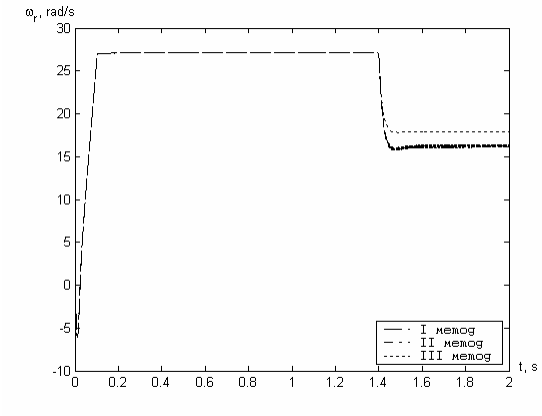

b)

Fig.4. Expression of the angular rotation speed of the rotor as a function of time for estimation the sensibility towards parameter variations: a) - $\omega_r = \omega_{rн}$ *; b) -* $\omega_r = 0.2\omega_{rн}$.

Total working capacity. The above quoted arguments show that the status observer has the best working capacity. However, it is the most difficult to realize. The main problem here is finding a stable observer matrix.

Conclusion

Algorithms, models and methods have been reviewed for sensorless estimation of the speed. System for sensorless control of an induction motor with magnetic filed orientation has been developed. With this system, the designed methods for sensorless defining of speed have been studied, in terms of different parameters of the quality of the transient process in the induction machine. The comparison of the developed methods per parameters of transient process quality proves that the observer-based method has the best working capacity, though it is most complicated for realization.

References

[1] Ilas C., A. Bettini, L. Ferraris, G. Griva, F. Profumo, Comparison of different schemes without shaft sensors for field oriented control drives, IEEE IECON, 1994, pp. 1579-1588

[2] Holtz J., Methods for speed sensorless control of AC drives, IEEE PCC-Yokohama, 1993, pp. 415-420

[3] Vladimirov P., D. Spirov, S.Rachev, Methods for sensorless determination of rotational speed of controlled induction motor drives, International Scientific Conference UNITECH `03 – Gabrovo, Gabrovo, 2003, pp. I-59-I-69

[4] Post R., E. Ritchie, Dynamic motor modelling, institute of energy technology – Aalborg University, 2001

[5] Filippich M., Digital control of a three phase induction motor, The University of Queensland, 2002

[6] Tajima H., Y. Hori, Speed sensorless field-orientation control of the induction machine, IEEE Trans. Indust. Appli., vol. 29, Jan/Feb 1993, pp. 175-180

[7] Sensorless control with Kalman filter on TMS320 fixed-point DSP, Texas Instrument Document BPRA057, 1997

[8] Kubota H., K. Matsuse, DSP-based speed adaptive flux observer of induction motor, IEEE Trans. Indust. Appli., vol. 29, March/April 1993, pp. 344-348

Dimitar Spirov *– Ph.D. Student, Department of Electrical Engineering, Technical University – Gabrovo, 4, Hadgi Dimitar str., 5300 Gabrovo, Bulgaria, dimitar_spirov@abv.bg*

Pencho Vladimirov *– Assoc. Prof. Dr., Department of Electrical Engineering, Technical University – Gabrovo, 4, Hadgi dimitar str., 5300 Gabrovo, Bulgaria, pvlad@iname.com*

An improved method for frequency control of an induction motor for different systems for pulse width modulation

Pencho Vladimirov, Dimitar Spirov

Abstract: *A system for frequency control of an induction machine has been developed and investigated, for loading with constant torque and regulation with constant stator flux, using sine and space vector pulse width modulation. The system performs compensation of the active resistance of the stator and of the slip frequency when effecting speed feedback.*

The advantages and disadvantages of the two methods for signal modulation and the efficiency of the system have been reviewed.

Keywords: *frequency control, constant load torque, constant stator flux, sine pulse width modulation, space vector pulse width modulation*

Introduction

The frequency control, while maintaining $U/f = const$ is widely used in systems for control of induction machines with lower requirements to the speed regulation quality, as, for example, the regulation of the speed in mechanisms with constant load torque. However, in order to maintain constant efficiency, $\cos\varphi$ and overload coefficient M_m / M_N it is necessary to maintain the magnetic flux Ψ_s constant and close to the rated one within the whole operation range [1]. With constant magnetic flux, control may be realized on the basis of the static mechanical characteristics of the induction machine by proportional changing of the stator supply voltage U_s and its angular frequency ω_s. This method may be applied for frequencies, which are close to the rated one, where $U_s >> I_s R_s$. For low frequencies different methods for accounting of this drop, such as introducing in the control system through current feedback [1] or compensating it via regulator [2].

The aim of this paper is to develop a model and system for frequency control of the induction machine when loaded with constant torque and when it is regulated with constant stator magnetic flux. The system performs compensation of the active resistance of the stator and the slip frequency when speed feedback is effected. By means of this system the positive and negative features of the two most used methods for signal modulation will be studied – the sine and space vector pulse width modulation.

A model and system for realization of frequency control at constant torque

Compensation of the active resistance of the stator.

The compensation of the active resistance of the stator is based on maintaining the amplitude of the stator magnetic flux Ψ_s constant and equal to its rated value. For the complex control for the stator winding voltage in established mode in the coordinate system which is fixedly connected with the stator we obtain [3]:

$$\overline{U}_s = R_s \overline{I}_s + j\omega_s \overline{\Psi}_s , \quad (1)$$

The expression (1) presents the relation between the voltage space vector U_s and its angular frequency ω_s. The stator current space vector is defined by two phase currents, measured directly at the outputs of the induction machine, with the expression (2) [4]:

$$i_{s\alpha} = \sqrt{\frac{3}{2}} i_A , \; i_{s\beta} = -\frac{1}{\sqrt{2}}\left(i_A + 2i_C\right), \quad (2)$$

The magnetic flux of the stator is set as equal to its rated value Ψ_{sN}. For angular frequency $\omega_s = 0$ from (1) we obtain:

$$\overline{U}_{s\min} = R_s \overline{I}_{sN} , \quad (3)$$

Compensation of slip frequency.

For the complex equation of the rotor winding voltage in established mode in coordinate system α, β we obtain [3]:

$$0 = R_r \overline{I}_r + j(\omega_s - \omega_r)\overline{\Psi}_r = R_r \overline{I}_r + j\omega_{sl} \overline{\Psi}_r , \quad (4)$$

where ω_r and $\omega_{sl} = \omega_s - \omega_r$ are the angular frequencies of the rotor voltage and the slip.

As well known, for established mode

$$\overline{\Psi}_s = L_s \overline{I}_s + L_m \overline{I}_r , \quad (5)$$

$$\overline{\Psi}_r = L_r \overline{I}_r + L_m \overline{I}_s$$

From the expressions $\overline{I}_r$ and $\overline{\Psi}_r$ we receive

$$\overline{I}_r = \frac{\overline{\Psi}_s - L_s \overline{I}_s}{L_m} , \quad (6)$$

(7) $$\overline{\Psi}_r = \frac{L_r \overline{\Psi}_s - L_e \overline{I}_s}{L_m},$$

where $L_e = L_s L_r - L_m^2$

After replacing (6) and (7) in (4), for ω_s we receive:

(8) $$\omega_s = \frac{R_r L_s \overline{I}_s - R_r \overline{\Psi}_s + \omega_r L_r \overline{\Psi}_s - \omega_r L_e \overline{I}_s}{L_r \overline{\Psi}_s - L_e \overline{I}_s},$$

This expression (8) defines the connection between the set electrical angular speed of the rotor ω_r and the electrical angular speed ω_s of the stator supply voltage.

Control system

The control system is used for the regulation of AC motors at frequencies, which differ from the rated supply frequency. It consists of to components: regulators for obtaining control frequency, and a three-phase inverter to generate the three-phase supply voltage.

Three-phase bridge inverter

The scheme of the three-phase bridge inverter consists of six power transistors, to which pulses by the voltage modulation system are fed, to open in a certain sequence. This system produces the pulse sequence on the base of the voltage fed by the regulator for producing of control frequency. Most often the three-phase generates three-phase AC system of voltages of the DC supply voltage using the pulse width modulation for controlling the power transistors. Here, two different ways for modulation of the input signal are considered: the sine pulse width modulation, and the space vector pulse width modulation.

Sine pulse width modulation.

The sine pulse width modulation (PWM) is obtained by comparing two signals – a modulating signal with frequency 10-20 kHz, and a three-phase sine system of voltages (Fig.1). At the output of this system positive and negative pulses with variable frequency and width are obtained. Increasing the number of the pulses for half a cycle decreases the frequency of the output sine wave, and increasing the width of the pulse increase the amplitude.

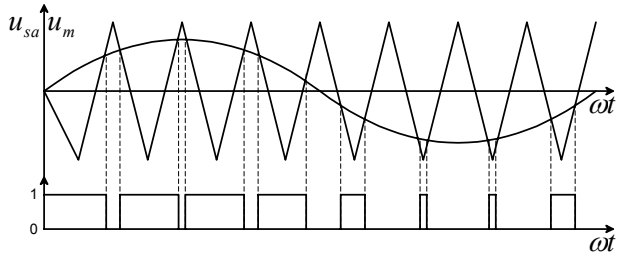

Fig.1. A scheme for obtaining sine pulse width modulation.

The three sine voltages with frequency f_s, obtained by the system for regulation of the variables, are compared with a triangular signal, whose frequency defines the working frequency of the inverter f_m. The modulation coefficient is defined by $k_f = \frac{f_s}{f_m}$. The value of k_f must be a round number and much greater than three, in order to decrease the losses due to high harmonics.

Space vector pulse width modulation.

For the presenting vector of the three-phase system of stator voltages while satisfying the requirements for invariability of the powers the following expression is obtained [3]:

(9) $$u_s = \sqrt{\frac{2}{3}}\left(u_A + a u_B + a^2 u_C\right),$$

There are eight combinations for switching the three bridges of the three-phase inverter (Fig.2). From expression (9) the space vector of the voltage for each of these combinations may be obtained. Fig.2 shows the location of the space vectors in the complex plane. The six vectors are at 60^o and the two zero vectors are in the beginning of the coordinate system.

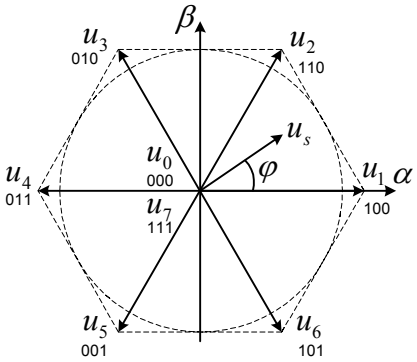

Fig.2. Location of the space vectors in the complex plane.

The space vector modulation must describe the input space vector of the voltage u_s through the eight vectors obtained. One of the ways is to set the average voltage of the inverter for the period T_{pwm} equal to the average voltage of the input space vector for the same period. Thus, the space vector is modeled through the two borderline vectors of the sector in which it is located. The binary representation of the borderline vectors differs with one bit only, which means that only one transistor shall switch over.

Assuming that the modulating frequency of the inverter is great, and the changes of the input space vector within this period are small, the modulating scheme may be presented with the following expression:

(10) $$T_{pwm} u_s = T_1 u_1 + T_2 u_2 + T_0 u_0,$$

where u_1 and u_2 are the two borderline vectors of the relevant sector, u_0 is the zero vector, and T_1, T_2 and

T_0 is the duration of the relevant vectors. To them the following expression applies:

(11) $$T_{pwm} = T_1 + T_2 + T_0,$$

The length of the input space vector defines the amplitude of the output voltage, and the speed, with which the vector rotates, defines the frequency of the output voltage.

Regulators for obtaining control frequency

Voltage regulator.

The voltage regulator has two zones: linear voltage variation as a function of the synchronous speed ω_s for frequencies around the rated frequency f_N, and for frequencies greater than the rated one the voltage remains constant and equal to the rated one. The linear part of the function does not start from zero point, but from $U_{s\min}$ as for frequencies close to zero the active drop of the voltage becomes greater than the inductive drop and must be taken into account (expression (1)).

Slip frequency regulator.

The slip frequency regulator compensates the speed reduction when the load increases. On its output the difference between the set speed ω_r^* and the speed ω_r, as measured at the rotor of the induction machine, is fed. The synchronous speed is obtained with the following expression:

(12) $$\omega_s = \omega_{sl} + \omega_r,$$

Results

The developed control system enables the realization of frequency control of an induction motor with the two methods of modulation of the input signal. The block scheme of the control system is given in Fig.3.

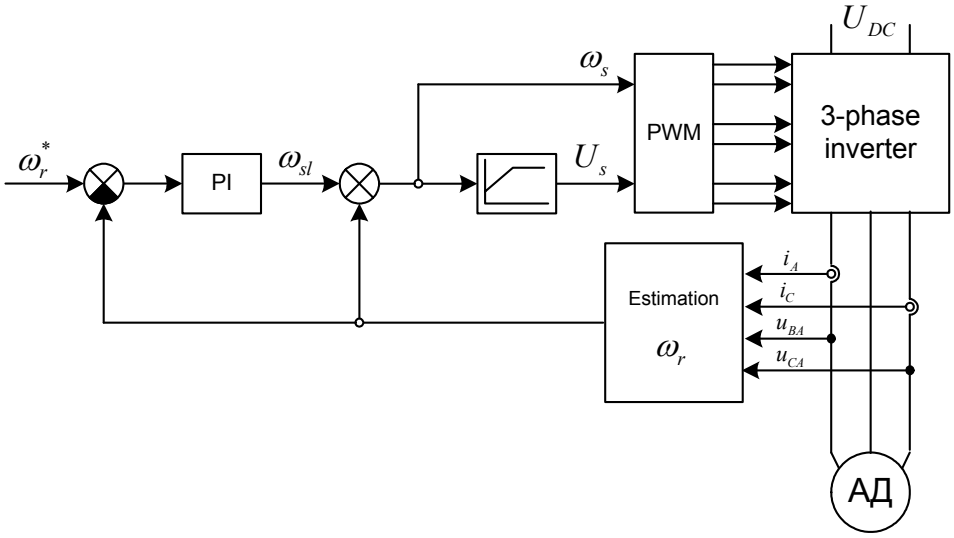

Fig.3. Block scheme of the control system.

In order to better illustrate the difference between the two methods, a study without the system for obtaining of control voltage has been made. To the modulating block the presenting vector of the stator voltage with rated amplitude and frequency is fed. The operation of the induction motor type T112 M-2 BR//B14 will be researched, a motor, which is designed to drive the lifting mechanism of electric hoists for such operation mode. During the studies the parameters of the replacement scheme of the motor are used, as defined by the calculation note of the producer ELMA AD – Troyan, for slip $s_N = 0{,}0575$. The rated data of the electric motor and the parameters of the replacement scheme for $s_N = 0{,}0575$ are given in an Appendix. By means of the developed models the operation of the electric motor has been studied for power supply from three-phase bridge inverter with using of sine pulse width and space-vector pulse width modulation in established operation mode and load $M_c = M_N = 16{,}89\ N.m = const$. The total inertia moment of the drive is $J_\Sigma = FI(J_m + J_{BR}) = 2.0{,}01153 = 0{,}02306\ kg.m^2$; the assumed inertia coefficient is $FI = 2{,}0$. The results obtained for the quantities for the two methods of modulation of the power supply are compared with the quantities, obtained for electric motor power supply from three-phase electricity net are summarized in Table 1. The full harmonic distortions of the voltage U_{WTHD} and the current I_{THD} are define in accordance with the expressions as given in [7]:

$$U_{WTHD} = \frac{\sqrt{\sum_{\nu=2}^{N}\left(\frac{U_\nu}{\nu}\right)^2}}{U_1},$$

$$I_{THD} = \frac{\sqrt{\sum_{\nu=2}^{N} I_\nu^2}}{I_1}$$

where ν is the consecutive number of the harmonic.

Table 1

Values of quantities for different ways of power supply

Power supply method	Three-phase network	Sine PWM	Space-vector PWM
Space vector for harmonic 1 of the stator voltage, V	381,05	331,74	384,00
U_{WTHD}, %	-	0,649	0,679
Phase stator current, A	9,126	10,701	9,362
I_{THD}, %	-	4,109	5,652

The researched made allow for the following conclusions to be made regarding the two methods of signal modulation:

- For the two methods the system allows reversing of the power flux, in which case energy is sent back to the electricity net when the motor operates in brake modes;
- With the space vector pulse width modulation the presenting vector for the first harmonic of the stator voltage is 384,00:331,74=1,1575 times greater than with the sine pulse width modulation (Fig.4); therefore it is better to apply DC supply voltage;
- The total harmonic distortion of the voltage U_{WTHD} [%], as defined according to [7] is approximately the same for the both methods;
- With the space-vector PWM the phase stator current is 9,362:10,701=0,8749 times greater than with the sine PWM, hence the electric losses in the windings will be less, they will depend on the current squares;
- The total harmonic distortion of the currents I_{THD} [%], as defined according to [7] is approximately the same for the both methods;
- The method of transistor switch over with the space-vector PWM improves the efficiency of the inverter and considerably simplifies the numerical realization of the algorithm.

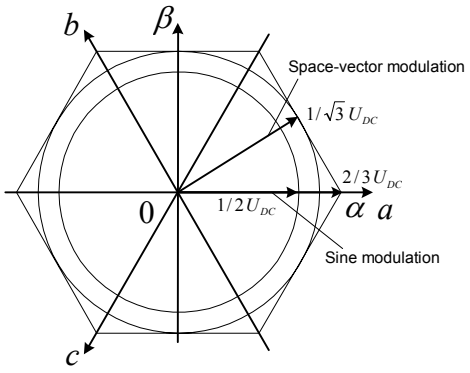

Fig.4. Comparison between the space vectors for the two methods of signal modulation.

Also, the operation of the system with frequency regulation of the speed through the regulators for obtaining of control frequency has been studied. The system has been realized with speed feedback, as the speed is calculated by means of the method, given in [5], by measuring two stator phase currents and two stator linear voltages. The regulators of voltage and frequency form the control signal, which is then fed to the modulating block. This block forms the pulses for controlling the three-phase inverter. The operation of the system for the two methods of modulation of the supply voltage has been studied too. Figs.6a and 6b show the curves of the phase current for both the cases. From the analysis made of the high harmonics it can be seen that with the sine PWM the total harmonic distortion of the current are 8,237%, and with the space-vector PWM they are 5,739%.

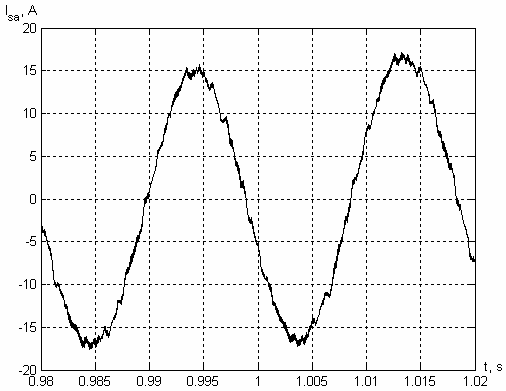

a)

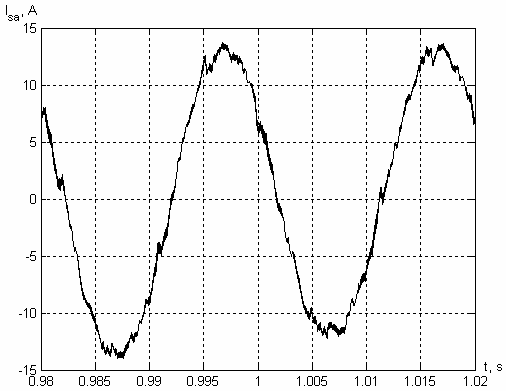

b)

Fig.5. Stator current variation as a function of time: a) – with sine PWM; b) with space-vector PWM.

Conclusion

A system for frequency controlling of an induction machine has been designed and studied, with constant torque loading and with regulation with stator magnetic flux through the application of sine and space-vector PWM. The system realizes compensation of the active resistance of the stator and slip frequency when realizing speed feedback.

With the space-vector PWM a better utilization of the DC supply voltage is realized, lower electric losses in the windings, improved efficiency of the inverter and significant simplification of the numerical realization of the algorithm. The efficiency of the system has also been confirmed.

Appendix

Induction motor type: T112 M-2 BR//B14

$P_N = 5\ kW$; $U_N = 380\ V$; $I_N = 9{,}774\ A$;

$f_N = 50\ Hz$; $n_N = 2827\ \text{min}^{-1}$;

$M_N = 16{,}887\ N.m$; $J_m + J_{BR} = 0{,}01153\ kg.m^2$;

Parameters for $s_N = 0{,}0575$:

$R_s^{75^oC} = 1{,}35\ \Omega$; $R_r^{90^oC} = 1{,}25\ \Omega$; $X_s = 2{,}164\ \Omega$;

$X_r = 2{,}206\ \Omega$; $X_m = 87{,}909\ \Omega$

References

[1] Munoz-Garcia A. et al., A New Induction Motor V/f Control Method Capable of High-Performance Regulation at Low Speed, IEEE Transaction on Industry Applications, vol. 34, № 4, 1998, pp. 813-821.

[2] Holtz J., Methods for Speed Sensorless Control of AC Drives, Sensorless Control of AC Motor Drives, IEEE PRESS, 1996, pp. 1-19.

[3] Vladimirov P., D. Markova, D. Spirov, Influence of replacement scheme parameters of the induction machine upon its energy characteristics, ELMA 2005.

[4] Vladimirov P., S. Rachev, Transient processes and dynamic loadings in the induction machines for lifting mechanisms, Journal of Technical University-Gabrovo, volume 30, 2004, pp. 135-150.

[5] Spirov D., P. Vladimirov, Realization of different methods for defining the speed in sensorless systems for orientation of the magnetic field, ELMA 2005

[6] Texas Instruments Document BPRA073 - Field Orientated Control of 3-Phase AC-Motors, 1998.

[7] Narayanan G., V. T. Ranganathan, Synchronized PWM Strategies Based on Space Vector Approach. Part 1 and Part 2, IEE Proc. Electric Power Applications, vol. 146, № 3, May 1999, pp. 276-289

Pencho Vladimirov *– Assoc. Prof. Dr., Department of Electrical Engineering, Technical University – Gabrovo, 4, Hadgi dimitar str., 5300 Gabrovo, Bulgaria, pvlad@iname.com*

Dimitar Spirov *– Ph.D. Student, Department of Electrical Engineering, Technical University – Gabrovo, 4, Hadgi Dimitar str., 5300 Gabrovo, Bulgaria, dimitar_spirov@abv.bg*

Frequency Method for Obtaining Low Velocities

Lubomir Genchev, Tsvetozar Petkov

Abstract: *The paper shows a new method for obtaining low regulated velocities of induction motor. This is a method, which uses direct conversion of frequency, created on the basis of a capacitive cycloconverter.*

This engineering solution achieves increasing the overload capacity and high energetic features by means of a cheap and not a complicated scheme.

Keywords – capacitive cycloconverter, frequency control

Essence of the problem:

In mechanisms that require restriction of the dynamic efforts, the main task of the electro motion system is achieving gradual starting and stopping. The most common electro motions solve this problem by using a DC-motor system, which is expensive, or an induction motor controlled by parametrical methods, which have a high-energy loss. Thus, it is necessary to find a solution that is cheap and reliable, with a low energy loss. The frequency control methods allow meeting these requirements.

At present the most perspective tendency is a change of the electro motions of the DC-systems and of the parametrical electro motions with induction motor controlled with frequency methods.

Purpose and tasks

The major purpose of this project is to create a new type of frequency electro motion, based on a converter for direct transformation of the frequency by using the advantages of the serial resonance.

The major task is to achieve wider range of velocities than two and tree speed induction motors, lower price than DC-AC invertors, higher energy parameters than the methods which use the decrease of the stator voltage, as well as the opportunity to work as a generator.

The device must not generate higher harmonics.

Solution of the problem

The suggested scheme of the device is shown in fig.1. It contains six two-way triacs, a separating capacitor and a three-phase induction motor.

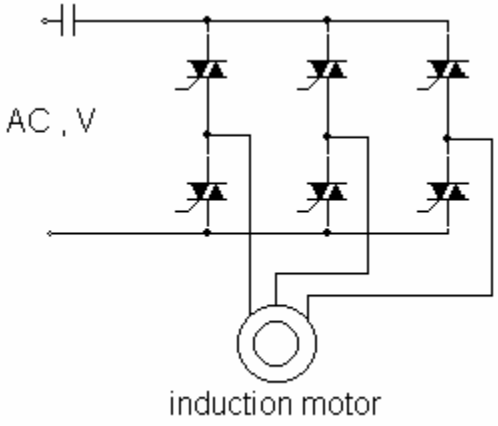

Fig.1 The suggesting scheme of capacitive cycloconverter

The control system (not shown here) passes impulses, which are synchronized to the supplying voltage. The current that is used by the electrical net has a sinusoidal form, because control impulses are passed when current crosses zero. As a result of this controlling method, in the stator coils of the induction motor flows a symmetrical tree-phase system of currents. The form of the current curve is shown on fig.2

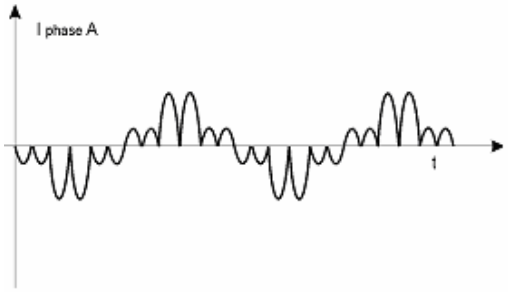

Fig.2 current curve for phase A

The result of changing the number of the semi waves in one period is a change in the frequency and the synchronic speed respectively.

Changing the value of the capacitor and keeping the same control, we can change the amplitude of the current and the work regime.

If the following conditions are fulfilled:

$$\omega^2 LC = 1 \qquad (1)$$

$$R \geq 2\sqrt{\frac{L}{C}} \qquad (2)$$

Where: L – equivalent inductance;

R – equivalent resistance of the motor, which is measured between two connectors of the cycloconverter.

With these conditions, we have a work regime very close to the resonance.

Results of the research

The form of the mechanical characteristics is shown in fig.3. They are made for induction motor type KT 63 B2 BR, made in Troyan Bulgaria with the following parameters:

P=0,25 kW, ω=314, rad/s, η=0,7, I=1,2 A U=220, V cosφ=0,75

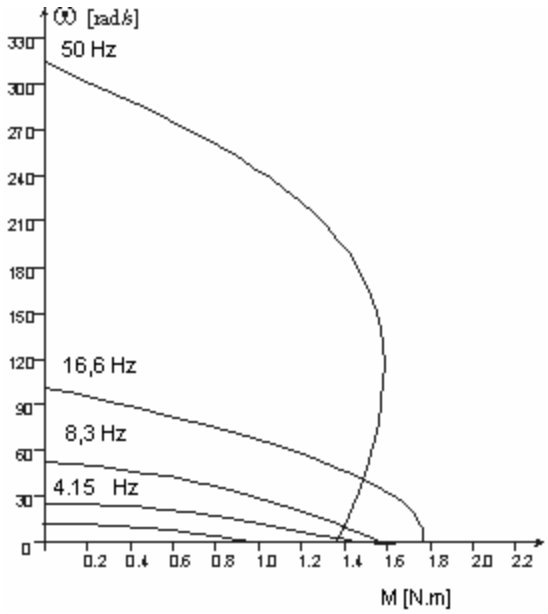

Fig.3 mechanical characteristic

The phase angle between currents in phases A, B and C is 120°, and the sum of their moment values always equals zero:

$$i_a(t) + i_b(t) + i_c(t) = 0 \qquad (3)$$

This allows implementing the method of the resulting vector for investigating the processes in the suggested electromovement.

The vector diagram can be easily found, because the current and the voltages around the capacitor and the converter have sinusoidal form.

The vector diagram is shown in fig. 4.

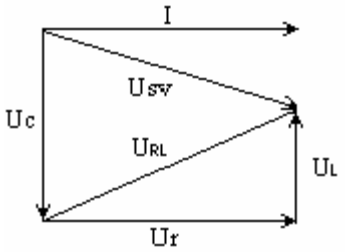

Fig. 4 The vector diagram

Where: Uc- voltage across the capacitor;

Usv- supplied voltage;

U_{RL}- voltage across the converter;

I - current from supplying net;

Ur – voltage across equivalent resistance;

U_L –voltage across equivalent inductance

When changing the frequency and keeping the current with the same sinusoidal form we can determine the equivalent parameters by measuring the voltages around the capacitor, the converter and the supplied voltage. In order the mentioned variables to be sinusoidal the angle of the control impulses must equal the phase angle between the current and the supplied voltage.

Opportunity for using in practice

One of the possible applications of this electro motion is its using as a starting and stopping device in mechanisms that require restriction of the dynamic efforts as cranes, elevators etc.

The device does not import in the supplying net higher harmonics, which is also an advantage of the method.

Obtaining low velocities when the duty cycle is S2 or S3 for avoiding transmissions with high price is an advantage of the method as well.

When the duty cycle is S1, it is necessary to use independent air-cooling system.

References

[1] B. Figaro, B.S. Gotovski,"Тиристорные циклоклоконверторы", Наука и техника, Минск 1973.

[2] V.Greko "Статические преобразувателей на несущей частоте" Электротехника" 1969 г. Pp 66-68

Lubomir V.Genchev *- associate professor at Technical University of Gabrovo, 4 H.Dimitar str. 5300 Gabrovo, Bulgaria*

Tzvetozar G. Petkov - *Assistant at Technical University of Gabrovo, 4 "H.Dimitar "str. 5300 Gabrovo, Bulgaria*

E-mail: tzvetozar_petkov@mail.bg

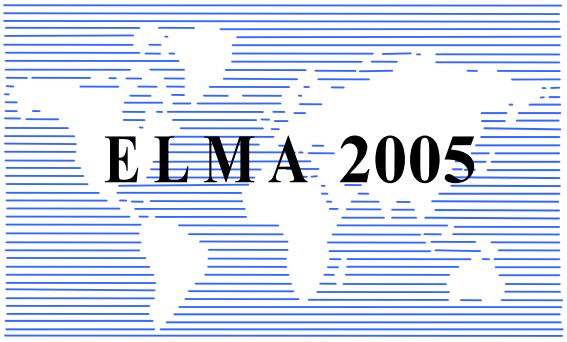

TECHNOLOGIES, NEW MATERIALS AND COMPONENTS I

Magnetic refrigeration at room temperature: from materials to applications

Afef Kedous-Lebouc, Farid Allab, Jean Marc Fournier and Jean Paul Yonnet

Abstract: *Based on giant magnetocaloric effect, the magnetic refrigeration promises high efficiency and ecological systems. A review of the recent researches and developments in the field is presented in this paper. The three following parts are discussed: giant magnetocaloric materials, magnetothermal cycles and the designed and built first systems. The paper describes in more details our experience and the main investigations carried out in collaboration with the Laboratoire de Cristallographie de Grenoble and the Laboratoire Louis Néel.*

Keywords: *giant magnetocaloric effect materials, magnetic refrigeration, active magnetic regenerative refrigeration.*

Introduction

Magnetic refrigeration at room temperature is a new and original method to produce cold at high efficiency and safe environment conditions. Its feasibility has been recently demonstrated [1], [2], [3] and several devices have been developed in order to study this new technology.

Magnetic refrigeration is based on the giant magnetocaloric effect (MCE), an intrinsic property displayed by some materials, which induces a change of the material temperature under an adiabatic magnetization or demagnetization. It can be used to make a magnetothermal cycle similar to the thermodynamic cycle of a classical vapor compression machine.

Compared to classical technologies, the magnetic refrigeration presents a high thermodynamic efficiency. This is mainly due to the reversibility of the MCE which takes place without loss. The theoretical efficiency can reach 60% of Carnot efficiency limit while it does not exceeds 40% in the best conventional thermodynamic systems. In addition, magnetic refrigeration allows air pollution to be reduced. In fact no CFC, HCFC or HFC are needed. The current developed systems work only with water.

These advantages agree with the current economic and environmental trends and offer a large potential of applications: domestic or industrial refrigeration, building or vehicle air conditioners, electronic systems cooling.

After a presentation of the concept of the MCE, this paper gives a review of the recent developments in magnetic refrigeration. It will focus on its three main components which must be mastered: MCE material, magnetothermal cycle and magnetic system and it presents the experience of the LEG in this field. This work is carried out with strong collaborations with two laboratories of physics in Grenoble: the Laboratoire de Cristallographie (LC) for giant MCE materials elaboration and the Laboratoire Louis Néel (LLN) for characterization and physical analysis.

MCE and giant MCE materials at room temperature

Magnetocaloric effect was first discovered by Warburg in 1881 [4] and explained later by Weiss and Picard in 1918. It is due to a coupling between the magnetic entropy and the lattice entropy of the material. The magnetization (demagnetization) induces a decrease (increase) of the material magnetic entropy. In adiabatic conditions, this leads to an increase (decrease) of the material lattice entropy and as a consequence a heating (cooling) of the material. The maximum effect is observed around material order/disorder transition temperature, Curie or Néel temperature, as shown in Fig.1. The entropy variation ΔS_m and the MCE can be expressed by equations (1) and (2):

$$\Delta S_m(T,B) = \int_0^B \left(\frac{\partial M}{\partial T}\right)_B dB \quad (1)$$

$$MCE(T,B) = -\frac{T}{C_p(T,B)}\Delta S_m(T,B) \quad (2)$$

with T the temperature, B the external applied magnetic induction and Cp the specific heat which is a function of T and B.

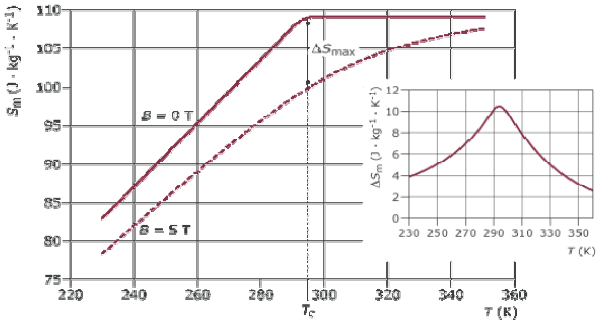

Fig.1. Magnetic entropy S_m evolution with temperature for 0 and 5T and corresponding variation ΔS_m [3]

For refrigeration applications, working temperature must be around room temperature. In this case the number of possible materials is drastically reduced. Up to now, only pure gadolinium has been used for demonstrative systems.

MCE characterization

Several methods can be used to characterize MCE: a direct method by measuring the temperature rise when the material is placed in an external field, a calorimetric method and a magnetic method. This last one is investigated in the laboratory using the LLN magnetometer. It consists in determining the magnetization curves M(T,B) at different temperatures and external field levels [3]. ΔS_m is then calculated from (1) using the following formula:

$$(3)\quad \Delta S_m = -\sum_j \frac{M_{i+1}(T_{i+1}, B_j) - M_i(T_i, B_j)}{T_{i+1} - T_i} \Delta B_j$$

Fig. 2 and Fig. 3 give the magnetocaloric properties for a sample of pure commercial gadolinium (99.99% Gd) characterized by this technique.

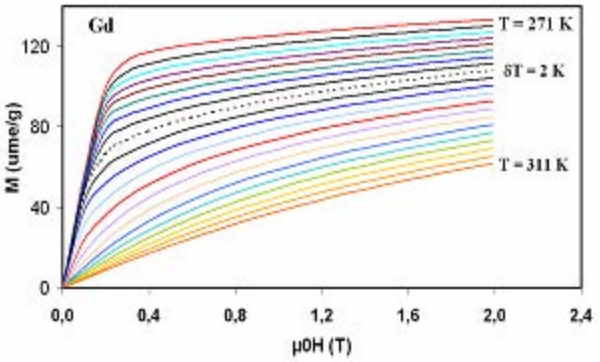

Fig.2. Experimental isothermal curves M(T,B) for Gd

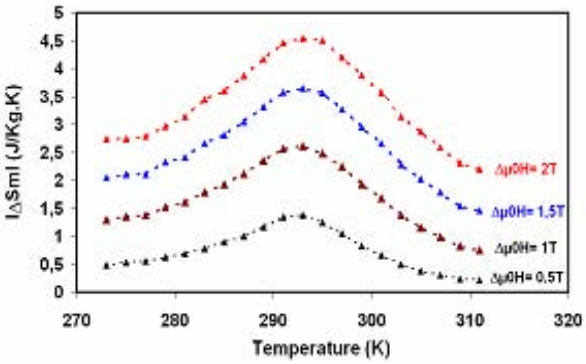

Fig.3. Calculated entropy variations $\Delta S_m(T,B)$

The Curie temperature of the material is 294 K. The maximum entropy variation and EMC are respectively 2.5 J/kg.K and 2.2 K/T. These results agree with those given in literature and are also confirmed by direct measurements.

Giant MCE materials

The main criteria for giant MCE materials are [5]:

- a T_c near room temperature
- a high ΔS_m
- a large temperature variation of ΔS_m
- a high MCE

Today, Gd is the only available material on the market which can verify these conditions. It is a 2nd phase transition metal and has smooth M(T) and $\Delta S_m(T)$ curves as shown in Fig.4 and Fig. 5.

To obtain higher magnetocaloric performances, researches are mainly oriented towards 1st phase transition alloys (Fig. 4). This leads to sharp $\Delta S_m(T)$ and MCE(T) curves. Upgraded magnetocaloric properties are obtained through a large reduction of the temperature working band (Fig. 5). The results obtained with such materials are already promising, especially with compounds like $Gd_5(Si_xGe_{1-x})_4$ [2],[6] and $MnFeP_{1-x}As_x$ [7], [8]. These last materials present especially higher MCE and lower cost than Gd and can be used with permanent magnet structures. Their Curie temperature can be adjusted by controlling the material compositions as shown for $MnFeP_{1-x}As_x$ in Fig. 6. Larger temperature working band can be so achieved by juxtaposing several compositions.

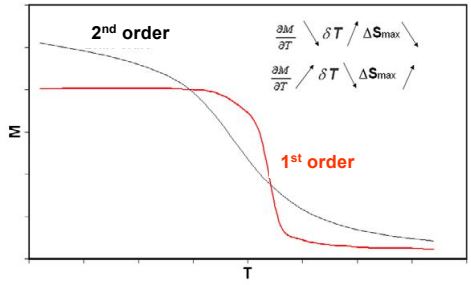

Fig.4. 1st and 2nd phase transitions

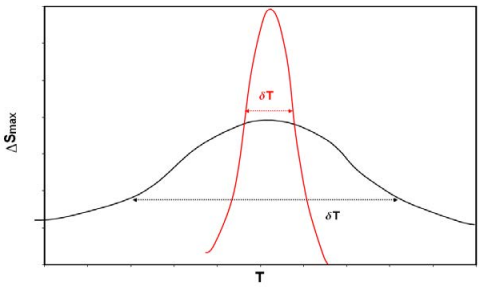

Fig.5. $\Delta S_m(T)$ induced by 1st and 2nd phase transitions

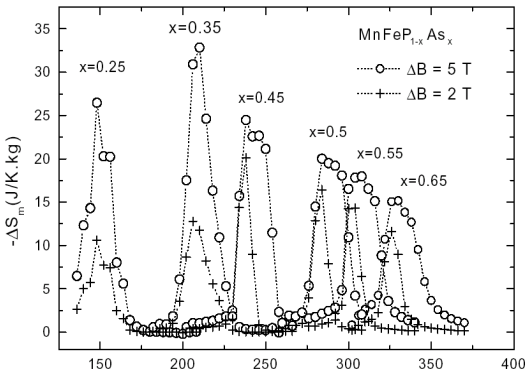

Fig.6. Influence of $FeMnP_{1-x}As_x$ composition on ΔS_m [7]

Today, thanks to the collaboration with LC and LLN several compositions of MCE material are under elaboration and test. Fig. 7 gives an example of the results obtained. It compares the properties of MnAs and $FeMnP_{0.45}As_{0.55}$ synthetized samples to the ones of a commercial Gd sheet and of GdSiGe developed in Ames Laboratory, USA.

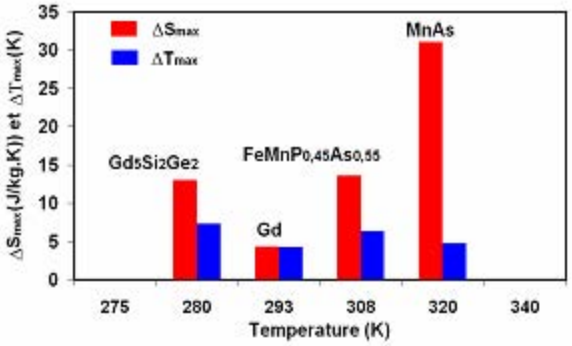

Fig.7. Magnetic entropy and MCE measured under an applied induction of 2T [3]

Active magnetic regenerative refrigeration cycle (AMRR)

The temperature span of a direct magnetic cycle is limited for actual giant MCE materials to a few K/T (e. g. 2 K/T for gadolinium). In order to obtain large temperature spans, magnetic refrigerators use a specific thermal cycle which is similar to a Stirling cycle and which is called Active Magnetic Regenerative Refrigeration cycle: AMRR [9], [10], [11].

AMRR cycle description

AMRR is a specific magnetic refrigeration cycle which creates a temperature gradient along the MCE material thanks to an energy exchange between the material and an intermediate fluid. Fig. 8 explains the principle of this cycle, the system starting from room temperature.

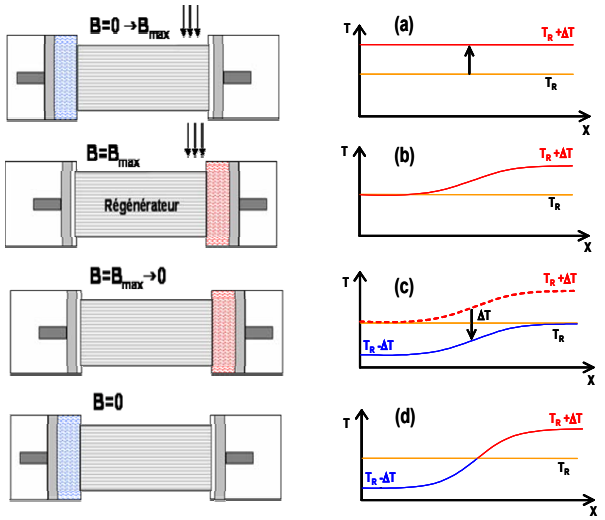

Fig.8. Schematic drawing of AMRR cycle

The four following steps are used:

(a) the material is adiabatically magnetized. Its initial temperature increases by ΔT (MCE)
(b) an external fluid flows along the material from the cold side to the hot side. A gradient temperature is created along the MCE material bed.
(c) the material is adiabatically demagnetized. The temperature of the bed decreases by ΔT (MCE)
(d) the fluid flows from the hot side to the cold side and enhances the temperature gradient.

The temperature span between the cold and the hot ends is amplified at each cycle and reaches at the steady state a level several times higher than the intrinsic ΔT of the material.

AMRR cycle modeling

AMRR cycle is an important component to master in order to achieve high efficiency magnetic refrigeration. Its modeling is necessary to analyze the heat exchange and to evaluate the parameters influences [12], [13]. We present in this paper a one dimensional numerical model we have developed. The considered active regenerator is a sheet of gadolinium with a length L of 50 mm and a thickness y_r of 1 mm. The fluid is a thin film of water (y_f = 0.1mm). It has a uniform flow with a constant velocity *v*. Only convection exchanges between the regenerator and the fluid are considered, the diffusion phenomenon along the bed is assumed to be negligible (Fig. 9).

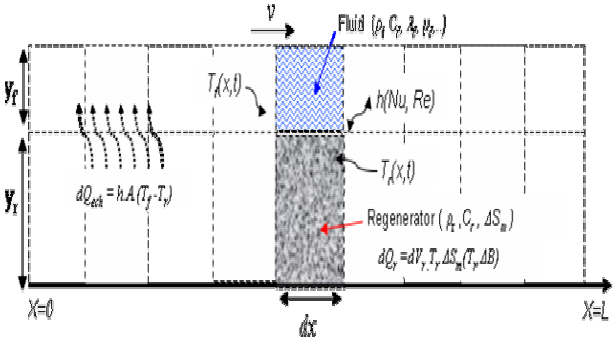

Fig. 9. A differential element of regenerator and fluid used to establish the model [13]

The heat exchanges between the fluid and the regenerator are described by the following equations for half of a cycle.

$$\rho_f C_f \left(\frac{\partial T_f}{\partial t} + v\frac{\partial T_f}{\partial x}\right) = h.\frac{A}{V_f}(T_r - T_f) \quad (4)$$

$$\rho_r C_r(\Delta B, T_r)\frac{\partial T_r}{\partial t} = h.\frac{A}{V_r}(T_f - T_r) \quad (5)$$

$$Q_r(T_r, \Delta B) = \rho_r T_r . \frac{f}{2}.\Delta S_m(T_r, \Delta B) \quad (6)$$

The indeces r and f represent respectively the material regenerator and the fluid.
T is the temperature; C the specific heat; t the time; x the position; h the heat transfer coefficient; A the cross-sectional area between the fluid and the regenerator; ρ the density; V the volume; Q_r the volumetric power heat released or absorbed when the differential element of the regenerator is magnetized or demagnetized; f the cycle frequency and ΔS_m the magnetic entropy change of the regenerator bed which depends on the temperature and the magnetic field change ΔB.

The equations are solved numerically by finite difference scheme. The problems of stability of the explicit numerical methods were analyzed by Courant-Friedrich-Levy criterion (CFL criterion) which ensures the solution convergence.

Fig. 10 shows the evolution with time of the temperature of the cold and the hot sources. The increase of the temperature span is clearly observed. The steady state is achieved after about 30 cycles. Elementary AMRR cycle is also reproduced with its four steps behavior: instantaneous increase and decrease of temperature during material magnetization and demagnetization and smooth evolutions during fluid and material heat exchanges.

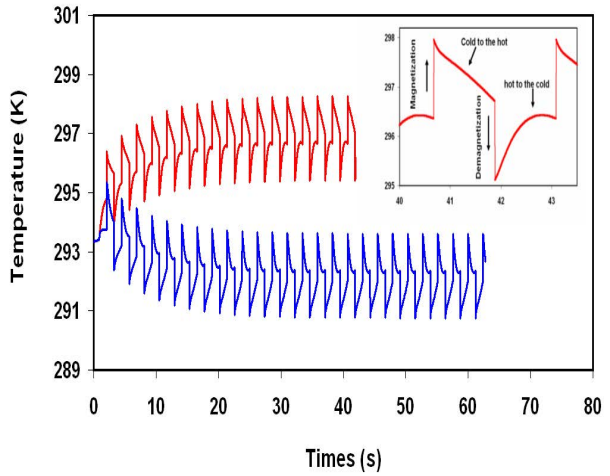

Fig. 10. Temperature evolution at hot and cold ends [13]
(T_{amb} = 293K, water flow = 5 ml/s , B= 0.8T, f = 0.5 Hz)

This model is a powerful tool to analyze the transient and the steady behavior of AMRR cycles. The influence of different parameters can be investigated and optimum conditions can be found for a given magnetic refrigeration application.

In Fig. 11 for example, the interest of FeMnPAs is clearly highlighted. The material MCE and ΔS_m are respectively two and three times higher than Gd. For the same volume and AMRR cycle conditions, the temperature span gain is about twice.

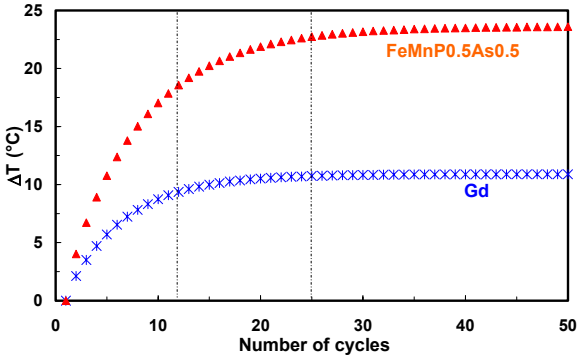

Fig. 11. Temperature span evolution obtained with Gd and $FeMnP_{0.5}As_{0.5}$

Giant MCE applications to magnetic refrigeration at room temperature

Up to now the different systems are developed as demonstrators in order to show the feasibility of magnetic refrigeration at room temperature or to study AMRR cycle. We present here three systems: two developed in USA by Ames Laboratory and Astronautics Technology Center and one made in our laboratory.

USA demonstrators

The first magnetic refrigeration system developed was presented in 1998 by Gschneider from Ames Laboratory in Iowa and Zimm from Astronautics Technology Center in Madison (ACA). It was used to demonstrate the feasibility of such a technology [1]. It is based on a superconducting field source of 1.5 to 5 T (Fig 13). Two beds of 1.5 kg of Gd powders constitute the active material and water is used as a fluid heat exchanger (flow = 5 l/min). Magnetization and demagnetization are achieved by an alternative movement of the material bed in the magnet thanks to a pneumatic drive. The force needed is about 2500N and the cycle frequency is 0.17 Hz.

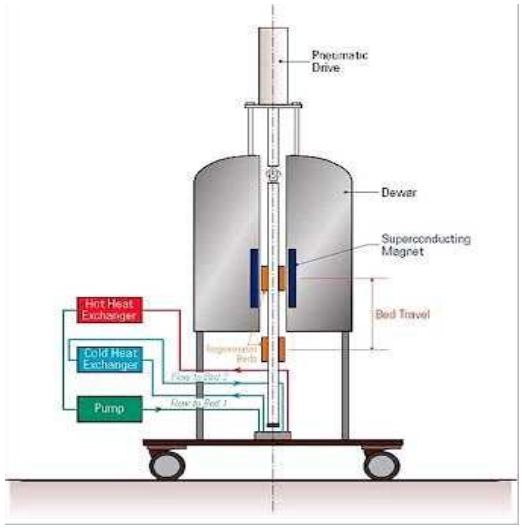

Fig. 13. Scheme of the first superconducting system [1]

The maximum measured cooling power is 600 W with a temperature span of 10 °C and a coefficient of performance COP of 6. Larger ΔT can be obtained for reduced powers: 24 °C for 100 W and 35 °C for 80 W.

A second device has been also studied by the same authors [2]. It is a rotating system in which the field is created by a modified Halbach cylinder made of NdFeB permanent magnets (Fig. 14). The induction level is 1.5 T in 1.25 cm airgap. In the theoretical project GdSiGe is considered as an active material. The system is designed for both refrigerator and freezer and the expected performances are respectively: 127 and 40 W for the cooling power, 33 and 11 °C for the temperature span, 3.9 and 6 for the COP.

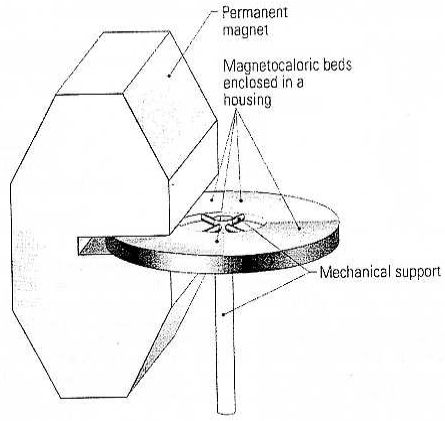

Fig. 14. Principle of the permanent magnetic refrigerator studied by ACA and Ames Laboratory [2]

Fig. 14 shows a photo of the prototype. It is a one stage refrigeration system in which Gd is used. For 0.4 to 2Hz cycle frequencies, 0.4 to 0.8 water flows, the obtained temperature spans vary from 4 to 20 °C and the cooling powers from 50 to 10 W.

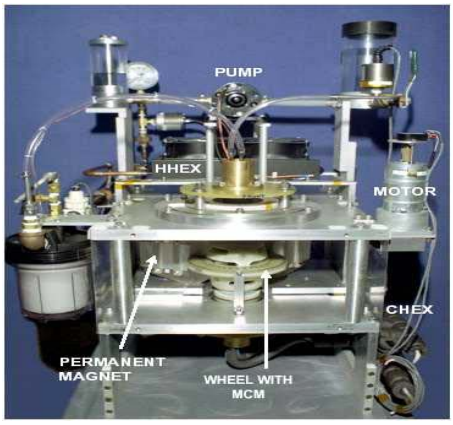

Fig. 14. Photo of the system [14]

A new system is under study and the expected performances are 10 kW for the cooling power, 20 °C for ΔT and 8 for COP.

The permanent magnet based device developed at LEG

In order to study the AMRR cycle, a magnetic refrigeration device has been developed [15]. Its principle is described in Fig. 15 and a photo is given in Fig.16. The magnetic field of 0.8T is produced by a Halbach magnet cylinder. The active block is a cylinder made of stacked Gadolinium sheets. It is equipped with thermocouples in order to measure the temperature variation along the material. Water is used as a fluid. Its transfer from one side to the other is driven by an external pump. No heat exchanger is used. The cycle period is equal to 2 s.

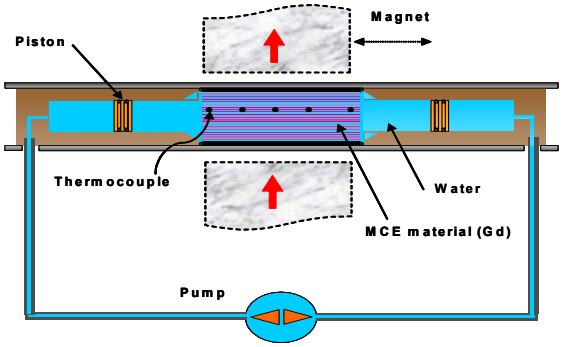

Fig. 15. Scheme of the active part of the LEG system [15]

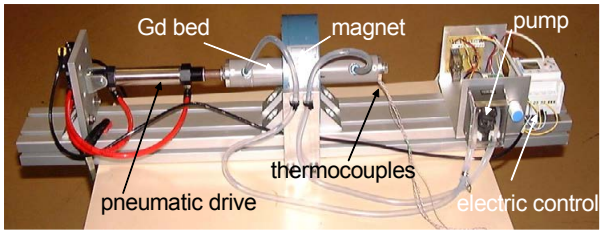

Fig. 16. Photo of LEG system [13]

Fig. 17 shows the temperature span obtained between the hot and cold ends for a 5 ml/s water flow. The cooling power is 37 W and the COP is 9. These curves are quite similar to those in Fig. 6 which are obtained by the model in the same AMRR cycle conditions.

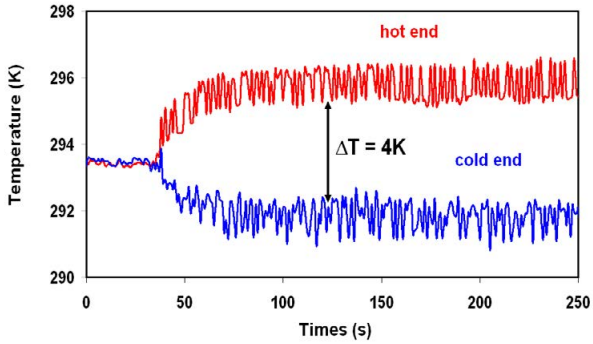

Fig. 17. Experimental evolution of the temperature at the hot and cold ends of the device [13]

For 0.5 ml/s water flow, the results are: ΔT=7 °C, cooling power = 7 W and COP=2. In that case the model

overestimates the ΔT because heat diffusion along the Gd sheet is no more negligible.

This experimental device and its associated test bench are easy to make and compact. They can work autonomously and can be modified very easily. It is a first step for magnetic refrigeration applications. The results already obtained have validated the AMRR model that we have developed [12]. This bench will be used to evaluate the potential of different MCE materials and the efficiency of different AMRR cycles.

Conclusion

Application of the MCE for refrigeration at room temperature is a recent and innovative research theme which should lead to higher efficiency and friendlier environment systems than the conventional thermodynamic ones. Giant MCE material is one key for the development of such a technology. Researches in this field have been enhanced during these last five years and advanced results have been already obtained. Besides high magnetocaloric properties, other criteria must be achieved as: easy elaboration, low cost, easy workability, no toxicity, weak ageing. The parameters of the magnetothermal cycle, the field source and the exchangers should also be optimized in order to achieve competitive systems.

Today, only demonstrative systems are developed. They are the first steps in magnetic refrigerator but the challenge is to reach industrial applications. Collaboration between LEG, LC and LLN, gathers competences in materials elaboration, thermal exchanges and magnetic systems. Out target applications are vehicle and building air conditioners.

Acknowledgements

The authors would like to thanks the ADEME (the French Environment and Energy Management Agency) PSA Peugeot Citroën and ELESA (INPG Federation) for their financial supports.

References

[1] Zimm C., Jastrab A., Sternberg A., Pecharsky V., Osbone Jr. M. and Anderson I. "Description and Performance of a Near Room Temperature Magnetic Refrigerator", Advances in Cryogenic Engineering, Vol. 43 (1998) pp.1759-1766.

[2] Karl A. Gschneider, Jr. and Vitalij K. Pecharsky "Magnetic refrigerators / freezers and air conditioners" Proceedings of Domotechnica Appliance Engineering Conference, March (2001), pp. 170-182.

[3] Lebouc Afef, Allab Farid, Fournier Jean Marc et Yonnet Jean Paul "Refrigération magnétqiue" Techniques de l'ingénieur, 2005, RE28-1 – RE28 -16.

[4] Brown G. V. "Magnetic heat pumping near-room temperature" J. Appl. Phys. 47 (1976), pp. 3673

[5] Yu B. F., GAO Q., Chen Z. "Review on research of room temperature magnetic refrigeration" International Journal of Refrigeration 26 (2003), pp. 622-636

[6] Pecharsky V. K. and Gschneider Karl A. Jr. "Giant Magnetocaloric Effect of optimally prepared $Gd_5Si_2Ge_2$" J. Appl. Phys. 93 (2003), pp. 4722-4728

[7] Tegus O., Brück E., Buschow K. H. J. and de Boer F. R. "Transition-metal-based magnetic refrigerants for room temperature applications" Nature/ volume 415/ 10 January 2002, pp. 150-152.

[8] Fruchart D., Allab F., Balli M., Gignoux D., Hlil E.K., Skryabina N., Tobola J., Wolfers P., Zach R. "On the magnetocaloric effect in d-metal pnictides" European Conference on Thermoelectrics of European Thermoelectric Society, September 15-17, 2004, Krakow, Poland.

[9] Brown G. V. "Magnetic Sterling Cycles- a new application for magnetic materials" IEEE Trans. Mag., Vol. 13, N° 5 (1997), pp. 1146-1148

[10] Barclay J. A. "Active and passive Magnetic regenerators in gas/ magnetic refrigerators" J. Alloys Compounds 207 (1994), pp. 355-361

[11] Barclay J. A., Steyert W. A. "Active Magnetic regenerator" US Patent N° 4, 332, 135 (1982)

[12] Allab F., Kedous – Lebouc A., Fournier J. M. and Yonnet J. P. "Numerical Modeling for Active Magnetic Regenerative Refrigeration" Intermag 2005, April 4 - 8, Nagoya – Japan, to be published in IEEE Trans. Mag.

[13] Shir Farhad, Bennett Lawrence H., Della Torre Edward, Mavriplis Catherine, Shull Robert D. "Transient response in magnetocaloric regeneration" IEEE Trans. Magn Vol. 41, N° 6 (2004), pp. 2129-2133.

[14] www.arti-21cr.org/research/ongoing/Astronautics-040107.pdf

[15] Clot P., Viallet D., Kedous-Lebouc A., Fournier J. M., Yonnet J. P., Allab F. "A magnet based device for active magnetic regenerative refrigeration", IEEE Trans. Mag., Vol. 39, n° 5, 2003, pp. 3349-3351.

Afef Kedous-Lebouc *– CNRS Researcher, Dr.,*
Laboratoire d'Electrotechnique de Grenoble (LEG), INPG/UJF – CNRS UMR 5529, ENSIEG, PB 46, 38402 Saint Martin d'Hères Cedex, FRANCE
e-mail: afef.lebouc@leg.ensieg.inpg.fr

Farid Allab *– INPG Ph.D. Student,*
Laboratoire d'Electrotechnique de Grenoble (LEG), INPG/UJF – CNRS UMR 5529, ENSIEG, PB 46, 38402 Saint Martin d'Hères Cedex, FRANCE
e-mail: farid.allab@leg.ensieg.inpg.fr,

Jean Marc Fournier *– UJF Professor, DSc.,*
Laboratoire d'Electrotechnique de Grenoble (LEG), INPG/UJF – CNRS UMR 5529, ENSIEG, PB 46, 38402 Saint Martin d'Hères Cedex, FRANCE
e-mail: Jean-marc.fournier@leg.ensieg.inpg.f,

Jean Paul Yonnet *– CNRS Researcher, DSc.,*
Laboratoire d'Electrotechnique de Grenoble (LEG), INPG/UJF – CNRS UMR 5529, ENSIEG, PB 46, 38402 Saint Martin d'Hères Cedex, FRANCE
e-mail: jean-paul.yonnet@leg.ensieg.inpg.f,

Micro heat pipe for electronic cooling

Mariya Ivanova, Christian Schaeffer, Yvan Avenas

Abstract: *The thermal problem caused by the increasing level of heat dissipation is further compounded by the trend of miniaturization in the modern power electronics. Consequently heat sinks have to dissipate very large heat flux densities. The consequence is the increasing level of heat dissipation densities in electronic equipment for that reason power electronics specialists are very interested in different cooling mechanisms. Heat pipes are very effective heat transfer devices and can be used to raise the thermal conductive path in order to spread a concentrated heat source over a much larger surface area. As a result, the high heat flux at the heat source can be reduced to a much smaller and manageable level that can be dissipated through conventional cooling methods.*

Keywords: *electronic cooling, heat pipe, silicon, DBC substrates*

1. Introduction

As the power densities of power components continue to grow, thermal issues are becoming extremely important and vital for the product quality. The primary causes of failures in electronic equipment are the excessive temperatures of the critical components, such as semiconductors and transformers.

Power systems for space application are usually housed in completely sealed enclosures due to safety reasons. Since the cooling of these systems primarily relies on natural convection, the effective management of the heat removal from a sealed enclosure poses a major thermal-design challenge.

In this context heat pipes are very effective heat transfer devices and can be used to raise the thermal conductive path in order to spread a concentrated heat source over a much larger surface area. As a result, the high heat flux at the heat source can be reduced to a much smaller and manageable level that can be dissipated through conventional cooling methods.

The objective of this work, presented in this paper is to describe the feasibility of a cooling system with micro heat pipes. We will present two types of micro heat pipes, one embedded in a Direct Bonded Copper structure (DBC) and second in silicon. The advantage of this kind of heat pipe is the integration of the electronic component layout directly on the heat pipe itself, which eliminates the existence of a thermal interface between the device and the cooling system.

2. Heat pipe

Heat pipe cooling is becoming increasingly popular in the field of electronics due to its advantages over extrusion heat sinks. The heat pipes are heat exchangers allowing a passive circulation of the coolant thanks to a phase shift and capillary wick (Fig. 1). Cotter [1] was the first who introduce the concept of micro heat pipes. It means that the hydraulic diameter is about 10 µm. Several authors [2, 3] studied silicon micro heat pipes; they present small sizes but cannot handle high heat flux. The length of the heat pipe is divided into three parts: evaporator section, adiabatic section and condenser section.

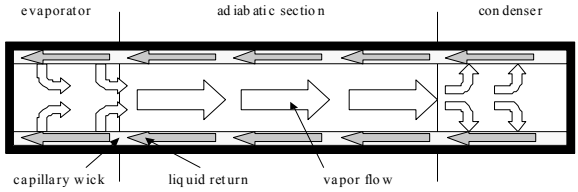

Fig.1. Heat pipe operation principle

Heat applied to the evaporator section by an external source is conducted through the pipe wall and wick structure, where it vaporizes the working fluid. The resulting vapor pressure drives the vapor through the adiabatic section to the condenser, where the vapor condenses, releasing its latent heat vaporization to the provided heat sink. The capillary pressure created by the menisci in the wick pumps the condensed fluid back to the evaporator section. That plays the role of driving force in the heat pipe. Many capillary wick designs and structures can be found in the heat pipe literature. Three structures are commonly used: groove wick, sintered metal powders and mesh screen [4], [5]. These devices use highly effective evaporation and condensation cycles to extend surfaces.

3. Heat pipe study process

The heat pipe study is divided in several steps. The first step of thermal experiments is the charging of the heat pipe with working fluid. Heat pipe operation is very sensitive to the quantity of injected fluid. In our case the working fluid is pure water and is injected in the heat pipe using a micro syringe. The injecting fluid has to be as pure as possible for eliminating the presence of incondensable gases, which can be harmful for the correct heat pipe operation. Before filling the prototype, its intern walls have to be degassed using a vacuum pump. The

first step of the experiment is the study of the heat pipe without working fluid. Thus the heat transfer between hot and cold sources is only convection and conduction through the heat pipe walls. Then the same experiment will be made with the heat pipe filled up with pure water. The thermal resistance of the system is defined as the temperature drop between the maximum temperature on the hot source level and minimum temperature on the cooler level divided by the input power (1).

$$Rth = \frac{(Tj - Tc)}{P} \quad (1)$$

The second step of this thermal study of a heat pipe is to determine the optimum quantity of a fluid injected in the heat pipe. The quantity of working fluid has to be enough to saturate the capillary wick.

We quantify that the best operation of the device is when its thermal resistance is lowest. Fillings with different water quantities have to be done. The heat pipe thermal resistance is calculated for each filling. And the filling with a quantity of water for which the level of the thermal resistance of the device is lowest we quantify like the optimum injected fluid for the best heat pipe operation. On figure 2 is shown the principle of this theory.

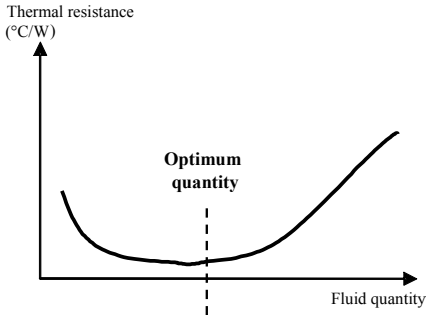

Fig. 2: Thermal resistance of the heat pipe depending on the injected quantities of fluid

The last step of the heat pipe experimental study is determination of its heat transfer limitation. We quantify the heat transfer limitation of the heat pipe with the knowledge of the evolution of the heat pipe thermal resistance in function of the input power for different cold plate temperatures. At the moment when the thermal resistance of the heat pipe increases with the increase of the heat flux (input power) we consider that heat transfer limit occurs (Fig.3). The more the power increases the more the heat pipe thermal resistance is high. There is a moment when the device operation is destroyed because of a dry out of the evaporator. The observed phenomenon present the capillary limit. The capillary limit is determined by the pumping capacity of the wick structure. The capillary limit is exceeded when the heat flux into the heat pipe is so high that the pumping force provided by the capillary wick can not provide for an adequate flow of working fluid back to the evaporator. When the mass flow rate of the vapour living the evaporator is greater than the mass flow rate of the liquid flow returned to the evaporator through the wick structure, the wick in the evaporator zone becomes depleted of working fluid and the evaporator path for heat removal is exhausted. In this case there is only conduction through the heat pipe wall and the wick structure.

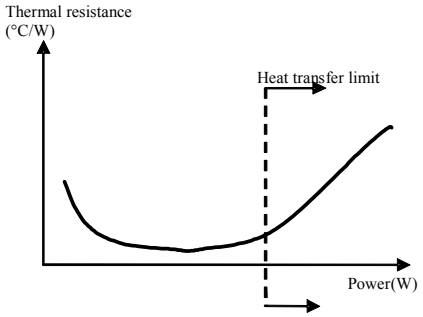

Fig. 3: Heat pipe thermal resistance for different input powers

4. Silicon heat pipe

Silicon provides several advantages compared to other materials. Thanks to silicon etching techniques, capillary groove wick can be very easily obtained with much smaller grooves dimensions. Thus, the effective thermal conductivity of the wick for the evaporator section is higher, at the same time the heat pipe made from silicon is very light thanks to his physical properties.

A prototype of a silicon flat miniature heat pipe was realized to demonstrate the feasibility of heat spreading of this type of heat pipe [4]. The selected working fluid is water.

The heat pipe is made with three silicon wafers (Fig. 4) with dimensions given in Table 1.

Table 1
Intern dimensions of the heat pipe

channel width W	90 µm
channel height t_g	100 µm
vapor passage thickness	500 µm
wick length	40 mm
wick width	10mm

The thickness of each wafer is 500 µm. Rectangular micro channels are machined in wafers A and C by deep etch technique. Grooves with rectangular section of very precise size can be obtained. In wafer B the vapor passage cavities are fabricated. Three wafers are assembled by the Silicon Direct Bonding technique.

On wafer A, filling hole is laser-drilled. A thin layer of metallization is sputtered around the hole laser-drilled in wafer A, which allows soldering a copper filling system.

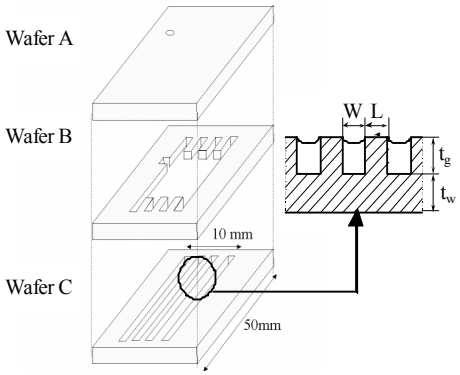

Fig.4. Silicon heat pipe assembling

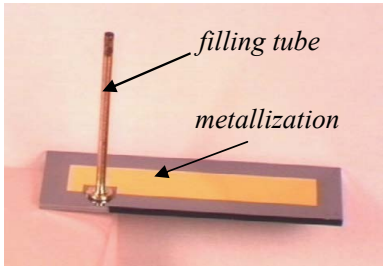

Fig.5. Silicon heat pipe

4.1. Experimental results

The heat source is constituted by a resistor. Its surface is 1 cm^2 and it is glued on the heat pipe. The device is cooled by a copper water cold plate.

Experiments have been realized with different water temperatures of the cold plate and different input power. Power dissipated in the system is calculated by measuring the voltage and the current in the electronic component.

Firstly, studies with empty heat pipe have been realized and then the same measurement has been made on the filled device with pure water. In the case of an empty device there is no heat pipe effect, the heat transfer between hot and cold sources is only conduction through the heat pipe walls.

Fig. 6,7 present the temperature distribution on the heat pipe surface obtained with infra red imaging. A temperature along the measuring line of the empty and filled devices for 12 W, applied on the resistor and 40°C temperature on the condenser is shown on Fig.7.

We can see that the temperature drop between the evaporator and condenser decreases of 75% in the case of micro heat pipe filled with 150 µl of pure water. This result shows the effectiveness of the heat pipe.

All experiments are realized with variation of the input power between 5W and 60W, and temperature variation of the water, circulating in the cold plate, between 30°C and 80°C.

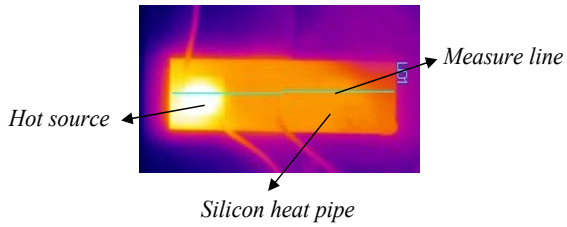

Fig.6. Infra red imaging

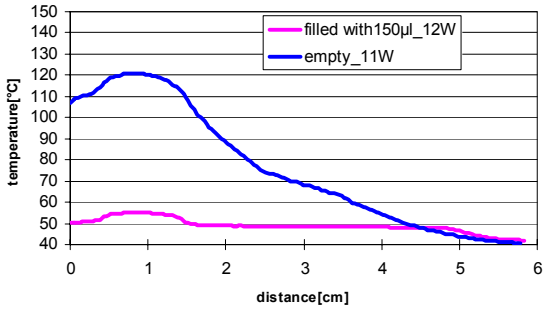

Fig.7. Temperature distribution along the heat pipe measure line

Study of the heat pipe heat transfer capacity has been realized. The conclusion is that the maximum heat transport capability of a silicon heat pipe is ranging between 30 and 55 W for all cooling water temperatures. Figure 8 shows the maximum heat transported in the heat pipe depending on the operation temperature. From values up to 60W the device thermal resistance increases. This increase is due to an area in the heat pipe where there is no more liquid because the capillary pumping action becomes insufficient to compensate the pressure drops in the capillary wick: the more the power increases, the more the length of this zone increases, what causes an increase in thermal resistance.

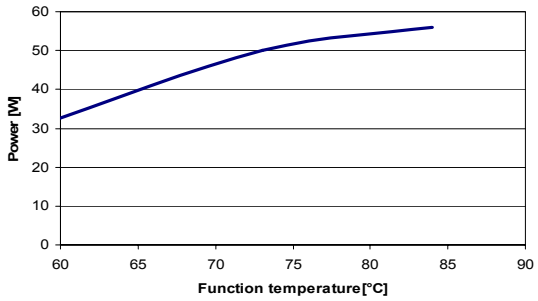

Fig.8. Silicon heat pipe

5. DBC heat pipe

Several authors have presented a heat pipe prototypes fabricated with ceramic materials. [6] [7]. We propose to integrate a heat pipe in DBC substrates.

Direct Bonded Copper technology is used for power applications, exhibiting good general features as a

medium thermal conductivity-24 W/mK for the Al_2O_3 (Alumina) and 380 W/mK for the copper, low coefficient of thermal expansion, a high current carrying capabilities due to the copper thickness (0.2 mm to 0.3 mm) and a basic fulfilling of packaging functions as electrical interconnection, mechanical fixation and thermal management. This technology has permitted to qualify an advanced packaging for power modules such as DC/DC converters for the space industry (figure 9).

Nevertheless and in spite of these advantages, thermal management remains crucial due to an increase of dissipative components.

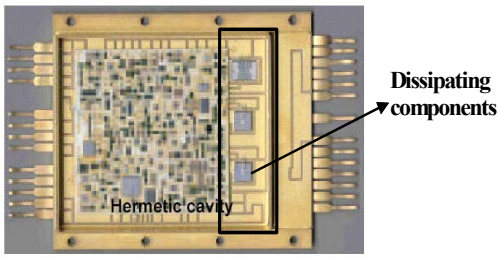

Fig. 9: DBC packaging for DC/DC converter with power components in hermetic cavity

When the traditional materials are limited in terms of conduction cooling, the heat pipe integration is a very interesting alternative. Generally the heat pipe is fabricated with metallic materials and in this case the electrical interconnections must be assumed by a specific board. The consequence is an additional integration for heat pipe it self and for the components.

The solution is to develop a heat pipe embedded in DBC structure able to assure an electrical interconnection directly linked on a high dissipative system and a mechanical fixation of the whole part of the frame (figure 10). In that way it can transfer heat dissipated by the components to a cooler (cool box, heat exchanger) and then reduces the thermal resistance between the component and the cooler. The temperature on the substrate is homogenized and the apparition of hot spots is eliminated.

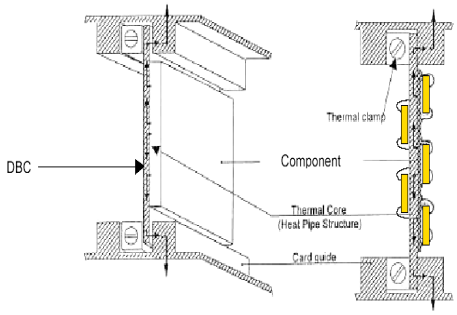

Fig. 10: Central core with heat pipes embedded in the interconnection substrate

An example of embedded heat pipe in an interconnection substrate is shown on figure 11. Using a heat pipe the heat flux dissipated by the components is spread through the heat pipe to the box walls playing role of a cold source and then evacuated in the ambient.

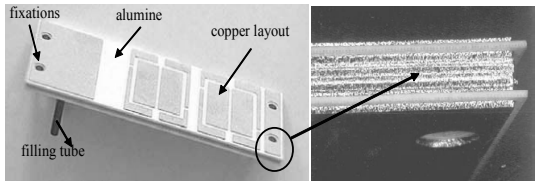

Fig. 11: Photography of the DBC heat pipe

5.1. Experimental results

A prototype or DBC heat pipe was fabricated by Curamik. A photograph of the heat pipe integrated in DBC layers is presented on figure 11. The filling of the heat pipe was realized through a copper tube fixed on the one side of the prototype. The design of the copper layout is made to assure the integration of thermocouple for the temperature measuring.

The heat source is constituted by an IGBT. Its surface is 1.2 cm^2 and it is glued on the heat pipe. The device is cooled by a copper water cold plate. The temperature of the water, circulating in the copper cooling system is controlled. The filling system contains a valve according to a vacuum pump and a filling device for the injection of the working fluid. Experiments have been realized with different water temperatures of the cooling system and different input power. The experimental setup is shown on figure 12. The first step of the experiment was the study of the heat pipe without working fluid.

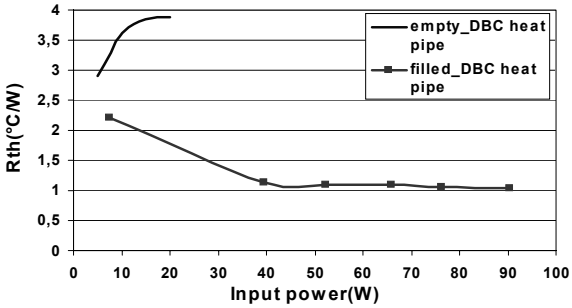

Fig. 12: Thermal resistance according to the input power

The second step of thermal experiments is the charging of the heat pipe with working fluid. The injecting fluid has to be as pure as possible for eliminating the presence of incondensable gases, which can be harmful for the correct heat pipe operation. Then the same experiment has been made with the heat pipe filled up with pure water. The thermal resistance of the system is defined as the temperature drop between the maximum temperature on the IGBT level T_j, measured on the heat pipe wall and minimum temperature of the cooler T_c divided by the input power P (1). Figure 12 shows the thermal resistance depending on the input power of

empty DBC heat pipe and the same prototype filled with 1100µl of pure water. The temperature on the cooler level is 50 °C. When the DBC heat pipe is filled and operational there is a decrease of 4 times of system thermal resistance. Low values of the heat pipe thermal resistance provide a decrease of the IGBT temperatures.

The third step of the thermal experiments is the study of the heat pipe heat transport capacities. We quantify the heat transfer limitation with the knowledge of the evolution of the heat pipe thermal resistance in function of the input power for different cold plate temperatures. At the moment when the thermal resistance of the heat pipe increases with the increase of the heat flux (input power) we consider that heat transfer limit occurs. The more the power increases the more the heat pipe thermal resistance is high. There is a moment when the device is destroyed because of a dry out of the evaporator. As we can see on Fig.13, the thermal resistance of a DBC heat pipe decreases and is constant until the input power reaches a values ranging between 100W and 110W. From these values the thermal resistance increases until the input power reaches 140W. This increase is due to an area in the heat pipe evaporator, where there is no more liquid because the capillary pumping action becomes insufficient to compensate the pressure drops in the capillary wick: the more the power increases, the more the length of this zone increases, this phenomenon causes an increase in the thermal resistance. The conclusion is that the maximum heat transport capability of the heat pipe integrated in DBC layers is ranging between 100 and 110 W for all cooling water temperatures.

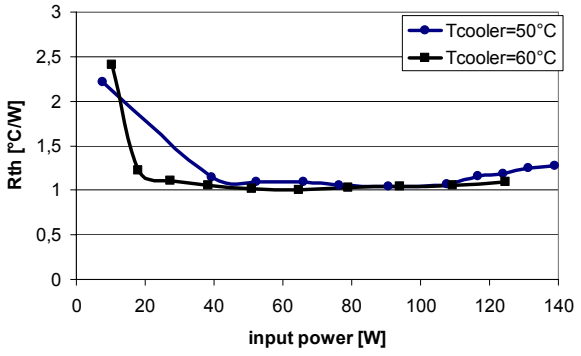

Fig. 13: Thermal resistance of the DBC heat pipe depending on the input power

6. Conclusion

This work shows that the silicon and DBC heat pipes can be used for the improvement of the embedded electronics cooling.

Two types of prototypes were fabricated: silicon heat pipe and heat pipe integrated in DBC substrates.

Experimental studies have been realized in order to demonstrate the operation of the heat pipe and to find the heat pipe heat transfer capacities.

For a silicon micro heat pipe we found that it has a capability to transfer more than 50W/cm^2 with a filling with 150 µl of pure water. An improvement of the thermal performance of the system of 75% was demonstrated with the integration of the micro heat pipe.

The DBC heat pipe has a best operation for a filling with 1100 µl. With the integration of this device we reduce the system thermal resistance 4 times. Experimental studies were realized in order to determine the heat transport limits of the DBC prototype. The heat pipe has a capacity of heat transfer of more than 100 W without a dry out in the evaporator zone. These results are very promising and two prototypes were tested in space orbit in order to finalize the study of this DBC application. The obtained results confirm the presented performances in this paper.

Acknowledgement

The authors thank the CEA-LETI in Grenoble, France for the fabrication process of the silicon thermal spreader. Contact for more information to GillotCh@chartreuse.cea.fr. The authors would like to thank also to B. Mallet from Laboratoire d'Electrotechnique de Grenoble and to A. Rogg, K. Exel from Curamik Electronics GmbH for their precious work in this project.

References

[1] T.P. Cotter, "Principles and properties of micro heat pipes," *Proceedings of 5th International Heat Pipe Conference*, Tsukuba, Japan, 1984, pp. 328-335.

[2] G.P Peterson, A.B. Duncan, M.H. Weichold, "Experimental investigation of micro heat pipes fabricated in silicon wafers," *Journal of Heat Transfer*, Vol. 115, Aug. 1993, pp.751-756.

[3] A.K. Mallik, G.P. Peterson, M.H. Weichold, "Fabrication of vapour deposited micro heat pipe arrays as an integral part of semiconductor device," *Journal of Micromechanical Systems,* Vol. 4, Sept. 1995, pp.119-131.

[4] Faghri A., "Heat Pipe Science and Technology", Taylor and Francis, 1995.

[5] Chi S.W., "Heat Pipe Theory and Practice", McGraw-Hill, 1976.

[6] Jones K.W., Liu Y., Gao M. "Micro heat pipes in low temperature cofire ceramic (LTCC) substrates", Inter Society Conference on Thermal Phenomena IEEE, 2002, p. 230-235

[7] Jones K.W., Liu Y., Gao M., "Micro heat pipes in low temperature cofire ceramic (LTCC) substrates", IEEE Transaction on Components and Packaging Technologies, vol. 26, No. 1, march 2003

Mariya Ivanova *– Ph.D. Student, INP de Grenoble, Laboratoire d'électrotechnique de Grenoble, France e-mail: mariya.ivanova@leg.ensieg.inpg.fr.*

Christian Schaeffer *– Professor, INP de Grenoble, Laboratoire d'électrotechnique de Grenoble, France. e-mail: christian.schaeffer@leg.ensieg.inpg.fr*

Yvan Avenas *– Associate Professor INP de Grenoble, Laboratoire d'électrotechnique de Grenoble, France. e-mail:yvan.avenas@leg.ensieg.inpg.fr*

Analysis of the Water Flow Behaviour in Water Modification Device

Yanko Slavtchev, Raina Tzeneva and Peter Dineff

Abstract: *This paper presents an analysis of the water flow behavior in an industrial maze-shaped device for modification of water and water solutions. Under the conditions, generated within the device, electric structural kinetic elements could be modified, by a Lorentz polarization, during their transverse motion through permanent magnetic fields when the fields exert max Lorentz forcing upon the flowing water.*

Keywords:*, polarization modification technologies, non-uniform magnetic field, finite elements method, fluid models, water velocity and pressure distribution.*

Introduction

It is admitted that the majority of the water and water solutions magnetic modification devices are constructed in such a way that the structural modification effect could not be bound uniquely to the existence of magnetic kinetic structure water's elements or electrical kinetic structure water's elements.

Furthermore, water's structure elements have electric as well as magnetic dipole moment, at molecular and over-molecular level, i.e. these are simultaneously magnetic and electric dipoles. Both moments are most commonly collinear due mainly to the anisomery of the water's structure element set-up, Fig. 1.

It means that one and the same water's structure element endures the direct influence that the magnetic field exerts on the magnetic moment and at the same time endures the Lorentz force, acting on the electric moment during motion through the same magnetic field.

The max Lorentz forcing on the water's structure elements is reached when establishing a scheme of transverse motion of water or water solutions in relation to the direction of the permanent magnetic filed intensity. This scheme develops progressively into a popular construction design for modification devices [1], [2], [3].

There is one more characteristic of the water modification device. It uses a monotonically increasing non-uniform magnetic filed intensity having gradient directed along the flow of water, Fig. 2.

That is how, by changing only the mutual position of the two permanent magnets, there emerges an area of max magnetic field intensity ***H*** and at the same time max water flow velocity ***V*** at the outlet, Fig. 2b.

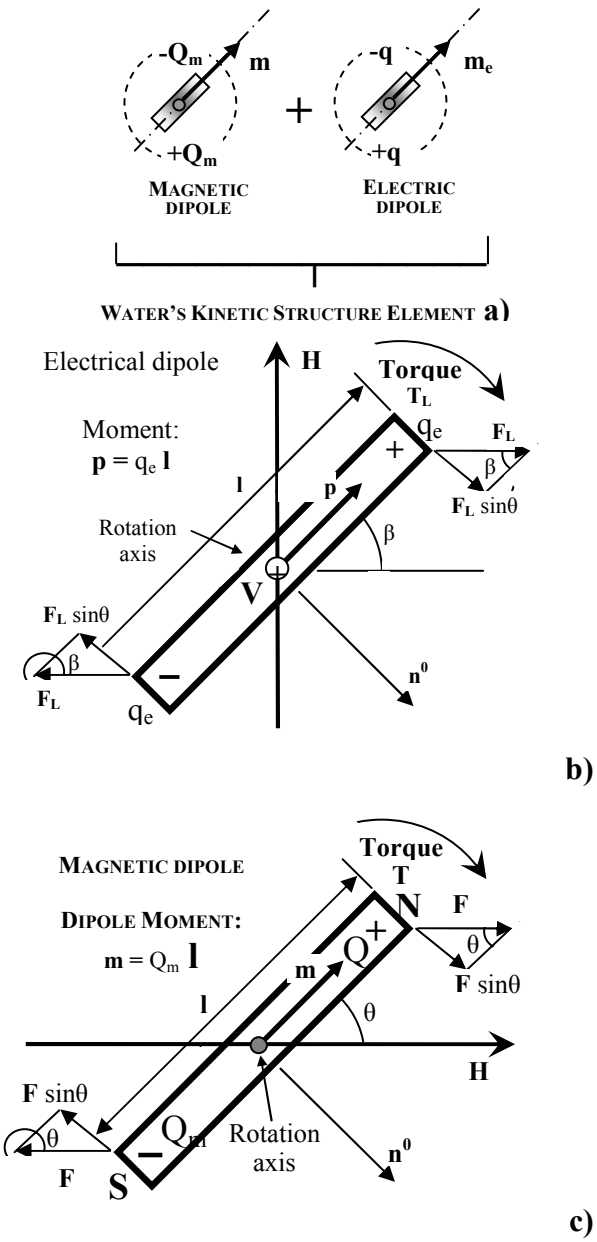

Fig.1. Water's structure element magnetic and electric dipole moments due to: (a) *structure anisomery*; (b) *Lorentz polarization torque* T_L *for the water's structure element motion with velocity* ***V*** *perpendicular to the sheet plane and the magnetic filed intensity* ***H****;* (c) *magnetization torque* ***T***

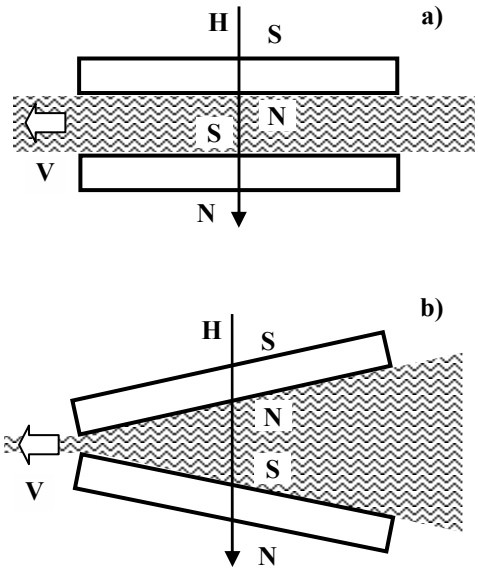

Fig.2. Magnetic device with pole pairs generating (a) *a uniform magnetic field;* (b) *a non-uniform magnetic field directed transversely to the flow of water with filed gradient along the flow*

There is a discussion in [4] of the magnetic filed of such a device for magnet slopes in the range of $9^0 \div 18^0$.

When fluids flow pass different resistances, like magnetic serpentines, usually applied for electro-magnetic water modification, then it is essential to be familiar with the velocity vector distribution on the serpentine surfaces.

It is quite hard to solve analytically and optimize the problem since it is needed to account for the influence of various parameters such as: fluid properties, geometry, fluid velocity, etc. The use of the finite elements method (FEM) facilitates this process and also allows for a more detailed study of the problem.

The FEA package ANSYS offers an efficient way of analyzing a 3-D water flow model [5], assembled by the CAD package SolidWorks.

This paper's goal is to study the velocity and pressure distributions of the water flow in a maze shaped device. The device consists of five pole pairs situated in such a way that generate a periodically varying Lorentz force along the flow. The force depends both on the magnetic filed intensity and the water flow velocity.

Theoretical basis

Fluid problems, in general, are described by the mass, moment and energy conservation laws. These laws are defined by the corresponding partial differential equations (PDE). The PDEs obtained are solved by the FEM discretization and the use of related FEA packages like ANSYS.

The ANSYS derived product ANSYS FLOTRAN CFD (Computational Fluid Dynamics), helps in solving numerous fluid problems.

When solving a given fluid problem, there exists a certain sequence of steps that include: determining problem domain, flow regime, meshing, determining boundary conditions and parameters, etc.

The flow regime is a function of the fluid properties, geometry and fluid velocity.

When analyzing laminar or turbulent flows, the procedure usually comes to examining pressure or velocity distribution results, given a 2-D or a 3-D geometry, under some assumptions regarding the fluid behavior: laminar or turbulent, compressible or incompressible. Fluids are most commonly defined by density and viscosity.

From the mass conservation law follows the continuity equation [5]:

$$\frac{\partial \rho}{\partial t} + \frac{\partial (\rho v_x)}{\partial x} + \frac{\partial (\rho v_y)}{\partial y} + \frac{\partial (\rho v_z)}{\partial z} = 0 \quad (1)$$

where v_x, v_y, v_z are the velocity vector components;

ρ – density; x, y, z – Cartesian coordinates; t – time.

The density rate of change could be replaced by the pressure rate of change and the density rate of change with respect to pressure, i.e.

$$\frac{\partial \rho}{\partial t} = \frac{\partial \rho}{\partial P}\frac{\partial P}{\partial t} \quad (2)$$

where P is pressure.

For an incompressible fluid $\partial\rho/\partial P$=const. The package interprets this constant as an infinitely fast pressure distribution in the fluid, i.e. a pressure change at the inlet, leads to an instant pressure change at the outlet. The Mach number (M) is used as an estimate to determine if the flow is a compressible or an incompressible one. For M > 0,3 the fluid is assumed to be a compressible one [6]

If inertia forces are higher than the viscous ones, then the flow is most probably a turbulent one. The Reynolds number (Re) is used as an estimate of this. For Re > 2300 – turbulent flow.

Fluid problems are commonly "internal flow", Fig.3 or "external flow" problems by nature.

The first type is associated with walls or planes (flows in pipes) that bound the flow except for the inlet and the outlet, Fig.3.

Investigation results

There has been analyzed the flow of fluid in a technological electro-magnetic device EM-WMD-01. This appliance is a 3-D assembly of six modules (permanent magnets) placed in series inside a non-

magnetic pipe. Thus, there are five working inter-polar cavities along the flowing water.

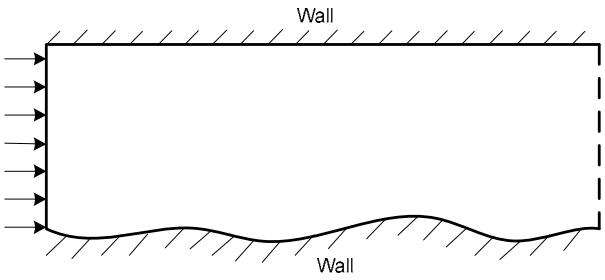

Fig.3. Internal flow problem

Each module consists of a permanent strontium magnet: Cf 24: 50 x 10 x 32 mm; Hc = 224 kA/m; Br = 037 T; (BH)max = 24 kJ/m^3, covered in epoxy resin. The modules are located inside the pipe and are rotated consequently to 180° with each other. That is how a working meander cavity is formed with a given rate of water flowing through it. Thus, it is the shortest technological link between polar pairs situated in series along the device.

Fig.4 shows the structure and dimensions of the device.

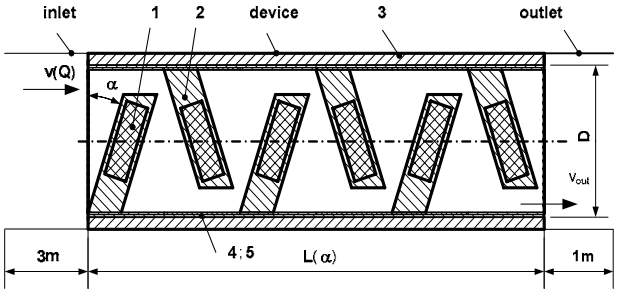

Fig.4. Device structure

1 – magnet; 2 – serpentine; 3 – pipe; 4, 5 – coating, α – serpentines slope; L(α) – device length

There have also been analyzed the EM-WMD-01-9, EM-WMD-01-12, EM-WMD-01-15, EM-WMD-01-18 and EM-WMD-01-21 configurations where the slope α is respectively 9^0, 12^0, 15^0, 18^0 and 21^0.

The Fig.4 model is assembled in SolidWorks and analyzed by ANSYS. Meshing is performed with FLUID142 elements, appropriate for 3-D problems.

The elements used have 8 nodes. The degrees of freedom are – velocities, pressure and temperature.

Fluid relaxation at the inlet and outlet is achieved with additional pipes of 3m and 1m lengths correspondingly, as shown in Fig.5.

The analysis procedure includes 5 main cases of the slope α of the magnets with respect to the vertical. These cases are α = 9^0, 12^0, 15^0, 18^0 and 21^0.

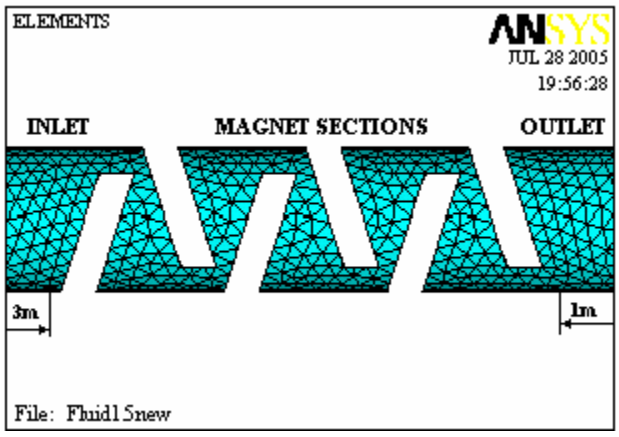

Fig.5. Device FE model

The fluid is water with properties:

- density ρ = 999.19kg/m^3,
- viscosity μ = 0.001139 kg/m.s,
- flow rate Q = 3.6m^3/h (and 10m^3/h),
- velocity in the straight 3m section v = 0.363m/s.

Pipe parameters:

- inner diameter D = 59.2.10^{-3}m,
- cross-section A = 2.753.10^{-3}m^2.

This is an internal flow problem.

The assumptions about the fluid are as follows:

- turbulent flow R_e = ρvD/μ ≈ 18900 > 2300 [4],
- incompressible flow: M ≈ 3.10^{-4} (Q = 3.6m^3/h),
- adiabatic case, T = 18^{0}C,
- smooth inner surface of the pipe.

Fig.6 shows the fluid velocity results for a) α= 12^0, b) α = 15^0 and c) α = 18^0 at a flow rate of 3.6 m^3/h. There are also obtained the velocity results for a 10 m^3/h flow-rate.

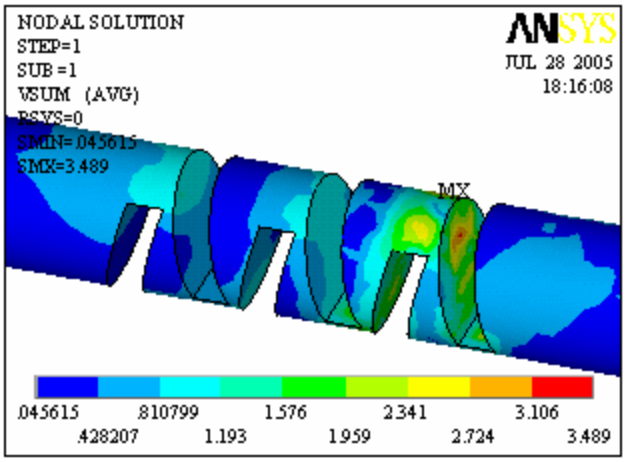

a)

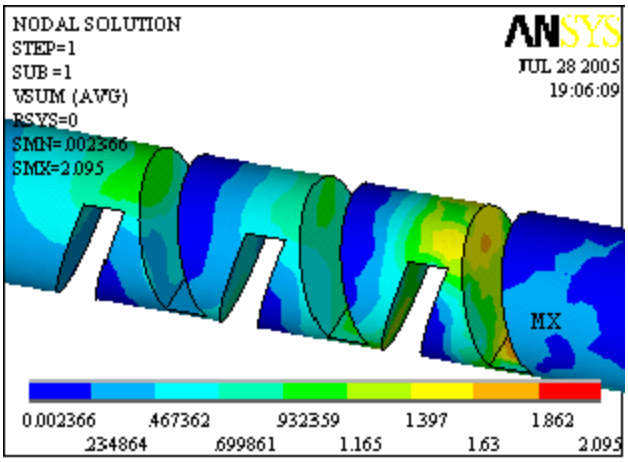

b)

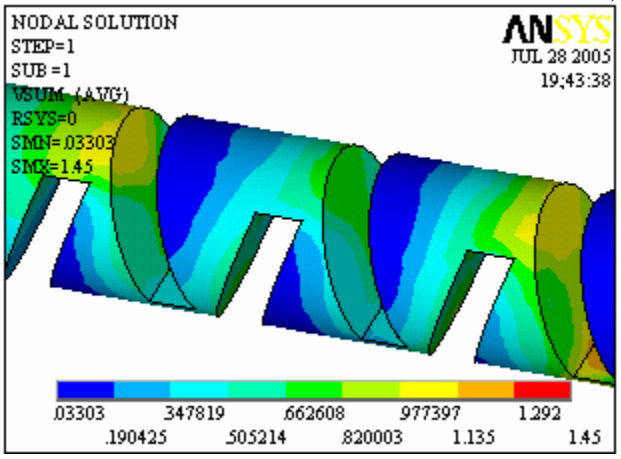

c)

Fig.6. Fluid velocity distribution in the device for a) α= 12^0, b) α = 15^0 and c) α = 18^0 at a 3.6 m^3/h flow rate

Fig.7 shows the water pressure distribution in the device at a 15^0 slope and at a 3.6 m^3/h flow rate.

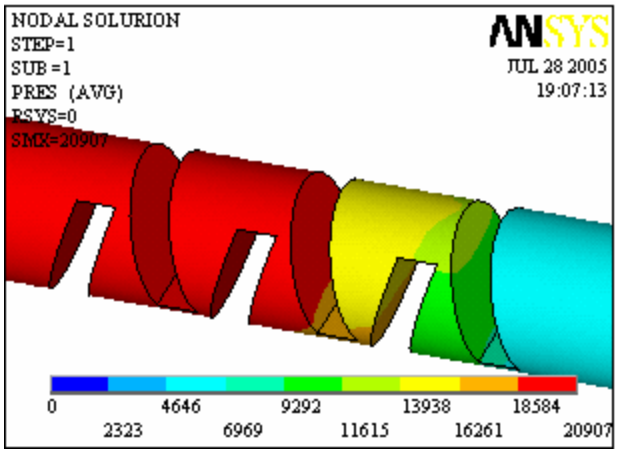

Fig.7 Water pressure distribution in the device α =15^0, Q = 3.6 m^3/h

Velocity distribution has been studied for the sections shown in Fig.8.

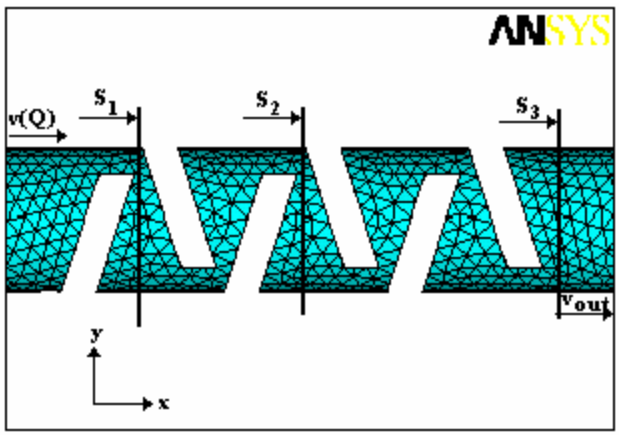

Fig.8 Sections of the water velocity analysis

Fig.9 and Fig.10 show the water velocity distribution for sections S_1, S_2 and S_3 along the y-axis for both flow rates.

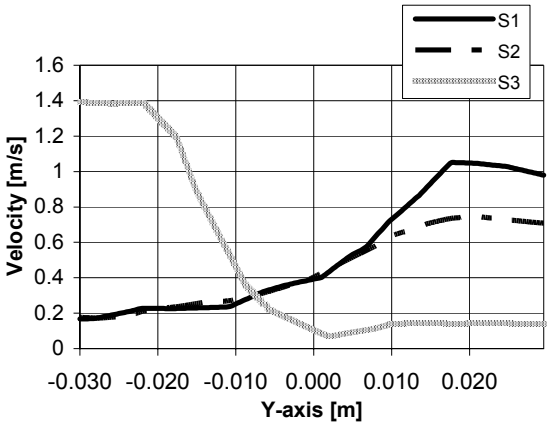

Fig.9 Water velocity distribution along the y-axis in sections S1, S2 and S3, α = 18°, Q = 3.6 m^3/h

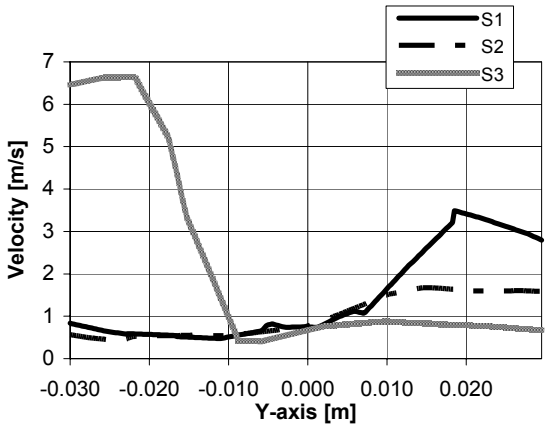

Fig.10 Water velocity distribution along the y-axis in sections S1, S2 and S3, α = 18°, Q =10 m^3/h

It could be seen that the largest velocity margin is for section S_3 (Δv = 1.4 - 0.1 = 1.3m/s at Q = 3.6m^3/h; Δv = 6.5 - 0.8 = 5.7 m/s at Q = 10m^3/h) and the smallest one is

for the intlet section S_1 ($\Delta v = 0.18 - 1.1 = -0.92$m/s at Q = 3.6m^3/h; $\Delta v = 0.8 - 3.5 = 2.7$m/s at Q = 10m^3/h).

Fig.11 and Fig.12 visualize the velocity change at the outlet of the device with respect to the slope α of the permanent magnets.

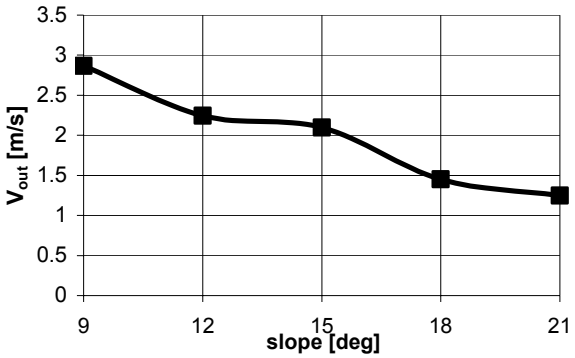

Fig.11. Water velocity change at the outlet with respect to the permanent magnets slope, Q = 3.6 m^3/h

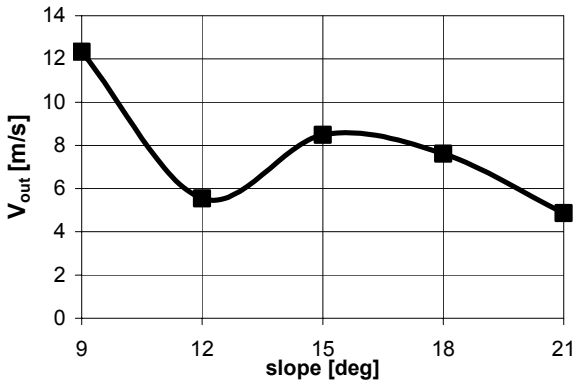

Fig.12. Water velocity change at the outlet with respect to the permanent magnets slope, Q = 10 m^3/h

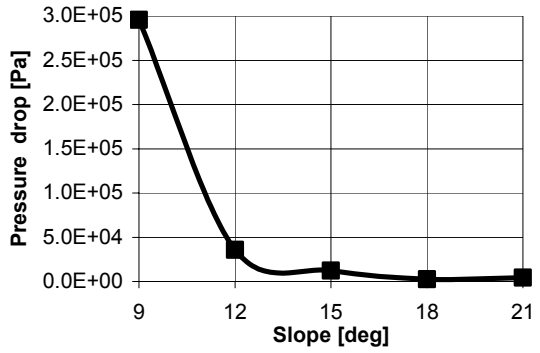

Fig.13. Pressure drop with respect to the slope of the permanent magnets, Q = 3.6 m^3/h

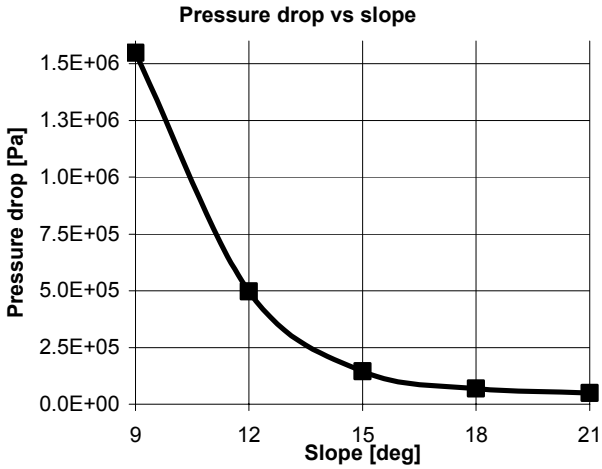

Fig.14. Pressure drop with respect to the slope of the permanent magnets, Q = 10 m^3/h

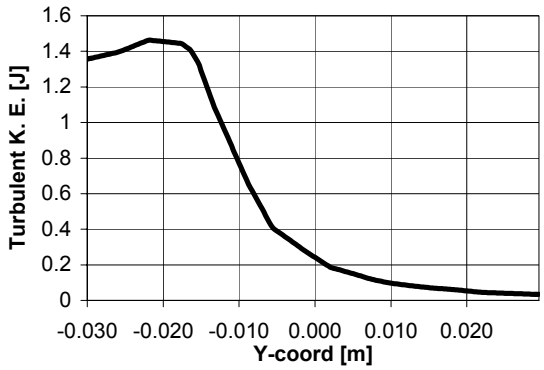

Fig.15. Water turbulent kinetic energy change in section S3, $\alpha = 18°$, Q = 10 m^3/h

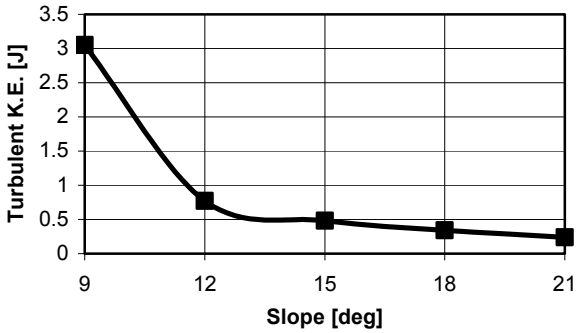

Fig.16. Water turbulent kinetic energy change at the outlet with respect to the permanent magnets slope, Q = 3.6 m^3/h

Fig.11 reveals an almost linear relationship between the water velocity change at the outlet and the slope α of the permanent magnets, at Q = 3.6 m^3/h. The linear interpolation polynomial obtained is $v_{out}(\alpha) \approx -0.134\ \alpha + 3.996$ with a coefficient of determination $R^2 = 0{,}965$.

The velocity change, at Q = 10 m^3/h, Fig.12, outlines a clearer non-linear behavior. There is a second extreme point at $\alpha = 15°$.

Fig.13 and Fig.14 imply that the water pressure drop with respect to the permanent magnets slope, for both flow rates, follows an exponential trend.

Water turbulent kinetic energy change in section S3, $\alpha = 18°$, $Q = 10\ m^3/h$ is given in Fig.15, while Fig.16 shows the water turbulent kinetic energy change with respect to the permanent magnets slope, at $Q = 3.6\ m^3/h$.

Conclusion

The water velocity change in the magnetic modification device is inversely proportional to the slope α of the permanent magnets generating a non-uniform magnetic field at a water flow rate of Q = 3.6 m^3/h.

At Q = 10 m^3/h, the water velocity behavior tends to non-linear and the graph has a second extreme point at $\alpha = 15°$.

When increasing the slope α of the permanent magnets, the water pressure drop retains an exponential behavior of decrease within the studied range.

Water turbulent kinetic energy follows an exponentially decreasing trace of change with respect to the slope α of the permanent magnets.

References

[1] Динев, П. Условия за диамагнитна поляризация. - Международна конференция по абразивно-магнитно обработване "АМО'89", Ботевград, България. Доклади, т. 2, 1989, стр. 258-267.

[2] Динев, П. Магнитна поляризация в неоднородно магнитно поле. Сили и моменти. Международна конференция по абразивно-магнитно обработване "АМО'89", Ботевград, България. Доклади, т. 2, 1989, стр. 248-257.

[3] Дорфман, Я. Диамагнетизм и химическая связь. Москва, Мир, 1961.

[4] Tzeneva, R., P. Dineff, Analysis of Technological Device with Permanent Magnets for Electromagnetic Modification of Water, XIII-th International Symposium on Electrical Apparatus and Technologies SIELA 2003, Plovdiv, Bulgaria, 29 – 30 May 2003, Proceedings of Papers Volume I, pp.198 – 203.

[5] ANSYS 9.0, Theory reference, 2005

[6] Башта, Т. М., Гидравлические приводы летательных аппаратов, М., 1967

Yanko Slavtchev *– Ph.D. Student, Department of Logistics and Materials Handling, Technical University of Sofia, 8 Kliment. Ohridski Str., 1000 Sofia, BULGARIA. e-mail: yatuworking@hotmail.com*

Raina Tzeneva *– Associate Professor, Dr., Faculty of Electrical Engineering, Technical University of Sofia, 8 Kliment. Ohridski Str., 1000 Sofia, BULGARIA. e-mail: tzeneva@tu-sofia.bg.*

Peter Dineff *– Associate Professor, Ph.D., Faculty of Electrical Engineering, Technical University of Sofia, 8 Kliment. Ohridski Str., 1000 Sofia, BULGARIA. e-mail: dineff_pd@abv.bg.*

An Application of the Piezoelectric Effect for the Generation of Mechanical Shocks

Marian Pearsica

Abstract: *This device constitutes a specific applications of piezoelectric transducers, which allow the generation of mechanical shocks. The equipment consists in a piezoelectric generator assembly and a command and supply system. The equipment was physically realized and it constituted the object of a research contract of the Optical-Electronic Institute of Bucharest.*

Keywords: *mechanical shocks, piezoelectric transducers.*

Introduction

The device operation is based on the process of achieving inverse piezoelectric effect, meaning the deformation of the crystalline network of the piezoelectric device caused by an external electrical field. The deformation power of piezoelectric transducer is approximately 450 W. The generator is a piezoelectric transducer, which belong to the series of piezoelectric devices with elastic wave of volume. The dimensions and the composition of the piezoelectric transducers were determined depending on the working conditions and on the datum mechanical power.

The equipment is used for the generation of seismological shocks or as electro-acoustical press. The kinetic energy for the seismologic shocks generating set developed in system is approximately 45 J and 100 J for the electro-acoustical press. Under the action of the electrical field produced by the excitation source, the piezoelectric generator will have an axial expansion of 0.15÷0.2 mm in a time of 0.1 s.

The command and supply system of the piezoelectric device is a switch mode power supply realized using a half bridge converter - the optimally variant for capacitive loads, high voltages and output powers up to 2 kW. A specific computer program is used to generate the series of datum impulses.

For certain values of frequency, the equivalent electro-elastic diagram of piezoelectric transducer could be represented as a circuit with discreet elements (fig. 1).

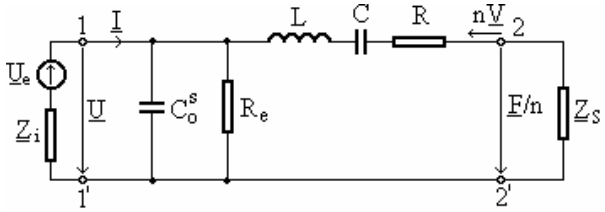

Fig.1. Equivalent diagram of piezoelectric transducer.

The elements of equivalent diagram have the following expressions and significations [2, 6]:

$$(1) \qquad C_o^s = \frac{1}{2\pi f}\,\mathrm{Im}\left\{\frac{1}{\underline{Z}_{oe}}\right\},$$

$$(2) \qquad R_e = \frac{Q_e}{2\pi f\, C_o^s},$$

$$(3) \qquad L = \frac{Z_{om}}{8n^2 v_f} = Z_{om}\frac{\lambda}{16\pi f_s n^2},$$

$$(4) \qquad C = \frac{4n^2}{\pi^2 f_s Z_{om}},$$

$$(5) \qquad R = \frac{\pi Z_{om}}{8Q_m n^2},$$

Where: $\underline{F}$ is the representative in simplified complex of elastic force at mechanical gate; $\underline{V}$ – the representative in simplified complex of vibration speed at mechanical gate; $\underline{U}$, $\underline{I}$ – the representatives in simplified complex of voltage and electrical current at electrical gate; n – the transformation ratio of ideal electro-elastic transformer; f – the oscillation frequency of electrical applied field; λ – the wave length of the gradual elastic wave; Z_{om} – the characteristic elastic impedance of the transducer; Q_m, Q_e – the qualitative mechanical and electrical factors of the transducer; f_s – the value of the frequency for which the constant phase of the transducer has the particular characteristic value at the mechanical resonance; v_f – the propagation speed of the elastic wave in the piezoelectric transducer; $\underline{U}_e$, $\underline{Z}_i$ – the complex electromotive voltage and the internal complex impedance of the supply source for the piezoelectric transducer; $\underline{Z}_S$ – the complex load impedance.

Concrete values of elements in equivalent diagram are determined by material parameters corresponding to transducer configuration and constructive sizes.

Equipment block diagram

Technical conditions for input and output were the following: the equipment supply is realized from the supply network – 220±15% V AC., f = 50 Hz; the length of the axial expansion of the piezoelectric assembly – 0.15÷02 mm; the period of the axial expansion of the piezoelectric assembly – 0,1 s; the operating regime – 1 pulse/10s; maximal voltage on piezoelectric device – 3500÷6000±1% V, supply voltage variation determining

the variation of the axial expanded of the piezoelectric assembly; the efficiency of excitation electronic source – ≥ 80%; the supply and command of the piezoelectric device were realized at maximum depth of 300 m; electrical resistance of supply cable, R_C = 80 Ω/km; supplementary command device which could short-circuit the piezoelectric assembly after a period of 0.2 s from the receiving of the command input; protection against overload, supra-voltage, electrocution, radio-electronic interferences in/from network; the electronic source and piezoelectric assembly were introduced into a stainless steel cylinder with inside diameter – 105 mm, outside diameter – 110 mm and maximal height – 1 m.

The block diagram of ultrasonic signals generating set, which is presented in figure 2, has two components: a surface equipment (A) and an equipment inside a stainless steel cylinder (B), which functions at 300 m depth. Considering the input and imposed output conditions there were established functional units, which compose the generating equipment.

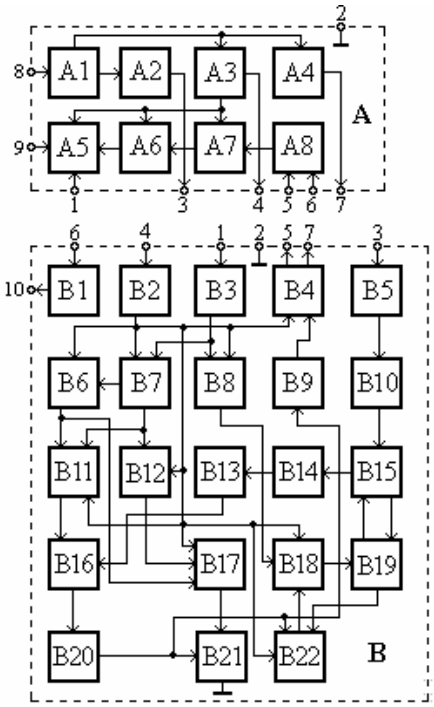

Fig.2. Block diagram of the mechanical shocks generating set.

The functional units of the surface equipment (A) are the following: protective unit against radio-electronic interferences in/from network (A_1); rectify and filtering unit for supply voltage (A_2); auxiliary power supply of ±18 V (A_3); auxiliary power supply for lifting motor (A_4); interface and command unit (A_5); frequency-voltage converter (A_6); circuit for amplitude discrimination of command pulses (A_7); low-pass filter (A_8). The equipment (B) has the following functional unit: steady voltage of ±29 V for lifting motor supply (B_1); steady voltage of ±15 V (B_2); low-pass filter (B_3); voltage-frequency converter (B_4); filter for radio-electronic interferences (B_5); power supply for triggering circuits (B_6); circuit for width discrimination of triggering pulses (B_7); circuit for amplitude and width discrimination of command pulses (B_8); reaction circuit (B_9); circuit for discharge the piezoelectric generator (B_{12}); condensers battery (B_{10}); triggering circuits (B_{11} and B_{17}); accumulation condenser (B_{13}); rectify unit for supply voltage of piezoelectric generator (B_{14}); high-voltage transformer (B_{15}); high-voltage switched circuits (B_{16} and B_{21}); command circuit of power module (B_{18}); power module (B_{19}); piezoelectric generator (B_{20}); protection overload and supra-voltage unit (B_{22}).

The interface and command unit realizes the interface between PC and functional unit (B), processes input and output data, and establishes working conditions. Because the command pulses are conducted through a 300 m long cable, it was necessary to utilize some receiving circuits for command pulses, like: low-pass filter, pulse height discriminator realized with a Smith trigger, circuit for time discrimination, circuit for reject the spikes and unlike interferences.

The block diagram of designing power module is presented in figure 3.

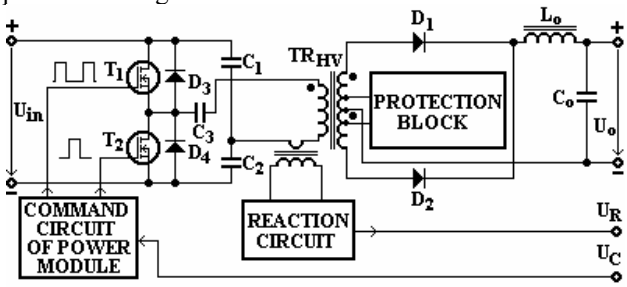

Fig.3. Block diagram of power module.

The half bridge converter is a converter with input-output galvanic isolation. The energy transfer of primary winding – load is realized during the conduction period of the switching elements. As switching elements there were used Power MOS transistors, because they allow obtain efficiency with at least 5 percentages higher than the switch mode power supplies using bipolar transducers.

The commutation frequency chosen is approximately 100 kHz. From that results a diminution of volume for the ferromagnetic core oh the high-voltage transformer.

Input and output parameters are presented on display, and working conditions are established with the computer keyboard.

The command circuit (B_{18}) realizes charge and discharge the gate-drain capacitance of Power MOS transistors, determining saturation or blocking them [7].

High-voltage transformer delivers necessary voltage to supply piezoelectric generator; also, it realized the load matching. The transfer of energy is made sin-phase.

Designing elements. Obtained results

The dimensions of the piezoelectric transducers used for the construction of the piezoelectric assembly are: external diameter, ϕ_{ext} = 38 mm; internal diameter, ϕ_{int} = 16 mm; height, h = 6 mm. The results of the experimental researches accomplished [6] (Table 1)

indicate that by supplying such a piece with a voltage of 6 kV, it will be axially expanded with approximately 4 μm.

For an axial expansion of 0.2 mm, the piezoelectric device must be realized using 50 piezoelectric pieces, parallel connected.

For the mechanical shocks generator, the developed kinetic energy is equivalent with a weight of 3 kg which is falling from a height of 1.5 m, resulting E_c = 45 J. Considering that the period of the axial expansion of the piezoelectric assembly is 0.1 s, the mechanical power developed by the piezoelectric device is 450 J/s. The equivalent capacitance of the piezoelectric device is determined using the relation:

$$C_e = \frac{2E_c}{U_o^2}, \quad (6)$$

Where: U_o is the supply voltage of the piezoelectric device.

As a consequence of the experiments achieved (Table 1), it results that for a 0.15 mm axial expansion of the piezoelectric device, the supply voltage necessary is 4.5 kV, and for an expansion of 0.2 mm, U_o = 6 kV.

According to relation (6), the value of the equivalent capacitance of the piezoelectric device will be: Ce = 2.5÷4.4 μF. Because of the low loading efficiency of the piezoelectric device through a resistor device, it results in a primary approximation that the value of the capacitance of the accumulation condenser is: Ca = 5.5÷9 μF.

In Table 1 there are presented a series of experimental results (axial expansion) obtained when a piezoelectric crystal and respectively an entire piezoelectric generator (stack) are supplied with different supply voltages.

For a supply of a piezoelectric crystal, the experiments were realized for a great number of crystals and there were calculated the average values of the axial expansion which were obtained.

Table 1

Experimental results

U_o [V]	Measured axial expansion (d)		Calculated axial expansion d [mm]
	Crystal d [μm]	"Stack" d [mm]	
3000	1.98	0.096	0.099
3500	2.31	0.109	0.116
4000	2.66	0.128	0.133
4500	3.00	0.147	0.150
5000	3.34	0.163	0.167
5500	3.67	0.178	0.184
6000	4.01	0.197	0.201
6500	4.32	0.211	0.216

From the presented table it results that the measured axial expansion of the piezoelectric device is smaller than the calculated one, because of the copper electrodes, situated between the piezoelectric crystals, which retard the expansion.

Piezoelectric generator assembly (stack) is show in figure 4, and it is composed by the following elements: metallic inertial mass (1); insulated pieces (2); non-conductive metallic axle (3); copper electrodes (4); piezoelectric transducers (5); metallic piece (6); sealing piece (7); anvil (8); cylindrical stainless steel tube (9); connections between electrodes (10). The piezoelectric generator consists in fifty piezoelectric radial polarized transducers, which are parallel connected. The piezoelectric transducers are made of ceramic materials as PZT (titanium, zirconium, lead) and the research was realized using a material as $Pb(Zr_{0,53}Ti_{0,47})O_3$ doped with Nb_2O_5, BiO_3 and MnO. The piezoelectric generator represents a preponderant capacitive load with a capacitance around 2.5 μF.

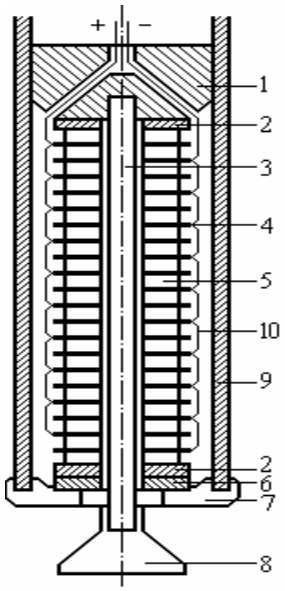

Fig.4. Piezoelectric generator assembly.

By PSpice simulation [4, 5] was tested in time and frequency domains the power supply of piezoelectric device. In order to simplify the analysis and to reduce simulation time, from designed power supply was considered only the power module.

The power supply is in essence a closed loop regulating system [1] (fig. 5), and it must be analyzed its stability.

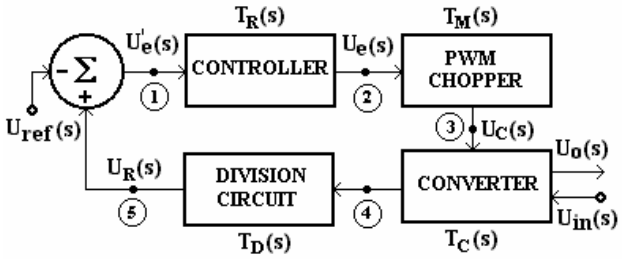

Fig.5. Power supply as a closed loop regulating system.

The waveforms for: drain currents, primary winding current of high-voltage transformer, filtering inductance

(L_o) current, and supply voltage of piezoelectric device are presented in figures 6 and 7.

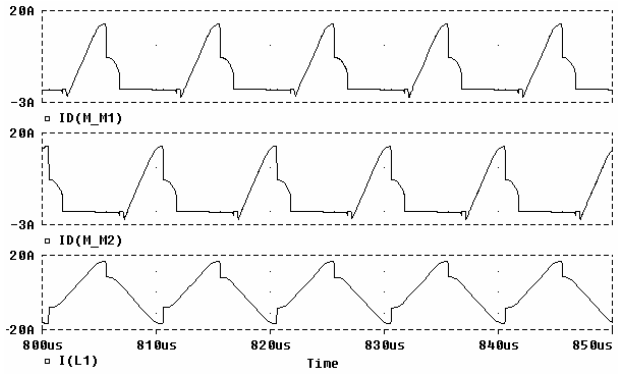

Fig.6. Waveforms for drain currents and primary winding current of high-voltage transformer

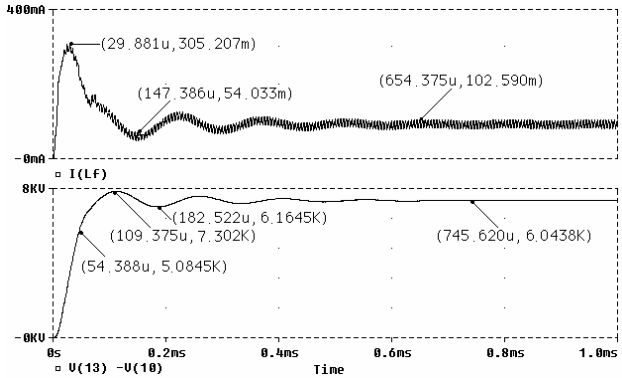

Fig.7. Waveforms for filtering inductance (L_o) current and supply voltage of piezoelectric device

The frequency attenuation characteristic and envelope-delay characteristic (phase response), for supply source, are presented in figure 8.

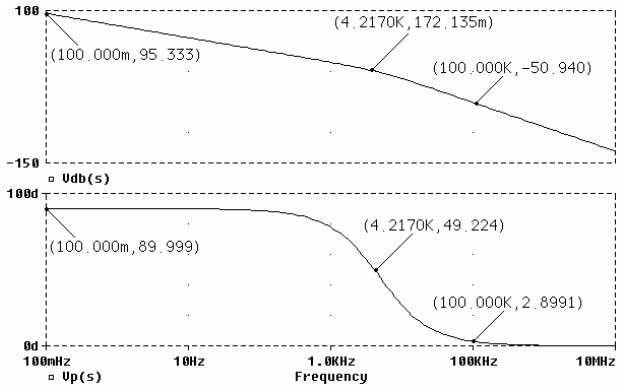

Fig.8. Waveforms in frequency domain.

The open loop transfer function of the system has a pole in fixed point, which is introduced by the controller, a double pole introduced by the converter, and two zero, one introduced by the controller and the other one introduced by the converter. The presence of pole in fixed point ensures a high gain at low frequencies. The zero introduced by the controller is placed near the double pole introduced by the converter, so that the passing through f_{cross} is realized with value: 20dB/dec.

It results f_{cross} = 4.2 kHz. The phase edge is positive and has the value equal to 49,3°.

Conclusion

The presented equipment is a complex system, purposed for generating seismological shocks or as an electro-acoustical press, by an unconventional method, using piezoelectric transducers.

It is constituted of a piezoelectric assembly composed of fifty piezoelectric transducers axial polarized, a switch mode power supply which supply the piezoelectric generator and a command block which allows to obtain the supply voltages of the electronically circuits and also to realize the operation mode.

The numbers of piezoelectric transducers also as their geometry were established considering the mechanic energy that the stack must develop.

Considering the results of performed analyze it is allowed to affirm that the open loop transfer function of the system ensures its stability.

As a consequence of the performed PSpice analysis, it results that the evolution in time of the electrical quantities and also the obtained signal levels has a good concordance with calculated values.

It was used an accumulation condenser which is discharging mediate through an high-voltage switched circuit on the piezoelectric assembly, at an external command, for transferring the electric energy from the power supply into the piezoelectric assembly.

References

[1] Mitchell, D. DC-DC Switching Regulator Analysis. McGraw-Hill Book Company, 1998.

[2] Nicolau, E. Radiotehnica, Vol.1, Editura Tehnica, Bucharest, 1988.

[3] Rasid, M., H. Power Electronics – Circuits, Devices and Applications. Prentice Hall, 1992.

[4] Radoi, C. SPICE – Simularea si analiza circuitelor electronice. Editura Amco Press, Bucharest, 1994.

[5] Pearsica, M. Methods of Pulsated Excitation of CO_2 Lasers Used for Material Processing. Analele Universitatii din Oradea, Anul I, Vol. I, 2002.

[6] Pearsica, M. Racuciu, C. Jula, N. Ultrasonic Signals Generator Based on Piezoelectric Transducers. International Conference Communications 2004, Bucharest, June 2004.

[7] * * * Power Semiconductor Applications. Philips Semiconductor Inc., 1994.

Marian Pearsica – *Associate Professor, Ph.D., Department of Electronic and Computer Science, "Henri Coanda" Air Force Academy, Mihai Viteazu St. 160, 500183, Brasov, Romania.*
e-mail: marianpearsica@yahoo.com

Frequency converter for plasma treatment with step-up transformer and paralel load circuit

Anastassia Krusteva, Plamen Avramov, Tsvetan Marinov

Resume: *The present paper presents the results of theoretical and experimental investigations of the developed high-frequency power supply for plasma surface treatment at atmospheric pressure and following conditions: operating frequency 20 ÷ 100 kHz, high-frequency discharge voltage U_{kp} =2÷6 kV – RMS, active power for plasma treating up to P_a = 20 ÷ 200 W, cos φ = 0.01 ÷ 0.10. A principle schematic of the converter is presented, as well as results from the experimental and simulation investigations. The test results of the converter show high operational reliability, which makes the investigation and application of the device interesting and useful.*

Keywords: *frequency converter, plasma technologies, computer simulations*

Introduction

Plasma surface treatment of materials at atmospheric pressure is obtained when barrier discharge is present. There are electrical and technological examinations conducted at industrial and higher frequency in terms to develop a concept for technology process control of the plasma-chemical modification of polymeric surfaces through electric characteristics and technological parameters of the electric capacitive (barrier) discharge at atmospheric pressure [1, 2, 3, 4, 7]. On the basis of the references [5,6,7], according to the requirements for high-voltage output in wide frequency range an alternative circuit is suggested, which is presented in [7]. The RC load, which represents the plasma discharge forms along with the secondary winding of the step-up transformer parallel resonant circuit, which has its own resonant frequency. The parallel load circuit could be tuned for lower frequency than the resonant by adding a parallel capacitor and for higher frequency – by connecting parallel inductance.

Realization

The suggestion is usage of half-bridge converter with serial power supply [8], but instead output step-down transformer and rectifier as it is in the switching-mode power supplies, here a special step-up transformer is connected to supply the electrode plasma-charge system. The power circuit from fig. 1 includes autotransformer, rectifier and half-bridge converter, operating with two switched mode *MOSFET*s **IRFP460** and two electrolytic capacitors (470 pF, 350 V) with output through the separating capacitor 10 μF, 750 V at the primary winding of the step-up transformer, which has ratio 1:30. The ferrite core of the transformer is made of the № 27 material, thyroidal type ∅ 140 /60 /60 for frequencies up to 100 kHz. Depending on the load's resonant frequency requirements, the control frequency is generated by IC TL **494**.

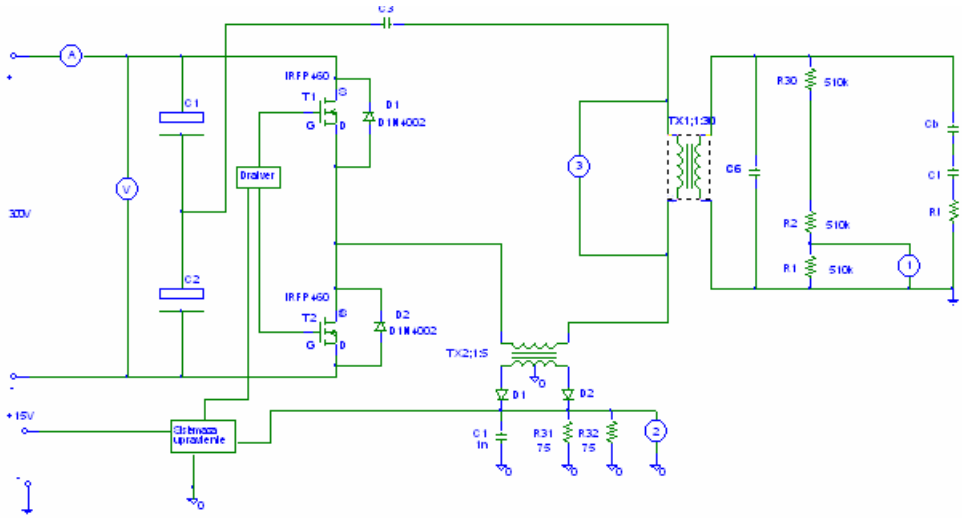

Fig. 1. Principle schematic of converter with output transformer and parallel resonant circuit

When varying the power supply voltage 100 ÷ 400 V, across the load capacitor (plasma gerator) could be obtained RMS values of the voltages in the range 2000 ÷ 6000V. The swing of the load voltage (300V) is measured, using the attenuator 1:30, i. e. 9000V, fig. 2. The RMS value of the load voltage is 3191,5V. It is seen a third harmonic at fig.2, because the resonant circuit has higher resonant frequency than the control.

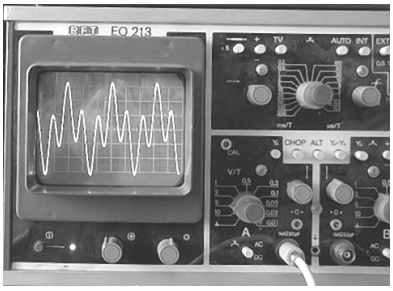

Fig. 2 Measuring the voltage across the load at resonant frequency, higher than the control

By adding a capacitor in parallel, which consists 6 equal capacitors of 470 pF in serial, i.e. total value 78,3 pF, the demanded frequency of the forced sine waveforms (30 kHz) match with the frequency of the new resonant circuit that is formed fig.3.

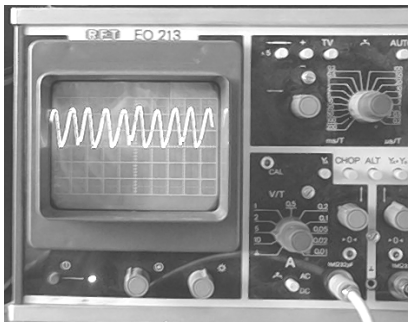

Fig. 3. Voltage across the load after tuning the resonance

Fig. 4 shows the waveforms of load voltage and current for one measurement of the real plasma-generator, which has dimensions of the electrodes (load capacitor) 350 x 175 mm, area 651.10^2 mm^2 and resonant frequency f = 30 kHz and cos (φ) = 0,066.

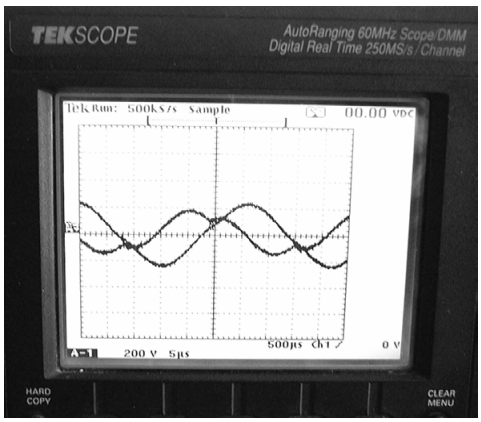

Fig. 4. One-plot load voltage and current waveforms at resonant frequency 30 kHz

Analysis of the load circuit electrical parameters

The analysis of the electrode system is presented in [7]. This system consists two flat electrodes with certain area, which have certain distance between themselves. This distance involves air (operating) interspace (1,5 to 15 mm) and potassium glass barrier (3 to 9 mm). The dimensions of the electrode plates are 350 x 175 mm, with rounded edges (5 mm) for avoiding the edge effects. The analysis shows that after ignition C_t gets the value of 110 pF, which is almost equal to the capacity of the barrier capacitor. R_t is in inversely proportion to the frequency, but C_t remains constant. As the reactive resistance Xc_t is in inversely proportion to the frequency it is assumed that cosφ=0,066 is constant [7]. The analysis of the resonant circuit parameters is implemented at these conditions of the electrode system, as observing the requirement for resonance of the parallel load circuit at the given frequency and RMS value U_t =6000V of the plasma. The obtained results are shown at Table 1.

Table 1

f [kHz]	20	40	60	80	100
R_t [kΩ]	4,8	2,4	1,6	1,2	0,96
X_C	72,34	36,17	24,11	18,08	14,47
X_{L2}[kΩ]-L_2=135mH	16,96	33,91	50,87	67,82	84,78
C_4/L_4 parallel	460pF	60 pF	121,6mH	49,06mH	23mH
I_t [mA]	82,9	165,88	248,8	331,8	414,65
P_a [W]	32,98	66,038	99,042	132,109	165,057
S [VA]	499,6	1001,3	1500	2001	2500,8
Pulse parameters					
TD [μS]	0 25	0 12,5	0 8,3	0 6,25	0 5
PW [μS]	24,9 24,9	12,4 12,4	8,2 8,2	6,15 6,15	4,9 4,9
PER [μS]	50	25	16,6	12,5	10
I_t [mA] - sim	92,89	180,63	240,15	318	418,6
P_a [W] - sim	41,42	77,76	92,27	121,34	168,21
$U_t$rms [V] - sim	5626	5877	5377	5390	5896
S [VA] -sim	513,31	1061,56	1291,29	1714,02	2468,06

The value of the secondary winding inductive resistance of the step-up transformer for inductance L_2=135mH is calculated for each frequency. This is just the inductance, which is determinative for the parallel resonant circuit, which involves the plasma-discharge capacitor. For frequency 20 [kHz] the value of the required additional capacity in parallel on the plasma-discharge capacitor could be determined C_4=560pF. At 40 kHz the resonance of the system occurs after adding a capacitor 60 pF.

For 60 kHz, 80kHz and 100kHz the values of the required parallel inductances are respectively L_4=121,6mH, L_4=49,06mH and L_4=23mH. These inductances are constructively acceptable.

If the RMS value of the voltage across the plasma-discharge capacitor is U_t = 6000[V], the following quantities could be determined: load current $I_t = U_t / Z_t$, active power $P_a = I_t^2.R_t$, and total power $S = I_t.U_t$, assuming that the plasma voltage and current are sinusoidal.

Modeling and simulations

A model for simulations is developed and there are simulated circuits using PSpice. For each frequency in Tables 1 there are parameters of the control pulses: period-PER, pulse width PW and time delay TD of the generators V_1 and V_2.

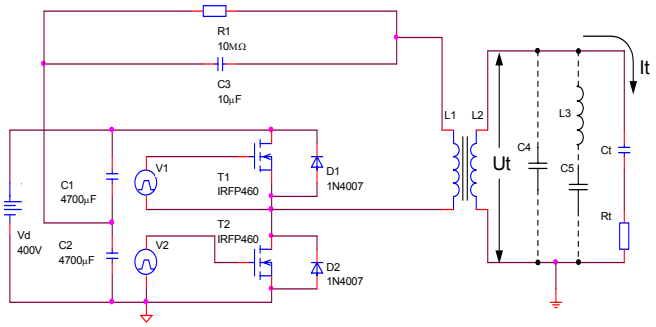

fig.5 Model for simulations

The capacitor C_5 is separating and its reactive resistance is negligible compared to the resistance of L_3. Fig.6 shows the waveforms of the voltage over the plasma and the discharge current. There is Fourier analysis of the current, which allows the spectrum to be evaluated.

Fig. 7 presents the waveforms of the voltage over the plasma and the discharge current at 40 kHz.

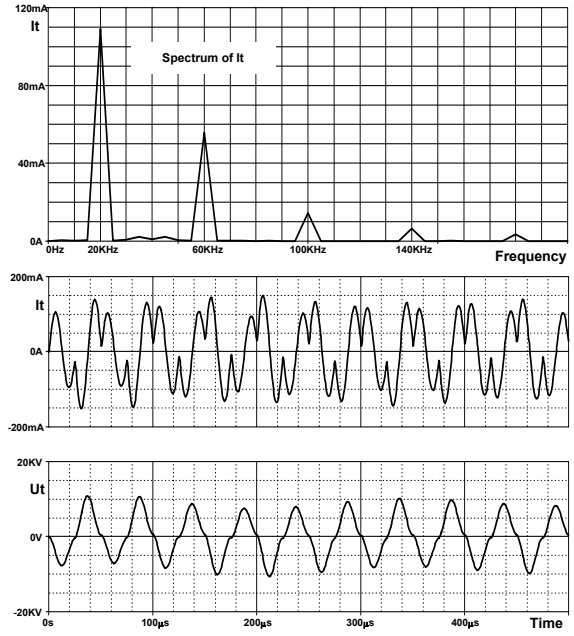

fig. 6 Waveforms at 20 kHz

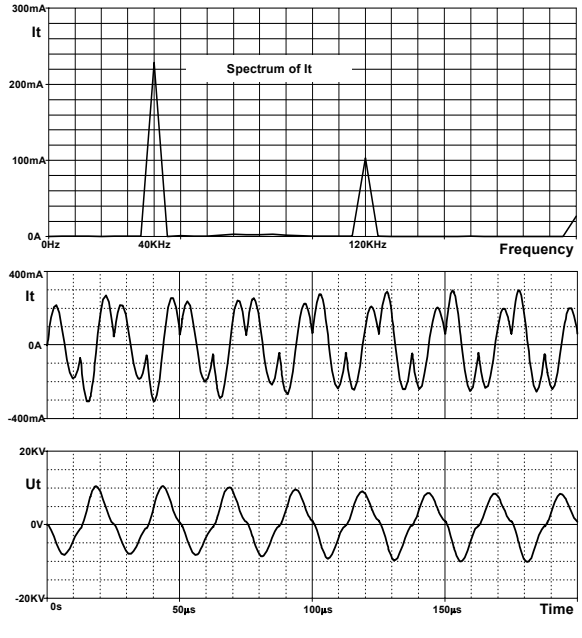

fig. 7 Waveforms at 20 kHz

Fig. 8 presents the waveforms of the voltage over the plasma and the discharge current at 100 kHz.

The waveforms of the voltage show sinusoidal shape. The current shape differs from the sinusoidal at lower frequencies. The spectrum shows considerable third harmonic.

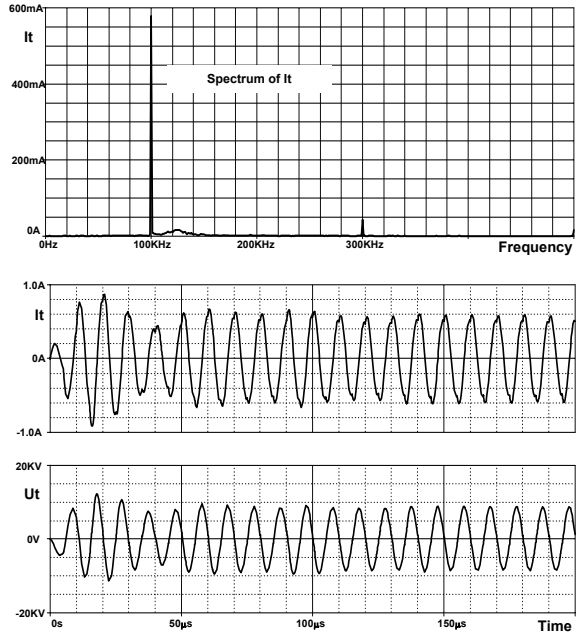

fig. 8 Waveforms at 20 kHz

The results for the RMS current and voltage from the simulations and the obtained values for the active and total power are filled in Table 1 as I_t [mA] – sim, P_a [W] – sim and S [VA] -sim. The presence of third harmonic at lower frequencies leads to increased values of the active power at these frequencies. The analysis from the calculated data and simulations shows good coincidence of the results.

The experiments over the test model, shown by the waveforms fig. 1, 2 and 3 corresponds to the simulations. The numerical analysis and the simulations show the possibility for obtaining increased active power at equal dimensions of the plasma-discharge capacitor. At the same time the total power also increases.

The designing and construction of the frequency converter must be conformable to the maximum value of the total power and the load current and voltage.

When varying the geometrical dimensions of the plasma capacitor, air (operating) interspace and the barrier thickness, then R_t, C_t respectively X_t also vary, which requires change of the resonant frequency tuning elements.

Conclusion

Here a frequency converter was realized, examined and simulated. It is based on the switch mode of the MOSFETs. At 100kHz the primary winding current does not exceed 5A maximum value and total power nearby 3000VA. The power supply is measured out according to the maximum total power.

The suggested method for analysis and simulation at various frequencies could be applied for bringing into line of the variable parameters of the high voltage RC

load for plasma technologies and power supplying frequency converter.

The extended possibilities for frequency changing at the desired voltage in the high-voltage range are precondition for developing plasma-surface technologies and obtaining new technology effects. The converter is developed and produced and it is successfully applied [9, 10] in technologies for burning-stability improvement of materials, used for interior and production devices and wooden materials, as portable plasma-activation device is included. It is used at multiple objects registering high operating reliability, which makes very interesting the examining and application of the circuit.

References

[1] Dineff, P., D. Gospodinova. The surface density of the power as a basic parameter of the plasma-chemical modification of materials in a barrier electrical discharge. Sofia, Bulgaria. Tenth international conference on electrical machines, drives and power systems ELMA 2002, volume I of proceedings, pp. 304-310;

[2] Gospodinova, D., P. Dineff. Low-frequency technological discharge at atmospheric pressure. XIII-th International Symposium o n Electrical Apparatus and Technologies SIELA 2003, Vol. 2, 29-30 May 2003, Plovdiv, Bulgaria, pp.94-99

[3] Dineff, P., D. Gospodinova. Electric characteristics of Barrier Electric Discharge. XXXVIII International Scientific Conference on Information, Communication and Energy Systems and Technologies ICEST 2003, 16-19 October 2003, Sofia, Bulgaria, pp. 442-445

[4] Dineff, P., D. Gospodinova. Atmosphere Barrier Discharges with Electrode Edge Effect. XXXIX International Scientific>> Conference on Information, Communication and Energy Systems and Technologies ICEST 2004, 16-19 June 2004, Bitola, Macedonia, pp.813-816

[5] A. P. Krusteva, P. D. Karamanski, N. P. Gradinarov, G. J. Maleev, G. Tz. Kanov, V. A. Jotev, St. Dentchev, N. L. Chinov, A. I. Dimitrova, M. E. Ivanov. *Etude des convertisseurs puissants de frequence d'energie*. ELECTRONIKA'2002, Sofia, Bulgaria, pp. 23-32.

[6] Metaxas A. C. FOUNDATIONS of ELECTROHEAT, UK, John Wiley & Sons, 1996

[7] Kunov G., A. Krusteva, G. Staychev. High-frequency converter with series resonance circuit for plasma-chemical surface treatment at atmospheric pressure, Scientific Conference with International Participation - ELECTRONICS ET'2003, Proceedings book 2, pp179-185

[8] Hirschamnn Walter Schaltnetzteile: Konzepte, Bauelemente, Anwendungen/von Walter Hirchmann u Elfred Hauenstein. Berlin ISBN 3-8009-1550-2

[9] Kostova L., Dineff P. Technologies and materials for improvement the stability toward burning of interior materials and treatment devices. "THIRD SCIENTIFIC CONFERENCE "FIRE AND EMERGENCY SAFETY'2005" Proceeding pp.209-214

[10] Dineff P., L. Kostova, T. Vladkova, Plasma-chemical technology for burning stability improvement of wooden materials "THIRD SCIENTIFIC CONFERENCE "FIRE AND EMERGENCY SAFETY'2005" Proceeding pp.189-194

Anastassia Krusteva *– assoc. professor, PhD, Faculty of electronic engineering and technologies, Technical University of Sofia, "8, Kliment Ohridski blvd.", 1000 Sofia, BULGARIA.*
e-mail: krusteva@tu-sofia.bg.

Plamen Avramov *– master-engineer, technology expert, dept. Power Electronics, Faculty of electronic engineering and technologies, Technical University of Sofia, "8, Kliment Ohridski blvd.", 1000 Sofia, BULGARIA.*
e-mail: p_avramov@tu-sofia.bg.

Tsvetan Marinov *– engineer, PhD Student, dept. Power Electronics, Faculty of electronic engineering and technologies, Technical University of Sofia, "8, Kliment Ohridski blvd.", 1000 Sofia, BULGARIA.*

e-mail: cmarinov@abv.bg.

Modeling of Starting Regimes of Tungsten Halogen Lamps

Angel Pachamanov, Kamelia Nikolova, Neli Ratz, Nikolay Matanov

Abstract: *The report describes a model of tungsten halogen lamp with the program environment Matlab. The starting regimes of the lamp are explored by this model in terms of minimum evaporation of the filament and corresponding minimum reduction of lamp's life. The processes modeled are compared with results from experimental investigations.*

Keywords: *filament-based incandescent lamps*

1. Introduction

The most popular lamps in the field of commercial and hotel building lighting are the tungsten halogen lamps (**THL**). The starting regimes of these lamps define to a great extent the average life expectancy. This type of lamps is very sensitive to the voltage level – the higher values lead to reduction of their life whilst voltage below the rated decreases the effectiveness of the halogen cycle, which leads to the same result.

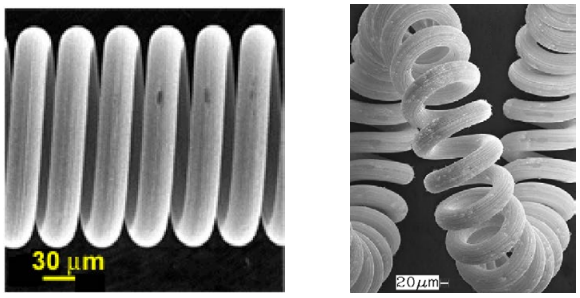

Fig.1 Pictures of coil and coiled coil tungsten filament [1,2]

Modeling of starting and working regimes in program environment Matlab by program models is extremely useful in terms of reducing the price for research work. Investigating the influence of supplied voltage over the lamp's life and the effectiveness of the halogen cycle by models is convenient, because of the long duration of real research work of this kind.

Sufficiently complete model of tungsten halogen lamp can be achieved by reading the constructive dimensions of lamp's components; type, quantity and pressure of the inert gas; concentration of the halogen element etc. In that case the lamp is considered as a system with distributed parameters and the models are used in optimization of working regimes of new lamps.

Models in time-area are used when designing electronic devices for controlling starting and working regimes of tungsten halogen lamps. They consider the lamp to be a system with concentrated parameters without rendering the characteristics of the construction. The construction as well as the processes in the lamp are read indirectly with the help of the equations and the constants of the mathematical model established on the bases of the electrical parameters of the wiring diagram. The main purpose of these models is by describing the change of lamp's electrical parameters to be described the change of the radiant flux as a whole and the luminous flux in particular.

The report describes a model verified on the basis of experimental investigations over a specially designed stand for measuring the starting processes of tungsten halogen lamps.

2. Main part

2.1. Analytical model of tungsten halogen lamp

The analytical model of tungsten halogen lamp for fixed regime is obtained through expressing the balance between the detached electrical energy in the filament $We=i(t)^2.R(T).dt$ and the dispersed by thermal energy radiation $p_r(t).dt$, convection $p_c(t).dt$ and heat conductivity $p_{hc}(t).dt$:

$$(1) \qquad i(t)^2.R(T).dt=p_r(t).dt+p_c(t).dt+p_{hc}(t).dt.$$

It has also to be considered in the starting regime the thermal energy, consumed for rising the temperature of the filament, the surrounding gas and the temperature of the bulb:

$$(2) \qquad [c_f(T).M_f+ c_g(T).M_g+c_b(T).M_b].dT=K(T).dT,$$

where $c_f(T)$, $c_g(T)$, $c_b(T)$ are the specific heat capacities corresponding to the tungsten, the gas surrounding in the lamp and the glass body, from which is made the bulb; M_f, M_g, M_b are respectively the masses corresponding to the tungsten filament, the gas surrounding and the glass bulb; dT is the change of filament's temperature for elementary time dt.

For energy balance it is received:

$$(3) \quad i(t)^2.R(T).dt= K(T).dT +p_r(t).dt+p_c(t).dt+p_{hc}(t).dt.$$

Therefore the elementary rising of filament's temperature after feeding the supplying voltage is expressed as a linear differential equation:

$$(4) \qquad dT/dt=\{ i(t)^2.R(T).-p_r(t)-p_c(t)-p_{hc}(t)\}/K(T).$$

After replacing of $i(t)=u(t)/R(T)$ finally it is received a more convenient for the model formula:

$$(5) \qquad dT/dt=\{u(t)^2/R(T) -p_r(t)-p_c(t)-p_{hc}(t)\}/K(T).$$

2.2. Program model of tungsten halogen lamp

Aiming at simulating and investigating the starting THL processes a program model, including a voltage source and contiguously plugged THL is developed (Fig.2).

2.2.1.Definition of the radiated power $p_r(t)$

The Plank formula for absolute blackbody radiation is used for defining the radiated from the filament thermal power:

$$(6)\quad m_0(\lambda,T)=2\pi hc^2\lambda^{-5}(e^{hc/\lambda kT}-1)^{-1}=37418.\,\lambda^{-5}.(e^{14388/\lambda T}-1)^{-1},$$

where $\boldsymbol{m_0(\lambda,T)}$ *[W/cm^2]* is the spectral density of the radiant luminosity emitted $\boldsymbol{M_e}$ (radiant flux, emitted from an unit of area of the blackbody, heated to temperature *T, K*); $\boldsymbol{h}$ and $\boldsymbol{k}$ are the corresponding constants of Plank (6,63.10^{-34}, J.s) and Boltzman (1,38.10^{-23}, J.K^{-1}), $\boldsymbol{c}$ is the speed of the light in vacuum (2,99.10^{-8} m.s^{-1}); $\boldsymbol{\lambda}$-wavelength, μm; $\boldsymbol{e}$ – the natural logarithm base.

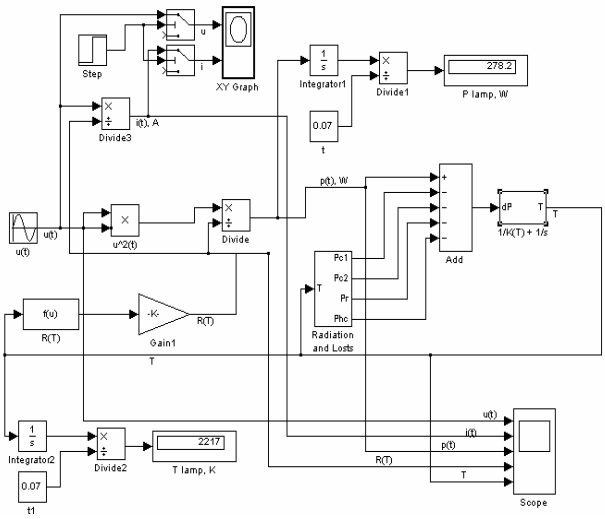

Fig.2. Program model in Matlab environment of tungsten halogen lamp

For obtaining of the spectral density of the radiant luminosity of tungsten filament is introduced a corrective spectral coefficient $\varepsilon(\lambda,T)$, reading the lower radiation ability of a real "gray" body (tungsten) in relation to this of a "absolute blackbody":

$$(7)\quad m(\lambda,T)=\varepsilon(\lambda,T).m_0(\lambda,T)=\varepsilon(\lambda,T).37418.\,\lambda^{-5}.(e^{14388/\lambda T}-1)^{-1}.$$

The density of radiation of the radiant luminosity is defined by integrating (7) in limits from 0 to ∞ (Stefan-Boltzman's law):

$$(8)\quad M_e=\int_{\lambda=0}^{\infty} m(\lambda,T).d\lambda=\sigma.T^4=p_r(t),$$

where σ=5,6687.10^{-12} W/(cm^2.K^4).

If formulae (6) is differentiated towards λ and the obtained expression is nullified we get the wavelength at which is the maximum of the radiation for a particular temperature of the radiating body. With increasing the temperature T the shifting of maximum spectral density of the radiant luminosity $m_0(\lambda,T)$ is towards the shorter wavelengths (fig.3 –Win's law) at which:

$$(9)\quad \lambda_{max}.T=2897800\ ,\ (\lambda,\ nm;\ T,\ K).$$

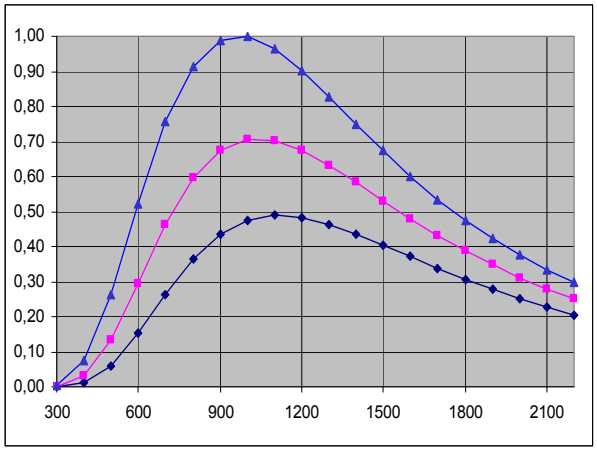

Fig.3. Blackbody radiation curves for three different temperatures (2600, 2800, 3000 K)

In fact for radiation of tungsten filament, placed in a glass bulb the temperature of the bulb T_{BULB}, has to be considered, which leads to getting the following radiated power:

$$(10)\quad p_r(t)=a_1.\,S_r.C_r\,.(T^4-T^4_{BULB}),$$

where a_1 is responsible for the type and the shape of the radiating surface with area S_r, C_r is adduced coefficient of radiant heat-exchange between the radiating area (tungsten filament) and bulb's walls, T and T_{BULB} are the respectively the temperatures of the radiating area and the bulb's wall.

2.2.2. Defining of the transmitted by convection heat flux pc(t)

According to Newton's law for this specific case, the flux released through convection is:

$$(11)\quad p_c(t)=a_2.S_c.C_c.(T-T_{MEDIUM}),$$

where a_2 takes into account the type and the shape of the area, releasing heat by convection with surface S_c, C_c is the coefficient of heat released by the surface to the surrounding gas through convection, T and T_{MEDIUM} are respectively the temperatures of the surface (the filament) and the surrounding gas.

2.2.3. Defining the heat flux released by heat conductivity $p_{hc}(t)$

According to the formulae for conducting heat through heat conductivity from the filament through the support wires and the lead-in wires to the metal socket there will be a heat flux:

$$(12)\quad p_{hc}(t)=a_3.q.K_{hc}(T-T_{SOCKET})/Lwires,$$

where a_3 takes into account the number, the type and the shape of the supporting and the leading-in wires; q is their cross section, K_{hc} – heat conductivity coefficient, W.m^{-1}.K^{-1}; L_{wires} – wire's length, m; T and T_{BULB} are respectively the temperatures of the filament and the socket, K.

2.3. Laboratory stand for verifying the correspondence of the model

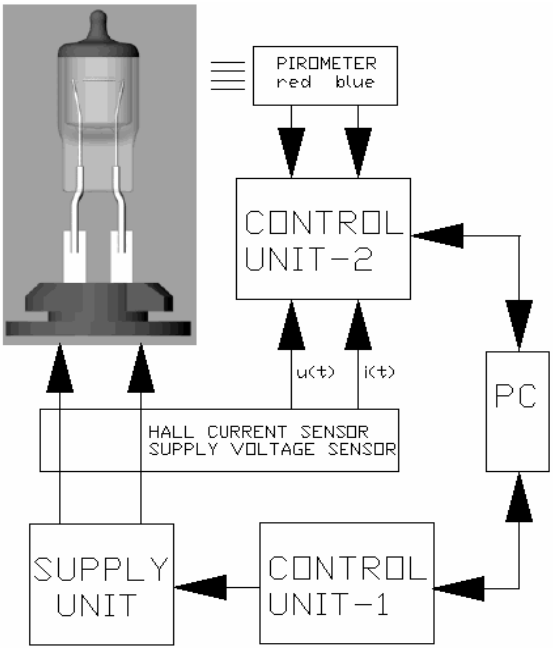

Fig.4. Stand for exploring the starting characteristics of THL

The block diagram of the developed stand for exploring the starting characteristics of THL is shown on fig.4. The stand consists of two microprocessor systems – for controlling the starting process (control unit -1) and for measuring the change in lamp's parameters: electrical (current and voltage), thermal (temperature of the filament), luminous (luminous flux). The adequacy of the developed program model is examined by recording these parameters in the memory of the registering microprocessor system (control unit-2) and the subsequent transfer into a personal computer (PC).

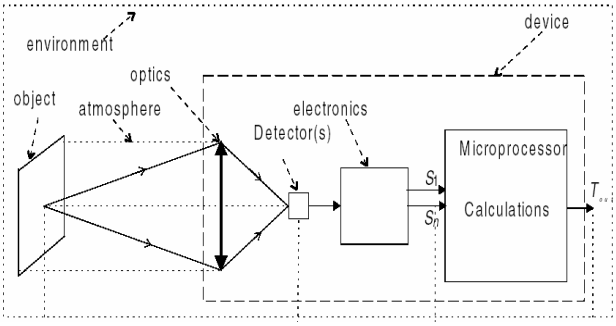

Fig.5. Typical simple objective thermometer [3]

Measuring the filament's temperature is realized by the classic principle for the "red-blue" interrelation at radiation of "gray" body (fig.5). For two wavelengths, admitted though red and blue filter, using (7) it can be calculated $m(\lambda_2,T)/m(\lambda_1,T)=\{\varepsilon(\lambda_2,T).\lambda_2^{-5}.(e^{14388/\lambda_2.T}-1)^{-1}\}/\{\varepsilon(\lambda_1,T).\lambda_1^{-5}.(e^{14388/\lambda_1.T}-1)^{-1}\}$ for values of the temperature T from 600 to 3300 K.

The dependence obtained (fig.6) $T=f(red_{665nm}/blue_{467nm}\_ratio)$ is brought in the registering microprocessor system (control unit-2) and through it the change of filament's temperature during the starting process is followed.

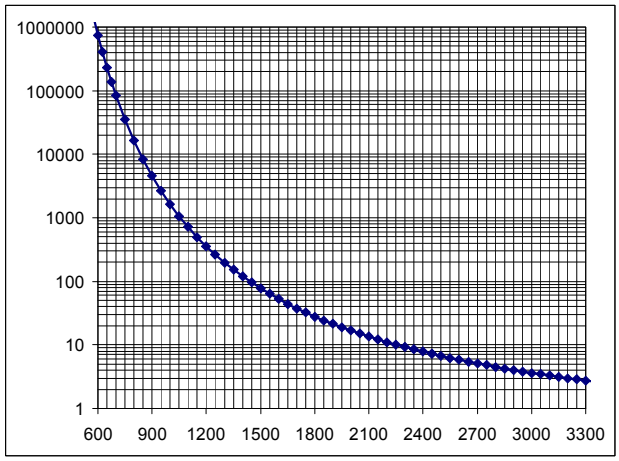

Fig.6. Correlation $red_{665nm}/blue_{467nm}$ at temperatures of the radiating body 600-3300K

2.4. Experimental results when investigating tungsten halogen lamp 150W/220V

A tungsten-halogen lamp with nominal supplying voltage 220 V and rated power 150 W is investigated. By specially developed microprocessor system is registered the alternation of the voltage supplied to the lamp's terminals and the current in the filament for an interval of 70 ms (100 reports). The results of the experimental investigations are shown on Figures 7÷11. The values of the instant power and filament's resistance during the transitional and the settled regime are calculated on the basis of the measured values of the current and the voltage.

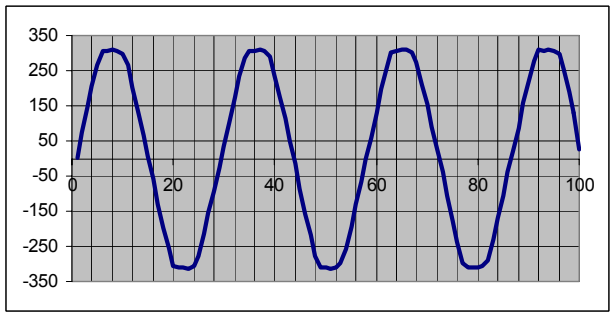

Fig.7. Registered voltage 220V (50 Hz) at switching-in the lamp

The observed deviations from the "logic" values of the lamp filament's resistance are due to the small resolving ability of the analogue-to digital converter used (ADC) and the error, obtained when dividing two small numbers (quantities).

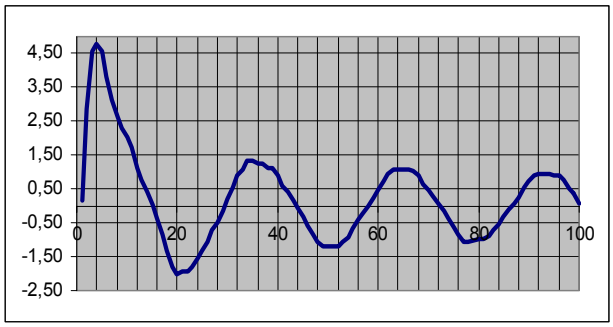

Fig.8. Registered current flow through the lamp at switching- in to voltage 220V, 50Hz

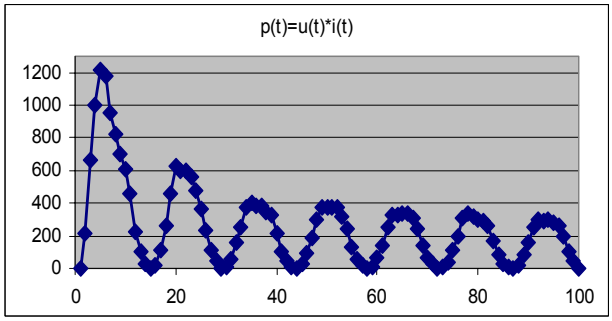

Fig.9. Instant power p(t)=u(t).i(t) at switching-in the lamp

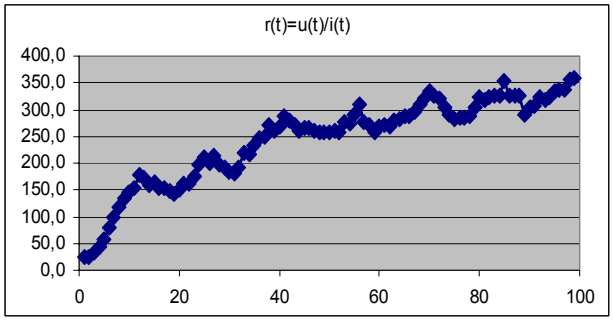

Fig.10. Instant values of the filament's resistance r(t)=u(t)/i(t) at switching-in to voltage 220V, 50Hz

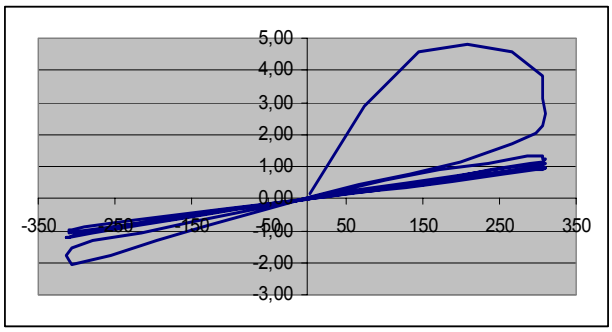

Fig.11. Measured dynamic current-voltage characteristics at switching-on the lamp to the supplying voltage 220V, 50Hz (till reaching steady state)

2.5. Simulation of the starting process of THL by using the developed program model

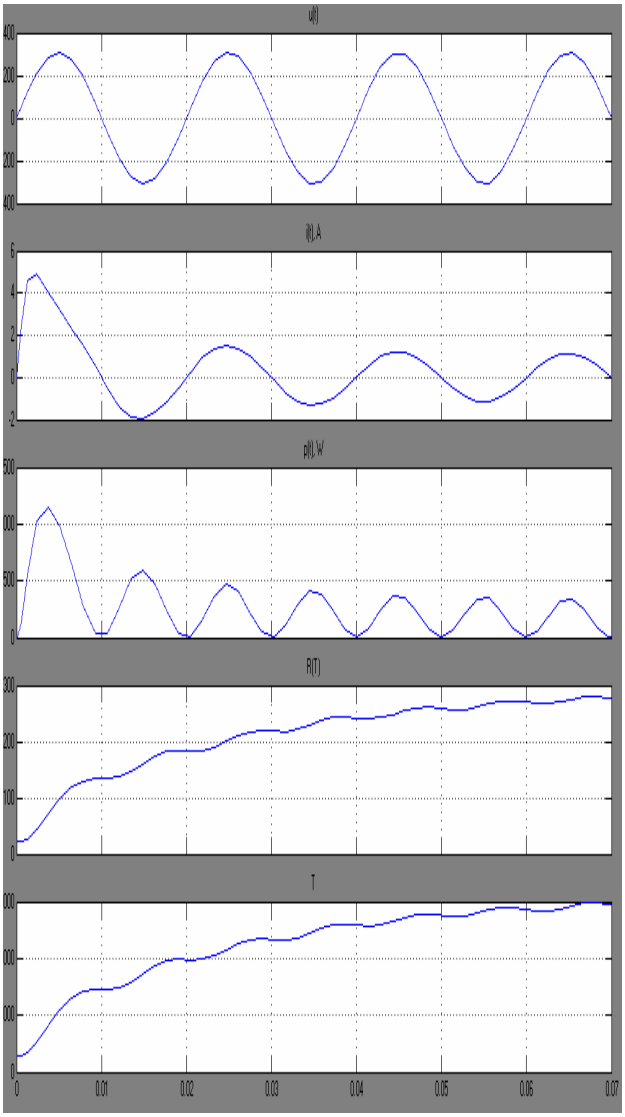

Fig.12.Simulated values of the voltage, current, instant power, resistance and temperature at supplying voltage 220V, 50Hz

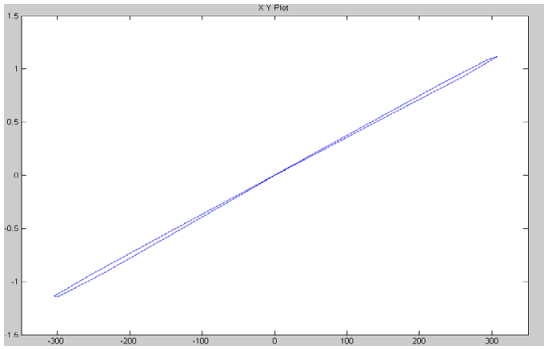

Fig.13. Simulated dynamic current-voltage characteristic at supplying voltage 220V, 50Hz (steady state)

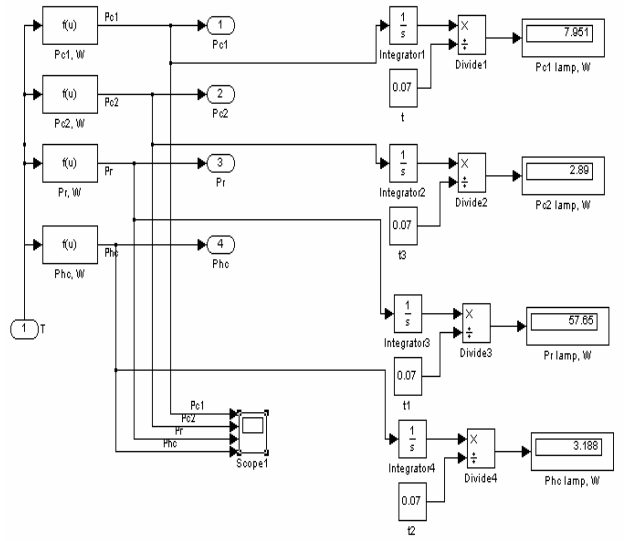

Fig.14. Block for simulating of the radiation and the losses from convection and heat conductivity

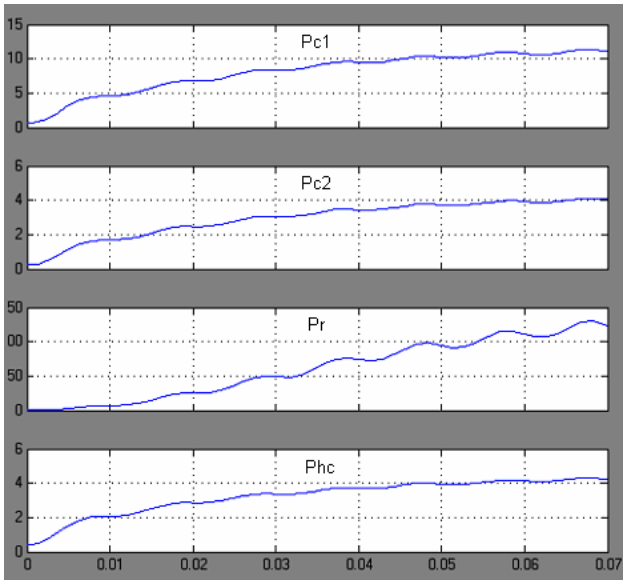

Fig.15. Simulating of the radiation and the losses from convection and heat conductivity

2.6. Model set-up

Two masks are used for set-up the program model parameters (Fig.16 and Fig.17) for concrete lamp:

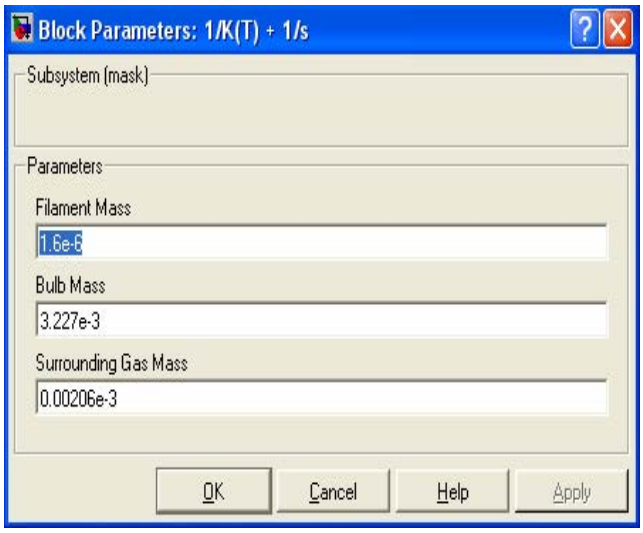

Fig.16. Mask for initiating the masses of filament, bulb and gas middle in the lamp

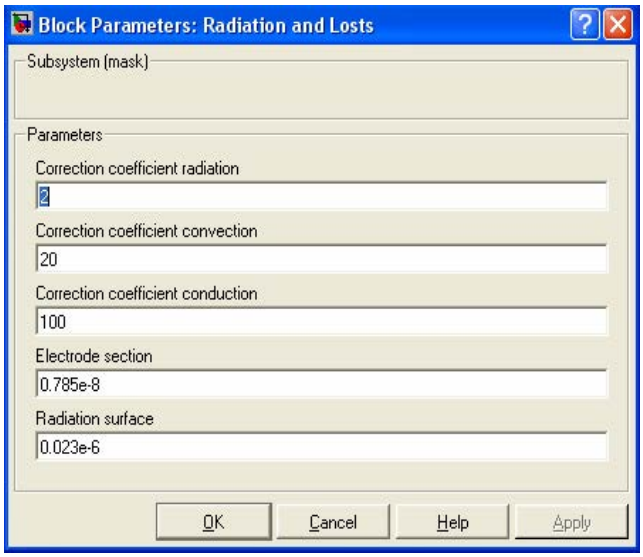

Fig.17. Mask for initiating correction coefficients, electrode's cross section and radiating area of the filament

Table 1

Used materials and technological fill gases in tungsten halogen lamps [4]

Name	Specific heat capacity c, $J.kg^{-1}.K^{-1}$	Density ρ, kg/m^3
Air	1005	1,2015
Nitrogen	1040	1,2506
Argon	520	1,784
Krypton	248	3,708
Xenon	158	5,9
Quartz	295	2600
Tungsten	142	19300

Table 2

Parameters of the explored lamp

Filament mass $M_f = \rho_f * V_f = \rho_f * \left(\pi d_f^2 l_f / 4\right), kg$	$1{,}6*10^{-6}$
Filament diameter d_f, m	$0{,}023*10^{-3}$
Filament length l_f, m	$200*10^{-3}$
Surrounding gas mass $M_m = \rho_m * V_m = \rho_m * \left(\pi d_{in}^2 l_m / 4\right), kg$	$0{,}206*10^{-6}$
Inner bulb diameter d_{in}, m	$4.5*10^{-3}$
Surrounding gas length l_m, m	$35*10^{-3}$
Bulb mass $M_b = \rho_b * V_b = \rho_b * \left[\pi\left(d_{out}^2 - d_{in}^2\right) l_b / 4\right], kg$	$3{,}2*10^{-3}$
Outer bulb diameter d_{out}, m	$7*10^{-3}$
Bulb length l_b, m	$55*10^{-3}$

3. Conclusion

The developed program model in program environment Matlab is an effective instrument for creating of electronic devices which provide a rational working regime for THL. The difference between the experimentally received and the simulated values for the electrical quantities is negligible (around 5%). By this model it is possible to examine the conditions for soft start of THL in order to lengthen their life. Improving the model in terms of the processes of lamp's life expectancy will enable improving the operating characteristics of THL on the basis of electronic devices for providing rational working regime.

4. References

[1] http://invsee.eas.asu.edu/nmodules/lightbulbmod

[2] Dan MacIsaac, Gary Kanner, and Graydon Anderson Basic Physics of the Incandescent Lamp(Lightbulb). Vol. 37, Dec. 1999 The Physics Teacher 521

[3] http://... Non-contact radiation thermometers.pdf

[4]http://nationmaster.com/encyclopedia

Angel Pachamanov *- Dr. Eng., Assoc. Professor, Electric Power Supply and Equipment Department, Technical University - Sofia, , E-mail: pach@tu-sofia.bg*

Kamelia Nikolova *– Ph.D.studentt, Electric Power Supply and Equipment Department, Technical University-Sofia*

Neli Ratz *- Mag. Eng., Assistant Profesor, OTK - Technical University – Sofia*

Nikolay Matanov *- Mag. Eng., Assistant Profesor, Electric Power Supply and Equipment Department, Technical University – Sofia*

Virtual Diagnosis of Cellular Manufacturing Systems

Călin Ciufudean, Alexandru Bogdan Larionescu and Valentin Popa

Abstract: *This paper considers techniques for computing the moments of certain cumulative diagnosis evaluations over a specified time horizon. We consider a generic cellular manufacturing system with finite buffers and prioritized repair, with multiple repairmen. We use stochastic Petri nets to model the failure-repair behavior as well as to obtain the performance measures of the cellular manufacturing system. A model of a cellular manufacturing system illustrates the theoretical approach. Extensions of this work are also discussed.*

Keywords: *automated manufacturing systems, discrete event systems, stochastic Petri nets.*

Introduction

In this paper, we study the diagnosability of discrete event systems (DES). The property of diagnosability is introduced in the context of the failure diagnosis problem, e.g. in the context of the availability of the DES by simulating Petri nets model, e.g. in a virtual manner.

We propose in this paper a DES approach to the problem of failure diagnosis of flexible manufacturing systems (FMS), respectively cellular manufacturing systems, because most of them are modeled by DES and because continuous variable dynamic systems can often be viewed as DES's at a higher level of abstraction.

The states of the discrete event model reflect the normal and the failed status of the system components, while the failure events form part of the event set.

The increasing requirements on performance and reliability of modern systems required the development of sophisticated and systematic methods for the diagnosis of systems failures.

This problem has received considerable attention in the literature and a wide variety of algorithms have been proposed. These include:

I) Quantitative methods based on mathematical models (see, for example [1], [2], [3])

II) Expert systems and other artificial intelligence (AI) – based methods ([4], [5], [6])

III) Discrete event systems methods ([7], [8], [9]).

The quantitative methods employ analytical models of the physical process, in order to compare the sensor measurement with their predicted values.

The AI – based methods incorporate the knowledge of human experts and reasoning mechanisms into diagnostic system.

The DES methods deal with the supervisory control problem with partial event observation. Usually one introduces a language-based definition of observability and state condition for the existence of a solution to the supervisory control problem in terms of observability and controllability of languages.

The control problem addressed there does not require explicit determination of the occurrences of failure events or identification of the system state. Thus, the notion of observability introduced in this manner is different from the problem of diagnosability.

We assume that the problem of diagnosability of a FMS is much more closely related to the problem of determining the availability of the respective system.

We propose in this paper a DES approach to the problem of failure diagnosis, e.g. to the problem of availability of complex manufacturing systems such as FMS's. We present a systematic procedure for detection and isolation of failure events using diagnosers. Therefore we model FMS's with controlled Petri nets (Ctrl.PN). The diagnoser is a Ctrl.PN which models the FSM. This model performs detection and isolation of failures (failure information and occurrences of failures can be detected by inspecting the states of the Ctrl.PN model), and it also permits the verification of the diagnosability properties of the system (e.g. permits the estimation of the availability of the system.

In section 2 "Diagnosability and Availability of DES's" we introduce the notion of diagnosability of DES's in correspondence with their availability.

In section 3 "Evaluation of Automated Manufacturing System" is discussed the theoretical support of our approach, e.g., the controlled Petri nets, and two illustrative examples of our work ("A Petri net model for virtual diagnosis of the AMS", respectively "A Petri net model of the availability of the AMS"), reported in this paper, from FMS virtual diagnosis are given.

Section 4 "Conclusion" summarizes the results of our work and extends them to other further researches and applications.

Diagnosability and Availability of DES's

The flexible manufacturing system to be diagnosed is modeled as a finite state machine of DES's formalism:

$$W = \left(S, E, t, m_0\right) \tag{1}$$

where S is the state space, E is the set of events, t is the partial transition function and m_0 is the initial state of system. The model W accounts for the normal and failed behavior of the system. Let $E_f \leq E$ denote the set of failure events which are to be diagnosed.

Our objective is to identify the occurrence of the failure events. Therefore we partition the set of failure

events into disjoint sets corresponding to different failure types:

$$E_f = E_{f_1} \cup E_{f_2} \cup \ldots \cup E_{f_m} \quad (2)$$

This partition is motivated by the following considerations [5]:

1) Inadequate instrumentation may render it impossible to diagnose uniquely every possible fault;

2) It may not be required to identify uniquely the occurrence of every failure event. We may simply be interested in knowing whether failure event has happened as the effect of the same failures in the system.

So, when we say that "a failure of type F_i has occurred", we mean that some event from the set E_{fi} has occurred.

In [5], [6] the diagnosability is defined as follows: A prefix-closed and live language L is said to be I-diagnosable with respect to the projection P, the partition E_f, and the indicator I if the following holds:

$$\left(\forall i \in E_f\right) \cdot \left(\exists n \in N\right) \cdot \left(\forall s \in E_{f_i}\right) \cdot \left(\forall t \in \frac{L}{s} : st \in I\left(E_{f_f}\right)\right), \left[\|t\| \geq n; \Rightarrow D\right] \quad (3)$$

Where the diagnosability condition D is:

$$\omega \in P_L^{-1}\left[P(st)\right] \Rightarrow E_{f_i} \in \omega \quad (4)$$

Note that $I(E_{fi})$ denotes the set of all traces of L that end in an event from the set E_{fi}.

The behavior of the system is described by the prefix-closed live language $L(A)$ generated by A (see relation (3)). L is a subset of E^*, where E^* denotes the Kleen closure of the set E [7]. $\|s\|$ denotes the length of trace $s \in E$. L/s denote the post language of L after s, i.e.,

$$\frac{L}{s} = \left\{t \in E^* / st \in L\right\} \quad (5)$$

We define the projection $P: E^* \rightarrow E$ in the usual manner [8]:

$$P(\varepsilon) = \varepsilon \text{ and } P(s_1 s_2) = P(s_1) \cdot P(s_2), \quad (6)$$

$$s_1 \in E^* \text{ and } s_2 \in E$$

Where ε denotes the empty trace.

The above definition, e.g. relations (3) and (4), means the following: Let s be any trace generated by the system that ends in a failure event from the set E_{fi}, and let t be any sufficiently long continuation of s. Condition D then requires that every trace belonging to the language that produces the same record of observable events, and in which the failure event is followed by certain indicator, should contain a failure event from the set E_{fi}. This implies that on some continuation of s one can detect the occurrence of a failure of the type F_i with a finite delay, specifically in at most n_i transitions of the system after s.

To summarize, here diagnosability requires detection of failures only after the occurrence of an indicator event corresponding to the failure.

In this paper we improve this approach by according a gradual importance of failure indicators, in correspondence with the availability of the system.

In our assumption the diagnoser is a controlled Petri net (Ctrl. PN) where the places are marked with the availability of the correspondent production cell. We may say that the diagnoser is an extended observer where we append to every state estimate a label. The labels attached to the state estimates carry failure information and failures are diagnosed by checking these labels. We also assume the system W is normal (functional) to start.

Evaluation of Automated Manufacturing System

Architecture of Automated Manufacturing System

Automated manufacturing systems (AMS's) are a complex interconnection of subsystems such as numerically controlled machine centers, assembly stations, automated guided vehicles (AGV's), robots and conveyors.

The structure of the interconnected manufacturing systems changes with failures and repairs and consequently the performance levels deteriorate or improve.

In this paper, we present an approach for the performance analysis of manufacturing systems in the presence of failures and repairs.

Throughput and manufacturing lead-time are two important performance measures in a manufacturing system.

Throughput is the number of parts produced per unit of time and lead-time is the amount of time the work-piece resides on the factory floor.

Most previous performance studies are conducted under failure free assumptions. Discrete event simulation, stochastic Petri nets are used to compute the performance measures.

This paper deals with the transient analysis of manufacturing systems in the presence of failures and repairs. The exact model is decomposed into:

- a structure state process, modeling the failure and repair events which typically occur at a slower time scale;
- a performance model, modeling the part processing and material movement events that typically occur at a faster time scale.

The solutions of these two models are combined to yield the mean and standard deviation of cumulative production over a finite time horizon.

Performability studies are carried out for a cellular manufacturing system, respectively for a two-cell manufacturing system featuring blocking and prioritized, centralized repair.

The approach followed here is the following: we first obtain a structure state process, which describes the system evolution as influenced by failures and repairs.

We define a performance model in each structure state and determine the throughput or lead-time, and use these values in the structure state process to determine the performability.

The basis for such an approach is the large difference in the frequencies of failure/repair events and the part processing events. This implies the following model:

a) A higher level (slow time-scale), structure-state process, describing the failure-repair process.
b) A lower level (fast time-scale), performance model, describing part processing and part handling activities.

We assume that in each state of the structure state process, the performance model reaches steady state. We mention several situations that can arise with regard to repair. These include non-repair, centralized repair, and decentralized repair.

The non-repair case is of interest in the case of night-shift operations.

If there is a separate repair station for each family of equipment it is termed decentralized repair.

If all equipment goes for repair to a unique repair station, then we are considering a system with centralized repair.

The automated manufacturing system consists of two cells linked together by a conveyor system. Each cell consists of a machine to handle within-cell part movement. Work-pieces enter the system at the Load/Unload station, where they are released from two buffers, *A* and *B*, and then are sorted in cells (pieces of type "*a*" in one cell, and pieces of type "*b*" in the other cell). We notice that in the buffer *A* there are pieces of types "*a*", "*b*", and others. In buffer *A* the number of pieces "*a*" is greater than the number of pieces "*b*". In the buffer *B* are pieces of types "*a*", "*b*", and others, where the number of pieces "*b*" is greater than the number of pieces "*a*".

The conveyor moves pieces between the Load/Unload station and those two cells. The finished (sorted) work-piece leaves the system, and a raw work-piece (unsorted piece) enters the system, respectively in one of those two buffers *A* or *B*.

The maximum number of work-pieces permitted inside a cell at any given time is limited, owing to the finite storage capacity available within the cell.

The conveyor along with the central storage incorporates a sufficiently large buffer space so that it can be thought of as possessing infinite storage capacity. Thus, if a work-piece routed to a particular cell finds that the cell is full is refused entry and it is routed back to the centralized storage area.

If a work-piece routed by the conveyor is different from the required types to be sorted respectively "*a*" and "*b*", it is rejected.

We notice that once a work-piece is blocked from entry to a cell, the conveyor does not stop service; instead it proceeds to the other work-pieces waiting for transport.

We also assume that within a cell no further blocking is caused once a work-piece is admitted. At the system level, we assume that the cells are functionally equivalent, so that each cell is sufficient to maintain production (at a reduced throughput).

We say the manufacturing system is available (or operational) if the conveyor and at least one of the cells are available.

A cell is available if its machine is available.

Over a specified period of operation, owing to the randomly occurring subsystem failures and subsequent repairs, the cellular automated manufacturing system will function in different configurations and exhibit various levels of performance over the random residence times in these configurations.

The logical model of our cellular automated system is given in Fig.1.

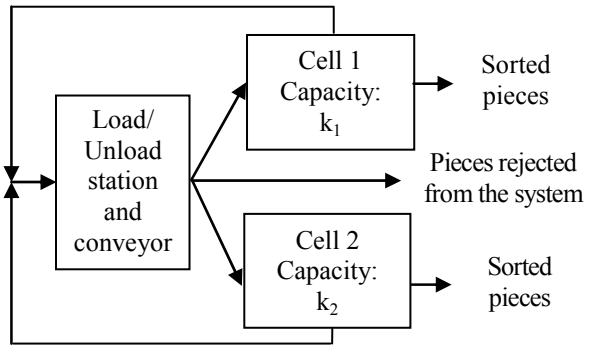

Fig.1. Logical model of a cellular automated manufacturing system (AMS)

A Petri net model for virtual diagnosis of the AMS

The Petri net model of the system appears in Fig.2.

Table 1 gives the interpretation of the places and transitions of the Petri net model.

In the initial marking, we have *n* tokens in P_{HC}, and k_i, i = 1,2 tokens in each $P_{Free\ Buffers\ i}$. We notice that places $P_{Buffer\ Ai}$ and $P_{Buffer\ Bi}$ allows the admission of the work – pieces from the corresponding buffers (*A*, and respectively *B*) in the moments when it is needed to sort more work-pieces from one category or from another one (*A* or *B*).

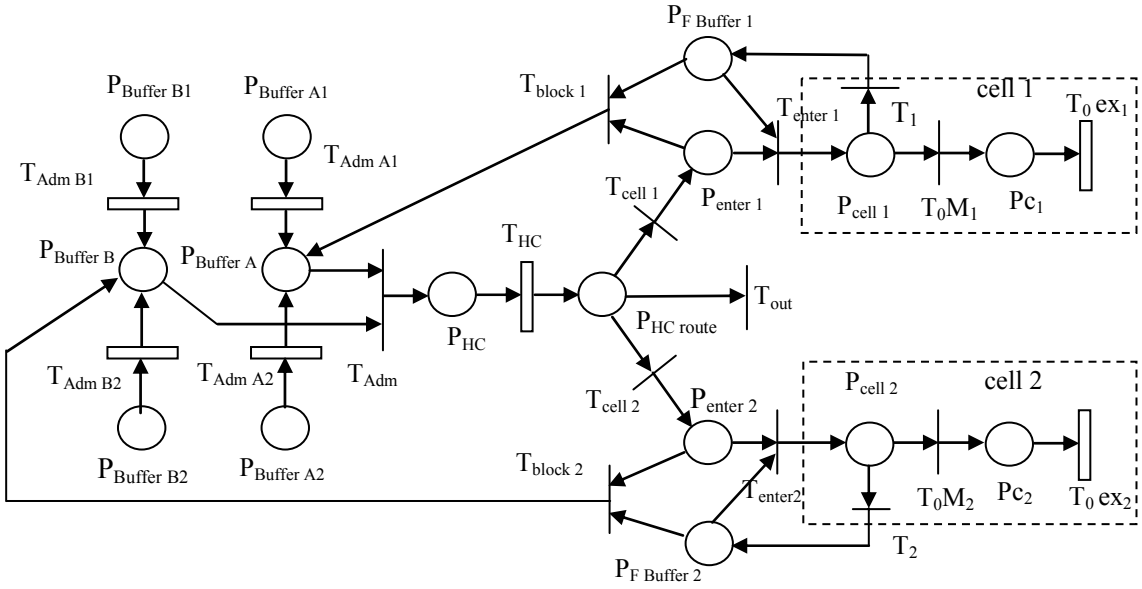

Fig.2. Petri net model for performance analysis of the AMS

Table 1

Legend for the Petri net model of AMS

Symbol	Places
P_{HC}	Work-pieces being admitted to the conveyor
$P_{HC\ route}$	Work-pieces being routed by conveyor
$P_{F\ Buffer\ i}$	Free buffer spaces in cell *i*
$P_{enter\ i}$	Work-piece attempting to enter cell *i*
$P_{cell\ i}$	A work-piece in cell *i* is being sorted by machine *Mi*
P_{ci}	Work-piece waiting to leave the cell *i*
$P_{Buffer\ A,B}$	Work-pieces in buffer *A*, respectively *B* waiting for admission to conveyor
$P_{Buffer\ Ai,Bi}$	A work-piece of type *a*, respectively *b* is expected to be sorted by machine *i.*
Symbol	**Transitions**
T_{HC}	Timed; firing rate (no. of tokens in P_{HC}) x μ_0; models the infinite server operation of conveyor
$T_{adm\ Ai,Bi}$	Timed; firing rate (number of sorted work-pieces *A* or *B*) x μ_0.
T_{adm}	Immediate; a work-piece is admitted (released) to conveyor
$T_{Black\ i}$	Immediate; a work-piece trying to enter cell *i* is blocked
$T_{cell\ i}$	Immediate; a work-piece is routed to cell *i* by machine *i*
$T_{enter\ i}$	Immediate; a work-piece is allowed into cell *i*
$T_{o\ Mi}$	Immediate; a work-piece is routed by machine *i*
T_i	Immediate a work-piece is sorted in cell *i*
$T_{o\ ex\ i}$	Timed; firing rate μ_i; a sorted work-piece is routed to exit the system

We mention that the processing time (part moving time in the case of the buffers A and B) at machine *i* is exponentially distributed with mean $1/\mu_i$, i = 1, 2. In all cases, the part moving time on the conveyor is assumed to be exponentially distributed with mean $1/\mu_0$. The queuing model of the system is produced under the First Come First Served queuing assumption, in spite of the blocking phenomena present in the model (if the cell capacity is fully occupied, the work-piece is blocked and re-enters in buffer *A* or *B*).

A Petri net model of the availability of the AMS

We assume an independent failure model. Let α_i, i=1,2 denote the mean failure rate of machine M_i and let its mean repair time be $1/\beta_i$. Also, let α_0 and β_0 denote respectively the failure and repair rate of the conveyor and buffers *A* and *B* material handling system seen as a whole. All failure and repair times we assume that are exponentially distributed. A pool of identical repairmen is available to work on the failed subsystem at a time. A failed subsystem can use the services of only one repairman. Fig.3. shows the Petri net model of the availability of AMS; it models the failure and repair of the different subsystems. Table 2 gives the interpretation of the places and transitions of this Petri net. Initially, all the subsystems are assumed to be functioning and all repairman are idling. Thus, in the initial marking, a token is placed in each of the places PU_{pj}, j=0,...,4; the number of tokens in the place $P_{F\ Rep}$ equals N_R (i.e., the number of repairmen in the system).

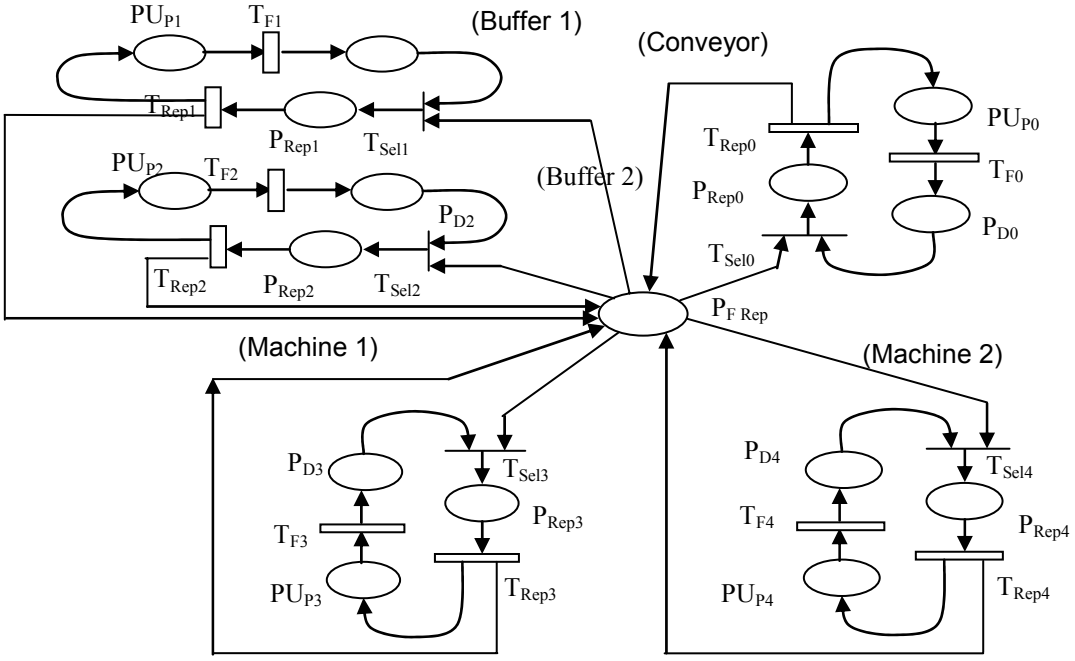

Fig.3. Petri net model of the availability of the AMS

Table 2

Legend for the Petri net model of the availability of the AMS

Symbol	Places
PU_{pi}	Subsystem *i* is working
P_{Di}	Subsystem *i* has failed, and is awaiting repair
$P_{Rep\ i}$	Subsystem *i* under repair
$P_{F\ Rep}$	Idle repairmen
Symbol	**Transitions**
T_{Fi}	Timed; models breakdown of subsystem *i*
$T_{Rep\ i}$	Timed; models repair of subsystem *i*
$T_{Sel\ i}$	Immediate; failed subsystem *i* taken up for repair

Evaluation of the performance and availability of the AMS is obtained by calculating the mean cycle time of the Petri net showed in Fig.1, respectively the Petri net showed in Fig.2, by using the algorithm given in [5]. The mean times obtained from the related graph gives us solutions for the analysis of the AMS over a finite time horizon. From Petri net showed in Fig.2 we calculate the probability of obtaining uptime of "u" hours during a finite interval of time containing a multiple of eight – hours shifts with one or more repairmen. From Petri net showed in Fig.1 we calculate the performability production index such as: expected cumulative production, coefficient of variation of cumulative production (i.e., standard deviation divided by mean), etc. For an example, our system has the next conditions: cell 1 can permit at most 15 work-pieces to be present at a time (k_1 = 15). Cell 2 allows a maximum of 16 work-pieces (k_2 = 16), $\alpha_1 = \alpha_2 = ½\alpha_0 = ½$ (failure rate, i.e., firing rate of corresponding transitions, of machine M_i and conveyor), $\beta_1 = \beta_2 = ½\beta_0 = ½$ (repair rate, i.e., firing rate of corresponding transitions, of machine M_i and conveyor). In such conditions, the expected cumulative production over a 96-hour period, over a six-day week, working two eight-hours shifts a day, with one, two, and three repairmen, shows an average cumulative production increases with the number of repairmen employed. The use of more than three repairmen has not increased the cumulative production.

Conclusion

This paper presented the framework for analyzing the virtual diagnosis of AMS's in the presence of system failures. The presented structures represent the Petri net model for an application built in our laboratory. In this application the sortie of pieces to cells is made automatically in a system driven by a video camera connected to a computer. The pattern recognition process, drive the AMS in a various functioning conditions for the process: random distribution of work pieces types in buffer A and B, different speeds for the conveyor, random break–down times for the machines, etc. We showed how this framework provides for unified, quantitative analysis of the availability, throughput and manufacturing lead-time related performance of a failure-prone manufacturing system. The results reported here can form the basic of several enhancements, such as conducting performability studies with multiple part types. Furthers research will focus on that theme.

References

[1] de Souza e Silva, E., Gail, H. R., "Calculating cumulative operational time distributions of repairable computer systems", IEEE Trans. on Comput., vol. 35, no 4, pp. 322-332, 1986.

[2] Viswanadham, N., Ram, R., "Composite performance dependability analysis of cellular manufacturing systems", IEEE Trans. on Rob. and Autom., vol. 12, pp. 245-258, 1994.

[3] Zurawski, R., Zhon, M. C., "Petri nets and industrial applications: a tutorial", IEEE Trans. on Ind. Electronics, vol. 41, no 6, pp. 567-583, 1994.

[4] Ciardo, G., Muppala, J., Trivedi, K. S., "On the solution of GSPN reward models", Performance Evaluation, vol. 12, pp. 237-253, 1991.

[5] Prath, J. M., Xie, X. L., "Cycle time of stochastic event graphs: evaluation and marking optimization", IEEE Trans. on Autom. Contr., vol. 39, no 7, pp. 1482-1486, 1994.

[6] Ciufudean, C., Larionescu, A. B., "Safety criteria for production lines modeled with Petri nets", Advances in Electrical and Computer Engineering, University "Stefan cel Mare" of Suceava, Romania, vol. 2(19), pp.15-20, 2002.

[7] Ciufudean, C., Popescu, D., "Modeling Digital Signal Perturbation with Stochastic Petri Nets", Advances in Electrical and Computer Engineering, vol. 4(II), no. 1 (21), pp. 71-75, Suceava, Romania, 2004.

[8] Ciufudean, C., "Petri nets in railway traffic systems", Advances in electrical and computer engineering, University "Stefan cel Mare" of Suceava, vol 1(18), no 1(15), pp.21-26, 2001.

[9] Ciufudean, C., "Discrete event systems for modeling the railway traffic", Matrix Rom, Bucuresti, Romania, 2002.

[10] Ciufudean, C., Filote, C., Graur, A., "Supervisory policies for flexible manufacturing systems", Acta Electrotehnica, Academy of Tehnical Sciences of Romania, Technical University of Cluj Napoca, vol.44, no.3/2004, pp.153-157.

[11] Ciufudean, C., Filote, C., Graur, A., Mahalu, G., "Scheduling Sequential Processes in Tree Network", Proceedings of the 13th International Symposium on Measurements for Research and Industry Applications and the 9th European Workshop on ADC Modeling and Testing, IMEKO 2004, 29th-1st October 2004, National Technical University of Athens, Greece,vol.I,pp.355-360.

[12] Ciufudean, C., Filote, C., Graur, A., "Process Monitoring for Flexible Manufacturing Systems with Error Recovering", Proceedings of 2004 IEEE-TTTC Quality and Testing, Robotics, AQTR 2004, May 13th-15th, pp.189-194.

[13] Ezpeleta, J., Colom, J. M., Martinez, J., "A Petri net based deadlock prevention policy for flexible manufacturing systems", IEEE Trans. on Rob. and Autom., vol.11, no2., pp.1028-1036, 1996.

[14] Murata, T., "Petri Nets: Properties, analysis and applications", Proc. IEEE, vol. 77, pp.541-580, 1989.

Călin Ciufudean – *Associate Professor, Dr., Faculty of Electrical Engineering, „Ştefan cel Mare" University of Suceava, str.Universitatii nr.13, RO-720225 Suceava*
e-mail: calin@eed.usv.ro

Alexandru Bogdan Larionescu – *Assistant, Ph.D. Student, Faculty of Electrical Engineering, „Ştefan cel Mare" University of Suceava, str.Universitatii nr.13, RO-720225 Suceava*
e-mail: lari@eed.usv.ro

Valentin Popa – *Associate Professor, Dr., Faculty of Electrical Engineering, „Ştefan cel Mare" University of Suceava, str.Universitatii nr.13, RO-720225 Suceava*
e-mail: valentin@eed.usv.ro

Energy Efficiency at Insurance Microclimatic Parameters in Livestock Building

Nikolay Mihailov, Valentin Stoyanov

Abstract: *Conceptual schemes for reconstruction of energyeconomical livestock buildings with controlled natural ventilation are considered in the paper. The microclimate control system structure is changed with decreased quantity of electrical equipment, new control algorithms and increased operational reliability.*

Key words: *Livestock Buildings, Controlled Natural Ventilation in Buildings, Integrated control systems.*

Introduction

The livestock building is energytransforming object, where the production efficiency depends on the energy utilization degree of the fodders, animals, environment and microclimate systems. Therefore, all these processes have to be considered in their unity and by means of the building construction and building thermal properties this unity be ensured. Every building design should lead to exergy increase of every energy flow forming building balance [1]. The pursuit of these aims has to be accompanied with creation of effective, module and accessible building constructions and types of livestock buildings. On this base, systematic investigations have been carried out at the University of Rousse and the main results are presented in this paper.

1. Model formulation

A synthesized scheme of the exergical contours and streams in a livestock building has been initial base during models' developing [2]. The simplified diagrams of buildings' models are presented in Fig.1. The basic variant is shown in Fig.1a. The all area of the enclosed construction is formed as recuperative heat-exchangers. The air circulation is carried out on the route: inlets (4) → inlet channels (1) → inlet (13) → premises → outlets (5) → outlet channels (2) → ridge vent (3) → atmosphere. The heat utilization is carried out on through air route. In order to air circulation be carried out, the heater contours have to be situated low in the animal zone. The use of a heated floor – contour (7) is more suitable to the occasion. The schemes allow a thermal-pump to be embedded. The valve (10) ensures fluent adjustment of the circulatory air through the building.

The building heat losses decrease, as the losses to the environment do not depend by temperature difference $(\theta_T - \theta_0)$. They depend by the difference $\left(\theta_0^* - \theta_0\right)$. The air warm temperature in inlet channels reach to several degree. For example, for θ_T =30 ^{0}C and θ_0 = -10 ^{0}C the air heating is about 6 ^{0}C [1]. The relation $(\theta_T - \theta_0)/\left(\theta_0^* - \theta_0\right)$ is 2.5 units.

During summer days the heating of the all area of the enclosed construction is restricted by reason of the presence of the air channels and the absence of accumulative mass.

The pressure head *(ΔP)*, being the driving force of the air circulation, due to thermal buoyancy, depends by

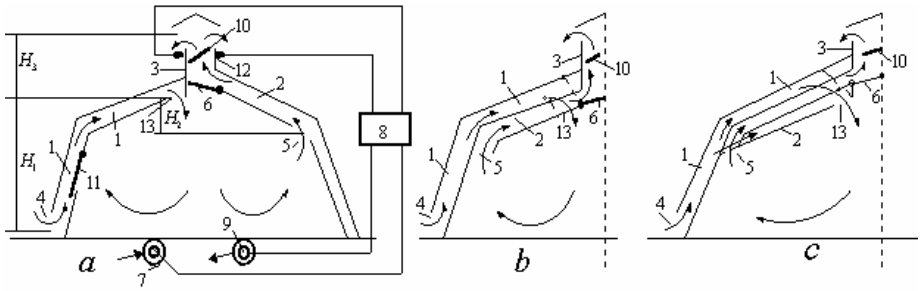

Fig.1. Construction schemes of energyeconomical livestock buildings:

a – alternation of inlet and outlet channels; b - parallel situation, with one contacting area of inlet and outle t channels; c - parallel situation, with two contacting areas of inlet and outlet channels: 1 - inlet channels; 2 - outlet channels; 3 – ridge vents; 4 – inlet; 5 – exhausting inlet; 6 – bottom valve; 7 – floor heating streamer of outer source; 8 – thermal pump; 9 - thermal pump capacitor; 10 – control valve; 11 – side wall valve; 12 - thermal pump evaporator; 13 – inlet.

temperature difference $(\theta_T - \theta_0)$ and geometric heights H_1, H_2 and H_3. The pressure head (ΔP) is given by the relationship [5]:

$$\Delta P = \left(H_1 + \frac{H_2}{2} + H_3 \right)(\rho_0 - \rho_T) - \frac{H_2}{2}(\rho_0 - \rho_0^*) \qquad (1)$$

where ΔP is the pressure head inside the building, Pa;

ρ_T - the air density inside the building, kg/m^3;

ρ_0 - the density of the outdoor air, kg/m^3;

ρ_0^* - the density of the outdoor air, after its heating in the inlet channel, kg/m^3.

The air circulation in the building by the route inlet-outlet channels 1 and 2 through whole year is ensured without use of the side wall valves 11 when the channels width is chosen by the conditions $(\rho_0 - \rho_T) \le 0.07$ and $(\rho_0 - \rho_0^*) \le 0.03$.

After substitution into Eqn (1), the relationship for maximum permissible air speed in the channels is obtained by

$$v_{max} \le \sqrt{\frac{4.7}{\sum_1^{\xi_n} \xi_i + \sum_1^{i_n} l_i}} \qquad (2)$$

where ξ_i are the coefficients of the local hydraulic losses;

l_i – the channels' lengths, m.

The maximum width of the channels (b) will be

$$b = \frac{G_{max}}{L v_{max}} \qquad (3)$$

where G_{max} is the maximum volumetric ventilation rate, m^3/s.

Thus suggested microclimate aeration schemes provide for more fully use of building energy potential (the air heat inside the building and heat emanated by animals), as and the potential of outdoor air. The processes exergy of the building ventilation increases [3]. As an example, the exergy coefficient of efficiency is determined and calculated for a restructured pig building. The exergy coefficient of efficiency of this building was compared with those of the buildings with force ventilation (Fig.2).

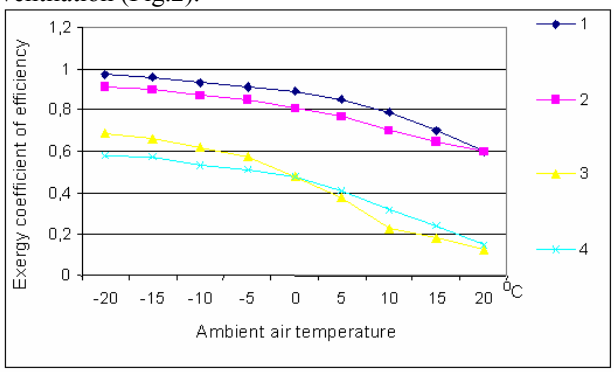

Fig.2. Exergy coefficient of efficiency of the buildings for finishing pigs:

1 - model building at the beginning of the technological cycle; 2 - model building at the end of the technological cycle; 3 - extant building at the beginning of the technological cycle; 4 -

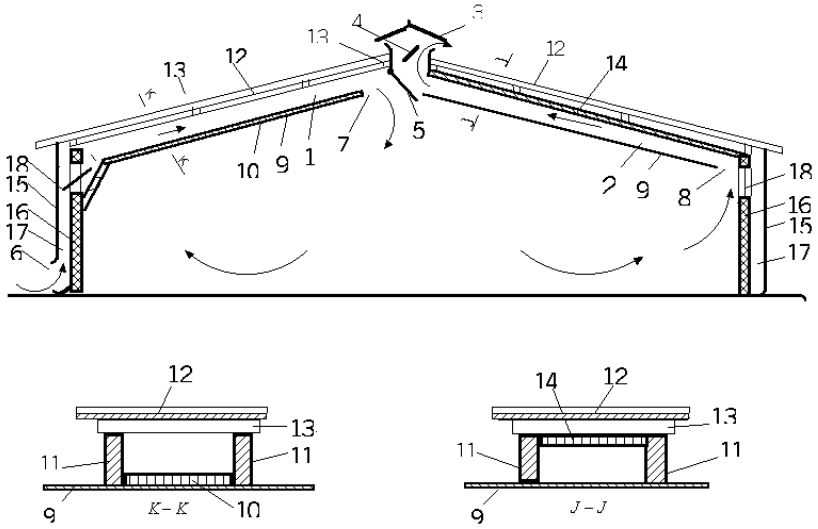

Fig.3. Reconstruction scheme of livestock building type "Gi&Gi":

1 - inlet channel; 2 - outlet channel; 3 – ridge vent; 4 – control valve; 7 – bottom valve-vent; 6 – inlet; 7 – inlet opening; 8 - exhausting outlet; 9 - outlet channel bottom; 10 - inlet channel bottom insulation; 11 - bearer frame; 12 - roof asbestos sheets; 13 – transverse beams; 14 - outlet channel insulation; 15 – insulation side-walls (mounted under reconstruction); 16 – extant wall panels; 17 - inlet channel to side-walls; 18 – windows

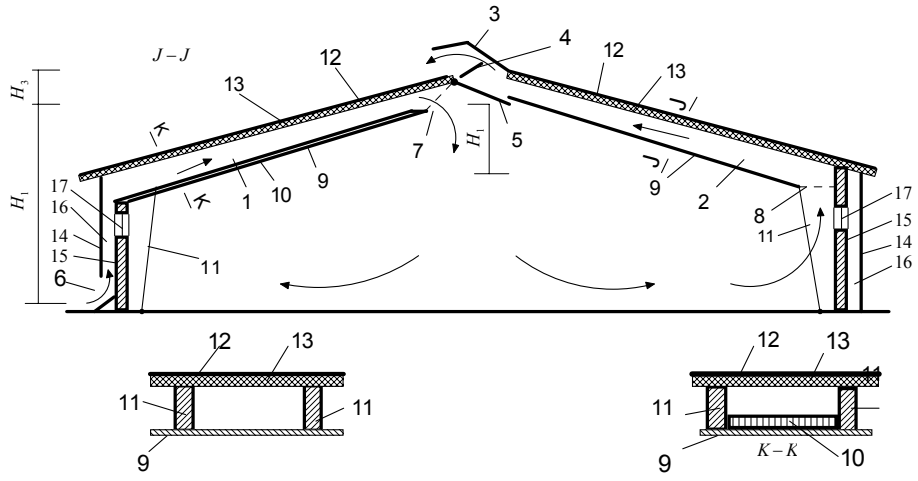

Fig.4. Reconstruction scheme of panel sectional livestock building:

1 - inlet channel; 2 - outlet channel; 3 – ridge vent; 4 – control valve; 7 – bottom valve-vent; 6 – inlet; 7 – inlet opening; 8 - exhausting outlet; 9 - outlet channel bottom; 10 - inlet channel bottom insulation; 11 - bearer frame; 12 - roof panels; 13 – insulation of the roof panels; 14 – insulation side-walls (mounted under reconstruction); 15 – extant wall panels; 16 - inlet channel to side-walls; 17 – windows.

extant building at the end of the technological cycle.

2. Model for reconstruction of livestock building type "Gi&Gi"

The livestock buildings type "Gi&Gi" are wide spread in the built farm and livestock complex in a lot of country and at home. It is suitable to carry out the reconstruction when the heat insulation of the roof is being changed. The reconstruction scheme is shown in Fig.3 [2,4]. The scheme from Fig.1a is suitable. The building construction is kept.

The inlet 1 and outlet 2 channels are built between bearer frames 11. The channels are manufactured from reinforced polyethylene foil, which covers the whole ceiling area. The polyethylene foil is mounted to frames 11. The bottoms of the inlet channels 1 are protected with insulation 10. On the outlet channels are put an insulating layer 14 by styrofoam, mineral batting or polypropylene on the area toward the roof. The insulating side-walls 15 are mounted over building sides. They cover the building walls fully and fix to the vertical columns of the bearer frames 15. The air exchange is controlled by the valve 4. The inlet channels connect to frameworks of the building windows.

3. Model for reconstruction of panel sectional livestock buildings

The reconstruction is carried out in like manner as the precedent building (Fig.4). The channels' bottoms take shape by means of affixing of the reinforced polyethylene foil 9 to bearer frames 11. The inlet channels 1 are insulated with the insulation layer 10. The outlet channels do not need by insulation. Along the building ridge some openings are taken form in which the ridge vents 3 and control valve 4 are mounted. The windows 17 are kept.

On the base of presented schemes, some pig buildings - type "Gi&Gi" for 2000 finishing pigs and 2 buildings for weaned piglets were reconstructed. The results of their investigation are shown in [5]. A decreased death-rate up to 3.3% is found, increase of the daily liveweight gain up to 12.8%, decrease of the fodder consumption up to 10.2%. The energy consumption for building ventilation dies out. The quantity of building electrical installations decreases two times.

4. Microclimate control system

The development of a modern control and management system for agricultural buildings must use recent advances in software design, and development tools, to provide an open system for rapid program development. VACQ (Virtual Aerial Control Qualitative) is a digital control system with generalized functions for process control, configurable to meet agricultural buildings control requirements. Intelligence is shared among the low-level control loops of the controller and the high level decisions made at the central process computer. The VACQ environment provides a vehicle through which all operations research achievements and management conclusions can be easily implemented in the field. It facilitates the development of artificial intelligence (AI) applications capable of collaborating with the agricultural building management system for the solution of common problems. Tools have been integrated at the level, which provides flexibility and freedom for the user, without loosing much of its friendliness. Moreover, there is a considerable potential

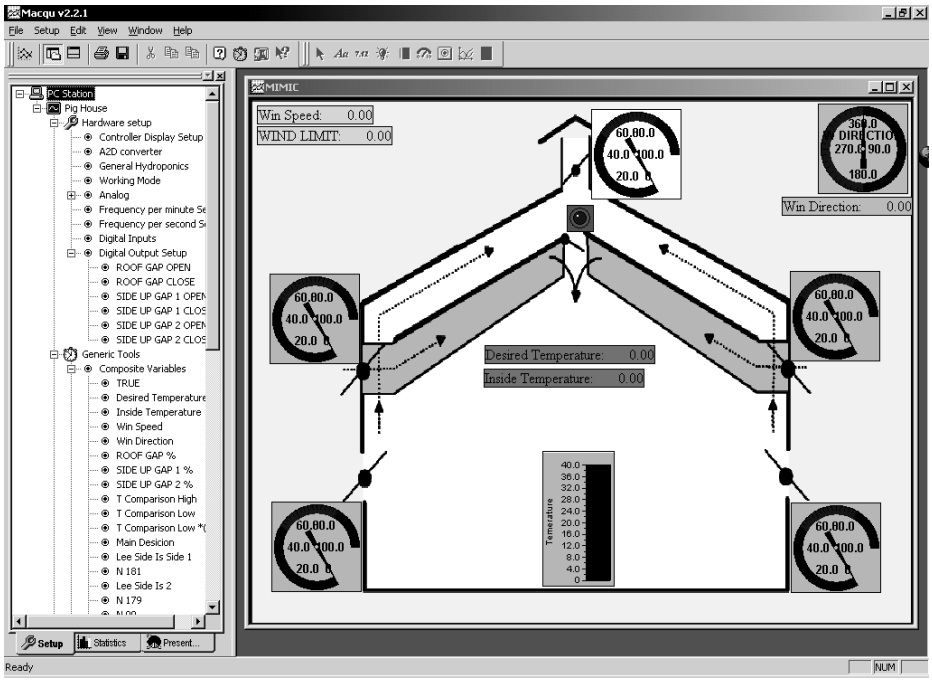

Fig. 5. VACQ's main window:

(1) Basic Menu Setup window; (2) Mimic diagram presentation window

for the development of hybrid systems that combine conventional applications with knowledge based systems.

The main innovative features implemented to provide a flexible system like VACQ are:

Functional objects: Object oriented design not only on the programming style but also on the "user_functionality". A complete set of "prime functions", needed at the different signal processing stages, [input stage]-[processing stage]-[output stage], were identified and designed as independent objects. These objects can be specified and chained to provide a "custom" higher level function.

Virtual variables (VV): The system starts with no variables defined, except the ones related to hardware and the program. At any time the "user" can institute, during execution, new variables as functions of other variables, starting with the hardware input variables, i.e. the measurements. A rich set of function templates (library) has been designed-in, from which the user can select his signal processing building blocks. Polynomials, adjustable Time-Integrated-Variables, digital delay lines with taps, first and second order system models, multi_in_one_out, thresholds/decisions, time_switches and multi-point day_clocks, hard and soft events, are some of such VVs which can be defined and used as input or control for other functions.

Output drivers (OD): Various type of equipment are used, depending on the technological status and the process involved. Output functions available are: bipolar or unipolar ON/OFF with hysteresis, PWM, Pulse Frequency Modulation (PFM) and analog. Control commands, supplied by a control loop, can be tied with a selectable output driver, to conform to the type of actuator used.

Virtual control loops: Almost any control philosophy can be implemented using a well-defined chain of building blocks and smart virtual variables. Non-linear PIDs controllers, starting from a VV reference and leading to configurable output functions and functional enable/disable switches are the tools to build control loops.

Presentation objects: A rich library of presentation tools was implemented to allow system customization on the site, to create an attractive and intuitive desktop. The screen can be organized to tile or cascade a number of windows, each including a real time presentation of the virtual variables. The real time graphics include scroll graphs, table type data viewer, dynamic bars, analog meters or a mimic diagram with animation of the work place.

On-line optimization tool: The system is also equipped with an on-line process optimization tool, which was built based on a modified search algorithm with accelerated learning. Each process, when entered under the optimizing monitor, must be performance driven. The system conducts real experiments on the site and uses a modified descent method to maximize performance.

Decision Support System (DSS): VACQ includes an advanced database system, which collects and organizes information from the connected agricultural buildings. The automatically collected information regards the external and internal environmental conditions, measurements of the root area microenvironment, the

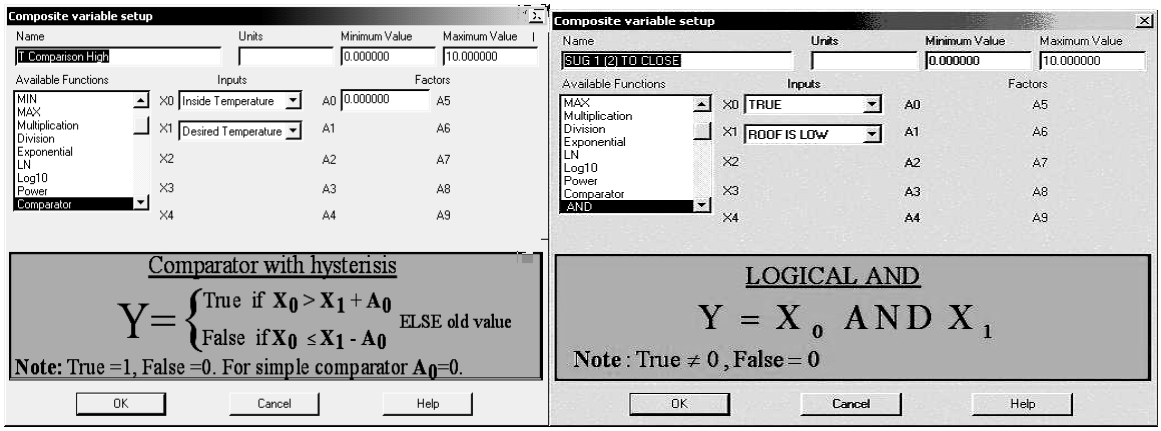

(a) *(b)*

Fig. 6. Composite Variable Setup windows for defining of virtual variables and functions: (a) example of defining of virtual variable called "T Comparison High" and use of "Comparator" function; (b) example of defining of virtual variable called "SUG 1 (2) TO CLOSE" and use of logical AND function

operational condition of several actuators inside the building a well as some sub-systems of VACQ.

Supervisory level: The central, PC Windows 95 based, VACQ software is intended to: a) provide menus to setup the management system, b) feedback the user with real time graphics and c) manage the overall operation by few rules.

VACQ suggests two modes for implementation of given algorithm.

The first mode requires the use of above-mentioned objects, as *Functional objects, Virtual variables (VV), Virtual control loops, Presentation objects* etc. Using the functional possibilities of the VACQ's *Basic Menu Setup window* (*Fig. 5(1)*) the user can create several types of virtual variables, control schemata and output drivers, in order to manage the microclimate in the livestock building. For example by *Generic Tools* and *Composite variables* (*Fig. 5(1)*) the variables *Inside Temperature, Win Speed* and *Win direction* can be assigned as measurement variables, but variables *T Comparison High* and *T Comparison Low* are assigned as virtual variables.

The logical rules of the algorithm are implemented by means of VACQ's built in functions as *Comparator* and *Logical AND* functions shown in *Fig. 6*. The values of the variables and the control commands are presented by a combination of a mimic background diagram and suitable number of real time presentation items, shown in *Fig. 5(2)*.

The second mode for implementation of the proposed algorithm suggests more facilities for the users. This mode requires creation of a special Graphical User Interface (Dialog), which to allow the necessary information to be entered by the user. For the needs of proposed algorithm a new control dialog box window was incorporated in VACQ system (*Fig. 7*). This control window allows in real time mode, all information for implementation of the proposed algorithm to be entered. The logical rules of the algorithm are built in the control window during its creation and they are not visible for the user.

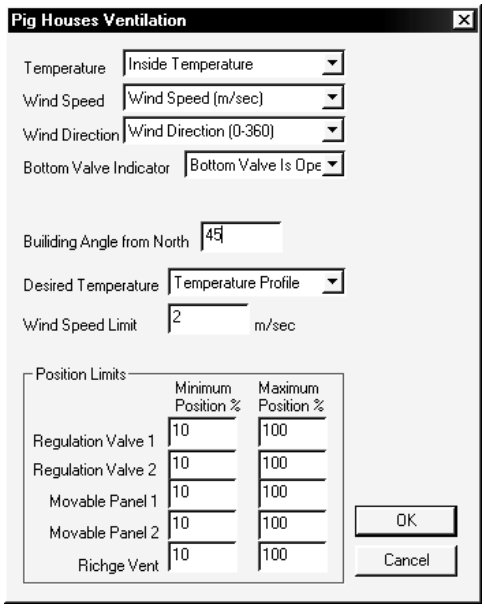

Fig. 7. Control dialog box window

Conclusions

The presented conceptual schemes of energyeconomical livestock buildings show that the manufacture of the livestock production can be put of the principled new base, if some preconditions for benefits in respect of the energy consumption, buildings'

construction and improvement of environmental norms are created.

The energy benefit is provided by building aeration during whole year, the heat-exchange realization through construction of the building, using of the heat emanated by the animals and utilization of the exhausted dirty air heat by heat-pump effect. The microclimate process exergy is increased.

The environmental improvement and providing of ecological cleaner production is achieved by means of uniform air distribution in the building, natural contact of the animals and poultry with surrounding environment, lack of noise, draughts and decreased dust.

The microclimate control system structure is changed with decreased quantity of electrical equipment (electrical motors, fans, control devises etc.), new control algorithms and increased operational reliability, independence by electrical interrupting.

REFERENCES

[1] Andonov, K. 1995. Investigation of livestock building aeration scheme. *Agricultural Engineering* №1, 26-31.

[2] Andonov, K., et al. 1993. Investigation of livestock buildings with aeration. *Agricultural Engineering* №5, 25-31.

[3] Stoyanov, V., 1999. Investigation of technological indicators, providing the microclimate in livestock building with aeration. *Ph.D. Thesis*. University of Rousse.

[4] Daskalov, P. I. 1997. Prediction of Temperature and Humidity in a Naturally Ventilated Pig Building, *Journal of Agricultural Engineering Research*, v.68, 329-339.

[5] Andonov, K., V. Stoyanov. 1995. A Scheme of Climatization in Livestock Buildings. *Journal of huaiyin teachers college* №5, 17-23.

Nikolay Mihailov *– Associate Professor, Dr., Faculty of Electrical Engineering, University of Rousse, 8 Studentska Str., 7017 Rousse, BULGARIA. e-mail: mihailov@ru.acad.bg*

Valentin Stoyanov *– Associate Professor, Dr., Faculty of Electrical Engineering, University of Rousse, 8 Studentska Str., 7017 Rousse, BULGARIA. e-mail: vstojanov@ru.acad.bg*

Three-Module Converter System for High Frequency Electrotechnological Applications

Georgi Kunov, Marian Popov and Elissaveta Gadjeva

Abstract: *In the present paper, a three-module converter system for high frequency electrotechnological applications is proposed. This system allows three fold increasing of load frequency with respect to switching frequency of the inverter transistors. This is achieved by a proper algorithm of transistor switching control on the connection of the represented module. PSpice simulation is performed and the switching losses are investigated. Based on parametric analysis, a design procedure is developed for the automatic calculation of the elements in the series resonant circuit.*

Keywords: *power electronics, transistor inverters, induction heating, computer modeling, PSpice simulation.*

Introduction

In practice, a number of electrotechnologies require power supply sources with frequencies above 1MHz. During the last years they have been realized as tube generators. As a result of the power semiconductor device improvement (mostly of MOSFETs) in the megahertz frequency range, power transistor frequency converters are successfully realized [1].

The maximal working frequency of the transistor converters is limited by the commutation losses. Similarly to the thyristor converters [1,2], the multi-module principle can be successfully applied to the transistor converters in order to reduce the commutation losses. This principle is reduced to a successive transfer of AC energy to the load from several (mostly three) inverters. As a result, the thyristor commutation frequency decreases and the turn-off time increases proportionally to the module number.

A series two-module resonant inverter is investigated in [3] realized using IGBTs. The load frequency is 200 kHz for the transistor commutation frequency of 100 kHz. In the present paper, a three-module MOSFET inverter circuit is proposed and investigated for the frequency range from 1.2 MHz to 2 MHz and load power of 15 kW, using the OrCAD PSpice circuit simulator [5].

Three-Module Converter System

Converter Circuit and Control Algorithm

The block scheme of the three-module converter system for high frequency electrotechnological applications is shown in Fig. 1. The realization of the converter circuit is shown in Fig. 2. It consists of three bridge transistor inverters (M11-M44). The first index corresponds to the inverter module number and the second – to the element sequence in the corresponding module.

The load circuit consists of a series resonant circuit. It is connected to the inverter modules by TX1-TX3 transformers. The energy is transferred to the load when the pair of diagonal transistors (1-3 or 2-4) is simultaneously turned on. The simultaneously turned on transistors follow in the sequence for a time interval equal to 1/6 of the load period in the following way: M11-M13, M21-M23, M31-M34, M12-M14, M21-M24 and M31-M34. When a transistor pair of a module is turned on, energy is transferred through the corresponding transformer from the power supply Vdc to the load resonant circuit. In the same time the transformers of the rest two modules are short-circuited by the turned-on lower transistor pair 3-4. The described algorithm of work is illustrated by the waveforms shown in Fig. 3. It is seen that the upper transistor pair (1,2) of each module is turned on during the time interval equal to 1/6 of the own transistor commutation period and the lower transistor pair - during 5/6 of this period. The commutation frequency of each transistor is three times lower than the load frequency. It follows from the consideration that the vertical transistor pairs 1-4 and 2-3 of each module are dephased by 180°. The control impulses of the transistors are defined in the *PSpice* model using independent voltage source of the **VPULSE** type. The corresponding parameters are presented in Table 1 in accordance with the input language of the *PSpice* simulator.

The SPICE model of the APT8011JFLL transistor (producer ADVANCED POWER TECHNOLOGY [4]) is used for the computer simulation (Fig. 4).

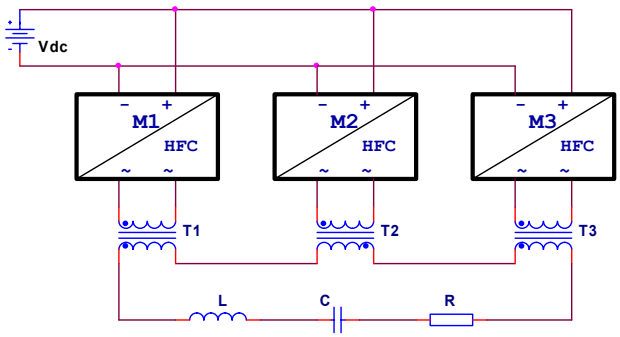

Fig.1. Block scheme of the three-module converter system

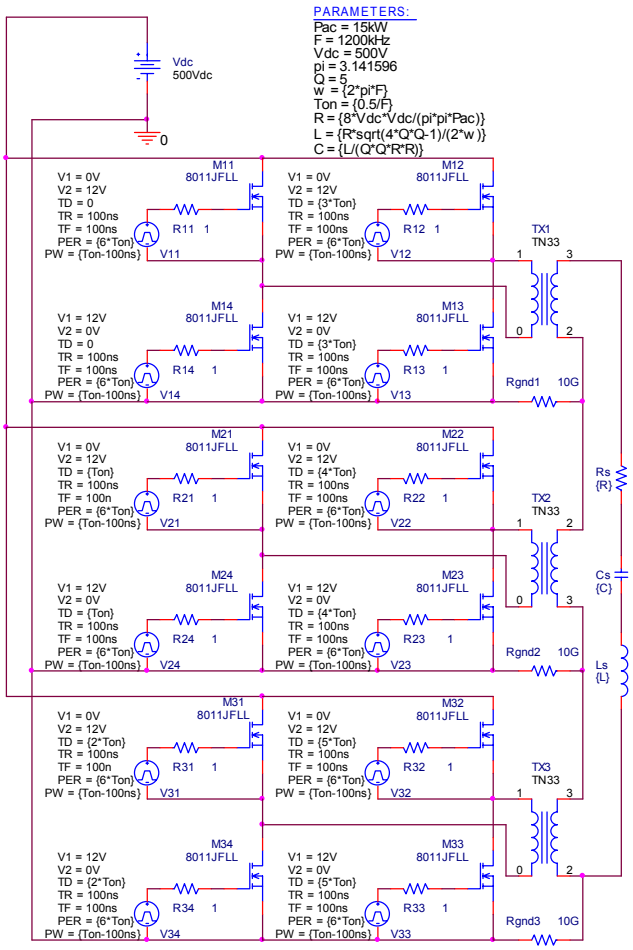

Fig.2. Three-module converter circuit

Table 1

Parameters of control impulses

1,2 – high level	3,4 – low level
V1 = 0V	V1=12V
V2=12V	V2 = 0V
TD11=0	TD14=0
TD21={Ton}	TD24={Ton}
TD31={2*Ton}	TD34={2*Ton}
TD12={3*Ton}	TD13={3*Ton}
TD22={4*Ton}	TD23={4*Ton}
TD32={5*Ton}	TD33={5*Ton}
PER={6*Ton}	PER={6*Ton}
PW={Ton-100ns}	PW={Ton-100ns}
Remark: Ton= {0.5/F} is a half of the load period	
PW={Ton-100ns}; 100ns – the deadtime	

Procedure for automatic design using PARAMETERS Statements

The parameter values of the elements in the load resonant circuit can be automatically calculated [8,9] using the PSpice **PARAMETRS** statement. The corresponding procedure consists of the following steps [4]:

– Pac=15kW – AC power on the resistor Rs;

– Fres=1200 kHz – resonant frequency of the series load resonant circuit (Rs, Cs, Ls);

– Vdc=500V - supply voltage;

– Q={sqrt(Ls/Cs)/Rs}= 5 - quality factor of the series resonant circuit;

– w= 2*pi*F; pi=3.141596;

– Ton= {0.5/F} is a half of the load period;

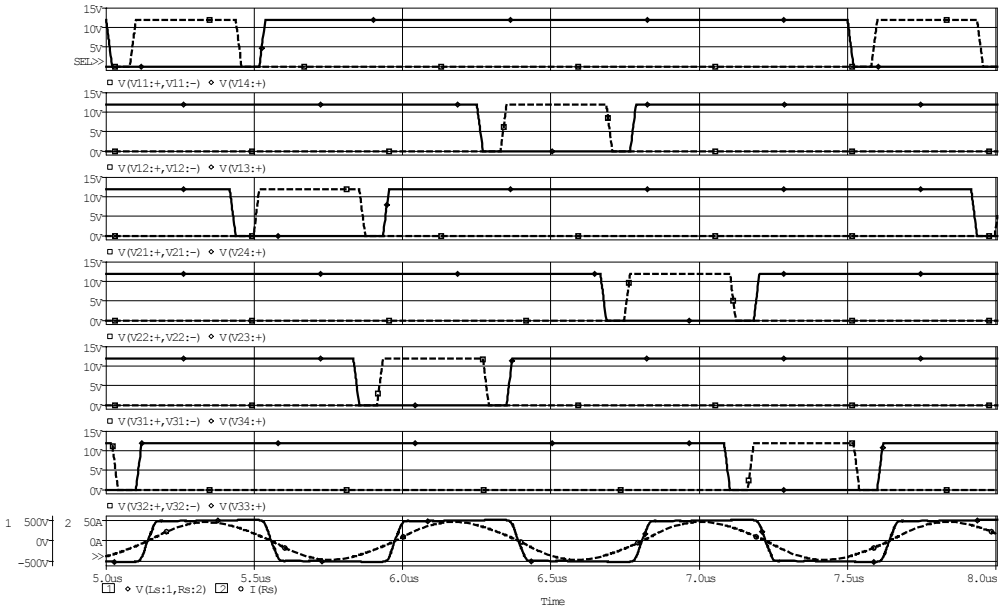

Fig.3. Waveforms of the gate control voltages

```
*SRC=8011JFLL;8011JFLL;MOSFETs N;
*APT 800V 51A 0.11ohm ISOTOP
.SUBCKT 8011JFLL 10 20 30
*    TERMINALS:  D  G  S
M1   1  2  3  3  DMOS L=1U W=1U
RD  10  1  51.2M
RS  40  3  3.75M
RG  20  2  2.94
CGS  2  3  9.7N
EGD 12  0  2  1  1
VFB 14  0  0
FFB  2  1  VFB  1
CGD 13 14  4.07N
R1  13  0  1
D1  12 13  DLIM
DDG 15 14  DCGD
R2  12 15  1
D2  15  0  DLIM
DSD  3 10  DSUB
LS  30 40  7.5N
.MODEL DMOS NMOS (LEVEL=1 LAMBDA=294U
VTO=4 KP=48.4)
.MODEL DCGD D (CJO=4.07N VJ=0.6 M=0.68)
.MODEL DSUB D (IS=212N N=1.5 RS=10.8M BV=800
CJO=6.94N VJ=0.8 M=0.42 TT=560N)
.MODEL DLIM D (IS=100U)
.ENDS
```

Fig. 4. SPICE model of the APT8011JFLL transistors

– R={8*Vdc*Vdc/(pi*pi*Pac)} – resistance value of Rs;

– L={R*sqrt*(4*Q*Q-1)/(2*w)}–inductance value of Ls;

– C={L/(Q*Q*R*R)} – capacitance value of Cs.

Using the described approach, a simulation of the circuit is performed. The results for the transistor pair (M11 and M14) are presented in Fig. 5, where:

– V(V11+,V11-) and V(V(V14+)) are control impulses of transistors M11 and M14;

– V(M11:10,M11:30) and I(M11:10) – drain-source voltage and drain current of M11;

– V(M14:10) and I(M14:10) – drain-source voltage and drain current of M14;

– ABS(V(M11:10,M11:30)*I(M11:10)) and ABS(V(M14:10)*I(M14:10)) – instant values of dissipated power in transistors M11 and M14.

It is seen that the lower transistor is characterized by greater power losses. The results in Fig. 5 are valid for each of the vertical transistor pairs.

Dependence of Power Losses in Transistors on the Working Frequency

The investigation of the frequency dependence of power losses in the transistors is performed by introducing the load frequency as a parameter (F={Fvar}). Its variation is defined in the range from 1.2 MHz to 2 MHz by an increment of 0.1 MHz. The simulation results are shown in Fig. 6 for the vertical transistor pair M11-M14.

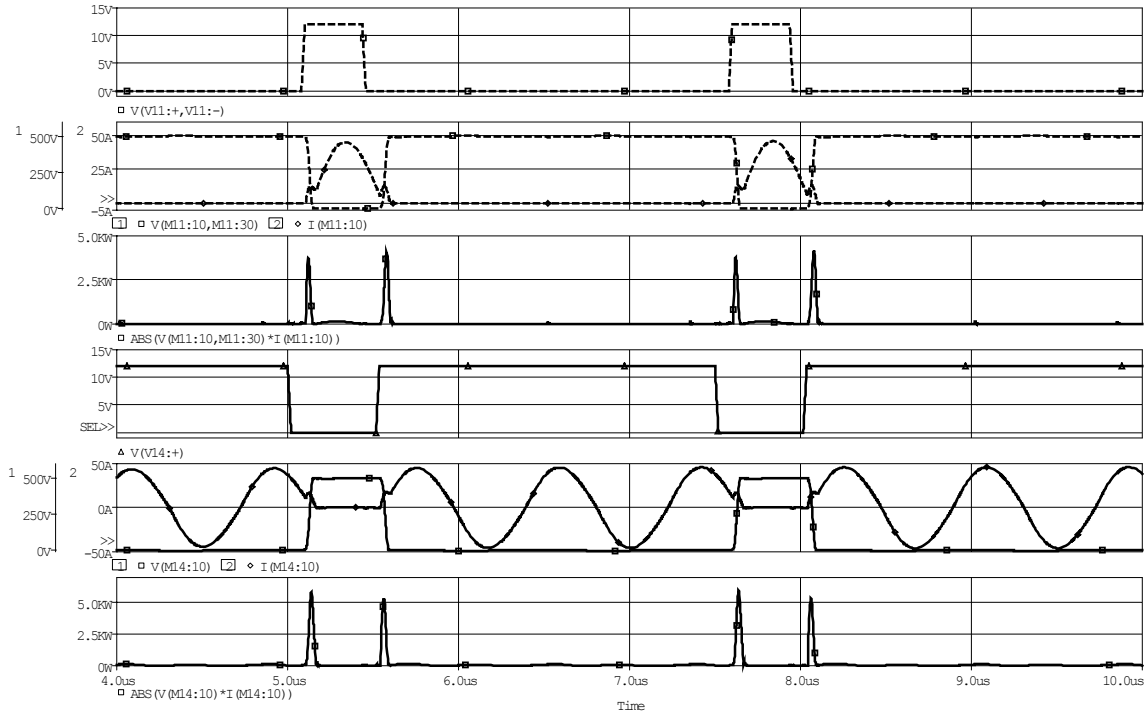

Fig. 5. Simulation results for the vertical transistor pair M11-M14

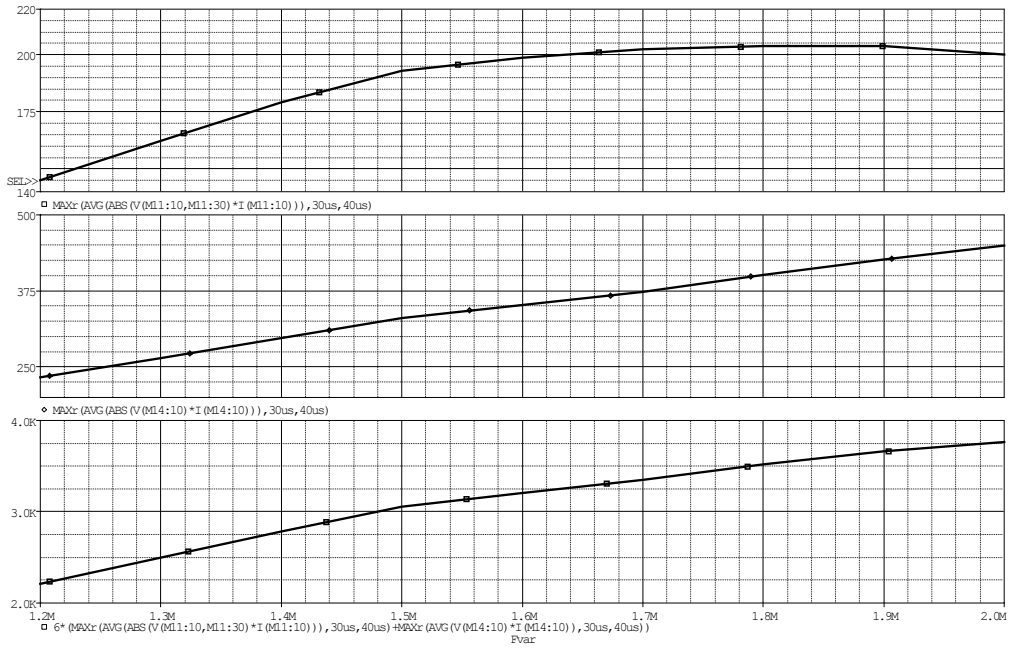

Fig.6. Dependence of power losses in transistors on the working frequency

The sum of the losses in M11 and M14, multiplied by 6, corresponds to the value of total power losses in all transistors. This value allows the assessment of the circuit efficiency. The corresponding powers are obtained in the graphical analyzer *Probe* using the expressions:

– MAXr(avg(abs(V(M11:10,M11:30)*I(M11:10))), 30us,40us)
– MAXr(avg(abs(V(M14:10)*I(M14:10))),30us,40us)
– 6*(MAXr(avg(abs(V(M11:10,M11:30)*I(M11:10))), 30us,40us)+MAXr(avg(abs(V(M14:10)*I(M14:10))), 30us,40us))

The Total Power Dissipation of the APT8011JFLL transistors is Pd=690W [5]. This power is not exceeded for the lower transistors (3-4) of the inverter bridges, which are working in a heavier mode of operation.

Conclusion

A three-module full bridge converter circuit has been developed, where the switching frequency of the transistors is three times lower than the load frequency. A proper algorithm of transistor control is presented. Based on parametric analysis, a design procedure is developed for the automatic calculation of the elements in the series resonant circuit. This procedure is implemented in the graphical editor *Capture* using the **PARAM** statement. The commutation losses in the transistors are investigated and the possibility is proved for covering the frequency range of up to 2 MHz and the load power of 15 kW.

References

[1] Tabacov, S. Power Electronic Circuits and Devices, Technika, 1987 (in Bulgarian).

[2] Natchev, N., Maleev, G. Power Electronics, Technika, Sofia, 1979 (in Bulgarian).

[3] Zied, H., P. Mutschler, G. Bachmann, A Modular IGBT Converter System for High Frequency Induction Heating Applications, PCIM 2002, 14-16 May 2002, Nürnberg, Germany.

[4] Brichant, F., Electronique de Puissance, E.T.S.F., Paris, 1977.

[5] http://www.advancedpower.com

[6] OrCAD PSpice and Basics, Circuit Analysis Software, OrCAD Inc., USA, 1998.

[7] Kunov, G., Popov, M., Gadjeva, E.: Comparison of Energy Factors of Transistor Inverters for Induction Heating Using PSpice, ICEST 2004, Bitola, Macedonia, 2004.

[8] Gadjeva, E., Kunov, G. Application of General-Purpose Simulators as a Design Tool for Transistor Inverters for Induction Heating, 4-th International Workshop CPE 2005, 1-3 June 2005, Gdansk, Poland.

[9] Kunov, G., Gadjeva, E.: Design and Simulation of Working in Parallel Transistor Inverters, 12-th International Symp. on Power Electronics, EE'2003, Novi Sad, Serbia & Montenegro, November 5-7, 2003.

Georgi Kunov *– Assist. Prof., Faculty of Electronic Engineering and Technologies, Technical University of Sofia, 8 Kl. Ohridski St., 1000 Sofia, BULGARIA. e-mail: gkunov@tu-sofia.bg.*

Marian Popov *– Ph.D. Student, Faculty of Electronic Engineering and Technologies, Technical University of Sofia, 8 Kl. Ohridski St., 1000 Sofia, BULGARIA. e-mail: mariannp@abv.bg*

Elissaveta Gadjeva *- Associate Professor, Dr., Technical University of Sofia, Faculty of Electronic Engineering and Technologies, e-mail: egadjeva@tu-sofia.bg.*

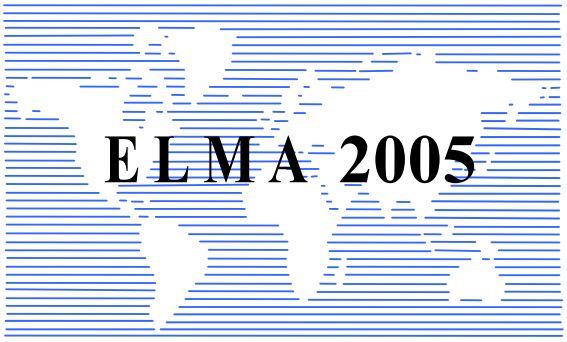

ELECTRICAL MACHINES II

Some Problems of Brushless Exciter for Synchronous Generator

Emil Sokolov

Abstract: *The m.m.f. harmonics produced by armature winding are analyzed. Amplitudes, number of poles and frequencies of two harmonic series are determined. The harmonics of first type depends from the armature winding structure. Non-sinusoidal armature current due to loading of rotating rectifier causes the second type harmonics. An example is considered and the effects of the high frequency eddy currents are discussed for case of a solid steel stator core. The influence of the exciter parameters on the stray load loss is studied.*

Keywords: *m.m.f. harmonics, current harmonics.*

Introduction

The brushless excitation system eliminates the slip rings and brushes of the conventional way for carrying of d.c. field current in the rotor of the synchronous machine. The exciter considered in this work is usually used for relative high-speed synchronous generators with ratings to about 10 MVA.

The typical arrangement of brushless exciter corresponds in principle to an inverse synchronous machine. The field winding of the salient-pole stator is supplied with direct current from an automatic regulator by which the field current of the synchronous generator is controlled. The rotor of exciter comprises three-phase armature winding. The output of the armature winding is connected to a diode rectifier. This rotating rectifier feeds the field winding of main rotor. The rotors of the generator and exciter are located on common shaft. The number of poles and frequency of the exciter are larger than these of the generator.

The brushless excitation systems have recently increasing applications since maintenance is not necessary and because of safety operation. From the viewpoint of reliability they are advanced technical solution.

In the present research some effects of the high frequency harmonics of the armature magnetic field are analyzed.

M.m.f. Harmonics of the Armature Winding

The exciter operates with frequency f_e which is higher than the frequency of the synchronous generator *f:*

$$f_e = \frac{2p_e}{2p} f \qquad (1)$$

where $2p_e$ and $2p$ is the number of poles of exciter and generator, respectively. The enhancing frequency enables to reduce the exciter dimension. Also, less ripple of the rectified current and greater rapidity of response is obtained.

It is well known that the three-phase system of sinusoidal currents in a balanced three-phase winding produces a series of m.m.f. harmonics. The analysis of the resultant waveform leads to high harmonics of order:

$$\nu = 6k \mp 1 \quad (k = 1,2,3,...) \qquad (2)$$

The fundamental space wave of armature reaction and the rotor of exciter rotate at synchronous speed n_S in opposite direction. Consequently, the fundamental wave is immovable relative to the salient-pole stator. The forward rotating harmonics (ν = 7, 13,…) have the same direction as the fundamental wave, the backward rotating harmonics (ν = 5, 11,…) rotate in opposite direction to the fundamental. The speed of harmonics in the rotor is:

$$n_{R\nu} = \frac{n_S}{\nu} \qquad (3)$$

The harmonic speed relative to the stator is:

$$n_{S\nu} = n_S\left(1 \pm \frac{1}{\nu}\right) \qquad (4)$$

where negative sign holds for the forward rotating and positive sign for the backward rotating harmonics.

Every harmonic has ν times larger number of poles than the poles of fundamental wave. Then the frequencies of harmonics in the stator and rotor can be easily calculated.

The high harmonics from described type are determined by the structure of armature winding. The magnitude of each harmonic depends on the distribution and pitch of the winding and decreases in proportion to the order of the harmonic. The amplitude of m.m.f. harmonic of order ν is given by the following expression:

$$F_\nu = 1{,}35\frac{w.k_{w\nu}}{\nu.p_e} I \qquad (5)$$

In Eq.(5) w is the number of turns in series per phase, $k_{w\nu}$ is the winding factor for the ν-th harmonic and I is the r.m.s. value of the phase armature current.

M.m.f. Harmonics due to Current Harmonics

The second type harmonics are formed when the armature current is non-sinusoidal. A three-phase full-wave bridge rectifier loads the wye-connected armature winding. In every time interval two diodes conduct and six such intervals pass per cycle. Due to the large inductance of the field winding of the synchronous generator the ripples of rectified current are negligibly small. Then for the armature current can be assumed rectangular shape in a half-cycle (Fig. 1). The amplitude of the rectangle is equal to the rectified current $\bar{I}$. The width of the rectangle is two thirds of a half-cycle or 120 degrees.

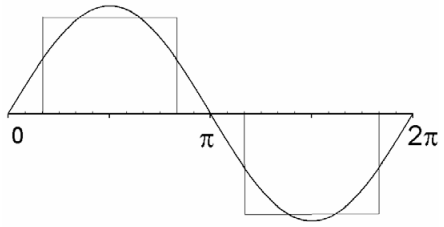

Figure 1

Fourier analysis of the armature current in a phase yields the following function:

$$i_a(t)=\frac{4}{\pi}\bar{I}\cos\frac{\pi}{6}\left(\sin\omega_e t-\frac{1}{5}\sin 5\omega_e t-\right.$$
$$\left.-\frac{1}{7}\sin 7\omega_e t+\frac{1}{11}\sin 11\omega_e t+\frac{1}{13}\sin 13\omega_e t-...\right) \quad (6)$$

As shown the analysis, the armature current comprises a series of high harmonics in addition to the fundamental. The order of the harmonics is:

$$\mu=6k\mp 1 \quad (k=1,2,3,...) \quad (7)$$

The frequency of these harmonics is μ times higher than the fundamental frequency. Triple current harmonics are not present.

Further only the fundamental m.m.f. space waves produced by the armature current harmonics are taken into account. Therefore the number of poles of all m.m.f. harmonics of order μ is constant and equal to the number of exciter poles, but their speeds are different. The space m.m.f. harmonics of order μ = 7, 13,… rotate in the direction of the fundamental wave, while the harmonics of order μ = 5, 11,… rotate in opposite direction.

The amplitude of m.m.f. harmonic produced by a current harmonic of order μ is determined from the relationship:

$$F_\mu=1{,}35\frac{w.k_{w1}}{p_e}\frac{I}{\mu} \quad (8)$$

The considered features of the two types m.m.f. harmonics are generalized in Table 1.

Table 1

	M.m.f. harmonics of the armature winding (ν-type)	M.m.f. harmonics due to current harmonics (μ-type)
Number of poles	$2\nu p_e$	$2p_e$
Speed relative to the rotor	$\frac{n_S}{\nu}$	μn_S
Speed relative to the stator	$n_S\left(1\pm\frac{1}{\nu}\right)$	$\mu n_S\left(1\pm\frac{1}{\mu}\right)$
Rotor frequency	f_e	μf_e
Stator frequency	$\nu f_e\left(1\pm\frac{1}{\nu}\right)$	$\mu f_e\left(1\pm\frac{1}{\mu}\right)$

Note: The negative sign relates to the forward rotating harmonics, the positive sign relates to the backward rotating harmonics. Clearly, with regard to the fundamental wave only one harmonic (ν=μ=1) should be comprehended. All time harmonics of order μ produce space harmonics with one and the same wavelength. Only they have amplitudes which merit attention.

Example and Analysis

The effects of the described harmonics will be discussed for a particular case. Let the synchronous generator has number of poles $2p=8$ and synchronous speed $n_S=750$ r.p.m. If the number of poles of exciter is $2p_e=16$ the frequency is $f_e=100$ Hz.

Table 2 shows calculated results for the fundamental wave and the harmonics of order 5 and 7.

Table 2

	Rotor frequency Hz	Stator frequency Hz	Number of poles
Fundamental wave	100	0	16
$\nu = 5$	100	600	80
$\nu = 7$	100	600	112
$\mu = 5$	500	600	16
$\mu = 7$	700	600	16

As follows from Table 1 and Table 2, the stator frequency for the pair forward and backward harmonics is equal. The same conclusion could be made for $\nu = \mu$. However, the rotor frequencies and number of poles are different for the two harmonic series.

When the armature winding is designed with number of slots per pole per phase q = 1 for the slot harmonics of first order is obtained:

$$\nu_Z=6q\mp 1=\begin{cases}5\\7\end{cases} \quad (9)$$

This pair of harmonics has winding factor equal to those for the fundamental wave $k_{w\nu}=k_{w1}$. Then from Eq.(5) and Eq.(8) it follows:

$$F_{\nu=5}=F_{\mu=5}$$
$$F_{\nu=7}=F_{\mu=7} \quad (10)$$

The above result shows that the magnitudes of the harmonics with order $\nu = \mu$ are even for the particular case q = 1. The amplitudes may be significant since numbers 5 and 7 are relatively small and windings factor is equal to unity. Similar relationship is available for the harmonics of greater order.

It is interesting to determine the depth of penetration for the eddy currents of frequency 600 Hz if the stator core is made from solid steel. The equivalent depth of penetration is expressed by:

$$\Delta=\frac{1}{\sqrt{\omega\mu_e\sigma}} \quad (11)$$

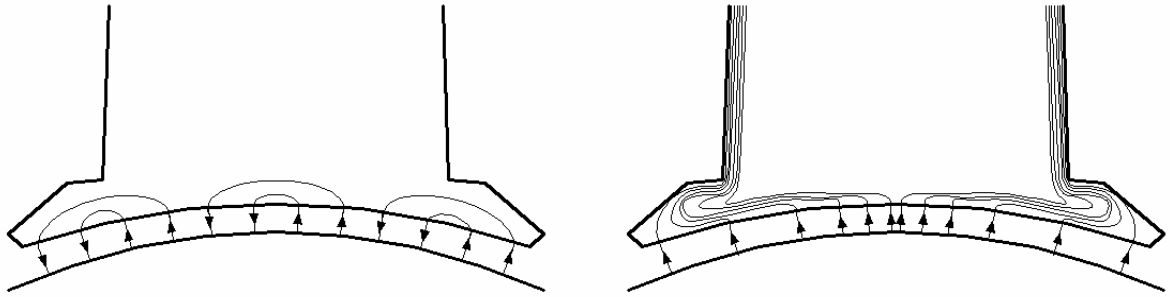

a **Figure 2** **b**

Assume that the permeability of iron is $\mu_e = 1{,}4.10^{-3} H/m$, the conductivity of iron is $\sigma = 8.10^6 S/m$ and the angular frequency is $\omega = 2\pi.600\ s^{-1}$. The depth of penetration calculated by means of Eq.(11) is $\Delta = 0{,}15$ mm. This result (known as skin effect) is important and demonstrates that the high frequency eddy currents and corresponding loss occur in a thin layer on the stator core surface. The eddy current loss will cause a considerable surface heating of the solid core. In a laminated stator the eddy current loss will be much smaller.

Special attention is required to analyze the effect of the number of harmonic poles. Figure 2 gives an idea for distribution of the harmonic fluxes when the depth of penetration is also takes into account. Because of the large number of poles the fluxes of ν-type harmonics could be closed only through the pole face (Fig. 2a). The number of poles of μ-type harmonics is the same as the stator poles. Therefore their fluxes can enter deep in the poles and yoke of the stator (Fig. 2b).

How is it possible to reduce the eddy current loss? In Table 3 four variants of the exciter with various design parameters are compared. The comparison is made under the condition that e.m.f. and current of the armature winding are kept constant. The number of turns per phase is also constant if the diameter of armature remains unchanged.

Table 3

Variant	1	2	3	4
f_e Hz	100	100	150	200
$2p_e$	16	16	24	32
Z	48	96	72	96
q	1	2	1	1
$\beta = y/\tau$	1	0,833	1	1
$f_{\nu=\mu=5}$ Hz	600	600	900	1200
$F_{\nu=5}$ %	100	6,7	66,7	50
$F_{\mu=5}$ %	100	100	66,7	50
$f_{\nu=\mu=7}$ Hz	600	600	900	1200
$F_{\nu=7}$ %	71,4	4,8	47,6	35,7
$F_{\mu=7}$ %	71,4	71,4	47,6	35,7

The parameters of the considered example with 16 poles and q = 1, full-pitch winding, are given in column 1. In this case it is assumed that the amplitudes $F_{\nu=5} = F_{\mu=5}$ are equal to 100 percent.

The following variant (column 2) has the same number of poles and q = 2. The armature winding is double-layered with fractional pitch. The amplitudes of harmonics $\nu = 5$ and $\nu = 7$ are very small, but the magnitudes of harmonics $\mu = 5$ and $\mu = 7$ practically are not reduced.

The last two variants presented in column 3 and column 4 have larger number of poles and higher frequency. The increasing of poles decrease the amplitudes of the harmonics as could be seen from Eq.(5) and Eq.(8). However the harmonic frequency rises. Thus for example, from the data of columns 1 and 4 it follows that when the amplitudes are double reduced the frequency is twice higher.

It can be approximately assumed that the eddy current loss is proportional to the squared product of amplitude and frequency. Then the stray load loss in core is independent on the exciter fundamental frequency as the results in Table 3 show.

The stray load loss can be reduced significant by laminated core. Another way to minimize the harmonic amplitudes is the air gap increase. The high frequency harmonics may be suppressed by means of a damper winding, but in a complicated and costly construction.

Conclusions

The armature m.m.f. wave of a brushless exciter contains two types high harmonics. The harmonics of the one group are typical for each three-phase winding and depend on its structure. The other group of harmonics is due to non-sinusoidal form of the armature current. The two series of harmonics have different features. This conclusion follows from the comparison between the relationships of their amplitudes, number of poles and frequencies.

The distribution of the harmonic fluxes in the stator core is considered. The depth of penetration of the high frequency eddy currents is determined for a stator from solid steel. In this case a significant surface heating because of skin effect is obtained.

The influence of various design parameters on the amplitude and frequency of harmonics is analyzed. Some measures to reduce the stray load loss are discussed.

Here can to ask the question: is it permissible to make the stator poles from solid steel. The fundamental component of the magnetic flux in the stator core is permanent. The production of solid poles cost lower than of laminated poles (a punch is not necessary). However, the high frequency harmonics of armature field cause high temperature of the solid pole surface, which will fault the isolation of the field coils. Undoubtedly a construction with laminated poles should be recommended.

The present investigation may by useful for the solution of critical problems in the design of brushless exciters for synchronous machines.

Appendix

The three-phase armatures current are:

$$i_a = \sqrt{2}I\left[\sin\omega_e t - \frac{1}{5}\sin 5\omega_e t - \frac{1}{7}\sin\omega_e t + ...\right]$$

$$i_b = \sqrt{2}I\left[\sin(\omega_e t - 120) - \frac{1}{5}\sin(5\omega_e t - 5.120)...\right] \quad \text{(A.1)}$$

$$i_c = \sqrt{2}I\left[\sin(\omega_e t - 240) - \frac{1}{5}\sin(5\omega_e t - 5.240)...\right]$$

If θ is space angle in a rotor coordinate system and considering only the fundamental waves, the phase m.m.f. as time and space functions are:

$$F_a(\theta,t) = k.i_a \sin p_e\theta$$
$$F_b(\theta,t) = k.i_b \sin(p_e\theta - 120) \quad \text{(A.2)}$$
$$F_c(\theta,t) = k.i_c \sin(p_e\theta - 240)$$

where

$$k = \frac{2}{\pi}\frac{w.k_{w1}}{p_e} \quad \text{(A.3)}$$

Using the relationship for $\sin\alpha.\sin\beta$ and after transformation of the total m.m.f.

$$F(\theta,t) = F_a(\theta,t) + F_b(\theta,t) + F_c(\theta,t) \quad \text{(A.4)}$$

a series of m.m.f. waves is obtained:

$$\begin{aligned} &F_1\cos(\omega_e t - p_e\theta)\\ &F_5\cos(5\omega_e t + p_e\theta)\\ &F_7\cos(7\omega_e t - p_e\theta)\\ &F_{11}\cos(11\omega_e t + p_e\theta)\\ &..... \end{aligned} \quad \text{(A.5)}$$

The above expressions shown that the m.m.f. harmonics of order μ = 7, 13,… are forward rotating while harmonics of order μ = 5, 11,… are backward rotating.

References

[1] Matsch L., J. D. Morgan. Electromagnetic and Electromechanical Machines. John Wiley & Sons, 1987.

[2] Pisinska C., R. Marvakov. Synchronous Generators for Electrical Plants. Technika, 1987.

[3] Nachev N. et al. Industrial Electronics. Technika, 1988.

Emil Sokolov – *Professor, D.Sc., Department of Electrical Machines, Technical University of Sofia, 8 Kl. Ohridski Str., 1000 Sofia, BULGARIA. e-mail: erso@tu-sofia.bg.*

Static characteristics of brushless switched reluctance motor, calculated with finite element analysis

Dimitar Sotirov, Plamen Rizov and Anton Kalapish

Abstract: *Reserch and comparisons between two brushless switched reluctance motors is made in this article. The comparison is between their static electromagnetic torque, self-inductance and used inverter. 2D model of FEA is used for solution of electromagnetic problem.*

Keywords: *Static characteristics, brushless switched reluctance motor, FEA.*

Introduction

Brushless switched reluctance motors have a comparatively simple design and low price. They have an application in electrical drives with power up to several hundred kW. They enable a reduction of rotor speed. For realization of this type motors can be use a classical designs of synchronous reluctance motors, but they are used very rarely. In brushless switched reluctance motors design with salient-pole rotor and stator most often is used. The number of phases of the stator is three or four. The rotor has four teeth, when the stator has three phases. The rotor has six teeth, when the stator has four phases. This design provides good characteristics of motors with low price. The object of this article is to make a model for calculation of static electromagnetic torque and the self-inductance depending on rotor's position and with reference to the swished on phase through the FEA in consideration of the saturation of the ferromagnetic sections of the magnetic circuit. The model enables an optimization of several proportions of the stator's teeth and the rotor's teeth. Using this model could comparison between the three and four phase's constructions of the motors.

Finite elements model

Numerical solution of the electromagnetic problem with FEA is made by computer package, developed in TU-Sofia. This computer package enables time-stepping solution of the problem [3].

The static electromagnetic torque is solved by Maksuel stress tensor:

$$(1) \quad M_\delta = \frac{l_\delta}{\mu_0} \int_\Gamma r B_n B_\tau d\Gamma$$

The self-inductance L of the switched-on phase is solved by energy into the magnetic circuit.

$$(2) \quad L = \frac{\int_S AJdV}{i^2}$$

Where: J is the current density in the coil and i is the current flowing through the coil

A 2D model of FEA is used. The area of research is located in the active part of the motor and it is a perpendicular to the axis of the rotor. The research implemented for four-phase brushless switched reluctance motor with salient-pole rotor and stator. Each phase winding has 2 series coils. These coils lay over two opposite situated stator poles. The spatial lag between the phases is π/m, where m is number of phases [figure 1].

The rotor has six salient teeth. Firstly we assume that the widths of rotor's and stator's teeth are equal. The arc of stator's teeth is equal π/2m. Stator's winding fill in area between stator's teeth. The stator's coil current density is 7,7A/mm. It creates a magneto motive force 3350 A for working current 18A. Maximum air gap length is $\delta_{\max} = 19$ mm, and minimum air gap length is $\delta_{\min} = 0.36$ mm. The external diameter of the stator is 194mm where a different sections of the magnetic circuit have such a size so that the inductions into them to be equal, when the axis of the stator's and rotor's pole coincide and when the respective stator's phase is excited. The experimental data about such motor are published by J.R. Hendershot [4]. The solution of the problem is made for a full cross-section area. It is taken into consideration the magnetic field doesn't distribute out of stator's package. The calculation starts with stator tooth lying opposite the rotor tooth. The exciters of the magnetic field are represented through the direct current which doesn't change by rotor's rotation. The step of the rotor's rotation is $\alpha=0.18^0$. The electromagnetic torque and self-inductance for every single step is calculated. The calculations are made for the angle of rotor's rotation, corresponding one period of the self-inductance respectively of the torque of the motor. The magnetic induction has value above 2T in some sections of the magnetic circuit mainly into the area of teeth and the parts from then where they overlap. Motor with m=3 and Z_R=4 is analyzed using the same procedure. The external diameter and the length of motor are equal. The sections of the magnetic circuit are calculated on the analogy of the four poles motor.

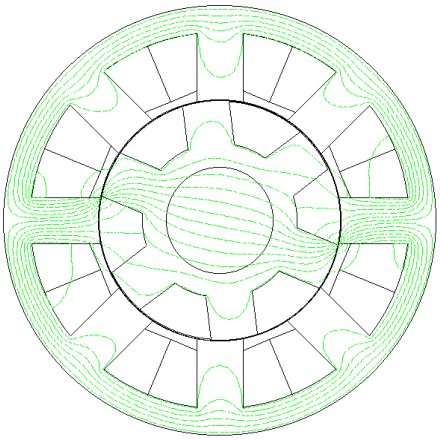

Fig. 1
I=18A $\alpha = 36.9^0$

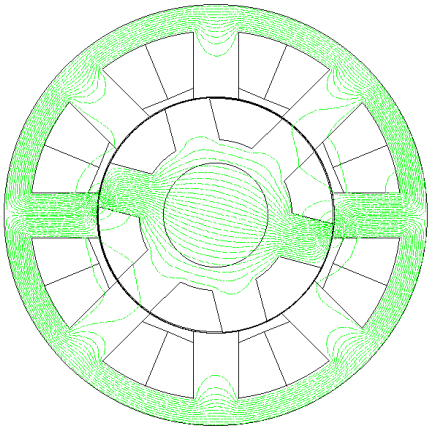

Fig. 2
I=18A $\alpha = 44.46^0$

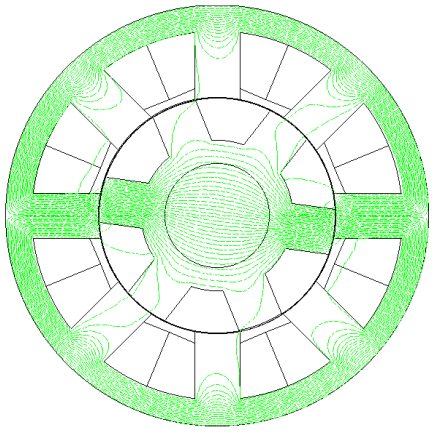

Fig. 3
I=18A $\alpha = 52.02^0$

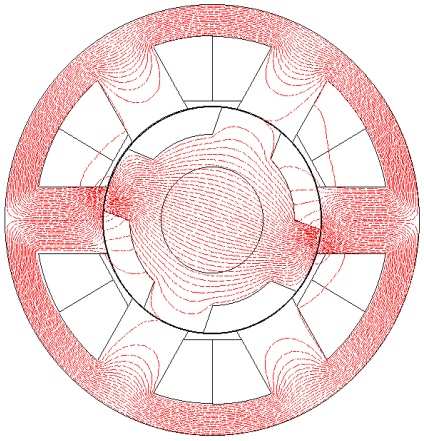

Fig. 4
I=18A $\alpha = 67.86^0$

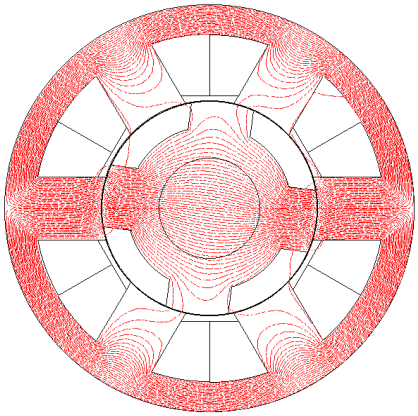

Fig. 5
I=18A $\alpha = 61.2^0$

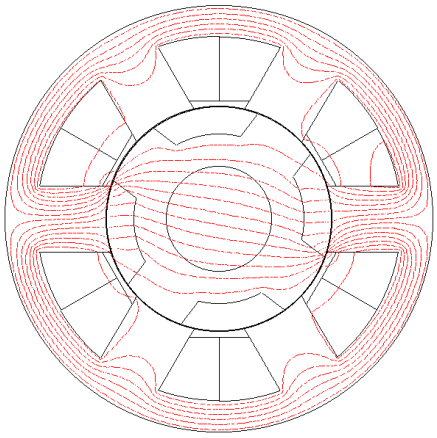

Fig. 6
I=18A $\alpha = 82.98^0$

The widths of the rotor's and stator's tooth are equal. The area of the stator's tooth is $\pi/2m$. The stator's winding fill in area between stator's teeth and the current density is 7,7 A/mm^2. It produces the magneto motive force 3870A for working current 18A. The rise in the magneto motive force, compared the four-pole motor, is due to the enlargement area between two stator's teeth. The magnetic core dimensions are enlarged in order to keep the value of the magnetic flux density. A calculation is made for finding optimum of size, so that the average value of static electromagnetic torque to be maximum for interval of commutation. Maximum air gap length is $\delta_{max} = 15$ mm and minimum air gap length is $\delta_{min} = 0.36$ mm. The magnetic induction has value above 2T into the different sections of the magnetic circuit mainly into the area of teeth and the parts from then where they overlap.

Interval of commutation determination

The interval of commutation α_k is the period during which the stator phase winding producing maximum torque is supplied. Minimum value of this interval is determined with accordance to the requirement for elimination of rotor's position which gives zero torque i.e. $\alpha_{\kappa min}=2\pi/(m.Z_R)$ The position of rotor for the start α_w and the end α_i of the interval of commutation is dependent on requirement the average value of the electromagnetic torque, for this interval, to be maximum. The minimum value of the torque at the beginning of interval must be above nil or given minimum value. The minimum value of the torque at and of interval also must be above nil or given value. We can increase interval of commutation, but electromagnetic torque of the winding must not have negative value. In fig. 11 and fig. 12 are shown interval of commutation $\alpha_{\kappa min}$ for motors with m=4 and m=3 about the curve of electromagnetic torque. For the motor with m=4, $\alpha_{\kappa min4}=15^0$ and for the motor with m=3 $\alpha_{\kappa min3}=30^0$. The flux density plots about three positions of the rotor are shown in figures 1, 2, 3 for the motor with m=4 and in figures 4, 5, 6 for the motor with m=3. The position of the rotor in figures1 and 4 is for the start position of the interval of commutation. The position of the rotor in figures 2 and 5 is for half of the interval of commutation. The position of the rotor in figures 3 and 6 is for the end of the interval of commutation.

Results

In result of the made calculations are shown the curves of the self-inductances L=f (α) of one fase for the two motors for three values of current flowing through the fase (I_{nom}=18A; I=12A; I=6A) with consideration of the saturation of the magnetic circuit. In a fig. 7 are shown curves of the four-fases motor. In a fig. 9 are shown curves of the three-fases motor. For the four-fases motor the maximum values of L is observed for $\alpha=0.18^0$, 59.94^0. The minimum value of L is observe for $\alpha=30.06^0$. They are:

Table.1

I_{nom} = 18 A	L_{max}= 0.109889 H	L_{min}= 0.011216 H
I = 12 A	L_{max}= 0.065866 H	L_{min}= 0.011216 H
I = 6 A	L_{max}= 0.047674 H	L_{min}= 0.011216 H

For the motor with m=3 the maximum values of L is calculated for $\alpha=0.18^0$, 90^0. The minimum value of L is calculated for $\alpha=45^0$. They are

Table.2

I_{nom} = 18 A	L_{max}= 0.175111 H	L_{min}= 0.016607 H
I = 12 A	L_{max}= 0.101128 H	L_{min}= 0.016607 H
I = 6 A	L_{max}= 0.072664 H	L_{min}= 0.016607 H

Inside the zone of the minimum in inductance, the magnetic circuit isn't saturated. For the four-fases motor this zone is $23<\alpha<37$ and for the three-fases motor it is $38<\alpha<52$. For this zone the inductance doesn't depend from current and the position of rotor. From these results we may conclude that in case of forced commutation it is possible to accelerate the current increase at switched-on so that the motor work with desired current value. With proper choice of the switch-on current angle the phase current reaches the value approximately equal to the desired before the rotor position makes the influence of the saturation significant. This gives an opportunity to use L=f(α) curve to determine the current at a given mode of operation in simplified models. Calculation for static electromagnetic torque M_δ at given values of the phase current are made for both motors. The curves of M_δ for one period are given. In fig. 8 are showed the curves of motor with m=4 and in fig. 10 are showed the curves of motor with m=3. For the motor with m=4 the maximum value of M_δ is calculated for angle $\alpha=39.96^0$ and it is:

Table.3

I_{nom} = 18 A	M_δ = 33.07129 N.m
I = 12 A	M_δ = 18.72429 N.m
I = 6 A	M_δ = 5.865085 N.m

For the motor with m=3 the maximum value of M_δ is calculated for angle l=28, 98 and it is:

Table.4

I_{nom} = 18 A	M_δ = 38.35624 N.m
I = 12 A	M_δ = 22.26777 N.m
I = 6 A	M_δ = 7.519559 N.m

For the motor with m=4 the curves of M_δ and L are calculated for angle between 0, 18 to 60,3 which is equal of 335 steps respectively for the motor with m=3 for angle between 0,18 to 90 equal of 500 steps. On the basis of giving curves for M_δ and L we can define optimum interval of commutation as it was shown above.

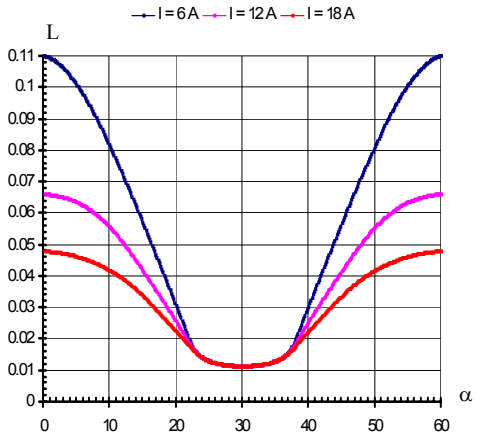

Fig.7

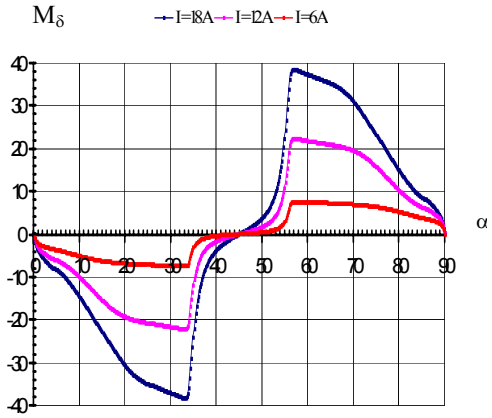

Fig.10

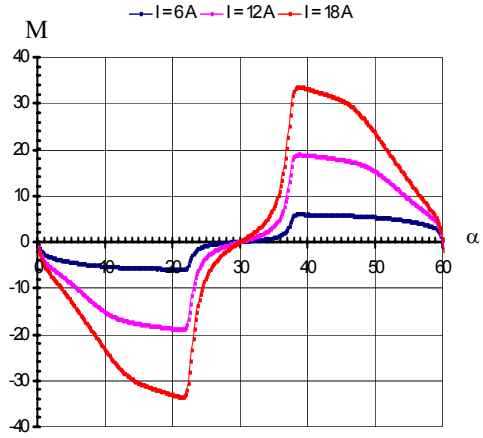

Fig. 8

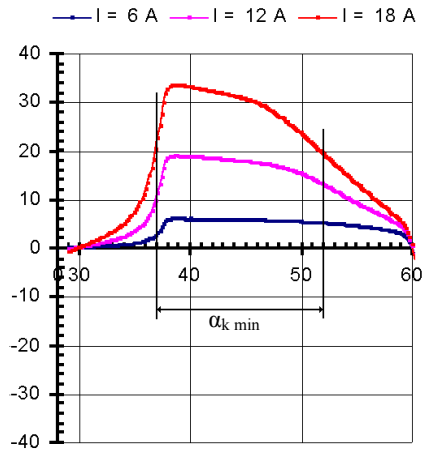

Fig. 11

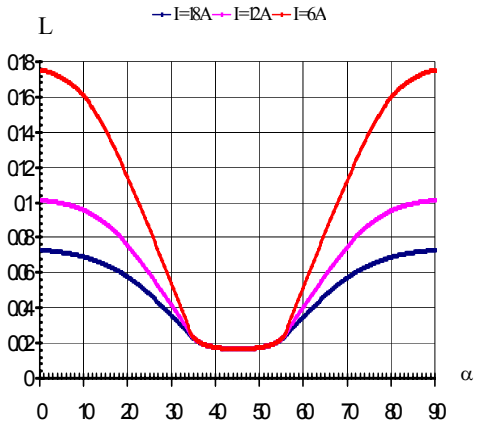

Fig.9

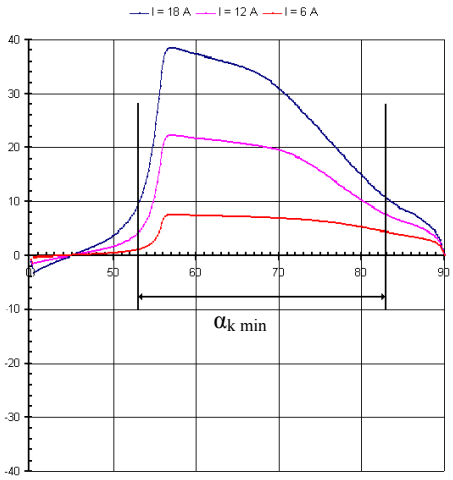

Fig.12

Comparison between the two motors

The volume of the active materials-magnetic steel, windings and constructional materials for the two motors is approximately equal. For equal values of the voltage and the current flowing through the phase we can evaluate:

-average value of electromagnetic torque Mav

-minimum value of the electromagnetic torque for the interval of commutation Mmin

- frequency of the commutation of the current

-the time for what is flowed the current for the interval of computation

-necessary number of elements for the inverter

Calculation of this quantity can be made with next expressions:

-frequency of the computation of the current $f_к=nmZ_к/60$ Hz

-an interval of commutation into the time $t_к = 60\alpha_к/(\pi n)$, sek

-a number of power switch of inverter $N_{inv}=2m$ where n is a rotor speed min-1.

The average value of M_δ is calculated for minimum interval $\alpha_{кmin}$ of commutation, defined above. The values for two motors, with nominal speed $n_{nom}=1800$ min^{-1} are:

Table.5

m	$f_к$	$t_к$	M_{av}	M_{min}	N_{inv}
number	Hz	ms	Nm	Nm	брой
4	720	1.4	28.8	20	8
3	360	2.8	27.35	10	6

Conclusions

From the results we can made the following conclusions:

1. The motor with m=4 has a bigger value of the average electromagnetic torque M_δ and a bigger value of minimum electromagnetic torque Mmin

2. The motor with m=4 has twice bigger frequency of commutation of the current and respectively twice smaller time for commutation of the current into the fase from motor with m=3

3. The number of the power switches of the inverter of the motor with m=4 are 8, while for the motor with m=3 they are 6.

From the making comparisons follows that:

-the motor with m=4 has priority for magnitude of Mav and Mmin, but it is with most complex and most expensive inverter. In the same time we may expect problems with commutation of current through the fase, because the rice time and fall time are too small.

The final conclusion about the priority of one of the motors could be made after analysis of dynamic behavior and optimization of the process of commutation.

References

[1] Takashi Kenjo, Akira Sugawara. Stepping Motors and their Microprocessor Controls. CLARENDON PRESS, OXFORD, 1995

[2] Динов, В.Р, Д.К.Сотиров. Безконтактни двигатели за постоянен ток, София, Техника 1981

[3] Ризов, П.М, Дисертационен труд ‘Изследване на установени режими на асинхронни двигатели с метода на крайните елементи’. София 1998

[4] James R. Hendershot, Jr. AC, Brushless Switched Reluctance Motor Comparison. Magna Physics Corporation, Hillsboro, OH 45133.

CAD System for Design and Teaching Distribution Transformers

Radoslav Spasov and George Todorov

Abstract: *In the paper the common structure of CAD system for distribution transformer's design is described. Student's teaching version is developed on the base of the design process algorithm. The teaching version contains only the modules that are necessary to perform the design and generate a solution, without optimization the dimensions and characteristics, but requires the student to define basic values and control the flow of the design process. Main goal of this teaching CAD system is to make students acquire how the transformer's characteristics depend on value's variation of the dimensions and electromagnetic quantities.*

Keywords: *distribution transformer, design, CAD system, teaching.*

Introduction

Transformer's design is a multivariable problem that implies knowledge in a wide range of fields – general theory of electrical machines; magnetic, insulation and construction material's characteristics; analysis and optimization methods; work with database; engineering skills. The realization of the design process should take into consideration the customer's and standard's requirements, production traditions and technological equipment of the producer and possibilities for implementation of modern design methods, using the power of today's computer technology.

Modern transformer production plants utilize powerful CAD systems that incorporate all components of transformer's life cycle. All CAD systems have been developed as interactive and the result of the design process depends on designer's skills and knowledge.

The aim of the present paper is to present an adaptation of a simple CAD system consisting of relatively small number of modules for implementation in education. The accent is to provide students with interactive learning framework that promotes experimentation with the fundamental laws and design principles and makes them to decide how to rule the design process.

Transformer Design Systems

The complete CAD system for distribution transformer's design contains big number of modules and provide with: development of design solutions; electromagnetic calculations; magnetic field analysis (2D and 3D); mechanical stress analysis; thermal analysis; cooling system analysis; link to CAM; PDM [5]. Implementation of such kind of CAD system requires high level of automation of the design and production cycles, it is expensive and only large producers could afford to buy. It is known that smaller producers do not have resources to automate all production process (in the transformer plants it usually is not profitable) and they use simplified or so-called hybrid CAD system [7]. The block diagram of such system is shown in Fig.1.

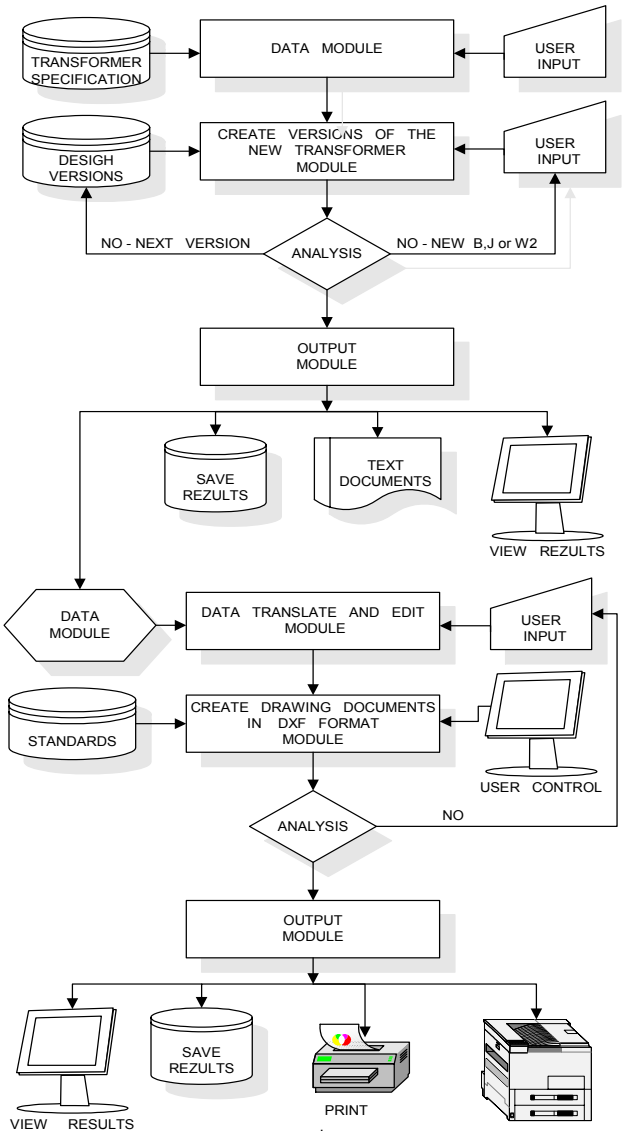

Fig.1. Block diagram of hybrid CAD system

Basic modules of the system are:

- DATA module – contains two groups of data. The first group is formed from the user-defined requirements to the transformer's characteristics, for instance: rated power, rated voltages, no-load losses, load losses etc. The second group contains database with

standard specifications for requirements that have not been defined by the customer, but the design engineer should take into consideration [3,8,9,10].

- CREATE VERSION OF THE NEW TRANSFORMER MODULE – calculation of the transformer's main dimensions, using design algorithms under user's control.
- ANALYSIS - electromagnetic, thermal and mechanical calculations have been performed in iteration cycle with variation of the magnetic flux density ***B***, current density ***J*** and secondary winding turns per volt ***W2***. Great number of design version (up to 1000) with different proportion between the dimensions is generated for each combination of the above values. The lower initial values of the magnetic flux density ***B*** and current density ***J*** had been chosen, the greater is number of the solutions, generated from the program module as a feasible design. This is an indication that it is possible to increase the values of ***B*** and ***J*** in order to reduce the transformer's dimensions.

The total owing cost (TOC) is commonly used as objective function for the analysis procedure. The TOC includes cost of acquisition, cost of core losses and cost of load losses over the transformer's life [4,6,8]. As a result of the analysis and comparison of all generated versions the program gives the best one or user's determined number of design solutions, put in descending order in accordance to the objective function.

- OUTPUT – gives an opportunity to view results for the optimal solution, save, print, develop text documents (technological and economic) and prepare data for the drawing phase of the design.
- DATA TRANSLATE AND EDIT MODULE – compiles the data from OUTPUT module under designer's control for basic construction.
- CREATE DRAWING DOCUMENTATION – using algorithmic model of the basic constructions and database for materials, standards, co-operating components and technological constraints creates all drawings, required to produce the transformer.
- ANALYSIS – makes mechanical and thermal analysis of the construction.
- OUTPUT - view results for the full set of drawings, save, print, develop digital documents for CAM.

Teaching System

It is known that the characteristics of electromagnetic phenomena depend on the parameters defining the construction of the transformer, the dimensions and the characteristics of used materials. The mathematical equations that are used to represent the phenomena are abstract and are hard to be understood by the students. The computer application in teaching could facilitate the understanding of scientific and technical concepts and the interaction between the complex studied phenomena and the real device. Implementation of teaching CAD system gives the students an interactive environment where they can test their understanding of a concept, make decisions for choosing dimensions and values of electromagnetic quantities and comprehend theirs relevance to the specific application.

The student teaching version of distribution transformer's CAD system has been developed (Fig.2) for one certain type of transformers – the most commonly used three-phase, core type, oil-immersed with conservator, self cooled transformer with multi-layer cylindrical primary winding and two-layer cylindrical strip-conductor secondary winding. The student's assignment is to develop a single design solution for the distribution transformer, applying their knowledge in basic principles of transformer's operation. They should calculate and give the initial values for the magnetic core flux density ***B,*** current density ***J*** and secondary winding turns per volt ***W2***. These values present the STUDENT INPUT.

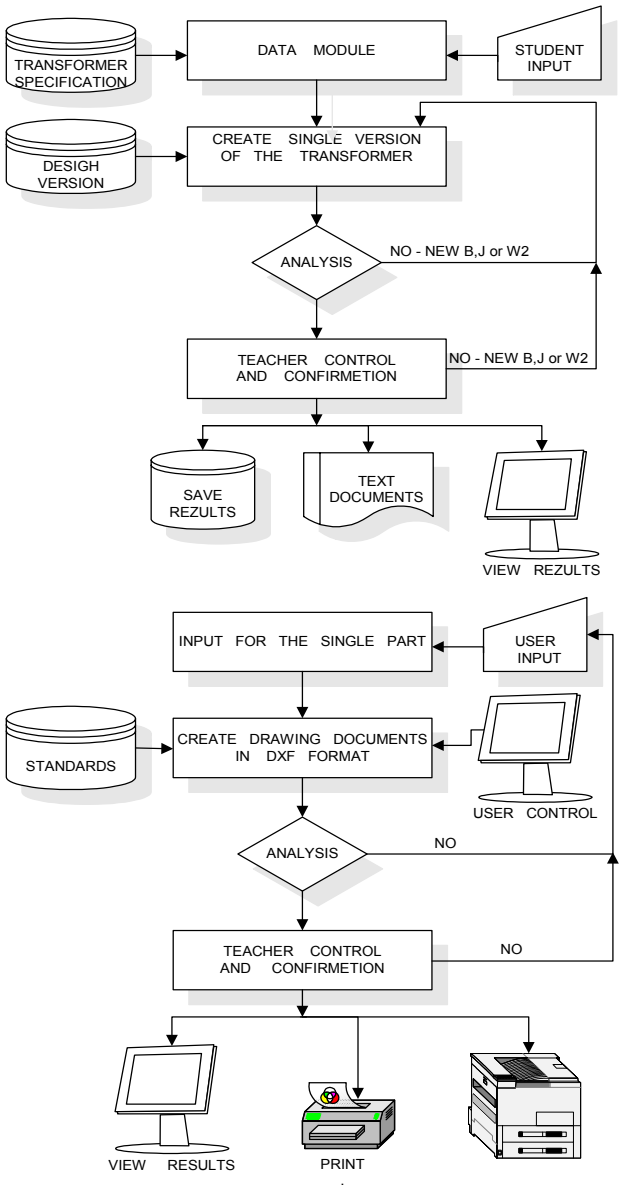

Fig.2. Block diagram of teaching version of the CAD system

The next module performs electromagnetic calculations with the student's data and gives the results. The computer program does not make evaluation or comparison of the results.

In the ANALYSIS module the student should review the results and make decision whether they give good solution or it is necessary to change the values of magnetic core flux density ***B,*** current density ***J*** and secondary winding turns per volt ***W2*** and how to make the changes. Then repeat electromagnetic calculations until the desired solution has been reached, according to the student's opinion.

TEACHER CONTROL – this is the point where the teacher compares the student's solution with an optimal one, developed with the real version of the CAD system. In case a good approximation has been obtained he approves the work at the stage of electromagnetic design and gives permission to continue with the next modules – save and print the results.

In case the student's solution does not comply with the assignment's requirements or big discrepancy with the optimal solutions has been obtained, the teacher discusses the reasons for the failure with the student and how to improve the results. The procedure has to be repeated until feasible design solution is obtained.

The second stage of the teaching CAD system is with separate input. The assignment for each student is to draw a drawing for a single transformer's part using general-purpose CAD software (for instance AutoCAD). In the end of this stage the transformer should be assembled from the separate parts, developed by the group of students. The geometric design is an iterative procedure and gives the students experience in team-work as each one should comply with the relevance to the results of the others.

The INPUT FOR THE SINGLE PART module contains the main dimensions of the transformer, which parts have to be drawn by the students. These dimensions should be taken into considerations as constraints during the geometric design of each part.

ANALYSIS – verification of dimensions and its deviations in order to enable the assemblage of the transformer.

TEACHER CONTROL – the teacher provides general supervision and oversight for all single drawings. The teacher also gives advices and rules the iterative procedure until the desired assembly is obtained.

Conclusion

Teaching CAD system for implementations in electrical machines design teaching is developed. It gives the students an opportunity to improve and test their understanding in the transformer's basic concept, usage of technical and economic database and gets them acquaint with the connection between theory and practice. The usage of teaching CAD system makes the students acquire knowledge and skills in production process of a real technological device and gives an experience in team-work.

References

[1] Bodger, P.S., Liew, M.C., and Johnstone, P.T., "A comparison of conventional and reverse transformer design", AUPEC'2000, Brisbane, Sept 2000, pp. 80-85.

[2] Chan J. H, A. Vladimirescu, X.-C. Gao, P. Liebmann, J. Valainis "Non linear transformer model for circuit simulation" IEEE Transactions on computer-aided design, vol. 10, no. 4, April 1991, pp. 476-482.

[3] Distribution Transformers: Technical Support Document. Available online: www.eren.doe.gov/buildings/codes_standards/applbrf/dist_transformer.html. Washington, D.C.: U.S. Department of Energy

[4] Distribution Transformer Rulemaking, Life Cycle Cost Analysis, Report to U.S. Department of Energy Office of Building Technology, State, and Community Programs.

[5] Groover M. P., E. Zimmers, Cad/Cam computer aided design and manufacturing, Prentice-Hall, New Jersey, 1984.

[6] Lokhanin A.K., Morozova T.I., Shifrin L.N., Savchenko A.L, Technical and economical efficiency of reducing the insulation level of power transformers and service experience concerned. Report 33-105, CIGRE, 2000.

[7] Spasov, R.L. CAD system for distribution transformers. Ph.D. dissertation, Technical University of Sofia, 2003.

[8] IEC standard 354: Loading guide for oil-immersed power transformers. IEC 1991. IEEE Guide for Loading Mineral-Oil-Immersed Transformers. IEEE Std C57.91-1995.

[9] ANSI C57.12.22 Requirements for Pad-Mounted, Compartmental-Type, Self-Cooled Three-Phase Distribution Transformers with High Voltage Bushings, 2500 kVA and Smaller: High Voltage, 34,500 GrdY/19,920 V and Below; Low Voltage, 480 V and Below.

[10] NEMA Standard No. TR 1 Transformers, Regulators and Reactors, 2000.

Radoslav Spasov *– Assistant Professor, Dr., Faculty of Electrical Engineering, Technical University of Sofia, 8 Kl. Ohridski Str., 1000 Sofia, BULGARIA. e-mail: rls@tu-sofia.bg.*

George Todorov *– Associate Professor, Dr., Faculty of Electrical Engineering, Technical University of Sofia, 8 Kl. Ohridski Str., 1000 Sofia, BULGARIA. e-mail: gtto@tu-sofia.bg.*

About Designing an Average Model of RL Loaded Single-Phased Transformers in Periodical ac-Switching Regime

Cristian-George Constantinescu, Constantin Strîmbu and **Mihai Miron**

Abstract: *This paper is proposing a method to find an average value of single-phased transformers magnetic core permeability, the transformer being supplying a current rectifier. This value may be used to study the RL loaded single-phased transformer in ac-switching mode. The paper consists in the following steps:*

- *Finding the magnetic core permeability average value. To complete this task it is performed first a study of the above-mentioned transformer, considering a non-linear magnetization curve (no hysteresis) [1] ,[2]. It results in this way a magnetic permeability average value, corresponding to each load circuit and firing angle.*
- *The periodical ac-switching study of a transformer working in the same conditions concerning the load circuit and firing angle, but characterized by a linear magnetization curve with the slope given by the appropriate magnetic permeability average value. The algorithms and mathematical methods used in this case are presented in [3] and [4].*
- *Comparisons between theoretical and experimental results.*

Keywords: *transformer, average model, ac-switching, magnetic permeability*

Magnetic permeability average value determination

This paper is presenting a study of a RL loaded transformer in ac-switching mode, assuming a constant magnetic permeability, depending on switch firing angle, α_0, and load phase shift, $\varphi = a\tan\left(\frac{\omega L}{R}\right)$.

The circuit (using a thyristor as main switch, V) are presented in fig.1 and 2.

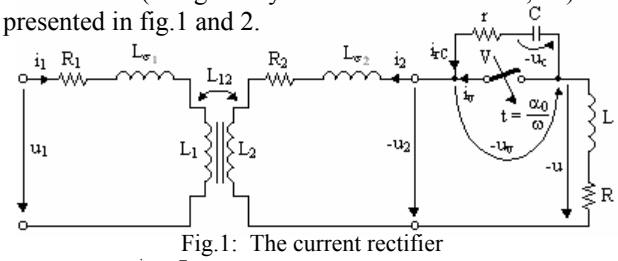

Fig.1: The current rectifier

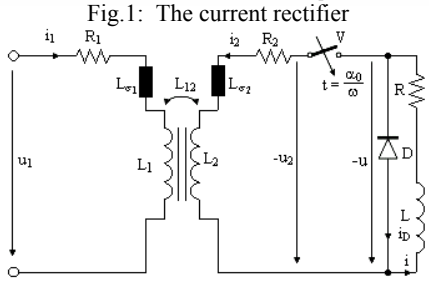

Fig.2: The current rectifier, leakage diode provided

To make clearer this paper novelty, a short review of approaching this theme (the RL loaded transformer periodical ac-switching mode) in other two ones will be inserted.

In [3] and [4] it was considering a transformer having a linear magnetization curve B(H) (linear transformer), assuming a constant magnetic core permeability, $\mu = \frac{dB}{dH}$, determined using the fundamental magnetization curve linear zone – fig 3.

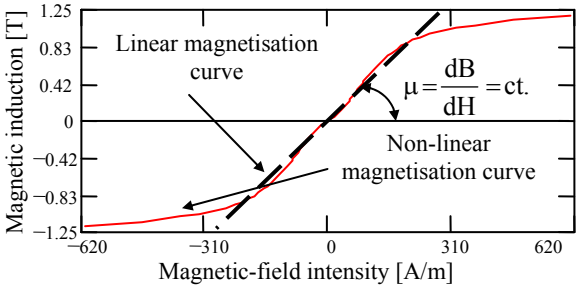

Fig. 3 Fundamental magnetisation curve B(H) (details)

As a consequence, the transformer inductances (L_1, L_2, L_{12}) are constant, being given by (1):

$$\begin{cases} L_1 = L_{\sigma 1} + \dfrac{\mu S_{Fe} w_1^2}{l_{mag}}; L_2 = L_{\sigma 2} + \dfrac{\mu S_{Fe} w_2^2}{l_{mag}} \\ L_{12} = \dfrac{\mu S_{Fe} w_1 w_2}{l_{mag}} \end{cases} \quad (1)$$

In [1] and [2] it was considering a transformer having a non-linear magnetization curve B(H) with no histeresis cycle (non-linear transformer). The experimentally determined fundamental magnetization curve, fig. 3, bases this study. The magnetization curve was considered as a piecewise-linear one. So, each piecewise-linearised curve line is characterized by a constant value of the magnetic permeability, the mathematical approaching in this case becoming a sequence of linear ones, like presented in [3] and [4]. The transformer inductances are given by (1), where the magnetic permeability, μ, is corresponding to each line of the magnetization curve.

In steady state, the point on the magnetization curve (corresponding to transformer operation) will trace the same portion (lines) in an ac cycle, as shown in fig.4, were two examples of magnetic permeability variation along an ac duty cycle are represented. It is coming out in this way that transformer core magnetic permeability becomes a periodical function.

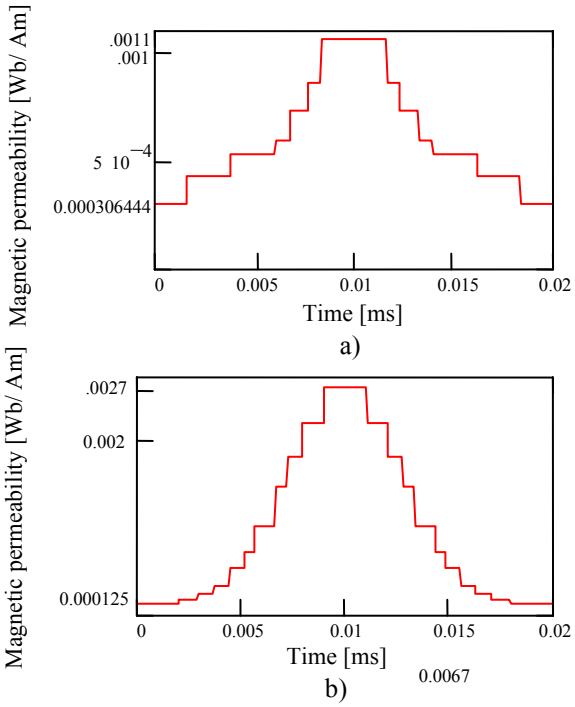

Fig. 4 Magnetic permeability variation along a period resulted by modelling the non-linear transformer
a) For the rectifier without leakage diode
b) For the rectifier with leakage diode

In [5] is presented a trigonometric regression algorithm, which fits an approximate harmonic Fourier series to a tabled periodical signal. The magnetic permeability average value is the dc component returned by this algorithm.

The studies [1], …, [4] were performed considering several firing angles, α_0, and load phase shifts, φ, covering a representative area of the possible domains: $0^0 \le \alpha_0 \le 180^0$; $0^0 < \varphi < 90^0$.

It was determined in this way a collection (a vector) of magnetic permeability average values, each one corresponding to a point $(\varphi ; \alpha_0)$.

Average magnetic permeability analysis

The goal is to find an approximating function, $\mu(\varphi, \alpha_0)$, for the average magnetic permeability. The method used to determine this (multiple regression) function is in detail presented in [5].

The function is of type:

$$\mu(\varphi, \alpha_0) = \sum_{i=0}^{n} \left(\sum_{j=0}^{p} b_{ij} \varphi^j \right) \alpha_0^i \ ; \ n = 5, p = 4 \qquad (2)$$

Fig. 5 and 6 are showing comparisons between the average magnetic permeability returned by the trigonometric regression algorithm (from the magnetization curve) and the approximate ones (level curves on the surface (2), corresponding to φ = constant), respectively the error level introduced by the regression function (2). The error level is at least acceptable.

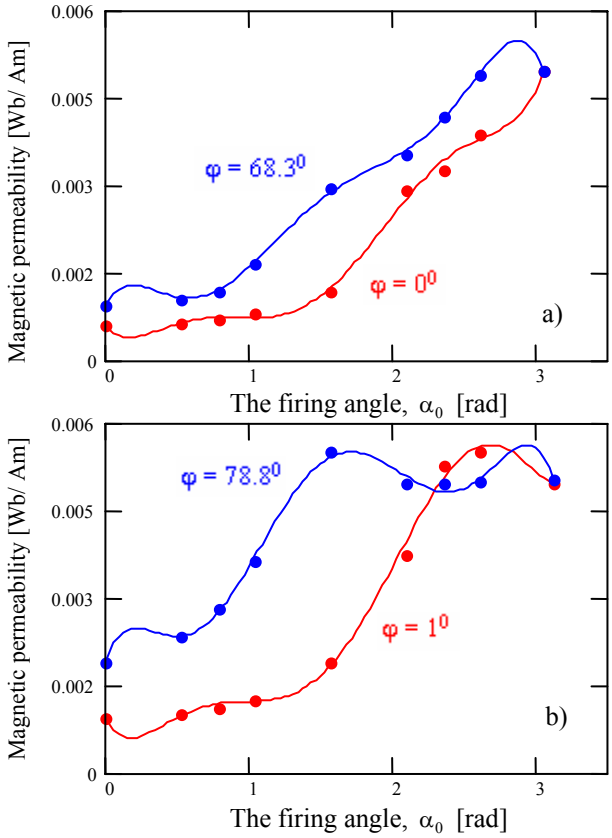

Fig. 5 Magnetic permeability variations for φ = constant
a) For the rectifier without leakage diode
b) For the rectifier with leakage diode

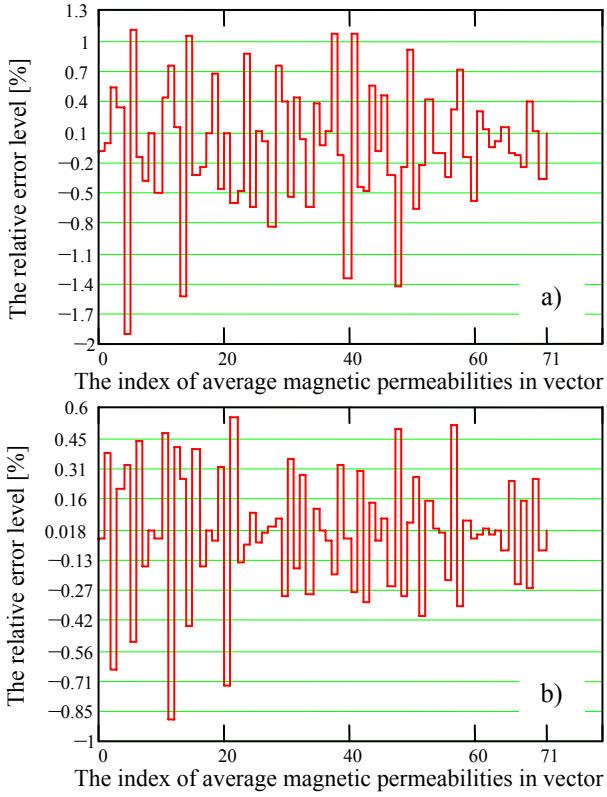

Fig. 6 The relative error introduced by the regression function
a) For the rectifier without leakage diode
b) For the rectifier with leakage diode

Owing to the low error level provided by the approximating function (2) and taking into account that transformers are likely from the magnetic quantities point of view and the representative sample of the possible domains considered for the firing angles and load phase shifts, the authors consider the above-mentioned function a suitable relation to determine the magnetic permeability of the discussed transformers magnetic core.

The steady-state regime waveforms

It is proposing as transformer (working in discussed conditions) average model a linear one, characterized by the core magnetic permeability given by (2). For such transformers, the algorithms presented in [3] and [4] (MathCAD implemented) were used.

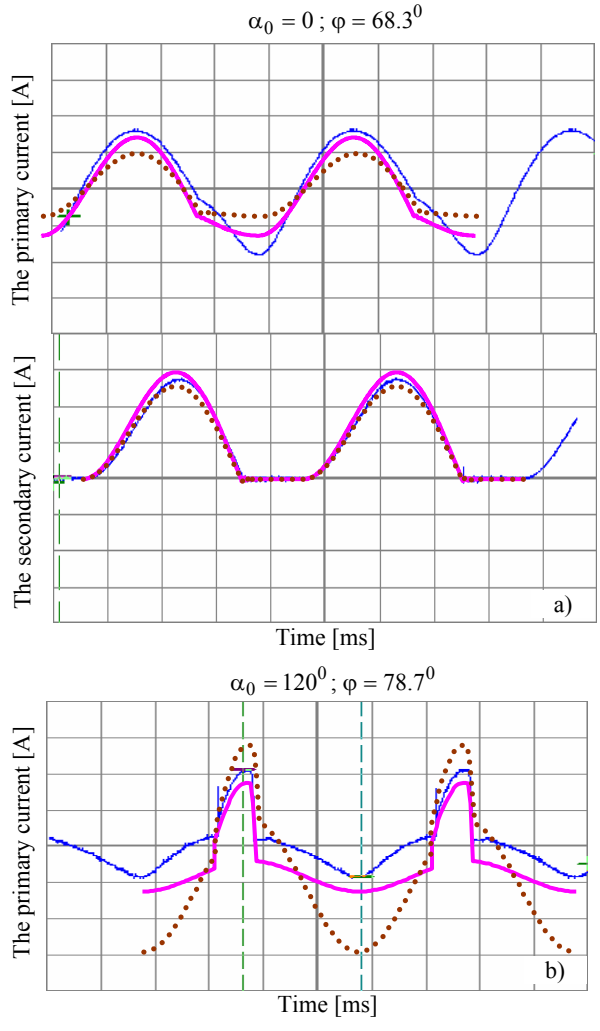

Fig. 7 Worst approaches
a) For the rectifier without leakage diode
b) For the rectifier with leakage diode
Time scale is 5ms /division, amplitudes are 2A/ division and 0.5 A/div, respectively.

The theoretical results were compared with the ones returned by the linear transformer characterized by the magnetic permeability computed like in fig. 3 and with experimental tests. This is necessary for evidencing the linear model improvement provided by the average model.
Fig. 7 and 8 are showing the worst and the best approaching between theoretical and experimentally determined waveforms, respectively.

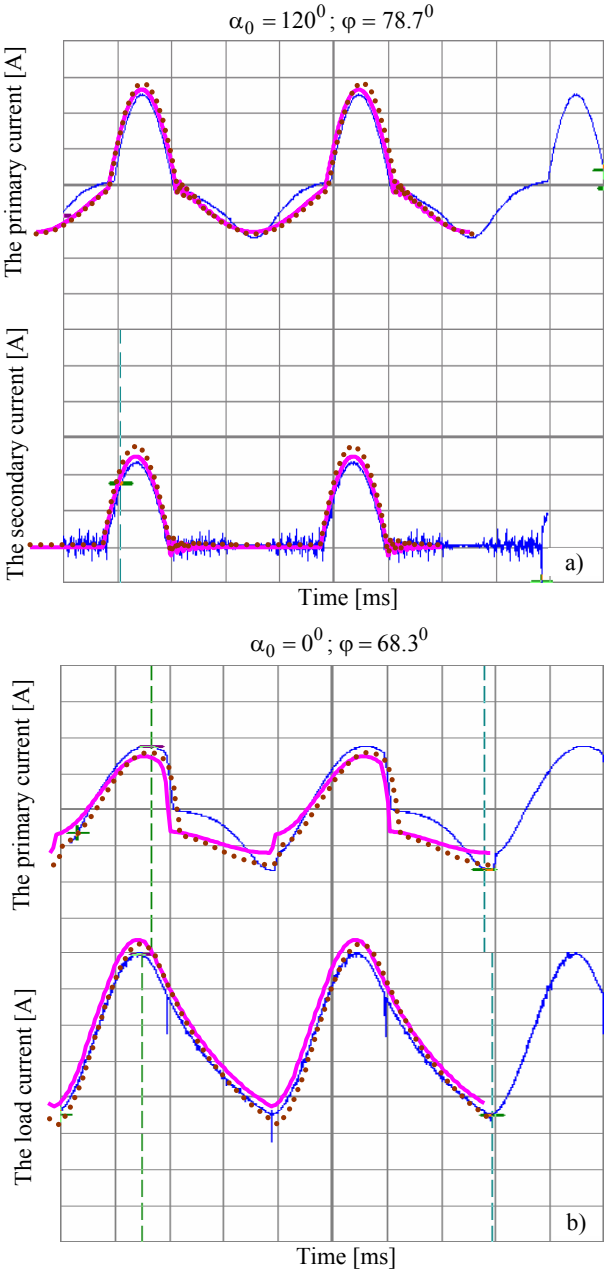

Fig. 8 Best approaches
a) For the rectifier without leakage diode
b) For the rectifier with leakage diode
Time scale is 5ms /division, amplitudes are 0.5 A/ division and 2 A/div respectively.

A certain improvement provided by the average model can be observed. Since the error level of the theoretical vs. experimentally determined waveforms is (in the worst case) between 15 and 50%, the average model decreased it at values between 7 and 20%.

Conclusions

This paper is focused in designing a linear model of the transformer in periodical ac switching mode in concordance with the working conditions (load circuit and firing angle), based on magnetic permeability average value, proposing a function that compute it. So, the transformer average model is a linear one, characterized by the magnetic permeability returned by the above-mentioned function. The advantage will be a computing time decreasing when modeling, simulating or designing such transformers. Because the error level is not entirely satisfactory, this goal was not yet completed, this approach being only a first step. However, it seems to be hopeful, owing to the certain improvement of the error level returned by the linear transformer, as fig. 7 and 8 are showing.

The following conclusions can be derived:

- Average magnetic permeability determination needs to study the non-linear transformer, several magnetization piecewise-linearised curve lines being stepped along an ac cycle;
- The average magnetic permeability depends on load phase shift, φ, and firing angle, α_0;
- Using an approximating function for the magnetic permeability, of type $\mu_{med} = \mu(\varphi, \alpha_0)$, introduces an acceptable relative error level comparing to its value obtained from the magnetization curve;
- Because all the transformers having the same ferromagnetic material in core structure are stepping approximately the same magnetization curve zone, (2) is proposed to be used as a general relation to determine the average model of transformers working in conditions like the ones discussed in this paper. This statement has to be validated with more experimental measurements.
- The transformer average model provides certain waveforms improvements comparing to its linear model, but the errors are still high. This is a reason to go on with the research work, either in transformer study (considering a hysteresis type magnetization curve and the power losses) or in average magnetic permeability determination.

List of used symbols:

- α_0: Turn-on angle;
- L_1: Primary winding self inductance;
- L_2: Secondary winding self inductance;
- L_{12}: Mutual inductance;
- $L_{\sigma 1}$: Primary winding leakage inductance;
- $L_{\sigma 2}$: Secondary winding leakage inductance;
- l_{mag}: Magnetic circuit average length;
- S_{Fe}: Magnetic flux crossing area surface;
- w_1: Primary winding number of turns;
- w_2: Secondary winding number of turns;

References

[1] CONSTANTINESCU, C.G.; STRÎMBU, C.; MATLAC, I.; MIRON, L: *The periodical ac-switching mode of the non-linear transformer supplying a leading load*. 7th International Conference of Applied and Theoretical Electricity ICATE 2004, Băile Herculane, October 14 –15, 2004, pag 154-159, ISBN 973-8043-554-4;

[2] CONSTANTINESCU, C.G.; STRÎMBU, C.: *A Periodical ac-Switching Mode Study of the Non Linear Single-Phased Transformer Supplying a Leading Load With Leakage Diode*. A XIX–a Sesiune de Comunicări Ştiinţifice cu participare internaţională "NAV-MAR-EDU 2005", 02-04 iunie 2005, secţiunea IV, pp 123- 130, ISBN 973-8303-54-0.

[3] CONSTANTINESCU, C.G.; PEARSICĂ, M.; MIRON, L.: *Periodical ac-switching study of the transformer supplying a leading load*. The 35th International Symposium of the Military Equipment and Technologies Research Agency, Bucharest, 27 – 28 May 2004, pp 229-234, ISBN 973-0-03501-6.

[4] CONSTANTINESCU, C.G.: *Comutaţia periodică a unui transformator liniar pe o sarcină inductivă cu diodă de nul*. Sesiunea Naţională de Comunicări Ştiinţifice, Academia Forţelor Aeriene "Henri Coandă", Braşov, 26 – 27 noiembrie 2004, pp 39-48, ISSN 1453-0139;

[5] CONSTANTINESCU, G.C.; MATLAC, I.; STRÎMBU, C.; IULIAN, L.: *Periodical ac-switching study of the transformer*. „SPEEDAM 2004", Symposium on Power Electronics, Electrical Drives, Automation & Motion, Capri (Italy), June 16 – 18, 2004, pp 293-298, ISBN 88-89389-00-1.

Cristian GeorgeConstantinescu – *Lecturer, Dr., "Henri Coandă" Air Force Academy of Brasov, 160 Mihai Viteazu steet, Brasov ROMANIA*
e-mail: ccg_cristi@yahoo.com
Constantin Strimbu – *Lecturer, Dr., "Henri Coandă" Air Force Academy of Brasov, 160 Mihai Viteazu street, Brasov ROMANIA*
e-mail: strimbu_c@yahoo.com
Mihai Miron – *Lecturer, "Henri Coandă" Air Force Academy of Brasov, 160 Mihai Viteazu street, Brasov ROMANIA*

A Comparative Study (Using Several Models) of the RC Loaded, Single Phased Transformer in Periodical ac Switching Mode

Constantin Strîmbu and **Cristian-George Constantinescu**

Abstract: *This is a synthetic paper, presenting the periodical switching of a transformer with RC parallel, working in the steady state. The operation of the transformer is studied using its following models: the T equivalent diagram, the linear magnetization curve and the non-linear magnetization curve (no hysteresis). In the paper are presented the resulted theoretical waveforms, compared with the experimental ones. The study was performed for several (capacitive) load circuits and turn-on angles. The mathematical support was MathCAD PLUS 6.0.*

Keywords: *transformer, numerical methods*

Introduction

The circuit (using a thyristor as switch) is presented in fig.1.

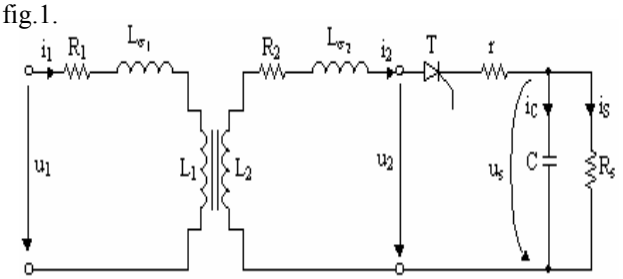

Fig.1. The voltage rectifier

In this study a comparative presentation of the circuit steady state waveforms (obtained using several transformer models) is performed. Experimental and theoretical waveforms were subjects of the comparisons. The models are the following:

- the T series equivalent diagram [1];
- the linear transformer (i.e. the core is characterized by a linear magnetization curve) [2];
- transformer with a core characterized by a non-linear magnetization curve, without hysteresis cycle [3];

The method used in [1], [2] and [3] consists in: writing the circuit equations, according to each working regime of the switch (On or Off);

- writing and solving the corresponding operational equations;
- determination of the time (original) expressions, corresponding to the operational ones.

The quantities above-mentioned are characterized by the following initial conditions:

- α_p: natural turn-on angle (the SCR voltage becomes positive);
- α_0 - SCR turn-on (firing) angle;
- β: turn-off angle (the SCR current is zero crossing); $I_{S\alpha p}$: load current in the α_p moment;
- $I_{S\alpha 0}$: primary current in the turn-on moment;
- $I_{S\beta}$: load current in the diode turn-off moment;

Mathematical determination of α_p and β impose to solve transcendental equations. For this reason numerical methods were used. The resulted algorithms were implemented as MathCAD functions. When the difference between two initial conditions consecutive values is less than the imposed accuracy, ε, the circuit is considered to be in the steady state regime.

The studies were performed in the following conditions:

- the resistors, inductivities and capacitors are characterized by linear and ideal characteristics;
- the semiconductor elements are ideal;
- the bias voltage is sinusoidal and no reactance (infinite power);
- the transformer is non-saturated (the work empty of the transformer is non-saturated).

The quantities characterizing the transformer models *(resistors, inductivities, number of turns, geometrical dimensions, ...) were previously experimentally determined, and the values of the load circuit (RC) and the SCR firing angles that are the input data for the study are the same with the ones used in the measuring circuits*.

Theoretical and experimental results and comparisons

In this section the most important studied quantities. All of them are determined for the three transformer models and will be inserted accompanied by their experimental values.

Angles (α_p and β)

The three theoretical models provided very low error levels, comparing to their experimental values.

- The α_p (β) variation, as a function of turn-on angle (α_0) and load (R_S) (also confirmed experimentally) are the following:
- The α_p (β) angle is an increasing (decreasing) function of the load, for the same value of the turn-on angle;

- The α_p (β) angle is a decreasing (increasing) function of the turn-on angle, for the same value of the load.
- A SCR type switch can be either a thyristor or a diode. Both cases were studied, providing the following results, in concordance with the experimental ones: $\begin{cases} \beta_{Thyristor} > \beta_{Diode} \\ \alpha_{p_{Thyristor}} < \alpha_{p_{Diode}} \end{cases}$.
- Taking in account that the circuit operates only respecting the constraint $\alpha_{p_{Thyristor}} < \alpha_0$, the firing angle setting is the result of the diode case, imposing a stronger constraint $\alpha_{p_{Diode}} < \alpha_0$. Results that it is necessary to find first the $\alpha_{p_{Diode}}$ value, so diode is not the thyristor particularly case $\alpha_0 = 0$.

The primary current

Theoretical waveforms presenting the primary current corresponding to the three transformer models, function of firing angle and load, are shown in figures 2, 3 and 4.

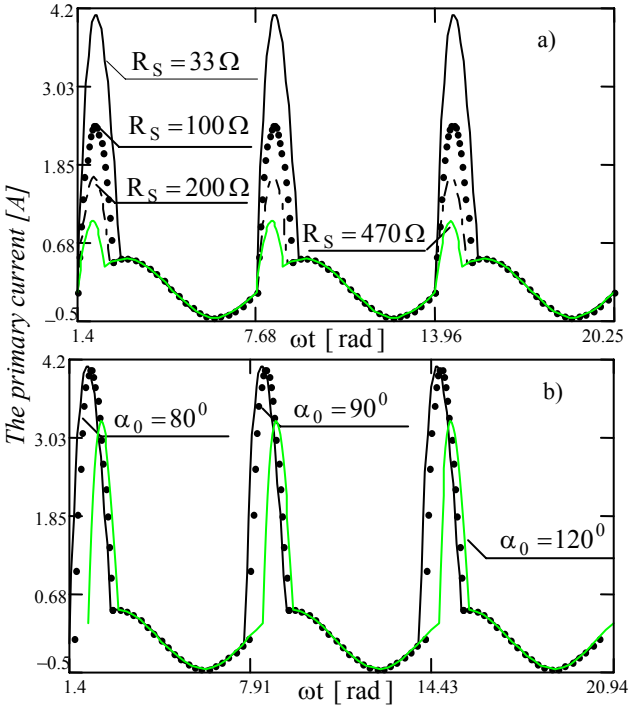

Fig 2. Variation of the primary current, i_1, resulted by modelling the transformer with the T series diagram, a) $i_1 = f(\omega t)\big|_{R;\alpha_0=\frac{4\pi}{9}}$, b) $i_1 = f(\omega t)\big|_{\alpha_0;R=33\,\Omega}$

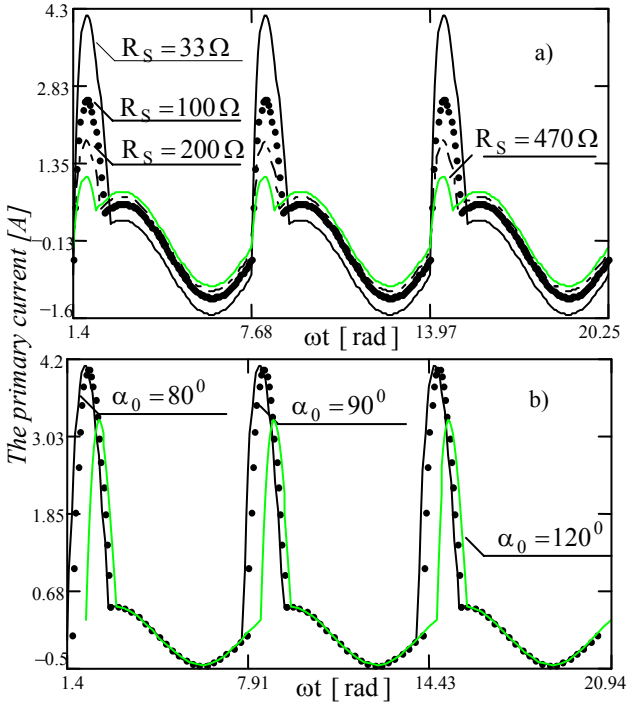

Fig. 3 Variation of the primary current, i_1, resulted by modelling the transformer with the linear model a) $i_1 = f(\omega t)\big|_{R;\alpha_0=\frac{4\pi}{9}}$, b) $i_1 = f(\omega t)\big|_{\alpha_0;R=33\,\Omega}$

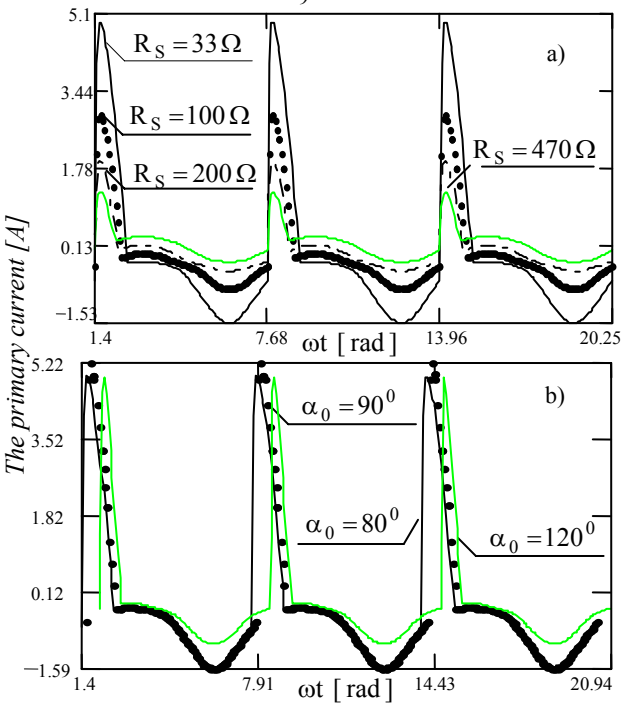

Fig. 4 Variation of the primary current, i_1, resulted by modelling the transformer with the non- linear model a) $i_1 = f(\omega t)\big|_{R;\alpha_0=\frac{4\pi}{9}}$, b) $i_1 = f(\omega t)\big|_{\alpha_0;R=33\,\Omega}$

Comparative (theoretical and experimental) waveforms (also for all transformer models studied), corresponding to a selection of firing angles and loads, are shown in figures 5, 6 and 7.

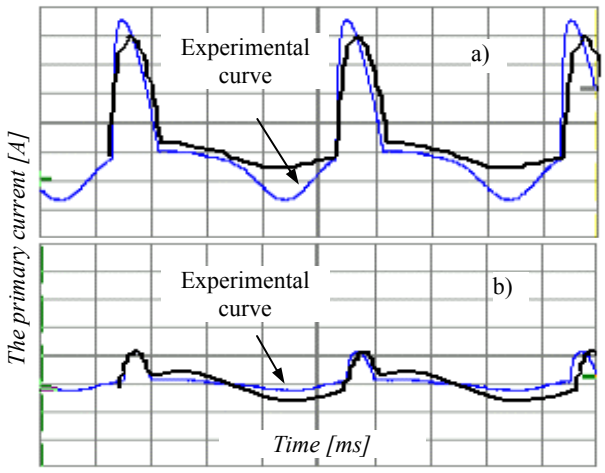

Time scale is 5ms per division, amplitudes are 1A per division

*Fig. 5. Comparison of i_1, resulted by modelling the transformer with the **T series diagram**, and the experimental one*

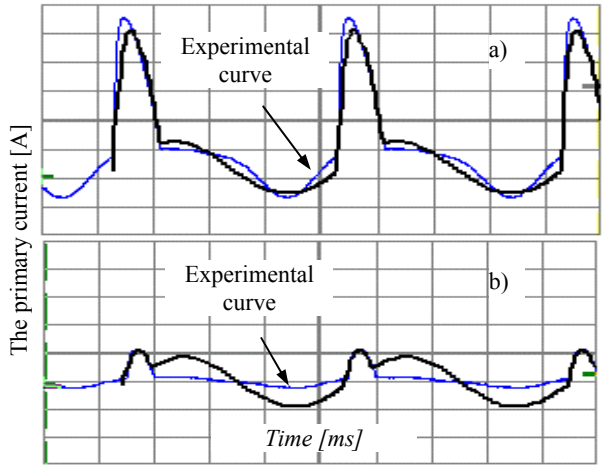

*Fig. 6. Comparison of i_1, resulted by modelling the transformer with **linear parameters**, and the experimental one*

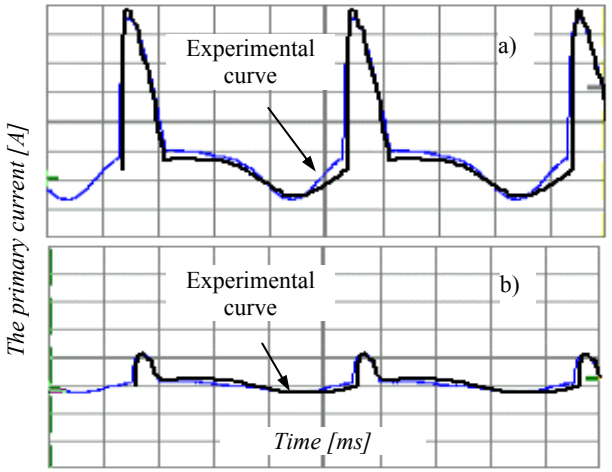

*Fig.7. Comparison of i_1, resulted by modelling the transformer with non- **linear parameters**, and the experimental one*

The comparisons were performed for:

a) $R_S = 33\Omega; \alpha_0 = 80^0$; b) $R_S = 470\Omega; \alpha_0 = 120^0$

The following observation can be derived:

- For T series equivalent diagram:
  - o the theoretical and experimental waveforms are similar, but the relative error level is very high (specially in the SCR turn-off period, because this model is insensitive to the load variation);
  - o the theoretical extreme values variation, function of load (R) and firing angle α_0 is not the same with the experimentally determined one.
- For the linear transformer:
  - o the theoretical and experimental waveforms are similar, but the relative error level is high enough (specially in the SCR turn-off period, this model being however more sensitive to the load variation during this time than the previous one);
  - o the theoretical extreme values variation, function of load (R) and firing angle α_0 is the same with the experimentally determined one.
- For the transformer with a core characterized by a non-linear magnetization curve, (without hysteresis cycle):
  - o the theoretical and experimental waveforms are quite identical, and the relative error level is at least acceptable;
  - o the theoretical extreme values variation, function of load (R) and firing angle α_0 is the same with the experimentally determined one.

The secondary current

Theoretical waveforms presenting the secondary current corresponding to the three transformer models, function of firing angle and load, are shown in figures 8, 9 and 10.

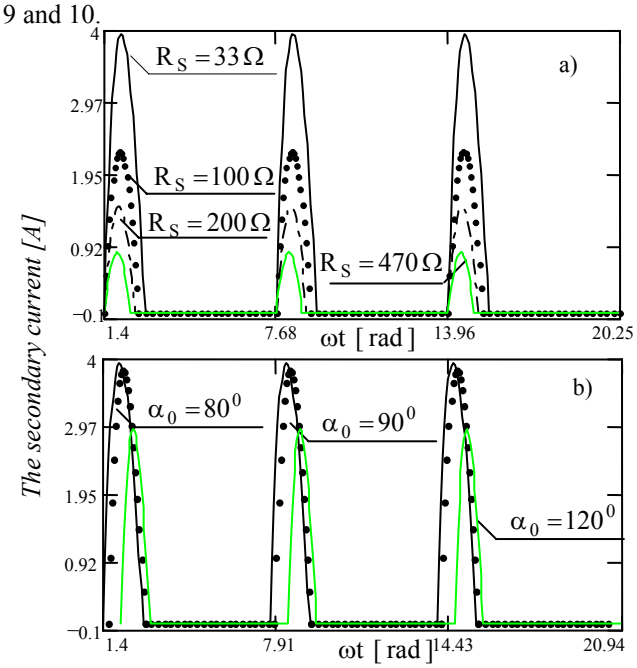

Fig 9. Variation of the secondary current, i_2, resulted by modelling the transformer with the T series diagram, a) $i_2 = f(\omega t)\big|_{R;\alpha_0=\frac{4\pi}{9}}$, b) $i_2 = f(\omega t)\big|_{\alpha_0;R=33\Omega}$

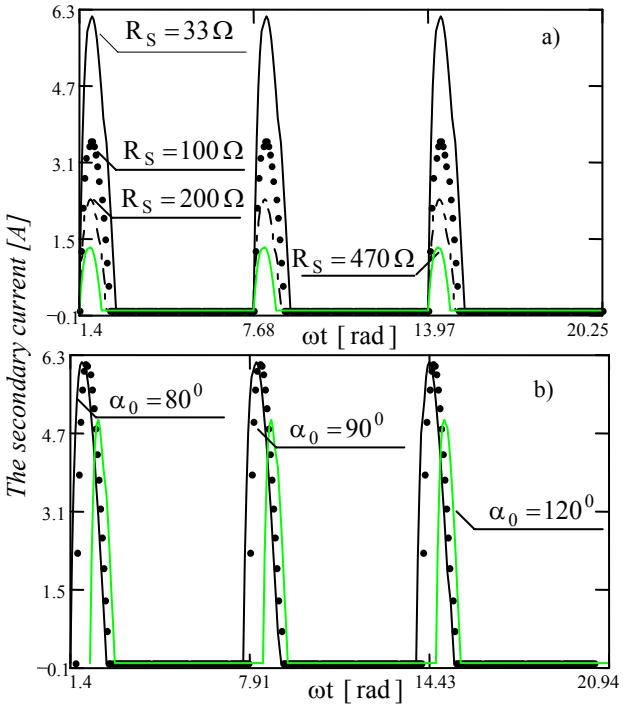

Fig 10. Variation of the secondary current, i_2, resulted by modelling the transformer with the linear model,
a) $i_2 = f(\omega t)\big|_{R;\alpha_0=\frac{4\pi}{9}}$, *b)* $i_2 = f(\omega t)\big|_{\alpha_0;R=33\Omega}$

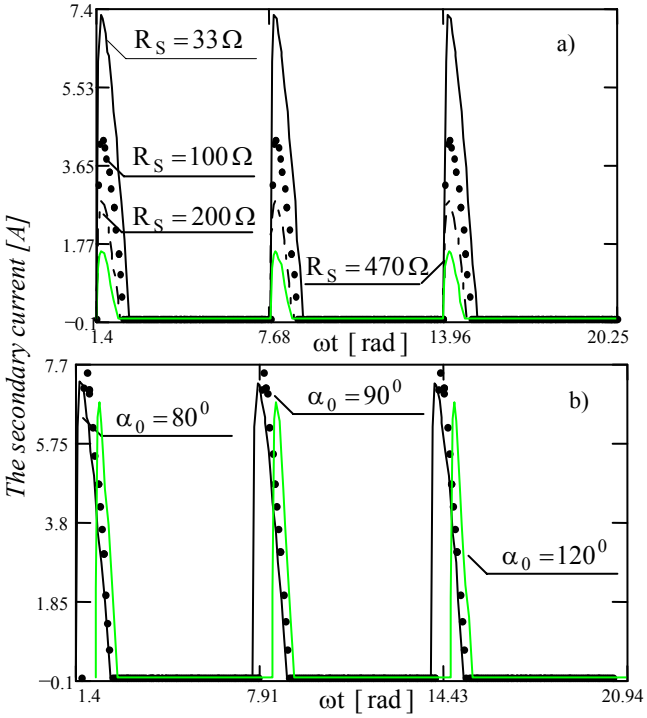

Fig 11. Variation of the secondary current, i_2, resulted by modelling the transformer with the linear model,
a) $i_2 = f(\omega t)\big|_{R;\alpha_0=\frac{4\pi}{9}}$, *b)* $i_2 = f(\omega t)\big|_{\alpha_0;R=33\Omega}$

Comparative (theoretical and experimental) waveforms (for all transformer models studied), corresponding to a selection of firing angles and loads, are shown in figures 12, 13 and 14.
The comparisons were performed for:
a) $R_S = 33\Omega; \alpha_0 = 80^0$; b) $R_S = 470\,\Omega; \alpha_0 = 120^0$

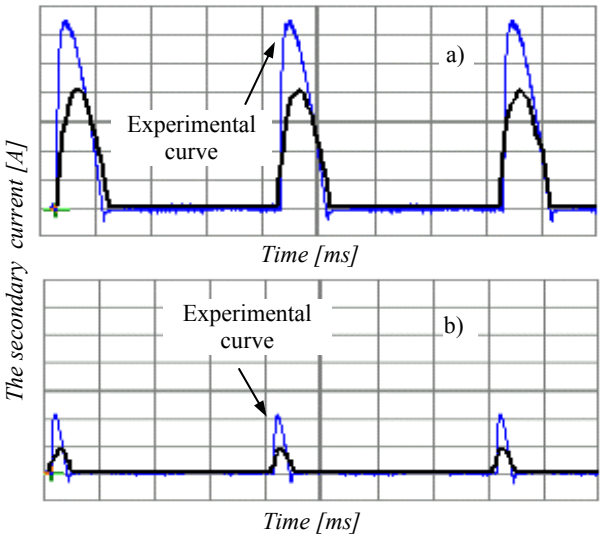

Time scale is 5ms per division, amplitudes are 1A per division

Fig.12. Comparison of the secondary current, i_2, resulted by modelling the transformer with the ***T series diagram****, and the experimental one*

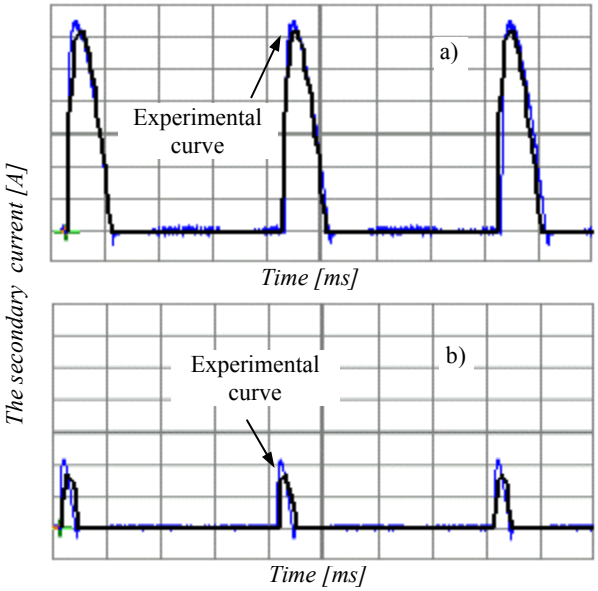

Time scale is 5ms per division, amplitudes are 1A per division

Fig.13. Comparison of i_2, resulted by modelling the transformer with ***linear parameters****, and the experimental one*

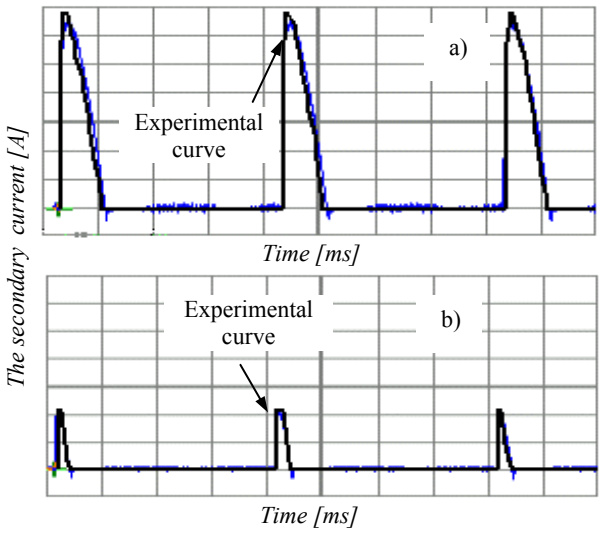

Time scale is 5ms per division, amplitudes are 1A per division

Fig.14. Comparison of i_2, resulted by modelling the transformer with non-linear parameters, and the experimental one

- The theoretical secondary current waveforms and the experimental ones are similar for the T series diagram and identical for the others;
- The relative error level is high for the T series diagram model and at least acceptable for the linear and non-linear transformer;
- The theoretical peak values variation, function of load (R) and firing angle is the same with the experimentally one only for the non-linear transformer.

The load voltage

Theoretical waveforms presenting the load voltage corresponding to the non-linear transformer model, function of firing angle and load, are shown in figure 15.

Comparative (theoretical and experimental) waveforms (for the non-linear transformer model), corresponding to a selection of firing angles and loads, are shown in figure 16.

The comparisons were performed for:

a) $R_S = 33\Omega; \alpha_0 = 80^0$; b) $R_S = 470\,\Omega; \alpha_0 = 120^0$

- All the three transformer models provide theoretical load voltage waveforms identical with the experimental ones and a very low error level. It is a confirmation of the statement saying that a transformer can be considered as an a.c. voltage source from the load circuit point of view.

In table 1 is shown a synthetic presentation of the results returned by the ac switching mode study of the RC loaded transformer, using the three models.

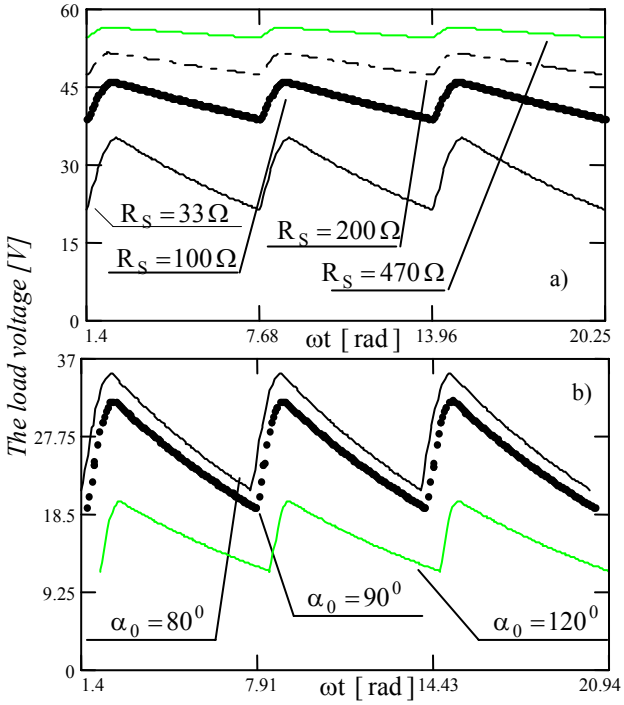

Fig 15. Variation of u_s, resulted by modelling the transformer with the non-linear model,

a) $i_2 = f(\omega t)\big|_{R;\alpha_0=\frac{4\pi}{9}}$, b) $i_2 = f(\omega t)\big|_{\alpha_0;R=33\Omega}$

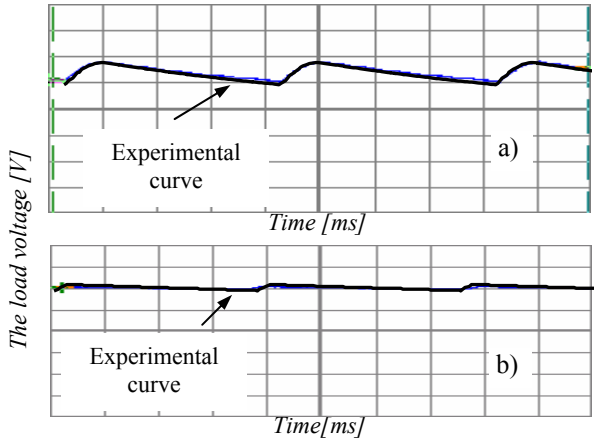

Time scale is 5ms per division, amplitudes are 20 V per division

Fig.16. Comparison of u_s, resulted by modelling the transformer with non-linear parameters, and the experimental one

Conclusion

As a conclusion the following observation can be derived: the periodical ac switching mode study of the transformer using the non-linear model, provides signals whose shape and values are close enough to the ones obtained by laboratory experiments.

Table 1.

Results returned by ac switching mode study of the RC loaded transformer

Analyzed quantities	T series diagram		Linear transformer		Non-linear transformer	
	Diode	Thyristor	Diode	Thyristor	Diode	Thyristor
$\max(\varepsilon_{\alpha pr})$ [%]	6.864		5.156		5.663	
$\alpha_p = f(R)$	Increasing		Increasing		Increasing	
$\max(\varepsilon_{\beta r})$ [%]	5.184	7.844	1.566	2.875	5.696	5.891
$\beta = f(R)\big\|_{\alpha 0=ct}$	Decreasing		Decreasing		Decreasing	
$\beta = f(\alpha_0)\big\|_{R=ct}$	Decreasing		Increasing		Increasing	
Primary current waveform	Similar		Similar		Quite identical	
$i_1 = f(\omega t)\big\|_{R;\alpha_0=ct}$	Decreasing (Th ON) **Constant** (Th OFF)		Decreasing		Decreasing	
$i_1 = f(\omega t)\big\|_{\alpha_0;R=ct}$	**Decreasing** (Th ON) Constant (Th OFF)		Extreme point for $\alpha_0 = \frac{\pi}{2}$		Extreme point for $\alpha_0 = \frac{\pi}{2}$	
$\max(\varepsilon_{I1\max r})$ [%]	**13.1**	**27.88**	9.265	**12.88**	5.864	9.545
$\max(\varepsilon_{I1\min r})$ [%]	**83.85**	**120**	**348.6**	**499.4**	**12.37**	**11.82**
Secondary current waveform	Similar		Identical		Identical	
$i_2 = f(\omega t)\big\|_{R;\alpha_0=ct}$	Decreasing		Decreasing		Decreasing	
$i_2 = f(\omega t)\big\|_{\alpha_0;R=ct}$	Decreasing		**Decreasing**		Maximum point for $\alpha_0 = \frac{\pi}{2}$	
$\max(\varepsilon_{I2\max r})$ [%]	**11.03**	**28.57**	7.229	**10.5**	9.677	**12.27**
Load voltage waveform	Identical		Identical		Identical	
$u_S = f(\omega t)\big\|_{R;\alpha_0=ct}$	Increasing		Increasing		Increasing	
$\Delta u_S = f(\omega t)\big\|_{R;\alpha_0=ct}$	Decreasing		Decreasing		Decreasing	
$u_S = f(\omega t)\big\|_{\alpha_0;R=ct}$	Decreasing		Decreasing		Decreasing	
$\Delta u_S = f(\omega t)\big\|_{\alpha_0;R=ct}$	Decreasing		Decreasing		Decreasing	
$\max(\varepsilon_{Us\max r})$ [%]	3.841	**15.33**	3.024	**10.13**	2.604	5.394
$\max(\varepsilon_{Us\min r})$ [%]	5.038	**15.29**	2.567	**10.69**	6.992	8.44

References

[1] Strîmbu, C. Comutația periodică (cu tiristor) a transformatorului cu sarcină capacitivă. Int. Conf. on Naval and Marine Education "Romanian Naval Academy's 130th anniversary ", Constanța, Romania, 2002, Vol I, pp 50- 59.

[2] Strîmbu, C., Matlac, I., Constantinescu, C.G., Iulian, L. Periodical ac switching study of the transformer,, Symposium on Power Electronics, Electrical Drives, Automation & Motion, "SPEEDAM 2004", Capri, Italy, 2004, pp W2D9-W2D12;

[3] Strîmbu, C., Constantinescu, C.G., Matlac, I., Miron, L. A study of the non-linear transformer suppplying a RC load in periodical ac switching mode, 7th Int. Conf. of Applied and Theoretical Electricity ICATE2004, Băile Herculane, Romania, 2004, pp 148-153.

[4] Strîmbu, C., Constantinescu, C.G. Determinări experimentale efectuate asupra comutației periodice în c.a. a unui transformator monofazat , Int. Conf. on Naval and Marine Education, Constanța, Romania, 2005, Vol I, pp 50- 59.

Constantin Strimbu *– Lecturer, Dr., "Henri Coandă" Air Force Academy of Brasov, 160 Mihai Viteazu street, Brasov ROMANIA*
e-mail: strimbu_c@yahoo.com
Cristian GeorgeConstantinescu *– Lecturer, Dr., "Henri Coandă" Air Force Academy of Brasov, 160 Mihai Viteazu street, Brasov ROMANIA*
e-mail: ccg_cristi@yahoo.com

Numerical approach for defining inductin motors parameters by catalogue data and data from no-load and short circuit tests

Miho P. Mihov, Andrei Krumov, Emil R. Ratz

and Petya Dimitrova

Abstract: *The parameters from the substituting scheme of the induction motors during variable slips are necessary for investigation their behavior in real working conditions. In the current publication is presented an approach for defining these parameters by catalogue and experimental data, without access to constructors documentation. The achieved dependences are successfully applied in simulation models of power systems.*

Key words*: induction motor, parameters of substituting scheme, current moving, saturation influence, rated data, tests of no-load and short circuit.*

Introduction

In modern researching simulation methods for the behavior of the induction motors (IM) as a recognized part of power systems, mainly – power stations, is required to be familiar with the parameters of the substituting scheme of IM, included in equations which reflect processes in the systems. Naturally,relationships which reflect on the ifluence on these parameters in the process of accelerating are needed.

$$\begin{aligned} x_{\sigma 1} &= f_1(s) \\ r_2' &= f_2(s) \\ x_{\sigma 2} &= f_3(s) \end{aligned} \qquad (1)$$

Therefore, the task should be resolved on the base of the user`s aaccessible data, for example [6,7] and with the additional feasible examinations help [1,3].

Generally, the output data complex doesn't include data of constructor sheets, to research the magnetic fields and related processes of the concrete machine – so called FEMM analysis [4], or a calculation of the necessary values- by the traditional relationships [2].

Method essence

The data used in the applied method are:

- The obligatory catalogue data from the firm-producer of the electrical motors: Pn- power rating, n_n-rated speed, work winding connection, U_n- rated supply voltage, f_1- supply power frequency, I_n- rated current, K_{mp}- coefficient of starting torgue $M_{пуск}=K_{mp}M_n$, Kmn-coefficient of maximum torgue $M_{макс}=K_{mn}M_n$.

- The experimental results during no-load and short circuit regimes, which are in the machine technical passports, are developed for machines with responsible purpose, as in thermoelectric power station "Maritza Iztok 2" and nuclear electric power station "Kozlodui" or they can be measured in lab conditions – in low powers. /When it's necessary r_1 is measured/. After result processing [1,3,8] values are defined $x_1 + x_\mu$ – the main reactance in no-load regime, r_k – the resistance in short circuit regime, x_k – the reactance of machine in short circuit regime.

The purpose is with suitable admissions, an algebraic system of equations to be developed, which solution would help for the formation of a relationship (1).

The admissions are:

1. It's generally accepted that the relationships (1) are:

$$\begin{aligned} x_{\sigma 1}(s) &= k_{ns1}(s)\, x_{\sigma 1(n)} \\ r_2'(s) &= K_r(s)\, r_{2\,(n)}' \\ x_{\sigma 2}'(s) &= k_{ns2}(s) K_X(s)\, x_{\sigma 2\,(n)}' \end{aligned} \qquad (2)$$

where,

- with index (n) are marked the substituting system parameters in full load;
- the coefficients $K_r(s), K_x(s)$ give the current moving influence on the rotor resistance and reactance [1,2,8];
- the coefficients $K_{ns1}(s), K_{ns2}(s)$ are designed to measure the influence of the saturation on the corresponding reactances.

2. It`s generally accepted, that there is a current moving and saturation in the whole winding capacity /and in the end windings/, which actually represents a

compromise, but with the chosen solution approach it reflects in an appropriate way.

3. It`s generally accepted that the rotor slots are with rectangular section, which in most cases corresponds to the reality, because it`s used in a large scale of construction for getting a higher starting torgue. In this way the coefficients $K_r(s), K_x(s)$ can be expressed with relatively not very complicated relationship [2,8,9]

4. Some of the parameter examinations of existing machines [7], made with the well-known computing methodics [2], allow to admit with approximation- $K_{ns1}(s) = K_{ns2}(s) = K_{ns}(s)$.

5. It`s generally accepted that the coefficient $K_{ns}(s)$ is linearly changing in the following intervals $1 \geq s \geq s_m$ and $s_m > s \geq s_n$, also $K_{ns}(s=1) = K_{nsp}$, $K_{ns}(s=s_m) = K_{nsm}$ and $K_{ns}(s=s_n) = 1$.

6. The lab examination of short circuit regime of IM – since $I_K = I_n$, the saturation has the same value as in full load.

7. The lab examination of short circuit regime of IM - since $s=1, f_2 = s\,f_1 = f_1$, the current moving is identical with this at the starting torgue of IM.

8. It`s generally accepted that

$$\frac{x_{\sigma 1(n)}}{r_1} = \frac{x_k}{r_k} \qquad (3)$$

/in this way $x_{\sigma 1(n)}$ is clearly defined/

Based on the input data, the admissions and in correspondence to the theory IM [1,2,8,9] is created an algebraic system of equations (4), where as the defined above parameters in nominal regime, $r'_{2(n)}, x'_{\sigma 2(n)}$, so and the conditional height of the rotor aluminum bar $\xi = 0.66\,h\sqrt{s}$ when $s=1$, which is a global argument in the equations for $K_r(\xi(s)), K_X(\xi(s))$.

(4)

$$M_n = \frac{pmU^2 \frac{r'_{2(n)}}{s_n}}{\omega_1[(r_1 + c_1\frac{r'_{2(n)}}{s_n})^2 + (x_{\sigma 1(n)} + c_1 x'_{\sigma 2(n)})^2]}$$

$$r_k = c_1 r_1 + c_1^2 r'_{2(n)}\,\xi\,\frac{\sinh(2\xi)+\sin(2\xi)}{\cosh(2\xi)-\cos(2\xi)}$$

$$x_k = c_1 x_{\sigma 1(n)} + c_1^2 x'_{\sigma 2(n)}\,\frac{3}{2\xi}\,\frac{\sinh(2\xi)-\sin(2\xi)}{\cosh(2\xi)-\cos(2\xi)}$$

The nonlinear system above is being resolved with Mathcad [5], with the help of built in constructions (options) of the software product.

The coefficient $K_{ns}(s=1) = K_{ns(1)}$ is defined at the moment of starting and $K_{ns}(s=s_m) = K_{ns(sm)}$ in critical slip is based on the preliminary coefficients of the following torgues K_{mp} , K_{mm} and with the help of the general relationship for electromagnetic torgue.

(5)

$$K_{ns(s)} = \sqrt{\frac{pmU^2 \frac{r'_{2(n)}}{s} K_r(s) - M_n K_{m(M)}[r_1 + c_1 \frac{r'_{2(n)}}{s} K_r(s)]^2}{M_n K_{m(M)}(x_{\sigma 1(n)} + c_1 K_x(s) x'_{\sigma 2(n)})^2}}$$

Here when $s=1, K_{m(M)} = K_{mp}$, and when $s=s_m, K_{m(M)} = K_{mm}$.

By the suggested approach during variable slips $1 \geq s \geq s_n$ are defined numerically the requested parameters of the substituting scheme of some of the high voltage IM, which are components of thermoelectric power station "Maritza Iztok 2" and nuclear electric power station "Kozlodui". It's made a verification for the deviation from the technical passport data – Table 1. In the same table it is shown conditionally the calculated admissions for the high of the rotor bar $h' \approx 1.4\,\xi_{(s=1)}$.

During the examination it was established that for some of the machines the system (4) has no solution. Then the equation of the rated torgue was successfully changed with this for the rated current . For other machines, other solutions exist in both cases, which are close in value – Table 1 and Table2.

Table 1

Type engine	Eq. №1 M_n , I_n	Deviation from technical passport data for:				h' cm
		$\mathbf{M_{пуск}}$	$\mathbf{M_{макс}}$	$\mathbf{M_n}$	$\mathbf{I_n}$	
		%	%	%	%	
ВАН215-41-16У3	I_n	0.26%	0.00%	3.14%	-0.21%	5.089
ВАН215-41-16У3	M_n	0.26%	0.00%	0.00%	2.89%	5.596
ДАЗО 17-54-10	I_n	0.23%	0.00%	0.00%	-0.05%	3.968
ДАЗО 17-54-10	M_n	0.23%	0.00%	0.00%	-23.09%	3.091
АО2 - 21-39-16У1	M_n	0.29%	0.00%	-0.04%	-3.80%	8.734
2А3М 500/6000 У4	I_n	0.27%	0.00%	-3.81%	-0.20%	7.425
2А3М-2500/6000 У4	I_n	0.29%	0.00%	-3.64%	-0.13%	5.920
4А3М-4000/6000УХЛ4	I_n	0.17%	0.00%	10.77%	0.00%	2.611
4А3М-4000/6000УХЛ4	M_n	0.17%	0.00%	0.00%	-10.53%	2.350
АОВ2 14 41-4	I_n	0.28%	0.00%	8.74%	-0.17%	5.485
АОВ2 14 41-4	M_n	0.31%	0.00%	-0.06%	-11.33%	4.692

Table 2

Type engine	Eq. №1 M_n , I_n	Nominal regime parameters			
		$\mathbf{r_1}$	$\mathbf{x_{\sigma 1(n)}}$	$\mathbf{r'_{2(n)}}$	$\mathbf{x'_{\sigma 2(n)}}$
		Ω	Ω	Ω	Ω
ВАН215-41-16У3	I_n	0.2058	0.950	0.211	8.491
ВАН215-41-16У3	M_n	0.2058	0.950	0.192	9.342
ДАЗО 17-54-10	I_n	0.3210	1.348	0.398	8.744
ДАЗО 17-54-10	M_n	0.3210	1.348	0.528	6.778
4А3М-4000/6000УХЛ4	I_n	0.0365	0.037	0.044	1.348
4А3М-4000/6000УХЛ4	M_n	0.0365	0.037	0.050	1.263
АОВ2 14 41-4	I_n	1.0200	1.020	1.646	63.765
АОВ2 14 41-4	M_n	1.0200	1.020	1.920	54.431

The outcome of numerical relationships of parameters from the slip and from the current during the accelerating process can be interpolated and presented with analytical relationships. This mathematical operation has the advance to make the simulation model construction lighter, but naturally, it supplements additional diversions from the input conditions – the technical passports.

Examples of interpolated relationships, applied for most of the machines above are:

(6)

$$x_{\sigma 1}(s) = y_1 + a_1 e^{-b_1 s} + c_1 s$$

$$r_2'(s) = y_2 + \frac{a_2}{1 + e^{-\frac{s - c_2}{b_2}}}$$

$$x_{\sigma 2}'(s) = a_3 e^{-b_3 s} + c_3 e^{-d_3 s} + g_3 e^{-h_3 s}$$

The coefficients in relationships (6) are defined with the software application Sigma Plot [10] and they differ for any concrete machine.

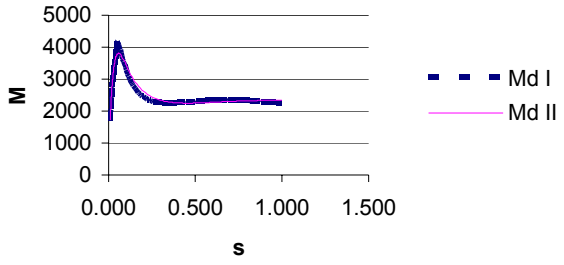

Fig.1

Fig.1 presents the curve line at the moment before the interpolation Md1, the one after the interpolation MdII for electric motor 2A3M 500/6000Y4, leading a pump for average supply (PAS) in nuclear electric power station "Kozlodui".

At Fig.2 and Fig. 3 are respectively presented the torgue curve and the current curve in the accelerating process of the same electric motor, obtained by it`s simulation model.

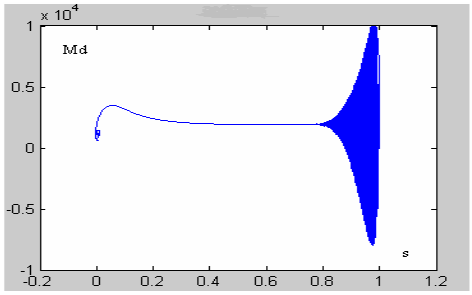

Fig.2

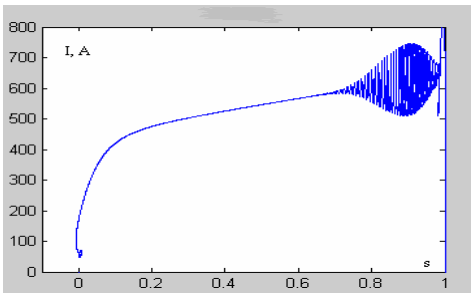

Fig.3

Conclusion

The suggested approach for defining the parameters of substituting scheme of IM has the following properties:

1. The deviations from the catalogue parameters Mstart , Mmax , Mn и I n are acceptable for the real practice.
2. The outcome parameter relationships, presented in numerical (tabular) or analytical mode are successfully applied in computer programs for simulation examinations.
3. It's recommended researchs for the difference in the solution values to be made and even when there is no solution in alternative inclusion of the equation for Mn or I_n in the algebraic system (4). They are subject of another development.

References

1. Динов, В. Електрически машини, " Техника", София, 1981
2. Копилов, И. и к-в, Проектиране на електрически машини, "Техника", София, 1988
3. Соколов, Е., Изследване на електрически машини, " Техника", София, 1977
4. Meeker,D.Finite Element Method Magnetics, ver.3.3. User's Manuel, 2002
5. Дьяконов, В. Mathcad 8/2000, "Питер", Санкт-Петербург, 2001
6. Неклепаев, Б.,И.Крючков, Электрическая часть электростанций и подстанций, "Энергоатомиздат", Москва, 1989
7. Асинхронные двигатели серии 4А, Справочник, "Энергоатомиздат", Москва, 1982
8. Волдек, А., Електрически машини, " Техника", София, 1971
9. Шуйский, В., Расчет электрических машин, "Энергия", 1968
10. Sigma Plot 8.02 Demo, User's Guide. SPSS Inc.2003

Miho Mihov *– Associate Professor, Dr., Faculty of Electrical Engineering, Technical University of Sofia, 8 Kl. Ohridski Str., 1000 Sofia, BULGARIA.*
e-mail: mpmi@tu-sofia.bg.

Andrei Krumov *– senior lecturer Eng.,, Faculty of Electrical Engineering, Technical University of Sofia, 8 Kl. Ohridski Str., 1000 Sofia, BULGARIA.*
e-mail: andrej_krumov@hotmail.com

Emil Ratz *– Associate Professor, Dr., Faculty of Electrical Engineering, Technical University of Sofia, 8 Kl. Ohridski Str., 1000 Sofia, BULGARIA.*
e-mail: emil_ratz@yahoo.com

Petya Dimitrova*– senior lecturer Eng.,United technical college, at TU-Sofia, Department Electrotechnics and Electrical Power Engineering, 8 Kl. Ohridski Str., 1000 Sofia, BULGARIA*
e-mail:dimovap@abv.bg

An Analysis of Stator and Rotor Leakage Reactance in Induction Motors Based on Slot Dimensions

A. Gökhan YETGİN, Nevra AKBİLEK

Abstract: *This paper examines the changes in the values of stator and rotor leakage in induction motors - commonly used in industry - based on stator back height, stator slot height and stator slot up width. An analysis is conducted using Artifical Neural Networks (ANN) and Finite Elements Method (FEM). A FEM package FEMM (Finite Element Method Magnetics) is used for the analysis. A NN model based on back-propagation is used for ANN analysis. The data used in this study is generated using a 3 kW squirrel cage induction motor. As one can easily relate the geometry of stator slot to the stator (X_1) and rotor (X_2) leakage, we show that how stator and rotor leakage changes when the geometry of stator slot is altered.*

Keywords: *Induction motor, stator slot geometry, stator-rotor leakage reactance, ann, fem.*

1. Introduction

Three-phase, low-voltage squirrel-cage induction motors are widely used in industrial applications [1]. Induction motors are used in commercial applications, various industrial fields, homes and electrical power plants [2–3]. They are produced from miliwatt to megawatts in various voltage range. Most of alternating current machines are induction motors [4] and are consuming the big range of the electrical energy produced in a country [5]. Therefore the improvement in design of induction motor parts (i.e, stator and rotor slots, air-gap lenght and ventilation) can yield improvement efficency and energy ecenomy [3].

Optimization of the induction motor design dates back to 1960, where Veinot proposed a digital computer based method in this area. The minimization of the production price was the main goal in the early works [3]. After the oil crisis, and the rise in the energy cost, some researchers, such as Buschart and Diamant put more effort on the optimization of the induction motor effeciency and estimation of its parameters. In recent works, neural network method, fuzzy logic method and also genetic algorithm are also employed in the optimization of induction motor design [3–6].

Chari and Silvester [7] were the first authors who used FEM in the analysis of electromagnetic problems, where it was followed by the implementation of FEM in the analysis of DC motors, SR motors as well as IM [3]. An early modelling of induction motors via ANN is done on linear induction motors. Later it is applied to multi-phased induction motors [8].

In this paper, by changing the stator slot geometry parameters of squireel-cage induction motor, the variation in stator and rotor leakage reactance is investigated. The modelling is achived by using the finite element method and artificial neural networks and the leakage reactance values are obtained.

2. Stator and Rotor Leakage Reactance Calculation Methods

2.1. Stator and Rotor Leakage Reactance Calculation Using FEM

To identify the parameters for an induction motor model, one must first have an equivalent induction motor model. A reasonable model to study might be the one pictured in Figure 1. This model is meant to represent one phase of an induction motor operating in steady state (*i.e.* at a constant electrical frequency and a constant mechanical speed) [9].

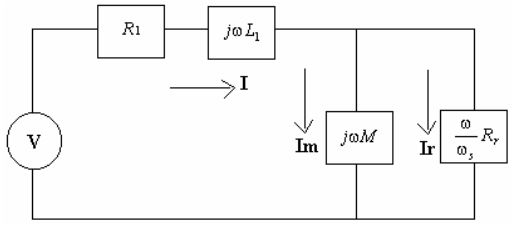

Figure-1. Simple steady-state per-phase induction motor model.

In this model, all leakage is lumped on the stator side of the circuit in inductance L_l. The coupling to the rotor and the currents on the rotor are represented by parallel paths through the inductor, M, representing the inductance of the magnetic circuit linking the rotor and stator. The symbol ω represents the applied electrical frequency (in radians/second). The symbol ω_s represents the difference between the rotor's mechanical frequency and its electrical frequency. If the stator is constructed with p pole pairs, we can define slip frequency ω_s in terms of electrical frequency and mechanical rotor speed ω_r as:

$$\omega_s = \omega - p\omega_r \quad (1)$$

We can imply that the flux, Φ, linking any phase is,

$$\phi = \left(L_l + M\left(\frac{1}{1 + j\tau\omega_s} \right) \right) i \quad (2)$$

Theoretically, the inductance is due to all flux that crosses the coil, and may be calculated by finding the energy stored in the coil and equating it to the energy stored in an equivalent inductance [10].

$$\frac{1}{2} L I^2 = \frac{1}{2} \int JA \, dv \quad (3)$$

For a 2D system, the inductance is,

$$L = \frac{1}{I^2} \iint JA dx dy \quad (4)$$

FEM equivalent of the previous defition is as follows,

$$L = \frac{1}{I^2} \sum_{e=1}^{N} \sum_{i=1}^{M} A_i \iint \alpha_i dx dy \quad (5)$$

where I is the current density in the coil, N is the element number, M is the node number of element used for discritization of the domain, A_i is the vector potential at ith node and α is the shape function of element. The final form of the inductance in finite element terms becomes,

$$L = \frac{1}{3I^2} \sum \int_{e=1}^{N} \Delta_e \int_{i=1}^{M} A_i \quad (6)$$

where Δ_e is the element area. In inductance calculation, only coil elements are considered in formula (6) [11].

FEMM can not model the rotor speed of an induction motor. Since it assumes that rotor is motionless, the problem is defined by giving the frequency. For a 3 kW motor the asynchronous speed is *3000 rpm* and nominal speed is *2844 rpm*. In this case, slip is *0.052* and therefore slip frequency is given as *0.052*50=2.6 Hz*. In order to determine motor inductance slip needs to be changed continiously. Slip frequency is varied between 0–3 Hz by incrementing 0.25 Hz.

Figure–2 shows structure of modelled induction motor whose stator is slot shaped. Here, h_s, h_{cs}, and b_{s2} represents original values of stator slot height, stator back height, and slot up width respectively. The values of h_{cs} and b_{s2} varies at certain degrees based the value of h_s.

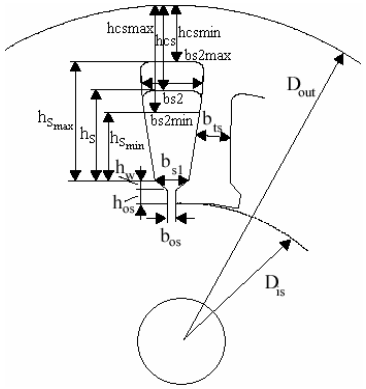

Figure–2. Stator slot structure of induction motor

2.2. Prediction Stator and Rotor Leakage Reactance Using Artificial Neural Networks

ANN are heavily used learning systems that explain the relations between many process parameters and are dependent on using samples which have potentially explanatory purpose to reveal the relationships between the process parameters. Probably the learning ability of ANN is the important reason that draws researchers' interests in this area. Because by using existing samples that shows input-output relations it is possible to solve new cases by making generalizations of previous relations [12].

ANN can be considered as a universal approximator [13–14]. ANN resembles human brain like neural systems in term of underlying structure. Learning ability of ANN, makes it powerful in partially known process control, complex mathematical description and control applications. Neurons are the basic process units of ANN [4]. Neurons receive the information (Receiving function) and process it (Processing function) and transfer it to the other neurons over the connection of the network [15]. Network evaluates the output according to some specific learning rules and improves the weights [12]. In conclusion an ANN consists of network, weights, multiplier, input variables, output variables and training data [16].

In this study, as a begining two dimensional geometrical model of stator slot for the specific values of parameters such as height, back iron height and slot up width of slot is done by using Autocad. Later these drawings are transferred to FEMM software to enable analysis by using finite element method. By doing this for each new stator slot geometry, stator and rotor leakage reactance values are calculated. While modelling is ANN 59 actual stator and rotor leakage reactance values are used for training and 52 values are used for the test purposes.

2.2.1. Multilayer Sensor Model (MLS)

There exist different types of ANN models in terms of the learning mechanisms. MLS sensors, LVQ, SOM,

ART, PNN, RBN, Elman Net, Hopfield Adaline and Modaline are examples of some ANN models [17]. In this study, MLS model is used.

MLS neural nets model is one of the higly used ANN models. The primary reasons that this model is popular are understandability and the possiblity to prove its working mechanism from a mathematical perspective [12]. There are numerous types of multilayer neural nets. The most general ANN has three layers. Multilayer neural networks have at least one hidden layer. The first layer consists of input neurons. The hidden layers are used for calculations. There is also one output layer.

In MLS networks a traning input is given to the net and it is taught what kind of output to produce for this input (Supervised learning) [12]. In multilayer neural nets a training set is given to the net and by using weights outputs are found. According to difference between the desired output and the actual output corrections are made on weights by using Delta Learning rules. In practice two types of stopping criteria are used. One of them is a threshold on error value and the other is the iteration number [18].

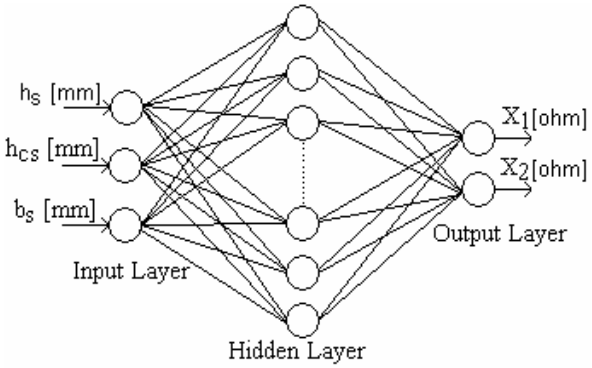

Figure–3. ANN model that is used in the calculation of stator and rotor leakage reactance

In the ANN model illustrated in Figure–3. Slot height, back iron height and slot up width of stator slot geometry are used as input parameters and the actual stator *(X_1)* and rotor *(X_2)* leakage reactance values is used for output value. Values of each input parameters changes for stator slot height and also back iron height between 7–22 mm, slot up width between 5.42–10.6 mm.

Sigmoidal Function which is used as an activation function;

$$f_x = 1/(1+e^{-x}) \quad (7)$$

Summation function used for summation;

$$Net_i = \sum Wij\,Iij \quad (8)$$

are the used is ANN structure.

2.2.2. Network Training Steps and Flow Diagram

The steps for the network training are definition of the network topology determining the input parameters (connection range, learning ratio, momentum coefficient), introducing training set to the network, determining the activation rule and finding the system output, determining the difference between the desired output and the system output, backpropogating of error from output layer towards the input layer and terminating the iteration when the error drops minimum level. Figure–4 illustrates the steps used in training.

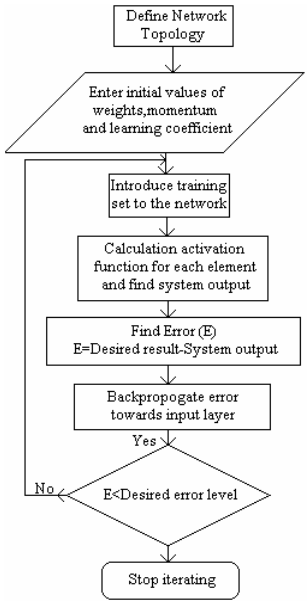

Figure–4. Flow diagram of network training

2.2.3. Creating ANN Model

Training the designed model is a natural consequence of developing an ANN of the system. In ANN h_s, h_{cs} and b_{s2} values are taken as input values. These values are normalized because of the software requirements. Stator slot height, back iron height and slot up width values are converted to values in between 0–1 interval. While normalizing the following Formula is used [17];

(9) $$X_{nor} = \frac{X_{actual} - X_{\min}}{X_{\max} - X_{\min}}$$

2.2.4. Learning Set and Model Training

In each iteration each sample at training set is entered to the model to find the error. The difference between desired output and actual output i.e. error is backpropogated and this procedure is done until a certain learning level is obtained. Training set consists of 59 samples. From these samples 52 of them are used in training and the remaining ones are used in testing level. Each sample has one input an done output layer levels but there are no restrictions on hidden layer. Values of network parameters are given at Table–1. Network's connection weights and bias input weights are initially determined randomly. The beter initial weight interval results will result in beter learning. Second important thing is to determine when training should be stopped. Increasing number of iterations is not the only technique to provide a good learning. Besides increasing the number of iterations accuracy rate is also important. Accuracy rate is calculated as follows;

*D % = (Number of truly classified sample / Total sample) *100*

Table–1

Network parameters

Number of Input Layer	3
Number of Output Layer	2
Number of Hidden Layer	15
Input Size	59
Test Size	52
Scaling Interval	0–1
Initial Weights Interval	-0.1 and 0.1
Learning Coefficient	0.3–0.4
Momentum Coefficient	0.8–0.7
Error Percantage	% 0.3

3. Results

After modelling the changing graph of stator slot height versus stator and rotor leakage reactance according to the ANN values are get from ANN and FEM is given at Figure–5–6. It can be seen from the graph that as the slot height increases then the leakage reactance value increases too. Results obtained from finite element methods and artificial neural network supports each other and there exists small difference between these values and actual values.

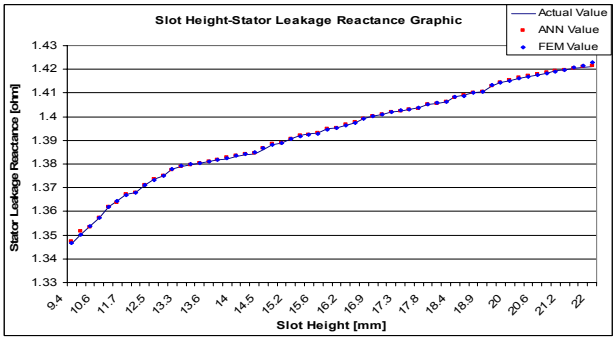

Figure–5. Stator slot height (h_s) versus Stator leakage reactance (X_1) graph

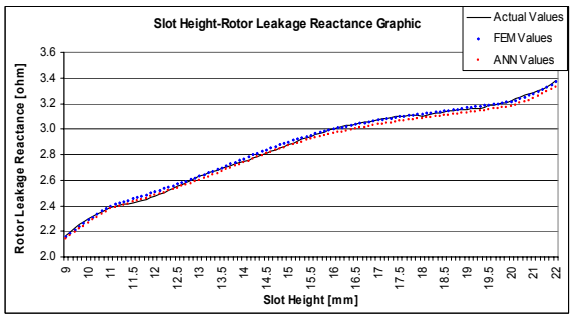

Figure–6. Stator slot height (h_s) versus Rotor leakage reactance (X_2) graph

It is shown in Figure–7 that maximum error after training is reduced based on increased hidden layers of neural networks. This, however, increases the training time. Therefore, 15 hidden layers is used.

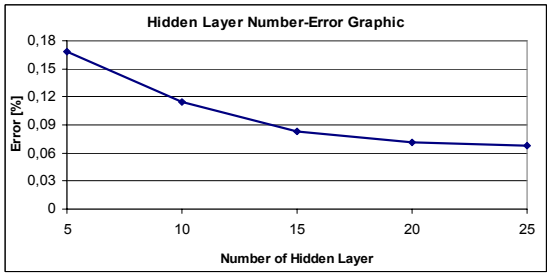

Figure–7. Hidden layer number-Error graph

In Table–2 true values of induction motor stator and rotor leakage reactance values for some specific h_s height values are given for comparision with the values found from FEM and ANN models. As we analyze Table–2 we see that the difference between the values we found from FEM and ANN and the actual values are very small. After training, the ANN the errors found between the results obtained and actual values are small and the error ratios are lower than the error ratios given in Table–1. That shows ANN is a powerfull tool to analyse stator and rotor leakage reactance values.

Table–2

Comparision of true values of stator and rotor leakage reactance and the values obtained by using FEM and ANN methods

	Stator Leakage Reactance [ohm]			Error [%]		Rotor Leakage Reactance [ohm]			Error [%]	
h_s [mm]	Actual Values	FEM Values	ANN Values	FEM	ANN	Actual Values	FEM Values	ANN Values	FEM	ANN
9.4	1.3464	1.34656	1,3467	-0.1654	-0.3	2.22440	2.21420	2.19081	0.0102	0.0335
10.2	1.3538	1.35381	1.35349	-0.0172	0.3044	2.31830	2.31150	2.28677	0.0068	0.0315
11.1	1.3618	1.36187	1.36199	-0.0792	-0.1910	2.39440	2.41080	2.38470	-0.016	0.0097
12.2	1.3713	1.37109	1.37124	0.2037	0.0536	2.50320	2.53200	2.50422	-0.028	-0.0010
12.7	1.3749	1.37493	1.37491	-0.0314	-0.0181	2.58300	2.59170	2.56310	-0.008	0.0199
13.3	1.379	1.37916	1.37901	-0.1617	-0.0184	2.66860	2.67040	2.64071	-0.001	0.0278
14.8	1.3882	1.38833	1.38841	-0.1305	-0.218	2.85110	2.87590	2.84338	-0.024	0.0077
15.9	1.3948	1.39460	1.39483	0.1907	-0.0334	2.99020	2.99030	2.95620	-0.0001	0.0340
16.7	1.3992	1.39922	1.39928	-0.0200	-0.0856	3.05210	3.04980	3.01488	0.0023	0.0372
17.3	1.4025	1.40259	1.40250	-0.0922	-0.0076	3.08920	3.08520	3.04979	0.0040	0.0394
18.4	1.4082	1.40826	1.40815	-0.0642	0.0443	3.12788	3.13820	3.10206	-0.010	0.0258
19.5	1.413	1.41315	1.41294	-0.1564	0.0500	3.18261	3.18830	3.15146	-0.005	0.0311
20.6	1.4177	1.41756	1.41792	0.1357	-0.2239	3.26320	3.25040	3.21271	0.0128	0.0504
21.2	1.4198	1.41988	1.41984	-0.0836	-0.0423	3.29770	3.29460	3.25630	0.0031	0.0414

At Figure–8 error versus number of iterations is illustrated. Although initially error drops fast, later it gets close to flat line. That shows after certain iteration learning of ANN does not change much.

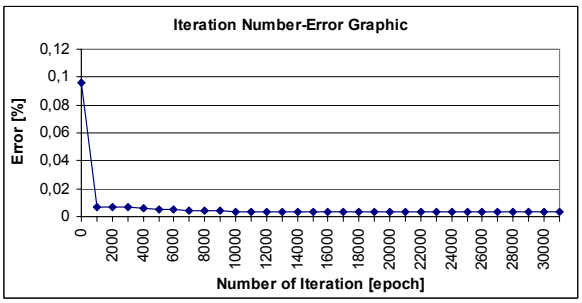

Figure–8. Iteration number-Error graph

4. Conclusion

In this study, effects of the changes in stator slot height, back iron height and slot up width parameters over stator and rotor leakage reactance values for induction motor are found by using finite element method and artifical neural networks. When we analyze the results it can be seen that results of FEM and ANN method approaches to the actual values. With this study it is shown that ANN can find stator and rotor leakage reactance values for different slot geometry. In addition to that ANN approach gives the results faster than time consuming and complex FEM approach.

Acknowledgment

The authors would like to acknowledge to ELSANAS I.C. (Emtaş) Motor Company for the motor datas.

References

[1] A., G., Yetgin, A., İ., Çanakoğlu, The affect of stator core length on efficiency in induction motors and select of optimum length, II. Ulusal Ege Enerji Sempozyumu ve Sergisi, ss 570–577, 16–17–18 Mayıs, Kütahya, 2004.

[2] R., M., Bharadwaj, A., G., Parlos, H., A., Toliyat, Adaptive Neural Network-Based State Filter for Induction Motor speed Estimation.

[3] M., R., Feyzi, H., V., Kalankesh, Optimization Of induction motor design by using the finite element method, pp 845-850.

[4] H., A., Al-Rashidi, A., Gastli, A., Al-Badi, Optimization of Variable Speed Induction Motor Efficiency Using Artificial Neural Network.

[5] S., B., Park, H., B., Lee, S.,Y., Hahn, Stator Slot Shape Design of Induction Motors for Iron Loss Reduction, IEEE Transaction on Magnetics, Vol:31, No:3, pp 2004-2007, May, 1995.

[6] A., G., Yetgin, A., İ., Çanakoğlu, Calculation of Induction Motor's Equıvalent Circuit Parameters Using Different Methods, ELECO' 2004 Elektrik-Elektronik ve Bilgisayar Mühendisliği Sempozyumu, ss 122–127, 8–12 Aralık, Bursa, 2004.

[7] M., V., K., Chari, P., Silvester, Finite element analysis of magnetically saturated DC machines, IEEE, January 31-February 5, New York, pp 2362-2372, 1971.

[8] K., Idir, L., Chang, Improved Neural Network Model for Induction Motor Design, IEEE Transaction on Magnetics, Vol:34, No:5, pp 2948-2951, September, 1998.

[9] Meeker, D., Induction Motor Example, 2002. www.femm.fostermiller.net.

[10] A., G., Yetgin, Desıgn and Finite Element Analysis of a Three Phase Induction Machine, Yüksek Lisans tezi, Dumlupınar Üniversitesi, Fen Bilimleri Enstitüsü, Kütahya, ss 139, 2004.

[11] A., İ., Çanakoğlu, İ., Şenol, D., N., Bekiroğlu, Analytical and Numerical Calculation Of Inductance Of Aplunger-Type Magnet, Eleco99 Interneational Conference on Elc-Elt. Eng., pp 455-458, 1-5 December, Bursa, 1999.

[12] N., Akbilek, S., Boran, Determination Function Using Artificial Neural Network, SAU Fen Bilimleri Enstitüsü Dergisi, 7. Cilt, 3. Sayı, ss 233-240, Eylül, 2004.

[13] L., Fausett, Fundamentals of Neural Networks, Prentice Hall, pp328-329, 1994.

[14] C., Lın, G., Lee, Neural Fuzzy Systems, Prentice Hall, pp 236-240,242,445-448.

[15] E., Öztemel, Artificial Neural Network, Papatya Yayıncılık Eğitim Bilgisayar Sist. San. ve Tic. A.Ş., 1. Basım, ss 232, Ağustos, 2003.

[16] D., Bea, D., Kim, H., K., Jung, S., Y., Hahn, Determination of Induction Motor Parameters by Using Neural Network Based on FEM Results, IEEE Transaction on Magnetics, Vol:33, No:2, pp 1924-1927, March, 1997.

[17] N., Akbilek, Determination Function Using Artificial Neural Network, Yüksek Lisans Tezi, SAU Fen Bilimleri Enstitüsü, ss 93, Ağustos, 2003.

[18] M., Ipek, I., H., Cedimoğlu, Due date Determining in a Job Shop Using Neural Networks, 4th International Symposium on Intelligent Manufacturing Systems, 6-8 September, 2004.

A. Gökhan Yetgin *- Ph.D. Student, Faculty of Engineering, Sakarya University, Dept. of Elc.-Elt. Eng., Campus of Esentepe, 54187, Adapazarı, TURKEY.*
e mail: agyetgin@sakarya.edu.tr

Nevra Akbilek *- Ph.D. Student, Faculty of Engineering, Sakarya University, Dept. of Industrial Eng., Campus of Esentepe, 54187, Adapazarı, TURKEY.*
e mail: nakbilek@sakarya.edu.tr

A dynamic computer model investigation of induction motor by loading with a static torques dependent from the rotor speed

Dinko Gospodinov, Pencho Georgiev

Abstract: *The purpose of this document is to show results received from investigation of computer model of induction machine. It will be used for a creation of a system for vector control and control by the orientation of the magnetic field. The investigations are made with tree type electrical motors produced by "ELMA-LTD" Troian and the results present the correct work of the model.*

Keywords: *induction motor, torque, revolutions, magnetic flux.*

Introduction

The contemporary systems of electromotion and regulation are characterized with a high effectiveness, precision, stability and safety of work. Now a days many firms produce devices for control of a different induction motors. The fundamental reason for that is they have a simple structure and low price. In the last years, the regulators of electromotion were created using microprocontrollers and microprocessors. They are generally DSP and have the necessary rapidity to make all mathematic calculations. These devices receive and transform all information from the sensors. At the same time they react in such way on the motor, that it keeps its number of revolution and magnetic flux. The work of processors in the regulators for electromotion is based of a software. Usually this is a model of induction motor.

Exposition

The objective of the present article is to show the results received from the investigations of a computer model of induction motor. The analyses are made by loading the model with a static torques dependent on the number of revolutions of the rotor. For the creation of the model are used fundamental equations from the theory of electromotion and the software MATLAB (SIMULINK). The equations which describe the dynamic processes in the induction machine are shown below (1-4):

$$(1)\quad \frac{d\Psi_{s\alpha}}{dt} = U_{s\alpha} - \frac{R_s.L_r}{L_s.L_r - L_m^2}.\Psi_{s\alpha} + \frac{R_s.L_m}{L_s.L_r - L_m^2}.\Psi_{r\alpha}$$

$$(2)\quad \frac{d\Psi_{s\beta}}{dt} = U_{s\beta} - \frac{R_s.L_r}{L_s.L_r - L_m^2}.\Psi_{s\beta} + \frac{R_s.L_m}{L_s.L_r - L_m^2}.\Psi_{r\beta}$$

$$(3)\quad \frac{d\Psi_{r\alpha}}{dt} = -\frac{R_r.L_s}{L_s.L_r - L_m^2}.\Psi_{r\alpha} + \frac{R_r.L_m}{L_s.L_r - L_m^2}.\Psi_{s\alpha} - \omega_{el}.\Psi_{r\beta}$$

$$(4)\quad \frac{d\Psi_{r\alpha}}{dt} = -\frac{R_r.L_s}{L_s.L_r - L_m^2}.\Psi_{r\beta} + \frac{R_r.L_m}{L_s.L_r - L_m^2}.\Psi_{s\beta} + \omega_{el}.\Psi_{r\alpha}$$

The model is presented in a frame of reference α-β. The different parameters are as follows:

$\Psi_{s\alpha}$ and $\Psi_{s\beta}$ are longitudinal and transverse components of the stator flux;

$\Psi_{r\alpha}$ and $\Psi_{r\beta}$ - longitudinal and transverse components of the rotor flux;

$U_{s\alpha}$ and $U_{s\beta}$ - longitudinal and transverse components of the voltage in the stator;

R_s – stator active resistance;

R_r – rotor active resistance;

L_s – stator inductivity;

L_r – rotor inductivity;

L_m – common inductivity;

ω_{el} – electrical frequency of rotation of the rotor.

$U_{s\alpha}$ and $U_{s\beta}$ are received after Klark transformation of tree phase stator voltage. After the magnetic fluxes are known, there are no problems to define the torque M using equation five:

$$(5)\quad M = Z_p.\frac{L_m}{L_s.L_r - L_m^2}.(\Psi_{s\beta}.\Psi_{r\alpha} - \Psi_{s\alpha}.\Psi_{r\beta})$$

where Z_p is the number of pole pairs.

In same way can receive the mechanical and electrical speed of rotor, respectively its revolutions.

To verify the correct work of the model, it was investigated by charging it with static torques dependent from the frequency of rotation of the rotor. The investigations are made with two type of torques. The first is when the torque depend in a linear mode, and the second when it is non linear function of the frequency of rotation of rotor. The equations of these parameters are shown below:

$$(6)\quad M_s = M_{s0} + \kappa.\omega_r$$

$$(7)\quad M_s = M_{s0} + \kappa.\omega_r^2$$

where:

Ms is the static torque

M_{s0} – initial static torque

k – coefficient of proportionality who's change from 0 to 1

ω_r – mechanical frequency of rotation of rotor

The such torques produce all machines working with fluids and some machines producing of paper.

The investigations are made with the parameters of real induction motors produced in "ELMA-Ltd" Troian. They are described with the following parameters:

ASM-1

$P_н$ = 1,5kW	R_s = 5,585 Ω	L_s = 0,304 H
$U_{н\,ф}$= 220 V	R_r = 4,220 Ω	L_r = 0,3066 H
$I_{н\,ф}$= 3,8 A	J = 0,00278 kg.m^2	L_m = 0,291 H

ASM-2

$P_н$ = 0,5kW	R_s = 4,495 Ω	L_s = 0,165 H
$U_{н\,ф}$= 127 V	R_r = 5,365 Ω	L_r = 0,162 H
$I_{н\,ф}$= 2,9 A	J = 0,00095 kg.m^2	L_m = 0,149 H

ASM-3

$P_н$ = 2,2kW	R_s = 3,614 Ω	L_s = 0,2445 H
$U_{н\,ф}$= 220 V	R_r = 2,874 Ω	L_r = 0,2453 H
$I_{н\,ф}$= 5,314 A	J = 0,00295 kg.m^2	L_m = 0,2336 H

The results of research are watches in the tables with the lower part, where can see the graphic dependences M=f(k) and ω_r=f(k).

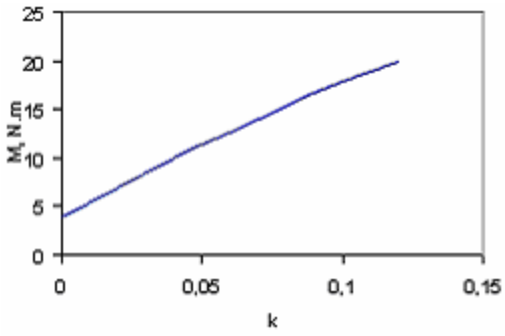

Fig.1 Graphical dependence of the function M=f(k) for ASM-1

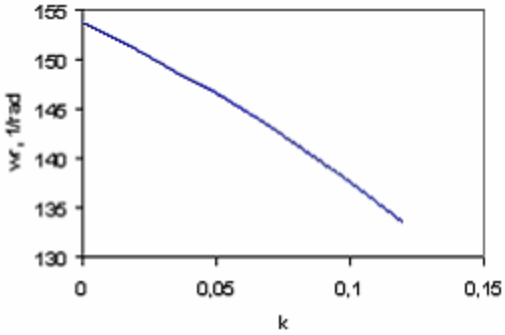

Fig.2 Graphical dependence of the function ω=f(k) for ASM-1

Results from the investigation of ASM-1 by charging with static torque Ms= Mso+k.ω_r

Mco=4 N.m Table1

k	0	0.02	0.04	0.06
M,N.m	4	7.02	9.922	12.69
ω_r, rad^{-1}	153.8	151	148	145
M_s, N.m	4	7.02	9.922	12.69

Table1-continuation

k	0.08	0.1	0.12
M,N.m	15.31	17.76	20
ω_r, rad^{-1}	141.4	137.6	133.5
M_s, N.m	15.31	17.76	20

Results from the investigation of ASM-2 by charging with static torque Ms= Mso+k.ω_r

Mco=1 N.m Table2

k	0	0.01	0.02	0.03
M,N.m	1	2.48	3.842	5.076
ω_r, rad^{-1}	153.6	148	142.1	135.9
M_s, N.m	1	2.48	3.842	5.076

Table2-continuation

k	0.04	0.05	0.06	0.07
M,N.m	6.168	7.106	7.875	8.469
ω_r, rad^{-1}	129.2	122.1	114.6	106.7
M_s, N.m	6.168	7.106	7.875	8.469

Table2-continuation

k	0.08	0.09	0.1
M,N.m	8.893	9.161	9.326
ω_r, rad^{-1}	98.66	90.76	83.26
M_s, N.m	8.893	9.161	9.326

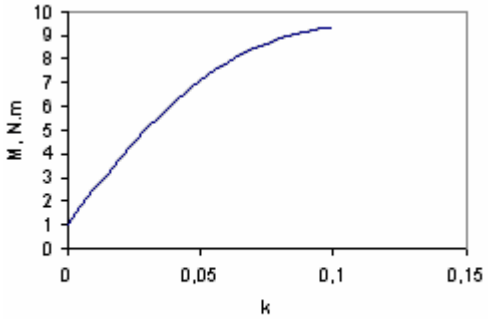

Fig.3 Graphical dependence of the function M=f(k) for ASM- 2

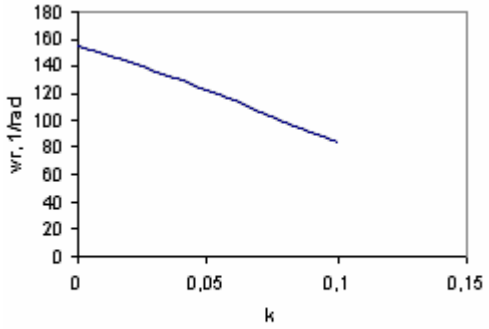

Fig.4 Graphical dependence of the function ω=f(k) for ASM- 2

Results from the investigation of ASM-3 by charging with
static torque Ms= Mso+k.ω_r

Mco=5 N.m Table3

k	0	0.01	0.02	0.03
M,N.m	5	6.533	8.049	9.545
ω_r, rad^{-1}	154.3	153.4	152.4	151.5
M_s, N.m	5	6.533	8.049	9.545

Table3 -continuation

k	0.07	0.08	0.09	0.1
M,N.m	15.32	16.71	18.08	19.42
ω_r, rad^{-1}	147.5	146.4	145.3	144.2
M_s, N.m	15.32	16.71	18.08	19.42

Table3 -continuation

k	0.17	0.18	0.19	0.20
M,N.m	27.91	29.04	30.07	31.06
ω_r, rad^{-1}	135.1	133.6	132	130.3
M_s, N.m	27.91	29.04	30.07	31.06

The graphical dependences ω_r= f(k) and M= f(k) for ASM-3 are shown on fig.5 and fig.6.

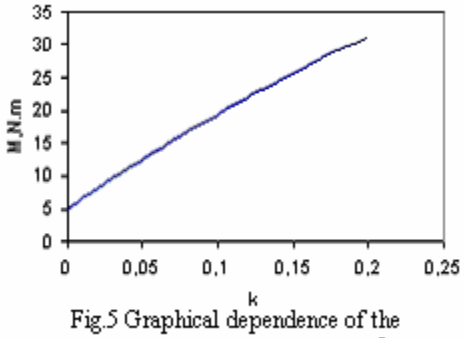

Fig.5 Graphical dependence of the function M=f(k) for ASM- 3

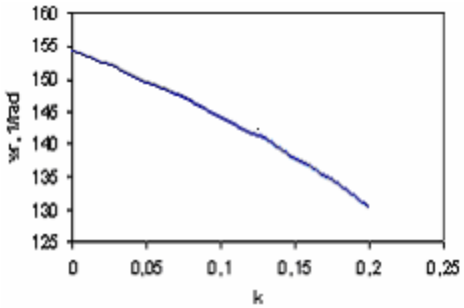

Fig.6 Graphical dependence of the function ω=f(k) for ASM-3

From the different graphical images can see that by increasing the coefficient of proportionality "k", the torque of the motor "M" increase too. In same time the revolutions decrease.

The same results are received after the investigation of the computer model by loading with the static torque according equation 7. They are shown below:

Results from the investigation of ASM-1 by charging with
static torque Ms= Mso+k.ω_r^2

Mco=4 N.m Table4

k	0	0.02	0.04	0.06
M,N.m	4	4.062	4.247	4.557
ω_r, rad^{-1}	154.9	154.8	154.7	154.5
M_s, N.m	4	4.062	4.247	4.557

Table4 -continuation

k	0.08	0.1	0.12	0.14
M,N.m	4.988	5.540	6.211	7
ω_r, rad^{-1}	154.3	154	153.6	153.1
M_s, N.m	4.988	5.540	6.211	7

Table4 -continuation

k	0.20	0.22	0.25	0.30
M,N.m	10.05	11.28	13.31	17.15
ω_r, rad^{-1}	151.2	150.4	148.9	146.1
M_s, N.m	10.05	11.28	13.31	17.15

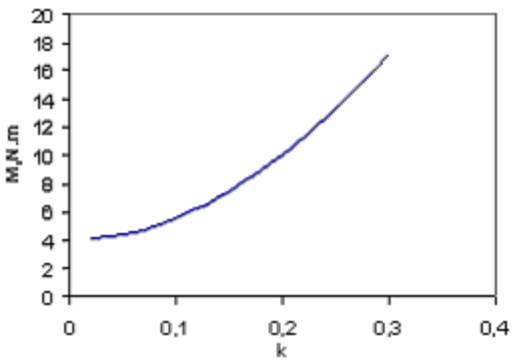

Fig.7 Graphical dependence of the function M=f(k) for ASM-1

Mco=0.5 N.m Table5

k	0	0.02	0.04	0.06
M,N.m	0.5	0.562	0.747	1.052
ω_r, rad^{-1}	155.4	155.1	154.5	153.3
M_s, N.m	0.5	0.562	0.747	1.052

Table5 -continuation

k	0.08	0.1	0.12
M,N.m	1.471	1.992	2.593
ω_r, rad^{-1}	151.6	149.2	145.4
M_s, N.m	1.471	1.992	2.593

The graphical dependences ω_r= f(k) and M= f(k) for ASM-2 are shown on fig.9 and fig.10.

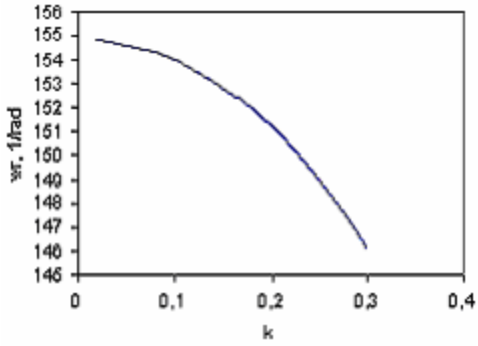

Fig.8 Graphical dependence of the function ω =f(k) for ASM-2

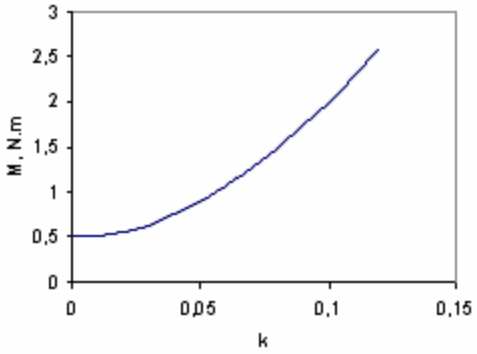

Fig.9 Graphical dependece of the function ω=f(k) for ASM-2

Results from the investigation of ASM-3 by charging with
static torque Ms= Mso+k.ω_r^2

Mco=5 N.m Table6

k	0	0.02	0.04	0.06
M,N.m	5	5.062	5.246	5.554
ω_r, rad^{-1}	154.3	154.2	154.1	154
M_s, N.m	5	5062	5.246	5.554

Table6 -continuation

k	0.14	0.16	0.18	0.20
M,N.m	7.988	8.889	9.901	11.02
ω_r, rad^{-1}	152.5	151.9	151.3	150.5
M_s, N.m	7.988	8.889	9.901	11.02

Table6 -continuation

k	0.34	0.36	0.38	0.40
M,N.m	21.45	23.22	25.02	26.84
ω_r, rad^{-1}	142.3	140.6	138.7	136.5
M_s, N.m	21.45	23.22	25.02	26.84

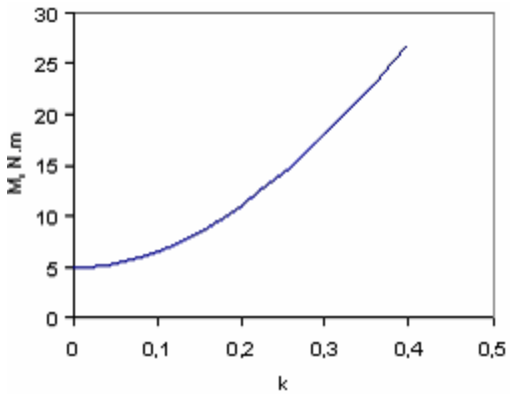

Fig.10 Graphical dependence of the function M=f(k) for ASM-3

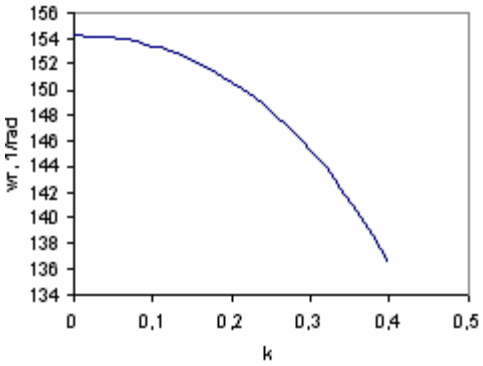

Fig.11 Graphical dependence of the function ω=f(k) for ASM-3

And here by seeing the results from the last investigation can see they are same like first.

Conclusion

At the end we can generalize that the model works correctly. It can be used for an investigation of a many type induction motors. Some results, received from the researches, are compared with data from the firm producer.

The accuracy of the results is more than 98%. The model will be used for a creation of system for a field oriented control of a induction motors.

References:

[1] Kluchev. V. Theory of electromotion. Technics 1989.
[2] Georgiev.P.V. Electronic regulators for electromotion, Gabrovo 1999.
[3] Rudakov.V.V.Asynchronous electromotions with vector regulation, Sanktpeterburg 1987.
[4] Vladimirov.P, Spirov. D., Rachev. Sv. Mode for sensorless speed determination of the rotor at the asynchronous electromotions.International scientific conference Gabrovo,2003.
[5] Nenov. N., Klissarov.G. „Electrical machines", Technics1979.

Pencho Georgiev- *Proph. d-r, Faculty of Electronics Technical Univercity- Gabrovo, H.Dimitar str.4, e-mail: pencho_georgiev2001@yahoo.com*

Dinko P. Gospodinov- *Ph. D. Student, Faculty of Electronics, Technical Univercity- Gabrovo, H.Dimitar str.4, e-mail: d.gospodinov@mail.bg*

A Software Method for Stator Current Values Processing during Induction Motor Rotor Faults Diagnosis

Lyubomir V.Dimitrov **Georgi P.Getzov**

Abstract:*The diagnosis of rotor faults by measuring the machine stator current is well known. If the values of the characteristic frequencies are available, it is possible to determine the possible defects. The aim of this research is to eliminate some problems appearing either in software or hardware during information processing.A software program AS is available, able to diagnose such cases, compiled on C++ with user friendly graphical interface extension. The result is obtained as a message about eventual presence of fault.*

Keywords: *Rotor faults , Induction Motor,Software*

Introduction

Rotor faults diagnosis (broken rotor bars and rings, excentricity, etc) by means of stator current is a well-known method [1],[2] which evaluates failure type on the existing characteristics frequencies. The presence of these frequencies is most often established with the Fast Fourier Transformation (FFT). Their calculation is based on the following dependencies:

- presence of a broken rotor bar

(1) $f_{bч} = (1 \pm 2.к.s).f$

where f is the power supply frequency, s is the normal slip, while k = 1,2,3…

- presence of excentricity

(2) $f_{ec} = \left[(kR \pm n_d)\left(\frac{1-s}{p}\right) \pm u \right] f_1$

where R is the number of rotor bars, p – the number of paired poles;
n_d = 0 with static and n_d = 1 with dynamic excentricity, u= 1,3,5 …

Simplified dependencies are often used:

(3) $f_{ec} = f\left[1 \pm k\left(\frac{1-s}{p}\right)\right]$,

where no motor design data are required, or

(4) $f_{ec} = f_1 \pm f_r$

where f_r is the rotation frequency.

Similar dependencies, related to bearing unit design data are presented both for bearing units and bearing faults [1].

Fig. 1 illustrates two spectra in overlay : one of a motor with normally operating rotor and one of a motor with a faulty rotor (with a broken rotor bar).

The difference in characteristic frequencies of amplidudes (1) is obvious, but it takes a specialist to read it, which is not always the case.

The aim of the present work is to eliminate the problems related to data processing on software and hardware level.

Fig. 2 is a flow chart representation of the stator current data processing arrangement.

Algoritms

The incoming signal from the current transformer is directly processed on a PC without an additional DSP board for the specific motor controlled, using the existing sound card of the computer and a suitable software tool for spectrum analysis of sound signals.

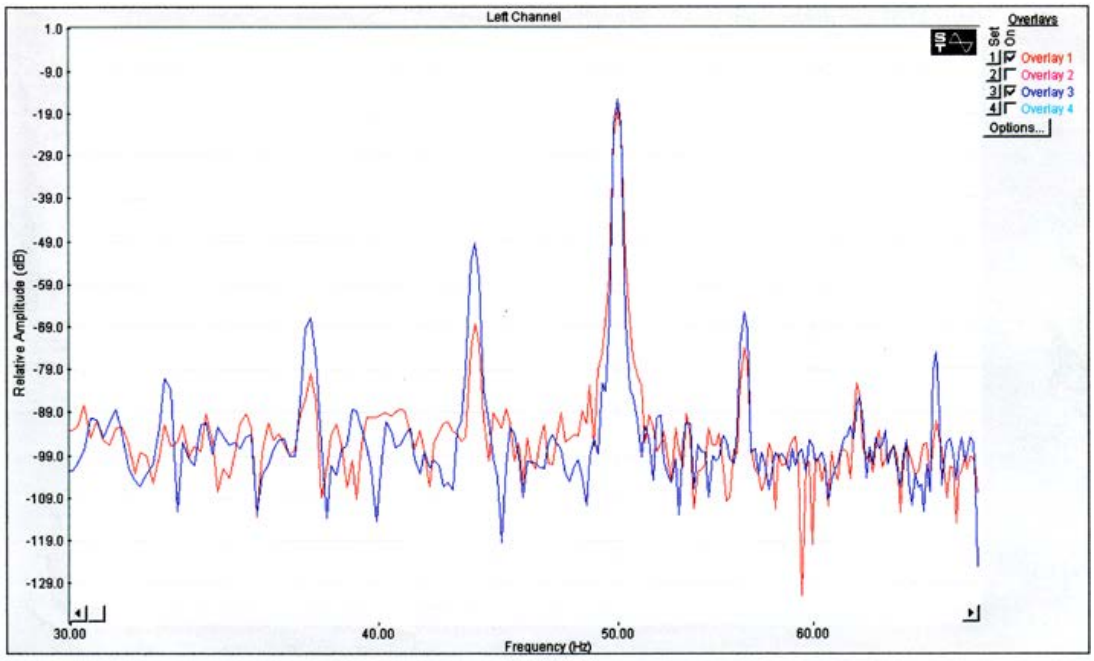

Fig.1.Two spectra in overlay

The Spectra Pro program is used in this case, but other programs can also be used allowing both real time operation and post processing where the signal can be WAV filed and then converted into numerical. This is extremely useful if more than one motors are monitored.

Fig. 3 illustrates the stator current spectrum of a normally operating (healthy) motor. The harmonics generated by a faulty rotor winding are marked. These harmonics increase with the existence broken rotor bars. This same file is simultaneously converted into a numerical one under data logging mode.

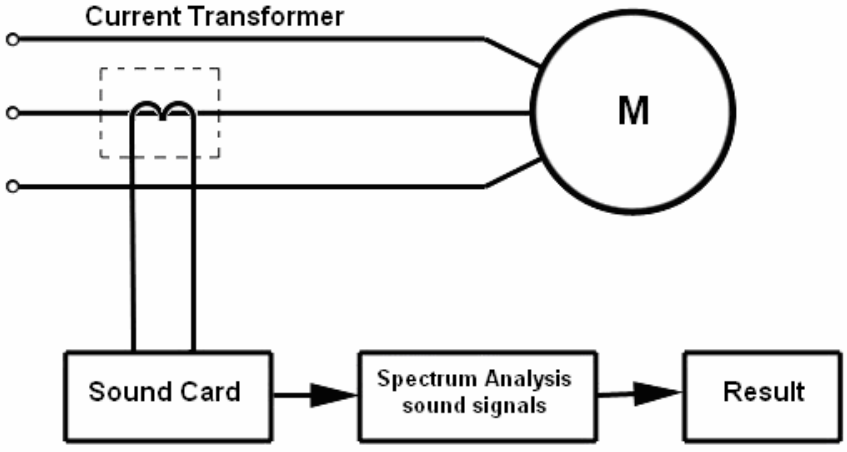

Fig.2.Configuration of the System

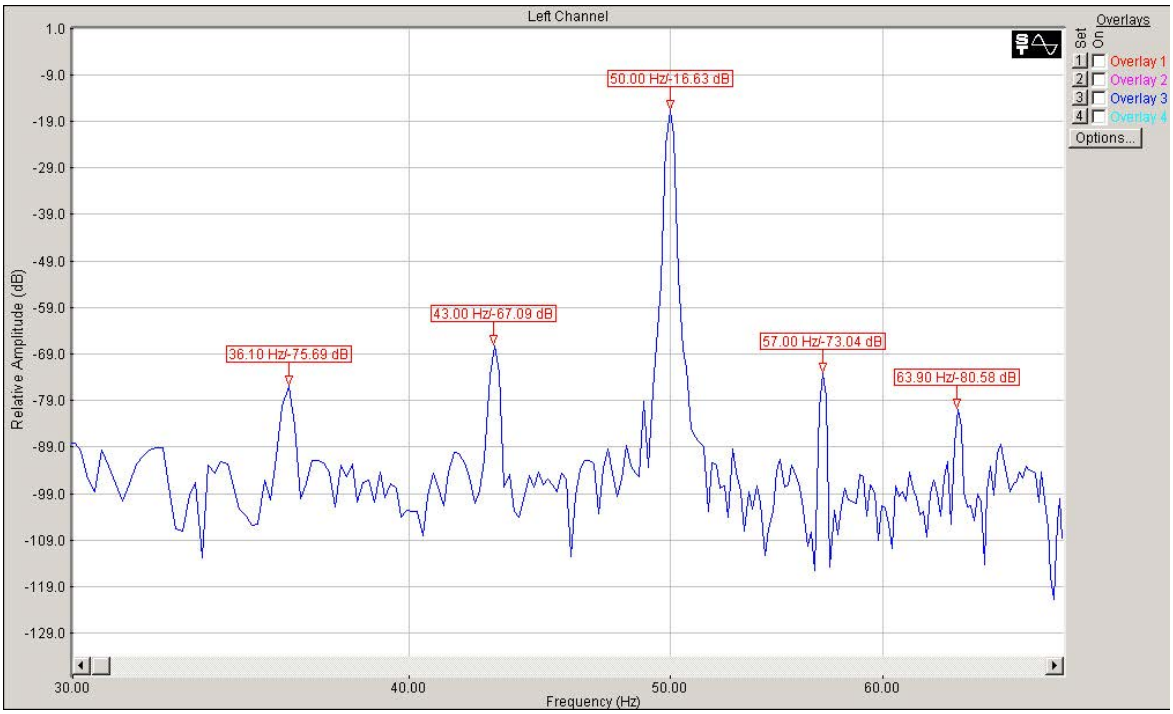

Fig.3.Stator current spectrum of healthy Motor

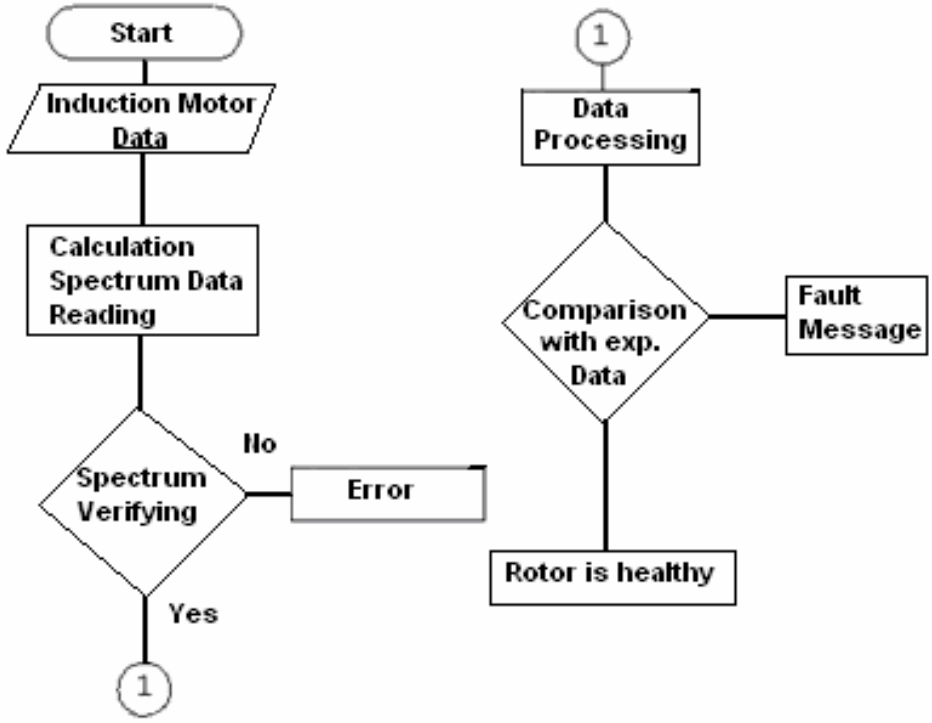

Fig.4. Block Diagram

A further diagnosis requires a tool. For this purpose a software program C++ (AsyncMotor) is created with a graphical interface matching it. Fig. 4 presents the flow chart (block diagram) of this program

Experimental Results

Fig 5 illustrates how the required motor label data are entered. The range of the adjacent harmonics (k=1 or 2) is additionally entered. It is important that both the spectrum data file and the software program be located in the same directory. After clicking the "Analysis" button , cyclic processing follows, based on the 'if-then' assumptions and the results are calculated. (Fig. 6)

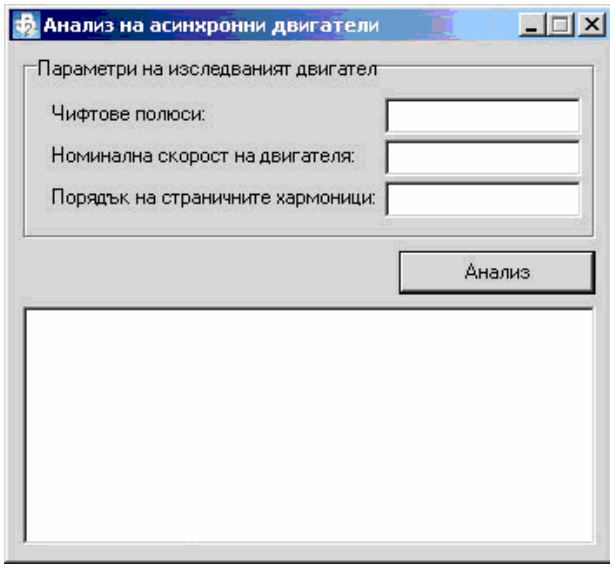

Fig.5 Induction Motor Data

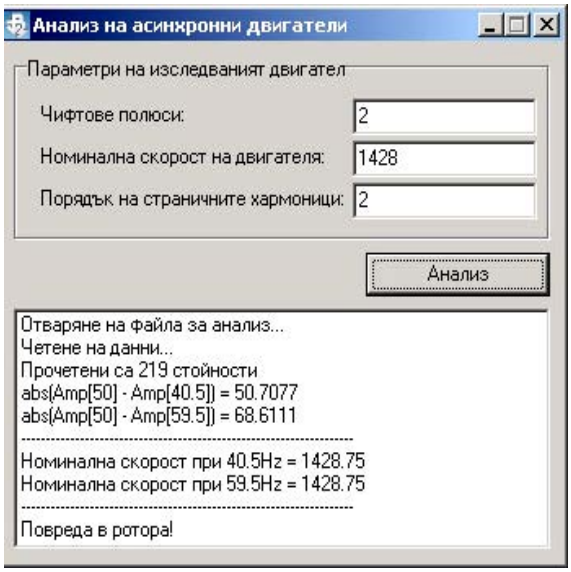

Fig.6.Application Results

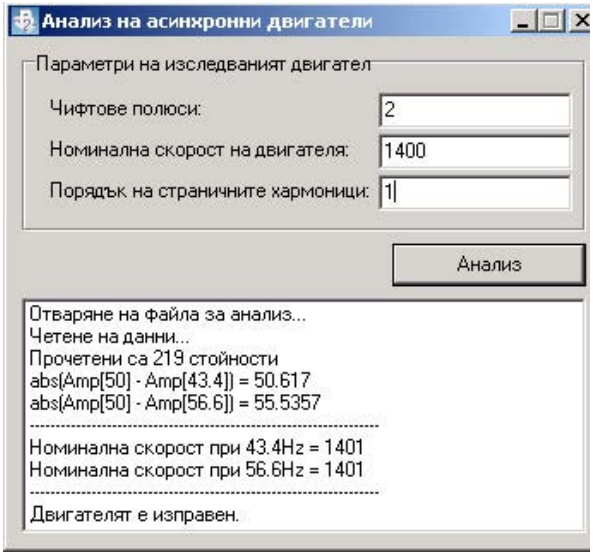

Fig.7.Application Results

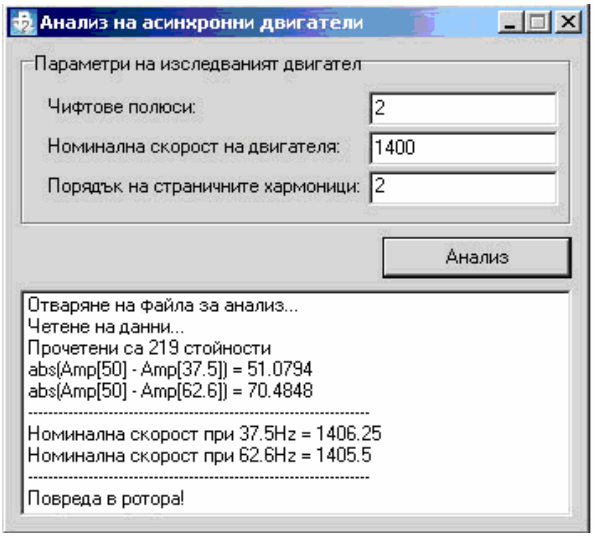

Fig.8.Application Results

In this case, the program is set to find broken rotor bars by comparing amplitude characteristics frequencies to those of the basic harmonic. Figs. 7 and 8 present the evaluation of harmonics for k = 1 with a normally running motor (Fig. 3) and a faulty motor.

Conclusion

It can be clearly seen that motor operation condition is adequately followed and read with required input data reduced to the possible minimum. If additional input parameters are entered, the program capabilities within the range of diagnosis will be increased including for instance excentricity or other rotor faults.

References

1].Benbouzid M.H."A Rewiew of Induction motors Sygnature Analysis as a Medium for Faults detection "IEEE Trans.on Industrial Electronies vol.47,№ 5,October 2000,p.984-993

2. Benbouzid M.H,Kliman G."What stator current processing – based technique to use?"IEEE Trans on Energy Conversion,vol.18, № 2,June 2003,p.238

Lyubomir Dimitrov *– Ass.Professor, Dr., Faculty of Electrical Engineering, Technical University of Varna Studentska Str1 ., 9000 Varna BULGARIA. e-mail: lubo.dimitrov@mail.bg.*

Georgi Gezov – *Student of TU-Varna, Faculty of Electrical Engineering,Technical University, Varna Studentska Str.1 9000 Varna BULGARIA*

Modelling of Heat Processes in Induction Motor and Determination of Thermal Life of Stator Winding Insulation by MATLAB 6.5

Totyo Iliev Iliev, Vladislav Tsvetanov Dimitrov

***Abstract*:** *The analysis of temperature modes of motors in solving of problems related to electric drive in most cases is directed to grounding of simplified methods and engineering ways for motor power preliminary selection and heating terms check. This investigation is a method for determination of electric machines heat parameters by means of computer simulation and modelling of temperature mode by MATLAB 6.5 program product.*

Keywords: electrical machines, thermal durability, electrical insulation, computer modelling

Investigation

The solving of the problem for full calculation of machine heating includes solving of a set of equations for its different parts by taking into consideration their mutual relation. The electric machine is presented with equivalent circuit consisting of several uniform bodies and sources of losses in the respective motor areas. Depending on the mode the heat capacities of separate parts are taken into consideration but this is in case the transition processes are examined. The preciseness of the results obtained depends on the number of bodies included in the equivalent circuit. Usually the preciseness necessary for the engineering practice is reached by examination of 4-5 uniform bodies. As a result of the set of equations solving, the temperatures in the examined areas are found and hence the residual resource can be predicted.

Exposition

The following assumptions are made in order to simplify the equivalent circuit:

1. The thermal conductivity and the heat release coefficients of different surfaces to the coolant are accepted independent of the coordinates and the temperature.
2. The losses are accepted independent of the temperature.
3. Steady-state operating duty is accepted

The equivalent circuit valid for the heating process in a steady-state regime contains conventionally 4 uniform bodies and it is shown in fig.1.

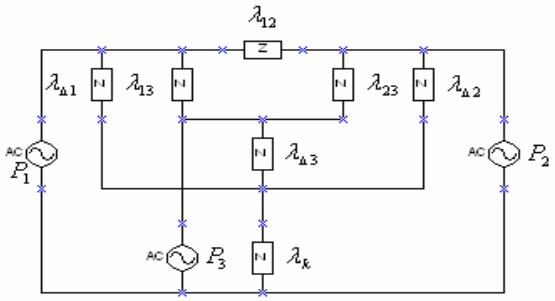

fig.1. Heat equivalent circuit

The individual symbols are as follows:

1. P_1, P_2, P_3- losses in the stator package, rotor and the stator winding;
2. λ_{12}-heat conductivity of the air gap;
3. λ_{13}-heat conductivity between the copper and the steel by the canal insulation;
4. $\lambda_{\Delta 1}$-heat conductivity of the contact gap between the package and the body;
5. $\lambda_{\Delta 2}$-heat conductivity of rotor to the case by shaft;
6. λ_{23}-equivalent heat conductivity between bodies 2 and 3;
7. $\lambda_{\Delta 2}$-heat conductivity between body 3 and the case;
8. λ_k-heat conductivity of the case to the environment;

The four bodies included in the equivalent circuits are as follows: stator package, stator winding, rotor and case. The set of equations describing the temperature regime is as follows:

(1) $$\Theta_1 = -(\lambda_{12}+\lambda_{13}+\lambda_{\Delta 1}).\Theta_1 + \lambda_{12}.\Theta_2 + \lambda_{13}.\Theta_3 + \lambda_{\Delta 1}.\Theta_4 + P_1(1+\alpha_1.\Theta_1)$$

(2) $$\Theta_2 = \lambda_{12}.\Theta_1 - (\lambda_{12}+\lambda_{23}+\lambda_{\Delta 2}).\Theta_2 + \lambda_{23}.\Theta_3 + \lambda_{\Delta 2}.\Theta_4 + P_2(1+\alpha_2.\Theta_2)$$

(3) $$\Theta_3 = \lambda_{13}.\Theta_1 + \lambda_{23}.\Theta_2 - (\lambda_{13}+\lambda_{23}+\lambda_{\Delta 3}).\Theta_3 + \lambda_{\Delta 3}.\Theta_4 + P_3(1+\alpha_3.\Theta_3)$$

(4) $$\Theta_4 = \lambda_{\Delta 1} + \lambda_{\Delta 2}.\Theta_2 + \lambda_{\Delta 3}.\Theta_3 - (\lambda_{\Delta 1} + \lambda_{\Delta 2} + \lambda_{\Delta 3}).\Theta_4$$

According to (1) the heat conductivity can be determined by the following relationships, having the constructive data for the respective motor:

(5) $$\lambda_{\Delta 1} = \frac{\lambda_{\gamma 1}.\lambda_{\gamma \Delta 1}}{\lambda_{\gamma 1} + \lambda_{\gamma \Delta 1}},$$

where: λ_{j1} is the general conductivity of the stator package and $\lambda_{j\Delta 1}$ varies from 0,0025 ± 0,003 cm - for small machines and 0,005 ± 0,0075 cm for big machines.

(6) $$\lambda_{12} = \frac{1}{2}.\alpha_{\delta}.\pi.\ell_1.d_2,$$

where:

(7) $$\alpha_{\delta} = 27.(1+\sqrt{v_{\delta}}),[\text{W/m}^2.^{o}\text{C}]$$

(8) $$v_{\delta} = \frac{1}{2}.\frac{\pi.D_2.n}{60},$$

where: D_2 – diameter of rotor.

(9) $$\lambda_{\Delta 2} = \frac{1}{\frac{1}{\lambda_{\gamma 2}} + \frac{1}{\lambda_{\gamma\Delta 2}} + \frac{1}{\lambda_{\text{в}n}}},$$

(10) $$\lambda_{\gamma 2} = 2.\pi.\lambda_{fe}.\frac{1}{\ln.\frac{D_{\text{в}} + h_{\gamma 2}}{D_{\text{в}}}}$$ -

conductivity of package back;

(11) $$\lambda_{\Delta\gamma 2} = \frac{\lambda_i}{\Delta_{\gamma 2}}.\pi.D\text{в}.l_2$$ - conductivity of the gap between the rotor and the shaft;

(12) $$\lambda_{23} = \alpha_{k2}.S_{k2}$$ - conductivity of rotor,

where:

(13) $$\alpha_k = 27.\left(1+\sqrt{v_{\alpha i}}\right),[\text{W/m}^2.^{o}\text{C}]$$- is determined with α sensors fixed to the fan;

(14) $$\lambda_k = \alpha_{c\Sigma}.\pi.D_c.L_c + \alpha_c.S_p,$$

where: λ_k is full heat abstraction coefficient.

The determination of heating and stator winding resource whose exhaustion is the cause for 70 ± 80 % of electric machines troubles is also interesting. The residual resource of the winding is determined by the following:

(15) $$T_p = \frac{1}{\sum_{1}^{n}\frac{a}{i}.e^{\frac{\Theta}{b}}},$$

where; a and b are coefficients depending on the insulation class. The complete block diagram of the realized mathematical model is presented in figure 2.

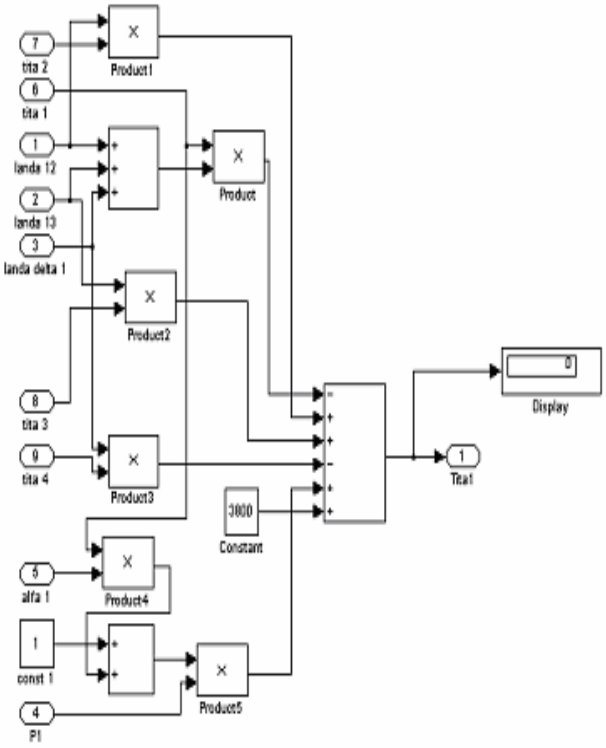

a) Subsystem for determining θ_1

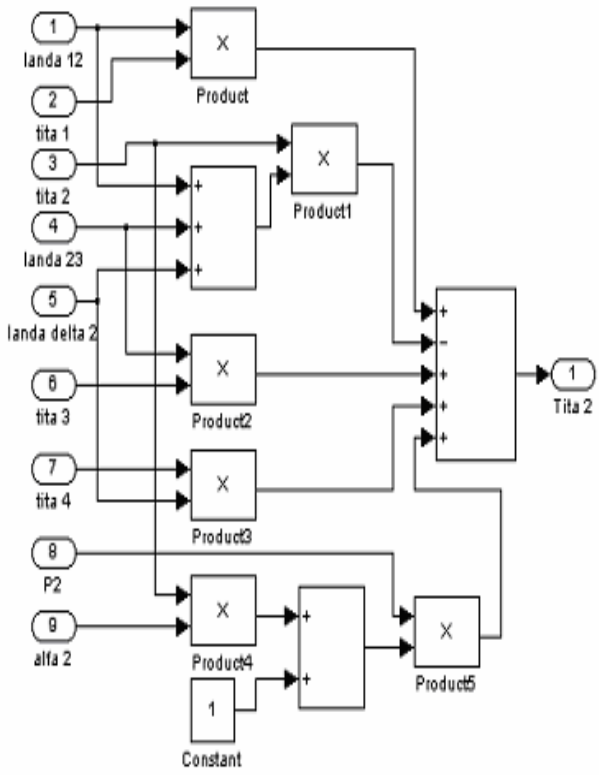

b) Subsystem for determining θ_2

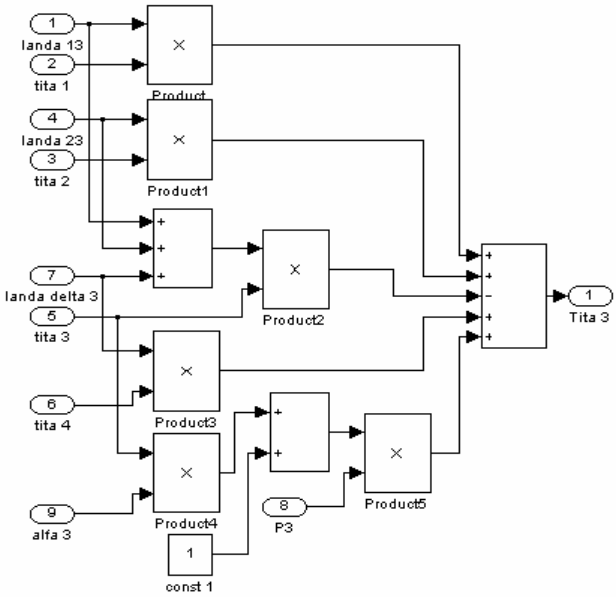

c) Subsystem for determining θ_3

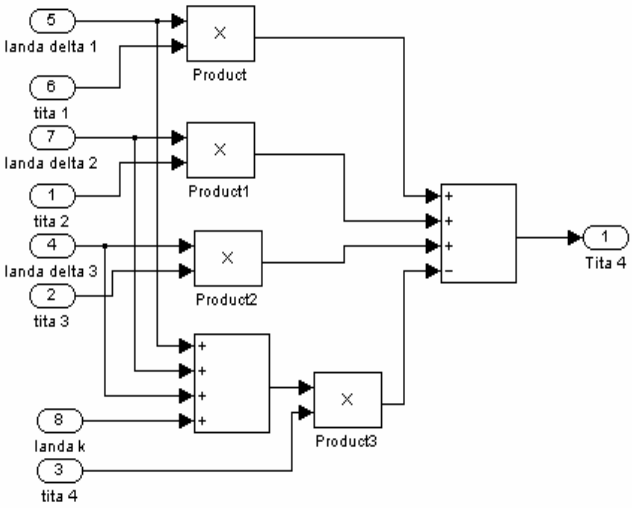

d) Subsystem for determining θ_4

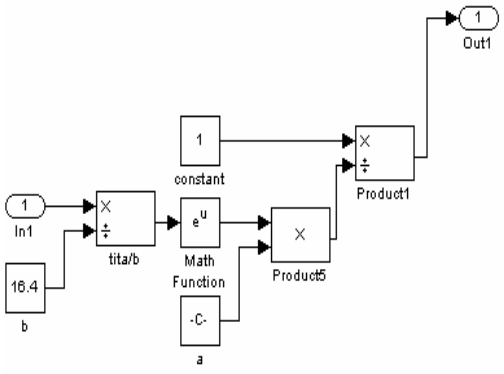

e) Subsystem for determining residual resource

Fig.2. Computer Modelling of the Temperature Regime

Figure 3 presents the graphically obtained temperatures in typical spots and the residual resource of the stator winding.

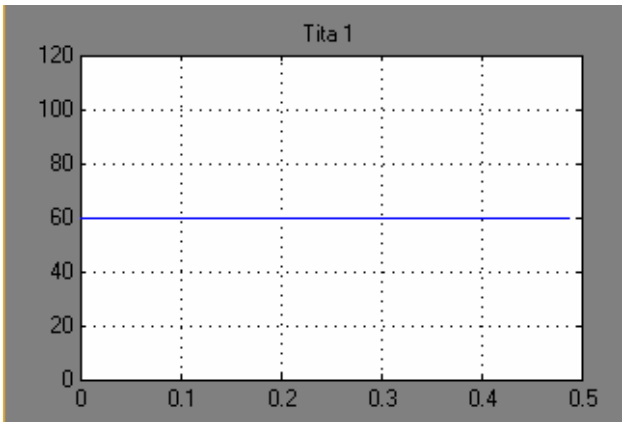

a)

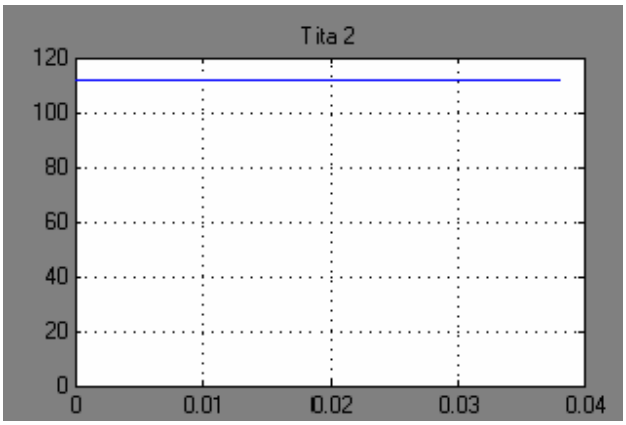

b)

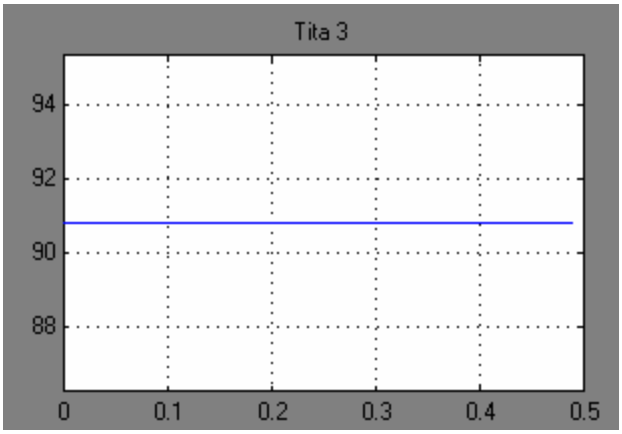

c)

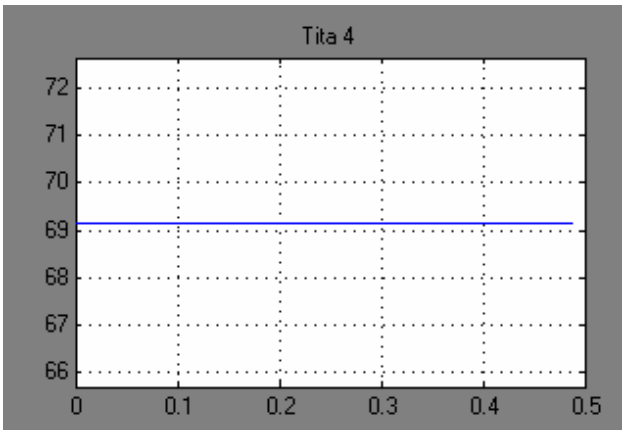

d)

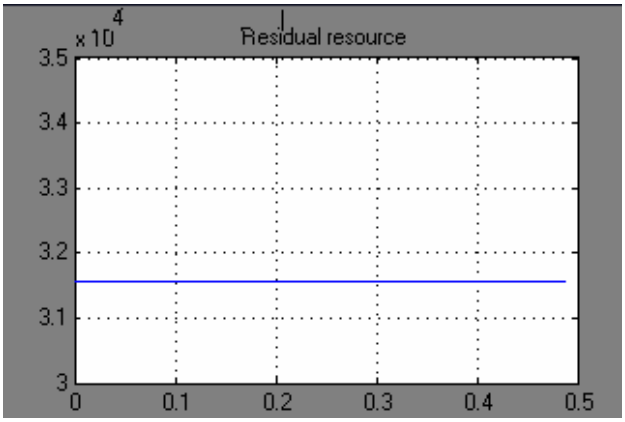

e)

Fig.3. Graphically obtained temperatures in typical spots and the residual resource of the stator winding
a) θ_1- temperature stator package: b) θ_2- temperature of rotor; c) θ_3- temperature of stator winding; d) θ_4- temperature of case

Appendix

AM type AT-104-4

P_n=250 kw, U_n=380V, I_n=470A, n=1470, η=0.93,
Losses : P_1=3850W, P_2=5844W, P_3=1755W
Calculated heat conductivity:λ_{12}=124 W/m^2.^{o}C,λ_{13}=0.2 W/m^2.^{o}C, $\lambda_{\Delta 1}$=117 W/m^2.^{o}C, λ_{23}=85 W/m^2.^{o}C, $\lambda_{\Delta 2}$=0.129 W/m^2.^{o}C,$\lambda_{\Delta 3}$=190 W/m^2.^{o}C, λ_k=42 W/m^2.^{o}C,α_k=0.004K^{-1}

Conclusion

Comparatively simple and generalized algorithm for determination of heating and thermal life of the stator winding insulation is developed and it can be placed in the basis of developing methods for heat calculation of different electric machines. Results of analytic and experimental tests of some of the most spread types of induction motors are also presented.

References

[1] G.G. Schastlivai, Heating of closed induction motors, Moskva 1966

[2] N.A. Koziryov, Insulation of electric machines and its testing, Moskva – Leningrad 1962

[3] Gotter G. – Heating and cooling of electric machines – Moskva 1961

Totyo Iliev Iliev– *Associate Professor, Dr., Faculty of Electrical Engineering and Electronic Technical University of Gabrovo,4 H.Dimitar Str. 5300,Gabrovo, BULGARIA.,e-mail:ilievt@mail.bg*

Vladislav Tsvetanov Dimitrov *- Ph.D. Student, Faculty of Electrical Engineering and Electronic, Technical University of Gabrovo, 4 H.Dimitar Str. 5300,Gabrovo, BULGARIA. ,e-mail:w.dimitrov@dir.bg*

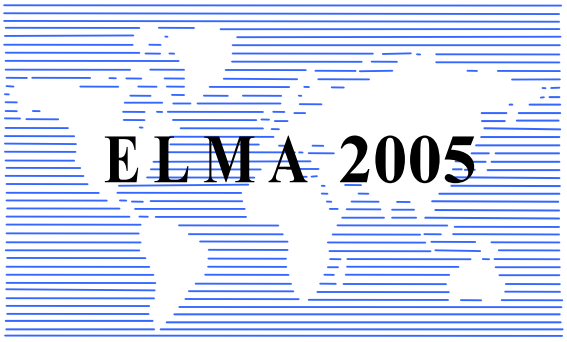

ELECTRICAL MACHINES III

A Comparison of the Main Classes of Brushless Motors by Analytical and Numerical Calculation

Daniel Fodorean, Ioan-Adrian Viorel, Adesslem Djerdir and Abdellatif Miraoui

***Abstract*:** *Analytical and numerical modeling is necessary to evaluate and validate the rated operating performances of the brushless motors. The main rotor topologies with permanent magnet (PM) excitation encountered in the literature are studied. The designing equations for these types of drives are employed. Performances comparison for the studied motors are presented by analytical approach and finite element method (FEM) analysis and conclusions are drawn.*

Introduction

The brushless motors, where the main flux is generated by the permanent magnets, are of a great interest in electric vehicle propulsion. They are usually divided into synchronous and brushless DC (**BLDC**) **PM** machines. This terminology is somewhat confusing since both types have no brushes and operate in synchronous mode. As it was pointed out in [1], the actual difference is rather the operation principle than the machine itself.

Inverter-fed synchronous **PM** and **BLDC** drives require the rotor position feedback to control the phase current synchronously with the rotor position. While for the synchronous PM machines the operation is characterized by sinusoidal stator currents, in the **BLDC** machines, the stator currents are square waves (or trapezoidal waves). In this paper we are dealing with the square waves supply.

For the specific applications in vehicle traction, the PM machines with surface or buried permanent magnets offer quite good performances. In terms of high efficiency and torque/weight ratio, low size and maintenance requirements, the surface mounted permanent magnets (**SMPM**) [2, 4] motors are the best solution. Otherwise, the buried permanent magnets machines, also called the interior permanent magnets (**IPM**) [3, 5] machines, combine the advantages of the permanent magnet motors with those of the reluctance machines, such as: good efficiency and power factor and flux weakening capability for variable speed applications.

The aim of this work is to evaluate the rated operating conditions by analytical design for the main classes of PM drives and to validate this approach by numerical analysis.

Several rotors structures are considered. Keeping on the same stator armature configuration, the ***surface*** **(a - SMPM)**, the ***flux concentrating*** **(b – IPM-fc),** the ***radial-inset*** **(c – IPM-ri)** and the ***u-type*** **(d** - with one or **e** – with two layers, **IPM-u1, u2**) permanent magnets topologies are considered (see figure 1). First of all, the main equations for each variant, modeling the airgap flux density, are presented. The design section consists of the electro-magnetic and mechanical parameters calculation. By analytical modeling, the rated operating point can be characterized (the rated current and torque, the efficiency etc...). Also, the finite element validation and the transient behavior are simulated using the *FLUX2D* to *SIMULINK* coupling technique.

Analytical Design

A design algorithm was developed for the main classes of PM motors. The saturation effect was neglected, for the sake of simplicity.

The drive specifications consist in: the rated power - 5.5kW, the rated speed - 1500 rpm, the dc battery voltage – 48V, 36 stator slots and 4 poles motor configuration. Rare earth PMs were utilized. A usual induction motor stator armature was considered.

Four types of rotor structures were employed to be analyzed. Their cross sections are given in figure 1. The main analytical design formulas are presented for each topology in table 1.

The meaning for the different values from the design formulae is:

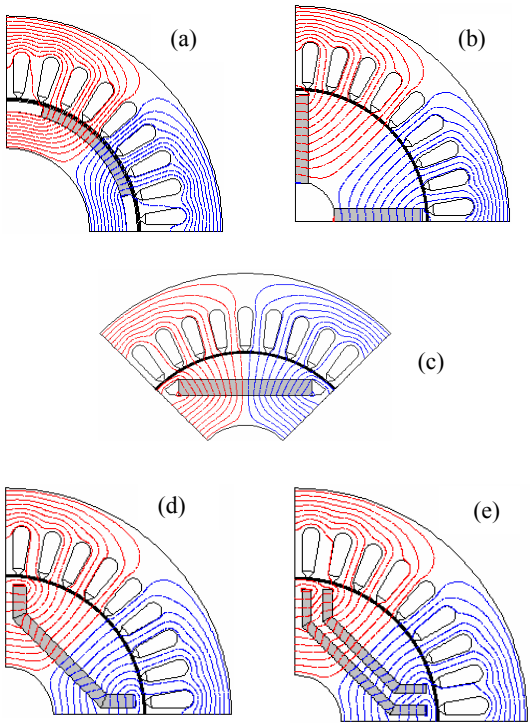

Fig. 1 Field lines distribution in the studied brushless drives

Table 1
The main mathematical expressions for the designed PMSM

Air gap flux density		**BLDCM**
(1)	$B_\delta = \dfrac{h_m \cdot B_r}{R_\delta\left(\ln\left(\dfrac{R_{si}-\delta_c}{R_{cr}}\right)+\mu_r \cdot \ln\left(\dfrac{R_{si}}{R_{si}-\delta_c}\right)\right)}$	**(a)**
(2)	$B_\delta = \dfrac{B_r}{\sigma \cdot \dfrac{S_p}{S_m}+\dfrac{1}{\mu_0}\cdot\dfrac{B_r}{H_c}\cdot\dfrac{2\cdot\delta_c\cdot k_s}{h_m}}$	**(b)**
(3)	$B_\delta = \dfrac{B_r - B_{\max}\cdot\dfrac{2\cdot x}{b_m}}{\dfrac{2\cdot R_{cr}}{p\cdot b_m}+\dfrac{\delta_c\cdot\mu_r}{h_m}}$	**(c)**
(4)	$B_\delta = \dfrac{B_r - B_{\max}\dfrac{2\cdot y+2\cdot y_2}{n_l\cdot(b_m+b_{m2})}}{\dfrac{\alpha_p\cdot D_{cr}}{p\cdot(b_m+b_{m2})}\cdot\dfrac{\delta_c\cdot\mu_r}{n_l\cdot h_m}}$	**(d, e)**
The *d* and *q* axis reactance		
(5)	$X_d = X_m\cdot\dfrac{k_{ad}}{k_{sq}}+X_\sigma,$	
(6)	$X_q = X_m\cdot\dfrac{k_{aq}}{k_{sq}}+X_\sigma,$	
	where,	
(7)	$X_m = \dfrac{4\cdot m\cdot f_s\cdot\tau_p\cdot l\cdot(N_s\cdot k_{ws})^2\cdot\mu_0}{\pi\cdot p\cdot\delta_c},$	
(8)	$X_\sigma = \dfrac{4\cdot\pi\cdot f_s\cdot {N_s}^2\cdot\mu_0}{p\cdot q}\cdot\sum\Lambda_\sigma,$	
	(for the **SMPM**, $k_{ad}=k_{aq}$, and $k_{sd}=k_{sq}$, $\Rightarrow X_d = X_q$.)	
Electrical and mechanical performances		
(9)	$E_{ph} = 4{,}44\cdot f_s\cdot N_s\cdot k_{ws}\cdot\phi_m\cdot k_{di},$	
(10)	$P_e = m\cdot U_{ph}\cdot\left(I_q\cdot\cos\psi - I_d\cdot\sin\psi\right),$	
	with,	
(11)	$I_d = \dfrac{\left(U_{ph}\cdot\left(X_q\cdot\cos\psi - R_{ph}\cdot\sin\psi\right)-X_q\cdot E_{ph}\right)}{R_{ph}^2+X_d\cdot X_q}$	
(12)	$I_q = \dfrac{\left(U_{ph}\cdot\left(X_q\cdot\sin\psi + R_{ph}\cdot\cos\psi\right)-R_{ph}\cdot E_{ph}\right)}{R_{ph}^2+X_d\cdot X_q}$	
(13)	$P_m = P_e - \sum Losses$	
(14)	$T = \dfrac{P_m}{\Omega_s},$	
(15)	$\cos\varphi = \dfrac{P_e}{m\cdot U_{ph}\cdot I_{ph}},$	
(16)	$\eta = \dfrac{P_m}{P_e}.$	

- for the PM: B_r, the remanent flux density; H_c, the coercitive field intensity; μ_r, the relative permeability; h_m, length on the magnetization direction; b_m (b_{m2} for **d** and **e** topologies), the width of the magnet pieces; S_m the PM surface area.
- concerning the rotor's pole: p, pole pair number; S_p, the pole surface area; τ_p, polar pitch.
- the air gap: B_δ, the flux density; δ_c, the air gap modified by Carter's coefficient; R_δ, the air gap radius; μ_0 air permeability.
- for the stator armature: m, number of phases; q, the number of slots/pole/phase; f_s, the frequency; N_s, number of turns per phase; k_{ws}, winding coefficient.
- geometrical parameters: R_{si}, inner stator radius; R_{cr}, rotor core radius; l, the active motor length; x, the iron bridge height (for the **c**, **d** and **e** structures); y (y_2 for **d** and **e** topologies), the number of PM layers.
- electro-magnetic values: X_m, the magnetizing reactance, Λ_σ, the leakage permeance, X_σ the leakage reactance; E_{ph}, the phase induced electromotive force; Φ_m, permanent magnet flux; U_{ph}, phase voltage; I_{ph}, phase current; $I_{d,q}$, direct and in quadrature current; P_e, the supplied power; $cos\varphi$, the power factor; ψ, the internal angle.
- mechanical parameters: P_m, mechanical power; T, motor torque; η, the efficiency; Ω_s, the speed.
- others coefficients: σ, leakage coefficient, $k_{ad,\,aq}$, the direct and quadrature axis coefficients which express the saliency ratio; $k_{sd,sq}$, the direct and in quadrature axis saturation coefficients; k_{di} the irreversible demagnetization coefficient.

The analytical approach being applied, the permanent magnet machines performances resulted. The first remark regards the **SMPM** structure, where, because of the unitary saliency ratio ($\xi=1$, $X_d=X_q$), the maximal stability point is found to 90° of the internal angle (see figure 2).

On the other hand, for all the **IPM** machines (*b* to *e* variants from figure 1), because of the reverse saliency ration ($X_q/X_d > 1$), a reluctance torque interferes. The maximal torque, which establishes the stability-operating limit, is obtained at around 100° of the internal angle (see also figure 2).

The rated torque (35 Nm) is reached for the surface brushless DC **(SBDC)** topology at 14° of the internal angle. For the second variant (**IPM-fc**), the rated torque is

reached for 20° of the internal angle. Rated current, 55A for both, (*a*) and *(b)* variants, is pointed on in the current vs. internal angle variation (see figure 3). The electrical and mechanical powers vs. internal angle dependencies on the stability zone are shown in figure 4. Also, the efficiency and the power factor, in the stability operating region, are presented in figures 5 and 6, respectively (without taken into account the inverter capability [2]).

Moreover, the same results can be performed for the other **IPM** machines (i.e. – the results for the *c* to *e* topologies were omitted in this paper for the sake of presentation).

The main performances for all variants, at the rated point operating, are presented in table 2.

Table 2

Performances comparison for the rated operating point of different rotor variants

Motor type	Power vs. Weight, [kW/kg]	Weight vs. Costs, [kg/€]	η	cos φ
SPMSM	5.5 / 22.5	22.5 / 283	0.95	0.98
IPM (b)	5.5 / 26.3	26.3 / 521	0.93	0.99
IPM (c)	5.5 / 24.7	24.7 / 325	0.93	0.99
IPM (d)	5.5 / 25.1	25.1 / 344	0.92	0.99
IPM (e)	5.5 / 25.4	25.4 / 350	0.92	0.99

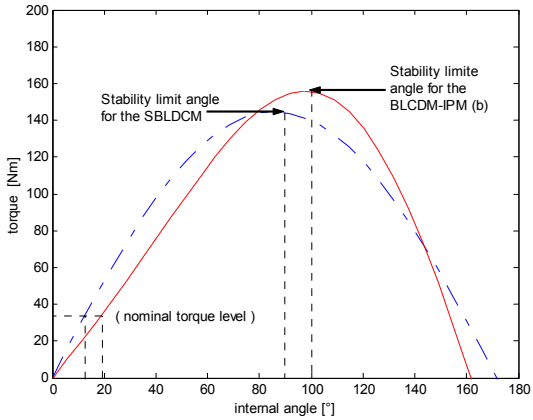

Fig. 2 Torque vs. internal angle dependencies

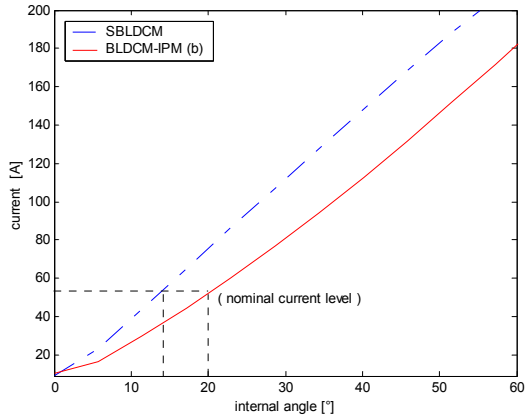

Fig. 3 Current vs. internal angle dependencies

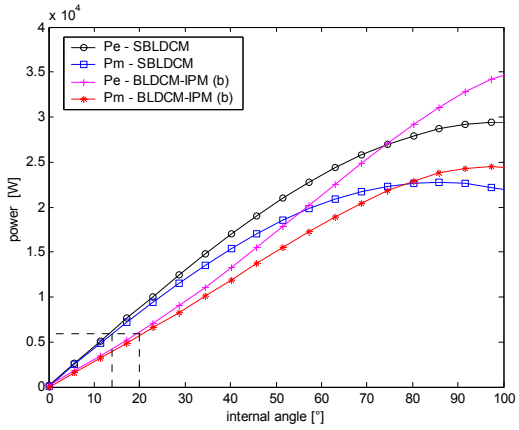

Fig. 4 Electrical and mechanical power vs. internal angle dependencies

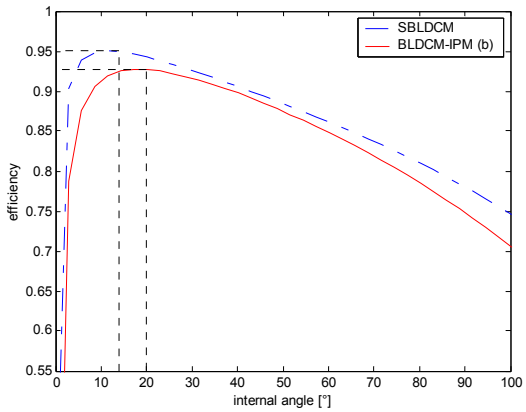

Fig. 5 Efficiency vs. internal angle dependencies

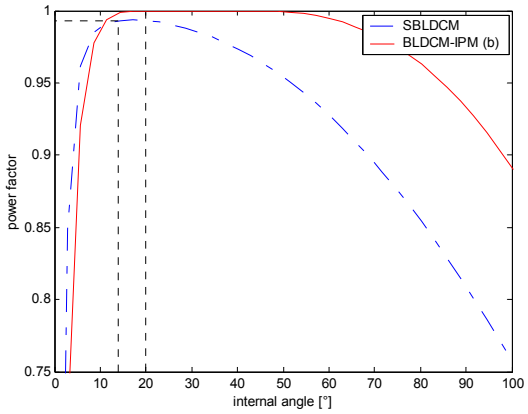

Fig. 6 Power factor vs. internal angle dependencies

FEM approach

The rated operating conditions were acquired by analytical modeling. In order to validate this approach, the numerical analysis must be taken into consideration. Despite of the fact that the FEM is time consuming, the accuracy of such a study brings out the real performances of the designed drive and the analytical model can be validate.

In our days there are many softwares developed for FEM analysis. The field lines, the flux density repartition and even the transient operating regime can be observed and assess. However, the special machines applications require much accuracy in the control process. The supplying capability and the switching behavior are more difficult when high drive performance applications are required. As a response to these complexity issues the *Flux2D to Simulink coupling technique* can accomplish our needs.

To simulate the transient operating regime, a classical 120° supply is considered for each studied variant. The main control panel is drawn as *Simulink* block.

The inverter-switching scheme, depending on the rotor position, is presented in figure 7a. The switches are modelled by resistances with a very low value to model *on*-state and very large value to model *off*-state (see figure 7*b* for the switching scheme and *7c* for the logic commutation). This approach is adopted since as input parameter we can have only an electrical (voltage, current, resistance, inductance) or a mechanical (speed, torque, inertia, position) quantity, respectively.

The middle part in figure 7 represents the coupling block with our application modelled in the numerical **FEM** software, *Flux2D*. A classical three phases inverter for brushless PM drives is behind this block. The battery source is one of 48 V-dc. A coil models each phase of the motor winding, with the correspondent resistance and the number of turns. The associated values for the electrical components must take into account the geometry structure. Only ¼ parts of the motor's geometry being represented, all the numerical parameters are divided by 4 – 12V for the voltage source and, because the phase resistance in the SBLDCM is 0.0223 ohm, the insert resistance value is 5.57e-3 ohm.

The field lines distributions in no-load operating of the studied brushless drives are presented in figure 1.

The 120° switching behavior of the three-phase inverter is plotted in figure 8.

The output parameters are, in our case, the speed, the torque, the position (which is the close loop parameter), the current and the voltage drop per phase - other electrical or mechanical parameters can be considered as outputs. To obtain the electrical position as input parameter, a *Simulink* block 'mod' is added to multiply the mechanical output position with the electric period (in our situation, it is about 4 poles motor and the electrical period is corresponding to a pair of poles, which means 180 electrical degrees).

For the transient operating, a resistant torque (rated torque) was imposed, and, off course, the moment inertia was also considered. All the results plotted in figures 9-12 correspond to the first permanent magnet structure, namely the SBLDCM, in order to have a comparison with the analytical results, (see figures 2 to 6).

The same kind of study and control strategy can be adapted for each permanent magnet topology. The results obtained after the transient regime simulations for each variant are not presented in this paper for the sake of space. In a further work, the flux weakening control and the wide speed range capability would be employed for comparison.

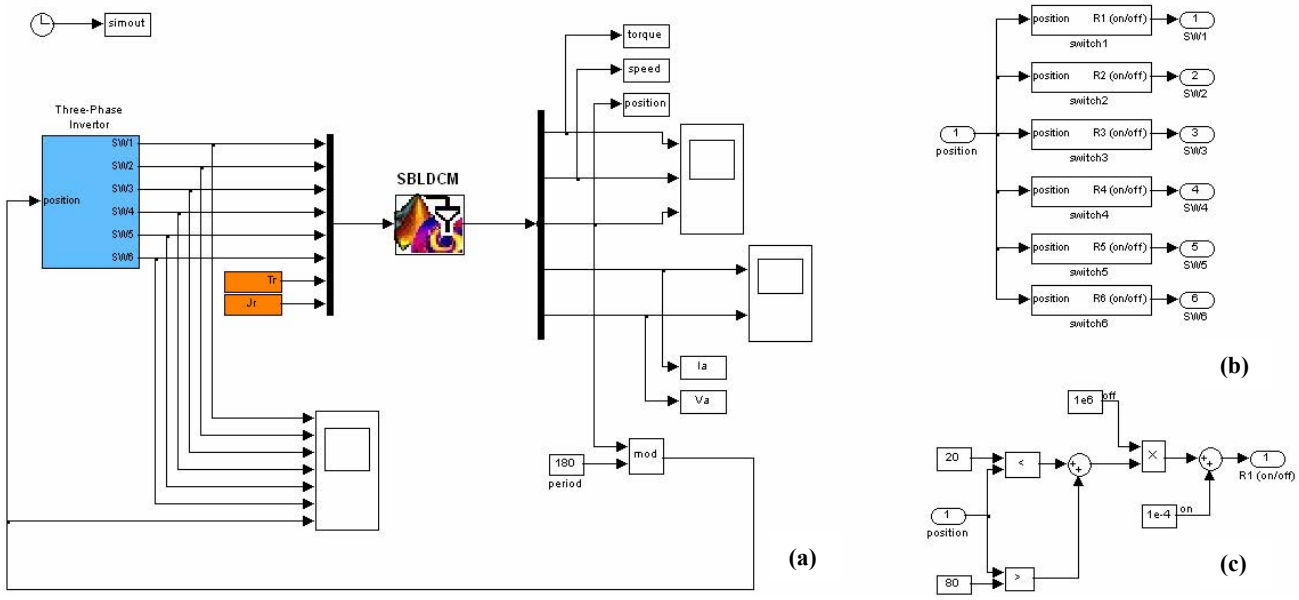

Fig.7 Control panel for the transient behaviour of a BLDC drive (a) – the switching scheme (b) – the logic commutation (c)

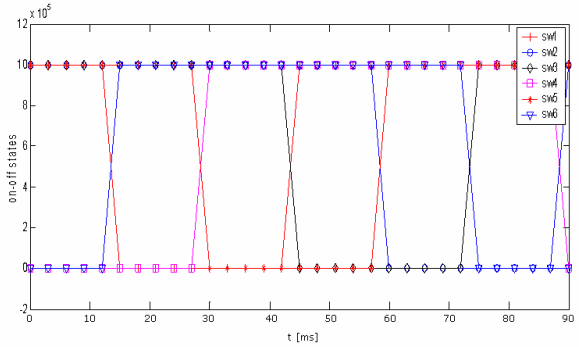

Fig. 8 The switching behavior for 120° control supply

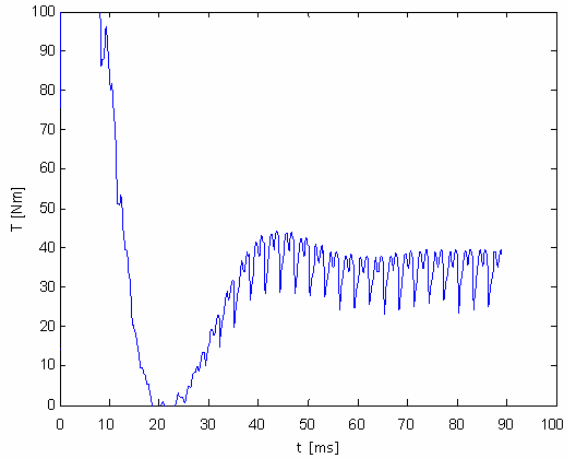

Fig. 9 The torque vs. time variation in transient operating for the SBLDCM

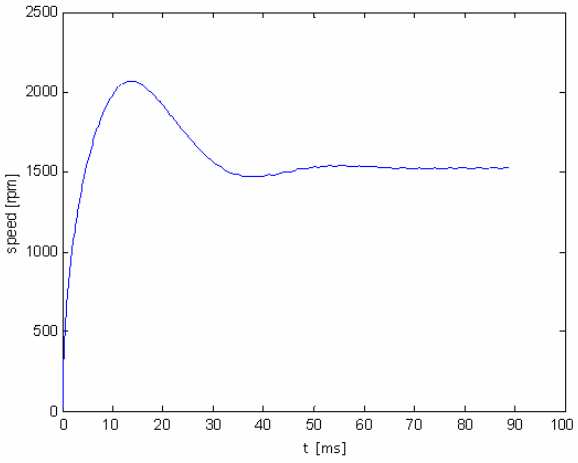

Fig. 10 The speed vs. time variation in transient operating for the SBLDCM

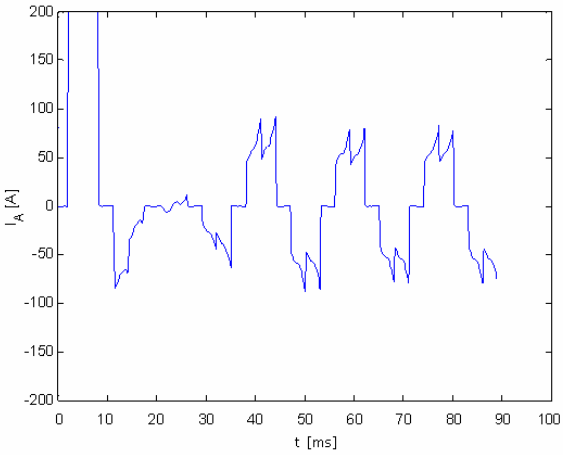

Fig. 11 The phase current waves, for the SBLDCM

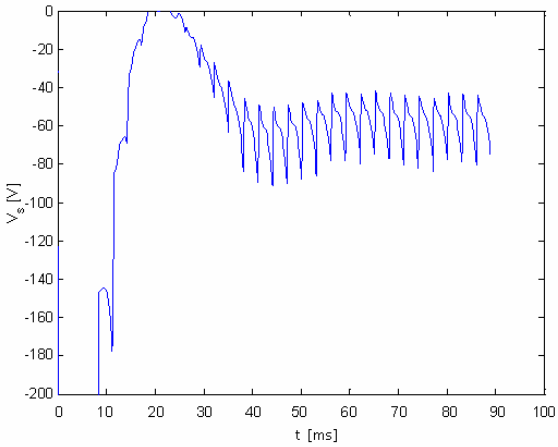

Fig. 12 The inverter current waves, for the SBLDCM

The rated torque obtained to the respective internal angle from the analytical model (see figure 2) is reached also (figure 9), at the rated speed - figure 10 -, in transient simulation. The rated current from the analytical approach (figure 3) is pointed on in the transient regime as the phase current (figure 11) supplied by the inverter source (figure 12).

From the results obtained in transient regime simulation at the rated operating point, a good concordance can be observed in terms of torque, speed and current performances.

Conclusions

The main permanent magnet brushless motors were introduced in this paper. An analytic design procedure was presented for the studied topologies and the rated operating point performances comparison was made. The numerical analysis is generally employed in order to validate the analytical design. Using the Flux2D to Simulink coupling technology the transient behavior of the surface permanent magnet brushless dc motor (**SBLDCM**) was simulated. At the rated point operating, a good concordance was found between the numerical and analytical approach.

References

[1] J.R. Hendershot, T.J.E. Miller: Design of brushless permanent magnet motors, Magna Physics Publications, Oxford, 1994, ISBN-0-19-859369-4.

[2] S. Meier: "Theoretical design of Surface-Mounted Permanent Magnet Motors with Field-weakening Capability", Master Thesis, Royal Institute of Technology, Stockholm, Sweden, March 2002.

[3] N. Bianchi: "Radially magnetized interior-permanent-magnet synchronous motor for high-speed drive: an analytical and finite-element combined design procedure", Electromotion, vol.6, 1999, pp.103-111.

[4] E. Nipp: "Permanent magnet motor drives with switched stator windings", PhD. Thesis, Royal Institute of Technology, Stockholm, 1999.

[5] E. Lovelace: "Optimization of a magnetically saturable interior permanent magnet synchronous machine drive", PhD. Thesis, Massachusetts Institute of Technology, June 2000.

Daniel Fodorean *– Ph.D. Student, Faculty of Electrical Engineering, Technical University of Cluj-Napoca, 15 Daicoviciu Str., 400020, Cluj-Napoca, Romania.*
e-mail: daniel.fodorean@personal.ro

Ioan-Adrian Viorel *– Professor, DSc., Faculty of Electrical Engineering, Technical University of Cluj-Napoca, 15 Daicoviciu Str., 400020, Cluj-Napoca, Romania.*
e-mail: ioan.adrian.viorel@mae.utcluj.ro

Abdesslem Djerdir *– Associate Professort, Dr., Technological University of Belfort-Montbéliard, Department of Electrical Engineering, 13 Thiery Mieg Str., 90010, Belfort, France.*
e-mail: abdesslem.djerdir@utbm.fr

Abdellatif Miraoui *– Professor, DSc., Technological University of Belfort-Montbéliard, Department of Electrical Engineering, 13 Thiery Mieg Str., 90010, Belfort, France.*
e-mail: abdellatif.miraoui@utbm.fr

Brushless DC Motor with Unsymmetrical Magnetization and Combination Control

Sameer H. Khader

Abstract: *This paper describe mathematical method which looks for optimized electromagnetic torque with reduced ripple in both single-phase and two-phase brushless dc motor with special rotor construction. The conventional two-phase two-pulse brushless dc motor requires special construction with aim to realize successful starting and ensuring relatively constant torque independent of the rotor position . Three methods are described:*

- *Pulse Width Modulation (PWM) control strategy with skewed stator poles, which introduce unsymmetrical airgap magnetic field with eliminated low-order current harmonics.*
- *PWM control strategy with symmetrical stator poles and shorted coil pitch.*
- *Combined PWM and continuous control signal energized two-phase three-windings motor and unsymmetrical rotor construction, where it is expected producing electromagnetic torque with reduced ripples and increasing stability, independent of the rotor position.*

The electromagnetic torque produced by motors using each of these methods is calculated by applying Co energy method. The numerically obtained results are going to be verified with experimental results in the next paper, and it is expected to obtained good coincidence between both results.

Keywords: *DC Motors, Synchronous Motors, and PWM.*

Introduction

Unlike a conventional dc motor, brushless dc motors has an " inside-out" construction [1-2], i.e. the field poles rotate and the armature is stationary . The field poles consist of permanent magnets mounted on the outside of the rotor surface, and the armature is wound on a slotted or a salient pole laminated sheets. The armature coils are switched by transistors instead of the commutator. This arrangement has several advantages over small conventional DC motor or AC motor such as 1) high efficiency, 2) adaptability for speed control, 3) high speed operation, 4) long operation life and absent rotor losses in additional with operation from low voltage dc supply .

Typical small-power applications is in dc fans for cooling electronic equipments and closed spaces . Brushless dc motor fans are smaller in size and weight than ac fans using shaded pole or Universal motors.

Ability to work with the available 24-v or 12-v dc supply makes the brushless dc motor fans convenient for use in electronic equipment, computers, mobile equipment, vehicles, and spindle drives for disk memories, because of its high reliability, efficiency, and ability to reverse rapidly. Brushless dc motors in the fractional horsepower range have been used in various types of actuators in advanced aircraft and satellite systems [3- 4].

Together with applying permanent magnet excitation, it is necessary to obtain an additional torque components, which could be obtained due to difference in magnetic permeance in both quadrant and direct axis, therefore, reluctance torque is developed and torque –null regions are eliminated [5-6]. Unsymmetrical air gap rotor construction are introduced to reduce the torque ripples and to increase the mean torque.

The low level of fluctuation in the magnitude and orientation of the armature-current patterns that is a standard future of well designed DC machines is normally absent in inverter-fed synchronous motors.

This seams from a relatively small number of switched armature-winding portions in the vast majority of synchronous motors and from the changes in phase angle between current and voltage that occur as load and speed varies. Fluctuations due to the latter usually occur relatively slowly and can be minimized by the use of current-forcing techniques or by appropriate control of switching instants.

Analysis

Motor windings and the Phase current

Brushless dc motors could be applied for various types of windings: single-phase single pulse, two-phase two pulse, three-phase three pulse or six pulse dc motors . The interest on two-phase brushless dc motor comes due to reduction of the driving circuit and total cost of the motor.

The elementary two-phase Brushless dc motor circuit usually consists of a permanent magnet rotor and stator with two windings located on the same magnetic axis, and drives by two power transistors controlled by sensing units, each transistor is switched on for 180°. The torque produced by the interaction of the rotor magnetic field and the winding current nulls each 180°. The presence of null points in electromagnetic torque are the main limitation for widespread application because of the following several reasons: first , the motor will not start from the null position, second, high ripples in the electromagnetic torque, therefore the speed will fluctuate with rotor position , and third, high current at low speed and additional losses. These disadvantages makes the motor impractical for commercial use unless one of the

following solutions are taken to overcome the main drawbacks :

❖Polyphase motor: this motor has no torque nulls and relatively constant torque. This motor is not a subject of this paper.

❖Unsymmetrical rotor construction : the rotor teeth are performed with predetermined high and width, this made with purpose to obtain unsymmetrical magnetic permance around the rotor surface .Taking into account motor design data and rotor construction illustrated on Fig.1, which is the subject of present study .

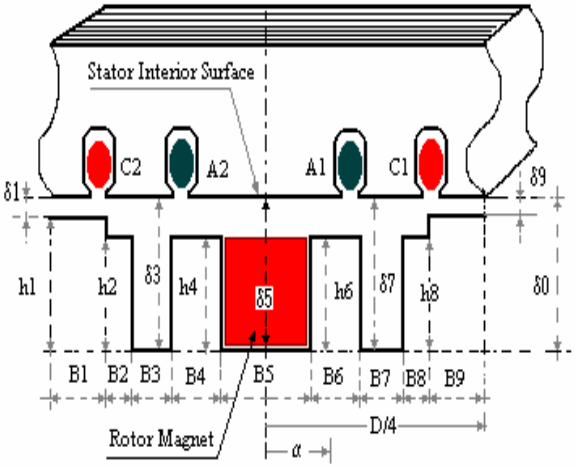

Fig.1. Motor construction

The magnetic permance yield due to the difference in the stator construction could be changed depending on the Rotor slots width and depth .

Fig.2 illustrates the harmonic spectrum of the magnetic permance distribution in the airgap with respect to rotor main tooth width , where it is clearly shown that by introducing some asymmetry in the rotor construction high order harmonic of magnetic permance are realized. This construction leads to avoiding null points in the electromagnetic torque .

By applying above mentioned construction the motor will produce two torque components: 1) an electromagnetic torque which form is expected to be sinusoidal positive change, and 2) a reluctance

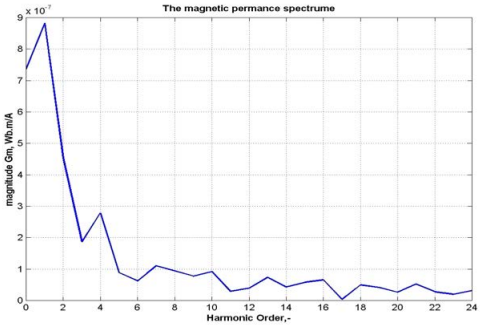

Fig2. the obtained harmonic spectrum of magnetic permance at variable airgap depth .

component with nulls of the torque does not coincides with the nulls of the electromagnetic torque .

The torque ripples could be reduced furthermore by representing an innovative way to resolve the two-phase limitation and to achieve relatively ripples-free torque. One of these solutions is presented in this paper ,which called a combination control method.

❖Combination control : This type of motor control presents two solutions at the same time – first one unsymmetrical rotor construction is introduced with purpose to avoid torque-nulls points, and second solution is PWM control drives additional bi-directional stator switching circuit as well shown on Fig.3a, where the time-switching diagram is shown on Fig.3b . Third winding S3 on the figure has uniform distribution in the stator periphery with aim to obtain approximately sinusoidal flux distribution in the airgap, this coil has less number of windings comparing with another two coils S1 & S2.

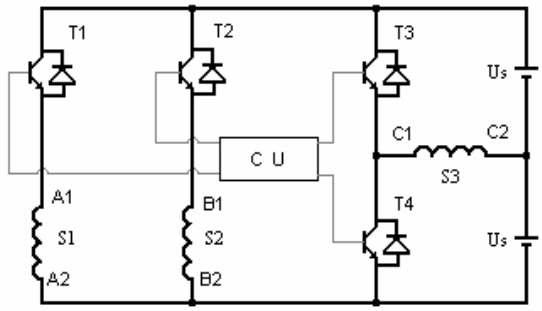

Fig.3a. Electrical simplified circuit

1. Switching pulse generation

Transistors T1 and T2 are switched continuously for 180° each one and connect the supply voltage to the coils S1 and S2 in complementary sequence.

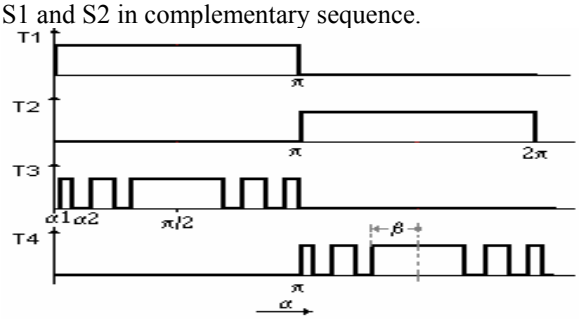

Fig.3b. Pulse generation wave form-illustration

Transistors T3 and T4 are connect the supply voltage to the third coil with polarity and time-duration determined from the applied PWM control strategy .

2. Phase current calculation

The motor phase current differs in coils S1,S2 and S3, where the current in first two coils has continuous character and approximately constant value at steady state operation, while the current in third coil takes form nearly to the sinusoidal form depending on the pulse PWM control strategy , induced counter EMF and magnetic permance .

Phase currents IA(ωt) :

Phase current of IA(ωt) and IB(ωt) in integral form are presented as follow for one phase only, second phase has the same relations:

$$\int_0^{\pi} 1 di_A(\alpha) = \int_0^{\pi} \frac{U_{dS} - e_A(\alpha)}{L_A(\alpha)} d\alpha + \int_0^{\pi} \frac{R_A i_A(\alpha)}{L_A(\alpha)} d\alpha + \int_0^{\pi} \frac{i_A(\alpha)}{L_A(\alpha)} \left[\frac{d}{d\alpha} L_A(\alpha)\right] d\alpha \quad (1)$$

The obtained results are displayed on Fig.4 for both phases, where each phase operates 180°. It is clearly shown that the phase current depends on the rotor position .

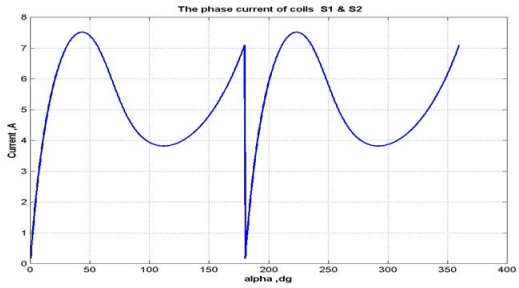

Fig.4. Phase current of both coils S1 & S2

Phase current IC(ωt) :

The coil current IC(ωt) could be calculated, taking into account the results of modulation function h(ωt) as well described in [7]. The time duration of generated train of pulses depends on the selected harmonic that must be eliminated while existing on the quarter wave interval from αmin to αmax.

The Fourier series could be presented by assuming the following harmonic function [8], which applied for elimination some of predetermined harmonics :

$$h(\alpha) = \sum_{n=1}^{\infty} A_n \sin(n\alpha)$$

$$A_n = \frac{4}{n\pi} \sum_{k=1}^{N_p} (-1)^{k+1} \cos(n\alpha_k) \quad (2)$$

where Np- odd or even numbers, α=ωt, and αmin <α1 <α2 ……...<αk < π/2, and n1, n2,……nNp are harmonics that to be eliminated.

A set of algebraic equations with respect to h(ωt) must be satisfied to reduce the coefficients of each harmonic to be eliminated to zero:

$$0 = \sum_{k=1}^{\infty} (-1)^{k+1} \cdot \cos(n_1 \alpha_k)$$

.

$$0 = \sum_{k=1}^{\infty} (-1)^{k+1} \cdot \cos(n_{Np} \alpha_k) \quad (3)$$

The obtained algebraic matrix is solved, where a set of pulse patterns are calculated, and the obtained waveform of applied phase voltage at certain speed and frequency is presented on Fig.5.

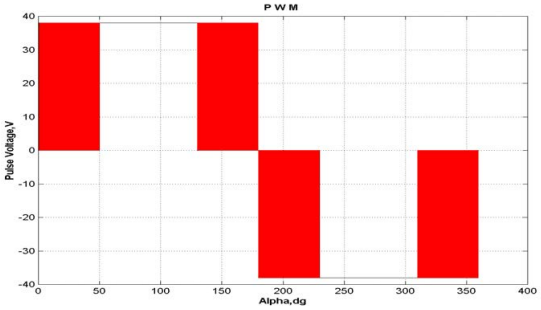

Fig.5. Phase voltage of coil S3

By applying KVL, and taking into account motor equivalent circuit with concentrated parameters the voltage equation for third coil, and back emf of the same coil are :

$$U_d = U_S \cdot h(\alpha)$$

$$U_d = R_C i_C(\alpha) + \frac{d}{d\alpha} \lambda_C(\alpha) + e_C(\alpha)$$

$$e_C(\alpha) = Em_C \sin(\alpha)$$

$$\lambda_C(\alpha) = L_C(\alpha) \cdot i_C(\alpha) \quad (4)$$

Where the leakage inductance of third coil and it's dependency on the rotor position is presented as follow :

$$L_C(\alpha) = L_0 + \sum_{q=1}^{\infty} L_{2m} \cos(2q\alpha) \quad (5)$$

Substituting eq.(5) in eq.(4), which can be expressed as follow :

$$U_d - e_C(\alpha) = R_C i_C(\alpha) + L_C(\alpha) \cdot \frac{d}{d\alpha} i_C(\alpha) + i_C(\alpha) \cdot \frac{d}{d\alpha} L_C(\alpha) \quad (6)$$

By applying the principle of implicit integration, which form is present below :

$$\int_{\alpha_1}^{\alpha_2} 1 di_C(\alpha) = \int_{\alpha_1}^{\alpha_2} \frac{U_d - e_C(\alpha)}{L_C(\alpha)} d\alpha + \int_{\alpha_1}^{\alpha_2} \frac{R_C i_C(\alpha)}{L_C(\alpha)} d\alpha + \int_{\alpha_1}^{\alpha_2} \frac{i_C(\alpha)}{L_C(\alpha)} \left[\frac{d}{d\alpha} L_C(\alpha)\right] d\alpha$$

(7)

The results of solving eq.(7) for various modulation index, modulation frequency and speed are graphically displayed on Fig.6.

$$i_C(\alpha) = \sum_{\nu=1}^{\infty} I_{m\nu} \cdot \sin\left(\omega t - \psi_\nu\right)$$

(8)

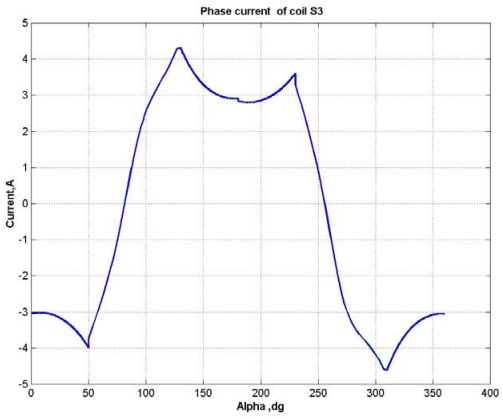

Fig.6.Phase current of S3 at given motor speed.

Electromagnetic Torque:

In this section two-types of two-phase, two-pulse brushless dc motors are going to be described :

a) Unsymmetrical rotor construction: the torque consists of two components[1-4] reluctance torque T_{RA} and electromagnetic torque T_{EA}, where this torque is going to be called " original " in this study .

The reluctance torque : this torque is independent of the excitation of stator coil and depends upon the permance of the airgap as seen by the rotor magnets. As stator consist of laminated sheets with slots , the rotor consist of massive iron core with special slots having different geometrical construction. The permance in the airgap varied periodically with the rotor position , being maximum at the axis of the stator poles. Consider the rotor construction shown on Fig.1, the reluctance torque is calculated using coenergy method as follow:

$$T_{RA} = \frac{d}{d\alpha} W_{RA}(\alpha) = 0.5 F_{SA} \cdot \frac{d}{d\alpha} G(\alpha)$$

where

$$F_{SA} = N_{phA} I_A K_{wA}$$

$$G(\alpha) = G_0 + \sum_{g=2}^{\infty} G_{mg} \cos\left[N_{tg}\left(\alpha - \beta_g\right)\right]$$

$$N_{tg} = g \cdot N_t$$

(9)

The final expression for reluctance torque is :

$$T_{RA} = \left(F_{SA}\right)^2 \left(G_2 \sin 2\left(\alpha - \beta_2\right) + 2 G_4 \sin 4\left(\alpha - \beta_4\right)\right)$$

(10)

The obtained reluctance torque expression indicates that null points torque occurs at $\alpha \neq 90°, 180°, \ldots\ldots$, which is good indicator for realizing self starting torque .

The electromagnetic Torque: this component of torque is obtained due to the interaction between stator coil current and rotor magnets , where the mathematical expression based on coenergy method [9,10] for determination the electromagnetic toque is presented as follow :

$$T_{EA} = \frac{d}{d\alpha} W_{EA}(\alpha) = F_{SA} \cdot \phi_R(\alpha)$$

(11)

where,

$$\phi_R(\alpha) = \int_{\frac{-\pi}{2}}^{\frac{\pi}{2}} F_R \cdot \cos(\theta - \alpha) \cdot G(\alpha) d\alpha$$

is the produced rotor flux in the airgap, which depends on the magnetic permance and rotor MMF produced form the permanent magnet intensity and length. The mathematical expression is given below:

$$\phi_R(\alpha) = F_R A \cos\alpha + F_R B \sin\alpha$$

where

$$A = 2 G_0 + \frac{2}{3} G_2 \cos 2\beta_2 - \frac{2}{15} G_4 \cos 4\beta_4$$

$$B = \frac{4}{3} G_2 \sin 2\beta_2 - \frac{8}{15} G_4 \sin 4\beta_4$$

$$F_R = L_m H_m$$

(12)

The final expression for electromagnetic torque for one coil S1 or S2 is :

$$T_{EA} = F_{SA} F_R A \sin\alpha - F_{SA} F_R A \cos\alpha$$

(13)

The total motor tor$T$que T_{TA}, presents sum of both torques taking into account eq.(10) and eq.(13), with graphically results illustrated on Fig.7. for certain speed, where its clearly shown that the motor achieved self starting condition.

$$T_{TA} = T_{EA} + T_{RA} \quad (14)$$

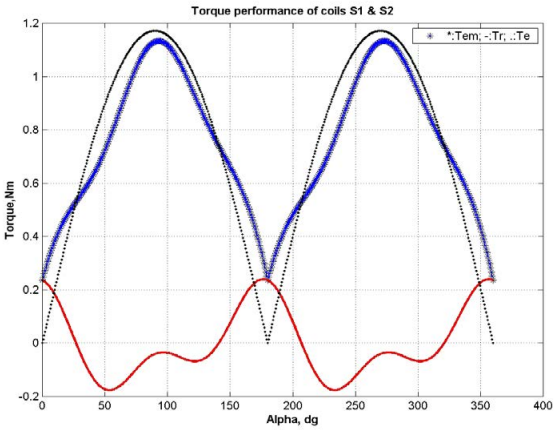

Fig.7. Total Electromagnetic torque of coils S1 & S2.

At the same time the generated torque ripples are relatively high, which is the main drawback of this design version . These ripples could be reduced extremely by applying the combination control method, where the produced torque is described hereinafter.

b) Combined control method: this method is concentrated in producing additional torque by third coil S3, and have a purpose to eliminate the weak regions of the original torque . Further more , the produced torque will play significant role in ripples reduction overall the speed range , average torque increasing, and finally as a result from this procedure achieving more speed stability with minimized fluctuations, which is important criteria in electrical drive technology . The torque expression is presented as follow, based on coenergy method:

$$T_{TC} = \frac{d}{d\alpha} W_{EC}(\alpha)$$

$$W_{EC}(\alpha) = \frac{1}{2}\left[F_{SC}(\alpha,\omega t)\right]^2 . G(\alpha) + . F_{SC}(\alpha,\omega t)\,\phi_R(\alpha) \quad (15)$$

The stator MMF produced by third coil S3 with current Ic(ωt) flow through distributed winding in the stator periphery has space time variation with stepped character and minimized space-time ripples. Writing the trigonometrically terms as sums and differences leads to the following expression :

$$F_{SC}(\alpha,\omega t) = \frac{N_{phC}\, I_{m1}}{\pi} \sum_{\nu=1}^{\infty} \sum_{\gamma=1}^{\infty} \frac{K_{\nu i}\, K_{\omega\gamma}}{\gamma} X(\nu,\gamma)\cos(\nu\omega t - \gamma\alpha) \; Y(\nu,\gamma)\cos(\nu\omega t + \gamma\alpha)$$

where

$$X(\nu,\gamma) = 1 + \cos(\nu-\gamma)\frac{\pi}{2} \qquad Y(\nu,\gamma) = 1 + \cos(\nu+\gamma)\frac{\pi}{2} \qquad K_{\nu i} = \frac{I_{m\nu}}{I_{m1}} \quad (16)$$

Since the phase current Ic(ωt) depends on the rotor position and induced back EMF, the electromagnetic torque produced by this coil T_{TC} will changes alternatively, which means that in some regions will added to the original torques and subtracted in another regions . As a result from this adding and subtraction the produced total electromagnetic torque is expected to be with reduced ripples. Hereinafter mathematical expression explaining the dependency of T_{TC} on many parameters expressed in eq.(15) and eq.(16), and leads to the following :

$$T_{TC} = T_{EC1} + T_{EC2} + T_{EC3} + T_{EC4}$$

where

$$T_{EC1} = F_{SC}(\alpha,\omega t) . G(\alpha) \frac{d}{d\alpha} F_{SC}(\alpha,\omega t)$$

$$T_{EC2} = \frac{1}{2}\left[F_{SC}(\alpha,\omega t)\right]^2 . \frac{d}{d\alpha} G(\alpha)$$

$$T_{EC3} = F_{SC}(\alpha,\omega t) . \frac{d}{d\alpha}\phi_R(\alpha)$$

$$T_{EC4} = \phi_R(\alpha) . \frac{d}{d\alpha} F_{SC}(\alpha,\omega t) \quad (17)$$

The obtained torque components of eq.(17) are graphically displayed on Fig.8. at the same conditions, where this torque has rich harmonic spectrum when operates alone, but will improve the total motor torque when acts together with the original torque .

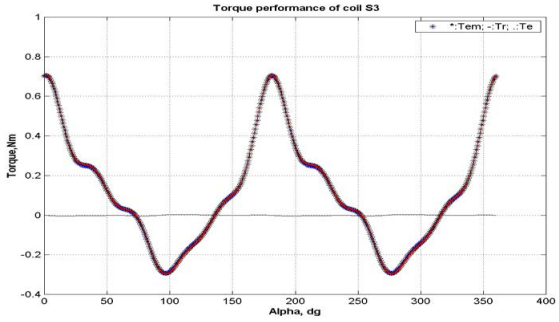

Fig.8.Total electromagnetic torque of S3

The total torque produced by three coils is the sum of eq.(14) and eg.(17) as follow:

$$T_{EM} = T_{TA} + T_{TC} \quad (18)$$

The torque results are graphically displayed on Fig.9a. for certain motor speed, and the torque harmonic spectrum is displayed on Fig.9b. From displayed .results it is shown that the put up tasks have been achieved .

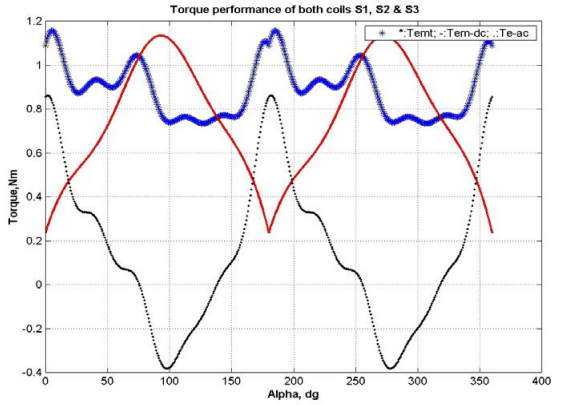

a)

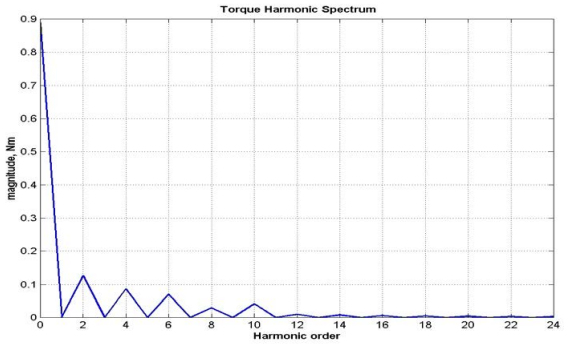

b)

Fig.9:a) The total electromagnetic torque of both coils S1, S2 & S3; b) The torque harmonic spectrum .

Results

Refer to the motor design parameters listed in Table1, with various rotor design parameter, the discussed results in previous section can be supported with additional conclusive parameters [11, 12] as follow :

Torque-Current ratio : this parameters presents the ratio of obtained mean torque to the root-mean square current :

$$T_{CR} = \frac{T_{AV}}{I_{TRMS}}$$

where

$$I_{TRMS} = \sqrt{\sum_{\nu=1}^{\infty} \left(I_{\nu RMS}\right)^2} \quad (19)$$

Torque ripple factor : this parameters presents the ratio of the torque ripples to motor mean torque :

$$T_{RR} = \frac{T_R}{T_{AV}}$$

where

$$T_R = \sqrt{T^{-1} \int_0^T \left(T_{EM} - T_{AV}\right)^2 d\alpha} \quad (20)$$

Current harmonic factor : this parameters presents the ratio of total rms current to the fundamental:

$$H_{FI} = \sqrt{\left(\frac{I_{TRMS}}{I_{RMS}}\right)^2 - 1} \quad (21)$$

These parameters are going to be discussed for the following cases :

Case#1 : The width of control signal β (see Fig.3b) could be varied, where the obtained results are graphically illustrated on Fig.10. From these results it is clearly shown that the motor mean (average) torque strongly increased by increasing β, but this increasing at the expense of torque-current ratio decreasing especially at certain value of β >65 ° . Furthermore the torque ripples factor reached it is minimized value at certain β=65° , while the current harmonic factor reached it is maximum value. This means that the pulse width must satisfy two contradict requirements high T_{CR} and relatively low H_{FI} .

Case#2 : The width of main rotor slot B5 (see Fig.1) could be varied, where the obtained results are graphically illustrated on fig11. From these results it is clearly shown that the motor mean torque strongly decreases by increasing B5, also T_{CR} decreases in the same manner . The torque ripples and the current harmonic factor have acceptable values at B5=5..10 mm comparing with these results obtained for B5 >10 mm . The torque ripples raised significantly at certain value of B5>12 mm, which means that the rotor construction must designed for B5 < 12mm .

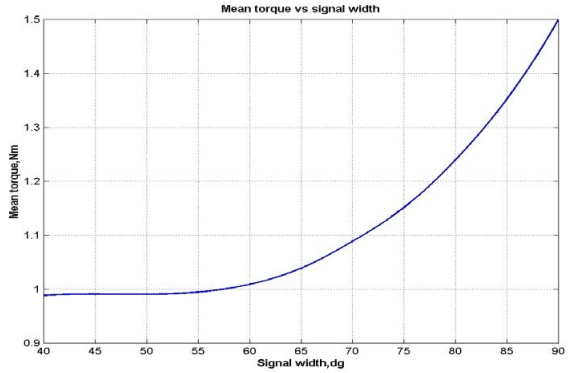

a)

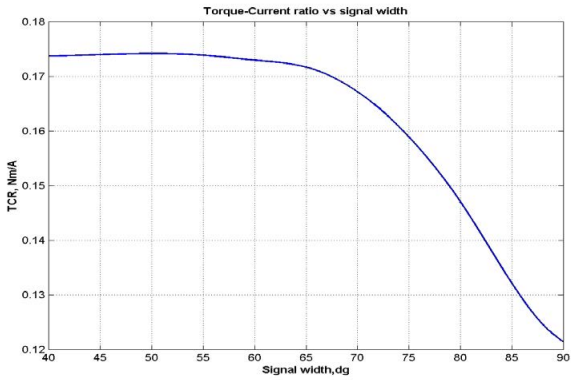

b)

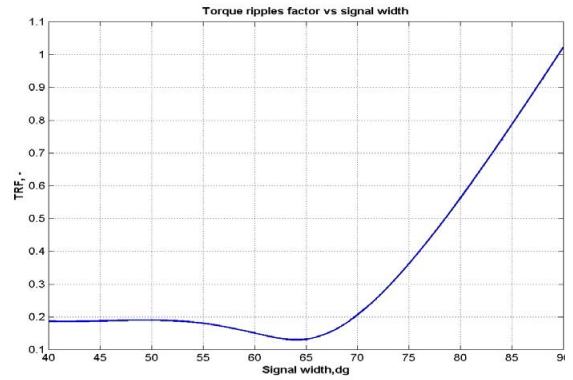

c)

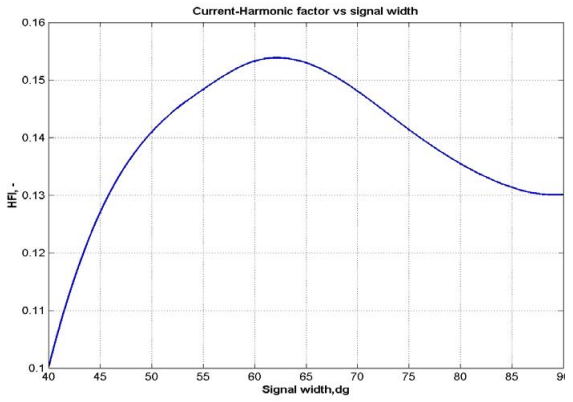

d)

Fig.10. a)The mean torque ; b)Torque-Current ratio ; c) Torque ripples factor ; and d) Current harmonic factor versus signal width β.

Tab.1: The motor parameters

Phase voltage Vs, V	38
The induced counter voltage in coil S1,EmA, V	33
The phase resistance of coils S1 & s2 RA, Ω	0.3
The phase resistance of coil S3 RC, Ω	8.5
The number of conductors of S1 & s2, NphA, conductors/ pole	60
The number of conductors of S3, NphC, conductors/ pole	80
The pole pairs number P	2
The induced voltage frequency f1, Hz	50
The modulation frequency fm, kHz	20
The stator interior diameter D, mm	54
The number of stator slots / pole S	4
The permanent magnet density Bm T	0.6
The stator active length Lδ, mm	65
The permanent magnet coercive force (intensity) Hm, kA/m	40

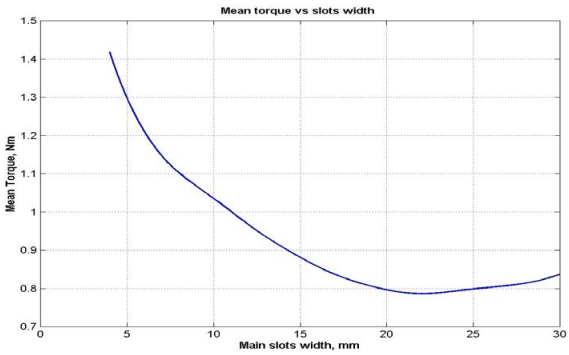

a)

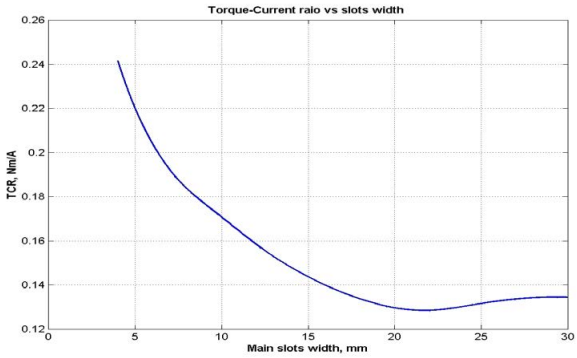

b)

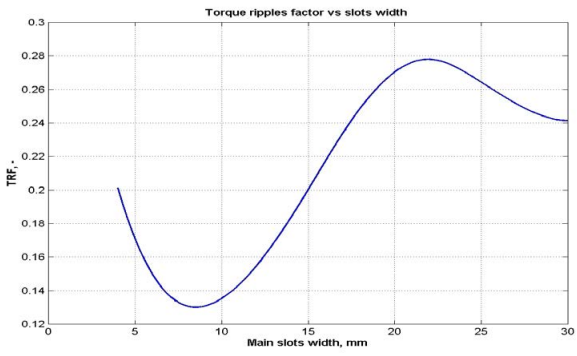

c)

Fig.11. a) Motor mean torque ; b) Torque-Current ratio ; and c) Torque ripples versus slots width B5, mm. .

Conclusion

The applied innovative design of two phase/ three coils two-pulse brushless DC motor with combined control produced electromagnetic torque having self-starting and reduced fluctuation . This is due to the dissymmetry in the rotor construction where the reluctance torque nulls do not occur at the same angles of the electromagnetic torque .

1-By introducing the PWM control of third coil torque ripples are further decreases, because of the generated train of pulses with variable width. Once torque ripples decreases, the additional stability in the motor torque could be achieved, dissipated power reduction and motor utilization ncreases. The motor electromagnetic performances are directly depends on the continuous width of the PWM signal β, where by increasing this angle the Torque-current ration keeps relatively acceptable result .

2-Discussed results related to rotor slots width, where illustrated graphically mentioned that by increasing the width of main rotor slot B5, the consumed phase current increases with purpose to cover the required MMF . At the same time the mean torque decreases because of additional reduction in the magnetic permance. The rotor has optimized slots width B5, which will be the design value in the future application of this motor.

3-The proposed design allow two operation modes depending on the required operation conditions and various rotor parameters :

- first mode: when the main criteria is to obtain constant stable torque with somewhat reduced mean torque, minimized ripples and fluctuations, thus three coils must energized with appropriate switching signals .
- second mode: when the main criteria is to obtain mean torque as great as possible, despite of the further increasing in the motor pulses and fluctuation, thus only two coils S1 and S2 are to be energized .
- Each described construction has certain advantages and disadvantages associated to moment of inertia, vibration and noises, which mean's that choosing the required construction must take these parameters into consideration .

List of Symbols

Us - motor supply voltage
Uds- supply voltage of coils S1 & S2
Ud- supply voltage of third coil S3
E_A- phase induced back emf of S1 & S2
E_C- phase induced back emf of S3
L_A- circuit inductance of S1 & S2
L_C- circuit inductance of S3
L2m magnitude of highest order harmonic of the circuit inductance
λ_C- flux linkage of third coil S3
R_A- circuit resistance of S1 & S2
R_C circuit resistance of coil S3
n - number of harmonic that must be eliminated
Np- number of generated pulses in the quarter interval (0..90°)
K- the sequence number of generated pulses
α_k the instant of k-ti pulse
h(α)- harmonic function
Em_C- magnitude of induced emf of coil S3
Em_A- magnitude of induced emf of coils S1 & S2
I_A, I_C- phase current of coil S1 and S3 respectively
Imν - magnitude of highest order current harmonics of S3
Ψν- phase shift of ν-ti harmonic current
ω- electrical angular frequency
T_{RA}- reluctance torque component of S1
W_{RA}- reactive component of magnetic coenergy of S1
F_{SA}- MMF of coils S1 and S2
Nph_A- number of coils conductor of S1
K_{WA}- winding factor of S1
harmonic order of circuit permance
Nt- number of rotor teeth per pole
magnetic permance in the airgap
Go- constant component of circuit permance
Gmg- magnitude of highest order harmonic of permance
βg- phase shift of highest order harmonics
W_{EA}- active component of magnetic coenergy
T_{EA}- active torque component of S1
coenergy of S1
ϕ_R- rotor magnetic flux per pole of used permanent magnet
F_R- rotor MMF
Hm- magnetic intensity of the permanent magnet
Lm- permanent magnet length
T_{TA}- total magnetic torque produced by S1 or S2
T_{TC} - total magnetic torque produced by S3
W_{EC}- magnetic coenergy of third coil S3
F_{SC}- space time MMF produced by S3
Nph_C- number of coils conductor of S3
Im_1- fundamental current of S3
K_{WC}- winding factor of S3
Kνi- ratio of ν-th current harmonic to the fundamental value Im1
ν, γ- time and space harmonic order respectively
T_{EM}- total electromagnetic torque produced by both coils S1, s2 and S3 .
T_{CR}- torque –current ratio
T_{AV}- mean value of total electromagnetic torque
I_{TRMS}- total root mean square of the current of both coils S1, s2 and S3
IνRMS- root mean square of highest current harmonic
T_{RR}- torque ripple ratio
T_R- torque ripples
H_{FI}- current harmonic factor
I_{RMS}- root mean square of fundamental current harmonic

Acknowledgment
The author would like to thank all the member of the team for their contribution in realizing the theoretical and practical implementation of the model .

References

[1] Alexander Kusko and Syed M. Peeran, " Brushless DC motor using usymmetrical Field magnetization " , in proc. IA Vol.23, No.2, march/april 1987, p.319 .
[2] Kenjo T. and Nagamori S., " permanent – Magnet and Brushless dc motors", Oxford, England, Clarendon press 1985.

[3] Bolton H. R. and Ashen R.A. , " influence of motor design and feed-current waveform on torque ripple in brushless dc motor", IEE proc. Vol.131, pt.B, No.3, may/1984, pp.82 –90.

[4] Miller, T. J. E., " Switched Reluctance Motors and their Control, Oxford /UK, Magna Phys. Publication and Clarendon, press 1993.

[5] Faiz, J. and Finch J.W.," Aspects of design optimization for Switched Reluctance Motors", IEEE trans. On energy conversion 8, 1993, No.4, pp.704-713 .
[6] Torrey D.A., Niu X.M. and Unkauf, E.J., " Analytical Modelling of Variable-Reluctance machine Mgnetization characteristics. IEEE proc.B-142/ 1995, No.1, pp.14-22 .

[7] Cathey J. J. and Krimm T. W., " A Theoretical Study of Reduction of Torque Pulsations in Low-Speed Self-Synchronous Motor Drives fed through a Cycloconverter Link.", Electric Machines and Power systems, No.13, 229-243, 1987, Hemisphere Publ. Corp.

[8] Krimm T.W, " harmonic Control to reduce torque Pulsations in brushless DC Motor Drives", MSEE Thesis, University of Kentucky , 1984.

[9] Stephen Chapman, " Electric machines Fundamentals", 3rd ed. 1998, McGraw-Hill International Edition.

[10] F. Piriou, A.Razek, R. Perret and H. LeHuy, "Torque characteristics of Brsuhless DC motor with imposed current waveform" , IEEE IAS Annual Meeting conference record, 1986 .

[11] Bolton H.R., Liu Y.D. and Mallenson N.M., " Investigation into a class of Brushless DC motor with quasiquare voltages and currents", IEE proc. Vol.133, Pt. B, No.2, March 1986.

[12] Sameer H. Khader, " Implementation Of An Accurate Mathematical Method For Modeling Electromagnetic Processes of Brushless DC Motor", MESM'2001, Amman 2-3 /Sept. Jordan, pp.31-38.

The Author

▪ ***Sameer Hanna Khader*** *(1962), Jenien, Palestine, received a Master's degree in Electrical Engineering from the Institute of Electrical & Mechanical Engineering, Sofia-Bulgaria in 1988. And Ph.D. degree from TU-Sofia in 1993.*
Since 1995 he worked in Palestine Polytechnic University (PPU) as a Lecturer and researcher in the Field of Electrical Machines and Power Electronics.
1999-2001: Chairman of department of Electrical & Computer Engineering at College of Engineering & technology, PPU.
2001-2004 Dean of College of Applied professions, PPU.
2004- till now Vice president for Academic Affairs at PPU.
He has various works in the field of Brushless dc machines, and several projects with local industry.

Phone: +972 2 2220620; Fax: +972 2 2224977;
E-mail: sameer@ppu.edu

Microstepping Control of 5-phase Hybrid Step Motor

Zahari J. Zarkov

Abstract: *The paper presents a method for calculation the values of the phase currents for microstepping control of a 5-phase hybrid step motor (HSM). This method uses the standard control of the step motor with rated currents and only during the commutation the currents of the switched phases change their values in small steps so as the natural step is divided into several micro-steps. The author has developed a mathematical model and computer programs for simulation of the motor operation under investigated microstepping control. The paper contains also the results from simulations and corresponding conclusions.*

Keywords: *hybrid step motor, microstepping control*

Introduction

Step motors are known as cost-effective, robust drives. They are used in a whole range of machines and devices and perform all kind of tasks from simple point-to-point positioning in handling and automation systems, fast, short-term movements in the textile industry to high-precision synchronized movements in printing applications. Step motors excel with a simple, sturdy construction (usually without feedback systems), they can be installed quickly and easily without requiring the user to set up complex control parameters.

Two-phase hybrid step motors (HSM) are usually employed for simple applications, while the 5-phase hybrid step motors have become the reliable solution for more demanding tasks. The advantages of the 5-phase step motors include the high natural resolution of 500 or 1000 steps per revolution, their low-noise and low-resonance operation. Their low detent torque makes them ideal for microstep operation [1], [2].

One of the advantages of the microstep operation of the step motor is much higher resolution of the motor shaft positioning. This is achieved without complex and expensive rotor position feedbacks or gear box. Another advantage is improved single-step response of the motor by substituting one big step for multiple microsteps [2].

Microstep operation of the step motors is achieved by suitable changes of the values of the phase currents. There are two basic ways for microstep control. The first way is to vary the currents in sinusoidal law. In this case the maximum static torque is constant and theoretically any step angle can be achieved [1], [3]. This method is used for step motors with permanent magnet rotors. The second way is to use the standard control with rated phase currents and only during the commutation in the new state the currents of the switched phases change their values in small steps so as the natural step is divided into several micro-steps – so called vernier control [3], [4]. The problem here is to find these current values that ensure uniform microstep angle.

The aim of the paper is to develop a method for calculating of the phase currents values for microstep control of 5-phase HSM and to investigate the motor operation under this type of control.

Static torque of a 5-phase HSM

The following study is made for 5-phase HSM with 500 steps per revolution. The natural step angle of this type of motor is Θ_{st}=36° electrical or 0,72° mechanical which is achieved at bipolar phase supply with 4 energized phases at time [2]. The idealized waveforms of the phase currents at low speeds are shown in Fig.1 [5], [6].

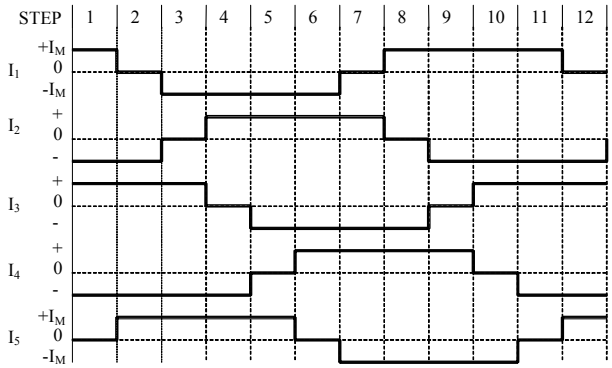

Fig.1. Idealized phase currents waveforms of a 5-phase HSM.

Here the author uses the model for the electromagnetic torque of the HSM without taking into account the non-linearity of the magnetic circuit and the magnetic permeance of the air gap. Under these circumstances the static torque curves of the phases and of the motor are sinusoidal and the relation between the current and the torque is linear. This allows for using vector diagrams for summing the torques of the phases [2], [6], [7].

Let's consider the state 1 from Fig.1 where the phase currents values are the following:

$$I_1 = I_M \qquad I_2 = -I_M \qquad I_3 = I_M \qquad I_4 = -I_M \qquad I_5 = 0.$$

Here I_M is the rated current value when the phase is supplied. The rated current is the value the step motor can operate with for an infinite long time in static mode without overheating. Of course the motor can operate also with currents different from the rated value - for example in static mode or in dynamic modes like acceleration, deceleration, entering resonant regions etc.

For the 5-phase HSD the static torque created by each phase is proportional to the phase current [6]. Taking into

account the values of the currents in state 1 in Fig.1 we have the following expressions for the static torques:

(1) $T_1 = k_M.I_M.\sin\Theta$

(2) $T_2 = -k_M.I_M.\sin(\Theta - 144°)$

(3) $T_3 = k_M.I_M.\sin(\Theta + 72°)$

(4) $T_4 = -k_M.I_M.\sin(\Theta - 72°)$

(5) $T_5 = k_M.0.\sin(\Theta + 144°) = 0$

where k_M is a factor with constant value for a given motor, I_M is the phase current, Θ is the angle of rotation of the rotor in electrical angle. The phase shift between the adjacent phases is 216° el. and the origin is the center of the stator tooth of the phase number 1 [7]. The magnitudes of the torque vectors correspond to T_m, where $T_m = k_M.I_M$ is the amplitude of the static torque sinusoidal curve created by one phase supplied by a current I_M.

The total torque of the motor T_E is a sum of the torques of the five phases. After summing the expressions for the torque (1) to (5) and corresponding rearrangements the total torque will be

(6) $$T_E = 4.k_M.I_M.\cos 72°.\cos 36°.\sin(\Theta + 54°) = \\ = 3{,}078.k_M.I_M.\sin(\Theta + 54°) = 3{,}078.T_m.\sin(\Theta + 54°).$$

Calculating of the current values for microstepping control of HSM

In order to obtain division of the natural step it is necessary to have the total torque vector turn by one microstep at each change of the values of the phase currents. The microstep angle value is defined by defining the angle positions of the total torque vector.

The current waveforms shown in Fig.1 are the basis for the definition of the proposed microstep control. Let's consider the transition from state 1 to state 2 in Fig.1. Here the current I_1 falls from I_M to 0, while the current I_5 rises from 0 to I_M. During this change of the state the rotor of the HSM is rotated in CCW direction by one natural step angle Θ_{st} = 36° el. The principle of the microstepping control is illustrated in Fig.2. In order to perform this control from the time t_1 the current I_1 begins to fall and the current I_5 – to rise. Here both currents have discrete pre-defined values. For each state (set of current values) the rotor turns by one microstep angle Θ_μ in CCW direction

(7) $$\Theta_\mu = \frac{\Theta_{st}}{n},$$

where n is a whole number, by which the natural step of the motor is divided. This is also the number of different states of the currents between the times t_1 and t_2 shown in the Fig.2.

The process shown in Fig.2 have to be done at each change of excitation state from Fig.1 in order to divide each natural step of the motor. In Fig.3 it is shown the torque-vector diagram for the first two states between the moments t_1 and t_2 from Fig.2 when dividing the natural step by 4.

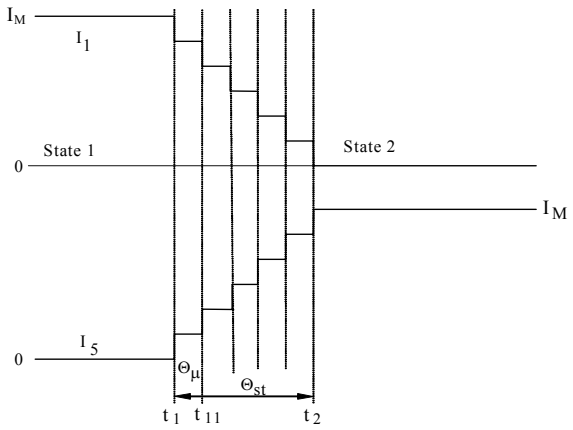

Fig.2. Principle of the microstepping control.

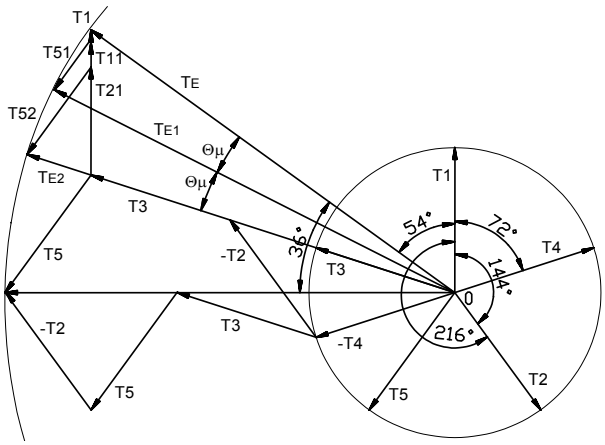

Fig.3 Torque-vector diagram when dividing the natural step by 4.

The T_{11} and T_{12} are the torques of the phase number 1, T_{51} and T_{52} – these of the phase 5 and T_E , T_{E1} , T_{E2} – the vectors of the total torque of the motor when changing the currents I_1 and I_5.

The problem for calculating the reference values of the phase currents can be solved at some limiting conditions. The following limiting conditions are formulated:

- the amplitude of the sinusoidal curve of the total static torque is constant, i.e. the vector magnitude is constant and equal to those when 4 phases of the motor are energized with current I_M;
- the vector of the total torque rotates by angle equal to one microstep Θμ at each subsequent state.

The vector-diagram shown in Fig.3 is drawn on the basis of these statements. Here one can see the variations of the torques when the currents in the two commutating phases change their values. The torque of the phase 1 decreases while this of the phase 5 – increases. As a result the total torque vector turns in CCW direction by

one microstep angle at each subsequent state. The locus of the total motor torque is a circle because his magnitude is constant.

In the formulated problem the unknown quantities are the magnitude of the torques $T_{11} \div T_{13}$ and $T_{51} \div T_{53}$. Considering that the relation between the static torque and the phase current is linear (expressions (1) to (5)), the expressions for the torque can be converted in such for the currents. After that these currents can be determined through of some trigonometric calculations.

For the state, shown in Fig.2 and taking into account the currents' signs from Fig.1 and on the basis of the expressions (1) ÷ (5), the total static torque of the HSM can be expressed as follows

$$\begin{aligned} & T_E = T_1 - T_2 + T_3 - T_4 + T_5 = \\ & = k_M \begin{bmatrix} I_1 \sin\Theta - I_M \sin(\Theta - 144°) + I_M \sin(\Theta + 72°) \\ - I_M \sin(\Theta - 72°) + I_5 \sin(\Theta + 144°) \end{bmatrix}. \end{aligned} \tag{8}$$

Here the currents I_1 and I_2 are unknown and change their values while the rest of the phases are energized by current I_M. After some transformations the expression (8) becomes

$$T_E = k_M \left[I_1 \sin\Theta + 2{,}62 I_M \sin(\Theta + 72°) + I_5 \sin(\Theta + 144°) \right]. \tag{9}$$

In order to fulfil the condition for keeping the magnitude of the static torque vector constant and taking into account the expressions (6) and (9), the following equation can be written

$$\begin{aligned} & k_M \left[I_1 \sin\Theta + 2{,}62 I_M \sin(\Theta + 72°) + I_5 \sin(\Theta + 144°) \right] = \\ & = 3{,}078 . k_M . I_M \sin(\Theta + 54° + p\Theta\mu) . \end{aligned} \tag{10}$$

Here p is the number of the consecutive microstep. After dividing the both sides of (10) by k_M and applying a phase shift of -54° to all terms in the equation we obtain

$$\begin{aligned} & I_1 \sin(\Theta - 54°) + 2{,}62 . I_M \sin(\Theta + 18°) + I_5 \sin(\Theta + 90°) = \\ & = 3{,}078 . I_M \sin(\Theta + p\Theta\mu) . \end{aligned} \tag{11}$$

This equation has to be solved for the currents I_1 and I_5. After rearrangements this yields

$$\begin{aligned} & I_1 \sin(\Theta - 54°) + I_5 \cos(\Theta + 90°) = \\ & = 3{,}078 . I_M \sin(\Theta + p\Theta\mu) - 2{,}62 . I_M \sin(\Theta + 18°). \end{aligned} \tag{12}$$

$$\begin{aligned} & I_1 \sin\Theta . \cos 54° + (I_5 - I_1 . \sin 54°) \cos\Theta = \\ & = I_M \begin{bmatrix} \sin\Theta (3{,}078 \cos p\Theta\mu - 2{,}62 \cos 18°) + \\ + \cos\Theta (3{,}078 \sin p\Theta\mu - 2{,}62 \sin 18°) \end{bmatrix}. \end{aligned} \tag{13}$$

And finally we obtain the following form of the equation (13)

$$\begin{aligned} & 0{,}59 . I_1 \sin\Theta + (I_5 - 0{,}81 . I_1) \cos\Theta = \\ & I_M (3{,}078 \cos p\Theta\mu - 2{,}49) \sin\Theta + \\ & + I_M (3{,}078 \sin p\Theta\mu - 0{,}81) \cos\Theta . \end{aligned} \tag{14}$$

It can be presented as following set of equations for the currents I_1 and I_5

$$\begin{cases} 0{,}59 . I_1 = I_M (3{,}078 \cos p\Theta\mu - 2{,}49) \\ I_5 - 0{,}81 . I_1 = 3{,}078 \sin p\Theta\mu - 0{,}81 \end{cases} \tag{15}$$

The solution of above set of equations for the currents I_1 and I_5 is as follows

$$\begin{cases} I_1 = I_M (5{,}235 \cos p\Theta\mu - 4{,}235) \\ I_5 = I_M (3{,}078 \sin p\Theta\mu + 4{,}235 \cos p\Theta\mu - 4{,}235) \end{cases} \tag{16}$$

Thus by using the expressions (16) we can calculate the values of the phase currents I_1 and I_5 that makes the p-th consecutive microstep after the state t_1 from Fig.2 and Fig.3.

The same form of the solution will be obtained for commutation of any another two currents, say I_1 and I_2, at the transition from the state 7 to 8 on Fig.1.

On the basis of the obtained solution the results for two particular cases are presented here. The study is done for above mentioned 5-phase HSM with 500 steps per revolution and natural step of $\Theta_{st} = 36° el.$ The following angle for the microstep is obtained when this natural step is divided by 4

$$\Theta_\mu = \frac{\Theta_{st}}{n} = \frac{36°}{4} = 9°. \tag{17}$$

The values of the currents I_1 and I_5 are calculated by using the expressions (16) in order to operate the motor with microstep of 9°. The results are shown in Table 1. These results are in units relative to the current I_M

$$I_1^* = I_1 / I_M \ ; \ I_5^* = I_5 / I_M \ . \tag{18}$$

Table 1

Θ, deg	0	9	18	27	36
I_1^*	1	0,9358	0,7439	0,4293	0
I_5^*	0	0,4293	0,7439	0,9358	1

With assumption that n=8 (dividing of the natural step by 8) the microstep angle becomes

$$\Theta_\mu = \frac{\Theta_{st}}{10} = 4{,}5° , \tag{19}$$

and the motor does 4000 microsteps per revolution. Again by using (16) and (18) the values for the currents I_1 and I_5 are calculated and are presented in the Table 2.

Table 2

Θ,deg	0	4,5	9	13,5	18	22,5
I_1^*	1	0,984	0,936	0,855	0,744	0,602
I_5^*	0	0,229	0,429	0,602	0,744	0,855
Θ,deg	27	31,5	36			
I_1^*	0,429	0,229	0			
I_5^*	0,936	0,984	1			

The current values for the natural step, divided by arbitrary whole number, can be calculated using above

approach. The waveforms of the currents I_1 and I_5 during the operation of the motor are shown in the next chapter.

Simulation of the HSM operation with microstepping control

The motor operation with above described microstepping control is simulated by a computer. The used mathematical model of the motor in conjunction with the current regulator is described in details in [8] and [9]. The model includes the voltage equations, the equation of motion of the rotor and the expression for the electromagnetic torque of the motor. The voltage equations are written on the basis of the equivalent circuit of one motor phase shown in Fig.4.

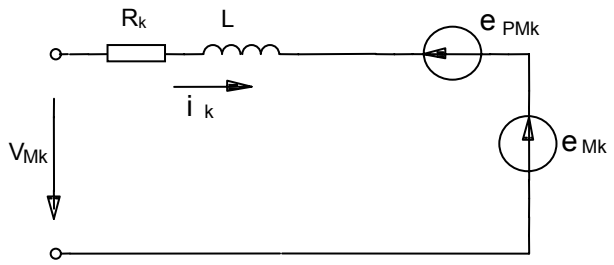

Fig.4. Equivalent circuit of one motor phase.

Hence the voltage equation for the phase number k is

$$V_M = R_k i_k(t) + L\frac{di_k}{dt} \pm \sum_{j=1, j\neq k}^{5} M_{kj}\frac{di_j}{dt} + e_{PMk}, \quad (20)$$

where $e_{PMk} = \frac{d\Psi_{PMk}}{dt}$ and $e_{Mk} = \pm \sum_{j=1, j\neq k}^{5} M_{kj}\frac{di_j}{dt}$.

The following notations are used here:
R_k – total resistance in the phase circuit (this includes the resistances of: the phase coil, the transistors, the current sensing resistor, the connecting wires);
L – phase inductance;
M_{kj} – mutual inductance between phases k and j;
e_{PMk} – EMF of the permanent magnet in the rotor;
e_{Mk} – EMF due to mutual inductances;
V_{Mk} – voltage applied to the phase;
i_k – phase current;
Ψ_{PMk} – phase flux linkage from the the permanent magnet in the rotor.

The equations for all 5 phases have the same form, the parameter Ψ_{PMk} being offset at $(6\pi/5)$ (see expressions (1) to (5)). The expression (20) is modified each time according to the current regulator state [8], [9]. This is a part from the algorithm simulating the work of the current regulator. The following set of differential equations represents the five phases of the motor

(21)

$$\begin{vmatrix} L_1 & -M_{12} & -M_{13} & -M_{14} & -M_{15} \\ -M_{21} & L_2 & -M_{23} & -M_{24} & -M_{25} \\ . & . & . & . & . \\ -M_{51} & -M_{52} & -M_{53} & -M_{54} & L_5 \end{vmatrix} \times \begin{vmatrix} di_1/dt \\ di_2/dt \\ . \\ di_5/dt \end{vmatrix} = \begin{vmatrix} V_1 - R_1 i_1 - e_{PM1} \\ V_2 - R_2 i_2 - e_{PM2} \\ .... \\ V_5 - R_5 i_5 - e_{PM5} \end{vmatrix}.$$

The equation of the rotor motion expressed in the form suitable for numerical integration is also added

$$\begin{vmatrix} \dot{\Theta} = \omega \\ \dot{\omega} = z\left(\left(T_E(t) - T_L\right) - k_D \frac{\omega}{z} \right) / J \end{vmatrix}, \quad (22)$$

where: J – moment of inertia of the rotor, k_D – damping coefficient, $T_E(t)$ – total electromagnetic torque of the motor, T_L – load torque, ω – electrical angular velocity of the rotor, Θ – angle of rotation of the rotor in electrical angle, z – number of the rotor teeth.

The relationship between the voltage equations (21) and the motion equation (22) is the expression for the electromagnetic torque $T_E(t)$ known from [8]

$$T_E(t) = -z\Psi_m \sum_{k=1}^{5} i_k(t)\sin(\Theta + \varphi_k), \quad (23)$$

where Ψ_m – maximal flux linkage of the phase from the permanent magnet, φ_k – phase shift angle according to expressions (1)÷(5).

The equations (21), (22) and the expression (23) form a set of differential equations describing the motor commutators in conjunction with the current regulator. The author developed also an algorithm describing the work of the current regulator embedded in the programs for numerical integration of the differential equations.

Accordingly to the described mathematical model the author developed a computer program in MATLAB for simulation of the 5-phase hybrid step motor

The operation of the 5-phase HSM in microstepping mode is simulated by means of the developed programs. The following parameters are used during the simulations:
L = 5,33mH; Ψ_m = 7,91mWb; M = 0,3L; $M1$ = 0,17L; R_k = 1 or 5Ω in dependence of the current regulator state; phase supplying current I_M = 4A; supplying voltage for the regulator and the motor V_M=150V; J = 0.0015kg.m^2, T_L = 0.

It is important to mention that the motor parameters L, M, $M1$, Ψ_m, R_k are the real parameters measured from the motor and they are not obtained by theoretical way.

The simulation model allows for investigating the motor behavior in different modes of operation – static, steady state and transient modes. Some results of these investigations are presented henceforward.

Fig.5 shows the rotor motion at microstepping control when the natural step is divided by 4. Here are used the current references shown in Table 1 multiplied by the value of I_M = 4A. It can be clearly seen that the rotor turns by 9° at each microstep (according to the expression (17)). The stepping rate is 15 SPS (SPS – steps per

second). The waveforms of the currents I_1 and I_5 obtained at the same conditions are shown in Fig.6.

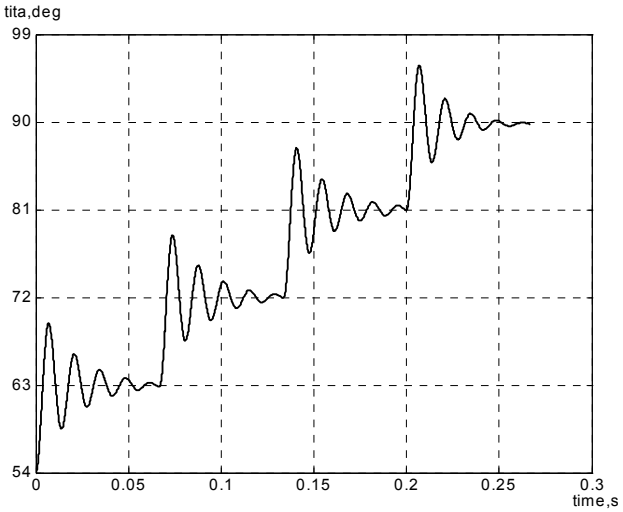

Fig.5. Rotor motion when the step is divided by 4 and step rate 15 SPS.

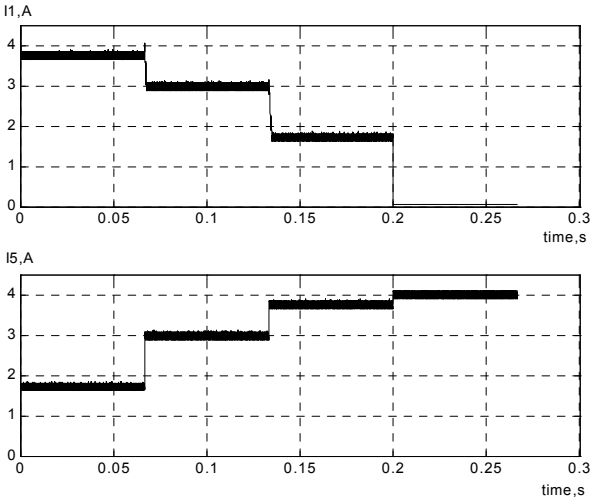

Fig.6. The waveforms of the currents I_1 and I_5 when the step is divided by 4 and step rate 15 SPS.

Figures 8, 9 and 10 show the rotor movement by angle of 36° that is exactly one natural step of the motor. In Figures 8 and 9 this is done when the natural step is divided by 4, i.e. Θμ= 9°. Respectively Fig.10 shows the motion of the rotor when the natural step is divided by 8, i.e. Θμ= 4,5°. In Fig.8 the step rate is 100 SPS and in Fig.9 is 300 SPS. Respectively in Fig.10 this step rate is 600 SPS that corresponds exactly to 300 SPS when the microstep angle is 9° (Fig.9). These results show that the quality of the rotor motion improves when one natural step is substituted for multiple microsteps. For comparison Fig.7 shows one-step response when the motor does one natural step of 36°. The rotor movement is much smoother and with smaller resonance oscillations. The time to settle in the new position is also decreased.

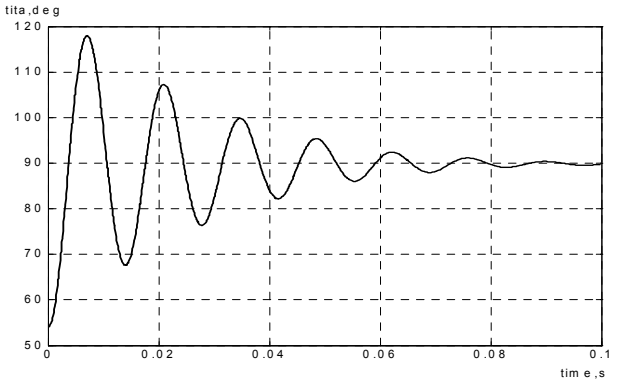

Fig.7. Rotor motion when the motor does one natural step of 36°.

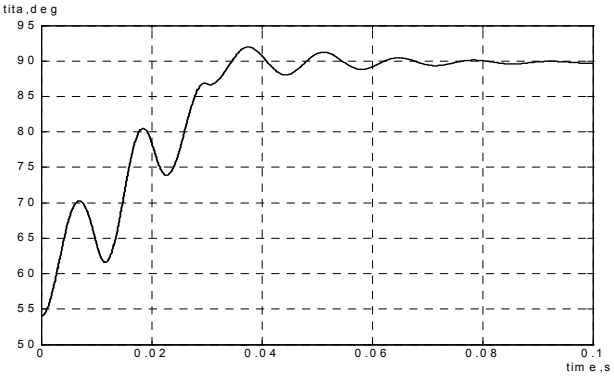

Fig.8. Rotor motion when the step is divided by 4 and step rate 100 SPS.

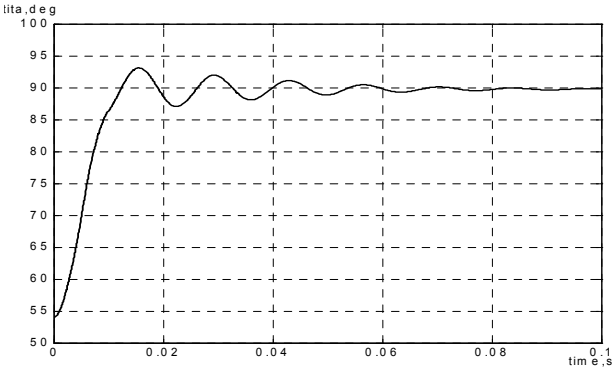

Fig.9. Rotor motion when the step is divided by 4 and step rate 300 SPS.

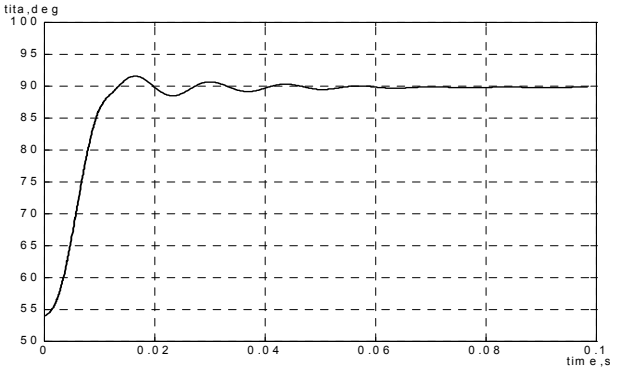

Fig.10. Rotor motion when the step is divided by 8 and step rate 600 SPS.

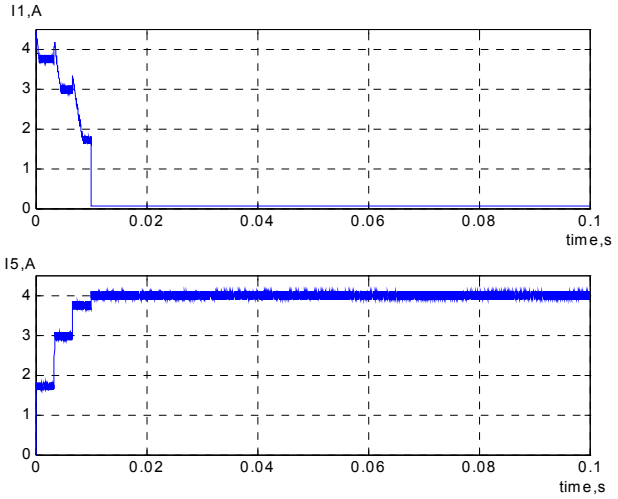

Fig.11. Waveforms of the currents I_1 and I_5 when the step is divided by 4 and step rate 300 SPS.

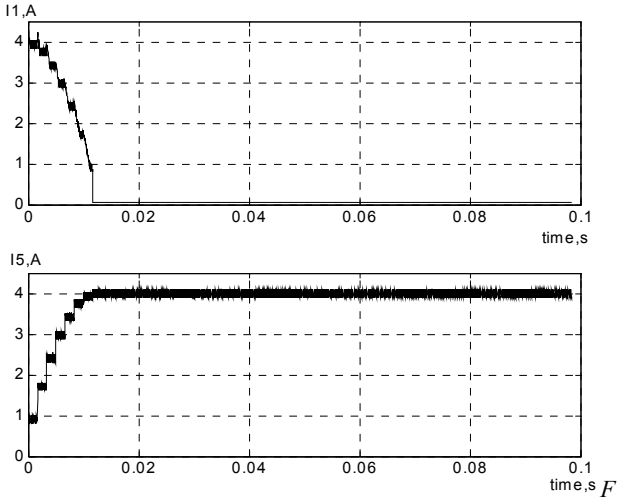

ig.12. Waveforms of the currents I_1 and I_5 when the step is divided by 8 and step rate 600 SPS.

In the same time by means of the developed programs can be calculated also another quantities characterizing the HSM operation. Fig.11 shows the waveforms of the currents I_1 and I_5, at same conditions like these on Fig.9. On the other hand Fig.12 shows the waveforms of the currents I_1 and I_5, at same conditions like these on Fig.10. It can be clearly seen how the currents accept the values calculated theoretically and shown in Tables 1 and 2. The current regulator sustains the reference value of the current with some pulsations due to his chopper mode of operation.

Conclusion

The presented in the paper microstepping control can be used effectively only for step motors with 3 and more simultaneously energized phases. These are the 3- and 5-phase HSM and also 4- and 5-phase switched reluctance step motors as well as all motors with greater number of phases.

The developed method for calculation the phase currents for microstepping control gives the opportunity to divide the natural step of the motor by any whole number. With this mode of operation the phase currents have values always smaller than the rated (I_M). So this leads to more uniform distribution of the losses in the motor phase windings and in the current regulators compared to the microstep control with sinusoidal current waveforms (especially in static modes). In the same time the static toque of the motor is preserved.

Using the presented mathematical model of the motor in conjunction with the current regulator the operation of the HSM can be simulated in different modes of operation. The obtained results show that the method for calculating of the reference values of the currents gives correct results. It can be concluded also that the proposed microstepping control leads to much better quality of the rotor motion – smoother and faster.

The further improvement of the model requires taking into account the saturation of the magnetic circuit of the motor in the model for the calculation of the reference currents as well as in the model describing the motor operation.

References

[1] Siefert,W. The 3-phase stepping motor system, Background, Functions. EPE Journal, Vol.5, 3/4, Jan., 1996, pp. 44-48.

[2] Kuo,B.C., J.Tal. Incremental motion control. Vol.II, Step motors and control systems. SRL Publishing Company, Illinois, 1983.

[3] Kant,M. Les actionneurs électriques pas a pas. HERMES, 1989.

[4] Rahman,M.F., Grantham,C. Design Approaches for microstepping step motor controllers. Int. Conf. on Power Electronics and Variable-Speed Drives, UK, 1990, pp. 253-257.

[5] Lazarov,V.D., R.V. Dinov, Z.J. Zarkov. Five-phase hybrid step motor drives. Proc. of Int. Conf. ELMA'93, Varna, Bulgaria, 1993, pp.417-422.

[6] Зарков, З.Ж., В.Д. Лазаров. Изчисляване на фазните токове при микростъпково управление на 5-фазен хибриден стъпков двигател. E+E, 1-2, 2005, стр. 49-55 (In Bulgarian).

[7] Лазаров, В.Д. Статичен синхронизиращ момент на хибридни стъпкови електродвигатели. Конференция по електрически машини ЕЛМА'87, Варна, 1987, стр.75-81 (In Bulgarian).

[8] Лазаров, В.Д., З.Ж. Зарков. Определяне на електромагнитния момент на хибриден стъпков двигател при токово управление в динамични режими. E+E, 7-8, 1995, стр. 33-36 (In Bulgarian).

[9] Лазаров, В.Д., З.Ж. Зарков. Теоретично изследване на нестабилността на хибридни стъпкови двигатели. E+E, 1-2, 1996, стр. 34-36 (In Bulgarian).

Zahari J. Zarkov *– Assistant Professor, Dr., Faculty of Electrical Engineering, Technical University of Sofia, 8 Kl. Ohridski Str., 1000 Sofia, BULGARIA. e-mail: zzza@tu-sofia.bg.*

Simulation and Measurement Study of Commutator DC Motor with Internal Asymmetries

Zygfryd Głowacz and Antoni Zdrojewski

Abstract: *The commutator of dc motor is approximated by resistance circuit. Extremely different values are assigned to parameters of commutator circuit depending on the angular position of the rotor. The set of internal asymmetries includes among others the broken and shorted rotor coils. Simulation and experimental investigations were performed for specially designed dc motor. Construction of this motor enables to realize the breaking of one loop rotor coil and shorting of two groups of rotor coils.*

Keywords: *Commutator DC Motor, Internal Asymmetries*

Introduction

Aim paper is increasing of knowledge about features of commutator dc motor. Special commutator dc machine with loop rotor winding was designed by BOBRME Komel in Katowice (Poland) for simulation and experimental investigations. Measurements and calculations have been carried out for two manner of motor supplying:
a) constant voltage (from dc separately excited generator),
b) rectified voltage (from 6T thyristor bridge),
and for different asymmetries of rotor winding.
The design data and values of the parameters of machine were: P_N =13 kW, U_N =75 V, I_N =200 A, U_{fN} =220 V, n_N =700 rpm, J = 0.9 kgm^2, D = 0 Nms/rad, K = 126, R_c =6.4 mΩ, R_f = 50 Ω, $R_{r1} = R_{r2} = \ldots R_K$ = 0.93 mΩ.
In paper are presented selected simulation and measurement results for considered commutator dc machine operating as a motor with internal asymmetries (i.e. breaking one rotor coil and shorting of two groups rotor coils). It was assumed that each group of three loop rotor coils is shorted through resistance R_{bz} =44.2 mΩ.

Mathematical description of dc motor

The mathematical description of commutator dc motor was derived on the following assumptions:
- the magnetic circuit is linear,
- the air-gap is uniform,
- the unipolar flux is neglected,
- the eddy currents in iron are not taken into account,
- the commutator of the motor is approximated by circuit with variable parameters.

The commutator of dc motor was approximated by resistance circuit. Extremely different values were assigned to parameters of commutator circuit depending on the angular position of rotor.
Constant voltage fed commutator dc motor is presented in Fig. 1 whereas rectified voltage fed commutator dc motor is shown in Fig. 2.

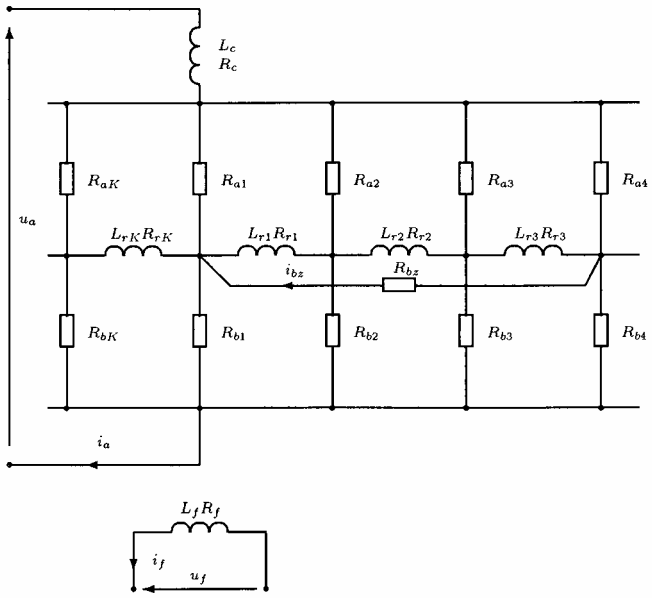

Fig. 1. Equivalent circuit of constant voltage fed commutator dc motor with shorted three loop rotor coils

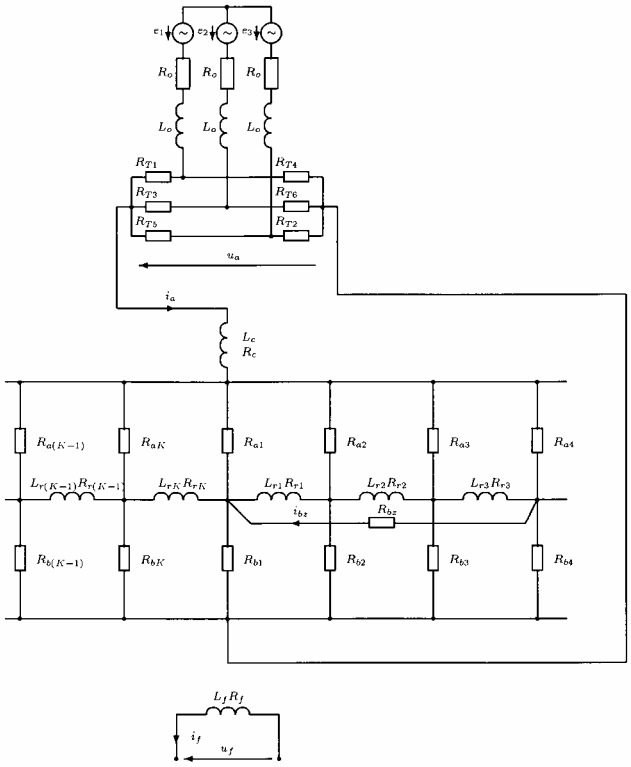

Fig. 2. Equivalent circuit of rectified voltage fed commutator dc motor with shorted three loop rotor coils

The commutator dc motor circuit is described by stiff differential equations:

$$\frac{d}{dt}\left(\mathbf{C}^{\mathrm{T}}\mathbf{L}_{\mathrm{b}}\mathbf{C}\,\mathbf{i}\right)+\mathbf{C}^{\mathrm{T}}\mathbf{R}_{\mathrm{b}}\mathbf{C}\,\mathbf{i}=\mathbf{u}, \tag{1}$$

$$\mathbf{i}_{\mathrm{b}}=\mathbf{C}\,\mathbf{i}, \tag{2}$$

$$\mathbf{C}^{\mathrm{T}}\mathbf{u}_{\mathrm{b}}=\mathbf{u}, \tag{3}$$

$$J\frac{\mathrm{d}}{\mathrm{dt}}\omega+D\omega=T_e-T_l, \tag{4}$$

$$\frac{\mathrm{d}}{\mathrm{dt}}\varphi=\omega, \tag{5}$$

$$T_e=\frac{1}{2}(\mathbf{i})^{\mathrm{T}}\frac{\partial}{\partial\varphi}(\mathbf{C}^{\mathrm{T}}\mathbf{L}_{\mathrm{b}}\mathbf{C})\,\mathbf{i}. \tag{6}$$

The inductances depend on the rotor position and are obtained by finite element calculations and then expressed in Fourier series [7]. A smaller accuracy is achieved when the inductances are calculated by means of the air-gap permeance function [3].

$$\lambda=\frac{\mu_o}{\delta'}\left[1+\sum_{\nu=1}^{N}a_\nu\cos(\nu y)\right]\left[1+\sum_{\rho=1}^{N}b_\rho\cos\left(\rho\left(y-\varphi+\frac{\mathrm{tg}\gamma}{r}z\right)\right)\right], \tag{7}$$

$$\delta'=k_C k_{Fe}\delta. \tag{8}$$

Resistances R_{am}, R_{bm}, $m=1,..,K$ depend on the rotor position. These resistancess in the machine with rotor loop winding are determined by the formulae:

$$R_{am}(t)=h\left(\left(\varphi(t)+\varphi_3+(m-1)\varepsilon+\frac{\pi}{2p}\right)\left(\mathrm{mod}\,\frac{2\pi}{p}\right)-\varphi_3\right), \tag{9}$$

$$R_{bm}(t)=h\left(\left(\varphi(t)+\varphi_3+(m-1)\varepsilon+\frac{3\pi}{2p}\right)\left(\mathrm{mod}\,\frac{2\pi}{p}\right)-\varphi_3\right), \tag{10}$$

for $m\in\{1,2,..,K\}$,

$$\varepsilon=\frac{2\pi}{K},\quad \varphi_3=0.5\left(\frac{b}{r_c}+\frac{2\pi}{K}\right). \tag{11}$$

A function $f(\varphi')$ is in the form:

$$h(\varphi')=\min\left\{\max\left\{\left(\frac{R_z-R_p}{\varphi_2-\varphi_1}\right)\left(\left|\varphi'\right|-\varphi_1\right),R_p\right\},R_z\right\}, \tag{12}$$

where: $|\varphi'|$ - absolute value of function,
$\varphi_1=\eta_1\,\varphi_3$, $\varphi_2=\eta_2\,\varphi_3$, η_1, η_2 - coefficients.

The motor inductances and commutator resistance depend on the angular position of rotor. Extremely different values are assigned to parameters of commutator circuit.
In the figures and mathematical description the following notation was applied:
$\mathbf{C}$ - matrix of constraints,
$\mathbf{L}_{\mathrm{b}}$ - matrix of branch inductances,
$\mathbf{R}_{\mathrm{b}}$ - matrix of branch resistances,
$\mathbf{u}_{\mathrm{b}}$ - vector of branch source voltages,
$\mathbf{i}_{\mathrm{b}}$ - vector of branch currents,
$\mathbf{u}$ - vector of mesh source voltages,
$\mathbf{i}$ - vector of mesh currents,
ω - angular velocity of rotor,
φ - angular position of rotor,
T_e - electromagnetic torque,
T_l - load torque,
L_o - self-inductance of supply network,
R_o - resistance of supply network,
L_{r1} ,..., L_{rK} - self-inductances of rotor coils,
R_{r1} ,..., R_{rK} - resistances of rotor coils,
L_c - self-inductance of commutation winding,
R_c - resistance of commutation winding,
L_f - self-inductance of excitation winding,
R_f - resistance of excitation winding,
R_{a1} ,..., R_{aK}, R_{b1} ,..., R_{bK} - commutator resistances,
R_{bz} - commutator bars shorting resistance,
R_p - min. value of $R_{a1},\ldots, R_{aK}, R_{b1},\ldots, R_{bK}$ resistances,
R_z - max. value of $R_{a1},\ldots, R_{aK}, R_{b1},\ldots, R_{bK}$ resistances and R_{bz} resistance,
b - width of brush,
r_c - radius of commutator,
r - mean radius of air-gap,
γ - skew angle of rotor slot,
μ_o - magnetic permeability,
y, z - motor coordinates,
N - number of components of series,
k_C - Carter's coefficient,
k_{Fe} - filling coefficient with iron,
p - number of pairs of poles,
K - number of commutator bars,
J - inertia moment of rotor,
D - damping coefficient.

The effective implicit integration method was used for solution of model equations. The set of system failures included among others the shorted and broken rotor coils (partly and totally). Constant voltage and rectified voltage fed commutator dc motor was operating in open regulation system.

Simulation results

Simulation results of excitation current in failure conditions for shorted three loop rotor coils and two manners of supply are presented in Fig. 3 - 4.

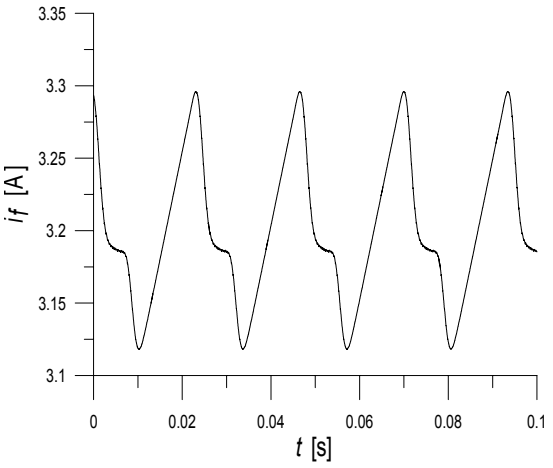

Fig. 3. Excitation current in conditions of shorting of first group of coils (constant voltage fed dc motor)

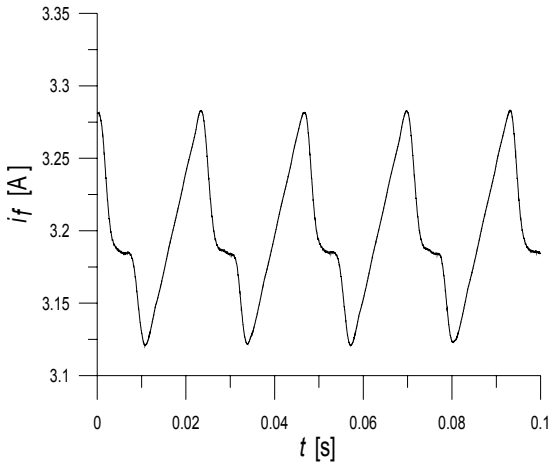

Fig. 4. Excitation current in conditions of shorting of first group of coils (rectified voltage fed dc motor)

Description of laboratory stand

Construction of this motor enables to realize the breaking of one loop rotor coil and shorting of two groups of rotor coils. Each group contains three loop rotor coils. In investigations these defects have been realized separately and simultaneously. Measurements have been developed by means of 16-bit a/d converter. Dc motor was supplied from constant voltage (from dc separately excited generator) and rectified voltage (from 6T thyristor bridge) and operated. Between converter and dc motor a choke has been inserted. Dc motor operated in open regulation system i.e. without rgulation of rotor velocity and armature current. The constant thyristor control angle was assumed The additional dc generator connected with external resistance produced the load torque. Supply network of 380/220 V and 220/127 V as well as converter transformer enabled the control of dc motor at nominal voltage of 75 V. Studied dc motor is presented in Fig. 5.

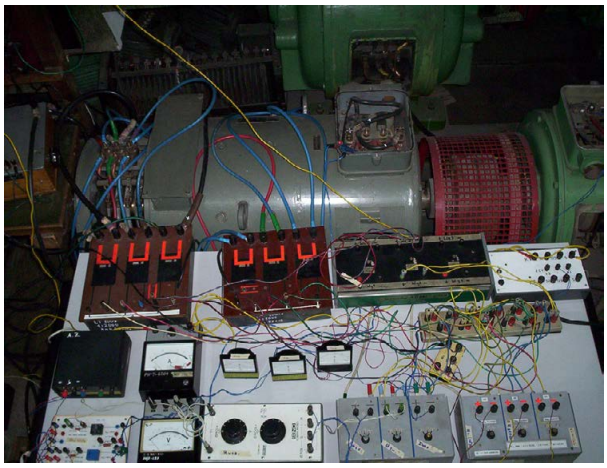

Fig. 5. Studied dc motor

Measurement results

Measurement results of excitation current in failure conditions are presented in Fig. 6 – 15.

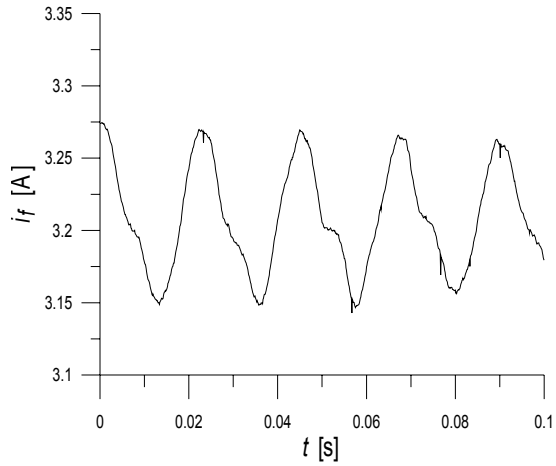

Fig. 6. Excitation current in conditions of shorting of first group of rotor coils (constant voltage fed dc motor)

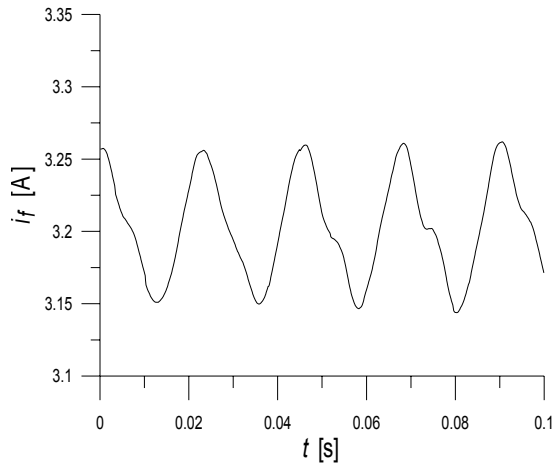

Fig. 7. Excitation current in conditions of shorting of first group of rotor coils (rectified voltage fed dc motor)

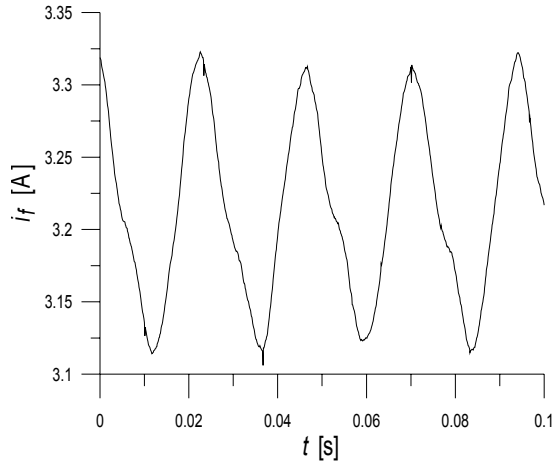

Fig. 8. Excitation current in conditions of shorting of first and second group of rotor coils (constant voltage fed dc motor)

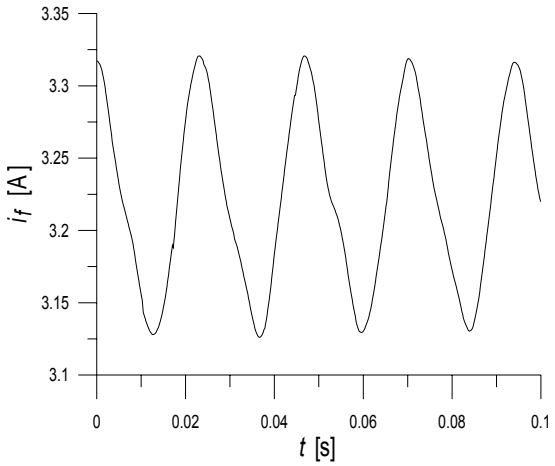

Fig. 9. Excitation current in conditions of shorting of first and second group of rotor coils (rectified voltage fed dc motor)

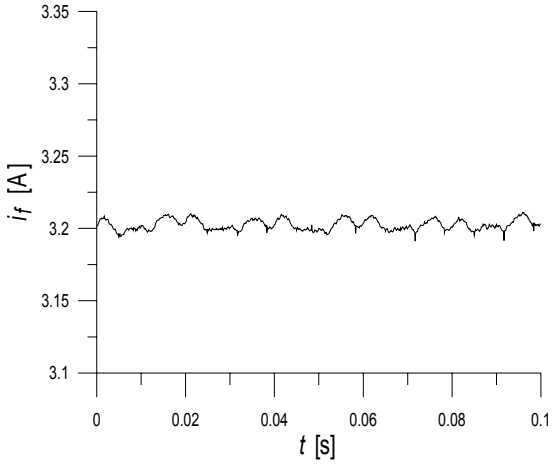

Fig.10. Excitation current in conditions of breaking of rotor one coil (constant voltage fed dc motor)

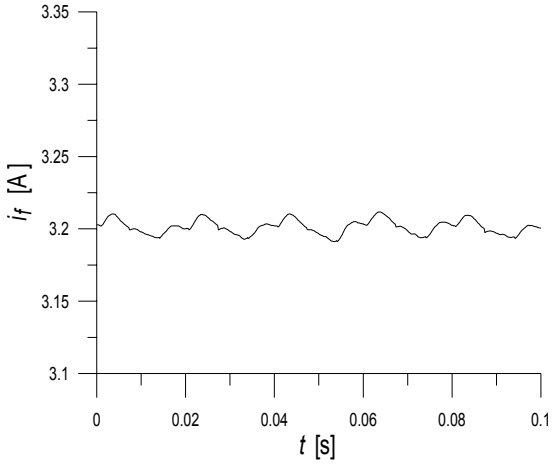

Fig. 11. Excitation current in conditions of breaking of rotor one coil (rectified voltage fed dc motor)

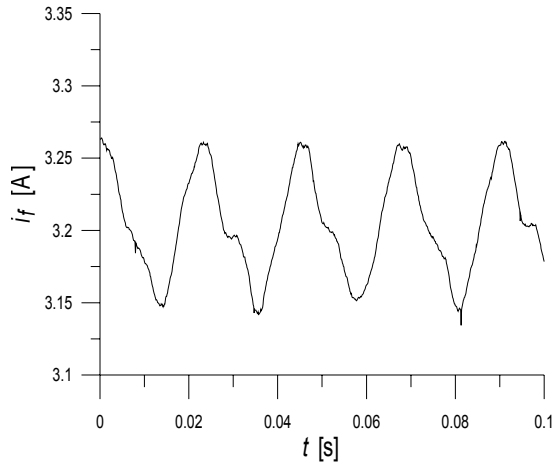

Fig. 12. Excitation current in conditions of breaking of rotor one coil and shorting of first group of rotor coils (constant voltage fed dc motor)

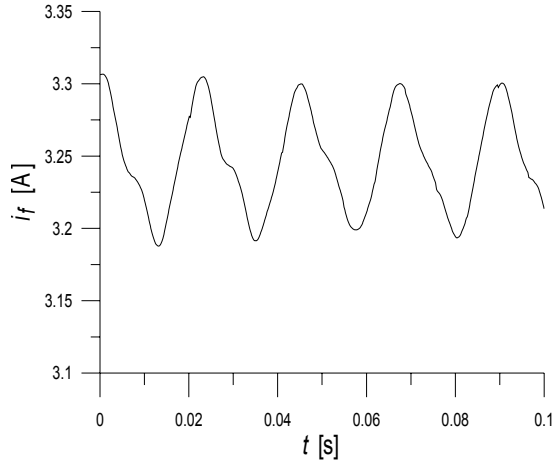

Fig. 13. Excitation current in conditions of breaking of rotor one coil and shorting of first group of rotor coils (rectified voltage fed dc motor)

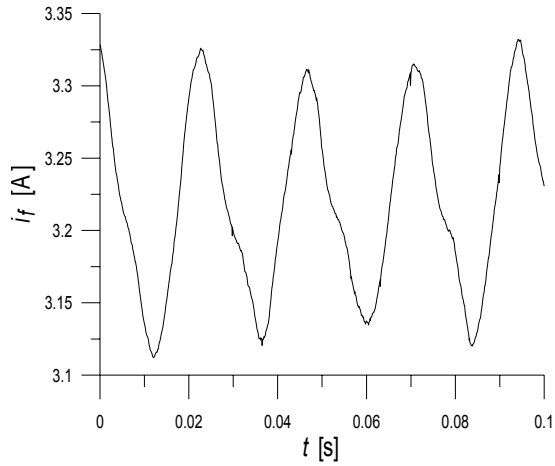

Fig. 14. Excitation current in conditions of breaking of rotor one coil and shorting of first and second group of rotor coils (constant voltage fed dc motor)

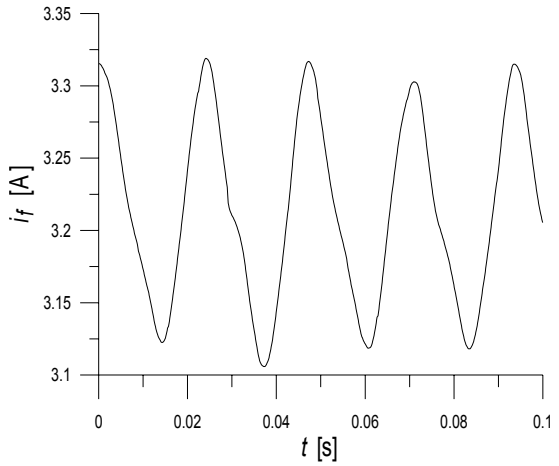

Fig. 15. Excitation current in conditions of breaking of rotor one coil and shorting of first and second group of rotor coils (rectified voltage fed dc motor)

In wave forms of excitation current shown in Fig. 10 – 11 are visible components corresponding to rotor coil breaking with different frequency and small amplitudes. From wave forms of excitation currents presented in Fig. 12 - 15 implies that breaking of rotor coil occurring simultaneously with rotor coil shorting deformes additionally the wave forms of excitation currents shown in Fig. 6 - 9.

Conclusions

Study of features of dc motor is purpose of this paper. The applied analysis parametrical method is competitive in comparison with other methods e.g. the variable structure method with a commutator model in the form of an ideal switch, the constant structure method with a commutator model in the form of series connection of inductive and resistive elements. From the carried out calculations it can be seen that this mathematical model is particularly advantageous in studies of rotor faults. Matrix of constraints existing in the model equations is easily obtained for commutator dc motor with loop rotor winding. It is possible to take into account the equalizing connections, compensating winding and other rotor winding types. Created for diagnostics the measurement stand uses modern computer equipment and software making easier the registration and analysis of phenomena occuring in the faulty states. Simulation and measurement studies enable to determine the qualitative and quantitative variations of electrical and mechanical quantities in failure conditions. Dc motor was investigated in different cases of shorting and breaking of rotor coils. Simulation and measurement results are generally conformed to expectations implying from theoretical analyses. The shorting of rotor coils causes the considerable deformations of currents and voltages in dc motor. In shorted coils of rotor occur current rushes which can damage the rotor. Excitation current contains the components which repeatability is closely connected with velocity of rotor. The calculations and measurements indicate that spectra of other electrical and mechanical quantities (i.e. armature current, current of shorted rotor coils, current in shorting resistance, electromagnetic torque, velocity of rotor) contain the harmonics corresponding to shorted and broken coils of rotor. Among the considered quantities practically useful for diagnostics are currents of excitation and armature circuits. Best diagnostics signal is excitation current which will be a subject of detailed Fourier analysis. Effects of commutation processes are perceptible in presented wave forms. Authors intend to perform the investigations which purpose will be further increasing of accuracy of simulation and measurement of physical phenomena in commutator dc motor.

Acknowledgements

Results presented in this paper concern partly the reasearch works No. MNiI/SGI2800/AGH/044/2005 and No. 10.10.120.557 sponsored in 2005 by University of Science and Technology in Cracow.

References

[1] Cash, J. R. A Class of Implicit Runge-Kutta Methods for the Numerical Integration of Stiff Ordinary Differential Equations. JACM, Vol. 22, No. 4, 1975, pp. 501-511.

[2] Chapman, S. J. Electric Machinery Fundamentals. New York: McGraw-Hill Book Company, 1999.

[3] Głowacz, Z. Mathematical model and simulation investigation of d.c. machine with equalizing connections in emergency states. Proc. of International Conference on Electrical Machines ICEM'00, Espoo, 2000, pp. 1447-1451.

[4] Krause, P. C. Analysis of Electrical Machines. New York: McGraw-Hill Book Company, 1986.

[5] Noga, M., Z. Głowacz, J. Rusek. Mathematisches Modell der Gleichstrommaschine zur Berechnung der Ströme in den Läuferwicklungen. Proc. 6. Wissenschaftliche Konferenz: Rationalisierung im Maschinenbau durch Schlüsseltechnologien, Fachtagung 8: Elektroautomatisierungstechnik, TH Zwickau, 1989, pp. 167-170.

[6] Pfaff, G. Regelung elektrischer Antriebe, I: Eigenschaften, Gleichungen und Strukturbilder der Motoren. München: R. Oldenbourg Verlag, 1987.

[7] Schröder, R., K. Oberretl. Neues Verfaren zur Berechnung der Kommutierung von Gleichstrommaschinen unter Berücksichtigung der Bürstenübergangswiderstände. Archiv für Elektrotechnik, Vol. 73, No. 2, 1990, pp. 69-79.

Zygfryd Głowacz *– Univ. Professor, DSc., Department of Electrical Machines, University of Science and Technology, Ave. Mickiewicza 30, 30-059 Cracow, POLAND, e-mail: glowacz@agh.edu.pl.*

Antoni Zdrojewski *– Academic Teacher, Department of Electrical Drive and Industrial Equipment, University of Science and Technology, Ave. Mickiewicza 30, 30-059 Cracow, POLAND, e-mail: zdrojton@agh.edu.pl.*

AC Commutator Motor: Calculation of Field, Parameter and Comutational Processes

V.Y. Bespalov, M.V. Panikhin

Abstract: *In the paper, different level mathematical model of the AC commutator motor is described. The goal of this study is to develop method and algorithm of calculation transients in commutating coils of armature winding. Field analysis in used to find inductive parameters of the machine. Some results of calculations are given.*

Keywords: *electromagnetic compatibility, finite-element program, winding coils commutating, self and mutual inductances.*

AC commutator motor (ACCM) still find wide use in consumer electronic devices, electrical instruments and other application thanks to their simplicity, low cost and reliability. Probably more important reasons for this their operation, from one-phase supply voltage and ability to exceed 3000 rev/min limit of the rotational speed. In spite of a notable progress of power electronics, EE companies don't trend to entire replacement of ACCM with brushless motors, inverter-fed AC motors or other machines with electronic commutation.

Such ACCM's negative feature as poor electromagnetic compatibility (EMC) till draw researchers attention. Physical phenomena in commutating coils and in the sliding contact are at the bottom of this drawback.

There are two ways to effectively solve this problem: experiment and computer simulation. Having broad experimental data, we have chosen the strategy of computer modeling.

For this purpose, the three levels ACCM mathematical model have been developed. The first one was reported in [1]. This paper deal with the other two.

The simulate transient processes in commutating coils and in sliding contact, one needs to know explicit values of machine parameters, first of all inductances of the armature winding. The best way to find them is to calculate, a magnetic field distribution over the machine structure [2].

Mathematical approach and models here in of course are universal. As the object for study we chose the AC commutator motor which is used in electric tool manufactured by one of the Russian firm. It is know that commutation in such machines is going much harder than in DC commutator motors because of transformer EMF in commutating coils, induced by the alternating stator flux [3,4].

Fig.1 shows a part of the armature winding of the motor under study. The brush overlaps 2,54 collector bars.

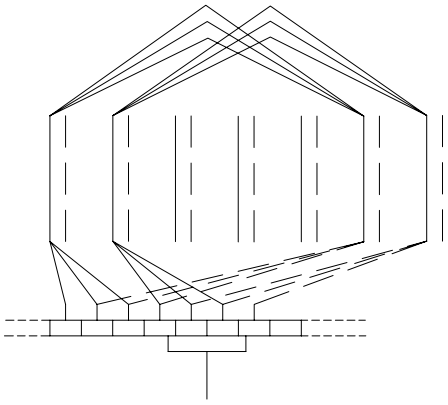

Fig.1. Armature winding drawing.

The winding coils commutating by one brush are described by the following system of ordinary differential equations, written under the assumption that distributed interconductors and commutator interbar capacitances are ignored:

$$
(1)\quad \begin{cases} i_{c1}r_{c1} + \Delta U_{сб} + \Delta U_{нб} = -(L_{1c}\dfrac{di_{c1}}{dt} + \\ + M_{21}\dfrac{di_{c2}}{dt} + M_{31}\dfrac{di_{c3}}{dt}) + e_{вр} + e_t; \\ i_{c2}r_{c2} + \Delta U_{сб} + \Delta U_{нб} = -(L_{2c}\dfrac{di_{c2}}{dt} + \\ + M_{12}\dfrac{di_{c1}}{dt} + M_{32}\dfrac{di_{c3}}{dt}) + e_{вр} + e_t; \\ i_{c3}r_{c3} + \Delta U_{сб} + \Delta U_{нб} = -(L_{3c}\dfrac{di_{c3}}{dt} + \\ + M_{13}\dfrac{di_{c1}}{dt} + M_{23}\dfrac{di_{c2}}{dt}) + e_{вр} + e_t. \end{cases}
$$

Here:

i_c - currents in corresponding commutating coils, A;

r_c - resistances commutating coils, Ω;

$\Delta U_{сб}$, $\Delta U_{нб}$ - voltage drop under run off and run over parts of the brush, V;

L, M - self and mutual inductances of the commutating coils, H;

Rotational EMF, V:

$$
(2)\qquad e_{вр} = (c_e \cdot n \cdot \Phi_m) \cdot \sin \omega t
$$

Transformer EMF,V:

(3) $$e_t = -W_c \cdot \frac{d(\Phi_m \sin \omega t)}{dt}$$

Φ_m - pole flux amplitude, Wb;

W_c - coil number of turns;

c_e - constant

To find inductances, we solved the field problem, making use the finite-element program package ELCUT® which allows to model two-dimension field. Core steel nonlinearity ha been included in consideration (μ is variable).

The problem was formulated for vector magnetic potential ***A*** coupled with flux density vector ***B*** by the relation ***B* = *rot A***. Vector ***B*** always lays on the plane of a machine cross section (xy), but vector of current density ***J*** and vector potential ***A*** are perpendicular to it (coordinate z). Only $\boldsymbol{J}_z$ and $\boldsymbol{A}_z$ components are not equal to zero. For such two-dimension problems Poisson equation is a follows:

(4) $$\frac{\partial^2 A_z}{\partial x^2} + \frac{\partial^2 A_z}{\partial y^2} = -\mu J_z$$

Additionally, the following assumptions have been accepted:

- at a given value of current, field in the region of calculation is stationary;
- coils inductances before and at the moment of commutation are assumed to be identical;
- coil-end leakage is calculated analytically;
- current in all parallel branches of the armature winding are equal;
- machine under study does not have any technological defects.

When field distribution is calculated, one can find inductances using well known formulas:

Self-inductance, H:

(5) $$L_{ii} = \frac{\psi_{ii}}{I_{ii}},$$

Mutual inductance of i and j contours, H:

(6) $$M_{ij} = \frac{\psi_j}{I_i},$$

where ψ - flux linkage, Wb;

I - current in each turn of the coil, A.

According to the commutation scheme, we took into account mutual influence of coils only in one slot layer. Fig.2 illustrates slot leakage field of one coil. Circles include only conductors without of insulation.

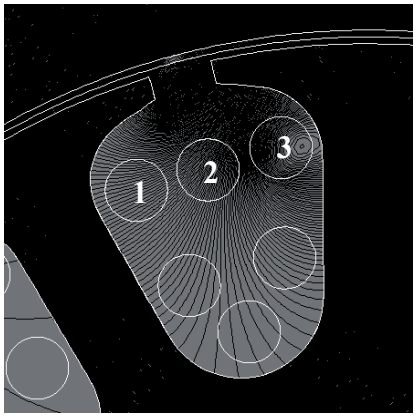

Fig.2. Slot leakage magnetic field line of the armature winding one coil (1, 2, 3 – coils numbers).

Calculations were carried out by two ways.

First: taking into account a real magnetization curve of the core steel at a given value of current in one coil.

Second (more precise): at the first step, for real distribution of current in all winding conductors and real magnetization curve, magnetic field is calculated. On the base of this result, we made a decision about the region of calculation splitting by subareas having linear magnetic properties. At the second step, the field problem for the region consisting of subareas with linear properties have been solved for a given value of current in one coil.

In result the following values of inductive parameter were received:

Table 1

Results of calculations

	$L_{1c.соб}$, мкГн	M_{21}, мкГн	M_{31}, мкГн	$L_{2c.соб}$, мкГн	M_{12}, мкГн	M_{32}, мкГн
1 way	33,099	32,7875	32,5885	33,1475	32,7953	32,7731
2 way	19,0269	18,786	18,5298	19,1638	18,7435	18,7343
Error concerning 2 way	74 %	74,5 %	75,9 %	73 %	75 %	74,9 %

	$L_{3c.соб}$, мкГн	M_{13}, мкГн	M_{23}, мкГн
1 way	33,1069	32,582	32,7704
2 way	19,0523	18,5252	18,772
Error concerning 2 way	73,8 %	75,9 %	74,6 %

Conclusions:

- Inductances of neighboring sections were got practically identical because of small difference between slot leakage fluxes;

- From above results it is seen that inductance calculated by 2nd way turns out to be more precise since this way allows to take into account saturation because of fluxes created by all conductors with currents;

- Because of low accuracy of the 1st way (about 14 %) it is not reasonable to use it.

From made calculation follows that self and mutual inductances of coils laying in one slot can be accepted by constants and in the first approximations equal each other:

$$L_{1c} \approx L_{2c} \approx L_{3c} \approx \ldots \approx L_c \approx const$$

$$M_{12} \approx M_{21} \approx M_{23} \approx M_{32} \approx \ldots \approx M \approx const$$

The system of the differential equations has been solved without armature movement that is it was in stall. In Fig. 3 the equations solution result, received with use of package Matlab, is shown.

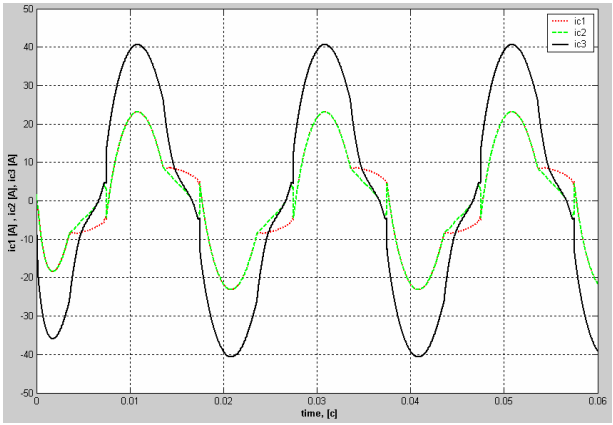

Fig.3. Curves of current in commutating coils.

Researches are executed within the framework of the grant of the Ministry of Education of the Russian Federation (A04-3.14-292; 2004).

References

[1] V. Bespalov, Y. Moschinsky, M. Panikhin, V. Tsukanov. Multilevel model of the AC commutator motors. Proceedings of the 6th International Conference on Unconventional Electromechanical and Electrical System, Alushta, Ukraine, 2004, vol. 3, pp. 811-814.

[2] V. Fisenko. FEM based numerical calculation of the electromagnetic field in electrical machines. Moscow, MPEI Publishing House, 2002.

[3] B. Tokarev. Electrical Machinery. Handbook for university students. Moscow, Energoatomizdat, 1990. – 624 pp.

[4] M. Kostenko, L. Piotrovskii. Electrical Machinery. Vol.2 “AC Machines”. Leningrad, Enegria, 1973. – 684 pp.

Victor Bespalov *– Professor, Dr. of Tech. Sciences, Dept. of Electromechanics, Moscow Power Engineering Institute (TU). 111250 Moscow, 14 Krasnokazarmennaya St. Russia. e-mail: elmech@srv-vmss.mpei.ac.ru.*

Mikhail Panikhin *- post-graduate, Moscow Power Engineering Institute (TU). 111250 Moscow, 14 Krasnokazarmennaya St. Russia. e-mail: misha3333@rambler.ru.*

Active Resistance of Rotor Winding of Large Turbogenerators

Natasa Mojsoska

Abstract: *In this paper will be elaborated a measuring of insulation systems of large turbogenerators. Basic characteristics of turbogenerator will be given as an importancy of prophylactical following. Main issue is prophylastic research of active resistance of rotor winding. The results in the paper will be analyzed for last eight years.. Also will be recalculated to 15℃ for comparing with factory values. The tables will be created and sistematized by years and grafical diagrams will be given.*

Keywords: *active resistance, measuring, turbogenerator, rotor winding*

Introduction

An annual repair in TPP are performed with purpose for bigger efficieny and reliability of work. In this paper work all analyses and examinations are considered to turbogenerator at unit 3 of TPP Bitola. The constructor of this generator is "Electricalforse" - Russia. Usually every year during the annual repair are made measures by strictly determined program. In that program besides other parameters of insulating system also is measured and active resistance of rotor winding. Analyse of presented results contributes to be observed behaviour of active resistance of rotor winding. Also the frame of variations would be founded, trend direction and duscused about prediction of values for further years.

Characteristics of turbogenerator

Type of generator		TBB-200-2A
Rated power		P=210MW
Rated voltage		U=15075kV
Rated current		I=9060A
Rated power factor		cosφ=0.85
Outer diameter of stator		D_n=2.5m
Inner diameter of stator		D_v=1.215
Length of stator magnetic core		L=4.2m
Effective length of st. mag.core		L_e=3.4782m
Wide of magnetic range		h=0.4395m
Number of stator grooves		Z=60
Height of stator grooves		h_k=203mm
Weight of stator grooves		b=20mm
Specific lose (W/kg) throught	B=1T	B=1.4T
parallelly to the rolling direct.	1.04	2.04
perpendicularly to the roll. dir.	1.71	3.35
Mass of range of mag. core		m_{fe}=77160kg
Effective surface of stator		S_{fe}=15286sm^2

Active resistance of rotor winding

Active resistance of sinchronous generators are defined by geometry of winding (length, cross-section and design) and with resistivity (specific resistance) of used material. At other side active resistance is defined by power (output), voltage and current of consumers and parameters of network. Active resistances of winding are changed by changing the temperature which is picture of loading of electrical machines.

Three-phases sinchronous generators had three exactly identical phases wich are consisted of sections connected between themselves. At some large sinchronous generators as the exeminated in this paper, phasses had halfwinding parallelly connected. The values of active resistance of all three phases are approximately equal.

Measuring

Measuring of active resistance of rotor winding is made by voltage-current UI method by laboratoric instruments with accuracy class 0.2 with purpose conclusions and the results to be valid [3]. Also is used digital instrument for measuring very low resistances tupe DLRO 24700-1 on scope of 200A and 100A [2]. During the measuring as a source for alternating current is used alternating generator with regulation of exitation. It is used electrical current of 200A. Also is measured a temperature of rotor winding by contact thermometer.

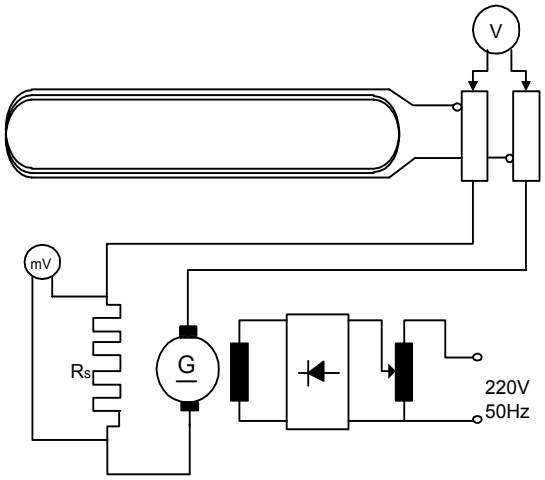

Fig.1 Survey of measuring of active resistance of rotor winding of turbogenerator.

Measuring of active resistance of turbogenerator's rotor winding at unit 3 of TPP Bitola is performed according to Fig. 1.

During the examination beside the temperature of winding also is measured an ambiental air temperature. Measured values of temperature are calculated to values of referent temperature wich according to rushion constructor of turbogenerator is 15°C. Calculated resistance is performed according to equation (1)

$$(1) \qquad \Theta_2 - \Theta_a = \frac{R_2 - R_1}{R_1} \cdot (235 + \Theta_1) + \Theta_1 + \Theta_a$$

where:

R_1 [Ω] is calculated resistance value to temperature of Θ_1=15°C

R_2 [Ω] is measured resistance value to temperature Θ_2

Θ_1 [°C] is temperature of 15°C

Θ_2 [°C] is temperature of particular measuring

Θ_a [°C] isambiental air temperature

From previous equation (1) follow eguation (2):

$$(2) \quad R_1 = R_2 \cdot \frac{235 + \Theta_1}{235 + \Theta_2} = R_2 \cdot \frac{235 + 15}{235 + \Theta_2} = \frac{250 \cdot R_2}{235 + \Theta_2}$$

Recalculated values to 15°C are compared with factory value of rotor's resistance wich for concrete generator is 0.0887Ω.

Results

Measured and calculated values of active resistance of rotor's winding at unit 3 of turbogenerator at PTT Bitola in period from 1997 till 2004 year are sistematized by years and given in following Table1:

Table 1

Result obtained from observation of active resistance of rotor's winding

god.	R [Ω]	Θ [°C]	$R_{15°C}$ [Ω]	g [%]
1997	0.0960	40	0.0872000	- 1.6910
1998	0.0949	32	0.0888576	+ 0.1780
2000	0.0928	23	0.0899200	+ 1.3750
2003	0.0928	23	0.0899200	+ 1.3750
2004	0.0958	35	0.0887040	+ 0.0045

In Table 1 is given a percentage mistake of recalculate values of active resistance to factory value. Percentage mistake is calculated according to equation 3:

$$(3) \qquad g = \frac{R_{15°C} - R_f}{R_f} \cdot 100$$

where:

g [%] is procentual mistake

$R_{15°C}$ [Ω] is calculated value of resistance to 15°C

R_f [Ω] is factory value of active resistance 0.0887Ω

On the base of previous Table 1 are created following diagrams, whereby are presented dependance of active resistance of rotor winding from time and dependnce of made procentual mistake from time, shown on Fig.2 and Fig.3.

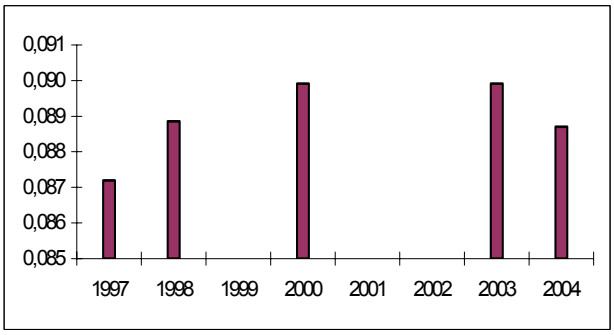

Fig.2 Dependance of rotor's active resistance from time.

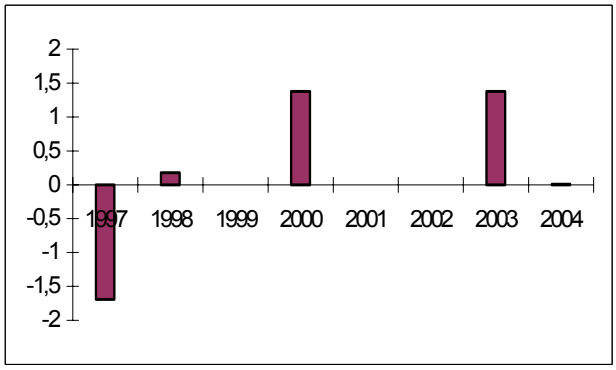

Fig.3 Dependance of percentage mistake from time.

Analyses of results

In experimental part of this paper work is followed the examination of active resistance of rotor winding with special view to results from 1997 till now.

Last eight years measurings were made by the same instruments and equipment, what contributes to bigger accuracy in comparison of the results by years.

From previous Table1 can be noticed that at years 1999, 2001and 2002 we don't have the results. At that years this kind of measuring were not be taken. When rotor of turbogenerator is shouting down , there is a very big temperature and it is imposible to measure the additional parametars. After turning off, the rotor is pulling out and immediately the team had started with cleaning and grinding the collector. And if the measuring were done after cleaning and grinding damage wiil be done of the grinding collector.

That's the reason why this measurings are not maden in particulary years, the short time predicted for repair.

With purpose for better analyse of the results of examination from Fig.2 is created diagram with linear trend of direction given on Fig.4.

Also if the results of made mistake presented by absolute values and add the direction of trend line we will obtain the follow diagram presented on Fig.5.

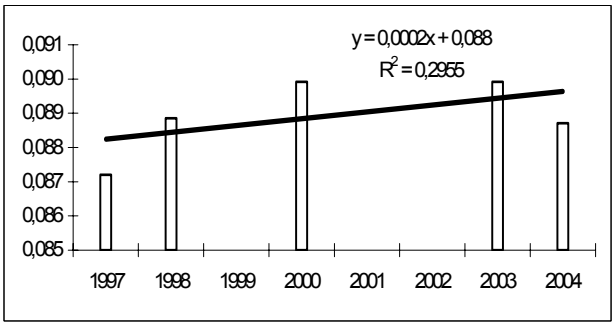

Fig.4 Trend of direction of active resistance of rotor winding.

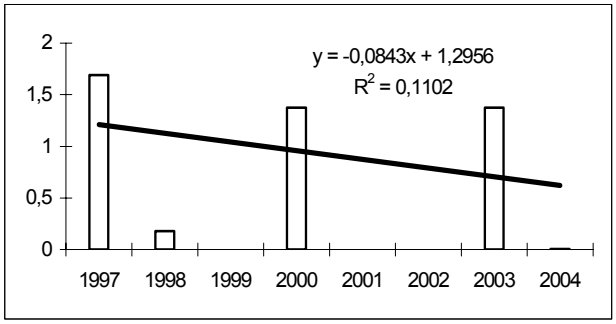

Fig.5 Trend of direction of procentual mistake.

Conclusion

On the base of presented results at Table 1 and given diagrams the conclusion is that in past years value of rotor's active resistance of particulary generator is moving into allowed bounderes and oscilating arround factory valye R_f=0.0887Ω.

According the direction of trend line can be expected that the value in further yaers will be moving around referent value.

Also the trend line of mistake according to fig.5 is decreased and incline at zero wich will be ideal state.

This year 2005 repair was not predicted for unit 3 of TPP, so with trend line from the diagram from this paper we can predict the value of resistance with accepted accuracy.

Despite the other advantages of this prophylactic research, this is the big contribution for continuing following the insulating system and the active resistance of rotor winding as a small piece from whole investigation program.

Acknowledgements

With this prophylactical research the biggest contribution is that if the measuring can't be made at some year we have predicted values for each parameter with particular accuracy which is acceptible.

References

[1] D. Hristovski - ″ Research of electrical machines ″ , ETF ZONIK kompjuteri - Skopje 1996.

[2] Elaborates, annual reports and protocols from annual year and capital repairs of turbogenerators at unit 3 of TPP Bitola

[3] T. Paspalovski. - " Examination of large turbogenerators in capital repair" MAKO CIGRE Conference Proceedings, pp. 39-46., Struga 1996.

[4] N. Mojsoska - "Teoretic and prophylactic research of effiency in exploatation of sinchronous turbogenerator at unit 3 of TPP Bitola" master thesis, ETF Skopje 2001.

Natasa Mojsoska *- Assistant, MSc., Technical Faculty, University St. Kliment Ohridski of Bitola, bb Ivo Lola Ribar Str., 7000 Bitola , MACEDONIA. e-mail: natasamojsoska@yahoo.com*

Partial Discharges of Insulating System at Large Turbogenerators

Natasa Mojsoska

Abstract: *In this paper will be elaborated a meaning of partial discharges in insulation systems of large turbogenerators. Theoretic and mathematical model will be given. The results in the paper are considered to* turbogenerator at unit 3 of TPP Bitola. *The tables will be created and grafical diagrams will be given.*

Keywords: *partial discharges, turbogenerator, gases holes, intensity.*

Introduction

Appearance of Partial Discharges (in further text PD) in insulating system of electrical machines is discovered many years ago and are as old as the electrotechnics. To PD was dedicated lot of attention for a long time.

Producing electrical machines with bigger single powers and higher voltages looking for long-lasting and more reliable operation. Operations and exploatation conditions are most different, from empty load to short circuit break with all kinds of loadings and transient appearances. During all operations insulating system must keep working in long time period during the live time.

PD in insulating system at rotating electrical machines

With plugging of voltage electrical current flows and creates electrical and magnetic field which together with voltage strained the insulation. With purpose break down do not happened, insulation is dimensioned with bigger electrical strength of material for endurance internal and external electrical, mechanical, thermal and chemical influences.

As a result of producing process, imperfections and breakdowns of row materials or influences on electrical machines in operation are shown gases holes with different dimensions. Electrical field in gases holes increased because of low dielectrical constant of air of others area dielectrics and give opportunity for creating PD inside of these holes although watching outside insulating system is o.k. The phenomena of PD in insulating system of electrical machines is manifested by several different kinds and had incidental character which is hard to predict.

The PD influenced to growing old and getting worst on insulating characteristics. It might be shown directly through effections of discharge and indirectly trough nus products. The destruction of insulation effects ultra radiation because of recombination, release of heat as a result of bombing of ions and electrons on internal surface of dielectric (gas hole).

Indirectly influenced with making of gases (ozone, slor,..) and pressure of gases and acids created by chemical process.

Internal and external influences of PD caused enlargement of dimension of holes, making inside conduct strata, erosion of surface and created dendrites and breakdown to all depths of insulation.

For producing the insulation which will annul or discrise PD is necessary to have thickness to gradient of potential to be small or to had a small electrical field. Also a producing price should be small. The heat which appears should relatively quick and easy to be taken away in environment. This referred conditions are contradictory which result to producing the insulation with PD.

The level of PD from 10^{-12} to 10^{-11} C is treated as small and it can not initiate quick destruction of insulation. These PD are named as early discharges.

Level of PD from 10^{-8} to 10^{-7}C is treated as relatively big value and it can distruct insulation, so they are known as critical discharges.

With early discharges in insulation are created the aggressive gases and acids which chemical and thermal distracted and enlarged the number of PD and also gases holes are getting bigger. Thus insulation growing old and exploitation time decline. Voltage which evolved from first PD is known by name threshold of ionization.

If number of PD increase and also gases holes than it is possible breakout of insulation. Rapide degradation can also begin from other processes such as thermal, chemical, mechanical, magnetic. Basic PD can act alone or in combination producing sudden acceleration of aging of insulation.

Ionization and discharges (early, critical and breakout) can evolve from neutral particles with large energy and from rest particles created by different incidentally possible ways on voltages under the threshold of ionization.

At high voltage machines PD are evolved from voltage. Their amplitudes are between 300 and 100000pC for voltage from 40 - 2000mV.

Research of PD are made from more aspects as: following aging of insulation, discovering troubles, detection of microlacation of mistake at insulation, predicting duration of exploitation, repairs and so on.

Theoretic and mathematical model of PD at insulation holes of rotating electrical machines

Pd happened in insulation are in three aggregate states: gas, fluid and hard. At holes there are different shapes of electrons with various mutual positions. Thereby exist

Different PD with low intensity caused current into surface of dielectric, avalanche discharges and intensity electrical arches. All PD enfeebed insulation and some of then breakout. Because insulation of generators predominantly is in hard aggregate state, here will be elaborated PD in hard dielectric.

In insulation there are gases holes. Amount electrodes in gases holes exist potential difference and gradient of that potential, in other words electric field which is distributed inside the hole. Distribution of electric field is contrary proportional with dielectrical constants. Gases in holes had smaller dielectric constant from insulation. Therefore electrical field strengten. Strengten electric field amount coused condition for appearance of ionization for which initial electron is necessary. Initial electron in holes where do not exist PD is formed under influence of radioactive or cosmical radiation, fotoelectronic emission in gases throught big values of electrical field.

In holes oxygen is presented and can accept the free electrons for connection what causes late of first PD with minute or more. Next PD begin with late of few microseconds or less, whereby initial electrons are released with bombing of dielectric surface with ions. After shown of first PD further development of discharges depends of many factors such as value of first initial free electron's voltage, age of gas hole, condition of dielectric, value of capacitive current which is allowed by dielectric and so on.

PD had differences according intensity and effects of aging and breakout of insulation. In following Table 1 and Table 2 classification is made.

Table 1

Kinds of PD and their dimensions

kind of PD	Dimension
surface emission	continually 10^{-10} to 10^{-3} A/m^2
pulsing currents	continually 10^{-15} to 10^{-8} A/m^2
sparkle discharges	continually ≈ 10 A/m^2
avalanches discharges	pulsing $\approx$ 100ns
strimers	pulsing 1 to 100ns; >100pC
liders	pulsing $\approx$ 100ns
sparks	pulsing $\approx$ 100ns
partial arches	pulsing $\approx$ 100ns

Table 2

Kinds of PD and their characteristics

kind of PD	detec-tion	importent for	
		aging	breakout
surface emission	no	no	no
pulsing currents	no	yes	yes
sparkle discharges	no	yes	no
avalanches discharges	no	yes	no
strimers	yes	yes	yes
liders	yes	yes	yes
sparks	yes	yes	yes
partial arches	yes	yes	yes

According intensity PD are grouped: weak intensive, intensive and express intensive.

Weak intensive PD are emission of surface, sparkle discharges with small value of current of discharging and can not be detected by usually used impulse methods of measuring. First initial electron is get by thermal ionization and cold emission.

Intensive PD are avalanches (Tausend) discharges and partial microdischarges with impulse nature. Can not be detected by usually used impulse methods of measuring, but can be detected by sensitive laboratory measuring technics.

Express intensive PD are strimers, liders, sparks, partial arches and breakout of insulation. Can be detected by ussualy used impulse measuring methods and technics.

At large electrical machines most frequently PD are expressed as intensive PD - strimers, the reason that will be presented in detail.

We examine one gas hole with initial electron get by previously described ways and surrounded by dielectrics. Under influence of electrical field initial electron is moving in opposite direction of electrical field and crushed with gases molecules ionized them and released another free electrons. This process continue, avalanchely enlarged number of free electrons and all number of positive ions moving with small speed in opposite direction of electrons. Each of the free electrons which are crushed with gases molecules do not create new electron (do not had ionization). It will be done critical condition and breakout will happened.

Slow moving ions on its way to opposite electrode made cloud which locally increase value of electrical field. If electrical field outdo critical value coursed ionization in cloud area and new electrons avalanches. This stretching out of strimer as tight lighten canal is very fast and released heat. Current of discharge is limited with insulation characteristics of dielectric. Discharge is extinguished an state when two ends of hole are separated with opposite space filling known by name dipole filling which create field opposite to the basic.

Dipole filling is equivalent to filling situated into ellipse with half axis a,b which are not determined by dimension of hole but by distribution of space filling into strimer process. Existing of space fillings to surface of dielectric caused free electrons into gases and with electrical field influenced to the field of hole which caused new PD.

Hole voltage consists of voltage of basic field and voltage of space filling perform according following equations (1), (2) and (3):

$$\Delta U = \Delta U_a + \Delta U_q \tag{1}$$

$$\Delta U_a = f \cdot E_0 \cdot l = f \cdot l \cdot U_0 \cdot \nabla u_0 = E_a \cdot l \tag{2}$$

$$\Delta U_q = \frac{q}{g \cdot \varepsilon_0 \cdot l} = E_q \cdot l \tag{3}$$

where:

ΔU [V] is change of voltage of hole

ΔU_a [V] is change of voltage caused by basic field

ΔU_q [V] is physical change of voltage caused by basic field and apparent physical space filling

f is coefficient determined by increase of field because the damage into hole

l is length of damage

U_0 [V] is contribute voltage

$\nabla u_0 = E_0/U_0$ [V] is reduced basic field

q is space filling

g is coefficient determined by geometry of damage and location of space filling, depends of relationship of axis of ellipse a and b.

Quantity of solid fulfill during the change time (decrease) with process of surface emission, drift of ions in holes and their distribution inside of dielectric.

Pd had differences between and there are three timing phases: young, middle old and old PD.

Young PD included PD from first to further PD till few minutes after it. At disk gases holes discharge are made through more solid displaced, approximately same by size and coincident PD. At spherical holes PD are made through one single discharge. Change - increase of PD voltage is around 500ps and duration of impulses from few microseconds. These values are typical for strimers PD.

After 5 minutes from beginning PD are shown middle old PD which lasted to 5 hours. They ere characterized by time of increase and duration of impulse from 5ns to 50ns. Space shape is diffuse as a result of chemical process into holes of dielectric. Gases products and water in the air created from chemical processes made acid drops located inside of hole. Dielectric conductivity increased also initial electrons and bombing surface with ions happened. Ionization at first moment is not intensive and produced PD with avalanches processes (Taunsend) which occupied bigger part of hole with diffuse shape of discharge. These middle PD are characterized by longer time of increasing and enlarging duration. They are known by name avalanches (Taunsend) discharges.

Amount time of 10h to 100h started the old PD. They aproximated to begging PD with fast enlargement and bigger duration because the drop off the impulse. Also frequency of impulse become bigger and amplitude of impulse is growing.

Characteristics of PD are different age, shape of impulse, time of increase and its duration. As a result of this characteristics PD can be differentieted from noises.

For mathematical calculation of PD usually is taken macroscopian view of hole and effects of PD to external circle. The most simply and the most used mathematical model of PD in holes is Germant-Philipoff method called as a-b-c model of capacivisity. Beside this model there are others which are better and with bigger accuracy, but more complicated for eg. model of Pedersen. This model takes care for shape and location of the hole.

Analyse of results of measuring of PD at turbogenerator at unit 3 of TPP Bitola

PD on this particular generator is measured only few years and the results are not clear enough. As important parameters for PD were measured apparent filling, middle current, square of filling at unit time and frequency of impulses, all as a function of voltage.

Apparent filling of PD and middle current of PD are generally parameters for definition of intensity of PD.

In years 1989, 1990, 1991and1999 measuring was made by team of experts from Electrotechnical Faculty in Skopje from High-voltage laboratory. For examination was used wide zonal amplifier. The values of basic noises are between 800-1000 to 1500pC.

The results from some measuring available to me, systematized and graphical presented are given in following Figs.1, 2, 3 and 4.

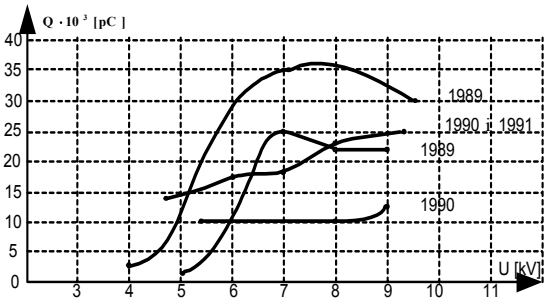

Fig.1 Apperent filling of PD as a function of voltage Q=f(U).

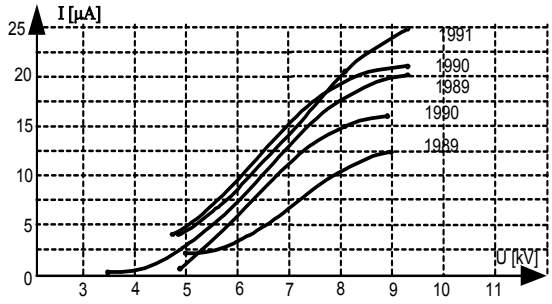

Fig.2 Middle current of PD as a function of voltage I=f(U).

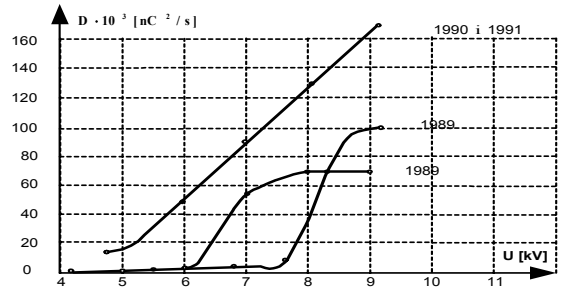

Fig.3 Square of apperent filling of PD as a function of voltage D=f(U).

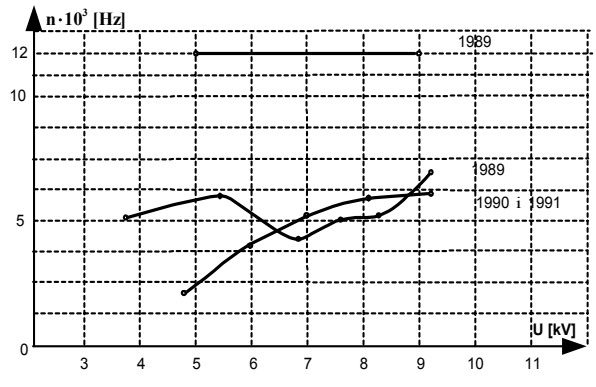

Fig.Frequency of impulses of PD as a function of voltage n=f(U).

In 2000 year the expert team from Canada in collaboration with our team from TPP made the measuring of PD in generator with new equipment by IRIS Power Engineering Inc.

Conclusion

This kind of measuring is not made regular every year. Maybe the problem is financial or short time of repair. But with proper equipment for "on-line" testing of PD can be obtained useful information about winding condition. It is propose examination of PD to be made every year with the same equipment and if it possible "on-line". Also it is recommended obtained results to be compared with results from previous years and analyzed differences of characteristics of measuring parameters. The main purpose is reliability and security of work.

Acknowledgements

Our team of experts do not have big experience for this kind of measuring of PD in insulation, which is one of basic elements for successful interpretation of the results and accuracy during the examination. Gradually after few years they will collect enough results to be compared and made conclusions about variation of parameters.

References

[1] N. Mojsoska - "Theoretic and prophylactic research of efficency in exploitation of synchronous turbogenerator at unit 3 of TPP Bitola" master thesis, ETF Skopje 2001.

[2] Elaborates, annual reports and protocols from annual year and capital repairs of turbogenerators at unit 3 of TPP Bitola

[3] J. Jankov - " Measuring of PD in insulation of stator winding of generators - predictive extend for security of work" MAKO CIGRE Conference Proceedings, P11-07, Ohrid 2001.

[4] V. Jankov, R. Minovski, T. Markovski, L. Klasninoski, V. Savevski, D. Jankovski - " PD of generator 1 at HPP Globocica" MAKO CIGRE Conference Proceedings, P33-05, Ohrid 2001.

[5] IRIS Power Engineering - Report for Bus Coupler Installation for Electric Power Company of Macedinia unit 1 Bitola PS, may 8-11,2000.

Natasa Mojsoska *- Assistant, MSc., Technical Faculty, University St. Kliment Ohridski of Bitola, bb Ivo Lola Ribar Str., 7000 Bitola , MACEDONIA. e-mail: natasamojsoska@yahoo.com*

Broken Part in Stator Core End Teeth Zone of AC Electrical Machine-Effects and Diagnosis

Rumena Stancheva and Ilona Iatchev

Abstract: *A part of stator core end teeth zone is simulated broken. Comparison between electromagnetic and temperature field values and their distribution under the normal working mode is carried out. Quasi three-dimensional electromagnetic and temperature field is solved as couple field forward problem applying FEM. A method for stator core state diagnosis is proposed as an identification problem solution on the basis of a statistical criterion. An application example is given referring to the 200MW turbine-generator.*

Keywords: *couple field, FEM, identification.*

Introduction

Typical example of electrical machine failures caused by broken teeth parts are the stator core end packages of large turbo-generators [1]. While the radial magnetic flux in the core of the machine remains approximately constant at a constant terminal voltage axial flux density at the surfaces of clamping flange or the stator end packages strongly depends on the load current and the power factor. Accordingly to the nature of the diurnal load graphics the working modes are changed. The most dangerous are the regimes at the leading power factor [2]-[4]. The temperature calculations in the stator core end regions show that there are local temperatures over permissible ones at some regimes at the leading power factor. This effect leads to additional thermo-mechanical stresses with grate magnitude and as a consequence the clamping thumbs fatigue and some remaining deformations results. Distances between the thumbs and the stator core end packages gradually arise as well as those ones between the stator core end lamellae in the region of the teeth. Their vibrations grow up under the influence of the electromagnetic field variations. Some elementary lamellae are possible to be tearing away. As a result the winding breakdowns and the breakdowns to the earth are possible. So the temperature control in the end region is obliged. The describing problems are very serious and impose investigations to be carried out in two directions: the temperature distribution in the end region at the presence of broken part in the teeth and the sequels of it to be discussed at first, the possibilities for forecast the disruptions at the stator core inner structure is the second.

The dangerous situations in the stator core end are too expensive to be reproduced in nature. Because of this a numerical example is simulated at fault in the teeth zone. Electromagnetic and the resulting temperature field are calculated at these circumstances. On the basis of the appreciated changes in temperature distribution the conclusions with respect to stator core state are made.

The second part of the presented paper is devoted to a new method description and evaluation of its application. Taking into account currently observed temperature values on the stator core boundary it concerns to the identification problem solution. On the basis of a statistical criterion [5] the methodology includes recommendations of stator core end structural changes prediction. The application example is referring to 200MW turbine-generator.

Coupled Field Model

Electromagnetic field

An axial section of 200MW (TBB-200-2A) turbo-generator end region is shown in Fig.1.

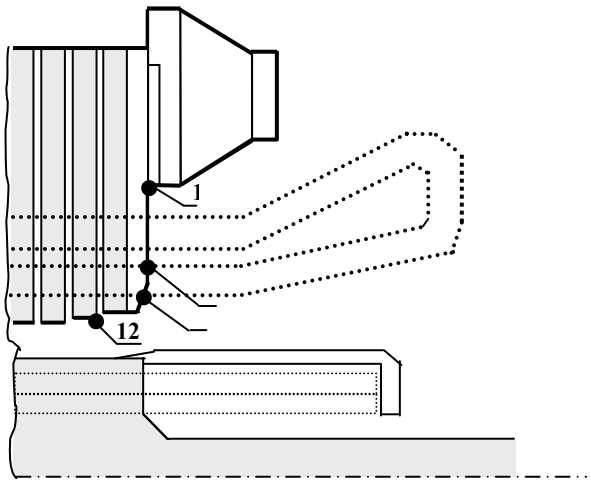

Fig.1. Axial section of generator end region with control points.

The following assumptions have been made.

- The field is quasi-three-dimensional and three spatial components of the currents in the windings are taken into account. The field is solved under steady-state mode as quasi-stationary. The separate parts of the stator and rotor end windings are represented as strips of finite dimensions with space-periodic currents defined by the actual winding currents. Only the effect of the first harmonic along the tangential coordinate is considered. Anisotropy in the teeth zone, eddy currents in the conductive media and the generator's operating mode (load angle and power factor) are also accounted for. The problem is considered linear.

The corresponding electromagnetic field equations for the steady state behaviour of the generator under sinusoidal input are given as

$$\text{rot}(\hat{\nu}\,\text{rot}\,\dot{\mathbf{A}}) = \hat{\gamma}\,\dot{\mathbf{E}} + \dot{\mathbf{J}}_e \tag{1}$$

$$\dot{\mathbf{E}} = -j\omega\,\dot{\mathbf{A}} - \text{grad}\,\dot{V}.$$

In (1) tensors $\hat{\nu}$ and $\hat{\gamma}$ present the specific magnetic resistivity and the electric conductivity respectively. They form is due to the anisotropy of the medium. The quantities are noted as follows: $\dot{\mathbf{A}}$ is the magnetic vector potential, $\dot{\mathbf{E}}$-the vector of electric intensity, $\dot{\mathbf{J}}_e$-the exciting current density in the coils cross sections and $\dot{V}$ - the scalar electric potential. In accordance with the assumptions that all electric and magnetic quantities vary only in sinusoidal manner vector and scalar variables in equations (1) are in complex form. The peculiarity of ordinary electrical machine is that axes of anisotropy and the co-ordinate axes of the device are coinciding. As a result the tensors $\hat{\nu}$ and $\hat{\gamma}$ are represented as diagonal matrices and the suitable gauge condition is valid [6,7]:

$$(\nu_r + \nu_\varphi + \nu_z)\,\text{div}\,\dot{\mathbf{A}} + (\gamma_r + \gamma_\varphi + \gamma_z)\,\dot{V} = 0. \tag{2}$$

Clearly in case of isotropy (2) is reduced to the well known gauge condition. The scalar electric potential $\dot{V}$ and the magnetic vector-potential $\dot{\mathbf{A}}$ are determined by solving the system of equations (1) and (2).

Temperature field

The eddy current losses of the conducting parts in the end zone of the machine are calculated and the distributed losses are applied as heat sources for the solution of the thermal problem. The temperature field is analysed as axisymmetrical. The following equation describes it

$$\text{div}(\lambda\,\text{grad}\,T) + Q = 0. \tag{3}$$

The quantity T denotes temperature, λ-the thermal conductivity and Q-the density of the heat sources. It depends on the eddy current's density $\dot{\mathbf{J}}$ determined by equation

$$Q = 0.5\hat{\gamma}^{-1}\dot{\mathbf{J}}.\dot{\mathbf{J}}^{*}. \tag{4}$$

On the basis of the describing models formulation electromagnetic and temperature field are calculated by FEM and their distribution is found. The comparison between calculated and measured temperature results at two control points for twenty regimes show good agreement [8] by error not exciding 12%.

Broken part at stator core end teeth zone

Simulation

Suppose that a part of the stator core tooth is broken. If the tooth height is h_z imagine that the m part of height is mh_z with $0 \le m \le 1$. The broken part depth is k-th part of the investigated end zone length l. The teeth region is considered anisotropic.

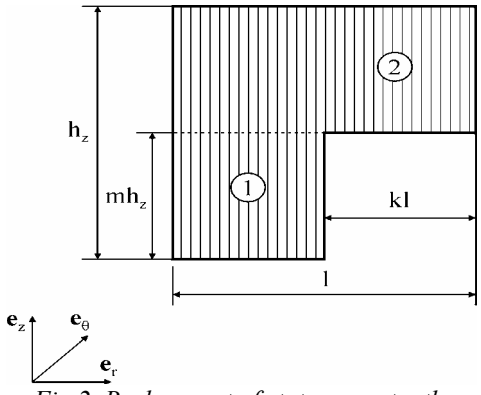

Fig.2. Broken part of stator core tooth.

In the region 1 equivalent relative magnetic permeability is calculated applying following expressions:

$$\mu'_{r1} = \frac{b_k + b_z[(\mu_r - 1)(1-k)k_f + 1]}{b_k + b_z}; \tag{5}$$

$$\mu_{\theta 1} = \frac{b_k + b_z}{b_k + \dfrac{b_z}{(\mu_r - 1)(1-k)k_f + 1}}; \tag{6}$$

$$\mu_{z1} = \frac{b_k + \dfrac{b_z\mu_r}{(1-\mu_r)(1-k)k_f + \mu_r}}{b_k + b_z}. \tag{7}$$

Here the quantities b_k and b_z are the tooth and the slot widths, respectively; k_f is the coefficient of the stator core filling and μ_r is relative magnetic permeability of the material. The terms with respect to μ'_r, μ_θ and μ_z in the region 2 are the same as (5), (6) and (7), but taking into account that $k = 0$. The theoretical results show that broken part mh_z of the height h_z does not participate in the expressions. For the investigated generator $b_k \approx b_z$, $k_f = 0.9$ and $\mu_r = 500$. If the depth of the broken part is referred to $k = 0.3$ the numerical results are: $\mu'_{r1} = 158.190$; $\mu_{\theta 1} = 1.994$ and $\mu_{z1} = 1.850$. For normal state without any fault the calculated values are: $\mu'_r = 225.550$, $\mu_\theta = 1.996$ and $\mu_z = 5.410$. The reduction of the values are: $\Delta_r\% = 29.8\%$; $\Delta_\theta\% = 0.7\%$ and $\Delta_z\% = 65.8\%$.

Temperature field distribution

The temperature distribution at rated mode is studied

in the presence and without broken part at stator core end teeth. The temperature map is presented in Fig.3.

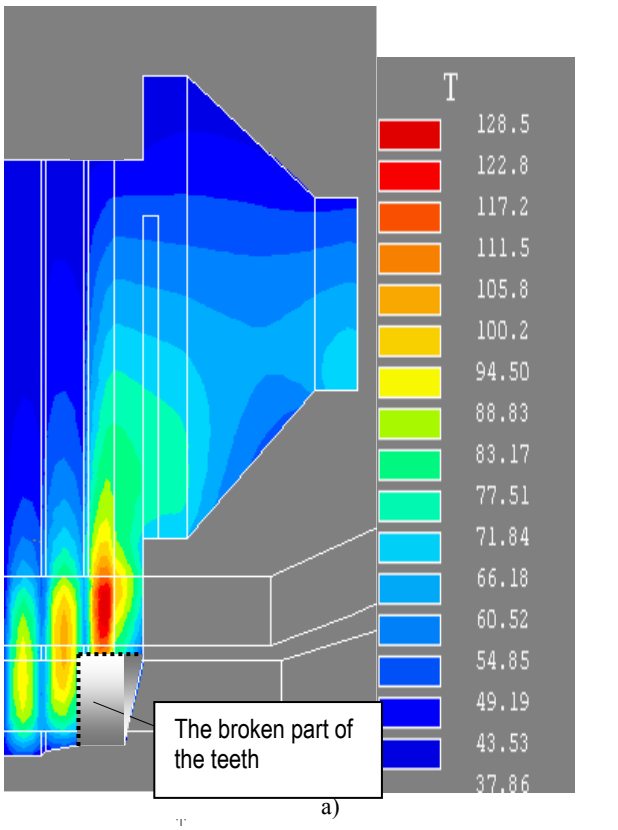

Fig.3. Temperature field distribution at the presence a) and without broken tooth b) in stator core end.

The temperature field distribution at rated mode in the presence of broken part at stator core end teeth zone is shown in Fig.3*a*. The temperature distribution in Fig.3*b* is referring to the case without any disruptions in stator core inner structure. The comparison between the results shows that so described damage leads to the following changes in the temperature field map:

-Considerable redistribution of the field;

-The highest temperature level increases more than 30 percents. Its absolute value reaches 120^0C. This is considerably more than permissible stator core temperature of 105^0C;

-The temperatures at the second and the third packages increase at the same rate as in the first package;

-The most temperature loaded region is sharply-outlined. Its position in the stator core end zone remains approximately the same situated at first core package. But its location descends near to the broken part.

-The flange temperatures are not changed.

As a result of 30 percent temperature increasing the thermo-mechanical loads and vibrations enhancing are also expected. Lamellae insulation disturbance is in short time possible and the temperature and the vibration arising are the sequels. The stator core end zone damage is impending nearly in the future.

These machines and their reappearing take a lot of money. So it is very important to predict the describing situation in its beginning. The identification of the broken tooth part is proved possible in its come into being.

Identification problem solution

In essence the proposed method [5] of identification problem solution consists of the following. On the stator core boundary the temperature is currently watched at N accessible control points. It is preferable to measure temperatures instead of boundary inductions because of the fact that the induction values are considerably influenced by ferromagnetic surroundings. Let note the calculated temperature values at i-th control point by θ_c, the measured one without any fault in the stator core inner structure by $\hat{\theta}_m$ and the temperature value at the presence of a broken tooth by θ_m. The calculated and measured results are only discrete values and they are both determined with some statistical errors. For example applying numerical procedure (usually FEM) the temperature θ_c is determined as a random variable. The similar variables are affected by casual factors: the round-off error and the error of investigation region discretization. The nature of these errors shows that this random variable is normal distributed. The measured quantities $\hat{\theta}_m$ and θ_m are also normal distributed random variables because these are the characteristics of the casual factors influencing on them. Consequently the absolute value of the difference $\Delta\theta^i$ between the couple θ_c and θ_m determined at i-th point of the boundary is also normal distributed random variable

(8) $$\Delta\theta^i = abs(\theta_c^i(x,y,z) - \theta_m^i(x,y,z)) .$$

The mean of the deviations at all investigated control points on the boundary is calculated by the expression

(9) $$\overline{\Delta\theta} = \frac{\sum_{i=1}^{N} \Delta\theta^i}{N} .$$

The unbiased variance estimator $s_{\Delta\theta}$ of the random variable $\Delta\theta$ is then defined by the term

(10) $$s_{\Delta\theta}^2 = \frac{\sum_{i=1}^{N} (\Delta\theta^i - \overline{\Delta\theta})^2}{N-1} .$$

In the case of numerous observation points N the estimator $s_{\Delta\theta}^2$ is also characterized by standard distribution. The sum of the deviation squares of N independent random variables each normal distributed gives the result with chi-squared distribution χ_N^2. Consequently the unbiased variance estimator $s_{\Delta\theta}^2$ of the random variable $\Delta\theta$ possesses the same distribution. When the set of new measured results is obtained during the time the ratio T_c between the currently calculated variance $s_{\Delta\theta}^2$ and the initial one $s_{\hat{\Delta}\theta}^2$ (in the beginning of the testing control without any accidents) is evaluated

(11) $$T_c = \frac{s_{\Delta\theta}^2}{s_{\hat{\Delta}\theta}^2} .$$

By this ratio two hypotheses are tested: the null hypothesis H_0 that the two compared variances are commensurable against the opposite hypothesis H_1 that $s_{\Delta\theta}^2 > s_{\hat{\Delta}\theta}^2$. The comparison between the calculated T_c ratio and the standard tabulated one T_t pointed which one of the hypotheses is correct. If inequality

(12) $$T_c \succ T_t$$

is realized it means that the hypothesis H_1 is right, Then the H_0 hypothesis is rejected. This means that the last obtained set of measuring values includes significant errors. In other words these errors haven't occasional character and it could be due only to the essential external influence. The right conclusion is that some structural disturbance in the inner structure of the stator core end zone has been appeared.

When the inner structure of the stator core end is broken the temperature values on the boundary ought to be sensitively changed. And taking into account the described methodology it is completely realistic detection of stator core end teeth zone break up.

Method realization

Numerical example

Consider 12 control points situated in a following way: the first one at the bottom of the tooth and all of the others to the 12-th is posed along the height of the tooth at equal distances to the bottom of the flange (Fig.1). The calculated θ_c, the measured temperatures without any fault $\hat{\theta}_m$ and the temperature values at the presence of a broken tooth θ_m are shown in the Tabl.1.

Table1

Calculated and "experimental" temperature results on the boundary

Point N	θ_c, ^{0}C	$\hat{\theta}_m$, ^{0}C	θ_m, ^{0}C
1	44.7	43.9	46.3
2	50.4	49.2	52.4
3	53.4	50.1	54.8
4	53.8	50.8	55.2
5	51.7	49.2	53.8
6	47.1	45.1	51.1
7	55.1	55.6	64.2
8	57.9	58.8	69.6
9	60.9	62.2	73.7
10	63.2	65.0	74.4
11	62.2	64.3	70.0
12	66.9	69.6	71.5

Because it is carried out only a numerical experiment as a simulation of the real situation the "measured" temperatures without any fault $\hat{\theta}_m$ are simulated as random generated values having normal distribution on the basis of the calculated ones θ_c. This acceptance takes into account the casual character of the errors of calculations and measurement and their probability distribution. These results are obtained considering that the generator has been worked at normal operating conditions. Therein the variable $\hat{\theta}_m$ is examined as initially measured set of temperature values. The temperature results θ_m are also calculated ones but at the presence of a broken tooth. Now the equivalent relative magnetic permeability along the coordinate axes $\mu_r^{'}, \mu_\theta$ and μ_z are calculated by the use of the expressions (5), (6), (7). The FEM calculations of the fields are made considering so presented anisotropy (2).

Statistical analysis

In accordance with the method described above the algorithm is implemented as follows:

- The mean (9) of deviations

$$\hat{\Delta}\theta^i = abs(\theta_c^i(x,y,z) - \hat{\theta}_m^i(x,y,z))$$

between calculated and initially measured results at all control points on the boundary is $\overline{\hat{\Delta}\theta} = 2.0$;

- The unbiased variance (10) of initially measured set of the values $\hat{\theta}_m$ referring to the state of electromagnetic device without any defects is $s^2_{\Delta\theta} = 0.89$;
- The mean (9) of deviations
$$\hat{\Delta\theta}^i = abs(\theta^i_c(x,y,z) - \theta^i_m(x,y,z))$$
between the calculated and the "experimental" temperatures at the presence of the broken tooth part is $\overline{\Delta\theta} = 6.05$ and the unbiased variance respectively is $s^2_{\Delta\theta} = 23.30$.
- On the basis of the obtaining results the ratio $T_c = 26.2$ is determined.
- Tabulated value of $T_t = F_{\nu_1,\nu_2}(\alpha) = 2.83$ criterion is found [9] characterized by $\nu_1 = \nu_2 = 11$ degrees of freedom and $\alpha = 0.05$ level of significance.

Results evaluation

The comparison $T_c >> T_t$ proves that the set of the "experimental" temperature values θ_m includes a significant errors. These errors have not casual character. The inequality between T_c and T_t quantities is possible to be due only to the broken inner structure of the stator core end package.

Conclusion

A part of stator core end teeth zone is simulated broken. The 30 percent temperature increasing at the region of the teeth in the stator core end packages is observed. This effect should be explains thermo-mechanical loads and vibrations enhancing in this zone.

The results of the new method realization are evaluated. The method is referring to the prediction of instantaneously came into being faults in the inner stator core end structure of the AC electrical machines.

A numerical example is regarded. In working mode instantaneously arising fault in the stator core end package is simulated. On the basis of a proposed statistical criterion the problem is specified.

Acknowledgements

The study is a part of the work carried out on the project "Couple and inverse problems in electrical machines" supported by NFSI of Ministry of Education and Science.

References

[1] Karmaker, H. An Experimental Study of Electromagnetic Field Distribution in Large Machines, Int. Conf. on the Evolution and Modern Aspects of Synchronous Machines, Zurich, Suitzerland, 1991, pp. 522-524.

[2] Silva, V., G. Meunier and A. Foggia, A 3D Finite-Element Computation of Eddy Currents and Losses in the Stator End Laminations of Large Synchronous Machines, IEEE Trans. Magn., vol. 32, No. 3, 1996, pp.1569-1572.

[3] Mecrow, B., G. Jack and C. Cross. Electromagnetic design of turbo-generator stator end regions, *IEE Proceedings*, Part C, vol. 136, No. 6, 1989, pp.146-149.

[4] Schastlivyi, G.,G..Fedorenko,V..Vigovskyi, Turbo and hydro generators under variable regimes, Kiev, Naukova dumka, in Russian, 1985.

[5] Stancheva, R. Statistical Analysis Application for the Solution of some Inverse Problems in Electrical devices, 5th International Conference on Applied Electromagnetics PES 2001, Nish, Yugoslavia, 2001, pp.143-146.

[6] Stancheva, R., I. Iatcheva. Numerical Determination of Operating Chart of Large Turbine Generator", Int. Conf.on Electr. Machines ICEM'2002, Book of Abstr., Full text on CD, Brugge-Belgium, 2002, pp. 329.

[7] Stancheva, R., I. Iatcheva. Investigation of the Electromagnetic Field in the Turbine-generator End Region Considering the Anisotropy". Electrical Engineering and Electronic, 1-2, Bulgaria, 1995, p.6-11.

[8] Stancheva, R., I. Iatcheva. Turbogenerator Stator Core Faults Diagnosis on load, International Agean conference on electrical machines and Power electronics, ACEMP 2004, Istanbul, Turkey, 2004, pp. 30-35.

[9] Smirnov, N., I. Dunin-Barkovski. Course of Probability and Mathematical Statistics, Science, M., in Russia, 1969.

Rumena Stancheva – *Associate Professor, Dr., Faculty of Automatics, Technical University of Sofia,8 Kl. Ohridski Str.,1000 Sofia, BULGARIA. e-mail: rds@tu-sofia.bg.*

Ilona Iatcheva – *Associate Professor, Dr., Faculty of Automatics, Technical University of Sofia, 8 Kl. Ohridski Str., 1000 Sofia, BULGARIA. e-mail: iiach@tu-sofia.bg.*

Steady-State Performance Analysis of a Salient-Poles Synchronous Generator based on the Finite Element Method

Zlatko Kolondzovski and Lidija Petkovska

Abstract: *In the paper a determination of parameters and performance characteristics of a small salient poles synchronous generator (SG) is presented. Generator's parameters and characteristics are determined via Finite Element Method (FEM) and for that purpose is used the software package FEMM version 3.3. When possible, a comparison with the measured values is presented too. Detailed performance analysis of the SG steady operation is carried out.*

Keywords: *Salient-pole synchronous generator, Finite Element Method, Magnetic field, Parameters, Characteristics.*

Introduction

When using the traditional methods for synchronous generator performance analysis the magnetic field is known only approximately. The evaluation of the machine characteristics is based on a rough idea of the field distribution in the magnetic core. These methods usually give satisfactory results for steady-state operation of the machine, but for transient operation the results are unreliable. It is one of the reasons why a lot of research work has recently been done associated with the numerical field analysis. The Finite Element Method (FEM) has been widely proved to be efficient when dealing with complicated geometries. The distribution of the magnetic field is solved by system of Maxwell's equations. Because of the nonlinearity of the core materials the system of equations must be solved iteratively. Equations should be solved simultaneously in the same iteration loop, if a fast convergence and a short solution time are wanted.

The proposed methodology is applied on experimental synchronous generator set, with rated data: S_n=3 kVA, U_n=400 V, f_n=50 Hz, I_{nf}=4.17 A, n_n=1500 rpm, I_{fn}=5.5 A.

Mathematical Formulation

The mathematical formulation for magnetic field problems description is based on the system of relevant Maxwell's equations, by which the magnetic field is described in closed and bounded system [1]. In our case the problem is 2D and here one can suppose that the axial length of the machine is infinite and the machine geometry is invariant along the z-axis. The synchronous generator is treated as a quasi-static magnetic system.

The field intensity $\boldsymbol{H}$ and flux density $\boldsymbol{B}$ must obey:

$$\nabla \times \boldsymbol{H} = \boldsymbol{J} \tag{1}$$

$$\nabla \cdot \boldsymbol{B} = 0 \tag{2}$$

The widely known subject to a constitutive relation between $\boldsymbol{B}$ and $\boldsymbol{H}$ for each material is:

$$\boldsymbol{B} = \mu \boldsymbol{H} \tag{3}$$

In the case of electric machines the stator and rotor core are made from saturating iron and therefore the permeability μ is a function of $\boldsymbol{B}$. The Finite Element Analysis (FEA) uses the magnetic vector potential approach about finding a field that satisfies Eqs. (1)-(3). The relationship between the flux density and the vector potential is

$$\boldsymbol{B} = \nabla \times \boldsymbol{A} \tag{4}$$

and from (4) we can express the distribution of the magnetic field by the following nonlinear partial differential equation:

$$\nabla \times \left(\frac{1}{\mu} \nabla \times \boldsymbol{A} \right) = \boldsymbol{J} \tag{5}$$

Assuming Coulomb gauge $\nabla \cdot A = 0$, for linear materials Eq. (5) reduces to a form:

$$-\frac{1}{\mu} \nabla^2 \boldsymbol{A} = \boldsymbol{J} \tag{6}$$

If there are no currents in the domain under consideration, the right side term in Eq. (6) is zero. In the general 3D case, $\boldsymbol{A}$ is vector with three components, but in the analyzed case, considered to be 2D planar, two components of $\boldsymbol{A}$ are zero, leaving just the component in the "out of page" direction.

The use of vector potential formulation is an advantage that all the conditions to be satisfied have been combined into a single equation. We can notice that if $\boldsymbol{A}$ is found, $\boldsymbol{B}$ and $\boldsymbol{H}$ can then be deduced by differentiating $\boldsymbol{A}$.

FEM Procedure

The procedure for numerical computation of magnetic field problems, by using the finite element method is divided into three steps:

- *Pre-processing* – the derivation of the FE model of the electric machine under consideration, defining material properties, boundary conditions and mesh generation;
- *Processing* – solving the problem by the relevant Maxwell's equations and obtaining the field distribution in the analyzed domain of the electric machine;
- *Post-processing* – calculation of characteristics, as well as parameters, of the analyzed electric machine.

Pre-processing

After the problem geometry is defined we have to complete the entire domain of the electric machine by defining the material properties and boundary conditions. The basic idea of FEM application is to divide that complex domain into elements small enough, under assumption to have linear characteristics and constant parameters. Usually, triangular elements are widely accepted shapes for 2D FE models. After this step is completed, the output is always generation of finite element mesh. It is recommended to make mesh refinements in the regions carrying the interfaces of different materials, or with expected or presumed significant changes in the magnetic field distribution. In Fig. 1 is presented the 2D mesh of the tested machine, which is consisted of 24975 nodes and 49452 elements.

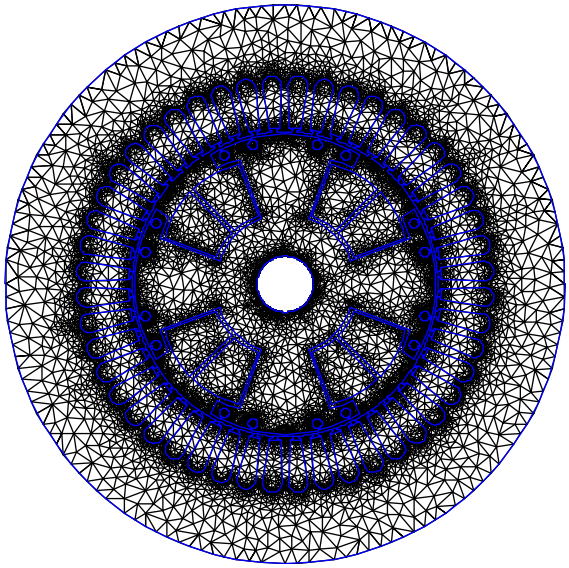

Fig.1. Finite element mesh

Processing

The solution of the problem, when the magnetic vector potential A is used, as an output from the 2D computations offers the values $A\{x, y\}$. The equipotential lines $A = const$. represent flux lines and the magnetic field distribution along any surface is obtained. As an example, in Fig. 2 is presented the distribution of the field flux per pole.

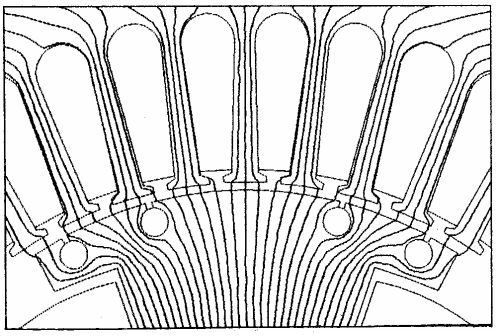

Fig.2. Field flux distribution at no-load of SG

Post-processing

This is the final and most important step of the FEM application. In this step we have possibility to compute various types of line and surface integrals numerically in terms of the magnetic vector potential A. This enables to determine different electric, magnetic and mechanic quantities and characteristics. In fact all the reactances and characteristics of the tested synchronous generator in this paper are determined in the step of post-processing.

Determination of Steady-State Reactances

The direct and quadrature axis synchronous reactances are important in steady state performance of a synchronous generator. Here is presented the procedure of their determination by FEM [2]. The results are obtained using the software package FEMM Version 3.3 and they are compared to the results obtained by the traditional methods.

Direct axis synchronous reactance

In the case of direct axis synchronous reactance X_d the currents in the armature winding are distributed sinusoidally such that the field produced peaks at the direct axis because the armature current peaks at the quadrature axis. The field winding is not energized. Magnetic flux distribution of the armature reactance field for this case is presented in Fig. 3.

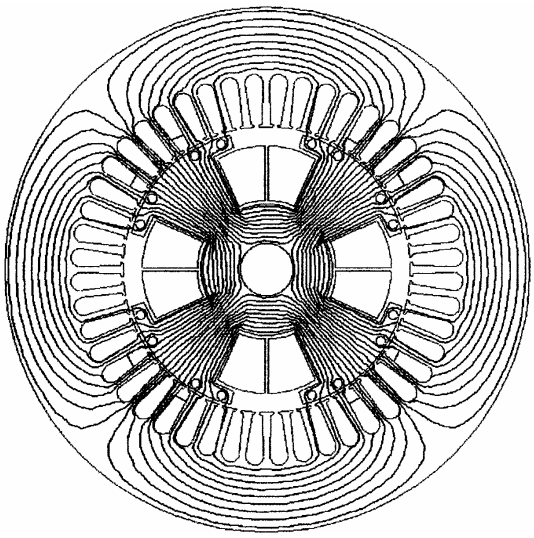

Fig.3. Magnetic flux distribution for X_d calculation

In general case, the inductance is calculated as a ratio of flux linkage to current:

$$L = \frac{\psi}{I}, \tag{7}$$

We can calculate the flux linkage as product of the number of turns N, the depth of the problem l and the difference in the vector potential $\Delta\mathbf{A}$ at the location of the two coil sides

$$\psi = Nl\Delta\mathbf{A}, \tag{8}$$

Here the difference in the vector potential ΔA is obtained directly from the finite element vector potential solution. If we assume that the fictitious winding on the direct axis has the same number of turns as the phase winding we need another factor to find the direct axis inductance. For a 3-phase machine, the current in the direct axis would have to be 3/2 times as great as the phase current to produce the same magneto-motive force in the direct axis as the 3-phase winding. Hence

$$L_d = \frac{L}{3/2}, \tag{9}$$

and the per unit value of X_d is

$$X_d = \frac{\omega_b L_d}{Z_b}, \tag{10}$$

The calculated value of the direct axis synchronous reactance by FEM is X_d=1.0139 p.u. In Table 1 there are compared the values obtained by different methods.

Table 1

Comparison of the results for X_d calculation

Method:	Numerical	Analytical	Experiment
X_d [p.u.]	1.0139	1.0181	1.0144

Quadrature axis synchronous reactance

The quadrature axis synchronous reactance X_q can be calculated in similar way as we calculated the direct axis synchronous reactance. The only difference is that the armature field is moved forward in space for 90^0 el. So, the field produced peaks at the quadrature axis and the current peaks on the direct axis. The field winding is also open circuited. Magnetic flux distribution for this case is presented in Fig. 4.

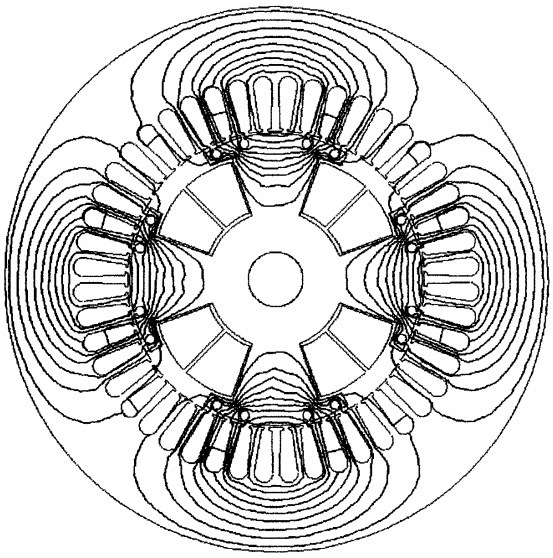

Fig.4. Magnetic flux distribution for X_q calculation

In this case the quadrature axis synchronous inductance is the ratio of quadrature axis flux linkage to quadrature axis current.

The calculated value of the direct axis synchronous reactance by FEM is X_d=1.0139 p.u. In the Table 2 are compared the values obtained by different methods.

Table 2

Comparison of the results for X_q calculation

Method:	Numerical	Analytical	Experiment
X_q [p.u.]	0.4822	0.4904	0.5072

Determination of Steady-State Characteristics

Here are presented some of the most interesting characteristics of a synchronous generator determined in the step of post-processing when calculating by FEM [3]. The results are obtained using the software package FEMM Version 3.3. We can prove that the most of these characteristics can be obtained only by using FEM.

Open Circuit Characteristic

The open circuit characteristic of the synchronous generator is determined for values of the field current $0<I_f<1.3I_{fn}$. For each value of the field current the flux linkage ψ is calculated from the finite element solution. Then the phase voltage E is calculated by

$$E = 4.44 N k_w f \psi, \tag{11}$$

where N is the number of turns of the phase winding, k_w is a winding coefficient and f is the frequency. The open circuit characteristic is presented in Fig.5.

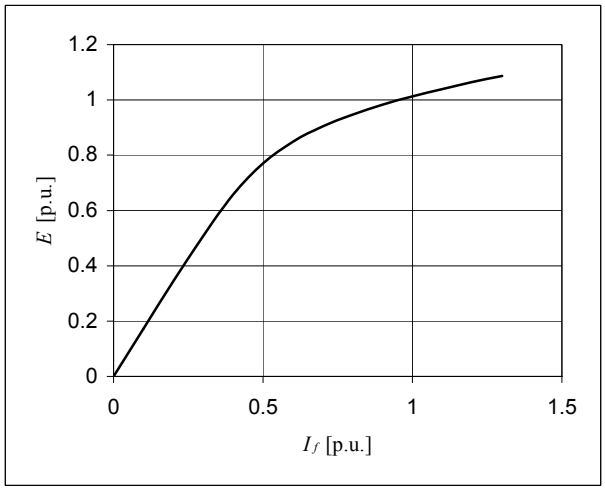

Fig.5. *Open circuit characteristic*

Air-gap flux characteristics

The characteristics of the flux in the air gap of the generator represent a dependence of the flux in the middle of the air gap against the rotor position for different values of the armature current I_a. In Fig.6 are presented the characteristics of the flux in the air gap for rated value of the field current I_f. Also, in Fig.7 are presented characteristics of the flux in the air gap for different values of the armature current I_a but for value of the field current $I_f=0$.

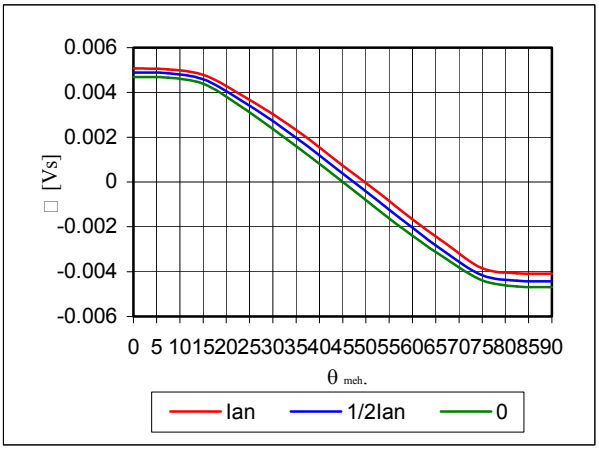

Fig.6. *Characteristics of the flux in the air gap for I_f=I_{fn}.*

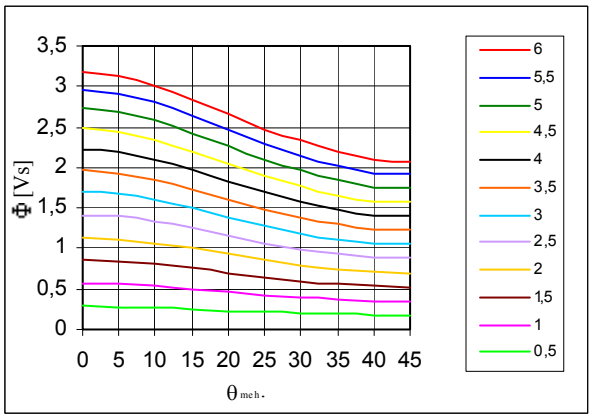

Fig.7. *Characteristics of the flux in the air gap for I_f=0.*

Distribution of the air gap flux density

In the post-processing step when using the FEMM package we can determine the distribution of flux density in an arbitrary selected region in the machine under consideration.

In Fig.8 is presented the distribution of the flux density in the middle line of the air gap over one pole pitch. The flux density is produced only by the field current I_f and we can notice the influence of the stator slots and teeth on the shape and values of the flux density.

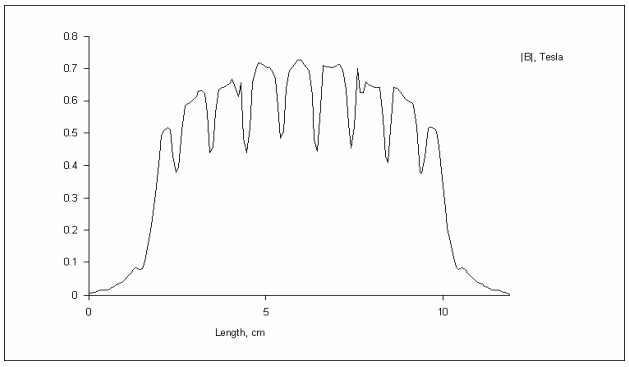

Fig.8. *Distribution of the flux density along the air gap*

Air-gap magnetic coenergy characteristics

The characteristics of the magnetic coenergy in the air gap of the synchronous generator represent a dependence of the air gap coenergy from the position of the rotor. Because the synchronous machine is a nonlinear system the magnetic coenergy is going to be calculated by

$$W_c = \int \left(\int_0^H B(H')\,dH' \right) dV \,, \tag{12}$$

In Fig.9 are presented the characteristics of the magnetic coenergy W_c in the air gap for different values of the armature current I_a and rated value of the field current I_f.

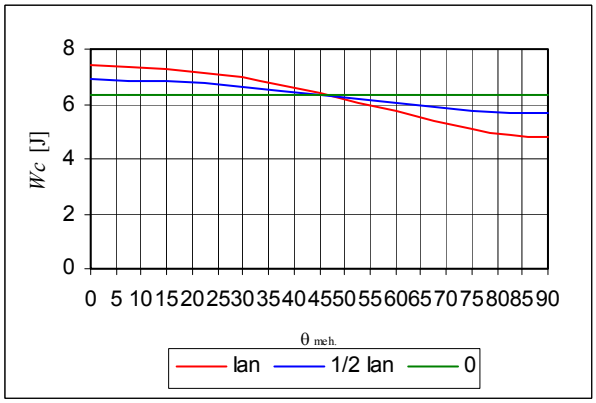

Fig.9. *Characteristics of the magnetic coenergy in the air gap*

Electromagnetic torque characteristics

The angle-torque characteristic is the dependence of the electromagnetic torque developed in the air-gap, against the rotor position. The electromagnetic torque here is calculated by the Maxwell's Stress Method. The calculation of this characteristic is less accurate then the other ones so we should use as fine a mesh as possible in order to obtain more accurate results. The determined characteristic of electromagnetic torque for rated field current I_f and rated armature current I_a of the synchronous generator is presented in Fig.10.

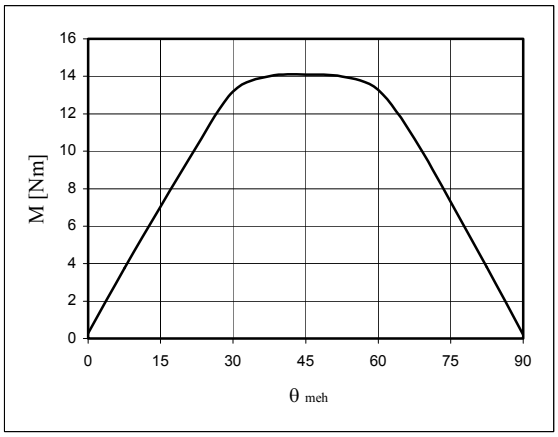

Fig.10. *Characteristic of electromagnetic torque*

Conclusion

As we can see, the most efficient analysis is carried out by using FEM for steady-state performance of a synchronous generator. From the comparison of the results we can conclude that FEM is very accurate method and its results are very close to the results of the traditional methods. Testing of the machine, when possible to be performed, is the only way to prove the results. On the other hand we can conclude that by using FEM results are obtained more easily and quickly compared to the other methods. We can conclude that the most of the characteristics described in this paper can be obtained only by using FEM. Also, an advantage is that FEM is excellent method when dealing with complicated geometries. Therefore, today FEM is considered to be the most powerful and elegant method for steady-state performance analysis of a salient pole synchronous generator.

References

[1] David Meeker, Finite Element Method Magnetics, User's Manual, FEMM Version 3.3, Massachusetts, USA, 2003;

[2] S. J. Salon, "Finite Element Analysis of Electrical Machines," Book, Kluwer Academic Publishers, Norwell, MA, USA, 1995.

[3] L. Petkovska, G. Cvetkovski and V. Sarac, Different aspects of magnetic field computation in electric machines, Book of Abstracts of the 10th International IGTE'2002 Symposium on Numerical Field Calculation in Electrical Engineering, p.p. 73; on **CD** p.p. 1-6, Graz, Austria, 2002.

[4] Kolondzovski, Z., Petkovska, L. Identification of a Synchronous Generator Parameters via Finite Element Analysis. Book of Abstracts of the 11th International IGTE'2004 Symposium on Numerical Field Calculation in Electrical Engineering, p.p. 96; on CD p.p. 1-6, Seggauberg (Graz), Austria, 2004.

[5] Kolondzovski, Z., Petkovska, L. Determination of a Synchronous Generator Characteristics via Finite Element Analysis. Book of digest of the 7th International Conference on Applied Electromagnetics, Nis, Serbia and Montenegro, 2005.

Zlatko Kolondzovski *– Ph.D. Student, Faculty of Electrical Engineering, P.O. box 574, Ss. Cyril and Methodius University, 1000 Skopje, MACEDONIA e-mail: zlatkokolon@hotmail.com.*

Lidija Petkovska *– Professor, D.Sc., Faculty of Electrical Engineering, P.O. box 574, Ss. Cyril and Methodius University, 1000 Skopje, MACEDONIA e-mail: lidijap@etf.ukim.edu.mk.*

Application of Hybrid Optimization Method on a Single Phase Shaded Pole Motor

Vasilija Sarac, Lidija Petkovska and Goga Cvetkovski

Abstract: *This paper presents an extension of previous authors' work in the field of Genetic Algorithms Method (GAM) used for optimization of a single phase shaded moto-SPSPM. The new optimized motor model is derived using electromagnetic torque as target function. As a result new optimized motor model is obtained with greater electromagnetic torque for rated slip s=0.16 but as well with increased efficiency factor. Further step in the optimization procedure is to implement the hybrid stochastic-deterministic optimization method, by coupling the results obtained from the GA optimization, with Hook & Jives Method (HJM).*

Keywords: *single phase shaded pole motor, GA optimization, Hook & Jives Method, hybrid method*

Introduction

In the paper is analysed a model of a small single phase shaded pole motor, with rated data: U_n=220 V; f_n=50 Hz; I_{1n}=0.125 A; P_{1n}=18 W; n_n=2520 rpm; 2p=2. The arrangement of the motor magnetic cores and windings is presented in Figure 1.

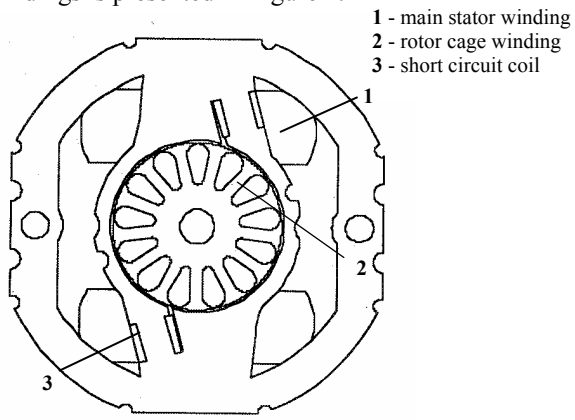

Fig. 1. Cross-section of the shaded-pole motor

At the beginning, the complex performance analysis is carried out on the original motor, adopting it as basic model - BM. The mathematical model is developed by an application of the revolving field theory. Accuracy of the shaded pole motor model is thoroughly examined and verified by experiments.

First step in optimization of basic model was by application of stochastic method of GA [1],[2]. Developed mathematical model was input into program of GA optimization. Electromagnetic torque was adopted as target function. As a result of optimization considerable increasment of electromagnetic torque was achieved.

Second step in optimization was implementation of hybrid method by coupling results from GA optimisation with deterministic method of Hook & Jives. On this way further more, improvement of electromagnetic torque is achieved. Basic model as well as new optimized motor model is analyzed by using Finite Element Method (FEM) in time harmonic domain. All relevant characteristics are calculated, and a comparative analysis of the both motor models is presented.

Method of Genetic Algorithms

Since fairly recent the Genetic Algorithms have been presented as computer algorithms, and wide range of applications have appeared in various scientific areas. Consequently, they have been proved as powerful tool for solving complicated tasks related to optimization problems. In their essence, the GAs are evolutionary searching algorithms, based on the rules of the natural genetics and the natural mechanics of unit selection. They are practically implemented in the most simplified natural way, based on the survival principles of the fittest unit.

In this stochastic process, the least-fit solution is receiving the minor chance for reproduction; to the contrary, the most-fit solution is receiving the major chance to be reproduced. The reproductive success of a problem solution is directly linked to the fitness value, which during the evaluation has to be previously assigned. The process starts from a randomly created population of strings, and after a sufficiently large number of generations, it stops giving the optimal solution with the best properties.

During the optimization, reproduction, mutation and crossover between the units and generations, determine the results finally achieved. The probability of their occurrence is recognized and determined through the corresponding genetic operators. Their percentage or per unit values of appearance in the genetic procedure, are always users' and problems' dependent.

Optimisation procedure

Design optimization of a shaded-pole motor is very important, but quite complicated problem. In general, it is a complex multi-variable, non-linear and constrained procedure. The optimization procedure is briefly explained.

In general case, during the process of design optimization, after the relevant machine parameters have been determined, depending on the problem which is solving, at the beginning target function is defined and derived by the user. The optimization procedure is always

searching for an extremity of this function, i.e. its maximum or minimum. In order to provide the derived solution to be practically acceptable, certain requirements should be satisfied. That means some important electrical or magnetic quantities, such as current density in the windings Δ [A/mm^2], or magnetic flux density in the air-gap B_δ [T] must be lower than the prescribed limits.

Knowing that the electromagnetic torque is one of the most important quantities of the motors motor mathematical model was developed with electromagnet moment as target function, based on method of symmetric components. Derived model is input in program of genetic algorithm which operates under C++ programming language. The optimization problem is considered to be maximizing one, and is carried out by the program GA-ODEM, originally developed. Program is using only one input file in which are defined ranges of variation of optimization parameters. The program is adjusted to create 6000 generations of each varied parameter.

Optimization procedure is extended regarding previous author's works by enlarging the number of varied parameters. Besides motor electrical parameters such as: current density, magnetic induction and angle of skew of rotor bars also parameters regarding motor cross section are changed : number of iron sheets in motor axial direction, width of stator pole and width of short circuit coil related to width of stator pole.

As an output program GA-ODEM gives a set of most favorable values of varied parameters with which achieved the largest target function i.e. electromagnetic torque.

Basing on the experience and expected results, the range of variation of the most important motor parameters mentioned above, is placed in certain constrains. Variation ranges as well as output set of most favorable parameters are presented in Table 1.

Table 1

Ranges of variations of motor parameters in GA method

Motor parameter	Variation ranges	Output set
Current density Δ [A/mm^2]	3.5 ÷ 8	5.0035
Number of iron sheets n[/]	20 ÷ 40	36
Magnetic induction B [T]	0.4 ÷ 0.5	0.45
Width of stator pole b_p [m]	0.01 ÷ 0.02	0.012
Width of short circuit coil related to width of stator pole	0.2 ÷ 0.3	0.2
Angle of skew of rotor bars [°]	10-20	10.023

In order to obtain motor parameters and characteristics after optimization procedure is finished output set of varied parameters is linked with originally developed computer program in FORTRAN, where is also input motor mathematical model. In Tables 2 and 3 are presented motor parameters and characteristics for basic as well as for optimized motor model at rated operating condition meaning slip s=0.16.

Table 2

Comparison of motor parameters

Basic model	Optimized model
Δ=8 [A/mm^2]	Δ=5 [A/mm^2]
$B_\delta = 0.404\,T$	$B_\delta = 0.449975\,T$
$\alpha_{sk} = 17^\circ$	$\alpha_{sk} = 10.023^\circ$
n=32	n=36
b_p=0,016 m	b_p=0,0120016 m
a=0,25	a=0,20002
$W_1 = 3488$	$W_1 = 2784$
$d_{cu} = 1{,}4 \cdot 10^{-4}$ m	$d_{cu} = 1{,}8 \cdot 10^{-4}$ m
$R_1 = 492{,}987\,\Omega$	$R_1 = 245{,}3024\,\Omega$
$R_2 = 497{,}0443\,\Omega$	$R_2 = 289{,}8911\,\Omega$
$R_3 = 18474{,}29\,\Omega$	$R_3 = 18723{,}5\,\Omega$
$X_1 = 498{,}1717\,\Omega$	$X_1 = 904{,}6708\,\Omega$
$X_2 = 76{,}7101\,\Omega$	$X_2 = 65{,}99443\,\Omega$
$X_3 = 127{,}5315\,\Omega$	$X_3 = 45{,}07528\,\Omega$
$X_{13} = 175{,}9108\,\Omega$	$X_{13} = 154{,}6218\,\Omega$
$X_{12} = 2163{,}34\,\Omega$	$X_{12} = 1970{,}399\,\Omega$

Table 3

Comparison of motor characteristics

Quantity	Basic model	Optimized model
Main winding turns per pole W	1744	1760
Stator current I_1 [A]	0.126	0.13
Short circuit coil current I_3 [A]	0.0063	0.00482
Rotor current I_2 [A]	0.0878	0.1009
Input power P_1 [W]	18.11	13.4713
Output power P_2 [W]	4.149	4.511
Efficiency factor η [/]	0.229	0.335
Electromagnetic torque M_{em} [mNm]	18.075	19.447

In Table 4 is presented percentage increasment of value of target function-electromagnetic torque in optimized model compared to basic model.

For the completeness of the analysis in Figures 2,3,4, are presented characteristics of currents in all three motor windings for the whole range of slip s=0÷1. Presented characteristics enable good comparative analysis of motor currents for basic and optimized motor model in whole range of motor slip.

Table 4

Percentage increasment of target function due to optimization

Basic model		Optimized model	
M_{em} [Nm]	η [%]	M_{em} [Nm]	η [%]
0.018075	0.229074	0.019447	0.334896
Improvement compared to basic model		**7,591**	**46,195**

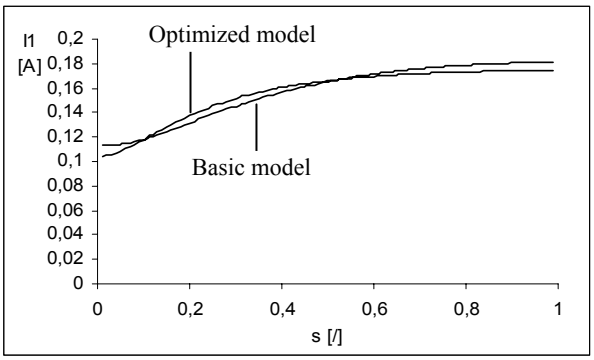

Fig.2. Comparative characteristic I_1=f(s)

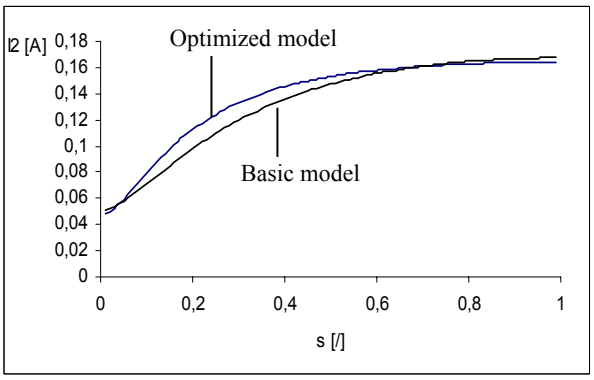

Fig.3. Comparative characteristic I_2=f(s)

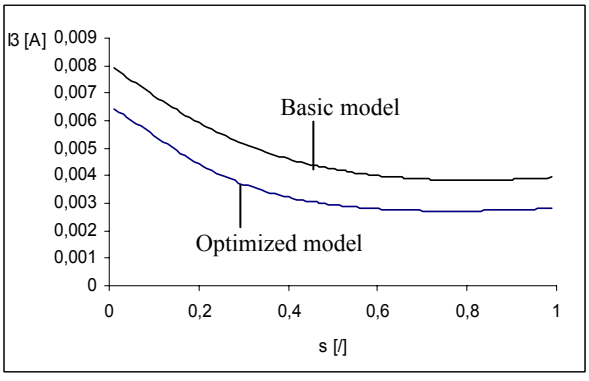

Fig.4. Comparative characteristic I_3=f(s)

In Figure 5 and 6 are presented characteristics of input power P_1=f(s) and output power P_2=f(s) which enables further analyses of characteristics of efficiency factor-η=f(s), electromagnetic torque-M_{em}=f(s) and power factor cosφ=f(s).

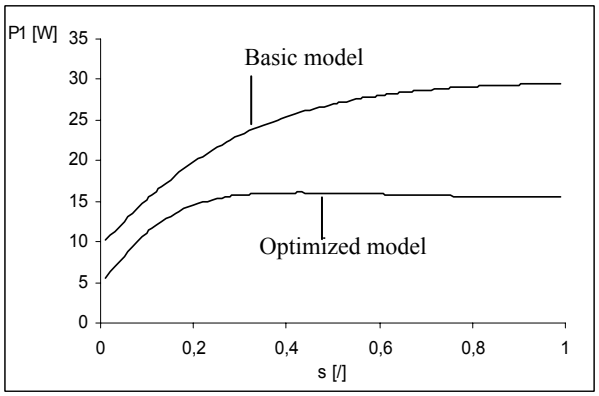

Fig.5. Comparative characteristic P_1=f(s)

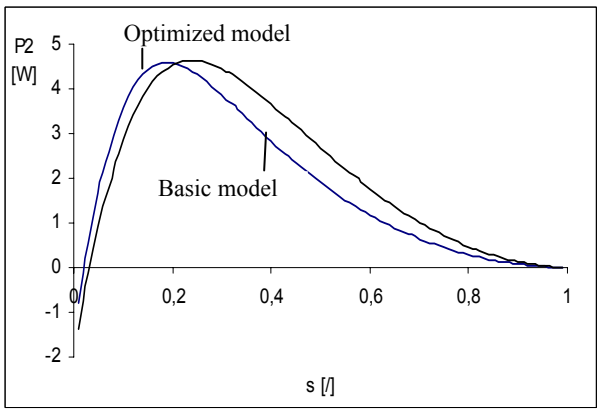

Fig.6. Comparative characteristic P_2=f(s)

As one the most interesting characteristics gained the optimization process are characteristic of target function of optimization –electromagnetic torque Mem=f(s), efficiency factor which is certainly one of the most important characteristic regarding motor performance η=f(s) and power factor cosf=f(s) presented in Figures 7,8 and 9 consequently.

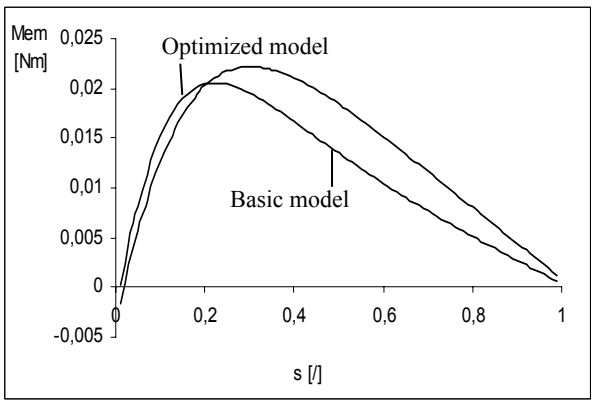

Fig.7. Comparative characteristic M_{em}=f(s)

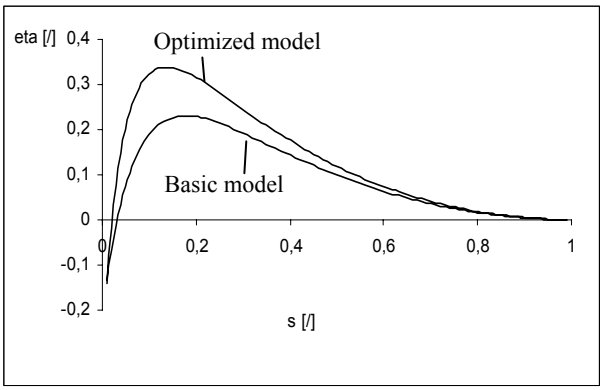

Fig.8. Comparative characteristic $\eta=f(s)$

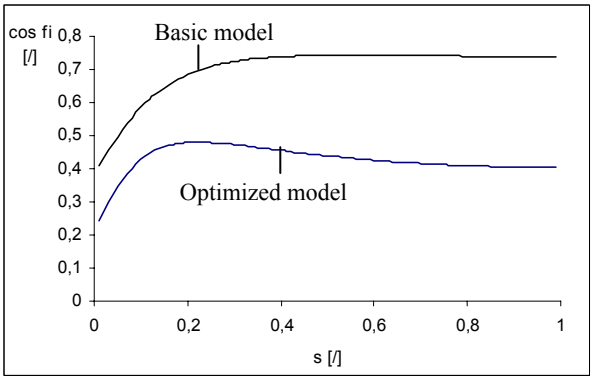

Fig.9. Comparative characteristic $\cos\varphi=f(s)$

Analysis of GA results

On the basis of presented results in Tables 2 and 3 after finished GA optimization of basic model for the performance of new achieved optimized model following general conclusions are derived:

- As a result of increased diameter on conductor in main excitation winding its resistance is decreased and consequently the current in main excitation winding as well as in rotor winding is increased. On the other hand, as a result of increased diameter of conductor current density is decreased which is certainly good improvement from operational point of view, leading to decreased copper losses in windings as well as to larger efficiency factor.
- As a result of increased current and decreased active resistance, but as well as a result of increased axial length of stator, electromagnetic torque is increased at rated load point and as a result of decreased losses efficiency factor is increased.
- From all relevant parameters of SPSPM only power factor is lower in optimized model, but for this special type of motors achieved values can be considered satisfactory high.
- In optimized model, angle of skew of rotor bars is changed which leads to decrease of space harmonics and contributes towards improvement of value of electromagnetic torque.

Hybrid method for optimization

One of the excellent features of GA method as main representative of stochastic methods for optimization besides its reliability is that it leads to the best possible solution defined in certain area which is searched. GA method is searching through the whole area of possible solutions of target function. In this way it is avoided possibility of locating only one optimum , which may not be the global optimum, i.e. absolute optimum of the target function.

Different from this method are deterministic methods which are searching from point to point within the space which is searched so very easily they are coming to the local extreme of the target function which may not be the best possible solution.

Hooke & Jeeves optimization method belongs to the group of deterministic optimization methods. Research of the optimization space of certain function starts in an arbitrary point, called *starting point*. From this point on, an optimum of the objective function is searched step by step, in the arbitrary directions of the searching space. Hooke & Jeeves method (HJM) operates as iterative method and each next starting point is closer to the local optimum of target function. Although it is found to be very robust method it has also some negative features which limit its implementation. One of this features is dependence of search quality and optimum reliability from the selection of starting point .This feature decreases the quality of the method, so very often obtained optimum is the optimum very close to the starting point, i.e. local optimum which is not always and the global optimum. Starting from the idea that GA method gives the global optimum of certain function, results obtained from GAM are used as starting point in HJM [3]. The further search is performed in the vicinity of this starting point and improves further more the target function. This optimization approach is called optimization by *hybrid method*. This means that good features from both methods are combined.

- In first phase by application of GA method and software program GA-ODEM the whole range of possible solutions is searched and it is located the point in which it is certainly the optimal solution.
- In second phase by application of HJM with starting point obtained from GAM further search in its vicinity is continued so optimal but more accurate solution of target function is obtained.

In Table 5 are presented ranges of variations of motor parameters, which are the same as in optimized model by Genetic Algorithms Method, and the starting point in the Hooke & Jeeves Method is actually the output set from GAM. In Table 6 are presented the output results obtained by the hybrid method (HM).

In Table 7 are presented results of optimization of target function-electromagnetic torque with both methods: GA and hybrid method. Slight improvement of electromagnetic torque as target function is achieved.

Table 5

Ranges of variation of motor parameters in hybrid method

Motor parameter	Variation ranges	Starting point
Current density Δ [A/mm^2]	3.5 ÷ 8	5.0035
Number of iron sheets n[/]	20 ÷ 40	36
Magnetic induction B [T]	0.4 ÷ 0.5	0.45
Width of stator pole b_p [m]	0.01 ÷ 0.02	0.012
Width of short circuit coil related to width of stator pole	0.2 ÷ 0.3	0.2
Angle of skew of rotor bars [°]	10-20	10.023

Table 6

Output results from hybrid method

Motor parameter	Output set
Current density Δ [A/mm^2]	5.0035
Number of iron sheets n[/]	36
Magnetic induction B [T]	0.449
Width of stator pole b_p [m]	0.0120005
Width of short circuit coil related to width of stator pole	0.2000089
Angle of skew of rotor bars [°]	10

Table 7

Output of electromagnetic torque from optimization methods

Electromagnetic torque	
GA-method	19.447
Hybrid method	19.617

From presented results in Table 7 it can be clearly seen that by using the output from GAM as starting point-imput in HJM value of target function obtained from GAM is further improved.

Small difference in final values shows that:

- Optimum of target function obtained by HJM is not local but global optimum of target function.
- Additional search in vicinity of global optimum by HJM dose not have major influence of optimal solution of target function.
- Starting point for HJM obtained by GAM is the point which includes the global optimum.
- GAM gives excellent results and it is an excellent optimisation tool.
- HM is a useful toll for further improvement of results of target function obtained from GAM and it is certainly a new idea how to combine the good features both methods: stochastic GAM and deterministic HJM.

FEM analysis of optimized models

The Finite Element Method is widely used for electromagnetic field calculations in electrical machines, in general. It is usually used as a non-linear magnetostatic problem which is solved in the terms of magnetic vector potential **A**. However, when analysing induction machines, considering their AC excitation, the air-gap magnetic field is always a time-varying quantity. In materials with non-zero conductivity eddy currents are induced; consequently, the field problem turns to magnetodynamic, i.e. non-linear time harmonic problem. Even more, when rotor is moving, the rotor quantities are oscillating at slip frequency, quite different from the stator frequency, and the direct implementation of the non-linear time harmonic analysis is improper. The problem is solved by adjusting the rotor bars conductivity σ, corresponding to the slip.

Magnetodynamic approach in FEM calculations, when magnetic filed is a time varying quantity, enables easy and direct analysis of electromagnetic phenomena. All calculations of magnetic filed distribution are done at $f=f_n=50$ Hz. As an input parameter in program is only the value of current in main excitation stator winding while currents in stator short circuit coil and rotor bars are left to be freely induced as a result of time varying magnetic field. During calculations non-linearity of magnetic material is taken into consideration. Excitation winding is connected to 220 V, 50 Hz [4]. The optimized motor model is obtained by coupling stochastic GAM and deterministic HJM. In Figure 10 is presented magnetic flux distribution at rated load condition $s_n=0.16$ for basic model – BM and for optimized model – OM.

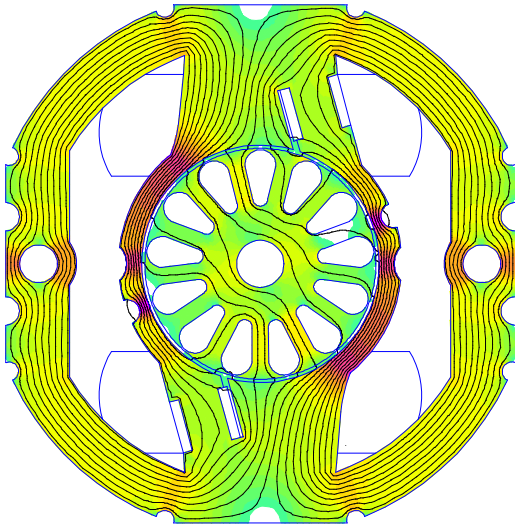

(a) BM

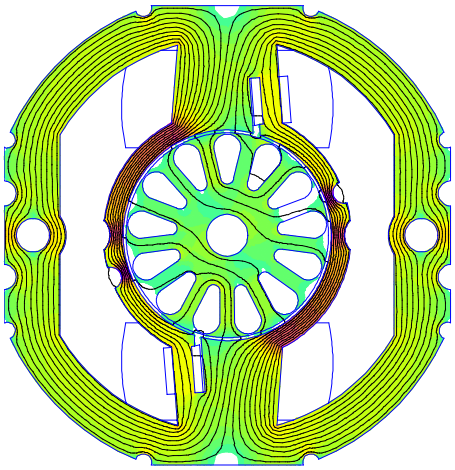

(b) OM

Fig.10. Flux distribution for basic and optimized model

In Figure 11 is presented space flux density distribution in the middle of the motor air gap for basic as well as for optimized model for rated load condition.

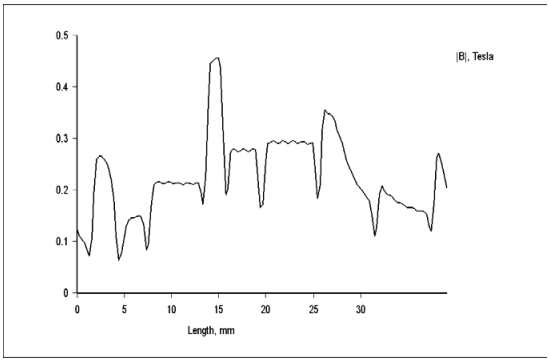

(a) BM

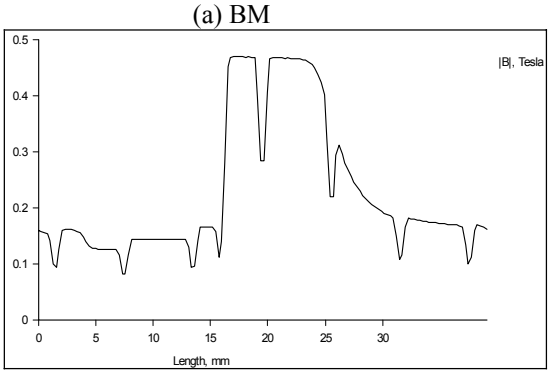

(b) OM

Fig.11. Space distribution of flux density

From graphic presentation of magnetic field distribution presented in Fig.10 it can be concluded that magnetic field distribution as well as magnetic flux density is different for basic and optimized motor model.

In basic model maximal value of magnetic flux density is: B_{mn}=2.61 T. Relatively large vale of flux density was one of the reasons for improvement of its construction and optimization of parameters and characteristics.

In optimized model maximal value of magnetic flux density is 2.4 T. Smaller vale of magnetic flux density in optimized model results in lower iron losses and consequently to greater efficiency factor.

Conclusion

Optimization procedure is conducted on single phase shaded pole motor using GAM with electromagnetic torque as target function. As a result of this optimization electromagnetic torque is increased for 7 % compared to basic motor model. In this paper is introduced new hybrid method for optimization. Hybrid method couples the good features of GAM which belongs to stochastic optimization methods and HJM which belongs to deterministic optimization methods. In this way optimization result of target function from GA method used as starting point in HJM is further improved.

Further more numerical analysis using FEM is performed on basic and optimized model. Numerical analysis shows that in optimized model maximal value of magnetic flux density is lower which results in lower iron losses and consequently greater efficiency factor. Stator bridges have the largest iron saturation which imposes new idea for motor construction by application of soft magnetic powders.

References

[1] V. Sarac, L. Petkovska, G. Cvetkovski: "*Comparison Between Two Target Functions for Optimization of Single Phase Shaded-Pole Motor Using Method of Genetic Algorithms*", Book of Digests from JAPMED'03, Athens, Greece, 2003 pp. 43-44.

[2] V.Sarac, L.Petkovska, M.Cundev, G.Cvetkovski: "*GA Based Optimal Design of a Shaded Pole Motor*", Proceedings of Int. Conf. of Electrical Machines – ICEM'04, Book of Abstracts pp.317-318, full manuscript published on **CD** pp.1-6, Krakow, Poland, 2004.

[3] G. Cvetkovski, L. Petkovska, M. Cundev: *"Hybrid Stochastic-Deteministic Optimal Design of Electrical Machines",* Proceedings on ISEF'2003, Vol. 2/2, p.p. 725-730, Maribor, Slovenia, 2003.

[4] V. Sarac, L. Petkovska, M. Cundev: "Non-linear Time Harmonic Analysis of a Shaded-Pole Micromotor", Proceedings of ISEF' 2003, Vol. 1/2, p.p. 137-142, Maribor, Slovenia, 2003.

Vasilija Sarac *- DSc.,Siemens A.E 11, Oktomvri br.6-1/1 Str,1000 Skopje, MACEDONIA e-mail: vasilija.sarac@siemens.com.mk*

Lidija Petkovska *– Professor, Dr., Faculty of Electrical Engineering, University Ss. Cyril and Methodius, P.O. Box 574, 1000 Skopje, MACEDONIA e-mail: lidijap@etf.ukim.edu.mk*

Goga Cvetkovski *–Associate Professor, Dr.,Faculty of Electrical Engineering, University Ss. Cyril and Methodius, P.O. Box 574, 1000 Skopje, MACEDONIA e-mail: gogacvet@etf.ukim.edu.mk*

A General Approach for Optimal Designing of Self-Starting Permanent Magnet Synchronous Micromotors

Iliya Stanev

Abstract: *In this paper a general approach for optimal designing of self-starting micromotors with permanent magnet is considered. The object of investigation is a synchronous motor with one group of unshaded poles and one group of shaded poles in ratio 3:4. Comparison data for designed micromotor are presented. The calculated and measured values coincide with sufficient accuracy from engineering point of view. The starting regime of the micromotor at favourable and unfavourable instant of switching on of the voltage is analyzed, too*

Keywords: *optimal designing, synchronous micromotor, permanent magnet, unshaded and shaded poles.*

Introduction

The self-starting permanent magnet synchronous micromotors are the motors that do not have any special starting devices, such as ratchets, catching up connectors and others. Practically, this name is generally accepted [1], [2], [3]. The starting in a determined sense of rotation is the main problem for these micromotors. Often an additional requirement for working both at frequency of 50 Hz and frequency of 60 Hz is presented. At single-phase supply the electromagnetic torque has a pulsating nature and the rotor has to reach the synchronous rotational speed by one half-period of the supply voltage. That is why the self-starting synchronous micromotors with permanent magnets are calculated for working at small moment of inertia and low speed of rotation (most often the number of the pole pairs is p=8 when at frequency of 50 Hz the rotational speed is $n_c = 375\ \mathrm{min}^{-1}$).

There is a large diversity of design solution of permanent magnet synchronous micromotors, not having special starting devices. But always an elliptical rotating magnetic field in the air gap is created. A series of patent designs rely upon the asymmetric spatial disposition of the stator poles [4], [5]. For the easiest and most effective way is to load one part of the stator poles by short-circuited copper turns called the shades.

Because of the design restrictions the system of shading when the unshaded and shaded poles of the same polarity follow one after another [6] is not possible to use. At self-starting permanent magnet synchronous micromotors the unshaded and shaded poles form groups, which alternate. The section along the axis of such micromotor is shown in Fig. 1. The micromotor consists of a cylindrical magnetized radially permanent magnet *1* and a knock-down stator, composed of pole pieces *2* and *3*, and locking clamp *4*, made from mild steel. At some designs the clamp *4* can be missed when the stator comprises two pole pieces only, one of them having a cup shape [7], [8]. Unshaded poles *5* and shaded poles *6* are cut off from pole pieces and bended axially. The shades *13* and *14* present copper discs with holes through which the poles pass. The axis of shaded poles are displaced from its symmetric position following the sense of rotation by an angle depending on the phasing angle φ between the magnetic fluxes of the unshaded and shaded poles. The symmetric position corresponds to the case of the circle rotating magnetic field at $\varphi = 90$ electrical degrees. In the holes of pole pieces *2* and *3* polyamide bearing *15* and *16* are injected and the shaft *17* is aligned. The multi-pole magnetized permanent magnet *1* is fixed to the shaft *17* by means of a plastic bush *18*.

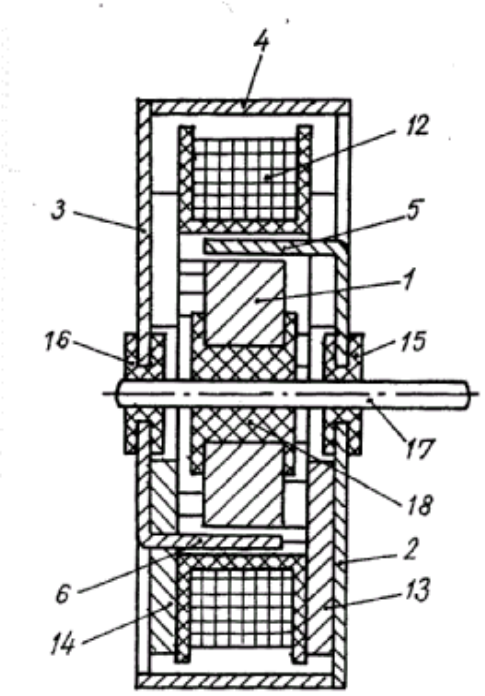

Fig.1. A section along the axis of the micromotor.

The main bibliography sources for these micromotors are the patent specifications.

A general approach for optimal designing of micromotors

The main aim of analysis of the electromagnetic processes in self-starting permanent magnet synchronous micromotors is the successful resolving the optimal design problem. The incessant improvement of computers allows utilizing the more complex mathematical models

of the processes within the design objects. In spite of this at present it is not possible to realize mathematical models without any simplifications. The use of non-linear programming involves great flexibility in the process of optimal design. But also realizing the general approach for optimal designing of self-starting permanent magnet synchronous micromotors, it is not possible to deflect our attention from the real fact that "independently of the large diversity of approaches, algorithms, and programs there is no algorithm having the vocation to be universal and capable to resolve the general problem of non-linear mathematical programming" [9].

Formally, formulating the problem for optimal designing of the micromotor from mathematical point of view is not complicated because it comes to the general problem of non-linear programming [10]

$$\min\{f(\mathbf{x}) | \mathbf{x} \in R\}, \tag{1}$$

where $\mathbf{x} = [x_1\ x_2\ \ldots x_n]^T$ is a vector of the variable quantities in Euclidean space E^n $(\mathbf{x} \in E^n)$ and R is the region of space where the constraints of the problem are satisfied:

$$R = \{\mathbf{x} | h_j(\mathbf{x}) = 0,\ g_j(\mathbf{x}) \geq 0\ \forall j\}. \tag{2}$$

In (2) $h_j(\mathbf{x})$ $(j = \overline{1, m})$ are equality-constraints and $g_j(\mathbf{x})$ $(j = \overline{m+1, p})$ are inequality-constraints.

When resolving the problem all variables are considered as having continuous values, and finally their values are rounded-off. Certainly, the optimization procedure can be continued, but this is not necessary always.

In the general approach of optimal design given below, the resolving of problem (1) is found by the slipping allowance method in accordance with the Nelder-Mead algorithm. In order to avoid a possible arithmetic interruption of the program, owing to the discrepancy of the coordinate of the current point in investigation space and the parameters of the micromotor, the problem of optimal design is carried out using the approximating functions method [11].

The objective function $f(\mathbf{x})$ and the constraints are replaced by second order full polynomials of the kind

$$\widetilde{Y} = b_0 + \sum_{i=1}^{n} b_i x_i + \sum_{i=1}^{n-1} \sum_{j=i+1}^{n} b_{ij} x_i x_j + \sum_{i=1}^{n} b_{ii} x_i^2, \tag{3}$$

which are obtained on the base of a rotatable or orthogonal central compositional design in accordance with the theory of experimental design [12]. The code values of the factors presenting independent variables in the problem of optimal design of the micromotor are expressed as

$$x_i = \frac{X_i - X_{i0}}{I_i}, \tag{4}$$

where X_{i0} is the value of the i-th variable X_i in the design centre, and I_i is the one-sided interval of variation of this variable. Consequently, the obtained approximating expressions are valid at $|x_i| \leq 1,\ i = \overline{1, n}$.

If the optimal vector $\mathbf{x}^*$ is found at the boundary of the area, a new cycle of optimization procedure has to be performed. Then as a centre of the design the point, corresponding to the local extremum, is taken.

Since the micromotor ought to have an electromagnetic torque as large as possible, for an objective function can be chosen [13]

$$f(\mathbf{x}) = -\frac{2}{\pi}(M_{dm} - M_{im}), \tag{5}$$

where M_{dm} and M_{im} is the electromagnetic torque of the forward and reverse rotated magnetic field, respectively.

Statement of the problem for optimal designing of the micromotor

The object of investigation in this paper is a self-starting permanent magnet synchronous micromotor with one group of unshaded poles and one group of shaded poles of the stator in the ratio of 3:4. The polarity of the adjacent poles at the boundary of both groups is different. A micromotor of this type is described in [14] with disposition of the stator poles in accordance with Fig. 2.

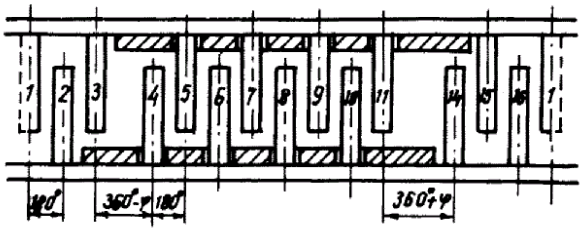

Fig.2. Disposition of the stator poles of the micromotor.

In published foreign patient specifications [1], [15], [16] of self-starting permanent magnet synchronous micromotors the width of shaded and unshaded poles is the same. In order to improve the characteristics of the micromotor an aspiration to equalize the magnetic fluxes of the pole groups exists. For this purpose the number of unshaded poles is taken smaller than the number of shaded poles. By this manner, however, it is not possible to reach a precise equalization of the magnetic fluxes.

The problem of optimal design of the micromotor is resolved at given overall dimensions when the generality of the approach does not decrease. The technical requirements of the micromotor are:

rated voltage $U = 220$ V;

frequency of the supply voltage $f = 50$ Hz;

output torque $M = 5.10^{-4}$ N.m;

overheat of the exciting winding $\Theta_b = 50$ K;

ambient temperature $\vartheta_0 = 20\,^\circ$C;

outer diameter $D = 42$ mm;

axial length $l_0 = 18$ mm;

outer diameter of the permanent magnet $D_M = 20$ mm;

axial length of the permanent magnet $l_M = 6{,}8$ mm;

mode of operation – continuous, S1.

The optimal designing of the self-starting permanent magnet synchronous micromotor comes to solving the following problem of non-linear programming:

Find out the minimum of the function

$$f(\mathbf{x}) = -\frac{2}{\pi}\left(\widetilde{Y}_1 - \widetilde{Y}_2\right), \mathbf{x} \in E^4 \tag{6}$$

at the constraints:

$$g_1(\mathbf{x}) = 1 - |x_1| \geq 0;$$

$$g_2(\mathbf{x}) = 1 - |x_2| \geq 0;$$

$$g_3(\mathbf{x}) = 1 - |x_3| \geq 0;$$

$$g_4(\mathbf{x}) = 1 - |x_4| \geq 0;$$

$$g_5(\mathbf{x}) = 1 - \frac{\widetilde{Y}_3}{\Theta_b} \geq 0;$$

$$g_6(\mathbf{x}) = \frac{3\tau - e_i - 0{,}5(a_{c1} + a_{c2})}{2.10^{-3}} - 1 \geq 0;$$

$$g_7(\mathbf{x}) = \frac{\tau + e_i - 0{,}5(a_{c1} + a_{c2})}{2.10^{-3}} - 1 \geq 0, \tag{7}$$

where:

$\mathbf{x} = [x_1\ x_2\ x_3\ x_4]^T$ is the vector of variable quantities, presented in dimensionless form in accordance with (4);

τ is the pole pitch;

a_{c1}, a_{c2} is the width of the unshaded and shaded stator pole, respectively;

e_i is the displacement of the axis of each shaded pole from its symmetric position.

In (7) the first four constraints describe the region where the approximating expressions are valid. The fifth constraint reflects the requirement for admissible overheat of the exciting winding Θ_b, and the last two constraints are linked with ensuring the sufficient space for short-circuited turns.

As independent variables of the problem are assumed: the amplitude of the scalar magnetic potential of the unshaded stator poles, $X_1 = V_{м1m}$; the width of the unshaded stator pole in parts of the pole pitch, $X_2 = \beta_1$; the width of the shaded stator pole in parts of the pole pitch, $X_3 = \beta_2$, and the angle of displacement of the axis of each shaded pole from its symmetrical position, $X_4 = \varphi_i$ (in electrical degrees).

Approximating expressions are found for the electromagnetic torque at synchronous of the forward magnetic field, $\widetilde{Y}_1$, electromagnetic torque of the inverse magnetic field, $\widetilde{Y}_2$, and the overheat of the exciting winding, $\widetilde{Y}_3$. There is a possibility to obtain approximating expressions for other quantities, too.

Program realization of the general approach for optimal designing

The general approach for optimal designing of self-starting permanent magnet synchronous micromotors consists of two principal stages: 1) obtaining the global quadratic approximations for the objective function and the constraints (stage of approximation); 2) finding out the solution of formulated general problem of non-linear programming for the area where the approximations are valid (stage of optimization). That is why the main program has as a core the calling to the subroutines EMS and SFPLX.

The important module of EMS is the subroutine PLMS where a full electromagnetic and thermal analysis of the micromotor is carried out using the subroutines CKF17P, CPQ17S, CPLS and TRZ.

The subroutine SFPLX for resolving the general problem of non-linear programming under constraints presents an improving of the program FLEXIPLEX [10] on the basis of a revised variant of the Nelder - Mead algorithm.

Numerical results

At a ratio of interval variation to the basic level of 0,05, the following optimal solution is obtained:

Value of the objective function

$$f(\mathbf{x}) = -16{,}15439.10^{-4}$$

and optimal vector

$$\mathbf{x}^* = \begin{bmatrix} x_1^* \\ x_2^* \\ x_3^* \\ x_4^* \end{bmatrix} = \begin{bmatrix} 0{,}519638 \\ -0{,}9972255 \\ -0{,}2124790 \\ 1{,}00037 \end{bmatrix}$$

$$\text{or } \mathbf{X}^* = \begin{bmatrix} V_{м1m}^* \\ \beta_1^* \\ \beta_2^* \\ \varphi_i^* \end{bmatrix} = \begin{bmatrix} 68{,}8 \\ 0{,}7036 \\ 0{,}8665 \\ 136{,}6 \end{bmatrix},$$

where

$$x_1 = \frac{V_{м1m} - 67{,}1}{3{,}355}; \quad x_2 = \frac{\beta_1 - 0{,}7405}{0{,}03702};$$

$$x_3 = \frac{\beta_2 - 0{,}8758}{0{,}04379}; \quad x_4 = \frac{\varphi_i - 130{,}1}{6{,}505}.$$

For obtained optimal solution the wire diameter is $d^* = 0{,}052012.10^{-3}$ m. With an accuracy of $0{,}1.10^{-3}$ m for the poles width is obtained $a_{c1} = 2{,}9.10^{-3}$ m and $a_{c2} = 3{,}5.10^{-3}$ m.

Owing to the small number of variables ($n = 4$) the final optimal solution is found out by the non-linear programming only (without approximating expressions) using a more precise value for the interval impedance of the shade obtained with the help of the finite element method [17]. Thus at $d = 0{,}05$ mm and $w = 13000$ is obtained:

Value of the objective function

$$f(\mathbf{x}^*) = -17{,}8905.10^{-4}$$

and optimal vector

$$\mathbf{x}^* = \begin{bmatrix} -0{,}8584227.10^{-1} \\ -0{,}1774977 \\ 0{,}2843388 \\ 0{,}999656 \end{bmatrix} \text{ or } \mathbf{X}^* = \begin{bmatrix} 67{,}4 \\ 0{,}7285 \\ 0{,}8692 \\ 135{,}1 \end{bmatrix}.$$

The area of variation of the variables when resolving the problem of non-linear programming in this case is

$$V_{м1m} = 67{,}7 + 3{,}38x_1,$$
$$\beta_1 = 0{,}735 + 0{,}0363x_2,$$
$$\beta_2 = 0{,}857 + 0{,}0428x_3,$$
$$\varphi_i = 128{,}7 + 6{,}435x_4.$$

Table 1

Comparative data for designed micromotor at voltage $U = 220$ V, frequency $f = 50$ Hz, and ambient temperature $\vartheta_0 = 60$ °C

Quantity	Calculation	Experiment	Relative error, %
Current *I*, A	$11{,}48.10^{-3}$	$12{,}1.10^{-3}$	-5,13
Supply power *P*, W	2,275	2,43	-6,38
cosφ	0,9007	0,9112	-1,33
Starting torque M_n^*, N.m	$9{,}75.10^{-4}$	$10{,}67.10^{-4}$	-8,62
Pull-out torque M^*, N.m	$24{,}63.10^{-4}$	24.10^{-4}	2,62
Overheat Θ, K	54,87	53	3,74

*At ambient temperature $\vartheta_0 = 20$ °C

In order to estimate the accuracy of the designing a specimen has been made. In Table 1 comparative data for designed permanent magnet synchronous micromotor with $a_{c1} = 3{,}1$ mm and $a_{c2} = 3{,}5$ mm are given.

In Fig. 3 the plots of the angle of rotation, θ, and angular velocity, Ω, versus the time, t, at favourable instant of switching on to the supply voltage at the limit load torque M_c=15,2.10^{-4} N.m are presented.

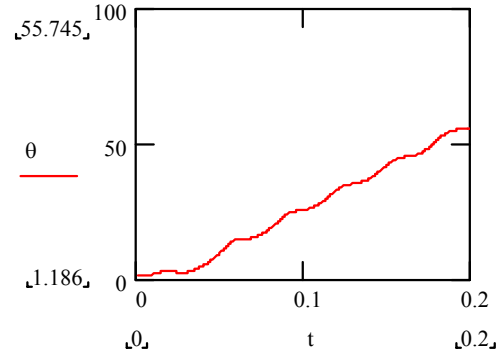

a)

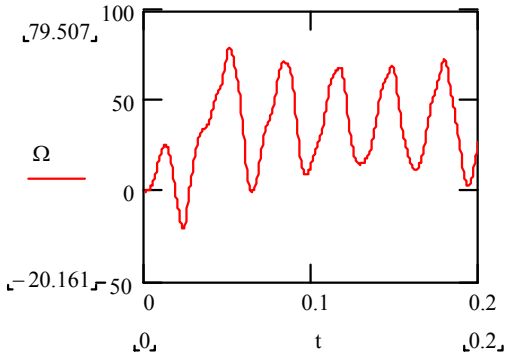

b)

Fig.3. Starting regime of the micromotor at favourable switching on instant to the supply voltage at load torque M_c=15,2.10^{-4} N.m

a) – angle of rotation; b) – mechanical angular velocity.

The curve $\Theta - t$ at unfavourable switching on instant of the micromotor at limit load torque M_c=10,3.10^{-4} N.m is shown in Fig. 4.

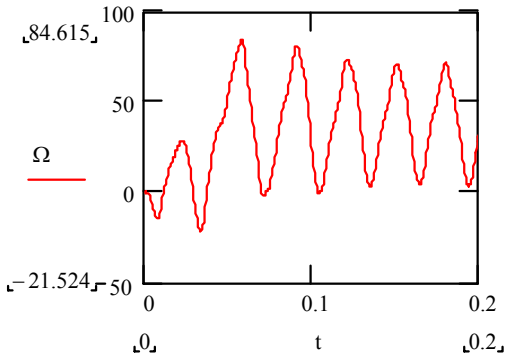

Fig.4. Starting regime of the micromotor at unfavourable switching on instant to the supply voltage at load torque M_c=10,3.10^{-4} N.m .

The curves of $\theta - t$ and $\Omega - t$ at unfavourable switching on instant to the supply voltage at load torque M_c=10,4.10^{-4} N.m are presented in Fig. 5. We can see that in this case the micromotor does not start and reach the synchronous mechanical velocity of 39,3 rad/s.

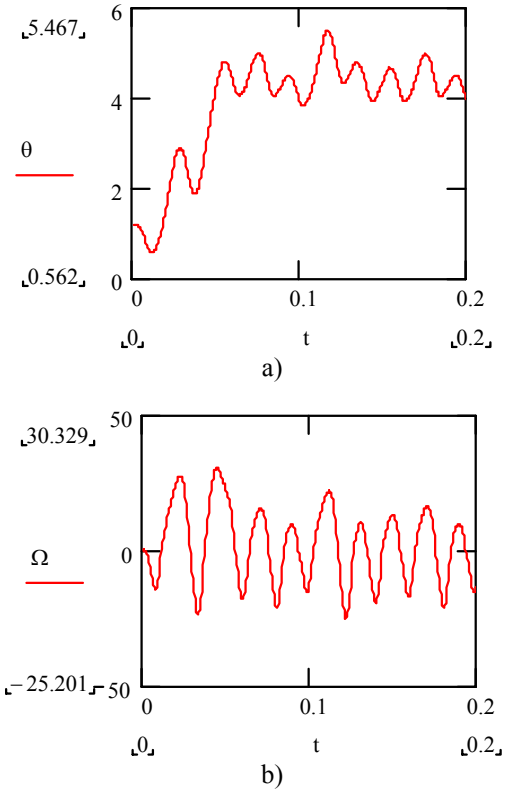

Fig.5. Starting regime of the micromotor at unfavourable switching on instant to the supply voltage at load torque M_c=10,4.10^{-4} N.m
a) – angle of rotation; b) – mechanical angular velocity.

The limit torque value of 10,3.10^{-4} N.m is in a good agreement with the measured value of the starting torque of 10,67.10^{-4} N.m in Table 1.

Conclusion

The offered general approach for optimal designing of self-starting permanent magnet synchronous micromotors based on the coupled using of the non-linear mathematical programming and the approximating functions method can be applied for comparative analysis of different designs. The coincidence of the calculated and experimental data in order of 10 % can be accepted as satisfactory from engineering point of view taking into account the small values of the quantities. The accuracy of the designing process depends in great degree on the adequacy of the mathematical model for electromagnetic processes in the micromotor which model can be improved incessantly.

References

[1] Gilbert, D. Unidirectional self-starting synchronous motors. Great Britain, Patent specification No 1397532, H02 k 1/14, 1975.

[2] Polujadoff, M., A. Abdel-Razek, J.-P. Chassande. Apport de l'ordinateur à l'étude des régimes transitoires des machines synchrones. Applications aux machines synchrones autopilotées, RGE, 10, 1982, pp. 694 – 697.

[3] Mörz, P. In einer Richting selbstanlaufender Synchron-Kleinstmotor. – DDR, Patentschrift No 90583, H02 k 21/12, 1972.

[4] Morly, E. R. Synchronous motor with improved starting characteristics. – United States, Patent No 3746900, Cl. 310/41 (H02 k 7/10), 1973.

[5] Browmick, A. K. Improvements in or relating to synchronous electric motors. – Great Britain, Patent specification No 1213377, H02 k 21/08, 1970.

[6] Ермолин, Н. П. Электрические машины малой мощности, Москва, Высшая школа, 1967.

[7] Vergues , J., G. Astic. Moteur synchrone monophasé à aimant permanent et bagues de déphasage. [Crouzet S. A.]. Brevet d'invention No 1598272, Cl. H02 k, 1970.

[8] Riggs, W. D. Shaded pole synchronous motor. United States, Patent No 3737695, Cl. 310/162, (H02 k 19/14), 1973.

[9] Терзян, А. А. Автоматизированное проектирование электрических машин, Москва, Энергоатомиздат, 1983.

[10] Химмельблау, Д. М. Прикладное нелинейное программирование (перевод с англ.), Москва, Мир, 1975.

[11] Папазов, С. П. Оптимално проектиране на електромагнитни системи, София, Техника, 1975.

[12] Ивоботенко, Б. А., Н. Ф. Ильинский, И. П. Копылов. Планирование эксперимента в электромеханике, Москва, Энергия, 1975.

[13] Станев, И. В. Оптимизация на самопускащ се синхронен микродвигател с постоянен магнит. Международна научна конференция УНИТЕХ'04, 18 – 19 ноември 2004, Сборник доклади, том I, Габрово, 2004, стр. I-57 – I-60.

[14] Станев, И. В. Синхронен микродвигател. Авт. св. на НРБ № 31353, Н 02 k 21/18, 1982.

[15] Hermann, G. Kleinsynchronmotor. Saia AG. Schweiz, Patent No 507612, H02 k 21/16, 1971.

[16] Traeger, F. Wechselstromkleinstmotor mit dauermagnetläufer und Polzackenkäfigen in Ständer. [Licentia Patent – Vervaltungs – GmbH]. Bundesrepublik Deutschland, Auslegeschrift No 1513936, Kl. 21 d2, 16 (H02 k, 21/16), 1973.

[17] Станев, И. В. Вътрешно комплексно съпротивление на екрана в синхронни микродвигатели с постоянни магнити. Електротехника и електроника "E+E", 7 – 8, 2004, стр. 35 – 39.

Iliya Stanev *– Assoc. Professor, PhD., Faculty of Electrical Engineering and Electronics, 4 H. Dimitar str., 5300 Gabrovo, BULGARIA.*
e-mail: staneviv@yahoo.com

The asynchronous machine for a starter - generating unit (SGU)

Pavel Grachev, Vladimir Anisimov, Elena Ejova

Abstract. *In the report the outcomes of designing and calculation an automobile starter - generator are submitted(shown) on the basis of the asynchronous machine for "a soft" hybrid. A feature of designing is the necessity of arrangement of an electric machine in essential(much) restricted space between an internal-combustion engine (ICE) and gear box of the automobile. The engineering solutions permitting to reduce mass and volume of an electric machine (SGU) are licensed.*

Keywords: *the automobile, starter - generator, asynchronous machine, stator winding.*

The introducing

In world motor industry the tendency of a heavy use in automobiles of electrical and electronic devices now is watched. Their part in the cost price of modern automobiles reaches 15 %, and in 2010 the growth up to 35 % is expected.

Exchange from hydrocarbon of fuel to hydrogenous, electrification and applying of electronic control systems enable to lower equipped weight of the automobile, to save fuel, to increase ecology, to simplify a control system, to increase comfortability and safety of automobiles. The competitive strength of transportation units is increased by improvement of these key consumer properties. Also the producer has a capability of occupation of new commodity markets.

The modern automobile has the tendency of association of different systems. The development of an electronics engineering, and also increase of power from the generator, allows to merge the system components of launch and electrical power supply in the integrated device (starter – generator) SGU [1].

Such solution allows to refuse a series of devices on the automobile engine the (of a flywheel, driving mechanism of a starter etc.), and also to extend functions executed usually by the generator and a starter. For example, together with a brake system to execute braking the automobile with power transmission in an accumulator battery and capacitive energy store. And also to serve the damper at engine run. Such solution allows to work in a mode of "start - stop". The high power of the starter - generator allows to lower power ICE, and to save fuel. At last, the starter - generator in definite situations can execute the motion of the automobile on electrical drive.

The high power of the starter - generator in a generating mode allows to electrify rudder control, the gas distribution system, the pump in a cooling system etc. However, too large current loads and voltage drop in valve inverters require the mode of heightened voltage.

Two electric machines of ordinary car are change for one integrated electric machine - starter - generator. Now competitive are the synchronous and asynchronous machine. The cost of a synchronous machine is increased at the expense of usage of expensive magnets, however, at definite control band, it better asynchronous under the power characteristics. From the point of view of the cost, the designs and maintenance are better for using the asynchronous machine.

The quality of activity of all installation depends on a design and know-how of manufacturing of the asynchronous machine in many respects. Therefore one of main problems solved during creation SGU, - designing and definition of parameters of the asynchronous machine.

Designing and definition of parameters of AM

The asynchronous machine is necessary for placing in restricted space of the automobile, therefore features of such machine are small length of a magnetic circuit increased minor diameter of the heart of a rotary table arranged on a special hub, the diminished frontal parts of winding of stators and rotary table.

If to construct the asynchronous machine on the basis of production AM (to use a magnetic circuit of such machine), on overall dimensions and weight it cannot be set on the customary automobile without essential changes in its design, therefore it is necessary to engineer special AM [2].

The main calculation of the machine is spent on the basis of the techniques which have been set up in [3, 4]. The calculation of a winding of stator and rotary table SGU is offered for executing in view of features of fulfilment of frontal parts of a winding of stator and rods of a winding of a rotary table, the design which one is licensed.

Feature of a winding of stator of AM is its running in a kind of a two-layer beam wave winding with a diameter step. It is connected to low voltages and considerable currents of phases. Besides such winding has a number of advantages as contrasted to by other winding. It - high space factor of a groove, that allows to reduce overall dimensions of the machine; the reduction of number of connections between bobbin groups, than is reached economies of a material of a winding and decrease of labour input of its manufacturing. The form of frontal parts of coils is rather simple.

To reduce a volume of a rotary table and to increase efficiency, the winding of a rotary table is made copper.

The designing of the asynchronous machine is conducted for a most heavy duty of activity - duty of start. The designing starts with definition of a design stress of a

winding of stator. For acceleration of process of start ICE it is necessary to change the frequency of a current of a stator of AM so that to back up slip close to critical, and voltage on a stator to change so that to save during launch close to constant saturation of a magnetic circuit of the machine. I.e. the launch is necessary for conducting with the constant moment. Thus the attitude of voltage to frequency should be supported approximately by constant, therefore at calculation we shall take advantage of the law of frequency regulation

$$\frac{U_1}{f_1} = const \cdot \tag{1}$$

As is said above, the demanded reduction of frontal parts of a winding of stator is reached by increase of number of pairs of poles *p* and fulfilment of a special two-layer beam wave winding. It also allows to increase number of orbits w1 in a phase of a winding of stator, since for a wave winding

$$\omega_1 = 2pq_1 . \tag{2}$$

The number of grooves on a pole and phase *q1* of a stator for AM should be selected probably smaller.

The computational voltage to neutral of AM for given computational rotational speed, receiving $n = n_1$ (s^{-1}), is connected to number of orbits of a phase of a winding by a ratio

$$U_{1РАСЧ} = \frac{w_1 222 k_{O1} \left(\frac{n}{50}\right) B_\delta D_1 l_1 10^{-6}}{k_H} . \tag{3}$$

Therefore, augmenting number of pairs of poles, at the given sizes and induction, is increased a design stress of a phase of a stator, that reduces a computational current of a stator and allows to reduce section of rods of a winding of stator. However increase *p* results in increase of a computational current frequency of a stator AM. Therefore it is necessary to limit an altitude of a groove, and also a sectional area of rods of a winding to reduce eddy-current losses.

The analysis of designs of AM with different numbers of pairs of poles *p* and grooves z_1, has shown, that the most reasonable version is the machine with $2p = 36$, $z_1 = 108$, $q_1 = 1$.

The minor diameter of a stator is selected outgoing, that a back of a stator and MMF in it were small. The lengths of hearts of a stator and rotary table are limited to length M.

To limit a phenomenon of replacement of a current in conductors of a stator, their section is selected no more than 20 mm^2. Outgoing from the adopted mark of a wire the altitude of a groove and altitude of a back of a stator is determined. Isolation is a little bit less advisable for standard wires, since. The AM works on undervoltages.

Feature of calculation of a minor diameter of a rotary table is its arrangement on a hub, bound with the arbor ICE.

Allowing a unorthodox design of frontal parts of a stator, the calculation of a pure resistance of a winding of stator includes definition of resistance of a groove, resistance of frontal parts, resistance of strips between by groups.

Expediently rotary table to execute without a taper of grooves, therefore at calculation of an induced drag a coefficient of conductivity of dissipation of a taper of grooves.

In a design of AM there are bearing boxs, therefore, there are no friction losses, besides there are no sliding contacts, therefore it is possible to admit, that the mechanical losses are peer to zero point.

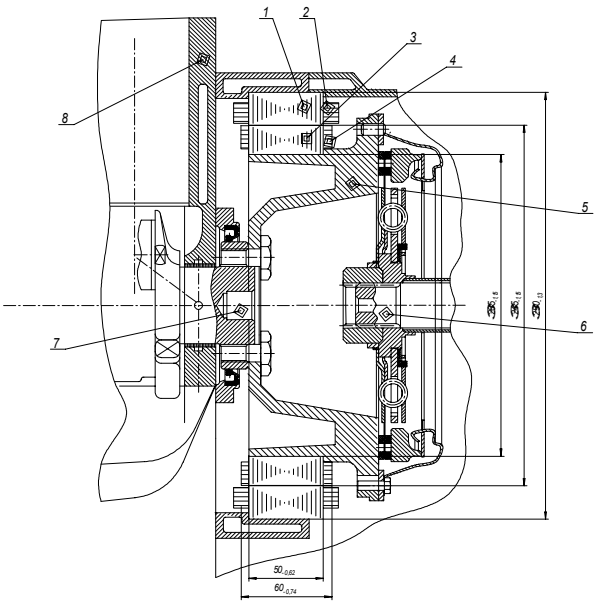

Ffig. 1

In view of described features of designing SGU the sizes of main bodies of a magnetic circuit and winding of this machine are counted and its delineation with applying of a packet “COMPASS” (fig. 1) is made.

In view of features of layout of the asynchronous machine SGU in the automobile is projected and the asynchronous machine of the starter - generator is counted. The designed starter - generator is cheaper, than existing, is more lighter and is more indiscrete.

References

[1] Автомобили с комбинированным энергетическим приводом. Обзор разработок за рубежом // Автостроение за рубежом. 2002.№3.С.5-11.

[2] Grachev P.Y., Ejova E.V. The electric drive alternating-current for the hybrid automobile with the multipolar asynchronous machine. Proceeding of the thirteenth conference « Electric drives alternating-current », Ekaterinburg, 2005, page 271-274.

[3] Goldberg O.D., Gurin J.S., Sviridenko I.S. Designing of electric machines. M.: a higher school, 2001.
[4] Balagurov V.A. Designing of special electric machines alternating-current. M.: a higher school, 1982.

Vladimir Anisimov *- D.Sc.Samara state technical university, Pervomajskay street, 18 - 45, 443010 Samara, RUSSIA.*

Pavel Grachev *- Samara state technical university, Pervomajskay street, 18 - 203, 443010 Samara, RUSSIA.*
e- mail: pgrachov@mail.ru

Elena Ejova *- post-graduate student, Samara state technical university, Pervomajskay street, 18 - 201 443010 Samara, RUSSIA.*
e-mail: eipo@sstu.edu.ru

AUTHOR INDEX

V

W

Y

Z

UNION OF ELECTRONICS, ELECTRICAL ENGINEERING AND COMMUNICATIONS (CEEC)

1000 Sofia. Bulgaria. 108, Rakovski Str.
Tel.: (+359 2) 987 9767, (+359 2) 986 5200 Fax: (+359 2) 987 9360
www.sees.hit.bg e-mail: ceec@mail.bg, sees_nts@abv.bg

Member of the

FEDERATION OF SCIENTIFIC AND TECHNICAL UNIONS IN BULGARIA /FNTS/

The Union of electronics, electrical engineering and communications /SEES/ is a non-governmental, non-political and non-profit professional association – part of the civil society.

The main goals of SEES are:

- To unite the efforts of its members and to facilitate the creation of improved conditions for their creative and professional development and progress as well to provide for more efficient participation in the process of formation of a civil society, acting as a consulting body and well-intended corrective in the field of the science and economics;
- To defend the interests of its members before the governmental and the local institutions;
- To enhance and expand its international contacts and develop mutually feasible collaboration with similar associations in Bulgaria and abroad;
- To provide for improvement in the scientific and professional qualification of its members by means of organizing conferences, workshops, discussions as well by collecting and dissemination of scientific and technical information and developing of own publishing activity;
- To raise the prestige of the electrical engineering, the electronics and the communications in the society, to form opinion about their progress and to stand up for them before the State and the local institutions;
- To work for promotion of the social status of the technical intellectuals by developing and submitting drafts for normative acts to the governmental institutions;
- Special focus of attention and care to be directed toward the joint activities with the firms and the young people.

Members of SEES are more than 1200 graduated engineers, scientists from the Technical Universities and the Bulgarian Academy of Sciences, specialists and managers in factories and firms, students and post-graduate students, organized in clubs and national scientific-technical divisions, devoted to the electrical engineering industry, electronics, telecommunications, electromagnetic compatibility, acoustics etc. The collective members include more than 50 firms, establishments and organizations in this field.

SEES organizes regular international and national scientific- technical events, such as the International Symposium on Electrical Apparatus and Technologies /"SIELA"/, the International Conference on Electrical Machines, Drives and Power systems /"ELMA"/, the International Conference "TELECOM", the National Conferences with international participation on the Earth-Sun interaction, acoustics etc.

SEES publishes an authoritative scientific journal – "ELECTRICAL ENGINEERING AND ELECTRONICS" and Information Bulletin.

Close and mutually feasible relations were established with VDE – the Union of German Engineers in the field of the Electrical Engineering, the Electronics and the Informatics as well with the Union of the Polish Electrical engineers, with concluded contracts during period of more than ten years. There is constructive exchange of information and experience with matching organizations from Russia, Romania, Macedonia etc. Three years ago frame contract was signed with IEEE.

SEES is an active member of FNTS. It carries out efficient work with the branch chambers of the electrical engineering, the electronic industry and the information technologies. It has own structures in all major cities in Bulgaria as well in the Technical Universities throughout the country.

ТЕХНИЧЕСКИ УНИВЕРСИТЕТ – ГАБРОВО

НАУКА

RESEARCH

TECHNICAL UNIVERSITY OF GABROVO

ОБЛАСТИ НА НАУЧНОИЗСЛЕДОВАТЕЛСКА ДЕЙНОСТ:

- Автоматизирано конструиране и технологии на финомеханични елементи и уреди
- Комуникационна техника
- Задвижваща и управляваща техника
- Динамика на машините
- Инструментална екипировка
- Машиностроителни конструкции и механизми
- Механика
- Мултимедийна техника
- Оптимално проектиране на механични конструкции и оптимизация на машиностроителни материали
- Възобновяеми енергийни източници
- Заваръчни, възстановителни, електротехнологични и термични обработки
- Безработица, политика на пазара на труда и социална политика

RESEARCH AREAS:

- CAD and fine mechanical element and instrument technologies
- Communication engineering
- Driving and control equipment
- Dynamics of machines
- Instrumental equipment
- Machine-building structures and mechanisms
- Mechanics
- Multimedia Technologies
- Optimum design of mechanical structures and engineering materials optimization
- Renewable energy sources
- Welding, recovery, electrotechnological and heat metal treatment
- Unemployment, labour market policy and social policy

Технически университет - Габрово, 5300 Габрово, ул. „Хаджи Димитър“ 4
тел.: 066 801 144; факс: 066 801 155; E-mail: rector@tugab.bg; **www.tugab.bg**

Technical University of Gabrovo, 4 Hadji Dimitar St., 5300 Gabrovo, BULGARIA
Tel: +359 66 801 144; Fax: +359 66 801 155; E-mail: rector@tugab.bg; **www.tugab.bg**

Quality Management System
DIN EN ISO 9001:2000

АББ е водещ световен Концерн предлагащ най-съвременни енергийни технологии и автоматизация на ютилити и индустриални фирми.

В областта на енергетиката предлагаме пълната гама продукти, системи и услуги от ниско до свръх високо напрежение (прав и променлив ток).

АББ е световен лидер на продукти и системи за автоматизация на непрекъснати и дискретни производства.

АББ България ЕООД
София 1000, ул. „Триадица” № 5
тел. +359 2 981 25 00; +359 2 981 29 00
факс: +359 2 980 08 46; +359 2 981 57 98
www.abb.com
e-mail: secretary@bg.abb.com

"ELPROM TRAFO CH" PLC

63, Dondukov str. . *tel.(+359 78) 2-37-96*
2500 KJUSTENDIL *fax:(+359 78) 2-36-18*
BULGARIA *e-mail:elpromch@infotel.bg*

1. HISTORY AND DEVELOPMENT

The factory was established on March 28 th 1968 in Kyustendil as a subsidiary of the existing Power Transformer Factory in Sofia. Back in 1968 the factory embarked on its activities for introducing the production of distribution transformers to meet the expanding demands of the Energy Sector of the Bulgarian industry marking a rapid development in those days.

In 1970 "Elprom Trafo" commenced the mass production of its first transformer type TM 100 kVA. Development and adoption of distribution transformers and new technologies as well as training of personnel were achieved in close collaboration with the mother company in Sofia. In a short period of the time the factory introduced the manufacture of several power ratings such as TM 160 kVA and TM 250 kVA. All three types of transformers were introduced into mass production to meet the demands of the local market as well as the huge consumption requests of the ex-Soviet market – Elprom's transformers were applied in the manufacture of package substations for export to Russia and the former Soviet republics.

The annual output in 1980 reached 6 200 pieces of transformers at an average rating of 212 kVA covering a very substantial order for Iran in the tune of 4 000 pieces. For the years to follow and in parallel with its increase of production, the factory managed to introduce some substantial reconstruction works and innovations such as: new production units, three automatic core-cutting lines delivered by the German company GEORG; the step-lap method for the core sheets stacking, a laboratory for the in-coming quality control of materials and a testing laboratory to perform routine and type tests on the manufactured transformers.

By the end of 1987 the factory adopted the manufacture of three new ratings: 630, 1000 and 1600 kVA thus covering the whole production range as per the existing Bulgarian State Standard 5034 of 1974 and reached its full production capacity of 8 313 pieces of transformers with an overall power rating of 2 532 MVA – at an average of 304.6 kVA.

2. LEGAL STATUS AND MANAGEMENT

From 1968 till 1996 the factory functioned as a completely state owned manufacturing entity. In 1996 it was transformed into a Public Liability Company, with the Ministry of Economy being its sole Principal. Following the government strategy for privatization of the industrial sector, in the middle of 1999 two private companies and individual share – holders acquired the public shares.

Nowadays "MEGA EL" LTD, Bulgaria is the majority shareholder being in control of 75% of the factory's shares.

The Principal is a private company established on 2001. Its main subject of activity covers: power supply engineering; electrification of construction projects; erection and repairs of indoor and out-door power supply installations – middle and low voltage; underground and overhead power distribution lines; package substations; lighting protective installations; ground protective installations, public and alley lighting; fire alarm installations; façade illuminations, etc.

"Elprom Trafo CH" PLC is managed by a Board of Directors and is headed by its Executive Director. The staff comprises 150 employees – highly qualified electrical engineers, skilled electricians, technicians and workers.

3. PRODUCT RANGE

At present "Elprom Trafo CH" PLC is the sole Bulgarian manufacturer of oil-immersed distribution transformers with operating voltages from 6 to 36 kV and power ratings from 25 up to 2 500 kVA.

A brief description of the main product range is given below:

- **Distribution transformers manufactured as per the prescriptions of CENELEC –** HD 428.1.S1:92 and Bulgarian State Standard (BDS) 3067/90 – three-phase, double coil, form 25 to 2 500 kVA and with operating voltage up to 20 kV;

- **Distribution transformers especially designed to operate in tropical climates -** (Middle East and Africa) with operating voltage 11 kV, 15 kV and 33 kV as well as with double primary or secondary voltages.
- **Standards** – the transformers are manufactured and tested according to the requirements of IEC 60076, the prescriptions of CENELEC - HD 428.1.S1:92 and BDS 3067/90 and can be also manufactured according to the requirements of other national standards.
- **Design –** the factory has its own design office and almost entirely depends upon its own developed technology and design. The engineering staff is well experienced and the design is completely computerized to guarantee the quality of the transformers.
- **ISO Certification –** The company holds a quality system certificate EN ISO 9001:2000 number Q 020808 issued by The MOODY Q-ZERT GmbH, Germany on 11.03.2003. The ISO 9001:2000 quality procedures are being widely applied to cover the whole process from control on the incoming materials through design and production to the outgoing testing and dispatch.

4. ANNUAL PRODUCTION AND SALES

The annual production rate of "Elprom Trafo CH" products is indicated below:

- **Capacity**

Distribution transformers up 36 kV and 2 500 kVA – total 750 MVA (about 3 000 pieces of 250 kVA)

- **Sales**

1999	2000	2001	2002	2003	2004
US $ 2.677 Million	US $ 3.128 Million	US $ 6.728 Million	US $ 3.385 Million	US $ 3.544 Million	US $ 3.880 Million

Detailed Sales Record could be attached upon request.

5. SERVICE EXPERIENCE

"Elprom Trafo CH" PLC supplies most of the transformers to customers of Africa, Asia, Latin America, Balkan region and Middle East as well as to the Bulgarian market and recently to EU. The factory is a well-established supplier of transformers to Russia, Nigeria, Ghana, Congo, Burkina Faso, Pakistan, Afghanistan, Uruguay, Albania, Serbia, Croatia, Lebanon, Syria, Iraq, Jordan, OAE, Greece and Italy (in 2002 the company was qualified as a transformer supplier to ENEL DISTRIBUZIONE and in 2003 was awarded its first contact for the supply of 2500 pieces of transformers).

The factory is a traditional supplier of transformers to the National Electricity Company of Bulgaria, the Regional Electricity Distribution Companies, Water utilities, National Railways, municipalities, construction companies and private entrepreneurs.

In addition to manufacturing of transformers the factory also carries out reconditioning/repair of distribution transformers.

6. CONTACTS:

Executive Director: Dipl. Eng. Kristina Mihailova
Tel.: 00359 2 920 9450; 00359 2 920 9440
Chief of Direction APPE: Dipl. Eng. Ivailo Panajotov
Tel.:00359 78 23796; mob. 00359 887 921832
Fax: 00359 78 23618
Sales: Orlin Itsov
Tel.:00359 2 920 8066; mob. 00359 888 666004
Fax: 00359 2 920 9450; 00359 2 920 9440
e-mail: elpromch@infotel.bg

ЕЛДОМ ИНВЕСТ ООД - ВАРНА
Бул. "Владислав Варненчик" 275А, тел. 052/ 502 109, факс 052/ 500 347

ЕЛДОМ ИНВЕСТ ООД е създадено през 1987 г., като през 1996 г. е приватизирано и към настоящия момент собствеността на дружеството е изцяло частна. Основният предмет на дейност са производство и търговия с електрически и газови домакински уреди и сервизна дейност. В предприятието работят над 450 работници и служители, като основната цел на ръководството и персонала във фирмата е непрекъснатото усъвършенстване на продукцията и нейната сертификация за успешното реализиране на нови пазари.

ЕЛДОМ ИНВЕСТ е най-големият производител на електродомакински уреди в България, в т.ч. електрически бойлери и преносими готварски печки, където заема пазарен дял от около 70%.

Заводът е разположен в промишлената зона на Варна, като общата заемана площ е 20826 декара. Енергийните източници са надеждно осигурени с дублирано захранване с електроенергия и вода. Транспортните връзки могат да се осъществяват посредством железопътен, автомобилен транспорт, така също по море и въздух, поради близостта на предприятието до летище, пристанище и ж.п.гара.

Годишният производствен капацитет на предприятието е :

- ❖ 250 000 бр. бойлери, от които:
- Проточни бойлери с мигновено действие (3, 6 и 8 kW) - за кухня, баня и комбинирани.
- Обемни бойлери от 5 л до 1000 л - под налягане с емайлиран или с неръждаем водосъдържател, за вертикален или хоризонтален монтаж, за окачване или свободно стоящи. Бойлерите от 80 до 1000 л, комбинирани с топлообменници, могат да се свързват към слънчеви, газови или централни (локални) отоплителни системи;
- Бойлери, произведени по специална поръчка на клиента.

- ❖ 20 000 бр. преносими готварски печки.
- електрически;
- в комбинация с газ
- изцяло газови.

Фирмата има потенциала и изпълнява поръчки за единични и малобройни серии продукти, които са извън основното производство, но са в техническите и технологичните възможности.

Благодарение на външно – търговската дейност над 25% от произвежданите уреди се изнасят за Италия, Великобритания, САЩ, Румъния, Словакия, Швеция, Дания и Украйна.

ЕЛДОМ ИНВЕСТ ООД притежава Система за управление на качеството, сертифицирана от SGS Yersley, Великобритания съгласно международния стандарт ISO 9001:2000. Фирмата притежава правото на CE маркировка, както и много други сертификати в съответствие с изискванията на нормативните уредби на няколко европейски страни.

ЕЛДОМ ИНВЕСТ гарантира надеждност на продуктите си, като дава следните гаранционни срокове:

- За бойлерите с емайлиран водосъдържател за окачване до 200 л включително - 5 години и от 150 до 500 л свободно стоящи – 3 години за водосъдържателя;
- За бойлерите с неръждаем водосъдържател за окачване до 200 л включително - 10 години и от 150 до 1000 л свободно стоящи – 5 години за водосъдържателя;
- За преносимите готварски печки – 3 години.

ЕЛДОМ ИНВЕСТ ООД традиционно участва на Международния панаир в Пловдив (България), където много от продуктите на фирмата са носители на златни медали. През 2004 г. бе получено поредното признание чрез връчването на Златен медал от 24 – тото Пролетно издание на панаира за Фамилията бойлери с мигновено действие.

В последните години фирмата успешно участва и на международни изложения - "Ромтерм" (Румъния), "ISH Франкфурт" (Германия), "Конеко-Рациоенергия" (Словакия), "Акватерм" - Нитра (Словакия), "ХоумТех" Берлин и Кьолн (Германия), "Мостра Конвеньо Експокомфорт" (Италия), „Климатизасион" (Испания) и др.

Фирмата е носител на редица награди и грамоти, между които:

- Иновативно предприятие на годината – диплом, получен от Министерството на икономиката, връчен на 22.10.2004 г.
- Юбилеен диплом за активна иновативна политика, завоюване на нови пазарни ниши и за успешна конкурентноспособност, връчен от Българската стопанска камара.

ЕЛДОМ ИНВЕСТ членува в следните асоциации: БТПП, БСК, Българска Камара на електротехниката, Българо-Руска Търговско-Промишлена Палата, Лондонска Търговско-Промишлена Палата.

В номенклатурата на продуктите на фирмата през 2005 г. се открояват няколко групи нови уреди, чието предлагане ще има за цел задоволяване на нарастващите потребности на нашите редовни и потенциални клиенти - първите български бойлери с микропроцесорно управление и цифров дисплей, промишлени бойлери 750 и 1000 л, нова серия компактни и удобни бойлери с мигновено действие, осигуряващи гореща вода по всяко време и готварски плотове за вграждане.

MOTOR DRIVE UNITS (MDUs)

MZ 4.1

MZ 4.4

MZ 8

- The MDUs are for side assembly to the transformer tank (deep or bell type) at vertical level convenient for control and maintenance.
- The MDUs execution covers all climatic conditions.
- The MDUs meet the requirements of IEC 60214-1-2003 Standard.
- The MDU type MZ 4.4 meets the requirements of ANSI Standard.
- The MDU type MZ 8 is with reduced weight and dimensions for light type OLTCs (RS 18 and RS 20).

TECHNICAL DATA

Motor Drive Unit		MZ 4.1 and MZ 4.4	MZ 8
Rated power of el. motor	kW	0,75 / 1,1	0,37
Rated frequency	Hz	50 / 60	50
Supply voltage	V	3 AC 400 / 230	3 AC 400 / 230
Synchronous speed	min^{-1}	1500	1500
Revolutions of hand crank per tap-change operation	revs	33	33
Torque on driving shaft	Nm	17 / 24	8
Running time per tap-change operation	s	4,5	5
Max. number of operating positions		35	27
Control circuits voltage	V	AC 230	AC 230
Insulation level	kV	2	2
Heating element power	W	250	250
Protection degree		IP 54	IP 54
Weight	kg	80; 90	60

The MDUs have also special executions to comply with client requirements. For example:
- Protection degree IP 65.
- Revolutions of out going driving shaft per tap-change operation: 0,5; 1; 6; 16,5.
- Number of steps - up to 99.

"Centralna Energoremontna Basa" AD (CERB) was founded in 1948 as a state-owned company providing repair services to the power facilities within the electric power sector in Bulgaria.

The necessity of performing various repair works determined the foundation and the further development of the following specialized sections:

- 1948 - electrical machines repair workshop
- 1956 - transformer repair workshop
- 1956 - mechanical workshop
- 1965 - transport department
- 1975 - welding and control of metals centre
- 1975 - vibration analyses and dynamic balancing Department

Today the company is recognized as a reliable supplier of repair services not only on the Bulgarian market but also in Macedonia, Albania and Greece.

CERB has approximately 200 employees and disposes of 20 000 m^2 built-up area including workshops, labs, store facilities and administrative buildings.

According to the machinery's content and specificity, diagnostics, test and repair works are performed on the spot or at the factory of CERB.

For more than 55 years of existence the company has specialized in the following sectors:

• Repair of all kinds of rotating electrical machines
• Repair of dry and oil immersed transformers, autotransformers and reactors
•Diagnostics, electrical measurement and tests of electrical machines, transformers, protective equipment and materials
• Manufacture of spare parts and non-standard equipment for electrical machines
•Vibration analyses and dynamic balancing of rotors and turbines, pumps and fans
•Control of metals
• Transportation of heavy and oversized loads by road & railway

REPAIR SERVICES IN BRIEF

1. REPAIR OF ALL KINDS OF ROTATING ELECTRICAL MACHINES WITHOUT LIMITATION OF RATED OUTPUT AND DIMENSIONS

Repair of the stators and rotors of hydrogenerators, turbogenerators, AC & DC motors, DC generators, induction generators and regulators.

2. REPAIR OF DRY AND OIL IMMERSED TRANSFORMERS, AUTO-TRANSFORMERS AND REACTORS

•Power transformers with rated output up to 250 MVA and rated voltages up to 400 kV.
•Distribution transformers with rated output up to 1600 kVA and rated voltages up to 35 kV.
•Autotransformers with rated voltages up to 400 kV.
•Special transformers: reactors, Petersen coils, welding transformers.
•Arc furnace transformers and shunt reactors with rated output up to 50 MVA.
•Measuring transformers: voltage, current, combined with rated voltages up to 220 kV.
•Manufacture of dry transformers with rated output up to 630 kVA and rated voltages up to 6 kV, reactors.

3. DIAGNOSTICS, ELECTRICAL MEASUREMENT AND TESTS OF ELECTRICAL MACHINES, TRANS-FORMERS, PROTECTIVE EQUIPMENT AND MATERIALS

I. ROUTINE TESTS
- Winding resistance
- Turns ratio and polarity
- Inter winding insulation, applied voltage
- In-winding insulation, induced voltage
- No load properties
- Impedance and load losses
- Control wiring, auxiliary operation, tap changer operation

II. SPECIAL TESTS
- Insulation resistance
- Insulation capacitance and its power factor
- Partial discharge observation
- Zero sequence impedance

III. TESTS ON TRANSFORMER OIL
- Appearance
- Breakdown voltage
- Density
- Water content
- Flash point
- Neutralization value
- Determination of particle concentration and particle size distribution.

4. VIBRATION ANALYSES AND DYNAMIC BALANCING

- Qualifying of the condition of : rotors, turbines, pumps and fans
- Dynamic balancing of the above mentioned units in own bearings
- Dynamic balancing of rotors with weight from 10 kg up to 110 t on test stand
- Adjustment of the regulation system of steam turbines

When it is costly to remove machinery for balancing, the engineers of CERB carries out dynamic balancing at customer's premises via apparatuses of "BRUEL&CAER" and "ENTEK IRD".

5. METAL TESTING CENTER

- laboratory tests for determination of the mechanical indicators and structure
- non destructive control – all kinds of methods
- long strength tests for determination of the residual life of the main equipment installed in electric power stations

6. MANUFACTURE OF SPARE PARTS AND NON-STANDARD EQUIPMENT FOR ELECTRICAL MACHINES

•Manufacture of casts with weight up to 2 t made of carbonic steel
•Manufacture of boiler equipment - shields, worm-pipes, steam heaters and others.
•Manufacture of conductive cable accessories for power cables and conductors: current terminals – aluminum, brass, bronze and bimetallic; insulating rods and portable earthing devices.

7. PVC PRODUCTION

At our premises we produce:

- reinforced pressure hoses
- ordinary free-flowing hoses
- transparent polyvinylchloride hoses

8. HAULAGE ACTIVITY

The Transportation Division of CERB is a licensed carrier of heavy and oversized loads within the country. We can haulage loads with weight up to 132 t by road and 250 t by railway. The transportation activities are carried out with: haulage trucks make "Mercedes", trailers make " SHOERLE", "Low bed" rail wagon make "MAN" 20 axles, which is unique and the only one available on the Balkans Peninsula.
The loading, unloading and supporting are performed by an experienced rigging team.

Since 2002, the company has possessed the Quality Management Certificate ISO 9001 issued by Moody International.
In the beginning of 2005 the specification OHSAS 18001:2002 was introduced.

`Троян Мотор`ООД

гр.**Троян** 5600, ул.`Македония`№46,пк102,тел. **0670 6 2208,** тел/факс: **0670 6 2219**
E-mail: **troyan-motor@dir.bg**, **adarsky@dir.bg**
Web: **http://www.troyan-motor.hit.bg** или **http://troyan-motor.hit.bg**

П Р Е З Е Н Т А Ц И Я

Нашето дружество е основано през 1993 година. Сградата е разположена в западната индустриална част на гр. Троян върху на 13,000 кв.м. земя. Разполагаме с 1,200 кв.м. производствена площ, 200 кв.м. офис.

Оборудването ни е предвидено за механична обработка на черни и цветни метали. Оборудвани сме с обработващ център с CNC управление, стругови машини с CNC управление, универсални металорежещи машини за стругови, фрезови,пробивни и шлифовъчни операции, ексцентър и хидравлични преси , заваръчна техника,намагнитваща техника за ротори и статори на електрически машини с постоянни магнити,бобинажно оборудване,специализирани стендове за изпитание на електрически машини-постоянно и променливотокови, линия за производство на вибратори за бетон.

Произвеждаме:

- ***Иглени вибратори и вибратори с външно регулиране за уплътняване на бетон и вибратори използвани при транспортиране на насипни товари.***

- ***Безчеткови алтернатори за автомобили и автобуси ,тягови ел.двигатели с постоянни магнити за електрически трактори и лодки, ел.двигатели с постоянни магнити за електромобили, паркови косачки , генератори за производство на електрическа енергия.***

- ***Помпи за охлаждаща течност на металорежещи машини, съединители,водни помпи за бита,електродвигатели за шевни машини, ротори и статори за генератори и ел.двигатели , ремонт на ел.двигатели***

Оборудването и специалистите , с които разполагаме ,ни позволяват да изработваме детайли и изделия с голяма точност и прецизност. Приемаме да работим както по техническа документация на клиента, така и да разработим такава по техническо задание (желателно е да ни предоставите мостра). Нашите изделия намират добър прием в САЩ, Канада, Турция, Гърция..

Контакт с нас:
Тел.: + 359 670 622 08 , + 359 670 622 93
Тел./Факс: + 359 670 622 19
GSM: 0888 67 92 13
Адрес: 5600 гр.Троян , ул.”Македония” № 46 , п.к. 102
E- mail: troyan-motor@dir.bg